NASA CP-2001

ADVANCES IN ENGINEERING SCIENCE

Volume 1

13th Annual Meeting
Society of Engineering Science
Sponsored by JIAFS
Hampton, VA, November 1–3, 1976

NASA
National
Aeronautics and
Space
Administration

Society of
Engineering Science

NASA Conference Publications (CP Series) contain compilations of scientific and technical papers or transcripts arising from conferences, workshops, symposia, seminars, and other professional meetings that NASA elects to publish.

The text of these proceedings was reproduced directly from author-supplied manuscripts for distribution prior to opening of the meeting. NASA has performed no editorial review of the papers other than those contributed by its employees or contractors.

NASA CP-2001

Advances In Engineering Science

Volume 1

13th Annual Meeting
Society of Engineering Science
Hampton, VA, November 1–3, 1976

Sponsored by Joint Institute for Advancement of Flight Sciences
NASA Langley Research Center
and
George Washington University

NASA
National
Aeronautics and
Space
Administration

Society of
Engineering Science

For sale by the National Technical Information Service
Springfield, Virginia 22161
Price – $10.25

PREFACE

The technical program of the 13th Annual Meeting of the Society of Engineering Science, Inc., consisted of 159 invited and contributed papers covering a wide variety of research topics, a plenary session, and the Annual Society of Engineering Science Lecture. Thirty-three of the technical sessions contained invited and/or contributed papers while two of the sessions were conducted as panel discussions with audience participation.

These Proceedings, which contain the technical program of the meeting, are presented in four volumes arranged by subject material. Papers in materials science are contained in Volume I. Volume II contains the structures, dynamics, applied mathematics, and computer science papers. Volume III contains papers in the areas of acoustics, environmental modeling, and energy. Papers in the area of flight sciences are contained in Volume IV. A complete Table of Contents and an Author Index are included in each volume.

We would like to express particular appreciation to the members of the Steering Committee and the Technical Organizing Committee for arranging an excellent technical program. Our thanks are given to all faculty and staff of the Joint Institute for Advancement of Flight Sciences (both NASA Langley Research Center and The George Washington University) who contributed to the organization of the Meeting. The assistance in preparation for the meeting and this document of Sandra Jones, Virginia Lazenby, and Mary Torian is gratefully acknowledged. Our gratitude to the Scientific and Technical Information Prgrams Division of the NASA Langley Research Center for publishing these Proceedings is sincerely extended.

Hampton, Virginia 1976

J. E. Duberg

J. L. Whitesides

Co-Chairmen

J. E. Duberg
NASA Langley Research Center

J. L. Whitesides
The George Washington University

Steering Committee

W. D. Erickson, NASA Langley Research Center
P. J. Bobbitt, NASA Langley Research Center
H. F. Hardrath, NASA Langley Research Center
D. J. Martin, NASA Langley Research Center
M. K. Myers, The George Washington University
A. K. Noor, The George Washington University
J. E. Duberg, NASA Langley Research Center, Ex-officio
J. L. Whitesides, The George Washington University, Ex-officio

Technical Organizing Committee

C. L. Bauer, Carnegie-Mellon University
L. B. Callis, NASA Langley Research Center
J. R. Elliott, NASA Langley Research Center
K. Karamcheti, Stanford University
P. Leehey, Massachusetts Institute of Technology
J. S. Levine, NASA Langley Research Center
R. E. Little, University of Michigan-Dearborn
J. M. Ortega, Institute for Computer Applications in Science and Engineering
E. M. Pearce, Polytechnic Institute of New York
A. D. Pierce, Georgia Institute of Technology
E. Y. Rodin, Washington University
L. A. Schmit, University of California at Los Angeles
G. C. Sih, Lehigh University
E. M. Wu, Washington University

SOCIETY OF ENGINEERING SCIENCE, INC.

The purpose of the Society, as stated in its incorporation document, is "to foster and promote the interchange of ideas and information among the various fields of engineering science and between engineering science and the fields of theoretical and applied physics, chemistry, and mathematics, and, to that end, to provide forums and meetings for the presentation and dissemination of such ideas and information, and to publish such information and ideas among its members and other interested persons by way of periodicals and otherwise."

OFFICERS

L. V. Kline, President
IBM Corporation

S. W. Yuan, First Vice President and Director
The George Washington University

C.E. Taylor, Second Vice President and Director
University of Illinois

E. Y. Rodin, Second Vice President and Director
The George Washington University

R. P. McNitt, Secretary
Virginia Polytechnic Institute and State University

J. Peddieson, Treasurer
Tennessee Technological University

DIRECTORS

B. A. Boley, Northwestern University
G. Dvorak, Duke University
T. S. Chang, Massachusetts Institute of Technology
E. Montroll, University of Rochester
J. M. Richardson, North American Rockwell Corp.
E. Saibel, Army Research Office
J. W. Dunkin, Exxon Production Research Co.
J. T. Oden, University of Texas

CORPORATE MEMBERS

Chevron Oil Field Research Company
Exxon Production Research Company
IBM Corporation
OEA Incorporated

CONTENTS

VOLUME I

ANNUAL SOCIETY OF ENGINEERING SCIENCE LECTURE

MATERIALS SCIENCE I
Chairmen: C. L. Bauer and E. Pearce

MATERIALS SCIENCE II
Chairman: R. E. Little

MATERIALS SCIENCE III
Chairman: J. H. Crews, Jr.

COMPOSITE MATERIALS
Chairman: E. M. Wu

DYNAMIC FRACTURE MECHANICS
Chairman: G. C. Sih

FRACTURE MECHANICS
Chairman: H. F. Hardrath

IMPACT AND VIBRATION
Chairman: H. L. Runyan, Jr.

VOLUME II

STRUCTURAL DYNAMICS I
Chairman: L. D. Pinson

STRUCTURAL DYNAMICS II
Chairman: S. Utku

BEAMS, PLATES, AND SHELLS
Chairman: M. Stern

COMPOSITE STRUCTURES
Chairman: J. Vinson

APPLIED MATHEMATICS
Chairman: J. N. Shoosmith

ADVANCES IN COMPUTER SCIENCE
Chairman: J. M. Ortega

VOLUME III

AEROACOUSTICS I
Chairman: D. L. Lansing

AEROACOUSTICS II
Chairman: A. Nayfeh

WAVE PROPAGATION
Chairman: E. Y. Rodin

ATMOSPHERIC SOUND PROPAGATION
Chairman: M. K. Myers

STRUCTURAL RESPONSE TO NOISE
Chairman: L. Maestrello

ENVIRONMENTAL MODELING I
Chairman: L. B. Callis

ENVIRONMENTAL MODELING II
Chairman: M. Halem

PLANETARY MODELING
Chairman: J. S. Levine

ENERGY RELATED TOPICS
Chairman: W. D. Erickson

VOLUME IV

INVISCID FLOW I
Chairman: F. R. DeJarnette

INVISCID FLOW II
Chairman: P. J. Bobbitt

VISCOUS FLOW I
Chairman: S. Rubin

VISCOUS FLOW II
Chairman: D. M. Bushnell

AIRCRAFT AERODYNAMICS
Chairman: R. E. Kuhn

EXPERIMENTAL FLUID MECHANICS
Chairman: J. Schetz

PROPULSION AND COMBUSTION
Chairman: A. J. Baker

FLIGHT DYNAMICS AND CONTROL I
Chairman: A. A. Schy

FLIGHT DYNAMICS AND CONTROL II
Chairman: M. J. Queijo

ANNUAL SOCIETY OF ENGINEERING SCIENCE LECTURE

CONTINUUM MECHANICS AT THE ATOMIC SCALE*

A. Cemal Eringen
Princeton University

ABSTRACT

Classical continuum mechanics has been successful in predicting a large class of physical phenomena for which the external characteristic length, λ, (e.g., wavelength, thickness, curvature) is much greater than the internal characteristic length, ℓ, (e.g., average atomic or granular distance, cell size). However, there exist large classes of physical phenomena that defy local description based on classical continuum theories. Among many we cite: the state of stress at a crack tip, dislocations, fatigue, turbulence, surface physics, dispersion of high frequency waves, etc. To explain these critical phenomena, one is often forced to revert to the atomic and molecular theories or approximate and heuristic models. By means of atomic theory of lattices, one can only deal with ideal crystal structures whose atoms are located in a perfectly periodic manner or deviate from it only slightly. All materials and engineering structures are, however, imperfect and cannot be represented by such perfect models.

Recently constructed nonlocal continuum mechanics, Eringen [1972a,b,c], [1973], [1974], [1976a], appear to have great potential in dealing with situations in which λ is of order of ℓ, i.e., the long range interatomic attractions are important. Nonlocal elasticity, for example, can be employed to determine the state of stress near a sharp crack and predict the cohesive stress to break the atomic bonds. Thus we have been able to produce a fracture criterion based on the maximum stress at the tip of a sharp crack and determine the shear stress that causes a dislocation of single atomic distance. These results are in excellent agreement with experiments and the atomic theory, cf., Eringen et al [1976], Eringen [1976b,c].

Similarly, the development of the secondary flow in a rectangular pipe can be predicted by means of the theory of nonlocal fluid dynamics.

In this lecture, I present a brief discussion of the physical and mathematical ideas underlying the nonlocal continuum mechanics. Afterwards, I shall present solutions of some problems in fracture mechanics, edge and screw dislocations, and secondary flow in a pipe. The results will be compared with experiments and atomic theories available.

---

*The research presented in this lecture was supported by the Army Research Office (Durham, North Carolina) and the Office of Naval Research (Washington, D.C.).

REFERENCES

Eringen, A. C. [1972a]: "Nonlocal Polar Elastic Continua," Int. J. Eng. Sci., 10, 1-16.

Eringen, A. C. [1972b]: "Linear Theory of Nonlocal Elasticity and Dispersion of Plane Waves," Int. J. Eng. Sci., 10, 425-435.

Eringen, A. C. [1972c]: "On Nonlocal Fluid Mechanics," Int. J. Eng. Sci., 10, 561-575.

Eringen, A. C. [1973]: "Theory of Nonlocal Electromagnetic Elastic Solids," J. Math. Phys., 14, 733-740.

Eringen, A. C. [1974]: "On Nonlocal Continuum Thermodynamics," Modern Developments in Thermodynamics, edited by B. Gal-Or, New York, John Wiley and Sons, 121-142.

Eringen, A. C. [1976a]: Continuum Physics, Vol. 4, New York and London, Academic Press.

Eringen, A. C.; Speziale, C. G.; and Kim, B. S. [1976]: "Crack Tip Problem in Nonlocal Elasticity," Princeton University, Civil Engineering Research Report 76-SM-13.

Eringen, A. C. [1976b]: "Screw Dislocation in Nonlocal Elasticity," Princeton University, Civil Engineering Research Report 76-SM-10.

Eringen, A. C. [1976c]: "Edge Dislocation in Nonlocal Elasticity," Princeton University, Civil Engineering Research Report 76-SM-11.

MICROSCOPIC ASPECTS OF INTERFACIAL REACTIONS IN DIFFUSION BONDING PROCESSES*

Michael P. Shearer and Charles L. Bauer
Center for the Joining of Materials
Carnegie-Mellon University

SUMMARY

This paper is concerned with microscopic aspects of interfacial reactions (occurring over distances less than one micrometer), such as interdiffusion, formation of intermetallic phases, generation and annihilation of lattice defects, effect of temperature, grain size, etc., which normally occur in diffusion bonding processes. Specifically, relationships between properties and microstructure in thin-film couples are examined utilizing a unique combination of contact resistance measurements and characterization by transmission electron microscopy. A thorough knowledge of these relationships is essential in order to control and improve all diffusion bonding processes.

INTRODUCTION

Diffusion bonding is a solid-state joining process wherein two materials are brought into intimate contact under the influence of elevated temperature and pressure in order to establish a bond across the resultant interface. This process may be characterized by four distinct steps: (1) preparation of surfaces to be joined, (2) development of intimate physical contact, (3) interdiffusion and (4) evolution of microstructure (recrystallization and grain growth) near the original interface. The joining of two metals by diffusion bonding, therefore, involves an intricate combination of surface and interfacial reactions which optimize continuity of macroscopic properties; e.g., electrical, mechanical, thermal, etc. Specific diffusion bonding processes, however, may promote contamination at the original interface, formation of intermetallic phases, generation of voids, etc., which degrade desirable engineering properties of the resultant bond. It is especially important to understand microscopic aspects of these reactions, since development of properties and establishment of long-term reliability are generally predictable from early stages of bond formation. The purpose of this paper is to examine relationships between properties and microstructure in thin-film couples utilizing a unique combination of contact resistance measurements and characterization by transmission electron microscopy.

*Financial support from the National Science Foundation is gratefully acknowledged.

BACKGROUND

Many techniques have been developed such as small-angle x-ray scattering (ref. 1), ion backscattering (ref. 2), Auger spectroscopy (ref. 3), and optical reflectivity (ref. 4), to study early stages of bond formation utilizing bimetallic thin-film (<10 μm) couples. These techniques provide useful information concerning interdiffusion of various chemical species (ref. 5), but cannot provide complimentary information concerning evolution of microstructure. Effect of microstructure on interfacial reactions in bimetallic thin films is demonstrated in studies of the copper-gold system (refs. 1,6,7), wherein results vary as to which intermetallic phases form as well as specific growth kinetics of each phase. These differences may be attributed to the large variation in microstructures of thin films.

Thin films often are characterized by dislocation densities greater than 10^{11} cm^{-2}, twin densities greater than 10^{17} cm^{-3} and grain sizes less than 10 nm (refs. 8,9). These defects often provide short-circuit diffusion paths which facilitate interfacial reactions. The ability to control grain size and, therefore, the extent of short-circuit diffusion is demonstrated in figure 1, wherein the grain size of copper thin films has been increased from 50 to 250 nm by increasing the substrate (sodium chloride) temperature from 25 to 200°C. Thus coefficients for bulk and short-circuit diffusion may be obtained as a function of grain size and other microstructural features. Grain size may also affect the number of nucleation sites available for intermetallic phase formation. Tisone and Lau (ref. 11) have shown that the resultant grain size of a TaAu intermetallic phase is dependent on the grain size of the tantalum and gold films. Orientation of grains can be controlled by epitaxial growth on suitable substrates (ref. 10), thereby permitting preparation and subsequent examination of specific grain boundaries with known atomic structure. Nucleation and growth of a specific phase among competing phases in bimetallic couples can also be examined by this method. Detailed information concerning defects generated or annihilated to accommodate nucleation and growth of a phase (ref. 12) can be obtained by high-resolution transmission electron microscopy.

The aforementioned discussion indicates the importance of continuously monitoring a property that reflects reactions occurring at or near the interface during diffusion bonding processess and correlation of these reactions with evolution of microstructure at the highest resolution possible. The remainder of this paper is devoted to a technique developed at Carnegie-Mellon University in which contact resistance is measured continuously in bimetallic thin films. In addition to the applicability of this technique to normal diffusion bonding processes, it is also relevant to degradation of contacts produced by multilayer metallization in semiconductor devices.

CONTACT RESISTANCE TECHNIQUE

Measurement of contact resistance can provide valuable information concerning interfacial reactions in bimetallic couples. For example, consider an

AB diffusion couple schematically represented by the binary AB phase diagram in figure 2. Initially, the composition vs. distance profile of this couple exhibits a single discontinuity at the original interface as well as a corresponding discontinuity in a given property (electrical resistivity). During interdiffusion, however, an intermetallic phase (γ) may form at the interface, separated from the original phases by discontinuous composition and resistivity profiles. The additional resistance associated with this reaction is denoted by the hatched area and is termed contact resistance. An additional contribution may arise due to chemical diffusion into the (originally) pure A and B phases.

Contact resistance $R_c(t)$ may be expressed by the sum of two terms:

$$R_c(t) = R_c(0) + \Delta R_c(t) \tag{1}$$

where $R_c(0)$ denotes an initial (temperature-dependent but time-independent) contact resistance and $\Delta R_c(t)$ denotes a time-dependent contribution. In general, time dependence of the contact resistance is given by the expression

$$\Delta R_c(t) = K(T)t^n \tag{2}$$

where t denotes time, K(T) denotes a temperature-dependent rate constant, and n denotes a characteristic time exponent.

Contact resistance is measured from a matrix of thin-film contacts consisting of AA, AB, BA, and BB couples, as illustrated in figure 3. A constant current I is then imposed across two adjacent legs of each couple and the potential drop ΔV across the other two legs is measured. The contact resistance then is obtained from the expression

$$R_c(t) = \Delta V/I \tag{3}$$

By continuously recording ΔV for each of four couples, evolution of contact resistance can be followed with great precision. In fact, since ΔV can be measured to 10^{-8}V, intermetallic layers as thin as 1 nm can be detected. Magnitude of $R_c(0)$ provides a measure of initial contact perfection, explicit values of n allow determination of rate-controlling mechanisms associated with interfacial reactions, temperature dependence of K(T) yields a measure of concomitant activation energies, and current dependence of K(T) permits resolution of effects due to Joule heating and electromigration. Artifacts can be separated easily by comparing results obtained from like and unlike metal couples.

TYPICAL RESULTS

A composite measure of current distortions in the region of each contact and an interfacial contribution associated with lattice defects is provided by the dependence of $R_c(0)$ on dc current density, temperature, film thickness, and fabrication conditions. Typical leg resistivities for thin films are about 50% greater than values for bulk materials, indicating presence of large

defect densities in the deposited films. For like-metal couples, Joule heating and electromigration effects occur at current densities in excess of 10^6 A/cm^2 due to a sharp, unstable, and irreversible increase in $R_c(0)$ and subsequent failure of some couples as a result of characteristic current-induced voids at or near the contact. For unlike metal couples (copper/nickel and aluminum/copper), Joule heating and electromigration effects are also observed, but relationships between contact resistance and current density become more complex as a consequence of interfacial reactions in the solid state.

For relatively simple systems, such as copper-nickel, values of the parameter n are about 0.5 indicating that evolution of contact resistance is characterized by a parabolic time law associated with interdiffusion of copper and nickel. An example of this time dependence is presented in figure 4 for a nickel/copper couple at 500°C. By conducting similar experiments as a function of temperature, an effective preexponential diffusion coefficient D_o of 4 x 10^{-4} cm^2/sec and an activation energy Q of 33 kcal/mol have been obtained. In general, D_o is orders of magnitude small and Q is about one-half of values expected for bulk diffusion. Combined with complimentary results from Auger electron spectroscopy, optical microscopy and transmission electron microscopy, data indicate that interdiffusion is facilitated by grain boundaries and other lattice defects. Further support of this conclusion is obtained through time-dependent contact resistance measurements on unlike couples with varying defect densities. In particular, when approximate grain sizes of the constituent copper and nickel films are increased from 20 and 120 to 65 and 250 nm, respectively, the effective interdiffusion coefficient is reduced by a factor of about 5. Deviation from linearity in figure 4 indicates that a characteristic diffusion distance has exceeded the film thickness.

For more complex systems, such as aluminum-copper, evolution of contact resistance is more complex than that presented in figure 4, although results still indicate that diffusion-controlled processes obtain. Namely, n assumes a value closer to 0.4 and the deviation from linearity is not nearly so evident. Nevertheless, by noting the time required for this deviation and the film thickness, a measure of the diffusion coefficient D can be estimated from the expression

$$D \approx x^2/t \qquad (4)$$

At 200°C, for example, the value of D obtained for aluminum-copper couples is about 3 x 10^{-13} cm^2/sec, compared to a value of about 3 x 10^{-18} cm^2/sec for copper-nickel couples. Subsequent examination of the surfaces by optical microscopy indicates that aluminum is more mobile in aluminum-copper couples whereas copper is more mobile in copper-nickel couples.

The principal contribution to the contact resistance in copper-nickel couples is expected to be due to chemical interdiffusion, whereas the principal contribution in aluminum-copper couples is expected to be due to formation of intermetallic phases. Indeed, five intermetallic phases of aluminum and copper are thermodynamically stable in the temperature range under investigation (ref. 13), each characterized by a unique value of electrical

resistivity. These phases and corresponding values of Knoop hardness and (relative) electrical resistivity are identified in figure 5. Since each intermetallic phase is characterized by a significantly smaller electrical conductivity (larger electrical resistivity) than either pure aluminum or copper it is expected that contact resistance will increase correspondingly.

Transmission electron micrographs and corresponding electron diffraction patterns confirm formation and growth of the intermetallic compound $CuAl_2$ at the interface of aluminum-copper thin-film couples during annealing at about $200^{\circ}C$. An example is presented in figure 6, wherein transmission electron micrographs and corresponding diffraction patterns are presented for unannealed and annealed couples. No indication of intermetallic phase formation is evident prior to annealing but small particles of $CuAl_2$ are easily discernible following annealing. Further annealing produces a continuous layer of $CuAl_2$. By depositing films of copper and aluminum of the appropriate thickness to produce $CuAl_2$ by extended annealing, values of $R_c(t)$ over 5 times larger than initial values have been measured. Similar changes in mechanical properties also occur. Therefore, it is evident that degradation of electrical and mechanical properties due to interfacial reactions represents an important limitation in diffusion bonding processes.

CONCLUDING REMARKS

Microscopic aspects of interfacial reactions in diffusion bonding processes have been investigated by combination of a sensitive contact resistance technique and microstructural characterization by transmission electron microscopy. Specifically, important interfacial reactions have been identified in the copper-nickel and aluminum-copper systems and specific information has been obtained concerning the nature of these reactions. Namely, degradation of engineering properties occurs predominantly by grain boundary diffusion between 300° and $500^{\circ}C$ in the copper-nickel system whereas degradation occurs predominantly by formation of the intermetallic phase $CuAl_2$ at $200^{\circ}C$ in the aluminum-copper system. A thorough knowledge of these reactions is essential in order to control and improve diffusion bonding processes.

REFERENCES

1. Tu, K. N.; and Berry, B. S.: X-ray Study of Interdiffusion in Bimetallic Cu-Au Films. J. Appl. Phys., vol. 43, no. 8, 1972, pp. 3283-3290.

2. Campisano, S. U.; Foti, G.; Rimini, E.; Lau, S. S.; and Mayer, J. W.: Kinetics of Phase Formation in Au-Al Thin Films. Phil. Mag., vol. 31, no. 4, 1975, pp. 903-917.

3. Chang, C. C.; Murarks, S. P.; Kumar, V.; and Quintana, G.: Interdiffusion in Thin-Film Au or Pt on GaAs (100) Studied with Auger Spectroscopy. J. Appl. Phys., vol. 46, no. 10, 1975, pp. 4237-4253.

4. Weaver, C.; Brown, L. C.: Diffusion in Evaporated Films of Gold-Aluminum. Phil. Mag., vol. 7, no. 8, 1962, pp. 1-16.

5. Weaver, C.: Diffusion in Metallic Films. Phys. of Thin Films, vol. 6, 1971, pp. 301-347.

6. Campisano, S. U.; Foti, G.; Grasso, F.; and Rimini, E.: Low-Temperature Interdiffusion in Cu-Au Films Analyzed by Helium back-scattering. Thin Solid Films, vol. 19, 1973, pp. 334-348.

7. Borders, J. A.: Ion Back-Scattering Analysis of Interdiffusion in Cu-Au Thin Films. Thin Solid Films, vol. 19, 1973, pp. 359-370.

8. Balluffi, R. W.; Blakely, J. M.: Special Aspects of Diffusion in Thin Films. Thin Solid Films, vol. 25, 1975, pp. 363-392.

9. Kang, S. K.; Bernstein, I. M.; Bauer, C. L.: In-Situ Observations of the Recrystallization Process in Single Crystal Thin Films of Gold. Scripta Met., August 1976.

10. Pashley, D. W.: The Study of Epitaxy in Thin Surface Films. Advances in Phys., vol. 5, no. 18, 1956, pp. 173-240.

11. Tisone, T. C.; Lau, S. S.: Interdiffusion and Compound Formation in Ta-Au Thin-Film Couples. J. Appl. Phys., vol. 45, no. 4, 1974, pp. 1667-1674.

12. Matthews, J. W.; Crawford, J. L.: Formation of Grain Boundaries During Diffusion Between Single Crystal Films of Gold and Palladium. Phil. Mag., vol. 11, no. 8, 1965, pp. 977-991.

13. Hansen, M.: Constitution of Binary Alloys, McGraw-Hill, 1958 (supplements by Elliot and Shunk).

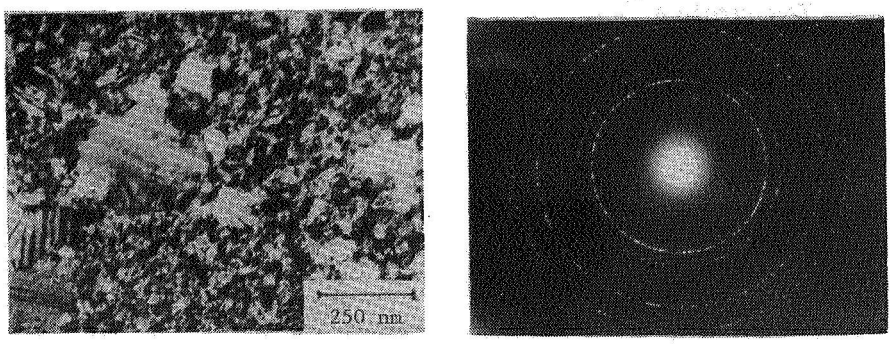

(a)

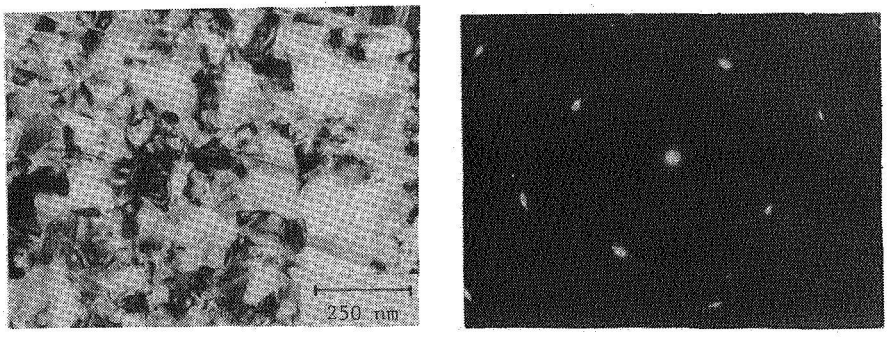

(b)

Figure 1.- Transmission electron micrographs and accompanying selected area diffraction patterns of copper thin-films deposited at (a) 25°C and (b) 200°C.

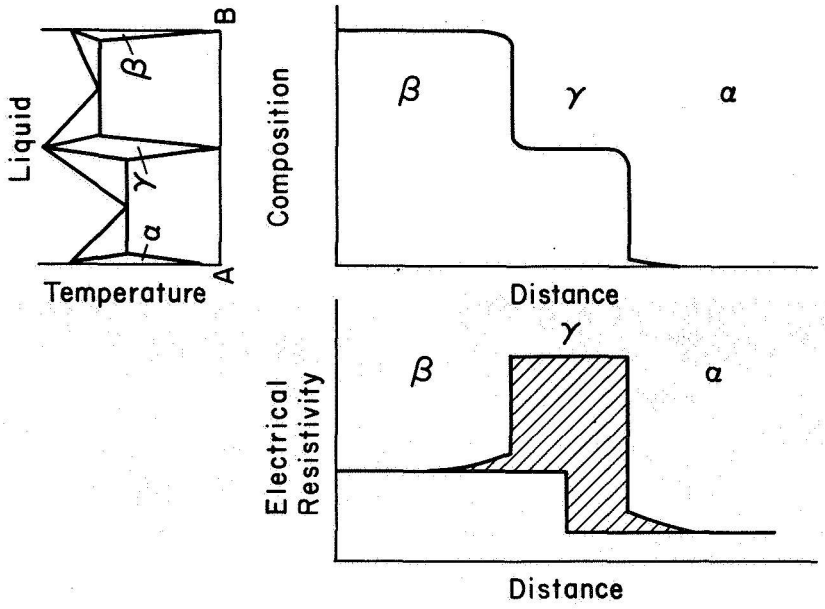

Figure 2.- Schematic illustration of a binary AB phase diagram along with composition and electrical resistivity profiles. The hatched area represents contact resistance.

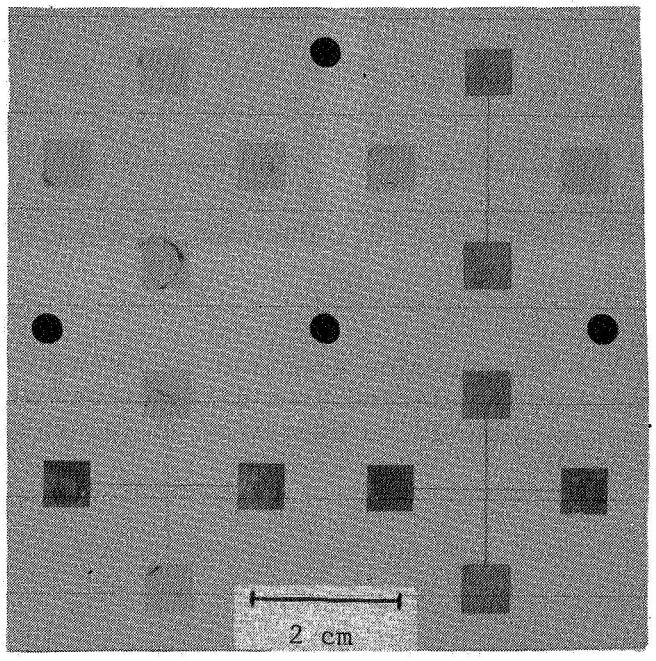

Figure 3.- Example of a typical AB thin-film (four-element) matrix. Contact resistance is measured at the point of crossover of each couple.

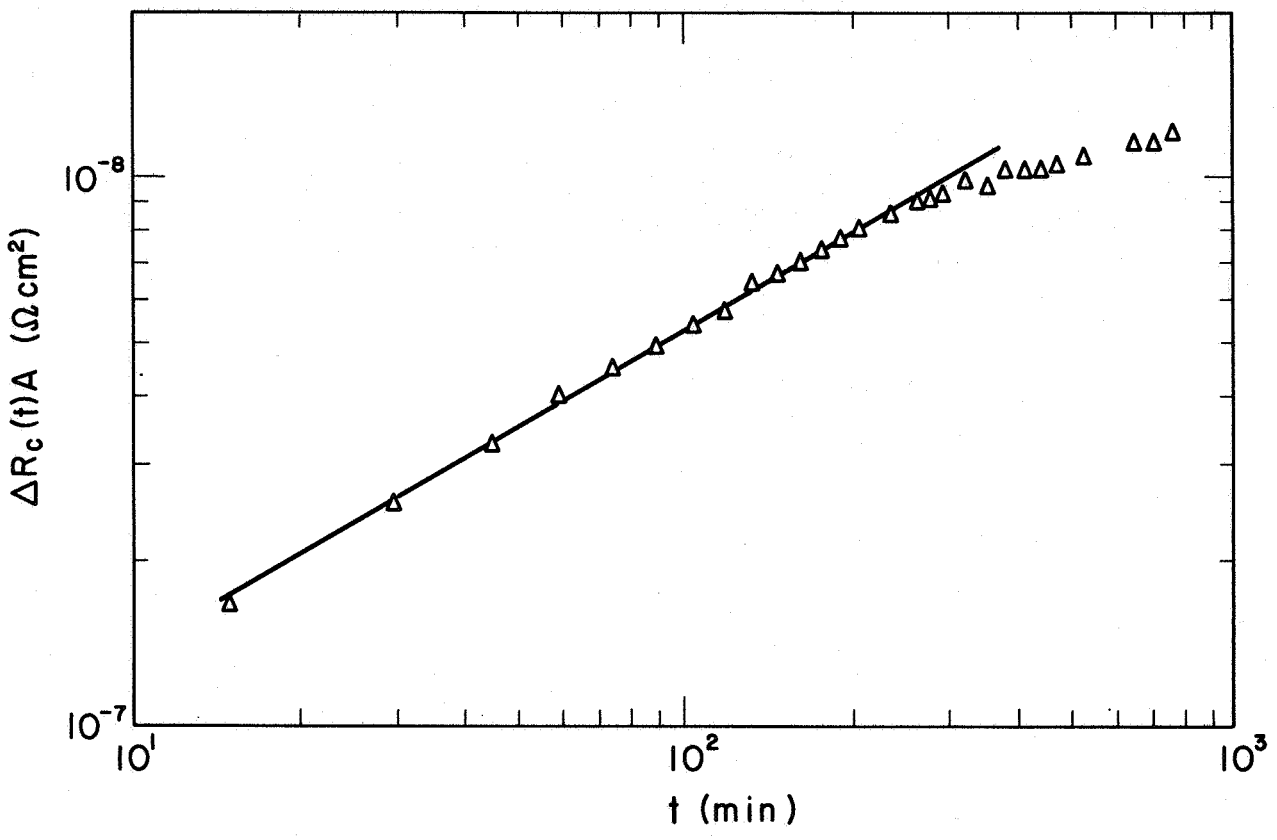

Figure 4.- Variation of the time-dependent component of specific contact resistance $A\Delta R_c(t)$ as a function of time t, where A denotes the apparent (geometric) contact area, for a copper-nickel thin-film couple at 503°C and a current density of 10^4 A/cm^2.

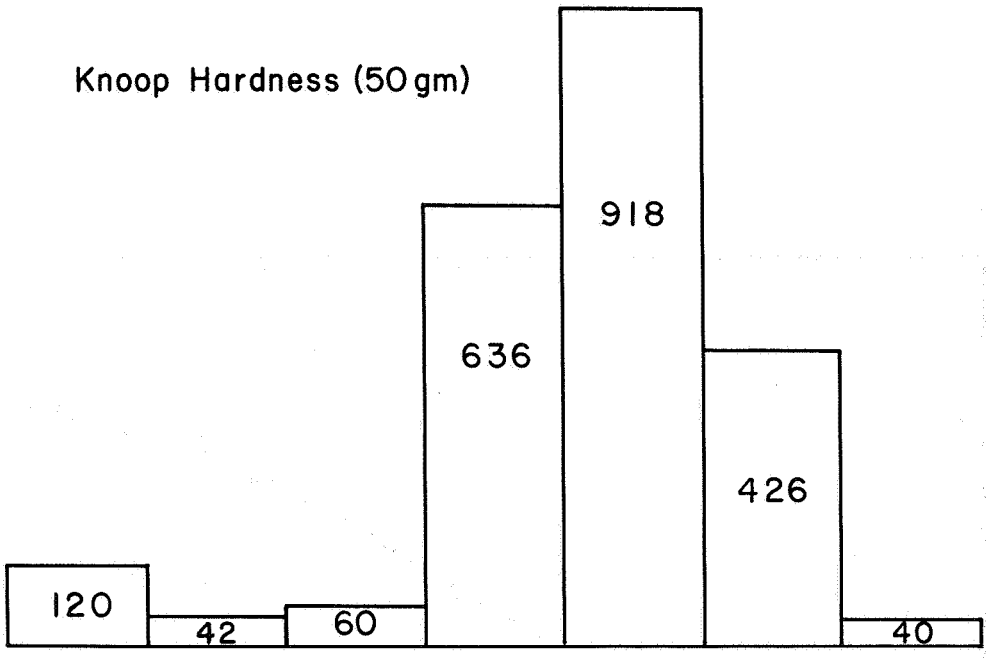

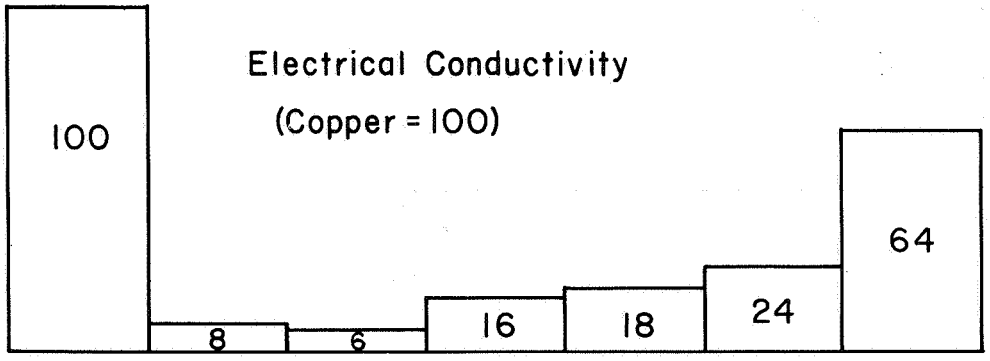

Cu	$Cu_2Al(\gamma_2)$	$Cu_3Al_2(\delta)$	$Cu_4Al_3(\zeta_2)$	$CuAl(\eta_2)$	$CuAl_2(\theta)$	Al
100/0	80/20	78/22	75/25	71/29	53/47	0/100

Figure 5.- Values of typical engineering properties (Knoop hardness and electrical conductivity) for thermodynamically stable phases in the copper-aluminum system.

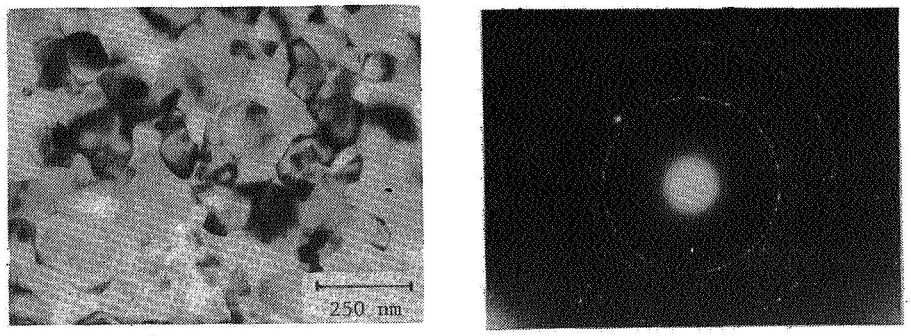

(a)

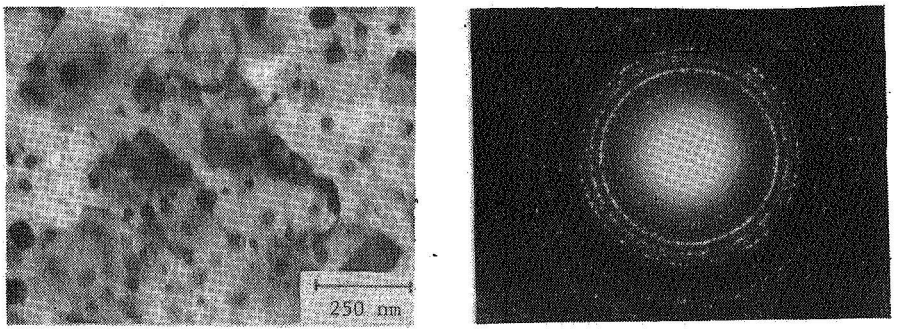

(b)

Figure 6.- Transmission electron micrographs and accompanying selected area diffraction patterns of aluminum-copper thin-film couples (a) unannealed and (b) annealed for 1 hr at 410°C. Extra rings in the diffraction pattern of (b) indicate formation of the intermetallic compound Al_2Cu.

MACROSCOPIC ASPECTS OF INTERFACIAL REACTIONS IN DIFFUSION BONDING PROCESSES*

R. W. Heckel
Department of Metallurgical Engineering
Michigan Technological University

ABSTRACT

The bonding of dissimilar metals and alloys frequently results in considerable interdiffusion in the vicinity of the bond zone. In addition, new phases not found in the metals being bonded can be formed. The extent of interdiffusion and formation of new phases is determined by the constitution diagram of the alloy system, the interdiffusion coefficients of the phases present, and the thermal conditions (temperature and time) associated with the bonding process and/or subsequent use of the bonded structure. In many instances the kinetics of interdiffusion and phase formation can be predicted from known parameters using numerical methods and computer techniques. This presentation will focus upon comparisons of such predictions with experimentally determined parameters for a variety of metallurgical alloy systems.

INTRODUCTION

The process of diffusion bonding is becoming more important with the increasing sophistication in materials technology. Solid state joining of metals and alloys is often used to weld structural components in instances where conventional fusion welding would result in poor properties due to the solidification process. In addition, diffusion bonding is of importance in the formation of adherent coatings, the fabrication of laminar and fibrous composites, and the consolidation of powders into structural components. It is clear that diffusion bonding offers a unique means of fabricating metals and alloys and should continue to grow in importance as more emphasis is placed on effective materials utilization.

Diffusion bonding is often carried out at temperatures approaching the melting point of the constituent parts, resulting in significant diffusional interaction. A small amount of interdiffusion is often necessary to achieve the properties desired in the bond; excessive interdiffusion can lead to too wide a bond zone and, for some alloy systems, the growth of intermediate phase layers which degrade the properties of the bond. Furthermore, the resulting

---

*Financial support from the National Science Foundation is gratefully acknowledged.

material is often subjected to use temperatures which promote additional diffusion. Typically, it is found that volume (or lattice) diffusion is the dominant transport process at these high temperatures and that the metallurgical phases present correspond to those present on the equilibrium phase diagram for the alloy system of interest.

The general nature of binary alloy system behavior during diffusion bonding can be defined in terms of the equilibrium phase diagram. The simplest types of behavior occur when the compositions of both components to be joined lie in the same field at the diffusion bonding temperature. If the field has two phases (e.g., ($\alpha+\beta$)), no long range interdiffusion will take place and the compositional discontinuity at the interface will remain. If the field has only one phase (e.g., α), interdiffusion will occur, a smooth transition in composition will develop and the width of the zone of interdiffusion will widen parabolically with time.

More complex situations develop when the components to be joined do not lie in the same field of the phase diagram. Components in adjacent one-phase fields (e.g., α and β) will give rise to interdiffusion, with a discontinuity in the concentration-distance profile of the magnitude of the compositional width of the ($\alpha+\beta$) field. Components in one-phase fields which are not adjacent (e.g., α and γ) will result in the formation and growth of a layer of the intermediate phase β at the joint interface; the concentration-distance profile will, in this instance, contain two compositional discontinuities representing the ($\alpha+\beta$) and ($\beta+\gamma$) two-phase fields. Components in adjacent two-phase fields (e.g., ($\alpha+\beta$) and ($\beta+\gamma$)) will result in the formation and growth of a layer of β phase at the joint interface. Thus, it is generally found during high-temperature diffusion bonding of binary systems that the concentration-distance profiles exhibit all of the one-phase fields between the compositions of the two components being joined; the two-phase fields are not observed and give rise to compositional discontinuities at the interfaces between phases.

Ternary and higher order alloy systems can give rise to much more complex phenomena. Both one- and two-phase fields can occur in ternary diffusion systems; one-, two-, and three-phase fields in quaternary systems, etc. Unfortunately, the diffusion paths cannot be predicted a priori from such phase diagrams, as in the case of binary systems, because of the additional degree(s) of freedom.

The kinetics of interdiffusion and possible intermediate phase growth associated with diffusion bonding is just as important as the understanding of which phases will form. Proper selection of the diffusion bonding temperature and time can often result in the necessary control of deleterious effects of interdiffusion. Furthermore, it is now possible to formulate predictive models for estimating the extent of interdiffusion and intermediate phase growth in binary systems since phase diagrams (solubilities) and interdiffusion coefficients are available for many systems. The formulation of predictive models for ternary and higher order systems is much more difficult due to the general lack of such data as well as the previously mentioned difficulties associated with the a priori definition of diffusion paths. How-

ever, in some instances binary kinetic models can provide significant approximations to more complex situations.

Predictive diffusion models require consideration of geometric factors as well as alloy system parameters (interdiffusion coefficients and phase solubilities) and process parameters (composition of components to be joined, temperature, and time). A planar joint interface between two large blocks of material (planar, infinite model) is the simplest situation. Solutions to this type of problem for both concentration-independent and concentration-dependent interdiffusion coefficients for one-phase systems are found in standard texts (ref. 1,2). Solutions for multiphase, planar, infinite problems with concentration-independent interdiffusion coefficients have been put forth as well (ref. 3). The use of these planar, infinite models is quite common and numerous comparisons between predictions and experimental data appear in the literature.

On the other hand, the development of predictive models which consider finite, non-planar (e.g., cylindrical and spherical), and multiphase situations has proceeded more slowly due to the complexities involved. These complexities, however, are often important in dealing with diffusion bonding problems. Finite situations arise when interlayers are used between the two components to be joined or when laminar composites are to be fabricated by diffusion bonding of many layers of metal foils; the cylindrical, finite geometry is important in the fabrication of continuous filament composites by diffusion bonding of alternate layers of metal foils and wires; the spherical finite geometry is important in the fabrication of components by the pressing and sintering of blends of powders.

Finite, non-planar geometry diffusion problems can be modeled using numerical methods and computer techniques. Solutions for problems where the components to be joined lie in adjacent one-phase fields (two-phase model) and in one-phase fields separated by an intermediate phase (three-phase model) have been developed for concentration-independent interdiffusion coefficients. The geometric elements of these models are given in figure 1. Thus, predictive models are now available to define the effects of alloy system and process parameters on the kinetics of interdiffusion and intermediate phase growth in a wide variety of diffusion bonding problems. It is the purpose of this presentation to compare the results of such predictions with experimental data obtained from diffusion bonding studies on finite, planar, multiphase systems.

DIFFUSION ANALYSIS

In general, the development of mathematical models for the description of binary interdiffusion phenomena in a situation of interest requires the simultaneous solution of Fick's Law (one equation for each phase) and the flux balance equation (one equation for each interface between phases) for the appropriate initial and boundary conditions and geometry. Fick's Law defines the change in solute concentration at any point with time:

$$\frac{\partial C}{\partial t} = \tilde{D}\,\frac{\partial^2 C}{\partial x^2} \quad \text{(planar geometry)} \tag{1}$$

where C is the concentration of solute, t is time, $\tilde{D}$ is the interdiffusion coefficient (concentration-independent), and x is distance. The flux balance equation defines the velocity of an interface between two phases (e.g., between α and β) in terms of the fluxes toward and away from the interface:

$$(C_{\beta\alpha}-C_{\alpha\beta})\frac{d\xi}{dt} = -J_\alpha+J_\beta \tag{2}$$

where $C_{\beta\alpha}$ is the concentration of solute (B) at the α-β interface in the β phase, $C_{\alpha\beta}$ is the concentration of solute (B) at the α-β interface in the α phase, $d\xi/dt$ is the interface velocity, J_α is the interdiffusion flux in the α phase at the interface and J_β is the flux in the β phase at the interface. It is typically found during high temperature diffusion bonding that the interface compositions ($C_{\beta\alpha}$ and $C_{\alpha\beta}$) can be closely approximated by the equilibrium phase solubilities; ($C_{\beta\alpha}-C_{\alpha\beta}$) (concentration discontinuity at the interface) can therefore be evaluated to be the width of the ($\alpha+\beta$) field of the phase diagram. After substitution for the flux terms in equation (2), it becomes:

$$(C_{\beta\alpha}-C_{\alpha\beta})\,\frac{d\xi}{dt} = \tilde{D}_\alpha\,\frac{\partial C_\alpha}{\partial x}\Bigg]_\xi - \tilde{D}_\beta\,\frac{\partial C_\beta}{\partial x}\Bigg]_\xi \tag{3}$$

For an example of a typical diffusional analysis, consider the problem of joining two components having compositions in one-phase fields (α and γ) separated on the equilibrium phase diagram by the intermediate phase β. Microstructurally, there will be three phases present (a thin layer of β between the α and γ components); the phases will be separated by the α-β and β-γ interfaces. Solution of the interdiffusion problem will therefore entail simultaneous solution of three equations of the form of equation (1) and two equations of the form of equation (3). A complete treatment of the solution to multiphase interdiffusion problems has been presented (ref. 4) for those persons interested in more detail on this topic.

The simultaneous solution of Fick's Law and flux balance equations can be carried out analytically or numerically. The numerical approach is usually necessary for more complex problems resulting from nonuniform initial conditions (ref. 5) and finite and non-planar geometries (ref. 6-8). Numerical methods could also be used to treat nonisothermal problems and have been used recently to treat problems associated with concentration-dependent interdiffusion coefficients (ref. 9).

DATA/ANALYSIS COMPARISONS

Two-phase, Planar, Finite Couples

Diffusion bonded laminar composites fabricated from multiple alternate layers of thin metal foils constitute an example of the planar, finite diffusion geometry shown in figure 1. If the foils have compositions in adjacent one-phase fields of a binary phase diagram (e.g., α and β phases), the interdiffusion phenomena characteristic of a two-phase situation should result during high-temperature bonding. The initial movement of the α-β interface is controlled by fluxes at the interface according to equation (2) as shown in figure 2 for the L/2 symmetry element defined in figure 1. ($C_{\alpha 0}$ and $C_{\beta 0}$ in figure 2 are the solute compositions of the foils being diffusion bonded.) If, however, the mean composition, $\bar{C}$, of the entire composite (and, therefore, the symmetry element):

$$\bar{C} = \ell/L \qquad (4)$$

lies in the α phase field, the β phase must ultimately dissolve by movement of the α-β interface to the left. This intermediate stage occurs in spite of the initial direction of the interface motion. Ultimately, the β phase dissolves completely with the final stage of the process, as shown in figure 2, being the leveling of concentration gradients in the α phase by one-phase, finite, planar diffusion.

The existing mathematical model for this two-phase problem (ref. 6,7) was tested by experimental diffusion bonding studies of alternate layers of Ni and W foils at temperatures in the vicinity of 1200°C (ref. 10). At these temperatures, this alloy system exhibits only the Ni-rich, face-centered cubic α phase and the W-rich, body-centered cubic phase (ref. 11). The W foil thickness (ℓ value in figure 1) was 2.46×10^{-5}m and Ni foil thicknesses ($L-\ell$ values in figure 1) were chosen to give mean compositions ($\bar{C}$) of 0.121 and 0.152 atomic fraction (a/f) W. Both of these values of $\bar{C}$ are in the Ni-rich α phase field of the Ni-W phase diagram, necessitating the ultimate complete dissolution of the W-rich, β phase layer.

A typical example of the progressive dissolution of the β phase is shown in the series of micrographs in figure 3. This system behaves according to case 3 described in figure 2 since the β phase continuously dissolves during the bonding process. (An example of initial β phase growth due to large β phase fluxes is given in ref. 12.) Electron microprobe analysis of the Ni and W concentrations across the four specimens shown in figure 3 are shown in figure 4. The correspondence between the W concentration trace across the symmetry element from x = 0 to x = L/2 in figure 4 and the schematic concentration-distance profiles (initial and intermediate stages) in figure 2 is noteworthy.

Mathematical diffusion model calculations using interdiffusion coeffi-

cient data ($\tilde{D}_\alpha$ and $\tilde{D}_\beta$) and solubility data ($C_{\alpha\beta}$ and $C_{\beta\alpha}$) from the literature (plus foil thickness (ℓ), mean compositions ($\bar{C}$), and temperatures from the experiments) were compared to experimental data. The first comparison was in terms of the decrease in thickness of the W-rich β phase as measured on photomicrographs such as figure 3. The model predictions and experimental data are presented together in figure 5, where the temperature dependence is accounted for in $\tilde{D}_\alpha$ in the abscissa. The second comparison was for the solute (W) concentration at the position $x = L/2$ (the midpoint of the Ni layers), as determined by electron microprobe analysis (see figure 4). Model predictions and experimental data are shown together in figure 6.

The close agreement between model predictions and experimental data shown in figures 5 and 6 illustrates the potential of diffusion modeling in accurately describing the effects of process variables. Furthermore, it should be noted that the agreement extends to $(C/\bar{C}) \cong 1.0$ in figure 6. Thus, the models are applicable to processing for times long enough to yield essentially homogeneous materials -- the end of any long-range interdiffusion phenomena.

Three-phase, Planar, Finite Couples

A companion study to that described above for Ni and W foils was carried out for composites fabricated from Ni and Mo foils in the vicinity of 1200°C (ref. 13). This alloy system contains the intermediate phase MoNi in this temperature range and is an example of a three-phase diffusion problem incorporating the formation and growth of an intermediate phase layer at the location of the original interface between the Ni and Mo. Thus, concentration-distance profiles for this system have two compositional discontinuities, one at the α-β interface and the other at the β-γ interface, where β is the MoNi phase. The mean composition in these couples was located in the Ni-rich α phase, resulting in the following sequence of events during the interdiffusion process:

a. formation of β (MoNi) at the original Ni-Mo interfaces

b. growth of the β phase at the expense of both the α and γ

c. complete dissolution of the γ phase, resulting in the conversion to a two-phase situation.

d. dissolution of the β phase resulting in the conversion to a one-phase homogenization problem.

The previously formulated mathematical model (ref. 8), employing available literature data and experimental parameters, was used to predict quantitatively the sequence of interdiffusion events indicated above. Predictions of the positions of both interfaces and the solute (Mo) concentration at the center of the Ni foils were in close agreement with experimental data, as was the case for the Ni-W bonding studies.

CONCLUDING REMARKS

Accurate predictions of high-temperature interdiffusion kinetics associated with complex multiphase problems are possible for systems where interdiffusion coefficients and phase solubilities are known. The verifications of this for the diffusion bonding of Ni-W and Ni-Mo laminar composites described in this paper are supported by similar comparisons in other types of related problems (ref. 5,12).

The availability of these predictive models is of benefit to workers in the area of diffusion bonding in several ways:

a. close correlation between models and data strongly implies a basic understanding of the phenomena involved,

b. the effects of variations in process and/or material parameters can be understood without the necessity for extensive experimental studies,

and c. the design of experiments, if in fact they are necessary to provide additional process information, is greatly simplified since interrelationships among various parameters are usually defined.

REFERENCES

1. Crank, J.: Mathematics of Diffusion, Oxford Clarendon Press, 1956.

2. Shewmon, P. G.: Diffusion in Solids, McGraw-Hill, 1963.

3. Jost, W.: Diffusion in Solids, Liquids and Gases, Academic Press, 1960.

4. Sekerka, R. F.; Jeanfils, C. L.; Heckel, R. W.: The Moving Boundary Problem. Lectures on the Theory of Phase Transformations, Aaronson, H. I. editor, The Metallurgical Society of AIME, 1975, pp. 117-169.

5. Hickl, A. J.; Heckel, R. W.: Kinetics of Phase Layer Growth During Aluminide Coating of Nickel. Met. Trans., vol. 6A, 1975, pp. 431-440.

6. Tanzilli, R. A.; Heckel, R. W.: Numerical Solutions to the Finite, Diffusion-Controlled, Two-Phase, Moving-Interface Problem. Trans. Met. Soc. AIME, vol. 242, 1968, pp. 2313-2321.

7. Tanzilli, R. A.; Heckel, R. W.: A Normalized Treatment of the Solution of Second Phase Particles. Trans. Met. Soc. AIME, vol. 245, 1969, pp. 1363-1366.

8. Lanam, R. D.; Heckel, R. W.: A Study of the Effect of an Intermediate Phase on the Dissolution and Homogenization Characteristics of Binary Alloys. Met. Trans., vol. 2, 1971, pp. 2255-2266.

9. Sarkhel, A. K.; Seigle, L. L.: Solution of Binary Multiphase Diffusion Problems Allowing for Variable Diffusivity, with Application to the Aluminization of Nickel. Met. Trans., vol. 7A, 1976, pp. 899-902.

10. Tanzilli, R. A.; Heckel, R. W.: An Analysis of Interdiffusion in Finite-Geometry, Two-phase Diffusion Couples in the Ni-W and Ag-Cu Systems. Met. Trans., vol. 2, 1971, pp. 1779-1784.

11. Hanson, M.: Constitution of Binary Alloys, McGraw-Hill, 1958 (supplements by Elliot and Shunk).

12. Heckel, R. W.; Hickl, A. J.; Zaehring, R. J.; Tanzilli, R. A.: Transient Growth of Second Phases During Solution Treatment. Met. Trans., vol. 3, 1972, pp. 2565-2569.

13. Lanam, R. D.; Heckel, R. W.: Diffusional Homogenization Behavior in Finite Ni-Mo Couples. Met. Trans., vol. 6A, 1975, pp. 421-423.

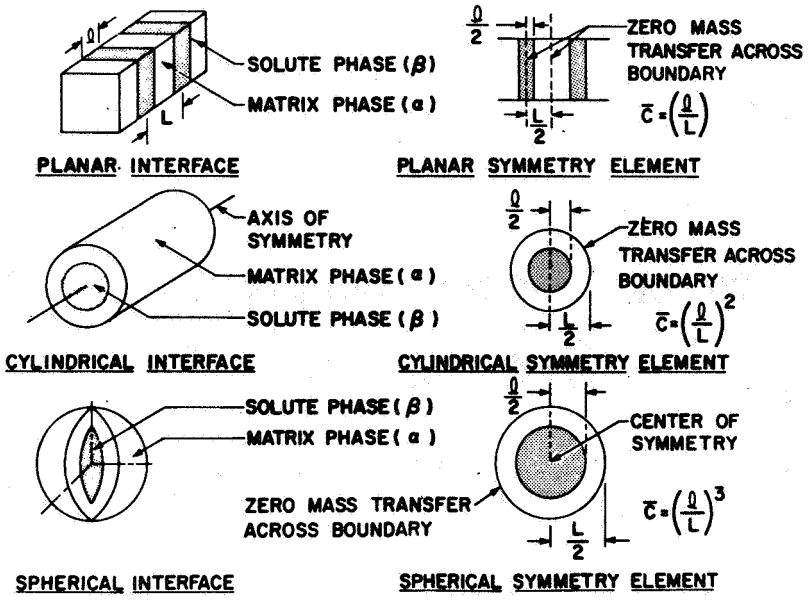

Figure 1.- Definition of planar, cylindrical and spherical geometries for finite diffusion problems. Symmetry elements for the diffusion models are also defined.

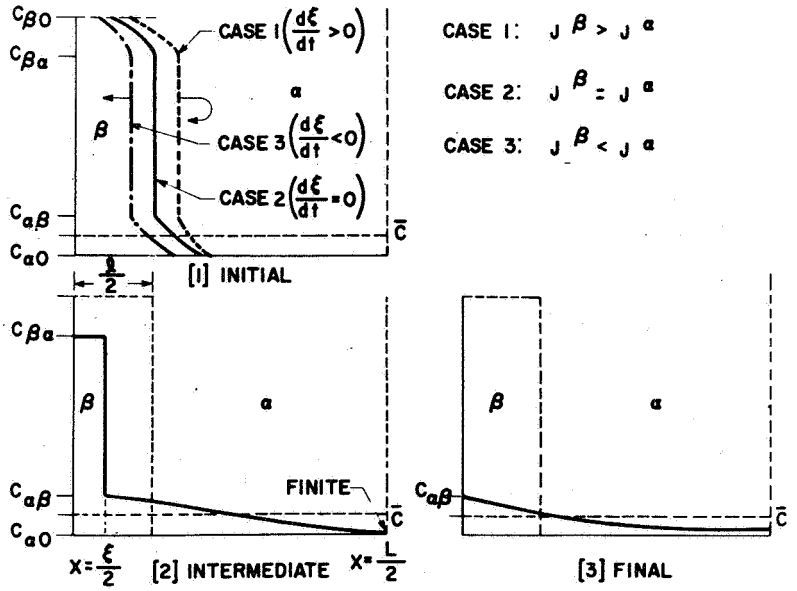

Figure 2.- Schematic solute concentration-distance profiles for the two-phase, finite, planar diffusion problem where the mean composition of the symmetry element lies in the α phase. Three stages of the process are shown along with three separate types of interface movement phenomena for the initial stage.

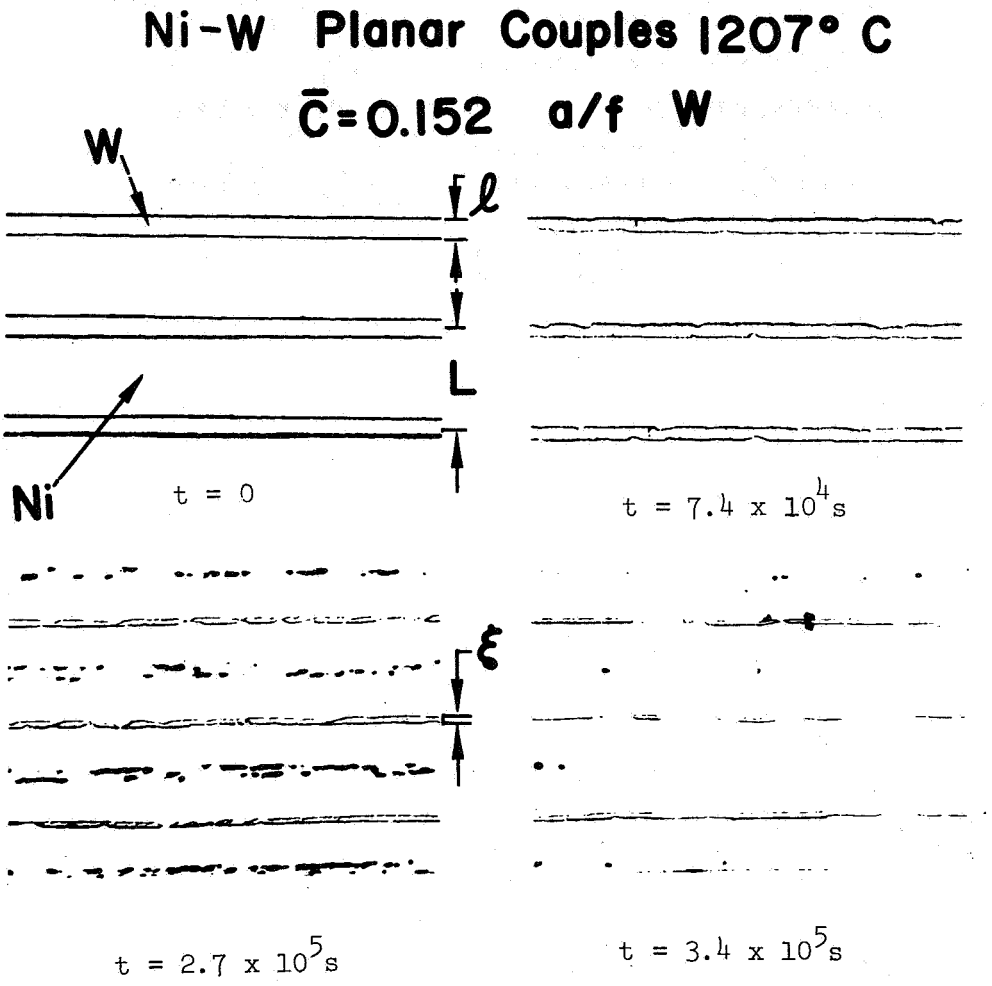

Figure 3.- Photomicrographs of laminar composites fabricated from alternate layers of Ni and W foils by diffusion bonding at 1207°C for the various times indicated. The initial W foil thickness (ℓ) was 2.46 x 10^{-5}m.

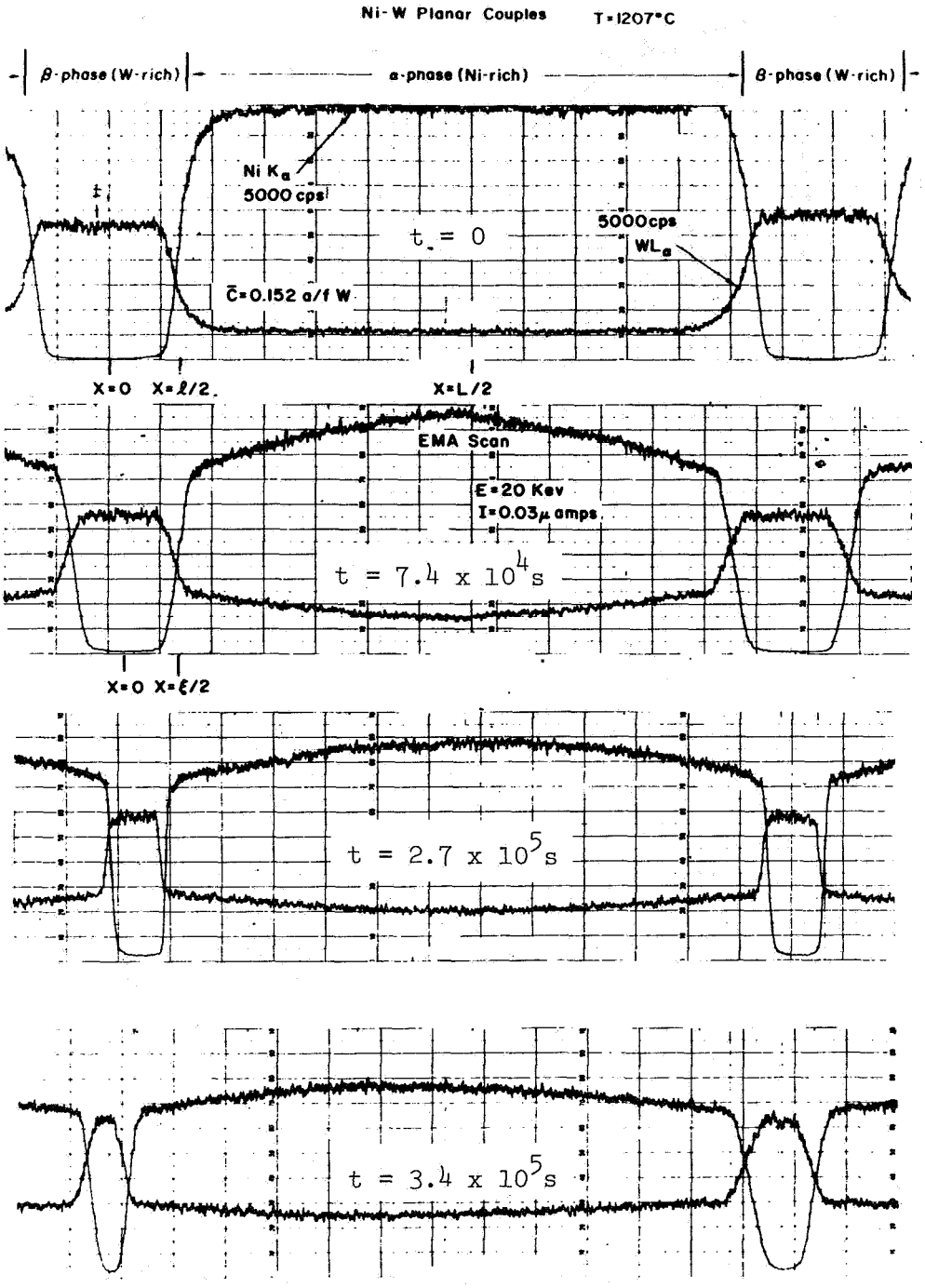

Figure 4.- Electron microprobe scans for both Ni (NiK_{α}) and W (WL_{α}) concentrations across the specimens whose microstructures are shown in figure 3.

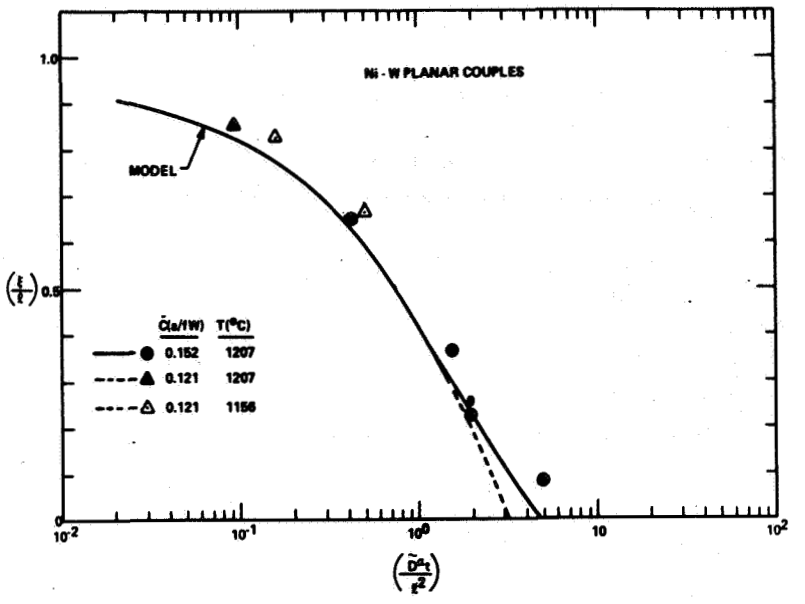

Figure 5.- Comparison of predictive model calculations and experimental data on the decrease of the thickness of the β phase (ξ) with time (t).

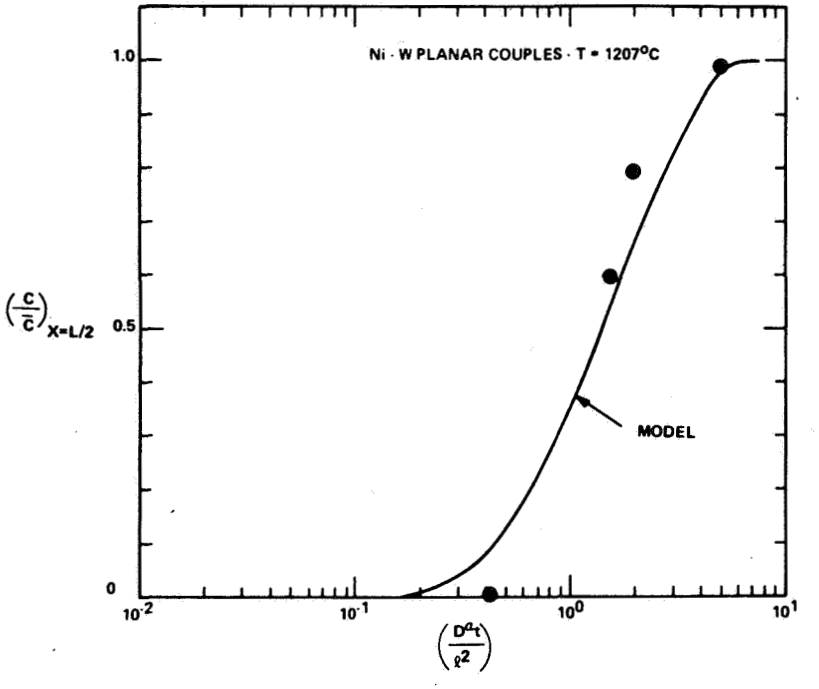

Figure 6.- Comparison of predictive model calculations and experimental data on the increase in solute (W) concentration at the center of the Ni foils (C at position x = L/2) as a function of time (t).

FRACTURE IN MACRO-MOLECULES

K. L. DeVries
Professor of Mechanical Eng.
University of Utah
Currently on leave as Program Director - Polymers
NSF, Washington, D.C.

INTRODUCTION

It is anticipated that the next decade will see greatly increased usage of polymers as structural loadcarrying members in engineering design. This increased usage will likely be stimulated by such factors as: (1) greater emphasis on weight savings, (2) concern with corrosion, (3) decreasing supplies and/or increasing costs of mineral resources and (4) increased emphasis on cost and ease of production. As polymer usage increases, it becomes more important that the engineers understand their mechanical behavior and, in particular, how to predict and optimize structural strength. Many designers have adapted (with some noteworthy success) the design criteria that are commonly used for designing with metals. The fundamental mechanisms responsible for damage and failure can be rather different for polymers than they are for metals. Some mechanisms of failure in polymers (e.g. crazing) do not even have direct analogs in metals. It would appear, therefore, that some caution must be exercised in transferring design technologies from one material type to another.

Most engineering design criteria currently being used view the material as a continuum (perhaps with mathematically introduced holes or flaws) and assume failure occurs when some function of the "macroscopic" stress and strain reaches a critical value. Approaches of this type have lead to such extremely useful design concepts and mathematical models as the Tresca and Von Mises yield theories and Griffith fracture theory. Nevertheless, real materials are not continuous on an atomic scale, but rather are made up of molecules and atoms. A true understanding of failure should include what happens on this scale. One might question the validity of using a criteria based on parameters obtained from laboratory tests to predict behavior under service conditions if there is a chance that the fundamental mechanisms (unknown) involved are unknown and might in fact possibly be different in the two cases. One might, for example, envision a laboratory test where in the time scale and under the conditions of the laboratory tests failure occurred by molecular slippage and shear, but in which service conditions were such that the molecules degraded and the mechanism of failure was accompanied by chain scission.

The need to understand molecular phenomena involved in failure is likely to be more acute in polymers than in other material because the mechanical properties of polymers are so intricately related to their macromolecular structure. For example, polymers that are chemically very similar but whose physical structures differ can have tensile moduli varying from as low as

10^7 dynes/cm^2 (typical of rubbers) to as high as 10^{11} dynes/cm^2 (typical of ultrahigh modulus fibers). The molecular morphology can have almost as drastic an effect on strength. Depending on the intricacies of structure, chemically similar polymers can exhibit practical strengths ranging from less than 10^7 dynes/cm^2 to as much as 5×10^{10} dynes/cm^2. A number of theoretical models of failure have been developed, but only recently have experimental techniques been developed that may be used to observe occurences that can be directly related to molecular phenomena associated with fracture. These techniques are comparatively new, but they have produced some interesting insights into the phenomena of polymeric fracture. The purpose of this paper is to discuss these methods and to review some of the results obtained.

METHODS AND TECHNIQUES

The methods used most extensively to date are Electron Paramagnetic Resonance (EPR) Spectroscopy, Infrared (IR) Spectroscopy and molecular weight (MW) measurements. All three methods are used to detect molecular bond rupture in the materials studied. They cannot be used to determine the amount of secondary bond rupture or slippage that might occur during the fracture process.

Each of the techniques are well established tools of analytical chemistry. For the formal development of EPR and IR Spectroscopy theory and techniques of molecular weight measurements, the reader is referred to the many texts on Spectroscopy and polymer characterization. For our purposes here the following very brief descriptions will hopefully suffice. (1) EPR is a form of microwave absorption Spectroscopy in which transitions are induced between Feeman energy levels with an applied magnetic field (ref 1). When homolytic chain scission of a polymer takes place, the two electrons composing a covalent bond may be uncoupled forming two free radicals. The net microwave absorption that takes place in the microwave cavity is proportional to the number of free radicals (and hence the extent of chain scission) present. The structure of the absorption Spectra provides clues as to the location of the unpaired electrons on the polymer chain. (2) Infrared absorption in a polymer can be due to a number of different causes (ref. 2). The absorption here is that due to resonant vibration of the chemical bonds between atoms, in particular the carbon atoms. The absorption bonds are characteristic of the nature of the bond and its associated atoms. As a consequence, those bonds associated with end groups of the molecular chain may have very different absorption frequencies from the other backbone carbon atoms. Careful monitoring of the change in the number of end groups, as a polymer is fractured, may be used as a measure of the extent of chain scission. (3) There are a number of means by which molecular weight can be measured. One method commonly used is "intrinsic viscosity." The viscosity of a dilute solution of polymers in selected standard solvents has been carefully calibrated as a function of the polymers molecular weight (ref. 3). By comparing viscosity (and hence molecular weight) for virgin and strained samples, we once again obtain a measure of bond rupture. Each of these methods has its advantages and limitations some of which will be discussed in the brief descriptions that follow.

EXPERIMENTAL RESULTS

To date the most extensively used method is EPR. This method was first suggested and used by Zhurkov and his associates in Leningrad (ref. 4-6). Since then EPR-Fracture studies have been reported in the United States (ref. 7-14), in Germany (ref. 15-16) and England (ref. 17-18).

The first and most extensive studies were on orientated polymer fibers and films, most notably nylon. Figure 1 shows the EPR spectra for nylon's fibers loaded to approximately 80% of its failure stress. Very briefly summarized these demonstrate that (1) The thermal motion of atomic partners in a covalent bond can be viewed as the fundamental process in fracture, at least in some materials; (2) an increase in temperature tends to bias the thermal motion in favor of bond dissolution. This process can be described analytically in terms of reaction rate theory with a characteristic activation energy (ref. 19). Application of an external applied load reduces the effective activation energy and further biases the thermal motion toward rupture; (3) some of the EPR behavior can be related to specific proposed polymer morphology (ref. 20); (4) it appears that the key to obtaining good agreement between experimental EPR observations of the extent of bond rupture (free radical concentration) and models, based on absolute reaction rate theory, is taking proper account of the variation of the "local" stress on the load carrying elements in the polymer structure; (5) finally, there is strong experimental evidence that the strength of a polymer can be significantly altered by processes that will alter and improve the stress distribution in the material. (See ref. 21.)

EPR has also been used to study fracture mechanisms in rubber; it has proven to be a very sensitive and informative means of monitoring bond rupture in unsaturated rubbers under combined stress and exposure to ozone (ref. 22-23). The EPR spectra shown in figure 2, resulting from the combined effect of ozone and stress, are four orders of magnitude above threshold sensitivity of the spectrometer. By comparing the EPR results, rate of macroscopic crack growth, stress relaxation (or creep rate) and using rubber elasticity, it is possible to arrive at some interesting deductions on the manner in which ozone cracks develop and proceed through a material (ref. 24). It has also been demonstrated that the EPR results can be correlated with a "molecular level" Griffith-type energy balance (ref. 22-23). That is, cracks propagate, i.e., bonds rupture only if (and at rates dependent on) sufficient strain energy being present. Excellent numerical correlation between the "energy released" from the stress field and the number of free radicals detected by EPR was observed for relaxation, creep and cyclic loading tests.

Cryogenic and space applications (in the binder of some solid propellants and in low-temperature seals, for example) require that rubber withstand very low temperatures, where it normally becomes brittle and cracks can propagate easily through the material. Andrews, Reed and co-workers (ref. 25-26) have demonstrated that prestraining the rubber before cooling can drastically modify its fracture behavior. In their studies and subsequent studies by Brown, DeVries, and Williams (ref. 27) a variety of rubbers ranging from natural rubber to silicone were prestrained (100% at room temperature) before reducing the temperature to -50°C (or below). When further stressed at these low temperatures, the rubbers did not fracture

in a brittle manner but exhibited a yield point followed by significant plastic deformation before failure. In a nutshell they had become "tough" in the engineering sense. Reed and his associates reported that this plastic deformation was followed by foaming and evolution of gases from the material upon warming. They also observed that samples that were prestrained and fractured at low temperature exhibited strong EPR signals, while samples that were fractured at the same temperatures but without prestrain showed little if any detectable radical production during deformation. This latter observation was confirmed by Brown and co-workers (ref. 28).

The free radicals produced by deformation in the prestrained rubber were characterized by a g value of approximately 2.00, characteristic of organic free radicals. Other than differences in the shape of the EPR spectra, no marked differences were noted in the behavior of natural rubber, acrylonitrile-butadiene, polybutadiene, and silicone rubbers though these rubbers reportably have very different crystallization characteristics (natural rubber crystallizes under stress while the others are often described as noncrystallizable). In each case, rubbers that were not prestrained fractured in a brittle fashion, while those that were preoriented by prestraining by 50% or more exhibited considerable ductility before fracture. Prestrain had only a slight effect on ultimate stress and initial modulus, but often increased the strain at fracture by orders of magnitude. During this plastic deformation the concentration of free radicals increased to easily detectable levels (10^{16} to 10^{17}spins/cm^3).

The large number of radicals (chain scissions) produced during this deformation suggest that fracture initiates in prestrained rubbers at a great many sites throughout the specimen volume. On the other hand, fracture is apparently much more localized in the unprestrained material and proceeds from an existing or easily developed flaw. In the language of fracture mechanics, the latter material might be called flaw-sensitive and the prestrained material "tough." The effect of room-temperature prestraining on the subsequent low-temperature ductility and fracture behavior of rubbers was interpreted by Brown and coworkers as probably being related to strain and temperature-induced ordering and orientation of the material. It is proposed that prestrain and subsequent cooling produces a great many small ordered regions throughout the sample that are comparatively impermeable to cracks. As the load is increased, a stress is reached at which microcracks begin to form. From analogy with studies of oriented semicrystalline nylon, these would be expected to originate in the more amorphous regions of the material, but their growth with further load increase is arrested by the more ordered or crystalline regions. As the deformation increases, more and more of the microcracks are produced with the associated bond rupture and free-radical production (detectable by EPR). Eventually, these microcracks start to coalesce and grow to a critical size, after which macroscopic failure ensues. In essence, if somewhat oversimplified, this model suggests that the low-temperature ductility of prestrained rubbers may be explained in terms of the conversion of the rubber into an oriented semicrystalline polymer as a result of the temperature and strain treatment.

As stated above, the behavior, in this respect of the easily crystallizable rubbers (e.g., natural rubber) and those normally termed noncrystallizing

(e.g., acrylonitrile-butadiene and silicone) is very similar. Indeed, there is evidence that some ordering occurs in all these systems. The X-ray diffraction patterns for prestrained samples of natural rubber, SBR, and silicone rubber at low temperatures show the Debye and Scherrer rings characteristic of crystallites and the transition to elongated areas indicative of orientation.

A major disadvantage to the use of EPR in studying polymeric fracture is the fact that most polymeric fibers are inherently unstable entities. The unpaired electron associated with the free radical has an affinity for other unpaired electrons; as a consequence, free radicals can combine with other free radicals or certain impurities. In this way the free radicals are annihilated. The spectrometer "sees" only the net number of radicals present. Radicals produced by fracture in nylon and ozone in rubber are fairly stable with a half life of approximately an hour at room temperature. Radicals in many other polymers are very unstable at room temperature with half lives of a second or less. In most rubber and plastic the radicals become stable at cryogenic temperatures, and hence some studies have been restricted to low temperatures. If one is to extrapolate from the number observed to the number produced by fracture, an understanding of the decay kinetics at the temperature of interest is necessary. Several studies of decay phenomena have been undertaken (ref. 29-31). and provide information helpful in this extrapolation.

The problem of free radical decay can be alleviated by "working" with more stable radicals. Ham and Davis suggest adding chlorinal to the polymer being fractured. They report that if chlorinal is present in the polymer it will react, with radical-produced bond rupture and result in a very stable secondary radical. Chiang et al. (ref. 32) have reported using oxygen as a free radical stabilizer in PET and PE with some success. Often, the radical observed by EPR is not that initially produced, but a secondary radical resulting either from radical migration along the polymer chain or interaction between the primary radical and impurities (most notably oxygen). A recent paper describes such phenomena (ref. 33) in some detail.

INFRARED SPECTROSCOPY

When chain scission occurs in polymers, new end groups can result that may be amenable to detection by Infrared (IR) Spectroscopy. IR Spectroscopy is not a new tool for polymeric end group analysis but to our knowledge it has only recently been used to study mechanical degradation during fracture. This interesting technique was first pioneered at the Institute of Materials Research, in Leningrad, USSR. Zhurkov, Novak and Vettegran have recently reported studies where the formation of CH_3 and C=C bonds during deformation of selected polymers (ref. 34-35) was monitored by IR. In these studies, two specimens, one unstrained and the other fractured, were interposed in the balanced light beams of a double beam spectrometer. In this mode the spectrometer records the difference in absorption, g-delta, of the undeformed and the fractured specimen. In principle, this should subtract out the end groups originally present in the material and indicate only those resulting from fracture. They report strong absorption bands at 910, 965,

1379 and 1735 cm^{-1}. These are attributed, respectively, to ($RCH=CH_2$), ($RCH-CHR^1$) $R-CH_3$ and (RCHO) groups. Their analysis of the IR results is both interesting and puzzling. They report that the analysis of these IR spectra indicate that each free radical detected by EPR may represent a great many broken bonds. They postulate that once backbone rupture has occurred with its associated pair of free radicals, these radicals may act as a catalyst for rupture of a number of neighboring bonds. This chain reaction presumably occurs in such a way and over a time scale that there is no net increase in the number of radicals. According to these investigators' interpretation of their study, the net number of broken bonds is proportional to, but much larger than, the number of radicals determined by EPR.

IR has a significant inherent advantage over EPR in that end groups once formed should be comparatively stable. This should allow the investigation of materials that cannot be studied by EPR, as well as facilitate investigations of long-term creep, fatigue, aging and similar behavior where the time required would allow too much radical decay. The intriguing prospects of this method have led to recent initiation of related studies at Case-Western Reserve University, the University of Utah, and the National Bureau of Standards. Our studies at the NBS and Utah, to date, have not reached the state of quantitative measurement of changes in end groups due to mechanical damage. A large part of our problem has involved trying to separate the effects of changes due to sample thickness, orientation, crystallinity, etc. with those due to new end groups produced by chain scission. We have, therefore, undertaken studies due to γ-irradiation damage in polymers. This treatment produces chain scission but reduces the other IR-sensitive effects and hopefully can be used for calibration purposes for the next and more interesting phase of the study. Figure 3 shows the resulting Spectra for polyethylene irradiated to produce levels of chain scission comparable to that reportably produced during fracture of some polymers. The oral presentation of the meeting will present a discussion of some of these results.

OTHER METHODS

The extent of bond rupture detected by EPR and IR would suggest that significant changes in molecular weight should occur during fracture. Preliminary studies at the University of Utah by R. E. Mehta and L. Shen (ref. 36), B. Crist of Northwestern University (ref. 37) and D. K. Roylance of Massachusetts Institute of Technology (ref. 38) demonstrate that this is indeed the case. In these studies the observed changes in molecular weight demonstrate roughly the same trends observed by EPR (see figure 4 by L. Shen). A quantitative comparison of these observations with those by the other techniques will be given in the oral presentation.

CONCLUSION

We have briefly outlined some of the techniques available for the observation of the extent of molecular bond rupture during fracture of polymers. Additional pertinent information can also often be inferred from microscopic and macroscopic measures. Individual or a combination of such methods should be invaluable in development of techniques for predicting material behavior and also as a tool for systematically studying and modifying structure in the effort to design materials to carry ever greater mechanical loads. The author feels these methods have the potential of helping us approach the goals of designing a material for a given usage.

Acknowledgements - Major portion of the authors research were supported by the National Science Foundation Grant #DMR74-03271. Many of the thoughts presented did not originate with the author but originated with his associates, graduate students, and other investigators.

REFERENCES

1. Carrington, A., and McLaehlon, A. D., Introduction to Magnetic Resonance, Harper and Row Publishers, New York 1967.
2. Miller, R. G. J. and Stace, B. C., Laboratory Methods in Infrared Spectroscopy, Heyden and Son, New York, 1972.
3. Brandrup, J. and Immugut, E. H., Polymer Handbook, Interservice, New York, 1966.
4. Zhurkov, S. N. et al., Soviet Phys. Solid State (in English) 9, 986, 1965.
5. Zhurkov, S. N. and Tomashevskii, E. E., Proceedings of the Conference on the Physical Basis of Yield and Fracture, p. 200, London: Oxford University Press, 1966.
6. Zhurkov, S. N., Int. J. Fracture Mech., vol. 1, p. 311, 1965.
7. DeVries, K. L., Roylance, D. K. and Williams, M. L., J. Polymer Sci., A-1 vol 8, p. 237, 1970.
8. Backman, D. K., DeVries, K. L. and Williams, M. L., J. Polymer Sci., A-1, vol. 7, 2125, 1970.
9. DeVries, K. L., Roylance, D. K. and Williams, M. L., J. Polymer Sci., A-2, vol. 10, 599, 1972.
10. DeVries, K. L., Lloyd, B. A., and Williams, M. L., J. Appl. Phys., vol. 42, 4644, 1971.
11. Roylance, D. K., DeVries, K. L. and Kausch, H., Eur. Polymer J., vol. 7, 105, 1971.
12. Campbell, D. and Peterlin A., J. Polymer Sci., vol. B6, 481, 1968.
13. Verma, G. S. P. and Peterlin, A., Polymer Preprints, vol. 10, no. 2, 1051, 1969.
14. Peterlin, J. Materials Sci., vol. 6, 490, 1971.
15. Becht, J. DeVries, K. L. and Kausch, H., Eur. Polymer J., vol, 7, 105, 1971.
16. Becht, J., and Fischer, H., Kolloid ZuZ. Polymer, vol. 229, 167, 1969.
17. Kausch, H., Int. J. Fracture Mechanics, vol. 6, 301, 1970.
18. Notarajan, R., and Reed, P. E., J. Polymer Sci., A-2, vol. 10, 585, 1972.
19. Glasstone, S., Laidler, K. J., and Eyring, The Theory of Rate Processes, New York, McGraw-Hill Book Co., 1941.

20. Peterlin, A., Textile Res. J., vol. 42, 20, 1972.
21. Park, J. B., Ph.D. Dissertation, University of Utah, 1971.
22, DeVries, K. L., Simonson, E. R. and Williams, M. L., J. Macromolecular Sci., vol. B-4, 671, 1972.
23. DeVries, K. L., Moore, N. B. and Williams, M. L., J. Appl. Polymer Sci., vol. 16, 1377, 1972.
24. DeVries, K. L., Simonson, E. R. and Williams, M. L., J. Basic Eng., vol. 91, 587, 1969.
25. Andrews, E. H., and Reed, P. E., J. Polymer Sci., vol. B5, 317, 1967.
26. Natarajan, R., and Reed, P. E., J. Polymer Sci., A-2 vol. 10, 585, 1972.
27. Mead, W. T., and Reed, P. E., Polymer Eng. Sci., vol. 14, 22, 1974.
28. Brown, R. D., DeVries, K. L. and Williams, M. L., Polymer Network: Structural and Mechanical Properties, New York: Plenum Publishing Co. p. 409-430, 1971.
29. Williams, M. L. and DeVries, K. L., Surfaces and Interfaces, p. 139, Syracuse: Syracuse University Press, 1968.
30. Brotskii, A. E., Doklady Akademiia Nauk USSR, vol. 156, 1147, 1967.
31. David, M. K., Electron Paramagnetic Resonance Studies of Molecular Fracture in Oriented Polymers, Ph. D. Dissertation, A&M Univ., 1970.
32. Chiang, T. C., and Sibilia, J. P., J. Polymer Sci., vol., 10, 2249, 1972.
33. Sakayuchi, M. and Sohma, J., J. Polymer Sci., vol. 13, 1233, 1975.
34. Zhurkov, S. N., Zakrevskii, V. A. Korsukov, EV. E., and Kuksenko, V. S., Soviet Phys. Solid State, vol. 13, no. 7, 1680, 1972.
35. Zhurkov, S.N and Korsukov, V. E., Riz. Tved. Tela, vol. 15, 2071, 1973.
36. Mehta, R. E., and Shen, L., appendix in paper by DeVries, K. L. and Williams, M. L., J. Macromol. Sci., vol. B8, 691, 1973.
37. Crist, B., Personal Communication, 1975.
38. Roylance, D. K., Personal Communication, 1976.

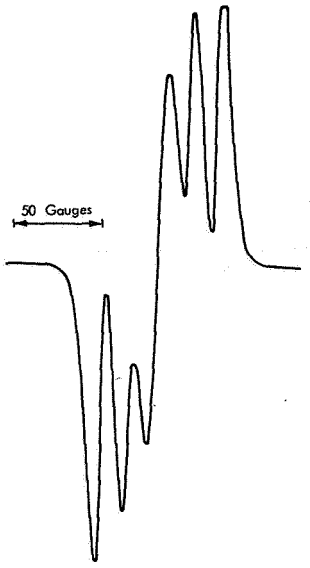

Figure 1.- Spectrum of secondary free radicals, formed in stressed 6 nylon fibers.

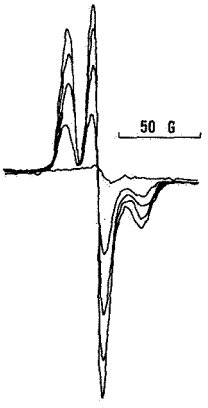

Figure 2.- EPR spectra of ozone-degraded NBR (HYCAR 1043). Ozone concentration 2.8 Mg/1. Lowest curve is residual signal; successively larger ones at 5 min intervals after application of 25% strain.

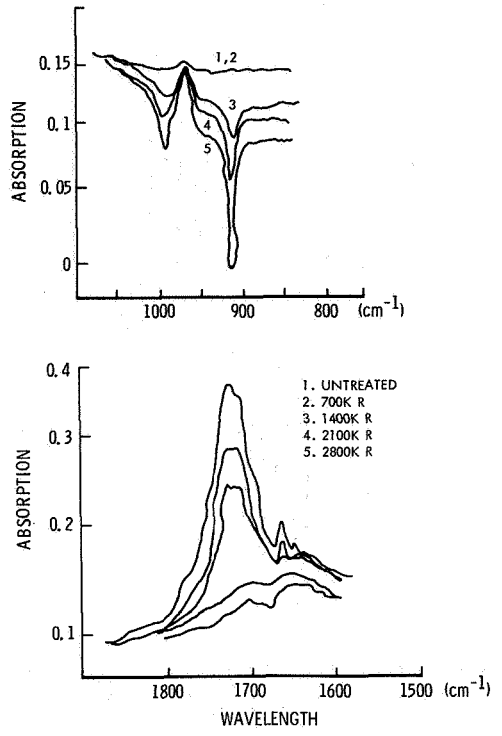

Figure 3.- IR difference spectra between an untreated PE sample and after different levels of irradiation.

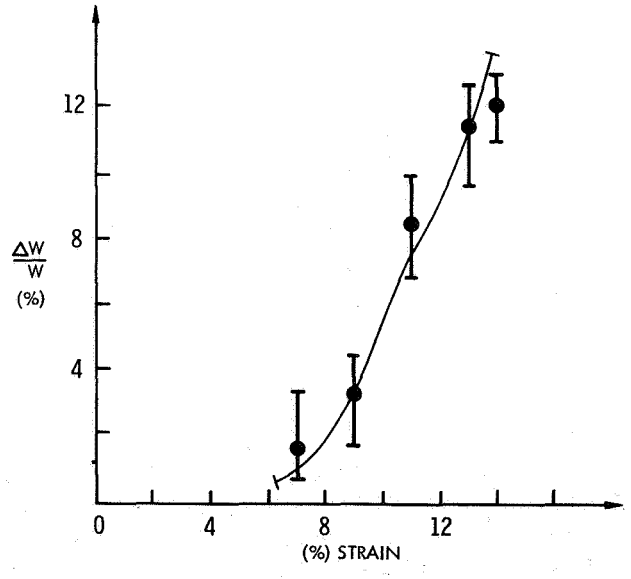

Figure 4.- Percent change in molecular weight versus strain for nylon 6 fibers.

STRUCTURE-PROPERTY RELATIONSHIPS IN BLOCK COPOLYMERS

James E. McGrath
Virginia Polytechnic Institute and State University
Blacksburg, Virginia 24061

ABSTRACT

Block copolymers are a class of relatively new materials which contain long sequences of two (or more) chemically different repeat units. Unlike random copolymers, each segment may retain some properties which are characteristic of its homopolymer. It is well known that most physical blends of two different homopolymers are incompatible on a macro-scale. By contrast most block copolymers display only a microphase (eg. 100-200 Å domains) separation. Complete separation is restricted because of a loss in configurational entropy. The latter is due to presence of chemical bond(s) between the segments.

Novel physical properties can be obtained because it is possible to prepare any desired combination of rubber-like, glassy or crystalline blocks. The architecture and sequential arrangement of the segments can strongly influence mechanical behavior. Thus, diblocks, A-B, are often quite different from A-B-A or $\{A\text{-}B\}_n$ systems. Moreover, B-A-B and A-B-A sequences possess dramatically different properties when the "A" segment is glassy or crystalline and the "B" block is elastomeric. The major differences are due to the fact that the microphase separated domains can associate to form a physical network in the tri- or multi-block architecture. Thermoplastic elastomers are possible if the end blocks are glassy or crystalline and can reinforce an elastomeric continuous matrix. Impact resistant transparent thermoplastics can be prepared where an elastomeric microphase can toughen a continuous glassy matrix. A number of block copolymers are now commercially available. The structure and properties of these materials are reviewed.

INTRODUCTION

Block and graft copolymers differ significantly from random or alternating copolymers (ref. 1-14). The main and most interesting feature of blocks and grafts is their ability to yield two phase systems in which the two phases are linked by a chemical bond. The latter insures a fine dispersion or intermixing of the phases thus yielding some very unique properties.

Blocks of varying structures can be linked together (ref. 1,4,11,15) by anionic (ref. 16-27), step growth (ref. 28-37) and other techniques. Both rigid-rigid rigid-soft (so-called A-B-A or $\{A\text{-}B\}_n$ "thermoplastic elastomers") and soft-soft block copolymers have been prepared and studied.

PHASE SEPARATION AND MORPHOLOGY

Homopolymer Blends

Homopolymer blends displaying even slight structural difference generally exhibit discrete two phase morphology. In order to achieve complete miscibility, basic thermodynamic principles (eq. (1)) require a negative value of the Gibbs free energy.

$$\Delta G = \Delta H - T\Delta S \qquad (1)$$

where ΔH = enthalpy of mixing
ΔS = entropy of mixing
T = absolute temperature

The detailed principles surrounding the thermodynamic analysis of phase separation in polymers has been treated elsewhere (ref. 38,39) and will not be repeated here. However, recent important studies related to polymer-polymer solubility such as the two-component solubility parameter approach by Shaw (ref. 40), the adaptation of Flory's equation of state thermodynamics by McMaster (ref. 41,42), and the solvent probe techniques discussed by Kwei (ref. 43) and Olabisi (ref. 44) are considered major advances and should be consulted.

In a typical polymer mixture, the morphology consistently varies as a function of the composition. Generally, in the 0.30 to 0.70 volume fraction range, both components can exhibit some degree of phase continuity. Geometric considerations require that components present at <0.30 volume fraction exist as dispersed phases.

Block Copolymers

The architecture of block copolymers can be varied from simple structures (i.e., AB) to tri- (i.e., ABA) and to multiple sequence blocks [i.e., $(AB)_n$]. The existence of covalent bonds clearly imposes a restriction to phase separation due to a decrease in the entropy caused by configurational considerations.

Two basic theories of microphase separation in block copolymers have been developed by Meier (ref. 45-47) and Krause (ref. 48). Both theories rely heavily on Flory's interaction parameter χ_{AB} and hence are somewhat limited to non-polar polymer systems where only dispersive interactions are important.

By using the simplest case of an AB block copolymer, Meier (ref. 45) established the thermodynamic criteria for domain formation. Meier calculated that higher block molecular weights were required for phase separation in a copolymer than in simple homopolymer blends. This theory predicted that in the case of a styrene-butadiene AB block copolymer, phase separation would occur when the polybutadiene block M_w is >50,000 and the polystyrene block M_w is >5,000 to 10,000. The most stable domain structure was also considered as a

function of block molecular weight (or composition). It was shown that the predicted spherical domains existed as the preferred morphology at low A block M_w (e.g., $M_A/M_B < .25$). When the ratio of $M_A/M_B > .30$ lamellar structure was favored. Cylindrical domains were predicted in the intermediate region. These predictions have qualitatively been shown to be correct via electron microscopy and small angle x-ray studies.

Note, however, that block copolymers can display various morphologies dependent upon the method of preparation. This is particularly true in solvent-cast systems where the solvent can be preferentially absorbed in one phase at the point of phase separation. The resultant morphology was theoretically treated by Meier (ref. 47) for block copolymer-solvent systems where it was emphasized that the morphology in the solvent free block copolymer will probably be fixed in a nonequilibrium state.

A different approach, which is strictly thermodynamic and not concerned with morphology, was developed by Krause (ref. 48). The critical interaction parameter $(\chi_{AB})_{cr}$ was related to the number of blocks per molecule, block molecular weight, homopolymer concentration, and component block concentration.

Experimental data on poly(α-methylstyrene)-polystyrene AB block copolymers (ref. 49,50) and the corresponding homopolymer blends has shown that phase separation occurs in homopolymer blends but that one phase behavior is observed in a block copolymer where the block molecular weights were greater than those of the homopolymers.

Krause's theoretical treatment also considers the important case where crystallization is a mode of phase separation.

TRANSITIONAL BEHAVIOR

Amorphous Transitions

Above certain critical block molecular weights, block and graft copolymers exhibit microphase separation. Exceptions can occur for blocks with similar polar and dispersive forces and/or specific interactions. The determination of phase behavior is commonly accomplished via modulus-temperature measurements, mechanical loss data and/or thermal analysis (i.e., differential scanning calorimetry).

Examples of phase separated systems include Bisphenol A polycarbonate-polysiloxane (ref. 31), polysulfone-polysiloxane (ref. 51) and polystyrene-polydiene (ref. 21) block copolymers. Single amorphous phase block copolymers (as determined by the existence of a single Tg intermediate between the constituents) include polystyrene-poly(α-methylstyrene) (ref. 49,50) and polysulfone-Bisphenol A polycarbonate (ref. 52).

The magnitude of the respective transitions has been shown to be influenced by the method of preparation. Casting from different solvents leads to

morphological changes and hence continuous structure variation. Examples of this dependence have been shown for polymethyl methacrylate-grafted-natural rubber (ref. 53) and polysulfone-polydimethyl siloxane block copolymer (ref. 51). Mechanical loss-temperature data (ref. 51) illustrates this feature for polysulfone-polydimethyl siloxane block copolymer.

Mechanical deformation has also been observed to yield changes in transitional characteristics. Canter (ref. 54) observed that pre-stressing styrene-diene block copolymers sharpened the polystyrene transition with a resultant lowering of modulus between the constituent Tg's.

In cases of limited solubility, sharp microphase separation may not occur, and the characteristic Tg's may be slightly shifted and, indeed, new intermediate transitions may emerge. This was observed by Beecher et al. (ref. 55) for styrene-butadiene block copolymers cast from different solvent systems. It is important to point out that in well phase separated block copolymers the Tg will show a predictable dependence on block molecular weight. Such behavior was observed for polysiloxane block copolymers for which the hard blocks were either polysulfone (ref. 51) or Bisphenol A polycarbonate (ref. 31). Similar dependence of Tg on molecular weight was reported for both systems (with appropriate correction for infinite M_w Tg's).

In the case of single phase block copolymers, Tg values intermediate between the infinite molecular weight Tg's are observed. This behavior was displayed by the 5000/5000 block M_w Bisphenol A polycarbonate-polysulfone block copolymer (ref. 52).

Crystalline Transitions

Crystallinity provides another means for promoting phase separation in block and graft copolymers (ref. 48). Thermoplastic polyurethanes are the earliest example of block copolymers in which phase separation occurs via development of crystallinity. Important differences in crystallinity and melting point are noted for block vs. random copolymers. The principle was illustrated in polyester block copolymers investigated by Charch and Shivers (ref. 29). In random copolymers a rapid decrease of the melting point (i.e., crystallinity) is observed with comonomer incorporation. This is much less pronounced in block systems because of the long sequences. Similar results have been reported for polyamide structures.

Other examples of copolymers containing crystalline segments include polysulfone-nylon 6 (ref. 56-58), polyethylene-polypropylene (ref. 59), and poly(butylene terephthalate)-poly(tetrahydrofuran) (ref. 60). In the polysulfone-nylon 6 block copolymer, the degree of crystallinity and melting point of the polyamide block are virtually the same as those of the nylon homopolymer.

One additional feature of the crystalline transition behavior is worthy of mention. Segments which are essentially amorphous in the isotropic undeformed

state may develop crystallinity upon deformation. This phenomenon is commonly referred to as stress-induced crystallization and its result is to produce excellent ultimate properties. Maintenance of elastomeric behavior (e.g., recovery) requires that stress-induced crystallization disappear upon stress removal. Rubbery segments exhibiting this behavior include certain polyether and polyester sequences (i.e., poly(tetrahydrofuran) and poly(ε-caprolactone)) present in thermoplastic polyurethanes. A recently commercialized material utilizing this principle is the poly(butylene terephthalate)-poly(tetrahydrofuran) $\{AB\}_n$ block copolymer (ref. 32,60).

Mechanical and Rheological Properties

One of the most important characteristics of elastomeric block copolymers is their ability to display rubbery properties while still retaining thermoplastic processability. The type of materials exhibiting this behavior are comprised of hard segments (high Tg and amorphous), soft segments (low Tg and amorphous), arranged in an A-B-A or an $\{A-B\}_n$ architecture. Phase separation of the hard block results in physical domains serving as tie points or "physical" networks which are similar to covalent bonds present in a crosslinked elastomer. The microphase separation of the hard segments results in highly dispersed rigid particles which reinforce the elastomeric matrix in a manner similar to carbon black reinforced vulcanizates. Judicial choice of the hard block content, block copolymer architecture, and a high degree of block purity is required to attain useful ultimate properties.

AB and BAB elastomeric block copolymers (A = hard block) have been shown to have inferior tensile strength and permanent set properties compared to ABA and $(AB)_n$ (n>1) systems (ref. 19,21). A new class of block copolymers termed radial block copolymers combine excellent ultimate properties with easier processing than their linear counterparts (ref. 61-63).

Elastomeric block copolymers, based on the thermoplastic polyurethanes and the polyester-polyether block copolymer exhibit high tensile strength (>5000 psi) and excellent wear and abrasion resistance. These properties are attributed to the ability of the soft block of these materials to stress-crystallize. The phenomenon can even be visually observed. High extension results in opacity which disappears upon removal of stress. The styrene-diene ABA block copolymers exhibit strengths characteristic of carbon black filled, crosslinked elastomers (~ 2000-3000 psi). Hydrogenated versions of styrene-butadiene (Kraton G) have tensile strengths approaching those of the thermoplastic polyurethanes (~ 5000 psi). This improvement has been suggested to be due to the better phase separation expected with an ethylene/butylene block compared to a polybutadiene block (ref. 64). Moreover, the presence of ethylene sequences in the center block may contribute to stress-induced crystallization.

Block copolymers exhibit a marked dependence of mechanical properties on the method of sample preparation. Variations in casting solvent (from an A block preferred solvent to a B block preferred solvent) bring about significant

variations in the stress-strain behavior.

If the solvent is preferentially dissolved in the "soft" block phase, lower modulus, "more elastomeric" materials are obtained. It must be pointed out that the resultant morphology of solvent cast samples will generally be in a nonequilibrium state as has been theoretically discussed by Meier (ref. 47). This behavior is not unique to block copolymers. In fact, the initial experiments showing this effect were conducted with a polymethyl methacrylate-natural rubber graft copolymer (ref. 53).

The modulus-composition behavior for polymer-polymer blends is generally quite similar to that of their block or graft copolymer counterparts. However, the ultimate properties of the block and graft copolymers are generally superior due to the excellent interfacial adhesion obtained by the imposition of a covalent bond at the phase boundary. Examples where block copolymers exhibited ultimate properties superior to their counterpart homopolymer blends include polysulfone-nylon 6, polystyrene-polysiloxane, and, of course, the polystyrene-polydiene ABA block copolymers.

Modulus-composition data can be used to assess the continuous phase of block copolymers. Kerner's analysis for a two-phase system has been used to determine the continuous-phase contribution of the respective components of the polysulfone-polydimethyl siloxane block copolymers (ref. 51). It was shown that the predicted continuous structure based on modulus data agreed well with a similar analysis derived from permeability data.

An interesting study of the behavior of styrene-butadiene ABA block copolymers was presented by Matsuo and Sagaye (ref. 65). Samples prepared by compression molding above 50 wt.% styrene gave superior strengths whereas samples prepared by casting from cyclohexane (a poor polystyrene solvent) were stronger below 50 wt.% styrene. Morphological characterization of the continuous-phase structure agreed with strength data.

A characteristic feature of block copolymers is that the melt viscosity is higher than that which would be expected from the homopolymer constituents. This has been attributed to the fact that the network structure exists above the major transitions of the constituent blocks (ref. 66-68).

Kraus and Gruver (ref. 67) noted that even at low shear rates non-Newtonian behavior was observed and a temperature-shear rate superposition of the data was not possible. At high frequencies, Arnold and Meier (ref. 68) found that typical thermoplastic behavior was observed, indicating that the network domains can be broken down.

Matzner, et al (ref. 66) hypothesized that the melt viscosity was related to the difference in solubility parameter between the constituent blocks. In a series of polydimethyl siloxane based block copolymers, it was shown that processability improved (melt viscisity decreased) as the hard block solubility parameter approached that of the soft block.

Recently, radial or star-shaped block copolymers have been shown to display lower melt viscosity while at the same time maintaining equal or superior mechanical behavior (ref. 61-63). Styrene-diene radial block copolymers have been cited as examples where these characteristics are achieved (ref. 61-63).

Transport Behavior

While mechanical properties of block copolymers have been investigated in detail, other physical properties have received less attention (i.e., electrical, thermal conduction, and permeability). The permeability of siloxane block copolymers is of particular interest (i.e., membranes for blood oxygenators) since high permeability (as well as penetrant selectivity) can be attained while permitting enhanced film properties (stiffness and strength) over those of crosslinked silicone rubber.

An example of this behavior is the permeability of polysulfone-polydimethyl siloxane block copolymers studied by Robeson et al (ref. 51,69). Maxwell's equation was utilized to determine the continuous-phase structure from O_2 permeability data. The continuous-phase structure determined from O_2 permeability data agreed well with modulus data determinations thus lending credence to both approaches. It was hypothesized that once the continuous-phase structure was determined (i.e., from modulus or permeability data) other transport properties could then be calculated (i.e., thermal conductivity or electrical conductivity) from values for the homopolymer constituents.

Blending Phenomena

Inoue et al carefully studied the addition of homopolymer constituents to an A-B styrene-isoprene block copolymer (ref. 70). It was concluded that if the homopolymer molecular weight was greater than that of the constituent block the homopolymer will form a discrete phase in a blend with the block copolymer. In studies of polysulfone-nylon 6 block copolymers, a desirable average of mechanical properties was obtained over a broad composition range of blends comprising either polysulfone or nylon 6 and the block copolymer (ref. 56-58). However, when both homopolymers were added to the block copolymer, brittle materials were obtained. The brittle behavior was believed to be the result of poor interfacial adhesion between the constituent homopolymers thus yielding a flaw in the composite.

Most blend studies have dealt with phase separated block copolymers. However, an investigation of blends of homopolymer constituents with the one phase α-methylstyrene-styrene AB block copolymers has been reported and is of considerable interest (ref. 49). At similar molecular weight, poly(α-methylstyrene) addition to the block copolymer produced a single phase system, whereas polystyrene addition resulted in a two phase system (polystyrene homopolymer and block copolymer phases). A ternary blend of the block copolymer and the homopolymer constituents resulted in a polystyrene-rich phase and a

poly(α-methylstyrene) - block copolymer phase. Blends of block and graft copolymer with rigid homopolymer have been cited in many examples where the impact strength of the rigid polymer is improved.

Applications

Commercial acceptance of block copolymers has centered upon their utility as thermoplastic elastomers. The primary advantages of the thermoplastic systems vis-a-vis their chemically crosslinked analogs include fast cycle injection moldability, reuse of scrap, transparency, color selections possible (e.g., no carbon black required for reinforcement), fabrication via solvent casting, etc. Large volume markets such as automotive tires cannot be penetrated due to property limitations such as high temperature compression set or poor solvent/oil resistance. Therefore, most of the market penetration has been directed toward mechanical goods and specialty products. These areas have shown dramatic growth in the last decade and this trend has been projected to continue in the future.

Thermoplastic polyurethanes were the first commercial thermoplastic elastomers. They have emerged as the major block copolymer used in demanding applications where excellent strength, wear, and oil resistance are required. Typical end uses include footwear, automotive bumpers and facia, adhesives and coatings, etc. Novel applications such as snowmobile treads and horseshoes have also been developed. Thermoplastic polyurethanes are available from a number of suppliers.

Polyester-polyether block copolymers based on poly(butylene terephthalate) and poly(tetrahydrofuran) are now commercially available under the trade name Hytrel. This material has property-profile characteristics which are similar to that of the thermoplastic polyurethanes. It has been reputed to display better processing stability and low temperature properties.

The styrene-diene-styrene ABA block copolymers have shown promising growth in a variety of end uses since their introduction in 1965. They have found applications in footwear, adhesives, sporting equipment, and general purpose rubber goods (e.g., toys).

Second generation ABA materials wherein the center polybutadiene block has been hydrogenated to yield a saturated ethylene/butylene structure have now been commercialized under the name of Kraton G (ref. 64). Obviously, this transformation results in vastly improved thermal oxidative and weather resistant properties. Such improvements should extend the end-use markets into areas where the precursor materials were marginal or unacceptable (e.g., automotive exterior parts).

Styrene-diene A-B block copolymers have been commercial for many years and have been utilized in various crosslinked applications. They have been shown to impart improved low temperature flexibility, increased hardness, and improve

processability in blends with other conventional elastomers.

Rigid, high styrene-butadiene radial block copolymers have been recently introduced under the trade name of K-Resins (ref. 62,63). These materials are transparent, relatively tough, and have been directed towards clear packaging applications.

Siloxane block copolymers wherein polydimethyl siloxane soft segments are combined with either polystyrene (ref. 71) or polycarbonate (ref. 31) hard segments have been proposed in membrane applications such as blood oxygenators. Polysiloxane containing materials such as these offers the possibility of achieving high oxygen and carbon dioxide permeabilities while at the same time displaying superior mechanical properties. Moreover, since external reinforcing fillers and crosslinking additives are not required, fabrication of thin pin-hole-free films is facilitated.

One of the oldest, but still important application areas for block copolymers is in nonionic surfactants. For example, polyurethane-foam stabilizers comprise alkylene oxide-silicone block or graft copolymers. The polyether segment is soluble in the polyurethane. The silicone block is phase separated and is believed to reside at the gas-urethane interface where it is of major importance in the production of uniform foam cell structures (ref. 72).

REFERENCES

1. Noshay, A. and McGrath, J. E.: Block Copolymers: Overview and Critical Survey. Academic Press, in press (1976).

2. Morton, M.: MTP (Med. Tech. Publ. Co.), Int. Rev. Sci.: Phys. Chem. Ser. One, Edited by C. E. H. Bawn, Buttersworth, London (1972).

3. Morton, M.: Encylopedia of Polymer Technology, 15, 508 (1971).

4. Ceresa, R. J.: Encyclopedia of Polymer Technology, 2, 485 (1964).

5. Symposium on Block Copolymers. J. Polymer Sci., Part C, No. 26 (1969).

6. Block Polymers. Ed. by S. L. Aggarwal, Plenum Press (1970).

7. Colloidal and Morphological Behavior of Block and Graft Copolymers. Ed. by G. E. Molau, Plenum Press (1971).

8. Estes, G. M.; Cooper, S. L.; and Tobolsky, A. V.: J. Macromol. Sci., Revs. Macromol. Chem., C4(2), 313 (1970).

9. Sagamore Conference on Block and Graft Copolymers. Sept. 5-8, 1972; J. J. Burke and V. Weiss, Editors, Syracuse University Press, 1973.

10. Kawai, H.; Soen, T.; Inoue, T.; Ono, T.; and Uchida, T.: Progress in Polymer Sci., Japan, 4, K. Imahori, Editor, Kodansha Ltd., (1972).

11. Block Copolymers. D. C. Allport and W. H. Janes, Editors, Halstead Press, New York (1972).

12. Holden, G.: in Block and Graft Copolymerization, p. 99, ed. by R. J. Ceresa, John Wiley & Sons, New York (1973).

13. Juliano, P. C.: New Silicone Elastoplastics. General Electric Co. Report No. 74 CRD 172, Presented at U. of Detroit Conf. Series, Aug. 1974.

14. Zelinski, R. P. and Childers, C. W.: Rubber Reviews, 41, 161 (1968).

15. Kennedy, J. P.: Recent Advances in Polymer Blends, Grafts and Blocks, ed. by L. H. Sperling, Plenum Press, 1974, p. 3.

16. Szwarc, M.; Levy, M.; and Milkovich, R.: J. Amer. Chem. Soc., 78, 2656 (1956).

17. Milkovich, R.: S. African Pat. No. 280, 712 (1963). Assigned to Shell Oil Company.

18. Morton, M.; McGrath, J. E.; and Juliano, P. C.: Presentation at ACS Division of Rubber Chemistry, Montreal, May 4, 1967.

19. McGrath, J. E.: Ph.D. Thesis, Akron University, Akron, Ohio (1967).

20. Morton, M.; McGrath, J. E.; and Juliano, P. C.: Presentation at Symposium of Block Copolymers, Pasadena, California, June 5, 1967.

21. Holden, G.; Bishop, E. T.; and Legge, N. R.: The Proceedings of the International Rubber Conf., p. 287, McLaren and Sons, London, 1967.

22. Hendus, H.; Illers, K. H.; and Ropte, E.: Kolloid - Z - Z, Polymere, 216, 110 (1967).

23. Fetters, L. J.: J. Elastoplastics, 4, 32 (1972).

24. Angelo, R. J.; Ikeda, R. M.; and Wallach, M. L.: Polymer, 6, 141 (1965).

25. O'Malley, J. J.; Crystal, R. G.; and Erhardt, P. F.: Block Polymers, ed. by S. L. Aggarwal, p. 163, Plenum Press (1970).

26. Bostick, E. E.: Block Polymers, ed. by S. L. Aggarwal, p. 237, Plenum Press (1970).

27. Szwarc, M.: Carbanions, Living Polymers and Electron-Transfer Processes, Interscience, New York (1968).

28. Schollenberger, C. S.; Scott, H.; and Moore, G. R.: Rubber World, 137, 549 (1958).

29. Charch, W. H. and Shivers, J. C.: Textile Research J., 29, 536 (1959).

30. Advances in Polyurethane Technology. Ed. by J. Burst and H. Gudgeon, Interscience (1968).

31. Kambour, R. P.: Block Polymers, ed. by S. L. Aggarwal, p. 263, Plenum Press (1970).

32. Witsiepe, W. K.: Polymerizations Reactions and New Polymers, p. 39, ed. by N. A. J. Platzer, Adv. Chem. Serv., No. 129, American Chem. Soc. (1973).

33. Noshay, A.; Matzner, M.; and Merriam, C. N.: J. Polymer Sci., A-1, 9, 3147 (1971).

34. Noshay, A.; Matzner, M.; and Williams, T. C.: Ind. and Eng, Chem. Prod. Res. and Dev. 12 (4) 268 (1973).

35. Matzner, M.; Noshay, A.; Robeson, L. M.; Merriam, C. N.; Barclay, R., Jr.; and McGrath, J. E.: Polymer Symp. 22, 143 (1973).

36. Schollenberger, C. S.: Polyurethane Technology, ed. by P. F. Bruins, p. 197, Interscience, New York (1969).

37. Harrell, L. L.: Macromolecules, 2, 607 (1969).

38. Flory, P. J.: Principles of Polymer Chemistry, Cornell University Press, Ithaca, New York (1953).

39. Scott, R. L.: J. Chem. Phys., 17, 279 (1949).

40. Shaw, M. T.: J. Appl. Polymer Sci., 18, 449 (1974).

41. McMaster, L. P.: Macromolecules, 6, 760 (1973).

42. McMaster, L. P.: Polymer Preprints, 15, No. 1, 254, 1974; and in Copolymers, Polyblends and Composites, Advances in Chem., Series No. 142, N. A. Platzer, Editor, ACS (1975).

43. Kwei, T. K.; Nishi, T.; and Roberts, R. F.: Macromolecules, 7, 667 (1974).

44. Olabisi, O.: Macromolecules, 8, 316 (1975).

45. Meier, D. J.: J. Polymer Sci., Part C, 26, 81 (1969).

46. Meier, D. J.: Polymer Preprints, 11, (2), 400 (1970).

47. Meier, D. J.: Block and Graft Copolymers, Syracuse University Press (1973).

48. Krause, S. J.: 19th Sagamore Conference on Block and Graft Copolymers, Sept. 5-8, 1972. Published in Block and Graft Copolymers, Syracuse University Press (1973).

49. Robeson, L. M.; Matzner, M.; Fetters, L. J.; and McGrath, J. E.: Recent Advances in Blends, Blocks and Grafts, p. 281, L. H. Sperling, Editor, Plenum Press, New York (1974).

50. Baer, M.: J. Polymer Sci., Part A, 2, 417 (1964).

51. Robeson, L. M.; Noshay, A.; Matzner, M.; and Merriam, C. N.: Die Angewandte Makromolecules, Chemie, 29/30, 47 (1973).

52. Matzner, M.; Barclay, R., Jr.; Robeson, L. M.; and McGrath, J. E.: 8th Regional ACS Meeting, Akron, Ohio, May 1976; J. Poly. Sci., Part C (in press) 1976.

53. Merrett, F. M.: J. Polymer Sci., 24, 467 (1957).

54. Canter, N. H.: J. Polymer Sci., Part A-2, 6, 155 (1968).

55. Beecher, J. F.; Marker, L.; Bradford, R. D.; and Aggarwal, S. L.: J. Polymer Sci., C26, 117 (1969).

56. McGrath, J. E.; Robeson, L. M.; and Matzner, M.: Polymer Preprints 14 (2), 1032 (1973).

57. McGrath, J. E.; Robeson, L. M.; and Matzner, M.: Polymer Blends, Grafts and Blocks, p. 195, Edited by L. H. Sperling, Plenum Press, New York (1974).

58. McGrath, J. E. and Matzner, M.: U. S. 3,655,822 (to Union Carbide Corporation) (1972).

59. Kontos, E. G.; Esterbrook, E. K.; and Gilbert, R. D.: J. Polymer Sci., 61, 69 (1962).

60. Hoeschele, G. K. and Witsiepe, W. K.: Angew, Makromol. Chem. 29/30, 267 (1973).

61. Bi, L. K. and Fetters, L. J.: Macromolecules, 8, 98 (1975); Macromolecules, in press (1976).

62. Foclor, L. M.; Kitchen, A. G.; and Biard, C. C.: Coatings and Plastics Preprints, 34, No. 1. 130 (1974).

63. Kitchen, A. G. and Szalla, F. J.: U. S. Patent No. 3,639,517 (1972) Assigned to Phillips Petroleum Co.

64. Kraton-G. Shell Chem. Co. Product Literature.

65. Matsuo, M. and Sagaye, S.: Polymer Physics Ed., 12, 2153 (1974).

66. Matzner, M.; Noshay, A.; and McGrath, J. E.: Polymer Preprints, 14, No. 1, 68 (1973).

67. Kraus, G. and Gruver, J. T.: J. Appl. Polymer Sci., 11, 2121 (1967).

68. Arnold, K. R. and Meier, D. J.: J. Appl. Polymer Sci., 14, 427 (1970).

69. Matzner, M.; Robeson, L. M.; Noshay, A.; and McGrath, J. E.: Encyloped. Polym. Sci. and Technol., in press (1976).

70. Inoue, T.; Soen, T.; Hashimoto, T.; and Haumi, H.: Macromolecules, 3, 87 (1970).

71. Saam, J. C. and Fearon, F. W. G.: I and EC Prod. Res. Develop., 10, 10 (1971).

72. Schwarz, E. G.: Appl. Polymer Symposia, 14, 71 (1970).

A CRITICAL REVIEW OF THE EFFECTS OF MEAN AND COMBINED STRESSES ON THE FATIGUE LIMIT OF METALS

R. E. Little
The University of Michigan-Dearborn

SUMMARY

The effects of mean and combined stresses on the fatigue limit of metals are critically re-examined. Data are presented which contradict the widely used fatigue limit analyses. Further study of basic fatigue mechanisms is required.

INTRODUCTION

Ten years ago it was widely accepted that fatigue cracks initiate in metals as a consequence of alternating shear deformations and propagate as the consequence of alternating normal deformations. However, scanning electron micrographs now indicate that fatigue cracks can initiate in the absence of slip, apparently as a consequence of local inhomogeneous strains and the associated local stresses (ref. 1). Thus, even for simple uniaxial states of cyclic stress, there remains considerable uncertainty regarding the respective roles of normal and shear stresses in the fatigue crack initiation process.

The discussion in this paper is restricted to fatigue limits so that cyclic stresses may be assumed to be proportional to cyclic strains. This assumption is almost universally employed in fatigue limit analyses even though in certain cases, depending on the material and on the mode of loading, the cyclic yield strength may lie well below the fatigue limit (ref. 2).

Engineering analyses of the effects of mean and combined stresses on the fatigue limit of metals may be classified as elementary and advanced. Elementary analyses generally combine an empirical mean stress relation with a common strength of materials failure criterion. Advanced analyses, on the other hand, are generally based on a proposed failure criterion that includes both mean and combined stresses.

SYMBOLS

A	parameter (material constant)
σ	normal stress
τ	shear stress

Subscripts:

a	alternating (allowable)
eqv	equivalent
m	mean
max	maximum
mr	maximum range
o	octrahedral
t	tensile
TU	true ultimate tensile strength
U	ultimate tensile strength
W	fatigue limit (Wohler)
Y	tensile yield strength
ϕ	orientation of critical plane
θ	direction in critical plane

ELEMENTARY FATIGUE LIMIT ANALYSES

Empirical Mean Stress Relations

The following equations summarize and extend the widely used empirical mean stress relations:

Goodman $$\left(\frac{\sigma_a}{\sigma_W}\right) = 1 - \left(\frac{\sigma_m}{\sigma_U}\right) \quad (1)$$

Little $$\left(\frac{\sigma_a}{\sigma_W}\right) = 1 - \left(A\frac{\sigma_m}{\sigma_U}\right) \quad (2)$$

Soderberg $$\left(\frac{\sigma_a}{\sigma_W}\right) = 1 - \left(\frac{\sigma_m}{\sigma_Y}\right) \quad (3)$$

Fischer $$\left(\frac{\sigma_a}{\sigma_W}\right) = 1 - \left(A\frac{\sigma_m}{\sigma_Y}\right) \quad (4)$$

Nishihara $$\left(\frac{\sigma_a}{\sigma_W}\right) = 1 - \left(\frac{\sigma_m}{\sigma_{TU}}\right) \quad (5)$$

Gerber $$\left(\frac{\sigma_a}{\sigma_W}\right) = 1 - \left(\frac{\sigma_m}{\sigma_U}\right)^2 \quad (6)$$

General $$\left(\frac{\sigma_a}{\sigma_W}\right) = 1 - \left(\frac{\sigma_m}{\sigma_U}\right)^A \quad (7)$$

Ellipse $$\left(\frac{\sigma_a}{\sigma_W}\right)^2 = 1 - \left(\frac{\sigma_m}{\sigma_U}\right)^2 \quad (8)$$

General $$\left(\frac{\sigma_a}{\sigma_W}\right)^{A_1} = 1 - \left(A_2\frac{\sigma_m}{\sigma_U}\right)^{A_3} \quad (9)$$

General $$\left(\frac{\sigma_a}{\sigma_W}\right)^{A_1} = \left(1 - A_2\frac{\sigma_m}{\sigma_U}\right)^{A_3} \quad (10)$$

General $$\left(\frac{\sigma_a}{\sigma_W}\right)^{A_1} = A_2 + (1 - A_2)\left[1 - \left(A_3\frac{\sigma_m}{\sigma_U}\right)^{A_4}\right] \quad (11)$$

General $$\left(\frac{\sigma_a}{\sigma_W}\right)^{A_1} = A_2 + (1 - A_2)\left[1 - A_3\frac{\sigma_m}{\sigma_U}\right]^{A_4} \quad (12)$$

The Gerber and Goodman relations were based on the pioneer axial load mean stress fatigue limit data for mild steels by Wohler. Gerber's relation is strictly empirical, whereas Goodman's relation was originally theoretical. It was widely accepted around the turn of the century that a live or dynamic load causes a stress that is twice as large as the stress caused by a dead or static load. It was also believed that the minimum cyclic load corresponds to the static load and that the range of cyclic load from minimum to maximum corresponds to the dynamic load. Accordingly, Goodman argued that the fatigue limit is reached when the minimum stress plus two times the range of stress equals the tensile ultimate strength. The predicted fatigue limit for mild steels, one-third of the tensile ultimate strength (refer fig. 1), agreed quite well with Wohler's data. Apparently this agreement and the simplicity of the relation led to its widespread use -- which continues to the present (with certain

modifications to be discussed). However, it was quite obvious even then that Goodman's relation did not agree with Wohler's data for finite fatigue lives. Moreover, it soon became apparent that not all materials exhibited fatigue limits equal to one-third of the ultimate tensile strength.

By the early 1920's there were sufficient fatigue limit data available for various materials to indicate that the ratio of the fatigue limit to the ultimate tensile strength depends on the material tested. Accordingly, the Goodman relation was modified to agree with the data. Approximately ten years later design influence led to a second modification; namely, limiting the maximum cyclic stress to a value less than the static tensile yield strength. The resulting modified-modified Goodman diagram is displayed in figure 1.

Ideally, tests conducted to investigate the effect of mean stress on fatigue limits pertain to various modes of loading, e.g., to bending, torsion, and combined bending and torsion. However, axial load tests with tensile mean stresses continue to dominate the scope and perspective of elementary fatigue limit analyses, perhaps because of the simplicity of the test and the ostensive design application of the data. This dominance, whatever the reason, causes several problems in analysis and interpretation of fatigue limits. For example, cyclic plastic deformations can become excessively large when testing with high mean stresses. (The specimen can undergo a change in area of 8 to 10% or more.) Moreover, the large cyclic plastic deformations associated with high mean stresses can, but need not, cause marked reductions in the fatigue limit (ref. 3). Unless the low and high mean stress fatigue limit data are separated, the reduced fatigue limits at high mean stresses may tend to give the erroneous impression that the Gerber relation accurately describes the aggregate data.

The Gerber and Goodman relations set the pattern for most subsequent mean stress relations. These relations are still being rationalized by alleging incorrectly that the allowable alternating stress must equal zero when the mean stress is equal to the ultimate tensile strength. This allegation is naive. The allowable stress diagram is three-dimensional, with the third axis out of the plane of the paper representing fatigue life, but is conventionally presented in the misleading two-dimensional format given in figure 1. Not only do the static and cyclic yield strengths differ markedly, the maximum cyclic stresses associated with the fatigue limit at high mean stresses may even exceed the static ultimate tensile strength. (The corresponding maximum cyclic stresses associated with the bending fatigue limit at high mean stresses may even exceed one and one-half times the static ultimate tensile strength.) The real purpose of plotting a static strength along the abscissa of an allowable or working stress diagram is merely to describe the fatigue failure locus in terms of a readily available material-dependent parameter.

The engineering emphasis on the fatigue limit of mild steels with tensile mean stresses has in effect promoted a set of elementary analyses which virtually ignore the remaining mean stress data, e.g., the contradictory data for cast iron with high compressive mean stresses displayed in figure 2 (ref. 4). These data cannot adequately be described by any of the empirical mean stress relations (1) through (12). Rather, the portion of the allowable stress

diagram pertaining to very high compressive mean stresses may indeed be quite complex, particularly if tensile residual stresses introduced by cyclic loading have a significant effect on crack initiation.

Strength of Materials Failure Criteria

The ratio of the torsional to bending fatigue limits depends on the material and its thermal-mechanical processing. Thus, elementary fatigue limit analyses usually include an impirical factor to correct for "anisotropy." For example, the modified principal shear stress criterion is

$$\tau_{eqv,a} = \frac{1}{2}[\sigma_a^2 + (\frac{\sigma_W}{\tau_W})^2 \tau_a^2]^{1/2} \tag{13}$$

Note that when $\sigma_a = 0$ and $\tau_W = \sigma_W/2$, $\tau_{eqv,a} = \tau_a$. Otherwise, $\tau_{eqv,a}$ is greater than or less than τ_a depending on whether τ_W/σ_W is less than or greater than 1/2. The other common strength of materials failure criteria are modified in a similar manner.

Theoretical fatigue limit analyses usually pertain to the plane of fatigue crack initiation. The primary issue is what combination of normal and shear stresses acting on this plane should be used to predict the influence of mean stress. For example, the elementary hypothesis that the fatigue limit corresponds to the amplitude of the shear stress acting on the plane of maximum range of shear stress ϕ_{mr}, modified by the magnitude of the mean shear stress acting on that plane, gives

$$\tau_{\phi_{mr},a} = A_1 + A_2 \tau_{\phi_{mr},m} \tag{14}$$

Although this criterion accurately describes certain fatigue limit data by appropriate selection of parameters A_1 and A_2, it does not distinguish adequately between tensile and compressive mean stresses to have general application. The complementary criterion

$$\tau_{\phi_{mr},a} = A_1 + A_2 \sigma_{\phi_{mr},m} \tag{15}$$

overcomes the objection to criterion (14), but has not been strongly advocated in the literature. The most widely accepted elementary criterion is based on the octrahedral shear stress, viz.,

$$\tau_{o,a} = A_1 + A_2 \sigma_{o,m} \tag{16}$$

Sines (ref. 5) shows that criterion (16) predicts the absence of a torsional mean stress effect on the fatigue limit under alternating torsion and under alternating bending, and also predicts that a tensile mean stress decreases the torsional fatigue limit whereas a compressive mean stress increases it. These predictions agree with the mean stress data examined by Sines. However, other data indicate that a mean torsional stress decreases the fatigue limit under alternating torsion (cast iron, aluminum, alloy steel) and under alternating bending (cast iron). Moreover, Nishihara's data (ref. 6) for both 0.10C (fig. 3) and 0.34C plain carbon steels indicate no decrease in the fatigue limit caused by superimposing tensile mean stress on alternating torsional stress.

Nishihara's data for a 0.72C plain carbon steel are also included in figure 3 to show that the effect of mean stress differs for a given mode of loading, depending on the material tested. Accordingly, advanced analyses generally involve failure criteria with parameters which permit the effect of mean stress to vary markedly for a given mode of loading, depending on the values assigned to certain material-dependent parameters.

ADVANCED FATIGUE LIMIT ANALYSES

Although several advanced fatigue limit analyses appear in the literature, e.g.,

Findley
$$\tau_{\phi,a} = A_1 + A_2\sigma_{\phi,max} \tag{17}$$

Stulen and Cummings
$$\sigma_{1,a} - A_1\sigma_{3,a} = A_2 + A_3\sigma_{1,m} \tag{18}$$

Nishijima
$$|\tau_{\phi,a}| = A_1(\sigma_W - \sigma_{\phi,t}) \tag{19}$$

(refs. 7 through 9 respectively), none of these criteria adequately describe typical axial load data for both mild steels and cast irons. In fact, it appears that only a fatigue limit analysis with multiple failure criteria (i.e., different criteria for different modes of loading and ranges of cyclic stress) will suffice to describe all data accurately. Even then, reliable prediction of fatigue limits is not a simple matter. For example, the multiple criterion analysis by Kawada and Kodama (ref. 10)

$$A_1\sigma_\phi + A_2\tau_\phi + A_3\tau_{\phi,a} = A_4 \tag{20}$$

can be used to describe the axial load data for cast iron and for mild steels (fig. 4), as can the Nishihara and Endo (ref. 11) analysis

$$\sigma_{1,a} - A_1\sigma_{3,a} = A_2 + A_3\sigma_{1,m} \tag{21}$$

but both analyses have shortcomings relative to accurate description of other mean stress data.

CONCLUDING REMARKS

Engineering fatigue limit analyses require several attributes to be reliable. First, the analyses should include both multiple failure criteria and material-dependent parameter values which permit a wide range of response for a given mode of loading. Essentially this means that fatigue limits should be categorized not only in terms of the mode of loading, but also in terms of the material. Moreover, the analyses should pertain to a more general state of cyclic stress where all (constant amplitude) stresses do not necessarily act in phase and at the same frequency. This aspect of fatigue limit analyses is virtually unexplored. Engineering fatigue limit analyses should also be amenable to simple modification to predict the fatigue limit of notched specimens. The primary reason in design for attempting to predict the fatigue limit of unnotched specimens is to obtain baseline data from which to estimate the fatigue limit of notched specimens. In turn, fatigue limit analyses for notched specimens should be amenable to simple modification to predict the fatigue life of specimens under complex stress-time histories, at least in the intermediate to long life domains of cyclic stressing. Further, fatigue limit and fatigue life analyses should be statistical. There is some evidence that the fatigue limit distribution for unnotched specimens is symmetrical, whereas the fatigue limit distribution for notched specimens is skewed (ref. 12). This area needs much more study.

The most urgent problem at present is how to use existing mean and combined stress data for unnotched specimens to predict the behavior of notched specimens. There has been very little progress made in estimating the fatigue limits of notched specimens since the introduction of the notch sensitivity index approximately forty years ago. Understanding the nature of crack initiation and the transition from initiation to propagation is evidently the key to predicting fatigue limits for notched and unnotched specimens.

REFERENCES

1. Wood, W. A.: Four Basis Types of Metal Fatigue. Technical Report 10, Institute for the Study of Fatigue, Fracture and Reliability, The George Washington University, June 1972.

2. Kawamoto, M.; and Nishioka, K.: Safe Stress Range for Deformation Due to Fatigue. Transactions, American Society Mechanical Engineers, Volume 77, 1955, pp. 631-634.

3. O'Connor, H. C.; and Morrison, J. L. M.: The Effect of Mean Stress on the Push-Pull Fatigue Properties of an Alloy Steel. Proceedings, International Conference on Fatigue, IME:ASME, 1956, pp. 102-109.

4. Pomp, A.; und Hempel, M.: Ueber das Verhalten von Gusseisen und Temperguss unter wechselnder Beanspruchung. Mitteilungen, Kaiser-Wilhelm-Institut Eisenforschung, Band XVIII, 1940, pp. 169-204.

5. Sines, G.: Failure of Materials Under Combined Repeated Stresses with Superimposed Static Stresses, NACA TN 3495, 1955.

6. Nishihara, T.; and Kawamoto, M.: A New Criterion for the Strength of Metals under Combined Alternating Stresses. Memoirs, College of Engineering, Kyoto Imperial University, Volume XI, 1944.

7. Findley, W. N.: A Theory of the Effect of Mean Stress on Fatigue of Metals Under Combined Torsion and Axial Load or Bending. Transactions, American Society Mechanical Engineers, Series B, Volume 81, 1959, pp. 301-306.

8. Stulen, F. B.; and Cummings, H. N.: A Failure Criterion for Multi-Axial Fatigue Stresses. Proceedings, American Society Testing Materials, Volume 54, 1954, pp. 822-835.

9. Nishijima, F.: Another Criterion for Endurance Limits of Steel. Proceedings, Third Japan National Congress Applied Mechanics, 1954, pp. 173-177.

10. Kawada, Y.; and Kodama, S.: A Criterion on Fatigue of Metals. Memoirs, Faculty of Technology, The Tokyo Metropolitan University, 1956, pp. 321-329.

11. Nishihara, T.; and Endo, K.: On the Theory of Fatigue Failure of Metals. Technical Report, Engineering Research Institute, Kyoto University, Volume II, 1952, pp. 171-185.

12. Nishijima, S.: Heat-To-Heat Variation of Statistical Fatigue Property for Two Types of Structural Steels. Journal, Society Materials Science, Japan, Volume 25, 1976, pp. 53-60. (In Japanese)

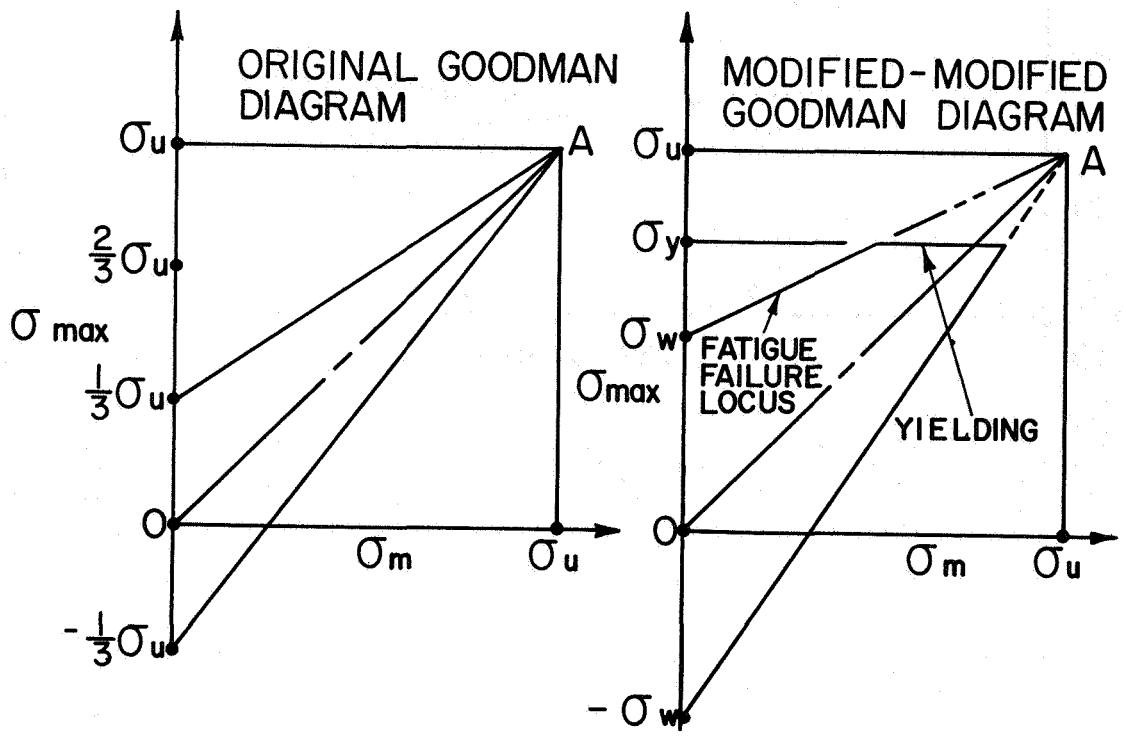

Figure 1.- Original and modified-modified Goodman diagrams plotted on σ_{max}, σ_m coordinates. σ_U = ultimate tensile strength; σ_W = fatigue limit; and σ_Y = tensile yield strength.

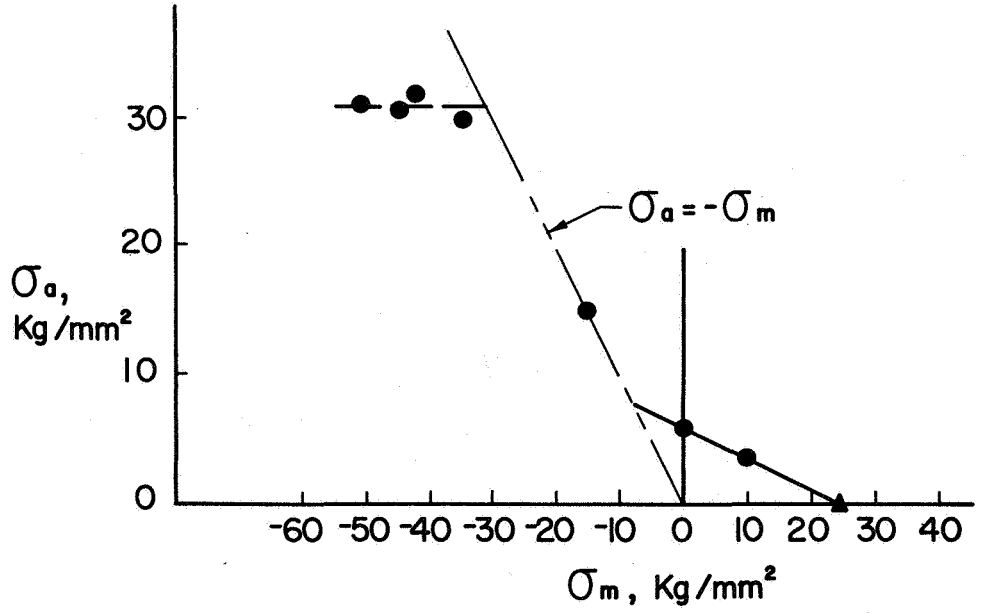

Figure 2.- Pomp and Hempel's axial load mean stress fatigue limit data for grey cast iron (ref. 4).

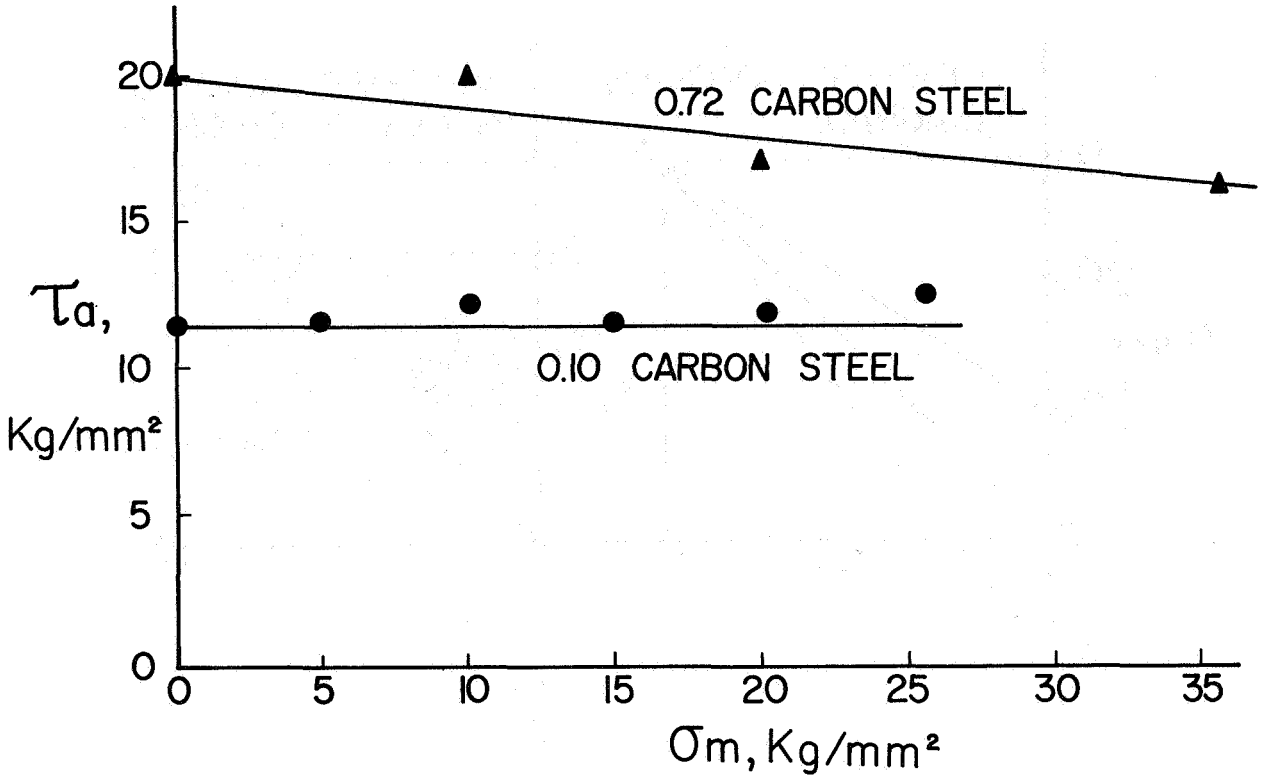

Figure 3.- Nishihara's fatigue limit data for two plain carbon steels subjected to static tension superimposed on alternating torsion (ref. 6).

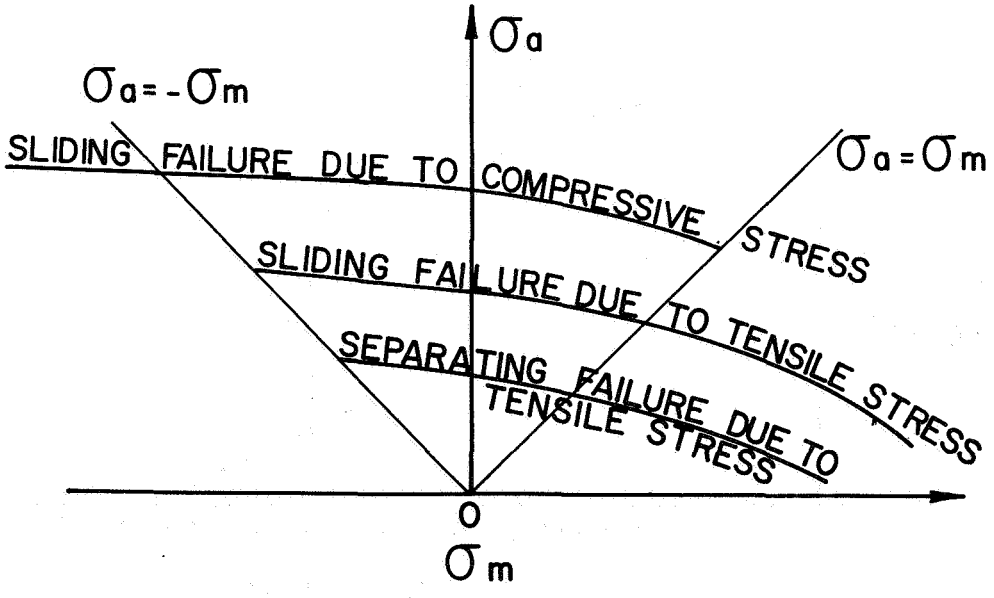

Figure 4.- Example allowable stress diagram established by multiple failure criteria for different domains of cyclic stressing (ref. 10).

INFLUENCE OF ACOUSTICS IN SEPARATION PROCESSES

Harold V. Fairbanks
West Virginia University

SUMMARY

The purpose of this investigation was to study the effects of introducing high energy acoustics into various filtering and drying systems. With very slow velocity filtration systems, it was found that the introduction of acoustics could substantially increase the flow rate and also aided in the coagulation of the particulates before reaching the filter media. In the drying of temperature sensitive powders, the rate was increased by the introduction of acoustics. The acoustic frequency used was 20kHz with power levels up to 3 watts per square centimeter.

FILTRATION

Figure 1 shows a schematic sketch of the filtration equipment used in this study. The special assembly of the acoustic horn on the top of the filter was built and consigned to us by the Branson Sonic Power Company of Danbury, Connecticut for this project. With this special head, the filter could be operated under pressure from both sides of the filtering media.

A porous stainless steel filter, 0.6 cm thick, was used to separate the solids from a viscous oil slurry which contained 7.5% solids by weight. The mean channel diameter in the stainless steel filter was 120 μm while the mean diameter of the solid particulates was 20 μm.

Figure 2 shows the filtration rates obtained when acoustics were introduced into the filtration system. The maximum flow rate was calculated to increase 9 times when using a system pressure of 0.91 kg/cm^2 with an acoustic intensity of 2.15 W/cm^2. The pressure drop across the 0.6-cm thick porous stainless steel filter media, 7.6 cm in diameter, was 0.05 kg/cm^2. The slurry consisted of 7.5% fine solids in motor oil. The slurry simulated oil produced from the hydrogenation of coal which contains a suspension of small mineral particles ranging from 1 to 100 μm in size. Besides increasing the oil flow rate, the acoustics also kept the filter media cleaner and aided in agglomerating the solids beneath the porous stainless steel filter.

DRYING

Figure 3 is a schematic sketch of the experimental tray type drying system used in this study. The special air-coupling acoustic bell horn used was consigned to us by the Branson Sonic Power Company of Danbury, Connecticut for this project. The temperature sensitive powders used included: (1) fine coal powder, after pyritic sulfur removal, made up of particles less than 150 μm in size, and (2) polymer powders having an approximate particle size of 20 μm.

Figure 4 compares drying rate curves with and without the introduction of acoustics. Two factors can be noted: (1) an increase in the drying rate during the constant drying rate period, and (2) an extension of the constant drying rate period.

The increase in the constant drying rate period is due to the increased air turbulence caused by the sound waves at the evaporation surface. R. E. Cline (ref. 1) showed that a minimum sound intensity of 130 dB was required at the evaporation surface for increased drying rate. J. M. Spain (ref. 2) showed that too high a sound intensity can decrease the drying rate due to cavitation being produced in the liquid phase.

The extension of the constant drying rate period is conjectured to be due to the acoustics ability to increase the liquid flow rate from the interior of the powder mass or agglomerate to the evaporating surfaces.

DISCUSSION

In both the filtering and drying processes, the introduction of acoustics increased the liquid flow rate. The main condition required was to satisfy Biot's relationship (ref. 3) where $F = \pi V/4d^2$. F is the sound frequency in hertz, V is the kinematic viscosity in square centimeter per second, and d is the mean channel diameter in centimeters. When the conditions of the experiments did not satisfy Biot's relationship, it was found that the effectiveness of introducing acoustics into the system was greatly reduced.

When Biot's relationship is satisfied the liquid flow changes from the normal viscous flow to a plug type flow. In other words, the friction factor for the liquid flow through the small channels is significantly reduced.

REFERENCES

1. Cline, R. E.: Acoustic Drying of Coal. M. S. Thesis, West Virginia University, 1967.

2. Spain, J. M.: Ultrasonic Effects on Critical Moisture Content. M. S. Thesis, West Virginia University, 1974.

3. Biot, M. A.: Theory of Propagation of Elastic Waves in Fluid-Saturated Porous Solid. J. Acoust. Soc. Am., Vol. 28, No. 2, 1956, pp. 168-191.

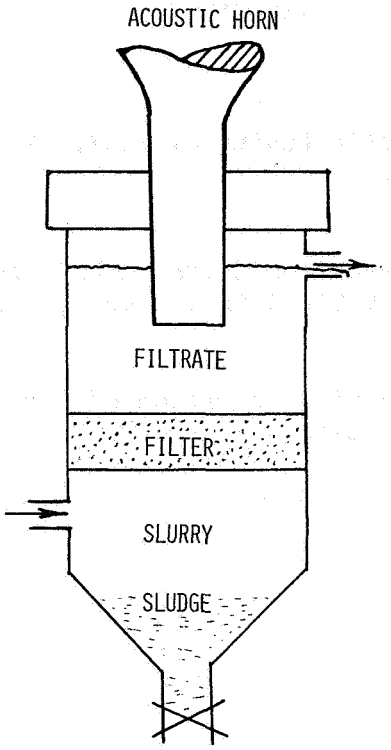

Figure 1.- Schematic sketch of equipment used for acoustic assist in filtration.

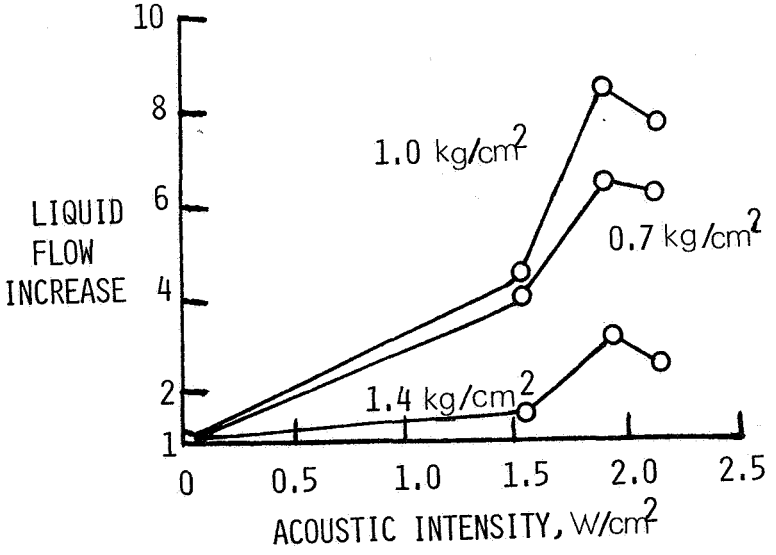

Figure 2.- Curves showing the effect of ultrasonic intensity upon filtration increase using various gauge pressures on the system.

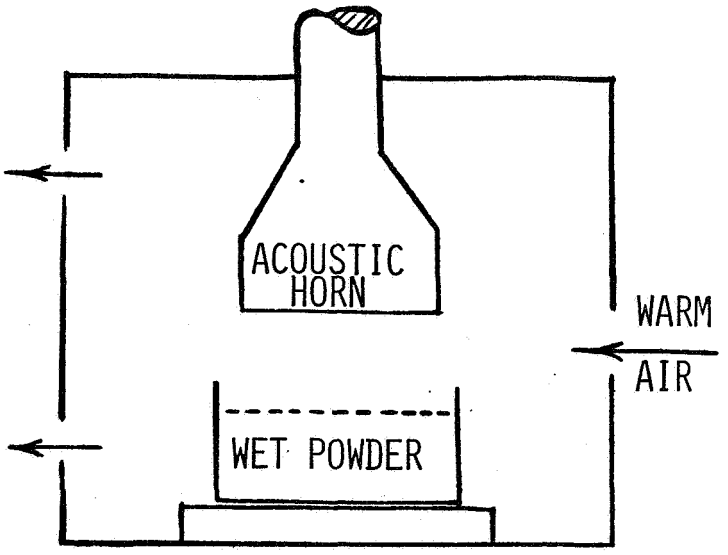

Figure 3.- Schematic sketch of equipment used for acoustic assist in tray drying.

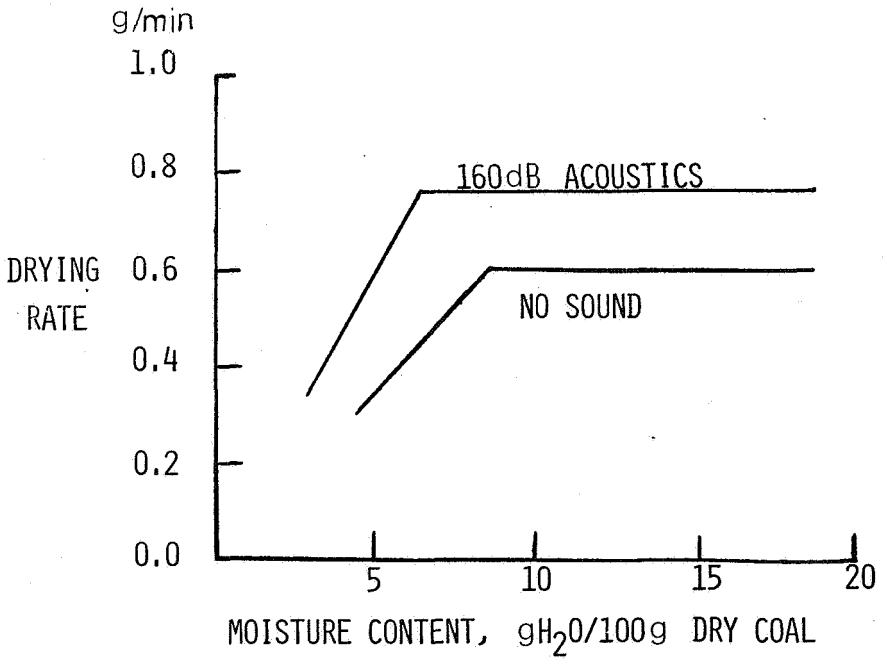

Figure 4.- Drying rate curves showing the influence of acoustics upon drying minus 150 μm powdered coal particles. Approximately two liters of air flow per second was used having a temperature of 200°C.

MICROMECHANICS OF SLIP BANDS ON A FREE SURFACE*

S. R. Lin**
The Aerospace Corporation

T. H. Lin
University of California, Los Angeles

SUMMARY

A micromechanics analysis for the formation and propagation of slip bands on the free surface of a polycrystal under monotonic loading is presented. For the growth of slip bands the analysis satisfies the conditions of both equilibrium and displacement continuity, as well as the relation between slip and the resolved shear stress throughout the polycrystal. Numerical calculations show how the microstress field causes the concentration of plastic deformation in discrete sliding bands and give results which are in good qualitative agreement with known slip band observations on aluminum single crystals.

INTRODUCTION

Slip bands on metal surfaces under loading have been observed since early in this century. Heidenreich and Shockley (ref. 1) found that slip bands visible in the light microscope were clusters of fine lines spaced about 100 atoms apart as resolved in the electron microscope. The number and intensity of slip bands increase with loading, and slip bands often run through the crystal (refs. 2 and 3). Many attempts have been made to explain the occurrence and growth of these slip bands observed both on the surface and at the interior of the deformed metal. It was commonly assumed that a single crystal first yields to an applied stress at some specific weak slip plane. Because the lattice around the active slip plane is so severely distorted as to require a higher stress to cause slip to continue, the slip does not continue on the plane until fracture occurs but shifts to others. As indicated by Brown (ref. 4), this hypothesis fails to explain why slip bands once formed can exhibit increasing shear strain at the same time as new bands are formed. If work hardening is due to distortion of lattice near the active slip plane, the planes on which slip has never occurred, being more nearly perfect, should be planes of easier slip than those which have slipped already.

---

*This work was supported by the National Science Foundation under Grant ENG 74-03809 at the University of California, Los Angeles, Calif.

**Formerly Post Doctoral Scholar at University of California, Los Angeles, Calif.

It is generally agreed that the interactions of slip bands determine their spacing. The observed mean slip band spacing of an aluminum single crystal is about 25μ at an extension of 0.7% and 12μ at 2.5%. Accumulation of large numbers of dislocations on slip planes produces residual stresses in the lattice causing difficulty for slip to occur within a zone on either side of the slip plane. As indicated by Mott (ref. 5), the difficulty of this hypothesis is that the range of the stresses due to dislocations in a plane array is much too small even to explain more closely spaced slip bands.

The microstress explanation of the nonuniform plastic deformation and slip bands in the interior of a polycrystal was proposed by Lin in 1972 (ref. 6), but that of the corresponding phenomena on the free surface is not available. Slip bands on the surface have great influence on the fracture characteristics of the metal. This paper aims to show, based on micromechanics, how slip bands are formed at the free surface under a monotonic loading. Micromechanics here means the variation of stress and strain from one band to the other.

RESOLVED SHEAR STRESS FIELD CAUSED BY SLIP

Among the different mechanisms of plastic deformation in metals, crystallographic slip has been shown to be the principal process of plastic deformations at low and intermediate temperature (ref. 7). This plastic deformation is mainly due to the movement of dislocations (ref. 8). Single crystal tests have shown that slip starts when the resolved shear stress reaches a certain value, known as the critical resolved shear stress. The initiation and continuation of slip depend on this resolved shear stress and are independent of the normal pressure on the sliding plane. Slip is caused by dislocation movement, and the force on a dislocation line to cause it to move varies linearly with the resolved shear stress (ref. 9). Hence, slip depends on the resolved shear stress.

Imperfections such as dislocations exist in all metals and cause an initial stress field denoted by τ^I_{ij}. Under loading, the elastic stress field caused by loading denoted by the τ^A_{ij} combines with the initial stress field to form a nonuniform stress field. The resultant stress field τ_{ij} gives a resolved shear stress field $\tau_{\alpha\beta}$ in a slip system, where α denotes the direction along the normal to the slip plane and β along the slip direction. The region with the highest resolved shear stress slides first, when the critical shear stress τ_c is reached. The amount of slip and the region of slip increase with loading. Should the load be removed after sliding in the region, the slip would remain and cause a residual stress field. If the load is applied again, assuming no further slip during the reloading, the resultant stress field $\tau_{\alpha\beta}$ is the sum of the initial stress $\tau^I_{\alpha\beta}$, the residual slip stress field $\tau^R_{\alpha\beta}$ and the applied stress $\tau^A_{\alpha\beta}$.

To find the residual stress field due to localized slip, use is made of the analogy between the plastic strain gradient and the body force developed by Eshelby (ref. 9) and Lin (ref. 10). Consider an aluminum polycrystal loaded

in tension. Due to different orientations of the crystals, the resolved shear stresses vary from one crystal to another. All crystals are assumed to have the same initial critical shear stress. Those crystals that have the highest resolved shear stress, known as the most favorably oriented crystals, will slide first. Under uniaxial tension along x_2 axis as shown in figure 1, the most favorably oriented crystal has a slip system with the slip direction and slip plane at 45 deg to the loading axis. Since the length of the slip band (dimension along x_3 axis in fig. 1) is much larger than its thickness, the plastic strain due to slip is assumed to be constant along the length. Hence, the deformation state due to plastic strain can be considered under plane strain. For numerical calculation, the slide region is divided into parallelogram elements in which, if slip occurs, the plastic strain $e''_{\alpha\beta}$ is assumed constant. The residual resolved shear stress in a semi-infinite medium due to a given plastic strain $e''_{\alpha\beta}$ in a parallelogram with width a, thickness b and centered at (x_{1_r}, x_{2_r}) was presented in closed form by Lin and Lin in 1974 (ref. 11) in the study of the surface fatigue crack initiation:

$$\begin{aligned}\tau^R_{\alpha\beta} = e''_{\alpha\beta}\,\frac{E}{4\pi(1-\nu^2)}\Bigg[&K\left(x_1, x_2; x_{1_r} + \tfrac{1}{2}a,\ x_{2_r} + \tfrac{1}{2}a + \tfrac{1}{2}b\right)\\ &- K\left(x_1, x_2; x_{1_r} + \tfrac{1}{2}a,\ x_{2_r} + \tfrac{1}{2}a - \tfrac{1}{2}b\right)\\ &- K\left(x_1, x_2; x_{1_r} - \tfrac{1}{2}a,\ x_{2_r} - \tfrac{1}{2}a + \tfrac{1}{2}b\right)\\ &+ K\left(x_1, x_2; x_{1_r} - \tfrac{1}{2}a,\ x_{2_r} - \tfrac{1}{2}a - \tfrac{1}{2}b\right)\Bigg]\\ \equiv\ & e''_{\alpha\beta}\,G\left(x_1, x_2; x_{1_r}, x_{2_r}\right)\end{aligned} \tag{1}$$

where

$$\left.\begin{aligned}K\left(x_1, x_2; \bar{x}_1, \bar{x}_2\right) = \tan^{-1}\left(\frac{w}{v}\right) - \tan^{-1}\left(\frac{w}{u}\right) + \frac{u(u+w)}{X_1} - \frac{u^2 + 2uv - v^2 + 2vw}{2X_2}\\ + \frac{v(v-w)(u^2-v^2)}{X_2^2}\end{aligned}\right\} \tag{2}$$

$$\left.\begin{aligned}u &= x_1 - \bar{x}_1 & X_1 &= u^2 + w^2\\ v &= x_1 + \bar{x}_1 & X_2 &= v^2 + w^2\\ w &= x_2 - \bar{x}_2\end{aligned}\right\}$$

and E and ν are elastic modulus and Poisson's ratio, respectively.

When the thickness of the grids is much smaller than the width, i.e., $b \ll a$, it is shown that

$$\tau^{R}_{\alpha\beta} = \frac{bEe''_{\alpha\beta}}{4\pi(1-\nu^2)} \left[K_o\left(x_1, x_2; x_{1_r} + \frac{1}{2}a, x_{2_r} + \frac{1}{2}a\right) - K_o\left(x_1, x_2; x_{1_r} - \frac{1}{2}a, x_{2_r} - \frac{1}{2}a\right)\right] \tag{3}$$

where

$$K_o\left(x_1, x_2, \bar{x}_1, \bar{x}_2\right) = \frac{2u}{X_1} - \frac{2u^2(u-w)}{X_1^2} - \frac{2v}{X_2} - \frac{3u^2v + u^2w + 2uvw - v^2w - 5v^3}{X_2^2} + \frac{4v^2(u^2-v^2)(v+w)}{X_2^3} \tag{4}$$

The relief of the shear stress is proportional to the product of the plastic strain and the slip band thickness, $be''_{\alpha\beta}$. Since the slip band is very thin, extremely large plastic strain $e''_{\alpha\beta}$ is required to have a finite value of shear stress relief in the sliding region.

INTERACTION OF SLIP BANDS

A most favorably oriented crystal at the free surface of a tensile specimen is considered (fig. 1). This crystal has a slip system with a slip direction and a slip plane at 45 deg to the loading axis. To simplify numerical calculation, slip is assumed to occur only in this slip system and has no strain-hardening. This crystal with linear dimensions of 50μ x 105μ (representing a typical grain size of pure aluminum) as shown in figure 2 is divided into fine parallelogram grids oriented 45 deg to the free surface. In a real metal specimen the initial stress field is a complicated function of material impurities and lattice flaws. For the numerical calculation, it is assumed that an idealized initial stress field of 0.034 MN/m^2 (5 psi) (approximately 10% of the critical resolved shear stress) uniform shear stress exists in a thin slice 45 deg to the free surface and zero stress elsewhere. The thickness of each thin grid is assumed to be 0.1μ corresponding approximately to the observed slip band thickness (ref. 12). The critical resolved shear stress τ_c is taken to be 0.369 MN/m^2 (53.5 psi), the elastic modulus E to be 68.9×10^3 MN/m^2 (10^7 psi) and the Poisson's ratio ν to be 0.3. These values also correspond approximately to those for pure aluminum (ref. 13).

For a slip system to start or continue sliding, the resolved shear stress $\tau_{\alpha\beta}$ has to reach the critical shear stress τ_c. Hence, the governing condition for the sliding region is

$$\tau^I_{\alpha\beta} + \tau^R_{\alpha\beta} + \tau^A_{\alpha\beta} = \tau_c \tag{5}$$

while in the non-sliding region, the magnitude of the resolved shear stress must be less than the critical. For zero strain-hardening, τ_c remains constant, and equation (5) can be differentiated with respect to the applied stress $\tau^A_{\alpha\beta}$

$$1 + \sum_r G\left(x_1, x_2; x_{1_r}, x_{2_r}\right) \frac{de''_{\alpha\beta}\left(x_{1_r}, x_{2_r}\right)}{d\tau^A_{\alpha\beta}} = 0 \tag{6}$$

where summation is over all sliding slip systems with slide regions centered at (x_{1_r}, x_{2_r}). This is a set of linear equations with as many non-zero unknowns, $de''_{\alpha\beta}/d\tau^A_{\alpha\beta}$, as there are equations. The change of the resolved shear stress in a nonactive slip system is given as

$$\frac{d\tau_{\alpha\beta}}{d\tau^A_{\alpha\beta}} = 1 + \sum_r G\left(x_1, x_2; x_{1_r}, x_{2_r}\right) \frac{de''_{\alpha\beta}\left(x_{1_r}, x_{2_r}\right)}{d\tau^A_{\alpha\beta}} \tag{7}$$

From the known values of $\tau_{\alpha\beta}$ at the nonactive points and the corresponding values of $de''_{\alpha\beta}/d\tau^A_{\alpha\beta}$, the increment in $\tau^A_{\alpha\beta}$ required for each nonactive point to initiate slip can be calculated and compared. The minimum of these increments in $\tau^A_{\alpha\beta}$ is applied, resulting in one additional active point for the next load increment. All $de''_{\alpha\beta}/d\tau^A_{\alpha\beta}$ obtained from equation (6) must be in the same sense as $\tau_{\alpha\beta}$ of the same slide grid, i.e., the incremental plastic work done by $\Delta e''_{\alpha\beta}$ must be positive. If some $\Delta e''_{\alpha\beta}$'s are of opposite sense to $\tau_{\alpha\beta}$, these grids must be deleted from equation (6) until all $\Delta e''_{\alpha\beta}$'s are in the same sense as $\tau_{\alpha\beta}$, and at the same time the shear stresses $\tau_{\alpha\beta}$ in all nonactive regions are less than the critical τ_c. Consequently, some iterations are often required to obtain the desired results. It should be noted that the incremental calculation of slip strains and stresses under monotonic loading outlined in the foregoing is rigorous within the framework of the discretized formulation.

The initially stressed band starts to yield when the applied stress reaches 0.668 MN/m^2 (97 psi), followed by the neighboring grids near the interior of the initially stressed band (fig. 2). As loading increases, grids in two regions away from this initially stressed band, one near the free surface and the other in the interior, join the previous bands in sliding. The distribution of active slip bands in this most favorably oriented crystal at the

applied load of 0.743 MN/m^2 (107.9 psi) is shown in figure 2. The formation of slip bands at the free surface at three different loading stages is shown in figure 3. It is seen that some originally active grids have become inactive while some grids remain active and the amount of their slip increases with loading. The spacing of the slip bands computed for this polycrystal is about 3μ, while the observed spacing for aluminum single crystal at 20°C is about 2μ (ref. 12). The computed slip band spacing was found insensitive to the assumed initial stress field when its magnitude was in the range of 0 to 0.069 MN/m^2 (10 psi). Tests conducted by Yamaguchi (ref. 12) indicated that the number of slip bands in a single crystal varies linearly with the shear stress. The present calculation for a polycrystal also shows an approximately linear variation of the number of slip bands with stress as shown in figure 4. The number and the magnitude of load increments are also indicated in figure 4. These numerical results show how the microstress field causes the concentration of plastic deformation in discrete sliding thin slices which are observed as slip bands.

CONCLUSIONS

A micromechanics analysis for the formation and propagation of slip bands on the free surface of a polycrystal under monotonic loading is presented. The displacement of dislocations observed as sliding of slip planes causes plastic shear strain. This localized plastic strain is shown as slip bands. The relief of resolved shear stress in the regions adjacent to the active slip system prevents the sliding in those regions and causes the concentration of plastic deformation of metals. Numerical calculations give results which are in good qualitative agreement with known slip band observations on an aluminum single crystal. The solution satisfies conditions of both equilibrium and displacement continuity, as well as the relation between slip and the resolved shear stress throughout the polycrystal.

REFERENCES

1. Heidenreich, R. D.; and Shockley, W.: Electron Microscope and Electron Diffusion Study of Slip in Metal Crystals. J. Appl. Phys., vol. 18, 1947, p. 1029.

2. Nye, J. F.: Plastic Deformation of Silver Chloride. Proc. Roy. Soc. A, vol. 198, 1949, p. 190.

3. Mori, T.; and Meshii, M.: Plastic Deformation of Quenched Hardened Aluminum Single Crystals. ACTA Met, vol. 17, 1969, p. 167.

4. Brown, A. F.: Surface Effect in Plastic Deformation of Metals. Adv. Phys., vol. 1, 1952, p. 427.

5. Mott, N. F. : The Mechanical Properties of Metals. Proc. Phys. Soc. B, vol. 64, 1951, p. 729.

6. Lin, T. H. : Microstress Field of Slip Bands and Inhomogeneity of Plastic Deformation of Metals. Proc. Int. Symp. Foundation of Plasticity, Noordhoff Int. Publishing, Gronigen, 1972, p. 77.

7. Dorn, J. F. ; and Mote, J. D. : On the Plastic Behavior of Polycrystalline Aggregates. Mater. Sci. Res., vol. 1, 1962, p. 11.

8. Read, W. T., Jr. : Dislocation in Crystals. McGraw-Hill, New York, 1953.

9. Eshelby, J. D. : The Determination of the Elastic Field of an Ellipsoidal Inclusion and Related Problems. Proc. Roy. Soc., vol. A241, 1957, p. 376.

10. Lin, T. H. : Theory of Inelastic Structures. Wiley, New York, 1968.

11. Lin, S. R. ; and Lin, T. H. : Effect of the Secondary Slip System on Early Fatigue Damage. J. Mech. Phys. Solids, vol. 22, 1974, p. 177.

12. Brown, A. F. : Slip Band and Hardening Process in Aluminum. J. Inst. Metals, vol. 80, 1951-52, p. 115.

13. Wu, T. T. : A Note on the Early Deformation of Aluminum Crystals in Simple Tension. J. Appl. Mech., vol. 31, 1964, p. 711.

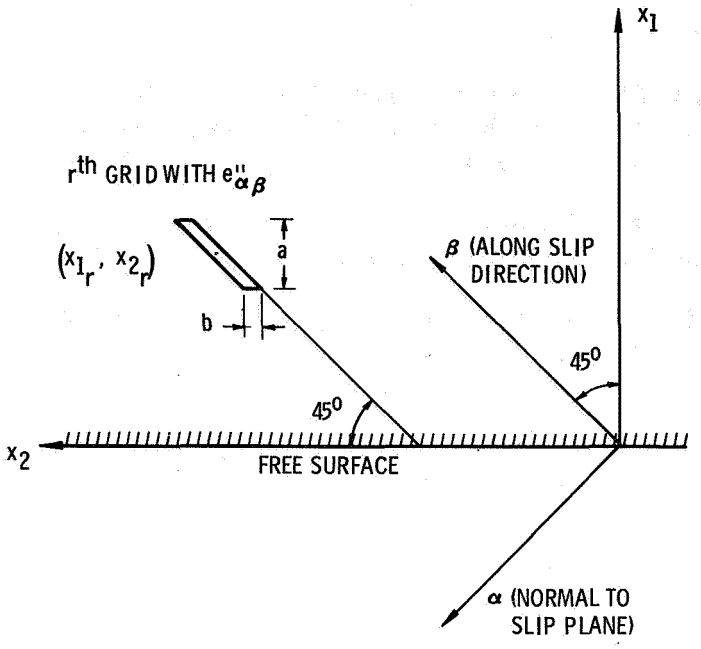

Figure 1.- Coordinates on a most favorably oriented crystal at the free surface of a polycrystalline aggregate.

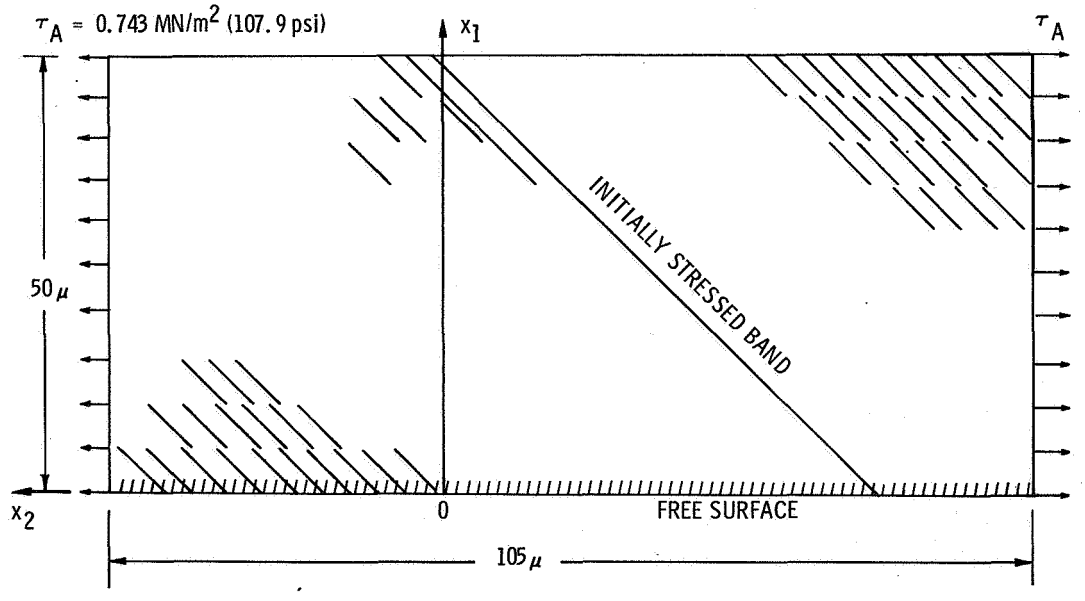

Figure 2.- Distribution of active slip bands in a most favorably oriented crystal under uniaxial loading.

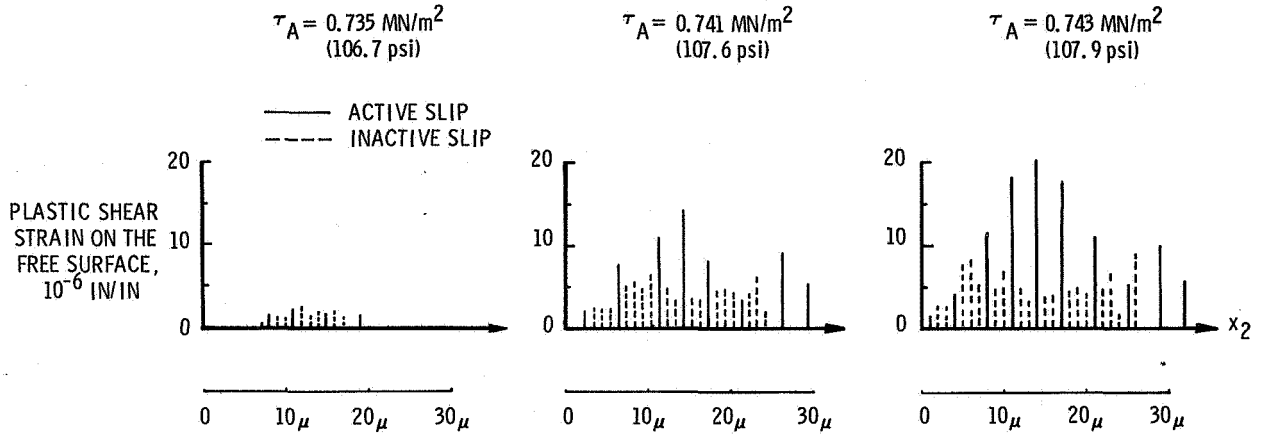

Figure 3.- Formation and propagation of slip bands at the free surface under monotonic loading.

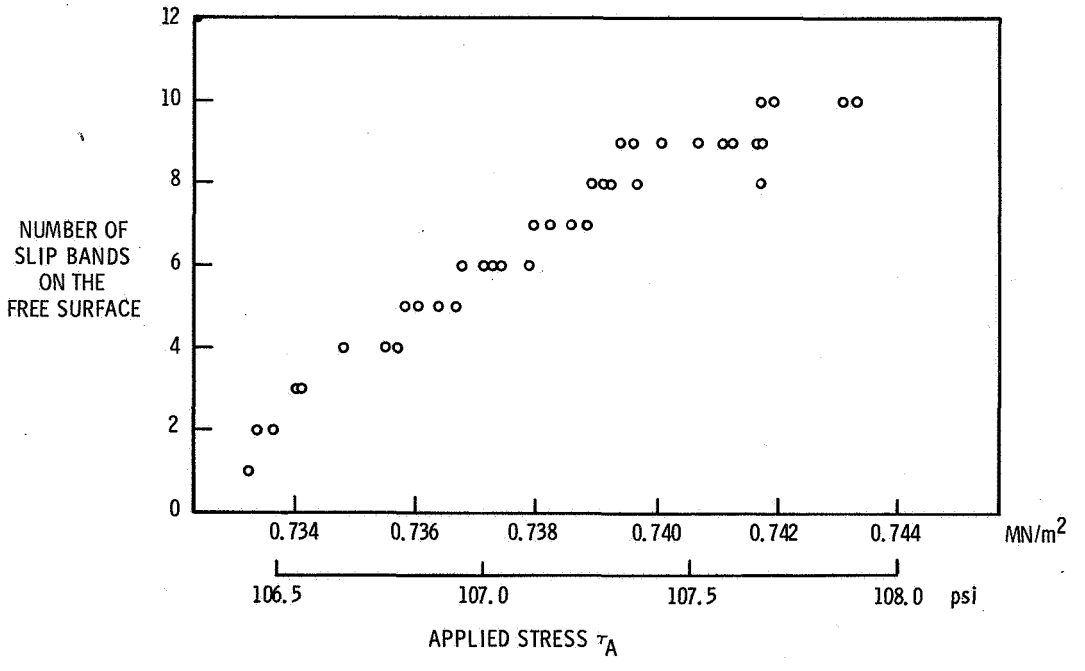

Figure 4.- Variation of number of slip bands on the free surface with applied load.

ON ONSAGER'S PRINCIPLE, DISLOCATION MOTION AND HYDROGEN EMBRITTLEMENT

M. R. Louthan, Jr. and R. P. McNitt
Virginia Polytechnic Institute and State University

SUMMARY

Onsager's reciprocal relationships from the linear theory of irreversible thermodynamics are applied to hydrogen - dislocation interactions. Existing experimental evidence shows that dislocation motion causes localized hydrogen accumulation; thus, from the Onsager principle, localized hydrogen accumulations will affect dislocation motion and therefore the properties of metals and alloys exposed to hydrogen environments.

INTRODUCTION

A major limitation in the design of many engineering systems is an incomplete understanding of the behavior of materials in hostile environments. This is particularly true for potential future energy systems based on thermonuclear fusion, hydrogen, coal gasification and liquification where the possibilities of high temperature errosion-corrosion, stress corrosion cracking and hydrogen embrittlement pose formidable problems. Interdisciplinary approaches have indicated that exposure to hydrogen adversely affects most high strength materials; fracture mechanics studies have shown hydrogen induced slow crack growth; metallurgical and mechanical evaluations have demonstrated hydrogen interactions with dislocations and chemical analyses have suggested that absorption is a precursor to embrittlement. Hydrogen exposures have caused changes in fracture mode, reductions in fatigue life, delayed failures and increases in creep rates. Rationalization of these various affects requires the use of interdisciplinary techniques. For example continuum mechanics, linear irreversible thermodynamics, and materials science might be combined to formulate a possible embrittlement mechanism.

HYDROGEN TRANSPORT BY DISLOCATIONS

The thesis that moving dislocations might transport significant quantities of hydrogen was first suggested by Bastien and Azou (ref. 1) in 1951. However, it was not until relatively recently that direct experimental support for that hypothesis was developed, although Frank (ref. 2) did report increased

hydrogen evolution during bending of hydrogen-charged mild steels in 1959. Fricke et al (ref. 3) made similar observations about a decade later but concluded that the deformation enhanced hydrogen release was due to the increased surface area. Subsequent studies at Savannah River Laboratory (ref. 4,5,6,7,8) confirmed the deformation enhanced release and demonstrated that the release was due to hydrogen transport by moving dislocations. These studies also demonstrated that when an initially hydrogen free specimen was plastically deformed while exposed to a hydrogen environment the apparent hydrogen diffusivity was increased. This increase in apparent diffusivity significantly increased the amount of hydrogen absorbed. Furthermore, localized high hydrogen concentrations were observed along slip lines emanating from regions of hydrogen embrittlement. Parallel studies with samples that were hydrogen charged before plastic deformation indicated that the plastic strain caused redistribution of hydrogen and that an initially homogeneous hydrogen distribution became quite heterogeneous as strain progressed. These observations are summarized in Figures 1 through 3 and have been interpreted as evidence that hydrogen is transported by dislocation motion. The strain enhanced hydrogen redistributions, the observed high hydrogen concentrations along slip lines, and the hydrogen release data from iron, austenitic stainless steels and aluminum provide the strongest evidence for this effect.

THE ROLE OF HYDROGEN TRANSPORT BY DISLOCATIONS

Various processes have been advocated to explain the mechanism by which hydrogen absorption reduces the load carrying capacity of a metal or alloy. These processes vary from assuming that hydrogen reduces the forces necessary to cause lattice decohesion to assuming that hydrogen either inhibits or enhances dislocation movement. However, the one common feature of most, if not all, proposed embrittlement mechanisms is that regions of localized, high hydrogen concentrations are necessary for embrittlement. Clearly the experimental evidence shows that indeed dislocation transport can lead to the development of such regions and correspondingly the role of dislocation motion may simply be its involvement in rapidly transporting and localizing hydrogen. However, most investigators have attempted to either directly involve the dislocation-hydrogen interaction in the embrittlement process (ref. 7-11) or discount altogether the importance of that interaction (ref. 12).

One model for embrittlement postulates that during plastic deformation dislocations with their associated hydrogen environments continually arrive at some deposition site. Inclusions, grain boundaries, phase boundaries, twins, strained lattices and other sites for possible dislocation annihilation are generally assumed to also be the hydrogen deposition sites. Continued deposition of hydrogen causes the hydrogen concentration to increase. Subsequently, molecular hydrogen will precipitate at defects in the areas of localized hydrogen concentrations. Because local equilibrium is maintained [i.e. $C = C_o p_{H_2}^{1/2} \exp(\Delta H/RT)$] the pressure of the precipitated hydrogen may be quite high and cause the defect to grow by mechanical processes. Such growth may involve either brittle fracture or plastic deformation and will continue until the pressure is relieved. The process by which the defect

grows will depend on specimen microstructure, local constraint conditions, hydrogen content, strain rate, temperature, and prior treatment.

The above model has recently been quantified by several investigators (ref. 13,14) and refuted by others (ref. 15) - in both cases by treatments of the kinetics of the accumulation processes. Furthermore, advocates of the decohesion model have tended to discount entirely the role of dislocation transport. In fact, at least one investigator has concluded that dislocation motion cannot be involved either directly or indirectly in the process of hydrogen embrittlement. This conclusion discounts any role for hydrogen transport by dislocations and implys that embrittlement cannot develop because of hydrogen effects on ductile rupture processes.

Beachem (ref. 16) in 1972, concluded that the term hydrogen embrittlement of metals was misleading and based on extensive microscopic observations stated that the term "hydrogen assisted cracking" more nearly represented the actual case. His work implies that somehow, hydrogen accumulations made dislocation motion easier. To date this work has not received wide support and in fact was quite controversial when initially presented. However, several subsequent investigators (ref. 7,8,17) have shown that hydrogen absorption may affect microvoid nucleation and/or microvoid growth. If, on the basis of such evidence, one accepts the premise that dislocation movement in a sample exposed to hydrogen causes localized hydrogen accumulations then one must ask if the converse is true. Do localized hydrogen accumulations effect dislocation motion?

IRREVERSIBLE THERMODYNAMICS CONSIDERATIONS

The question as to how seemingly diverse thermal, electrical, and chemical events may be interrelated during a process has long been of interest to the academic community. Onsager (see ref. 18 for a bibliography and background), surmised that the common factor of all real processes was the production of entropy. Through this factor, he sought relationships between the various changes in the thermodynamic properties. Indeed he was successful in this endeavor, for at least small excursions about equilibrium states, through the formulation of what is now known as linear irreversible thermodynamics. A main point of this theory is that entropy production is given by

$$T \frac{dS}{dt} = \sum_{i=1}^{N} \bar{X}_i \frac{dQ_i}{dt} \qquad (1)$$

where T = temperature

$\frac{dS}{dt}$ = rate of entropy prediction

Q_i = an extensive variable describing the state of the body (volume, electric charge), thermodynamic coordinates

$\bar{X}_i$ = an intensive variable (pressure, electric field, etc.), thermodynamic forces

If one chooses the extensive coordinates to cover the system and yet be independent, and then recalls that in any real process the entropy production must be positive semi-definite then some dependence between forces $\bar{X}_i$, and $\frac{dQ_i}{dt}$ must exist, or

$$\bar{X}_i = b_{ij}\frac{dQ_j}{dt} + b_{ijk}\frac{dQ_j}{dt}\frac{dQ_k}{dt} + \cdots \quad (2)$$

(note repeated subscripts imply summation) where b_{ij} = 1st order, b_{ijk} = 2nd order Onsager coefficients. Through the use of a time symmetry principle Onsager was able to show that (in the absence of a magnetic field and on an inertial platform) the first order coefficients were symmetric; that is

$$b_{ij} = b_{ji} \quad (3)$$

This simple statement is very powerful in relating seemingly diverse processes. As an example of the usefulness of this relationship, consider the case of an electrical current through the junction of two dissimilar metals; one metal will cool and the other heat up. Equations 2 and 3 then tells us that if we were to heat one junction and cool the other, then electric current would flow, which of course is precisely what happens. This type of observation can also be useful in considering the dislocation-hydrogen interaction problem.

Dislocation motion ($\frac{dQ_i}{dt}$) under irreversible shear stress (i.e. local shear stresses exceeding the yield values) results in local plasticity in most materials. This is an irreversibility and hence would supply a term for the right hand side of Equation 1. Experimental evidence shows that when dislocations move hydrogen is redistributed through the material. The redistribution leads to entropy production in various ways, particularly if the local lattice solubility is exceeded. The particular mechanism of entropy production is not required for this discussion. We need only to assume the condition that under the driving fugacity hydrogen redistribution irreversibility occurs and entropy is produced. Thus defining

$\bar{X}_1$ = plastic shear stress

$\frac{dQ_1}{dt}$ = dislocation motion

$\bar{X}_2$ = Fugacity or hydrogen driving "force"

$\frac{dQ_2}{dt}$ = Hydrogen redistribution rate

We have from Equation 2

$$\bar{X}_1 = b_{11} \frac{dQ_1}{dt} + b_{12} \frac{dQ_2}{dt} + \cdots \quad (4)$$

$$\bar{X}_2 = b_{21} \frac{dQ_1}{dt} + b_{22} \frac{dQ_2}{dt} + \cdots$$

from Equation 3 that $b_{12}=b_{21}$. We know that $b_{12}\neq 0$ because the experimental results show that dislocation motion transports hydrogen. Thus we conclude from Equation 4 that hydrogen redistribution will indeed influence the dislocation motion which in turn will surely affect the fracture process! Thus Beachem's hypothesis seems to be bolstered by the thermodynamics of irreversible processes. It remains for further work to show precisely how this is accomplished.

In summary we have described experimental evidence to demonstrate the transport of hydrogen by dislocation motion and then applied Onsager's reciprocal relations to show that an effect of localized hydrogen accumulation will be to enhance dislocation motion. On the macroscopic level such effects have been observed as hydrogen induced changes in fracture processes and are in agreement with Beachem's evidence of hydrogen assisted cracking. Hence a powerful new argument can be utilized to better understand some of the mechanisms of hydrogen embrittlement.

REFERENCES

1. P. Bastien and P. Azou, C. R. Acad. Sci., Vol. 232, p. 1845 (1951).

2. R. G. Frank, Internal Stresses and Fatigue in Metals, G. M. Rassweiler and W. L. Grube (eds.) p. 411, Elsevier, New York (1959).

3. E. Fricke, H. P. Stuwe and G. Vibrans, Met. Trans., Vol. 2, p. 2697 (1971).

4. M. R. Louthan, Jr., G. R. Caskey, Jr. and J. A. Donovan, Microstructural Science, Vol. 3, p. 823 (1975).

5. M. R. Louthan, Jr., J. A. Donovan and G. R. Caskey, Jr., Nuclear Technology, Vol. 26, p. 192 (1975).

6. M. R. Louthan, Jr., Process Industries Corrosion, p. 126 National Association of Corrosion Engineers, Houston, Texas (1975).

7. M. R. Louthan, Jr., Hydrogen in Metals, I. M. Bernstein and A. W. Thompson (eds.) p. 53, American Society for Metals, Metals Park, Ohio (1974).

8. M. R. Louthan, Jr., G. R. Caskey, Jr., J. A. Donovan and D. E. Rawl, Jr. Materials Science and Engineering, Vol. 10, p. 357 (1972).

9. M. R. Louthan, Jr. and R. P. McNitt, p. 496, Effect of Hydrogen on Behavior of Materials, A. W. Thompson and I. M. Bernstein (eds.) The Metallurgical Society of AIME, New York (1976).

10. B. C. Odegard, J. A. Brooks and A. J. West. p. 116, Ibid, reference 9.

11. A. W. Thompson, p. 467, Ibid, reference 9.

12. R. A. Oriani and P. H. Josephic, Acta Met., Vol. 22, p. 1065 (1974).

13. J. K. Tien, page 309, Ibid, reference 9.

14. J. K. Tien, A. W. Thompson, I. M. Bernstein and R. J. Richards, Met. Trans.,A, Vol. 7A, 1976.

15. H. H. Johnson and J. P. Hirth, Internal Hydrogen Supersaturation Produced by Dislocation Transport, report COO-3166-17, Materials Science Center Ithaca, New York (Nov. 1975).

16. C. D. Beachem, Met. Trans., Vol. 3, p. 437 (1972).

17. M. R. Louthan, Jr., D. E. Rawl, Jr., J. A. Donovan and W. G. Holmes, Trans. ANS, Vol. 21, p. 158 (1975).

18. R. P. McNitt and M. M. Stanesic, Acta Mechanics, Vol. 7, p. 187 (1969).

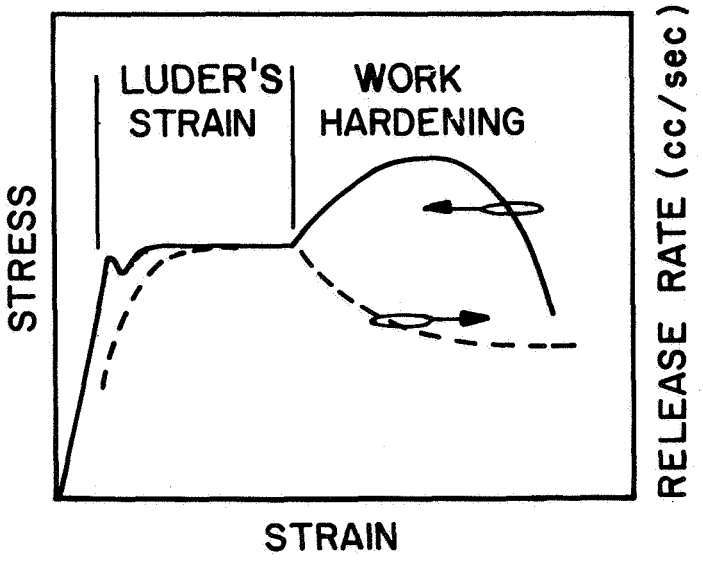

Figure 1.- Deformation - enhanced hydrogen (tritium) release during tensile test of precharged armco iron sample.

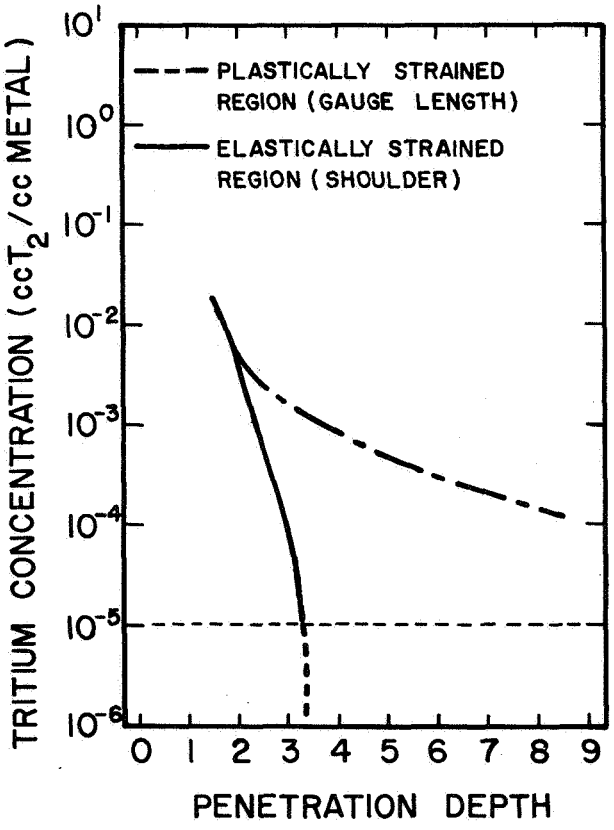

Figure 2.- Deformation - enhanced hydrogen (tritium) uptake during plastic deformation of austenitic stainless steel.

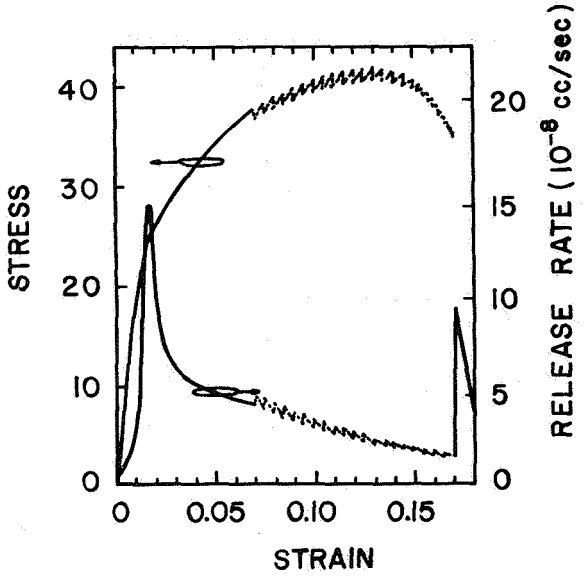

Figure 3.- Hydrogen release and serrated yielding in hydrogen (tritium) charged aluminum alloy.

WAVE SPEEDS AND SLOWNESS SURFACE IN ELASTIC-PLASTIC MEDIA OBEYING TRESCA'S YIELD CONDITION*

T. C. T. Ting
University of Illinois at Chicago Circle

SUMMARY

The plastic wave speeds in elastic, isotropically work-hardening materials obeying the Tresca's yield condition are obtained. With the coordinate axes chosen along the principal axes of the stress, the plastic wave speeds c_f and c_s depend on the direction of propagation, not on the stress components. The directions along which c_f and c_s assume the largest and smallest values are determined. A means of determining the slowness surface when the coordinate axes are not along the principal axes of stress is presented.

INTRODUCTION

When the material is in an elastic state, the relation between the stress σ_{ij} and the strain ε_{ij} in a rectangular coordinate system x_i is given by

$$\sigma_{ij} = 2\mu\varepsilon_{ij} + \lambda\delta_{ij}\varepsilon_{kk} , \tag{1}$$

where λ and μ are the Lame constants. Inversion of equation (1) is

$$\varepsilon_{ij} = \frac{1}{2\mu}\sigma_{ij} - \frac{\lambda}{2\mu(2\mu+3\lambda)}\delta_{ij}\sigma_{kk} . \tag{2}$$

When the stress state is such that

$$f(s_{ij}) = k^2, \qquad s_{ij} = \sigma_{ij} - \frac{1}{3}\delta_{ij}\sigma_{kk} , \tag{3}$$

where f is a homogeneous function of s_{ij} and k is the yield stress which depends on the work-hardening, the material is in a plastic state. The relation between ε_{ij} and σ_{ij} is given by Hill (ref. 1) ,

---

*This work is supported by the U.S. Army Research Office - Durham, Grant DAAG 29-76 G 0121 through the University of Illinois at Chicago Circle.

$$\dot{\varepsilon}_{ij} = \frac{1}{2\mu}\dot{\sigma}_{ij} - \frac{\lambda}{2\mu(2\mu+3\lambda)}\delta_{ij}\dot{\sigma}_{kk} + G\dot{f}f_{ij} \quad , \tag{4}$$

where G is a known function of k, a dot stands for differentiation with respect to time t, and

$$f_{ij} = \frac{\partial f}{\partial \sigma_{ij}} \quad . \tag{5}$$

To ensure zero plastic volume change, we must have

$$f_{ii} = 0 \quad . \tag{6}$$

Equation (4) can be inverted as

$$\dot{\sigma}_{ij} = 2\mu(\dot{\varepsilon}_{ij} - G\dot{f}f_{ij}) + \lambda\delta_{ij}\dot{\varepsilon}_{kk} \quad , \tag{7}$$

where the property (equation (6)) has been used. Since $\dot{f} = f_{ij}\dot{\sigma}_{ij}$, multiplying both sides of equation (7) by f_{ij} yields

$$\dot{f} = (1-h)2\mu f_{ij}\dot{\varepsilon}_{ij} \quad , \tag{8}$$

$$(1-h) = (1 + 2\mu G f_{ij} f_{ij})^{-1} \quad . \tag{9}$$

With equation (8), equation (7) can be written as

$$\dot{\sigma}_{ij} = 2\mu\dot{\varepsilon}_{ij} + \lambda\delta_{ij}\dot{\varepsilon}_{kk} - 4\mu^2(1-h)G f_{ij}f_{k\ell}\dot{\varepsilon}_{k\ell} \quad . \tag{10}$$

By specializing equation (10) for the case of a simple shear, it can be shown that (when the Tresca's yield condition is used),

$$1 - h = \mu_p/\mu \quad , \tag{11}$$

where μ_p is the slope of the simple shear stress-shear strain curve. Hence, $0 \le h \le 1$. When the material is elastic $h = 0$ and when the material is perfectly plastic $h = 1$.

If we write equation (10) in the form

$$\dot{\sigma}_{ij} = M_{ijk\ell}\dot{\varepsilon}_{k\ell} \quad , \tag{12}$$

the wave speed c, which depends on the direction of propagation n_i, is given by reference 2

$$\|Q_{ik}\| = 0 \quad , \tag{13}$$

$$Q_{ik} = M_{ijk\ell} n_j n_\ell - \rho c^2 \delta_{ik} \ , \tag{14}$$

$$n_1^2 + n_2^2 + n_3^2 = 1 \ , \tag{15}$$

where ρ is the mass density of the medium. Therefore, for the stress-strain relation given by equation (10) we have

$$\frac{Q_{ik}}{\rho} = (c_1^2 - c_2^2) n_i n_k + (c_2^2 - c^2)\delta_{ik} - 4\mu c_2^2 (1-h) G \, f_{ij} f_{k\ell} n_j n_\ell \ . \tag{16}$$

By a direct calculation, or using the identity derived in reference 3, it can be shown that

$$\frac{\|Q_{ik}\|}{\rho^3} = (c_2^2 - c^2)\{(c_2^2 - c^2)(c_1^2 - c^2) - 4\mu c_2^2 (1-h) G[(c_1^2 - c^2) f_{ij} n_j f_{i\ell} n_\ell - (c_1^2 - c_2^2)(f_{ij} n_i n_j)^2]\} \ . \tag{17}$$

From equation (17), we see that $c = c_2$ is always a plastic wave speed regardless of the form of yield function (equation (3)) one assumed. The other two wave speeds are obtained from the equation

$$(c_2^2 - c^2)(c_1^2 - c^2) - 4\mu c_2^2 (1-h) G\{(c_1^2 - c^2) f_{ij} n_j f_{i\ell} n_\ell - (c_1^2 - c_2^2)(f_{ij} n_i n_j)^2\} = 0 \ . \tag{18}$$

WAVE SPEEDS

For materials which obey the Tresca's yield condition, let the principal deviatoric stresses be denoted by S_1, S_2 and S_3, respectively. We will assume that

$$S_1 > S_2 > S_3 \ . \tag{19}$$

For the discussion of wave speed, we take the coordinate axes x_1, x_2, x_3 along the directions of the principal stresses. Hence

$$s_{ij} = \begin{bmatrix} S_1 & 0 & 0 \\ 0 & S_2 & 0 \\ 0 & 0 & S_3 \end{bmatrix} \ , \tag{20}$$

$$f = \left(\frac{S_1 - S_3}{2}\right)^2 = k^2 \ , \tag{21}$$

$$f_{ij} = \begin{bmatrix} k & 0 & 0 \\ 0 & 0 & 0 \\ 0 & 0 & -k \end{bmatrix} , \tag{22}$$

$$(1 - h) = (1 + 4\mu k^2 G)^{-1} . \tag{23}$$

Equation (18) then simplifies to

$$(c_2^2-c^2)(c_1^2-c^2) - hc_2^2\{(c_1^2-c^2)(n_1^2+n_3^2) - (c_1^2-c_2^2)(n_1^2-n_3^2)^2\} = 0 . \tag{24}$$

Equation (24) shows that the wave speeds c depend on the direction n_i only, not on the stress components. Let c_f and c_s be the two roots of equation (24) where the subscripts f and s stand for "fast" and "slow" wave speeds, respectively. Since the left-hand side of equation (24) is positive when $c = 0$ and $c = c_1$, and negative when $c = c_2$, the two roots c_f, c_s must lie in the ranges given by

$$0 \leq c_s \leq c_2 \leq c_f \leq c_1 . \tag{25}$$

In reference 4, Clifton obtained the plastic wave speeds for n_i which lies on one of the principal planes. Equation (24) is valid for arbitrary n_i.

DEPENDENCE OF c_f, c_s ON n_i

It is more convenient to write equation (24) in a nondimensional form by introducing the following notations:

$$\bar{c} = \frac{c}{c_2} , \qquad \eta^2 = \frac{c_1^2}{c_2^2} = 1 + \frac{1}{1-2\nu} \geq 2 , \tag{26}$$

where ν is the Poisson's ratio. We then have

$$(1-\bar{c}^2)(\eta^2-\bar{c}^2) - h\{(\eta^2-\bar{c}^2)(n_1^2+n_3^2) - (\eta^2-1)(n_1^2-n_3^2)^2\} = 0 . \tag{27}$$

To see the dependence of the two roots $\bar{c}_f$, $\bar{c}_s$ on n_i, we draw on the (n_1,n_3) plane curves of constant $\bar{c}_f$ (fig. 1) and curves of constant $\bar{c}_s$ (fig. 2) with h and ν being fixed. It is seen that the curves are symmetric with respect to the n_1 axis, n_3 axis, and the 45° diagonals. Since $n_2^2 = 1 - (n_1^2 + n_3^2)$ by equation (15), $n_2 =$ constant represents a circle in the (n_1,n_3) plane. In particular, the circle of radius unity corresponds to $n_2 = 0$ and the origin corresponds to $n_2 = 1$. One may consider the curves in figs. 1 and 2 as the projection on the (n_1,n_3) plane of curves drawn on the surface of a unit sphere in the (n_1,n_2,n_3) space. With figs. 1 and 2, c_f and c_s are readily obtained when the direction of propagation n_i is given.

A particularly interesting result is the straight-lines for the particular value $c_s = c_s^*$ shown in fig. 2. By letting

$$n_1 = \pm n_3 + b \ , \tag{28}$$

we see that equation (27) is satisfied if

$$b^2 = \frac{2(\eta^2-1)}{\{4(\eta^2-1) - h\}} \ , \tag{29}$$

$$c_s = c_2 \left\{ 1 - \frac{h(\eta^2-1)}{4(\eta^2-1) - h} \right\}^{1/2} = c_s^* \ , \quad \text{say.} \tag{30}$$

It can be shown that $1/2 < b^2 < 2/3$ for $2 < \eta^2 < \infty$, $0 < h < 1$.

If we use the polar coordinates:

$$n_1 = r \cos\theta \ , \qquad n_3 = r \sin\theta \ , \tag{31}$$

we can verify from equation (27) that

$$\frac{\partial \bar{c}_f}{\partial \theta} \geq 0 \ , \qquad \frac{\partial \bar{c}_s}{\partial \theta} \leq 0 \ , \qquad \text{for} \quad 0 \leq \theta \leq \frac{\pi}{4} \ , \tag{32}$$

where the equality holds at $\theta = 0$ and $\pi/4$. By rewriting equation (27) as

$$\bar{c}^4 - (\eta^2 + 1 - hr^2)\bar{c}^2 + \ldots = 0 \ , \tag{33}$$

we see that

$$\bar{c}_f^2 + \bar{c}_s^2 = \eta^2 + 1 - hr^2 \ . \tag{34}$$

Hence $\bar{c}_f^2 + \bar{c}_s^2$ is a constant along any circle $r = \text{constant}$.

THE LARGEST AND SMALLEST c_f and c_s

From equation (25), the largest c_f is c_1. If we let $\bar{c} = \eta$, equation (27) is satisfied when $h = 0$ (elastic) or $n_1 = \pm n_3$. In fig. 1, $c_f = c_1$ along the two 45° diagonals. The locus of $n_1 = \pm n_3$ is two orthogonal planes on which the shear stress has the largest value k.

The largest c_s by equation (25) is c_2. When $\bar{c} = 1$, equation (27) is satisfied if $h = 0$ or

$$(n_1^2 + n_3^2) - (n_1^2 - n_3^2)^2 = 0 \ . \tag{35}$$

The solutions of equations (35) and (15) are $n_i = (\pm 1,0,0)$, $(0,\pm 1,0)$, or $(0,0,\pm 1)$. In other words, the largest c_s occurs along the principal directions.

From equation (34), the smallest $\bar{c}_f$ is obtained by letting $\bar{c}_s$ and r assume the largest values. Hence

$$(\bar{c}_f^2)_{min} = \eta^2 - h, \text{ at } \underset{\sim}{n} = (\pm 1,0,0), \quad (0,0,\pm 1) \ . \tag{36}$$

Since η depends on the Poisson's ratio ν (equation (26)), $(\bar{c}_f)_{min}$ depends on ν and h. This dependency is shown graphically in fig. 3. It is seen that the smallest c_f/c_1 is obtained when $\nu = 0$ and $h = 1$ (perfectly plastic).

By a similar argument using equation (34), the smallest $\bar{c}_s$ is

$$(\bar{c}_s^2)_{min} = 1 - h, \quad \text{at} \quad n_1 = \pm n_3 , \quad n_2 = 0 \ . \tag{37}$$

Therefore, $(\bar{c}_s)_{min}$ depends only on h, not on ν.

THE SLOWNESS SURFACE

In the (x_1,x_2,x_3) space, the slowness surface is obtained by the locus of points:

$$\underset{\sim}{x} = \frac{1}{c} \underset{\sim}{n} \ . \tag{38}$$

The slowness surface is useful in studying the reflection and transmission of a wave front at an interface boundary. In fact, we do not need the entire slowness surface. All we need is a cross section of the slowness surface given by equation (38) and a plane

$$\alpha n_1 + \beta n_2 + \gamma n_3 = 0 \ , \tag{39}$$

where α, β, γ are components of a unit vector. In figs. 1 and 2, the locus of (n_1,n_3) subjected to the conditions (equations (15) and (39)) is an ellipse (dotted line in figs. 1 and 2) whose semi-major axis is unity and the semi-minor axis is β. The orientation of the major axis depends on α and γ. When $\beta = 0$, the ellipse is reduced to a straight-line (a diameter). $\beta = 1$ corresponds to the unit circle.

In the analysis presented so far, the x_1, x_2, x_3 axes are assumed to be in the directions of the principal stresses. If the deviatoric stress s_{ij} is given on the X_1, X_2, X_3 axes which are not the principal axes, one can obtain the wave speeds c_f and c_s in the following way. Let $\underset{\sim}{N} = (N_1,N_2,N_3)$ be the direction of propagation referred to the (X_1,X_2,X_3) coordinates while $\underset{\sim}{n} = (n_1,n_2,n_3)$ be, as before, the direction of propagation referred to the

principal axes (x_1,x_2,x_3). Both $\underset{\sim}{N}$ and $\underset{\sim}{n}$ are unit vectors. If we diagonalize the matrix $\underset{\sim}{s} = \{s_{ij}\}$ as

$$\underset{\sim}{s} = \underset{\sim}{Q} \begin{bmatrix} S_1 & 0 & 0 \\ 0 & S_2 & 0 \\ 0 & 0 & S_3 \end{bmatrix} \underset{\sim}{Q}^T , \tag{40}$$

where the matrix $\underset{\sim}{Q}$ is an orthogonal matrix, it can be shown that

$$\underset{\sim}{n} = \underset{\sim}{Q}^T \underset{\sim}{N} . \tag{41}$$

As an example, consider

$$s_{ij} = \frac{k}{\sqrt{2}} \begin{bmatrix} 0 & 1 & 0 \\ 1 & 0 & 1 \\ 0 & 1 & 0 \end{bmatrix} . \tag{42}$$

From equation (40), we find $S_1 = k$, $S_2 = 0$, $S_3 = -k$, and

$$\underset{\sim}{Q}^T = \frac{1}{2} \begin{bmatrix} 1 & \sqrt{2} & 1 \\ \sqrt{2} & 0 & -\sqrt{2} \\ 1 & -\sqrt{2} & 1 \end{bmatrix} . \tag{43}$$

If we are interested in the slowness surface for $\underset{\sim}{N}$ in the (X_1,X_2) plane, we have $\underset{\sim}{N} = (\sin\theta, \cos\theta, 0)$ where θ is the angle between $\underset{\sim}{N}$ and the X_2-axis. Equation (41) then furnishes $\underset{\sim}{n}$ and $\bar{c}_f$, $\bar{c}_s$ are obtained from equation (27). The dependence of $\bar{c}_f^{-1}$ and $\bar{c}_s^{-1}$ on θ for the stress state given by equation (42) is shown in fig. 4. Only half of the figure is shown because of symmetry about the X_1 axis.

CONCLUSION

We summarize the results obtained in the following.

1. When the coordinate axes (x_1,x_2,x_3) are taken along the principal directions of the stress, the plastic wave speeds c_f and c_s depend on the direction of propagation $\underset{\sim}{n}$ referred to (x_1,x_2,x_3). c_f and c_s are independent of the stress components.
2. The largest c_f is c_1 which occurs along the directions $n_1 = \pm n_3$. The smallest c_f is

$$\left(\frac{c_f}{c_1}\right)^2_{\min} = 1 - h\left(\frac{c_2}{c_1}\right)^2 , \tag{44}$$

which occurs along the x_1 and x_3 directions.

3. The largest c_s is c_2 which occurs along the three principal directions x_1, x_2 and x_3. The smallest c_s is

$$\left(\frac{c_s}{c_2}\right)^2_{min} = 1 - h \tag{45}$$

which occurs along $n_1 = \pm n_3$, $n_2 = 0$. In particular, $(c_s)_{min} = 0$ when $h = 1$ (perfectly plastic).

4. $c_f = c_s = c_2$ when $\nu = 0$ and $h = 1$. The directions along which $c_f = c_s = c_2$ is the x_1 and x_3 directions.

The significance of equation (44) is that for $\nu = 1/3$ (which is the value for most materials) and $h = 1/2$ (which represents a moderate loading), $(c_f/c_1)_{min} = 0.935$. That is, the difference between the fast plastic and elastic wave speeds is no more than 6.5%. Therefore, if a three-dimensional analysis is used for ealstic-plastic waves, the plastic precursor wave front will arrive at a speed within 6.5% of elastic wave speed. In many cases, this percentage will be smaller because not all plastic waves propagate at the slowest speed. This is in direct contrast with one-dimensional analysis in which the plastic wave speed can be much lower than the elastic wave speed.

REFERENCES

1. Hill, R.: The Mathematical Theory of Plasticity. Clarendon Press, Oxford, 1950.

2. Courant, R.; and Hilbert, D.: Methods of Mathematical Physics, Vol. II. Interscience, New York, 1962.

3. Ting, T. C. T.: Elastic-Plastic Boundaries in the Propagation of Plane and Cylindrical Waves of Combined Stress. Quart. Appl. Math., Vol. 47, 1970, pp. 411-449.

4. Clifton, R. J.: Analysis of Dynamic Deformation of Elastic/Plastic Solids Under Conditions of Plane Strain. Ph.D. Thesis, Carnegie Institute of Technology, 1963.

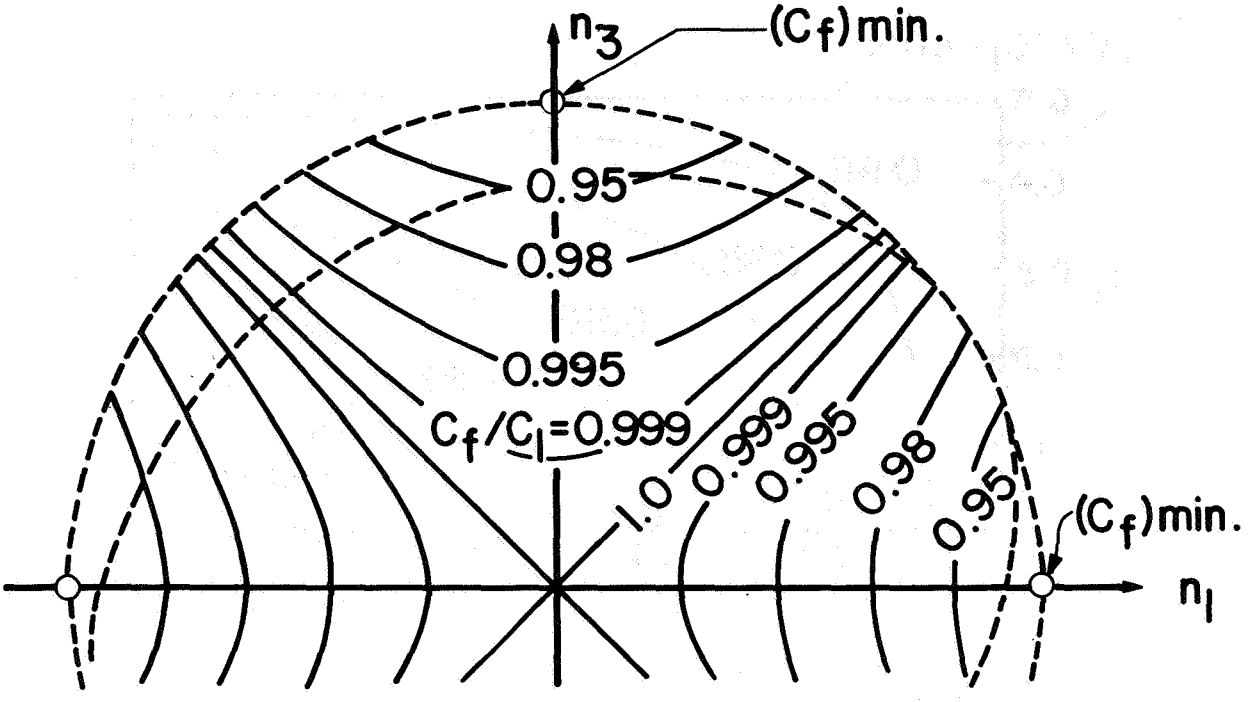

Figure 1.- Contour lines for constant c_f/c_1 (drawn for h=1/2,ν=1/3).

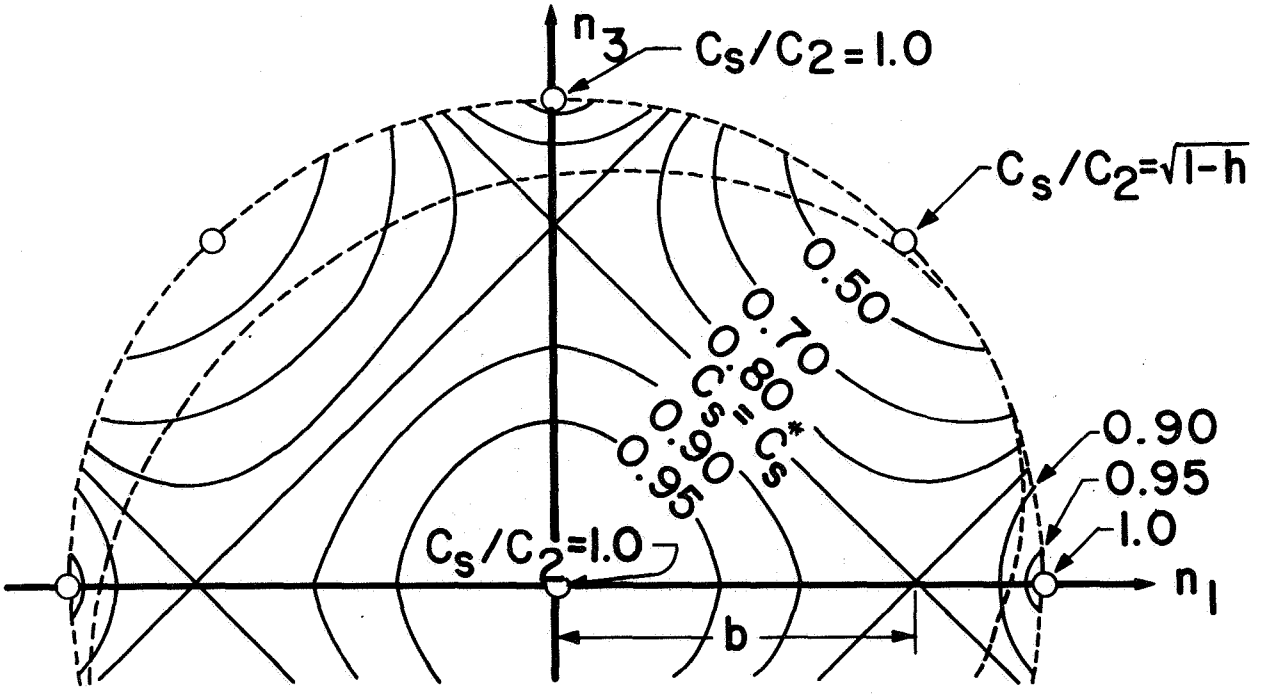

Figure 2.- Contour lines for constant c_s/c_2 (drawn for h=1/2,ν=1/3).

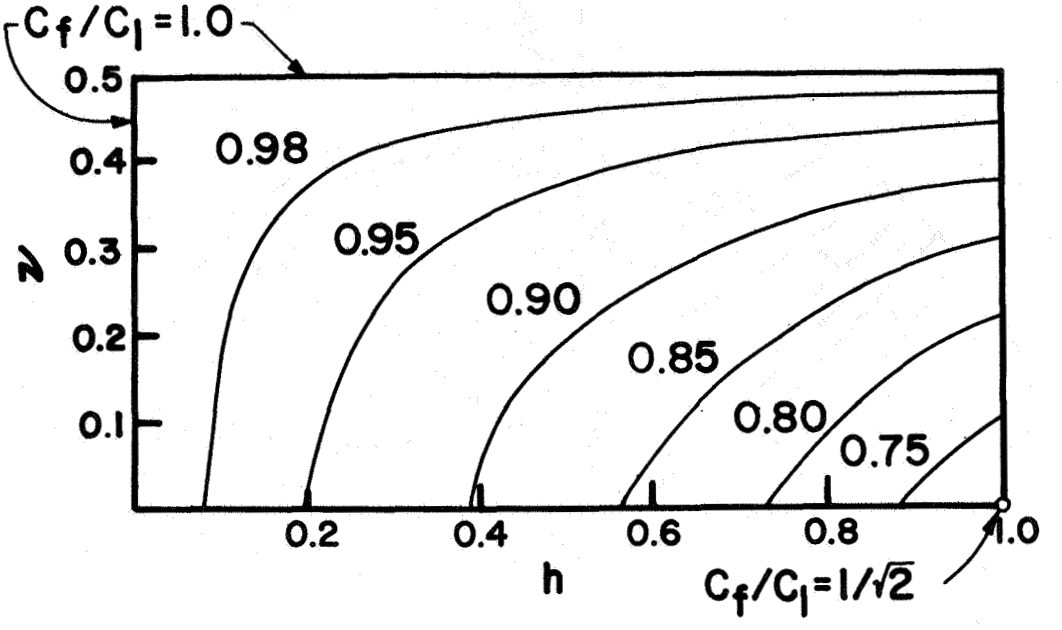

Figure 3.- Dependence of (c_f)min. on h and ν.

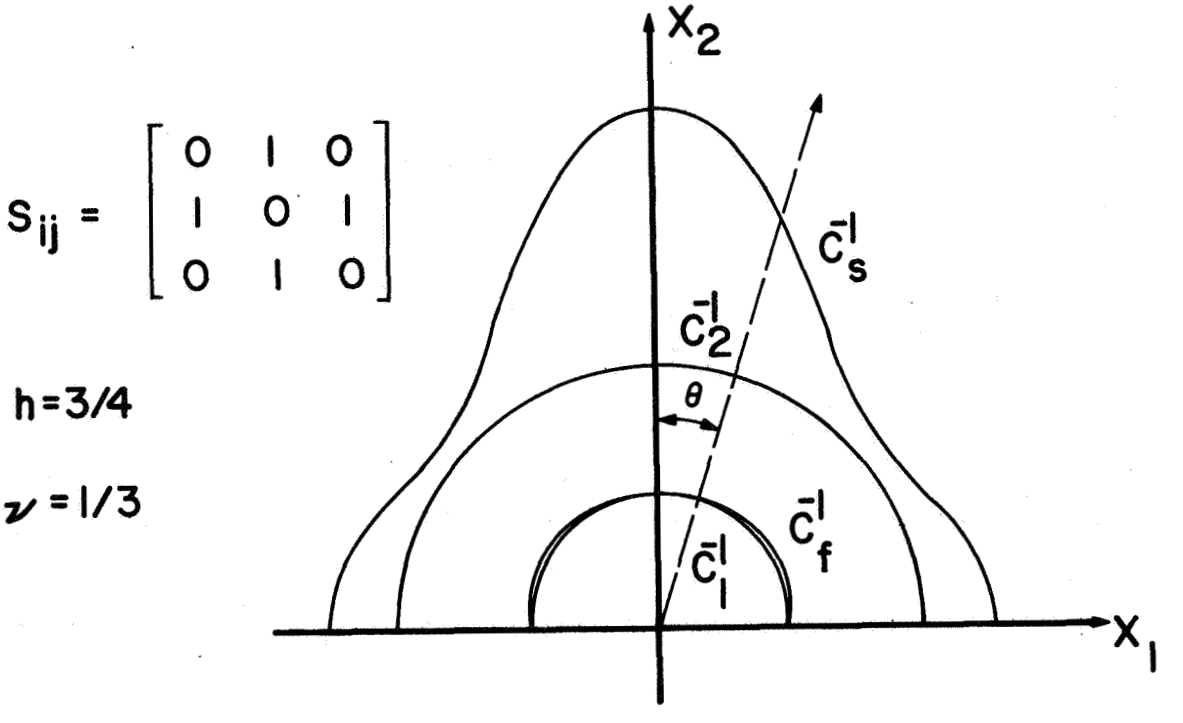

Figure 4.- Intersection of the slowness surface with the (X_1, X_2) plane.

MATHEMATICAL MODELLING OF UNDRAINED CLAY BEHAVIOR

Jean-Hervé Prévost and Kaare Høeg
Norwegian Geotechnical Institute

SUMMARY

The proposed general analytical model describes the anisotropic, elasto-plastic, path-dependent, stress-strain properties of inviscid saturated clays under undrained conditions. Determination of the model parameters is achieved by using results from strain-controlled simple shear tests on a saturated clay. Thereafter, the model's accuracy is evaluated by applying it to predict the results of other tests on the same clay, including monotonic and cyclic loading. The model explains the very anisotropic shear strength behavior observed for weak marine clays.

PROPOSED MATHEMATICAL MODEL

The details of the proposed mathematical model are given in reference 1. In order to separate the contributions of the elastic and plastic properties in the total deformations, it is assumed that the material's elasticity is linear and isotropic, and that non-linearity and anisotropy result from the material's plasticity. The model combines properties of isotropic (ref. 2) and kinematic (ref. 3) plasticity by introducing the concept of a field of plastic moduli (refs. 4 and 5). This field is defined in stress space by a collection of yield surfaces $f_o,\ldots,f_n$ of respective sizes $k^{(o)},\ldots,k^{(n)}$. A plastic shear modulus H'_m is associated with each of the surfaces, and the associative flow rule is used to compute the plastic strains. The total strain is the sum of the elastic and plastic strains. The hardening rule (ref. 5) specifies that all yield surfaces may be translated in stress space by the stress point without changing in form and orientation. The yield surfaces will consecutively touch and push each other but cannot intersect. For any loading (or unloading) history, the instantaneous configuration of the yield surfaces is determined by calculating the translation and expansion (or contraction) of each yield surface during successive changes in load. The material behavior can thus be determined for complex loading paths and for cyclic loading.

During undrained loading, the yielding of saturated clay is independent of the imposed octahedral normal total stress component. The yield surfaces may therefore be expressed by equations of the form

$$\left[\frac{3}{2}\,(s_{ij}-\alpha_{ij}^{(m)})(s_{ij}-\alpha_{ij}^{(m)})\right]^{1/2}-k_{(\lambda)}^{(m)}=0 \qquad (m=0,1,\ldots,n) \tag{1}$$

where the tensor $\alpha_{ij}^{(m)}$ represents the translation of the yield surface f_m and $k_{(\lambda)}^{(m)}$ is a measure of its current size. s_{ij} denotes the deviatoric stress tensor components. λ is a scalar parameter monotonically increasing during the deformation process:

$$\lambda = \int \left[\frac{2}{3}\, de^{p}_{ij}\, de^{p}_{ij}\right]^{1/2} \qquad (2)$$

where the integration is carried out over the strain path. de^{p}_{ij} denotes the incremental plastic deviatoric strain tensor components.

DETERMINATION OF MODEL PARAMETERS

The clay samples were initially preconsolidated under a vertical effective stress of 400 kPa with the condition of no horizontal strains, and thereafter were unloaded to a vertical effective stress σ'_{vc} = 100 kPa before undrained shearing. The model parameters are determined based on the observed experimental behavior of the clay in slow monotonic (strain rate = 4.5%/hr) and rapid cyclic (period = 10s.) two-way strain-controlled simple shear tests.

Figure 1a presents the results from a test with monotonic loading. τ_h denotes the average horizontal shear stress measured experimentally. In the interior of the specimen, it has been shown that $\tau_{xy} = \tau \simeq 1.11\ \tau_h$. Figure 1a also shows typical hysteresis loops obtained in one of the cyclic strain-controlled tests for which the strain amplitude is γ_1 = 1.3%. After a number of cycles, the loops develop an S-shape which becomes even more marked as the number of cycles increases. However, it is an experimental finding that the gradients of all hysteresis loops at peak shear stress stay the same and are approximately equal to the gradient observed in the monotonic test at γ_1 = 1.3%. The test results are summarized in figure 1b by plotting the shear stress amplitude for different imposed shear strain amplitudes at different numbers of cycles. The vertical axis shows the ratio τ_h/τ_{hf} where τ_{hf} = 0.714 σ'_{vc} = undrained shear strength measured in the monotonic test. It is of importance to note that the shear stress which is necessary to produce a specified strain amplitude during the first quarter cycle N = 1 of the cyclic tests is larger than the one observed in the monotonic test. The stress-strain curve constructed from the cyclic test results at N = 1 is shown by the upper curve in figure 1a.

Complete specification of the mathematical model parameters requires the determination of (1) the initial positions and sizes of the yield surfaces before undrained shearing, (2) their associated plastic moduli, and (3) their size changes as loading proceeds. For simplicity, it is assumed that the yield surfaces change negligibly in size during the first loading sequence because λ is then small and therefore $k^{(m)}(\lambda)$ = constant. Moreover, it is assumed that the length λ of the cyclic plastic deviatoric shear strain trajectory is the same as the length of the total one because the elastic strains are not cumulative and therefore their contribution is very small.

Under an axisymmetric stress state ($\tau_{yz} = \tau_{zx} = \alpha_{yz} = \alpha_{zx} = 0$) with equal horizontal normal stresses ($\sigma_x = \sigma_z$ and therefore $\alpha_x = \alpha_z$), the position in stress space of the yield surfaces is defined by the determination of only two parameters $\alpha^{(m)}$ and $\beta^{(m)}$ (m=0,...,n), and equation (1) simplifies to

$$\left[\left[\sigma_y - \sigma_x\right] - \alpha^{(m)}\right]^2 + \left[\tau_{xy}\sqrt{3} - \beta^{(m)}\right]^2 - \left[k^{(m)}(\lambda)\right]^2 = 0 \qquad (3)$$

where $\alpha^{(m)} = \alpha_y^{(m)} - \alpha_x^{(m)} = 3\,\alpha_y^{(m)}/2$ and $\beta^{(m)} = \alpha_{xy}^{(m)}\sqrt{3}$. It is convenient here to refer to the shear modulus H_m defined as

$$\frac{2}{H_m} = \frac{1}{G} + \frac{2}{H'_m} \tag{4}$$

for all m, where G is the elastic shear modulus. Simple analytical functions for the field of yield surfaces and for H_m and $k^{(m)}$ will be suggested so that mathematical solutions may be achieved in closed form.

The initial locations $(\alpha_o^{(m)}, \beta_o^{(m)})$ in stress space of the yield surfaces are determined by the soil's consolidation history (ref. 1), and

$$\alpha_o^{(m)} = \frac{d}{2}\left[1 - \left(\frac{k_o^{(m)} - d}{d}\right)^2\right] \quad ; \quad \beta_o^{(m)} = 0 \tag{5}$$

for all m, where $d = \sigma'_{vc}$ and $k_o^{(m)}$ denote the sizes of the yield surfaces under slow monotonic loading conditions. Their associated shear moduli are deduced from the monotonic simple shear stress-strain curve shown in figure 1a:

$$H_m = 2\,\frac{d\tau}{d\gamma}\bigg|_{\tau\sqrt{3} = k_o^{(m)}} = \frac{2}{3}\,\frac{\left[\tau_f\sqrt{3} - k_o^{(m)}\right]^2}{a'\tau_f} \tag{6}$$

where $\tau_f = 1.11\,\tau_{hf}$ and a' is an experimental constant. In the course of cyclic loading, the yield surfaces all change in size:

$$k^{(m)}(\lambda) = k_o^{(m)} + \delta(\lambda) \tag{7}$$

until they reach their ultimate limiting sizes $k_L^{(m)}$, experimentally determined to be:

$$k_L^{(m)} = 0.08\,k_o^{(m)} \tag{8}$$

The cyclic two-way simple shear strain-controlled experimental test results (fig. 1b) may be combined to yield a single analytical expression for the isotropic softening function $\delta(\lambda)$:

$$\delta(\lambda) = \left[\delta_1 - \delta_{ult}\right] \exp\left[-A\,\mathrm{Ln}\,\frac{\lambda'}{\lambda_1}\left(B + \mathrm{Ln}\,\frac{\lambda'}{\lambda_1}\right)\right] + \delta_{ult} \tag{9a}$$

with

$$A = \frac{\mathrm{Ln}(1 - \delta_1/\delta_{ult})}{\mathrm{Ln}(5 + b/\lambda_1^c)\left[B + \mathrm{Ln}(5 + b/\lambda_1^c)\right]} \tag{9b}$$

in which δ_1, δ_{ult}, b, c, and B are experimental constants: $\delta_1 = 0.15\,\tau_f\sqrt{3}$, $\delta_{ult} = -0.70\,\tau_f\sqrt{3}$, b = 1.45, c = 5.96 and B = 1.67. λ_1 denotes the current deviatoric shear strain amplitude of the cyclic loading ($\lambda_1 = \gamma_1/\sqrt{3}$). λ' denotes the equivalent length of the deviatoric shear strain trajectory which corresponds to the current λ_1 value after N cycles of loading: $\lambda' = \lambda_1[1 + 4(N - 1)]$. Under cyclic two-way strain-controlled loading conditions, λ_1 is constant and thus $\lambda' = \lambda$.

Once the yield surfaces reach their ultimate limiting sizes $k_L^{(m)}$ (eq.(8)), their respective shear moduli start to vary, and the experimental test results

(fig. 1a) suggest that:

$$H_m = \frac{\tau_f\sqrt{3} - k_L^{(m)}\, y_L}{x_L\, \tau_f} \sqrt{\left(\tau_f\sqrt{3} - k_L^{(m)} y_L\right)^2 + \left(k_L^{(m)} x_L\right)^2} \tag{10a}$$

with

$$x_L = 3a'\tau_f^2 \frac{(\sinh \gamma_L)^2}{(\cosh \gamma_L)\left[\delta(a' + \gamma_L) + \tau_f\sqrt{3}\gamma_L\right]} \tag{10b}$$

$$y_L = \frac{\tau_f\sqrt{3}\ (a' + \gamma_L)}{\delta(a' + \gamma_L) + \tau_f\sqrt{3}\gamma_L} - \frac{x_L}{\sinh \gamma_L} \tag{10c}$$

$$\gamma_L = a'\delta \frac{84/92}{\tau_f\sqrt{3} - 84\delta/92} \tag{10d}$$

where $\delta(\lambda)$ is given by equation (9).

APPLICATIONS - MODEL PREDICTIONS

In the previous section, the model parameters were determined by using the results from monotonic and cyclic strain-controlled simple shear tests. The model should be able to predict the results of other tests, and it was therefore applied to predict the results of (1) cyclic two-way stress-controlled simple shear tests (fig. 2), (2) monotonic triaxial compression and extension tests (fig. 3), (3) cyclic two-way strain- and stress-controlled triaxial tests (figs. 4 and 5, respectively) on the same clay. All theoretical predictions are found to agree very well with the experimental test results shown in figures 2 to 5.

CONCLUSIONS

It is concluded that the proposed general mathematical model for undrained soil behavior is very promising. In subsequent work, the model will be used in finite element formulations for the analysis of the complete general boundary value problem, in order to compute stresses and deformations under a structure subjected to cyclic loading, such as waves or earthquake excitations.

REFERENCES

1. Prévost, J.H. and K. Høeg: Mathematical Model for Static and Cyclic Undrained Clay Behavior. Norwegian Geotechnical Institute, Oslo, Norway, Report 52412, 1975, 142 p.

2. Hill, R.: The Mathematical Theory of Plasticity. Oxford Un. Press, London, 1950, 356 p.

3. Prager, W.: The Theory of Plasticity: A Survey of Recent Achievement. Proc. Ins. Mech. Eng., London, Vol.169, 1955, pp. 41-57.

4. Iwan, W.D.: On a Class of Models for the Yielding of Continuous and Composite Systems. Jnl Appl. Mech., ASME, Vol.34, Series E, No.3, 1967, pp. 612-617.

5. Mróz, A: On the Description of Anisotropic Workhardening. Jnl Mech. Phys. Solids, London, Vol.15, 1967, pp. 163-175.

NOTATION LIST

a', b, c, d, B, x_L, y_L, γ_L = experimental constants

$d\lambda = \left[\frac{2}{3} de^p_{ij} \; de^p_{ij}\right]^{1/2}$ = incremental plastic deviatoric shear strain

$e_{ij} = \varepsilon_{ij} - \frac{1}{3}\delta_{ij}(\varepsilon_{kk})$ = deviatoric strain

$f(\;)$ = general yield function

G = elastic shear modulus

$H = \left[\frac{1}{2G} + \frac{1}{H'}\right]^{-1}$ = shear modulus

H' = plastic shear modulus

$k(\;)$ = instantaneous yield surface size

k_L = yield surface limit size

N = number of applied cyclic loading

$s_{ij} = \sigma_{ij} - \frac{1}{3}\delta_{ij}(\sigma_{kk})$ = deviatoric stress

x,y,z = reference coordinate axis fixed with respect to the element and specified to coincide with the axis of preconsolidation

α,β = yield circle center coordinates in $\tau_{xy}\sqrt{3}$ vs $(\sigma_y - \sigma_x)$-stress plane

$\gamma = \gamma_{xy}$ = shear strain in simple shear test

$\delta(\;)$ = isotropic softening function

δ_1, δ_{ult} = experimental constants

$\varepsilon_v = \varepsilon_y$ = vertical strain

σ'_{vc} = vertical effective consolidation stress

$\sigma_v (= \sigma_y)$, $\sigma_h (= \sigma_x = \sigma_z)$ = vertical and horizontal stresses

$\tau = 1.11\,\tau_h \; (= \tau_{xy})$ = horizontal shear stress in simple shear test

τ_h = average horizontal shear stress in simple shear test

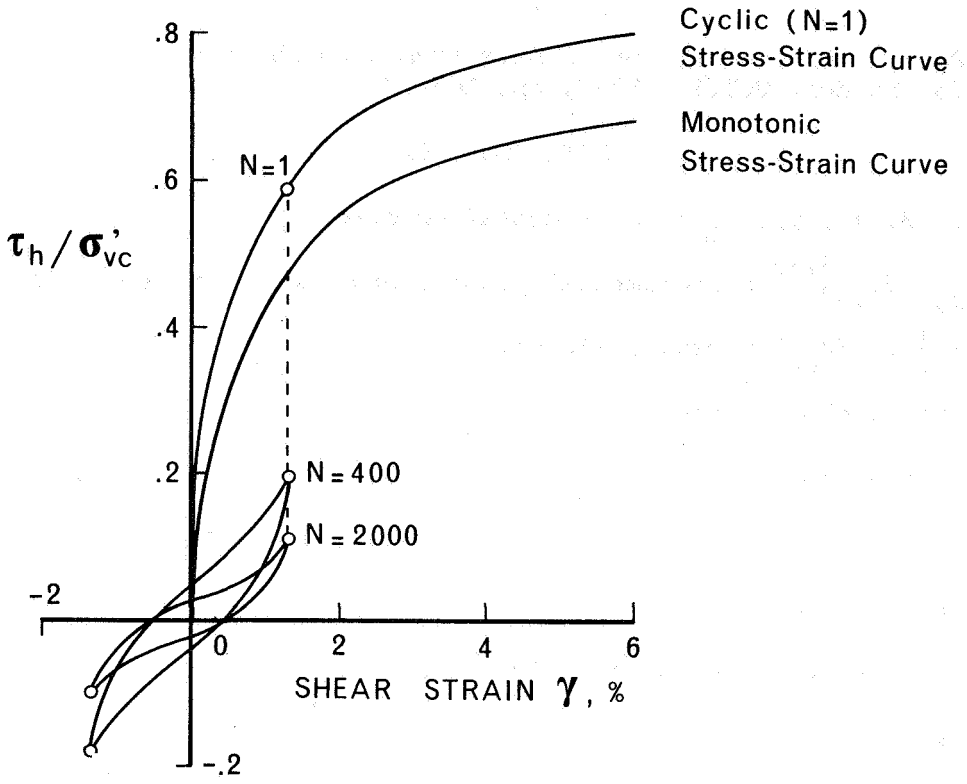

(a) Stress-strain curves.

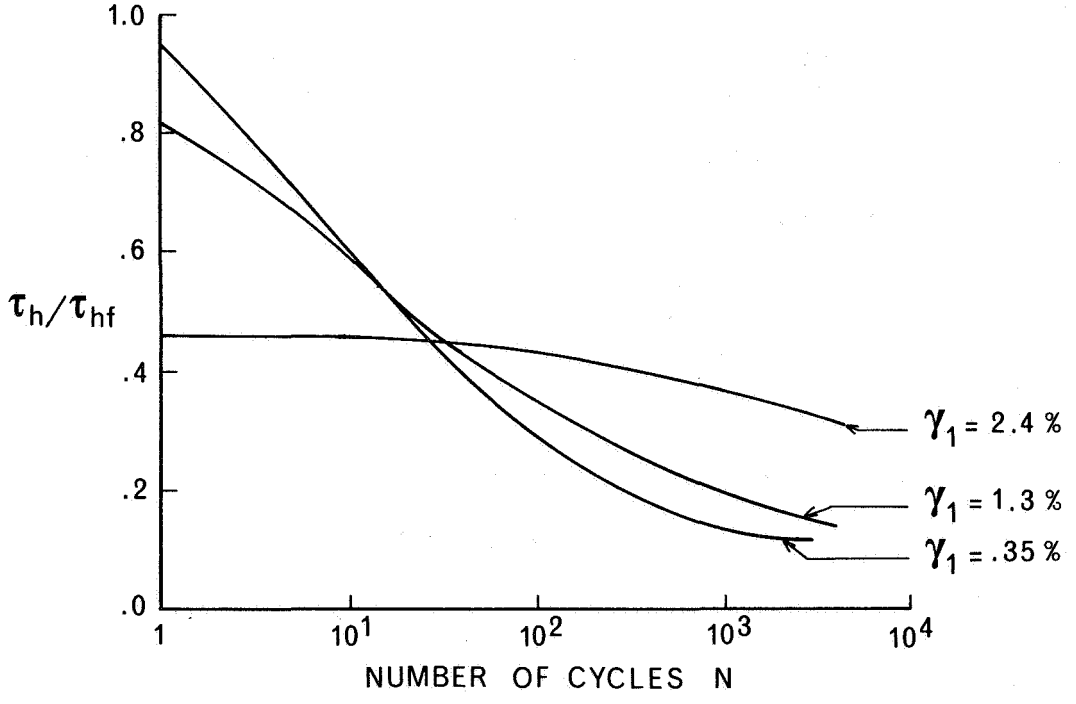

(b) Summary of test results.

Figure 1.- Simple shear strain-controlled experimental test results.

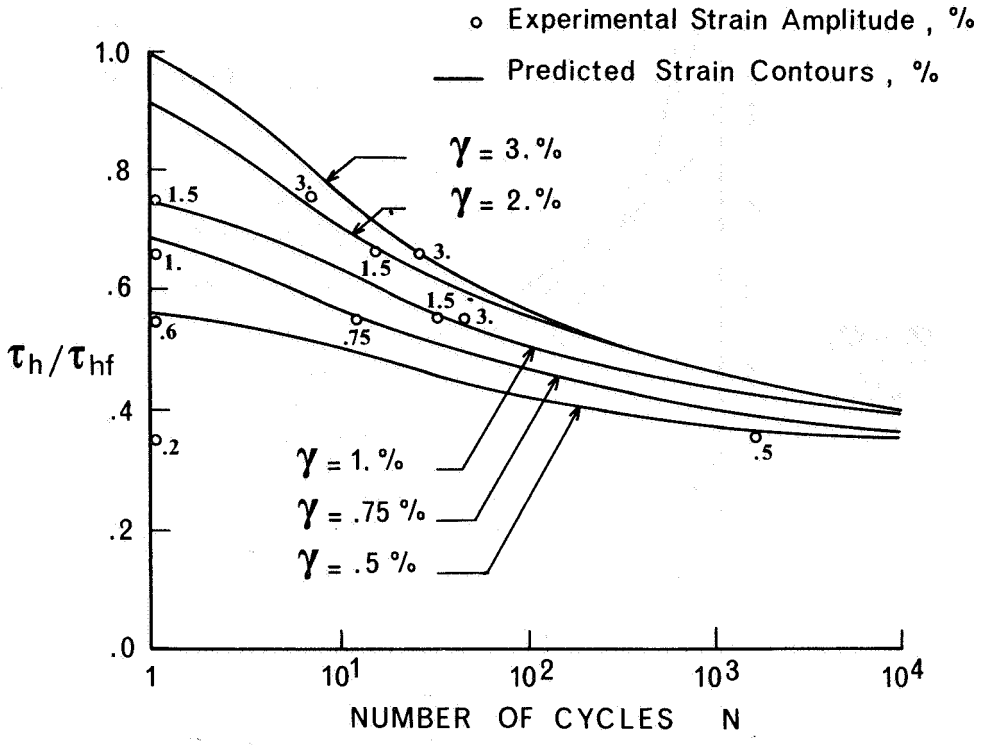

Figure 2.- Cyclic simple shear stress-controlled tests; model predictions; strain contours.

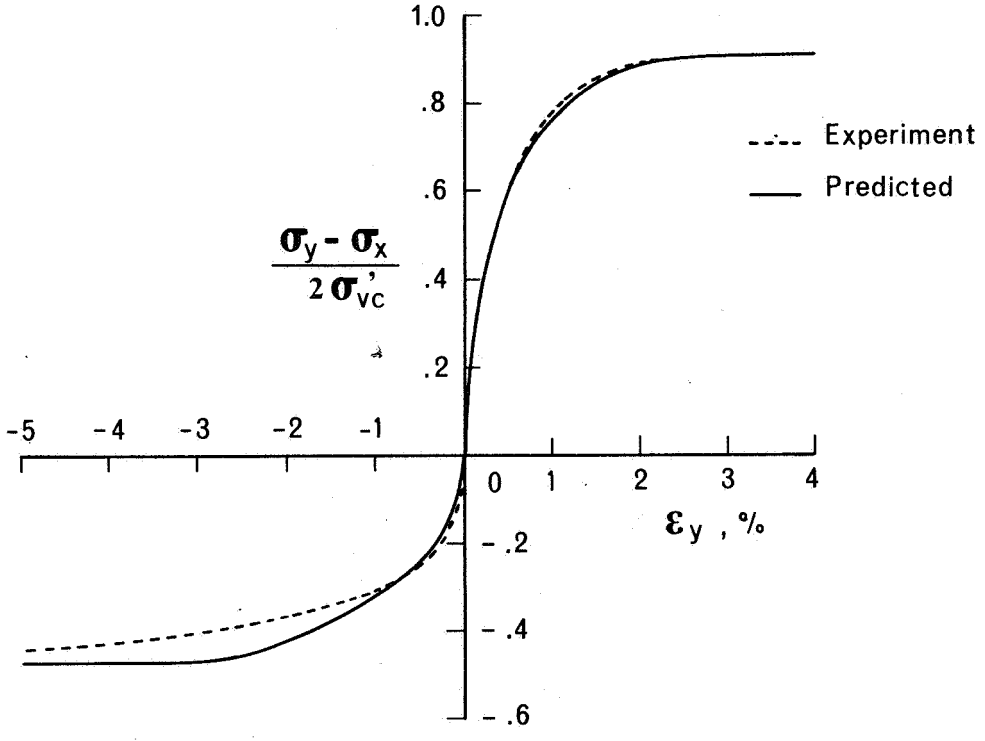

Figure 3.- Monotonic undrained triaxial tests; model predictions.

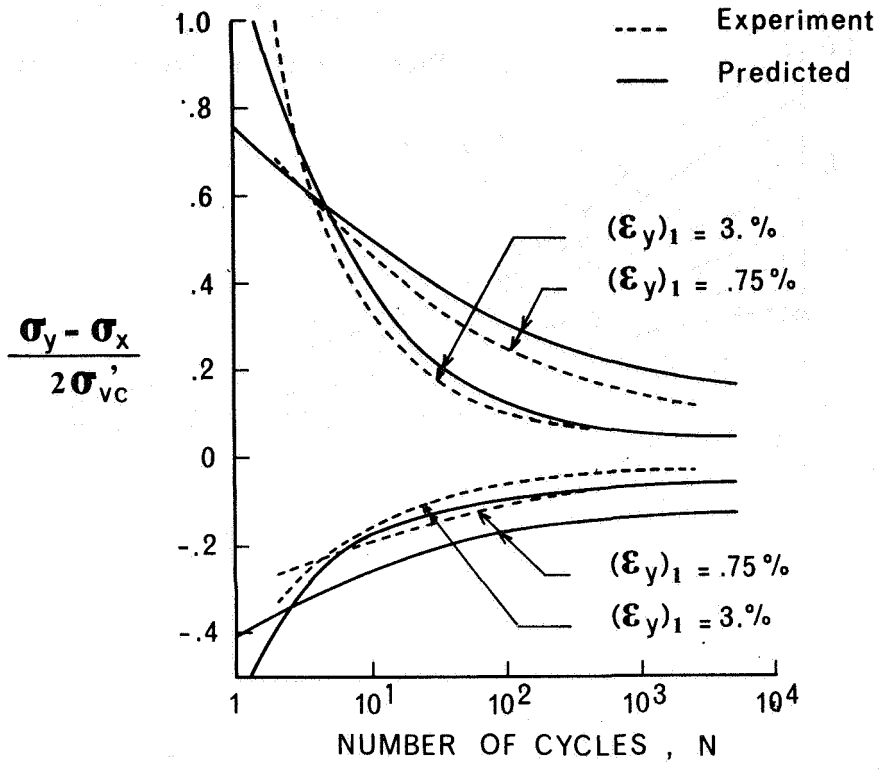

Figure 4.- Cyclic undrained triaxial strain-controlled tests; model predictions.

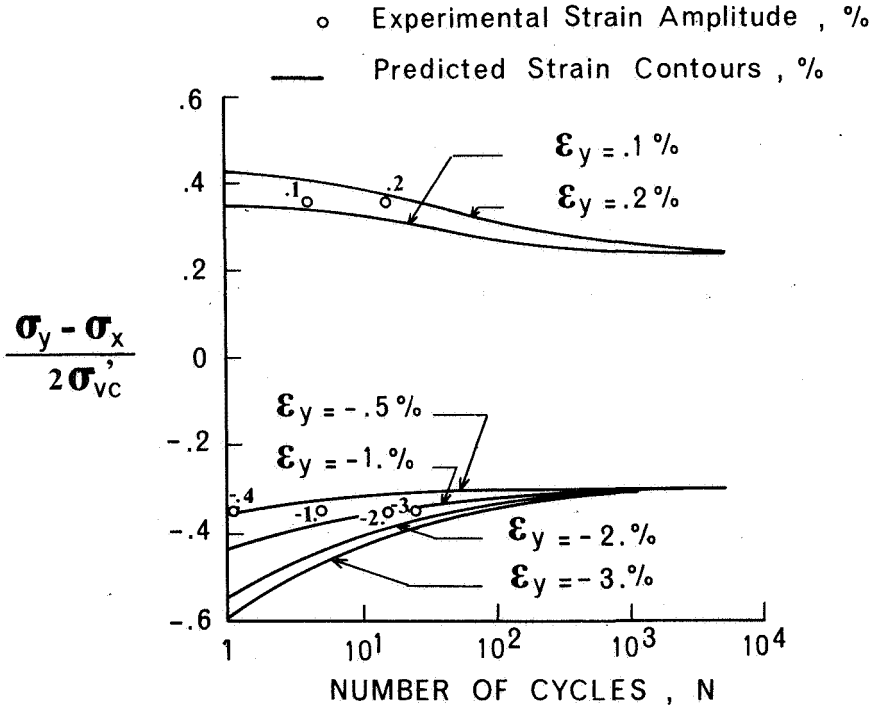

Figure 5.- Cyclic undrained triaxial stress-controlled tests; model predictions; strain contours.

THEORY OF ORTHODONTIC MOTIONS

Susan Pepe
School of Dental Medicine, University of Connecticut

W. Dennis Pepe
Connecticut General Insurance Co.

Alvin M. Strauss
Engineering Analysis Dept., University of Cincinnati

SUMMARY

A general theory of orthodontic motion is developed that can be applied to determine the forces necessary to induce a given tooth to move to the predetermined desirable position. It is assumed that the natural (non-orthodontic) forces may be represented by a periodic function and the orthodontic forces may be superimposed upon the natural forces. A simple expression is derived for the applied stress.

INTRODUCTION

The objective of this paper is to lay the foundation for a theory that may be used to predict the movement of teeth loaded by orthodontic appliances over moderately long periods of time, i.e. several hours to several years. There is some literature on the short term movement of teeth and on the response of the periodontal ligament to loading. Thus, given a tooth occupying a given position in its bone matrix, the theory seeks to predict the loads one needs to apply to the tooth to achieve the appropriate state of stress in the surrounding bone matrix that will yield the desired motion of the tooth to another position and will retain it there. The objective as stated above would not have been realistic a few years ago, because of a lack of quantitative knowledge of the forces normally experienced by human teeth and a corresponding lack of knowledge of the forces produced by various orthodontic appliances. The force systems delivered by these appliances are known to be statically indeterminate. Thus, there is little in the literature concerning the solution of problems involving orthodontic forces. However, advances are being made toward the solution of problems involving orthodontic force systems (ref. 1 - ref. 3).

At this time, one useful piece of information would be an appropriate constitutive equation that can be used to describe the properties of the bone matrix that the teeth are imbedded in, i.e. alveolar bone. However, the constitutive equations are not completely determined for any biomaterial, primarilly because of the difficulty in experimental programs (ref. 4). Orthodontics is unique among the biological disciplines for it exploits the viscoplastic nature of alveolar bone to move teeth from one state of equilibrium in the alveolar bone to another and to retain them there until the alveolar bone's memory of its stress history fades and the movement does not relapse. A variety of experimental programs are available in the orthodontist's office if only one were to collect the appropriate data. To this end, a number of assumptions must be made to obtain tractable relations if the equations that are derived are to be useful to practitioners in the field.

ASSUMPTION I. The teeth may be considered to be rigid bodies. Of course, the teeth are not rigid, however, the deformation of any tooth itself will be small compared to the osseous deformation. Also, a tooth does not remodel, per se, whereas the alveolar bone can. The crown of a tooth undergoes no remodeling. Root resorption and cemental tears are known to take place especially when a tooth is subjected to high forces. Since orthodontic treatment is usually initiated prior to the complete formation of the permanent dentition, some apposition of root structure normally occurs during the period of tooth movement. The adult root form can be somewhat altered by these orthodontic forces. Still, there is little lost in assuming that a tooth transmits forces like a rigid body.

Thus, in this theory only the alveolar bone deformation must be taken into consideration since the osseous remodeling determines the tooth movement. There exists a significant literature available on the qualitative aspects of tooth movements (refs. 5 to 7).

SYMBOLS

$\underset{\sim}{C}$	strain measure
$\underset{\sim}{e}$	strain tensor
$\underset{\sim}{E}$	strain tensor
$\underset{\sim}{f}$	see equation (4)
$\underset{\sim}{F}$	deformation gradient

$\underset{\sim}{F}_o$	see equation (3)
$\underset{\sim}{I}$	identity tensor
$\underset{\sim}{K}$	kernel function
K^*	functions of frequency
p^*	dynamic pressure
$\underset{\sim}{Q}$	functional operator
$\underset{\sim}{R}$	pure rotation
t	present time
u	displacement
$\underset{\sim}{V}$	pure stretch
$\underset{\sim}{x}$	present position
$\underset{\sim}{X}$	orthodontically deformed position
$\underset{\sim}{\xi}$	reference coordinates
$\underset{\sim}{\sigma}$	stress tensor
$\underset{\sim}{\sigma}^*$	complex dynamic stress
$\underset{\sim}{\sigma}_n$	natural stress
τ	time variable
ϕ	constant
ω	frequency

THE LOADING SITUATION

Orthodontic loads are applied to a tooth by wires, elastics, springs or other devices that can be manipulated by the orthodontist to supply a wide range of forces and moments, and it is these loads that the theory will specify. The other loads a tooth experiences will be called natural loads. These are defined as loads experienced by a tooth in the absence of any prosthetic devices. These forces are

a) Occlusal Forces; due to the process of mastication, grinding, clenching and other situations where the maxillary

(upper) and mandibular (lower) teeth come into contact.

b) Tongue Forces; due to the contact of the tongue upon the teeth. These forces can be of considerable magnitude. Tongue postures during speech, chewing, swallowing, playing wind instruments, resting, etc. produce a variety of loads upon the dentition.

c) Buccal Forces; due to the pressure of lips, cheeks and circumoral musculature on the teeth.

d) Air Pressure; due to swallowing, speaking, breathing and the general movement of air in and through the oral cavity.

e) Tooth Eruption; due to the absence of opposing teeth or the natural eruption of a developing tooth. This phenomenon is not well understood.

f) Other Forces; due to habits such as thumb sucking and nail biting, pipe smoking, sleeping with the face resting against an object, trauma, etc.

These forces play an important role in the prediction of tooth movement and must be taken into consideration in any theory that attempts accurate predictions. However, the complexity of the various forces and their interactions preclude their being used in the theory at this time in any detailed manner. This leads us to

ASSUMPTION II. The natural forces may be represented by a time-harmonic expression of frequency ω. In terms of the stress experienced by the bone due to these natural forces, the natural stress may be written as

$$\underset{\sim}{\sigma}_n = \underset{\sim}{\sigma}^* \exp(i\omega\tau) \tag{1}$$

where $\underset{\sim}{\sigma}^*$ is the complex dynamic stress.

The loading situation has now been decomposed into two distinct parts; the orthodontic load and the natural load.

THE CONSTITUTIVE EQUATION

Let the alveolar bone be considered as physically standardized at some time prior to the application of the orthodontic appliances and let this time be set at $\tau=0$, where τ is the time variable. Now let us deal with the symmetry of the bone.

ASSUMPTION III. The alveolar bone is an isotropic material.

The alveolar bone is not isotropic, but the order of magnitude of this error is of the order of magnitude of the error introduced by the other assumptions. When moving the tooth through modulary bone in a buccal-lingual and/or mesial-distal

direction, the bone behaves essentially as an isotropic material. Unfortunately, the alveolar bone does not react as an isotropic material to intrusive and extrusive loads placed upon a tooth. Further, the thin layer of cortical bone covering the modulary bone is denser than the modulary bone and remodels at a somewhat slower rate. A tooth can be moved partially or entirely out of its surrounding alveolar bone, but no one has demonstrated intrusion of a tooth into basal bone. However, as a preliminary theory we shall make this assumption.

The position of a generic particle in the reference configuration, $\tau=0$, is denoted $\underset{\sim}{\xi}$ in a rectangular Cartesian coordinate system. The time of application of the orthodontic appliance is denoted by t_o. The generic particle $\underset{\sim}{\xi}$ is first orthodontically deformed to the position $\underset{\sim}{X}$. The bone is then subjected to the natural forces, inducing the generic particle to occupy the position $\underset{\sim}{x}(\tau)$ (ref. 8).

The deformation gradient may be written as

$$\underset{\sim}{F}(\tau) = \underset{\sim}{f}(t_o)\underset{\sim}{F}_o \tag{2}$$

where

$$\underset{\sim}{F}_o = \frac{\partial \underset{\sim}{X}}{\partial \underset{\sim}{\xi}} \tag{3}$$

and

$$f = \frac{\partial \underset{\sim}{x}}{\partial \underset{\sim}{X}} \tag{4}$$

Let us use Johnson's (ref. 8) history dependent constitutive equation to describe the properties of the alveolar bone.

$$\underset{\sim}{\sigma}(t) = \underset{\sim}{f}(t)\ \underset{\sim}{Q}\ [\underset{\sim}{E},\underset{\sim}{e}(\tau)]\underset{\sim}{f}^T(t) \tag{5}$$

where $(\ )^T$ denotes the transpose, $\underset{\sim}{C}(\tau) = \underset{\sim}{f}^T\underset{\sim}{f}$ is a measure of the strain relative to the orthodontically deformed bone, and by polar decomposition $\underset{\sim}{F}_o = \underset{\sim}{V}\ \underset{\sim}{R}$, then

$$\underset{\sim}{E} = \frac{1}{2}\ (\underset{\sim}{V}^2 - \underset{\sim}{I}) \tag{6}$$

and

$$\underset{\sim}{e}(\tau) = \frac{1}{2}\ (\underset{\sim}{C}(\tau) - \underset{\sim}{I}). \tag{7}$$

The functional operator $\underset{\sim}{Q}$ is defined on the interval $\tau\varepsilon[0,t]$.

At this point another key assumption must be introduced.

ASSUMPTION IV. The phenomena of creep and bone remodeling can be represented by the constitutive equation (5).

This assumption has been made because creep and remodeling are, to a large extent, experimentally indistinguishable from a macroscopic point of view. Bone remodeling due to the application of orthodontic loads to a tooth occurs by alveolar bone being removed from areas where the stress is high - the direction in which the tooth is to be moved - and deposited in areas where the stress is low - areas where the tooth was prior to its movement. This is analogous to what one would observe in the situation of a rigid cylinder imbedded in viscoelastic medium with the cylinder loaded in a similar manner to the tooth.

ASSUMPTION V. The natural forces produce motions $\underset{\sim}{e}$ of magnitudes such that the squares and products of the components of $\underset{\sim}{e}$ may be neglected.

Therefore, the functional $\underset{\sim}{Q}$ may be approximated by a linear functional in $\underset{\sim}{e}$

$$\underset{\sim}{Q}[\underset{\sim}{E},\underset{\sim}{e}(\tau)] = \underset{\sim}{Q}_o(\underset{\sim}{E}) + \int_o^t \underset{\sim}{K}(\tau,\underset{\sim}{E})\ \dot{\underset{\sim}{e}}(t-\tau)d\tau \tag{8}$$

and as a consequence of Assumption III, one may write

$$\underset{\sim}{Q}_o = \phi_o \underset{\sim}{I} + \phi_1 \underset{\sim}{E} + \phi_2 \underset{\sim}{E}^2 \tag{9}$$

$$\underset{\sim\sim}{K}\dot{\underset{\sim}{e}} = K_o \dot{\underset{\sim}{e}} + K_1(\dot{\underset{\sim}{e}}\underset{\sim}{E}+\underset{\sim}{E}\dot{\underset{\sim}{e}}) + K_2\ (\dot{\underset{\sim}{e}}\underset{\sim}{E}^2+\underset{\sim}{E}^2\dot{\underset{\sim}{e}}) + \sum_{m,n=0}^{2} K_{mn}\,\mathrm{tr}(\dot{\underset{\sim}{e}}\underset{\sim}{E}^n)\underset{\sim}{E}^m\ . \tag{10}$$

Let

$$\underset{\sim}{u} = \underset{\sim}{x} - \underset{\sim}{X} \tag{11}$$

be the displacement vector that is a measure of the displacement relative to the orthodontically deformed bone, and let

$$\underset{\sim}{e} = \frac{1}{2}\ (\nabla\underset{\sim}{u} + (\nabla\underset{\sim}{u})^T) \tag{12}$$

Recall equation (1) and decompose the stress into a orthodontic part, $\underset{\sim}{\sigma}_o$, and a natural part, $\underset{\sim}{\sigma}_n$. Further

$$\underset{\sim}{u}(\tau) = \underset{\sim}{u}^*\ \exp\ (i\omega\tau) \tag{13}$$

$$\underset{\sim}{e}(\tau) = \underset{\sim}{e}^* \exp(i\omega\tau) \tag{14}$$

It can be shown (ref. 8) that to a second-order approximation

$$\underset{\sim}{\sigma}^* = -p^*\underset{\sim}{I} + \phi_1(\nabla \underset{\sim}{u}^* \underset{\sim}{E})'' + Ko^* \underset{\sim}{e}^* + K_1^*(\underset{\sim}{e}^* \underset{\sim}{E})' \tag{15}$$

where $(AB)' = \underset{\sim}{A}\,\underset{\sim}{B} + \underset{\sim}{B}^T\underset{\sim}{A}^T$, p^* is the dynamic pressure corresponding to the dynamic stress $\underset{\sim}{\sigma}^*$, K_1^* and K_o^* are functions of frequency only. The orthodontic part is given by

$$\underset{\sim}{\sigma}_o = -p_o\underset{\sim}{I} + \phi_1\underset{\sim}{E} + \phi_2\underset{\sim}{E}^2 \tag{16}$$

The forces applied by the orthodontic appliances are periodically varied as the tooth-bone system moves. After each adjustment one may apply the theory relative to the new forces applied. In this manner one may incrementally apply the theory. One may thus use the input-which is the motion desired - to calculate the desired stress that will cause the desired motion. The natural forces, taken as an average, are assumed to be invariable in time. Therefore, it is only the orthodontic forces that can be manipulated to induce tooth movement. So by incrementally measuring the displacement, the force increment can be calculated that will cause the tooth to move to its next incremental position. Alternatively, but not as accurately, the motion of the tooth may be predicted at time, knowing the motion for t, using the constitutive relation and the forces applied to achieve a desired movement, much as the orthodontist does in the office.

REFERENCES

1. Terlingen, P.J.A.M.: Material and Mathematical Model Experiments on Orthodontic Extraoral Traction. Thesis, University of Michigan.

2. Burstone, C. J.; and Koenig, H. A.: Force Systems From an Ideal Arch. Am. J. Ortho., Vol. 65, 1974, pp. 270-289.

3. Koenig, H. A.; and Burstone, C. J.: Analysis of Generalized Curved Beams for Orthodontic Applications. J. Biomechanics, Vol. 7, 1974, pp. 429-435.

4. Fung, Y. B.: Stress-Strain-History Relations of Soft Tissues in Simple Elongation. Biomechanics (Fung, Y. C., Perrone, N., Anliker, M., Eds.), Prentice-Hall, 1972.

5. Nikolai, R. J.: Periodontal Ligament Reaction and Displacements of a Maxillary Central Incisor Subjected to Transverse Crown Loading. J. Biomechanics, Vol. 7, 1974, pp. 93-99.

6. Burstone, C. J.: The Biomechanics of Tooth Movement in Vistas in Orthodontics (B. S. Kraus, ed.) Lea and Febiger, 1962.

7. Graber, T. M.: Orthodontics, Principles and Practice, 3rd ed. Saunders, 1972.

8. Johnson, A. F.: Small Amplitude Vibrations in Prestrained Viscoelastic Solids. J. Hult (Ed.), Mechanics of Viscoelastic Media and Bodies, Springer, Berlin, 1975.

NONLINEAR EFFECTS IN THERMAL STRESS ANALYSIS OF A SOLID PROPELLANT ROCKET MOTOR

E. C. Francis, R. L. Peeters, and S. A. Murch
United Technologies, Chemical Systems Division,
Air Force Rocket Propulsion Laboratory,
MB Analysis

INTRODUCTION

Microstructural damage causes solid propellants to exhibit a nonlinear mechanical response when used under normal service conditions. Before such materials can be used in structural designs, accurate material descriptions of the observed phenomenological behavior must be obtained, and the structural analysis procedures modified to include this material nonlinearity.

In this paper, direct characterization procedures were used to determine the relaxation modulus as a function of time, temperature, and state of strain. Using the quasi-elastic method of linear viscoelasticity, these properties were employed in a finite element computer code to analyze a thick-walled, nonlinear viscoelastic cylinder in the state of plane strain bonded to a thin (but stiff) elastic casing and subjected to slow thermal cooling. The viscoelastic solution is then expressed as a sequence of elastic finite element solutions. As will be seen, the material is regarded as nonhomogeneous in the nonlinear case.

The strain-dependent character of the relaxation modulus is included by replacing the single relaxation curve used in the linear viscoelastic (LVE) theory by a family of relaxation functions obtained at various strain levels. These functions may be regarded as a collection of stress histories or responses to specific loads (in this case, step strains) with which the cooldown solution is made to agree by iterations on the modulus and strain level.

SYMBOLS

Values are given in both SI and U.S. Customary Units. The measurements and calculations were made in U.S. Customary Units.

a_T	time-temperature shift function
A	cross-sectional area of large test sample
E	Young's modulus
$E(t,T)$	relaxation modulus
E_a	apparent modulus in large test samples
E_I	effective value of modulus for use in a linear viscoelastic (LVE) analysis
E_{In1}	effective value of modulus for use in a nonlinear analysis (NLVE)
E_i	modulus response to ith step strain
F	axial force on large test samples
I	subscript denoting equivalent or effective value
i	subscript denoting one in a series of values (i = 1,2,3, . . .)
k_F	factor relating apparent modulus in large test samples to actual uniaxial modulus
L	length of large test samples
m	subscript denoting specific value in a series
r	coordinate in radial direction in polar cylindrical system
t, t'	time
T	temperature
T_i	specific temperature level
T_0	stress-free temperature
$\bar{t}$	time corresponding to E when E is associated with a relaxation curve
T_g	glass transition temperature

u_z axial displacement in large test samples

x symbolic reference to coordinates r, θ, Z

z coordinate in axial direction in polar cylindrical system

Greek Symbols:

ϵ uniaxial strain

ϵ_0 strain of constant value

ϵ_I von Mises "effective" strain

ϵ_θ circumferential component of strain

ϵ_r radial component of strain

$\epsilon_{z_{AV}}$ average axial strain in large test sample

ξ reduced time

ν Poisson's ratio

θ coordinate in circumferential direction in polar cylindrical system

σ uniaxial stress

σ_θ circumferential component of stress

$\sigma_{z_{AV}}$ average axial stress in large test sample

$\sigma_{k\ell}$ stress tensor ($k, \ell = 1,2,3$)

$\bar{\sigma}_{k\ell}$ stress response to a unit step temperature change

ANALYSIS

In a linear viscoelastic, the state of stress and strain depends on the history of loading through integrals of the type (refs. 1 and 2)

$$\sigma(t) = \int_0^t E(t-t') \frac{d\epsilon}{dt'} dt' \tag{1}$$

so that the current stress is determined by the past strain as well as the current value. The function $E(t)$ is called the relaxation modulus and is determined from the stress response to a fixed strain input ϵ_0, i.e.,

$$E(t) = \frac{\sigma(t)}{\epsilon_0} \quad , \quad \epsilon = \begin{cases} \epsilon_0, t \geqslant 0 \\ 0, t < 0 \end{cases}$$

In linear viscoelastic (LVE) materials, the relaxation modulus is independent of the magnitude of the imposed strain. The notation $E(t, T_i)$ refers to the standard $\epsilon = 2\%$ relaxation function at temperature T_i.

For the class of nonlinear viscoelastic materials considered here, the relaxation modulus varies considerably with strain level, decreasing monotonically with increasing values ϵ_i ($i = 1, 2, 3, \ldots$). When the notation includes ϵ_i — for example, $E(t, \epsilon_i, T_1)$ — reference is being made to the relaxation function obtained for $\epsilon = \epsilon_i$. The presence of a subscript I — for example, $E_I(t_1, T_1)$ — denotes a calculated effective modulus to be used in an elastic finite element program to obtain an LVE solution valid at a particular time t_1 and temperature T_1. In the nonlinear viscoelastic (NLVE) solution, the subscripts $n1$ are added, i.e., $E_{I_{n1}}$.

The procedure for linear viscoelastic grain analysis is presented in the ICRPG Handbook (ref. 3), which shows how elastic solutions with different Young's modulus may be used with the relaxation modulus function to construct time-dependent, linear viscoelastic responses. This paper modifies the ICRPG procedure by incorporating the observed dependence of the relaxation modulus on strain level. Since solid propellants are nearly incompressible, Poisson's ratio is taken near one-half ($\nu = 0.499$).

This quasi-elastic treatment of LVE problems (refs. 3 and 4) essentially replaces Young's modulus in an elastic analysis by the instantaneous value of the relaxation modulus for the response to a step load. Let $\sigma_{k\ell}$ be the elastic state of stress at a point in a body subjected to a unit temperature change. The LVE response to a step temperature change ΔT_i, applied at time t_i, may be represented as

$$\sigma_{k\ell}(t) = \bar{\sigma}_{k\ell}[E(\xi - \xi_i)] \quad \Delta T_i \tag{2}$$

where, assuming a thermorheologically simple (TRS) material, ξ is the "reduced time"

$$\xi = \int_0^t \frac{dt}{a_T} \quad , \qquad \xi_i = \int_0^{t_i} \frac{dt}{a_T} \tag{3}$$

and $a_T[T(t)]$ is the temperature shift factor that relates relaxation functions at different temperatures. Since the solution for more general loads consists of the appropriate superposition of solutions for step loads, a property of such LVE solutions is that the stress and strain fields at any given moment may be duplicated by an elastic analysis at the same temperature and a suitably chosen uniform value of Young's modulus, termed the effective modulus E_I.

For a sequence of step temperature decreases, the total stress by equation (2) is

$$\sigma_{k\ell}(t) = \sum_i \bar{\sigma}_{k\ell}[E(\xi - \xi_i)] \quad \Delta T_i \tag{4}$$

For the class of problems being considered (i.e., grains that are nearly incompressible mechanically and that are bonded to an elastic but stiff motor case), the stresses obtained in an elastic analysis are closely represented over the range of interest ($E < 1000$ psi) by

$$\bar{\sigma}_{k\ell} = A_{k\ell} E \alpha \Delta T \tag{5}$$

where $A_{k\ell}$ depends on geometry and coordinates only. Substituting equation (5) into equation (4)

$$\sigma_{k\ell}(t) = A_{k\ell} \alpha \sum_i E(\xi - \xi_i) \ \Delta T_i \tag{6}$$

so that by comparing equations (5) and (6), the effective modulus is

$$E_I(t) = \frac{\sum_i E_i \Delta T_i}{\sum_i \Delta T_i} \tag{7}$$

where $E_i = E(\xi - \xi_i)$

When the material is not TRS, E_i may be obtained from a set of relaxation functions $E(t, T_i)$ by moving at constant stress from one relaxation curve to the next as the temperature is stepped (fig. 1). Note that after the first step, the time t is no longer given by the abscissa of the graphs of $E(t, T)$ but by the sum of the separate times spent on each relaxation curve.

Suppose $E_I(t_n, T_m)$ has been obtained using LVE methods and duplicates, by elastic analysis, the stress-strain fields arising in a motor cooled to temperature T_m at time t_n. The resulting strain field (near zero at case wall and 10–15% at the bore surface) covers a range of strain levels which indicate that the strain dependency of the propellant modulus should be important. For a material whose relaxation curve is sensitive to strain level, the resulting change in the stress history throughout thermal loading can be accounted for in the calculation of effective modulus.

The procedure suggested in this paper corrected the strain level at each temperature step during cooldown by moving to the relaxation curve corresponding to the current strain level. (An appropriate measure of strain level for multiaxial states of strain is discussed later.)

The effective modulus thus becomes a field variable and, in general, differs in every element of a finite element model. Finite element iterations are required following each temperature step to adjust the modulus in every element until no further strain change can be detected. Denote the value of E_I obtained by this iteration procedure with the subscript $_{n1}$, i.e., E_{In1}. The basis for calculating E_{In1} is to relate it to the value of E_I obtained in the linear viscoelastic solution. Specifically, if the effective strain is ϵ_I in an element whose LVE modulus is $E_I(t_n, T_m)$, then

$$E_{In1} = E(t_{I_n}, \epsilon_I, T_m) \tag{8}$$

where t_{I_n} is obtained from

$$E(t_{I_n}, T_m) = E_I(t_n, T_m) \tag{9}$$

in general $t_m \neq t_{I_m}$.

In practice, the procedure is simpler than implied above and will be outlined briefly.

Effective Strain Level for Multiaxial States of Stress

The state of strain in a body has several components upon which to base a strain level. Some special consideration must be given to define a measure of "effective" strain. An acceptable definition should satisfy the following criteria:

- Incorporate all given components of strain
- Relate to the uniaxial values associated with the strain-dependent relaxation curves
- Be independent of the coordinate system
- Recognize that only the portion of the strain that produces stress should contribute, since the thermal strains $\epsilon_1 = \epsilon_2 = \epsilon_3 = \alpha\Delta T$ represent a change in the reference state of stress.

One definition meeting these criteria is the so-called von Mises strain, which is an invariant of the strain deviation tensor normalized to the uniaxial state; i.e.,

$$\epsilon_I = \frac{\sqrt{2}}{2(1+\nu)}\left\{(\epsilon_1-\epsilon_2)^2 + (\epsilon_2-\epsilon_3)^2 + (\epsilon_3-\epsilon_1)^2\right\}^{1/2} \tag{10a}$$

where $\epsilon_1, \epsilon_2, \epsilon_3$ are the principal strains.

ϵ_I is proportional to the octahedral shear strain at a material point; hence, it is independent of volume changes and, for the uniaxial state $(\epsilon, -\nu\epsilon, -\nu\epsilon)$ gives $\epsilon_I = \epsilon$.

Note that other combinations of strain invariants also meet the requirements listed above, but the von Mises strain was selected for this paper.

Procedure for Selecting Nonlinear Effective Modulus

The cooling of a case-bonded, solid propellant rocket grain can now be discussed in greater detail. The time-dependent temperature field in the strain is assumed to be spatially uniform and to produce a stress-free state at T_0. If the temperature-time curve is replaced by a series of steps such as shown* in figure 2, then suppose the first temperature step ΔT_1 to be imposed at time t_1.

*The stress due to polymerization shrinkage has been considered by assuming that the initial motor cooldown starts from zero stress temperature, which is slightly above the rocket motor cure temperature.

Since this is the first temperature increment to be applied, the expression for the effective modulus has only one term, so that equation (10) reduces to

$$E_I(t, T_1) = E(t - t_1, T_1) \tag{10b}$$

This expression is valid until the application of the second increment of temperature at time t_2. For purposes of analysis, the time t_2 was selected for the first set of nonlinear iterations. The LVE solution must first be obtained, however. The effective modulus is calculated by evaluating the above at $t = t_2$. Using the thermal ΔT_1 and the spatially uniform modulus $E_I(t_2, T_1)$ for Young's modulus in an elastic finite element (FE) program, the result is the LVE solution at time t_2. The resulting strain field prescribes the starting values for the first nonlinear iteration.

The strain level $\epsilon_I(x)$ in each element is calculated using equation (10). The spatial dependence of ϵ_I is emphasized with the argument x, which is a symbolic reference to the coordinates r, θ, z.

To select an effective modulus $E_I(x)_{n1}$ associated with $\epsilon_I(x)$, consider the strain-dependent family of relaxation curves $E(t, \epsilon, T_1)$ at temperature T_1. One member of this family is standard relaxation curve $E(t, T_1)$, used to obtain $E_I(t_2, T_1)$ in the LVE solution. If E_I is identified with a point on $E(t, T_1)$, an effective time t_{I_2} is defined through equation (9) with $n = 2$, $m = 1$, i.e.,

$$E_I(t_2, T_1) = E(t_{I_2}, T_1)$$

Using t_{I_2} as the time for which the nonlinear iterations are to be performed, an interpolation curve of modulus versus strain level may be constructed from the points $E(t_{I_2}, \epsilon_i, T_1)$ obtained from the strain-dependent family of relaxation curves at the same temperature and time. Values of $E_{I_{n\ell}}(x)$ corresponding to various $\epsilon_I(x)$ may then be read and input to the finite element program to implement the first nonlinear iteration.

From the new FE results, a second set of values of $\epsilon_I(x)$ is calculated, compared to the previous set, and (if necessary) used to find revised set $E_{I_{n\ell}}(x)$ for another iteration. This procedure is repeated until the change in the effective strain is insignificant. After two iterations, the LVE solution usually shows the desired consistency between $E_{I_{n\ell}}$ and ϵ_I. The FE results so obtained constitute the nonlinear solution at time t_2 just prior to the application of the next step temperature.

Returning to the LVE solution, at time t_2 a second step temperature change ΔT_2 is imposed and the grain temperature is reduced to $T_2 = T_1 - \Delta T_2$. There are now two stress responses present: (1) the response to ΔT_2

$$\Delta T_2 E(t - t_2, T_2) \tag{11}$$

and (2) the response of ΔT_1, which now obeys $E(t, T_2)$; i.e.,

$$\Delta T_1 E(t - \bar{t}_2, T_2) \tag{12}$$

where $\bar{t}_2$ is given by solving

$$E(t_2 - t_1, T_1) = E(\bar{t}_2, T_2) \tag{13}$$

In practice, recalling figure 1, the value of E on the curve for T_1 at $t_2 - t_1$ is transferred to the curve for T_2 and the corresponding time is read as $\bar{t}_2$. The effective modulus becomes

$$E_I(t, T_2) = \frac{\Delta T_1 E(t - \bar{t}_2, T_2) + \Delta T_2 E(t - t_2, T_2)}{\Delta T_1 + \Delta T_2} \tag{14}$$

Suppose a solution is desired at time t_3, just before ΔT_3 is applied, then equation (7) is evaluated at t_3 and $E_I(t_3, T_2)$ is used in a finite element computer run which becomes the LVE solution at t_3, and provides the starting values for the first nonlinear iteration. The effective time t_{I_2}, corresponding to $E_I(t_3, T_2)$, is given by equation (9) with $n = 3$, $m = 2$.

An interpolation plot is next made of values of E versus ϵ from the strain-dependent family $E(t, \epsilon_i, T_2)$ at t_{I_3}. The effective strains $\epsilon_I(x)$ calculated from the LVE solution are then used to obtain $E(\epsilon_I)$ for the first iteration. This procedure is repeated until convergence is obtained for each step temperature assumed.

NONLINEAR MATERIAL BEHAVIOR

Many materials, such as filled plastics, advanced composites, etc., exhibit a nonlinear viscoelastic behavior that is now commonly termed permanent memory behavior. The Mullins effect in rubbers and elastoplastic response are simple examples of such behavior.

The microstructural variations change the macroscopic response properties following a given displacement, which is termed deformation or load-induced damage. This damage is seen primarily as a decrease in the relation modulus – that is, a softening that is a function of the loading/strain condition. Furthermore, it has been observed that a given deformation produces a new equilibrium zero-state of stress of the material with respect to which a new material constitutive relation exists (ref. 5).

Typical constant strain-stress relaxation data for a highly filled solid propellant (TP-H1011 – 86% solids) are presented in figure 3. End-bonded test samples 6 in. × 0.5 in. × 0.5 in. (15.24 cm × 1.27 cm × 1.27 cm) were ramp-loaded to the 2.64% strain level and held fixed while the stress relaxation was monitored as a function of time. These uniaxial stress data were then converted to the viscoelastic modulus data in figure 3, using an experimental time-temperature shift that is reasonably close to the theoretical shift (ref. 6) developed for pure polymers (fig. 4). The master viscoelastic modulus curve in figure 3 has been used for routine solid propellant rocket motor structural analysis. However, if the stress relaxation test is conducted at different strain levels, a family of modulus curves can be determined which shows that modulus is a strain-dependent parameter. These strain-dependent data for the same propellant are shown in figure 5.

These data represent the viscoelastic modulus behavior of a solid propellant tested at four different strain levels from small to intermediate strains. Modulus differences due to the damage incurred at each strain level are significant. Small strain modulus numbers at 0.5% strain are nearly three times greater than the modulus at 5% strain. Accurate modulus data below the 2.5% strain level have generally been difficult to obtain. In the past, machining and handling of the small, soft viscoelastic samples prior to testing has damaged the propellant. To avoid this damage to the pretest sample,

a larger specimen was cast, which required no machining and which was large enough not to be damaged by careful human handling. Samples used for these tests are shown in figure 6. Both circular and rectangular samples have been tested, but the circular samples were selected for this study because they can be readily analyzed as a result of their symmetry. These large test specimens are cast like the rocket motor grain when the propellant is fluid. Over a period of 5–10 days at approximately 140°F (333°K), they cure in casting molds into a nonlinear viscoelastic solid. Samples are removed from the casting hardware and are ready for immediate testing. These large cast bulk samples have been a major factor in obtaining reliable modulus data in the small strain range typical of most solid propellant grains.

These large samples can be adjusted in length/diameter ratio to match any kind of loading, stress, or strain axiality needed for accurate simulation of full-scale motor grain conditions.

The much higher modulus detected at small strains with the larger specimen would be expected to cause a large difference in motor stresses, since the strain gradient in the rocket motor from the case wall to the internal bore surface (where combustion occurs) varies from a fraction of a percent to as much as 15% strain. This same modulus strain softening has been reported by Francis *et al.* (refs. 7 and 8) for other propellants at larger strain levels and at lower temperatures.

LARGE SAMPLE FINITE ELEMENT ANALYSIS

When these large samples are loaded in axial tension, the resulting state of stress is not simple tension. The bonded end restraint prevents the lateral contraction that would be present due to the effect of Poisson's ratio. Because of the low length/diameter ratio (L/D < 2), the multiaxial stress field near the ends makes a significant difference in the overall displacement when compared to that due to a simple tensile state. There is enough similarity between the two tests to interpret the results of the large sample using a finite-element-determined factor applied to the test results. Specifically, an axial force F, when applied to the sample, produces an average axial stress

$$\sigma_{z_{AV}} = \frac{F}{A}$$

where A = cross-sectional area. If the axial displacement noted by the finite element is u_z, then the average strain is

$$\epsilon_{z_{AV}} = \frac{u_z}{L}$$

where L = sample length. The apparent modulus is then

$$E_a = \frac{\sigma_{z_{AV}}}{\epsilon_{z_{AV}}}$$

which is always greater than the E employed in the finite element program. Defining k_F by

$$E_a = k_F E$$

then

$$u_z = \frac{FL}{AEk_F}$$

In a laboratory test, an effective large sample E_I may be obtained from the apparent value by

$$E_I = \frac{E_a}{k} = \frac{FL}{Au_z}$$

Examples of this k_F value were determined for two sample geometries using finite element analysis to demonstrate the magnitude of the uniaxial large sample correction factors.

The analyzed test sample geometries and computer-determined k_F values are listed below:

Sample No.	Length	Radius	k_F
1	5 in. (12.7 cm)	1.4625 in. (3.71 cm)	1.115
2	3 in. (7.62 cm)	3 in. (7.62 cm)	1.51

STRUCTURAL ANALYSIS

The impact of this variation in modulus as a function of strian level has been assessed by comparing linear elastic analysis, linear viscoelastic analysis, and iterative nonlinear analysis. Data presented in figure 3 were used to select the linear viscoelastic behavior. Figure 7 presents modulus strain sensitivity data for specific motor analysis time-temperature loading increments. These data were obtained by shifting data to the appropriate time-temperature conditions and selecting the correct modulus versus strain response for this condition.

The iterative nonlinear solution included analysis for five different temperature cooling steps. This cooldown history was selected so that the rocket motor would be cooled from a zero stress state at 141°F (334°K) to 21°F (267°K) in 50,000 minutes, using five evenly spaced temperature-time steps.

Plane strain finite element analyses were conducted with the Texas Institute for Computation Mechanics Grain Analysis Program (TEXGAP-2D). TEXGAP-2D was selected because of its highly accurate determination of stress and deformation fields in solid propellant rocket motors, especially in the critical areas near the interfaces of the case, insulation, liner, and propellant (ref. 9). Although material nonlinearities are introduced in the analyses under consideration, TEXGAP-2D is a linear elastic finite element computer code.

The solid propellant rocket motor, with its assumed infinite length, is shown in figure 8. A 0.010-in. (0.0254-cm) thick liner is applied directly to the 0.235-in. (0.597-cm) thick steel case. The liner, which consists of a thin layer of adhesive, is used to improve the chemical bond between the propellant and the case and is included in the structural analysis. The grain is composed of TP-H1011 propellant, in a center-perforated, 0.438-in. (1.113-cm) bore-radius, circular port with an outside radius of 1.990 in. (5.055 cm). The elastic moduli for the liner and case were 150 psi (1.03×10^6 N/m^2) and 30,000,000 psi (207×10^9 N/m^2), respectively, while the corresponding linear coefficients of thermal expansion were -2.5×10^{-4} in./in.-°F (4.5×10^{-4}/°K) and -6.0×10^{-6} in./in.-°F (10.8×10^6/°K). The effective propellant equilibrium elastic modulus was approximately 120 psi (8.26×10^5 N/m^2) and the linear coefficient of thermal expansion was 5.0×10^{-5} in./in.-°F (9×10^5/°K). Poisson's ratio for the case (0.310), liner (0.499) and propellant (0.499) was assumed constant for all analyses.

The solid propellant rocket motor was modeled as shown in figure 9. The grid, generated using the TEXGAP-2D polar option, spanned a 30° (0.524 rad) segment with 5° (0.0873 rad) per angular element and ten evenly spaced radial propellant elements between the liner and the bore. Both propellant and liner were modeled with the QUAD element, which is a reformulated isotropic, quadrilateral element. Minor modifications in TEXGAP-2D allowed the material properties to be decoupled element by element (i.e., normally the hydrostatic variable would be constrained). The case was modeled using a subparametric quadrilateral element entitled QUAD 8. The r axis was aligned as shown in figure 9 so that numerical values of stress and deformation as a function of radial location could be read directly from the computer printouts. SLØPE boundary conditions with zero value were specified along the outer sides of the propellant, liner, and case elements, resulting in sloping rollers on a ±15° (±0.262 rad) angle.

DISCUSSION OF RESULTS

Figures 10 to 14 compare circumferential stress as a function of grain radius for linear and nonlinear viscoelastic analysis at various times during cooldown. The times selected for analysis are chosen to precede directly the application of each temperature increment, i.e., $t = t_i$. This minimizes errors introduced by the high values of the relaxation modulus at short times.

Since the effective modulus for the LVE cases is uniform throughout the grain, the familiar form of $\sigma_\theta(r)$ is observed, with a maximum at the bore monotonically decreasing to a lesser value at the propellant liner bond. At any given station, the stress is essentially proportional to the temperature change from the stress-free state and to the modulus which also increases here as the temperature decreases.

The strain axiality varies significantly from the bondline to the free bore surface as shown in figure 15 for linear elastic analysis with a propellant modulus of 300 psi. The ratio of radial strain to hoop strain is −1.08, indicating a near one-to-one field at the bore surface. At the bond line, this ratio has changed to −124. Clearly, a single component of strain is not an indicator of strain level, which should depend instead on all nonvanishing components.

The nonlinear distribution $\sigma_\theta(r)$ changes its shape during cooldown, eventually reaching a form similar to the linear case. For higher temperatures, the modulus dominates the determination of the distribution, producing a curve that increases toward the bond. This is due to the low strain levels

which imply high modulus values. The strains, which are primarily determined by the temperature field, agree with the LVE pattern, i.e., monotonically decreasing toward the bond. The associated effective modulus values thus increase toward the bond (see table 1) producing a stress field that also tends toward higher values with radius, in contrast to the linear distribution.

In general, the accounting for strain dependence of the relaxation modulus increases the bond stresses early in cooldown and decreases them at lower temperatures as strains increase. This is evident from figure 16, which shows the circumferential stress in the grain next to the bond during cooling. In this bond region, strain levels are low (<0.2%), so that the high associated modulus drives the stress above the corresponding linear result, which employs a (lower) relaxation function obtained at approximately 2% strain level.

In contrast to this result, the nonlinearly obtained circumferential stress at the bore surface $\sigma_\theta(a)$, which exceeds the 2% strain level at 130°F (328°K), operates with an effective modulus below that used in the linear viscoelastic theory. This nonlinear surface stress remains below the linear viscoelastic values throughout the remainder of the cooldown (figure 17).

This high-strain, low-bore stress agrees with the work of Martin (ref. 10), who used a similar approach to evaluate this nonlinearity. The low strain consequences of the strain-dependent modulus method were not discussed by Martin because he did not have access to accurate, small-strain modulus data.

In figure 10, the upturn in the nonlinear distribution at the bore is indicative of a tendency, evidenced later in figures 11 to 14, to assume a shape similar to the distribution for a linear material.

As cooling continues and strain levels increase, the modulus values decrease (see table 1) and approach a more uniform distribution. This follows as the strain-sensitivity of the solid propellant modulus diminishes as the strain increases.

At 93°F (307°K) and 20,000 minutes, the linear and nonlinear distributions (fig. 11) approach each other. Also, the nonlinear distribution begins to assume the shape of the linear curve.

At 69°F (294°K) and 30,000 minutes (fig. 12), the two distributions are very close in shape and magnitude, crossing at station 4.

At 45°F (280°K) and 40,000 minutes (fig. 13), the strain level specifies modulus levels below the linear values. The crossover point of the stress distributions moves out to station 7 as the two curves move apart.

Finally, at 21°F (267°K) and 50,000 minutes (fig. 14), the two distributions no longer cross, and although the effective modulus near the case is double that near the bore, the modulus distribution is flat enough that the familiar, monotonically decreasing (with radius) stress distribution is observed.

Comparison should be made with a previous higher rate cooldown analysis (ref. 11) on this same geometry in which the circumferential strain in each element was used as a measure of strain level. Using a hoop strain modulus selection criterion increases the stress levels near the motor case. A high relaxation modulus was selected since ϵ_θ gets vanishingly small in this neighborhood due to case restraint. This could be misleading as the radial strain is of the order of $3\alpha\Delta T$. The von Mises strain

here is about $2\alpha\Delta T$, leading to a lower modulus selection and hence lower stresses. Near the bore, the difference in predicted stress is small because (1) the von Mises stress is close numerically to the hoop stress (within 20%) and (2) the strains are large enough that strain level changes produce only small changes in modulus. Use of the von Mises strain is expected to yield more realistic analytic predictions since it meets the earlier criteria, which account for stress-strain axiality variations that occur between the bore surface and case bond region of a solid propellant rocket motor.

This nonlinear rocket motor grain bond stress buildup over the conventional linear elastic and linear viscoelastic analysis is a new phenomenon that has been observed only as more accurate small strain modulus test methods have been developed for soft propellant material. The very small strain modulus limit of 1580 psi (10.9×10^6 N/m^2) was obtained from a Duomorph test and was supplied by Dr. R. Schapery of Texas A&M University. Strain data ranging from 0.5% to 3% were obtained at Chemical Systems Division with large cast test samples that minimized sample handling damage prior to testing. These large cast samples have been a major factor in obtaining good reliable test data in this smaller strain range. This small strain modulus sensitivity of highly filled solid propellants has been predicted by Schapery (ref. 12), using a nonlinear constitutive theory that is based on time-dependent microstructural damage, crack growth theory, and material statistical representations.

Samples normally used for laboratory testing of propellant are damaged by machining and handling before test initiation and have as much as 0.5% permanent strain damage. This level of damage essentially removes the higher modulus portion of the propellant response. In a rocket motor, the propellant grain is cast while propellant is in the liquid state and then cured to the solid state at an elevated temperature. The stress builds up very slowly during the cooldown process so that the bulk of the strain never sees a large strain value and is not damaged as are conventional laboratory samples.

CONCLUSIONS

Stresses predicted using the nonlinear effects considered here are in general higher than those calculated by linear theory in the early part of cooldown over the bulk of the grain, i.e., $T > 69°$F ($T > 294°$K). The nonlinearly determined stress is consistently higher near the bond for $T > 25°$F ($T > 269°$K). Nonlinear bore stress predictions are lower than linear results because of the large strain levels arising in this region throughout cooldown. (See figures 16 and 17.)

Stresses predicted using linear analysis methods are generally lower because the properties used for the conventional analysis reflect a significant damage state before and during the test. The rocket motor does not experience this damage during the initial cooldown cycle. Conventional laboratory test samples have already gone through a permanent set and are in a secondary softened material status for normal viscoelastic modulus evaluation. Accurate motor analysis requires a more detailed, small strain modulus evaluation of undamaged propellant and usage in a complete or approximate nonlinear analysis.

REFERENCES

1. Muki, R. and Sternberg, E.: On Transient Thermal Stresses in Viscoelastic Materials with Temperature Dependent Properties. *J. Appl. Mech.*, vol. 23, 1961, pp. 193–207.

2. Christensen, R. M.: *Theory of Viscoelasticity,* Academic Press, 1971.

3. Hufferd, W. L and Fitzgerald, J. E.: *JANNAF Solid Propellant Structural Integrity Handbook.* CPIA Publication, 230, AFRPL and ONR, September 1972.

4. Schapery, R. A.: Approximate Methods of Transform Inversion for Viscoelastic Stress Analysis. *Proceedings of Fourth U.S. National Congress of Applied Mechanics,* vol. 2, 1962, pp. 1075–1085.

5. Hufferd, W. L. and Fitzgerald, J.E.: Permanent Memory Effects in Solid Propellants. *Proc. 1974 JANNAF SMBWG and OSWG Meeting,* CPIA Publication No. 253, The Johns Hopkins University, July 1974, p. 345.

6. Williams, M. L., Landel, R. F., and Ferry, J. D.: The Temperature Dependence of Relaxation Mechanisms in Amorphous Polymers and Other Glass-Forming Liquids. *The Journal of The American Chemical Society,* vol. 77, July 20, 1955, pp. 3701–3707.

7. Francis, E. C. and Carlton, C. H.: Some Aspects of Nonlinear Mechanical Behavior of A Composite Propellant. *Journal of Spacecraft and Rockets,* vol. 6, No. 1, January 1969, pp. 65–69.

8 Francis, E. C., Deverall, L. I., and Lostrie, J.: Nonlinear Propellant Characterization and Analogue Motor Analysis. ICRPG Mechanical Behavior Working Group – 6th Meeting, CPIA Publication No. 158, vol. 1, October 1967, pp. 203–218.

9. Francis, E. C. *et al.*: Case Liner Bond Analysis. AFRPL-TR-74-23, Air Force Rocket Propulsion Laboratory, Edwards, CA, June 1974.

10. Martin, D. L., Jr.: An Approximate Method of Analysis of Nonlinear Transient Thermoviscoelastic Behavior. *JANNAF Mech. Behavior Working Group, 8th Meeting,* CPIA Pub. 193, vol. 1, 1969, pp. 45–52.

11. Francis, E. C., Peeters, R. L., and Hufferd, W. L.: Considerations in the Applications of Nonlinear Structural Materials. Second International Conference on Mechanical Behavior of Materials Proceedings, Boston, August 1976.

12. Schapery, R. A.: A Nonlinear Constitutive Theory for Particulate Composites Based on Viscoelastic Fracture Mechanics. JANNAF Operational Serviceability and Structures and Mechanical Behavior Working Groups – 1974 Combined Annual Meeting, CPIA Publication No. 253, July 1974, pp. 313–328.

TABLE 1. – DISTRIBUTION OF EFFECTIVE NONLINEAR MODULUS IN GRAIN AT HIGH AND LOW TEMPERATURES

T = 117 °F (320°K) (Reference linear viscoelastic modulus = 132 psi)

Finite Element Station	Nonlinear E	
	(psi)	($N/m^2 \times 10^3$)
1 (bore)	117.5	810
2	175	1205
3	220	1516
4	270	1860
5	350	2412
6	460	3169
7	630	4341
8	780	5374
9	875	6029
10 (next to liner)	940	6477

T = 21°F (267°K) (Reference linear viscoelastic modulus = 173 psi)

1 (bore)	130	896
2	140	964
3	150	1034
4	158	1089
5	163	1123
6	175	1206
7	195	1344
8	225	1550
9	255	1757
10 (next to liner)	285	1964

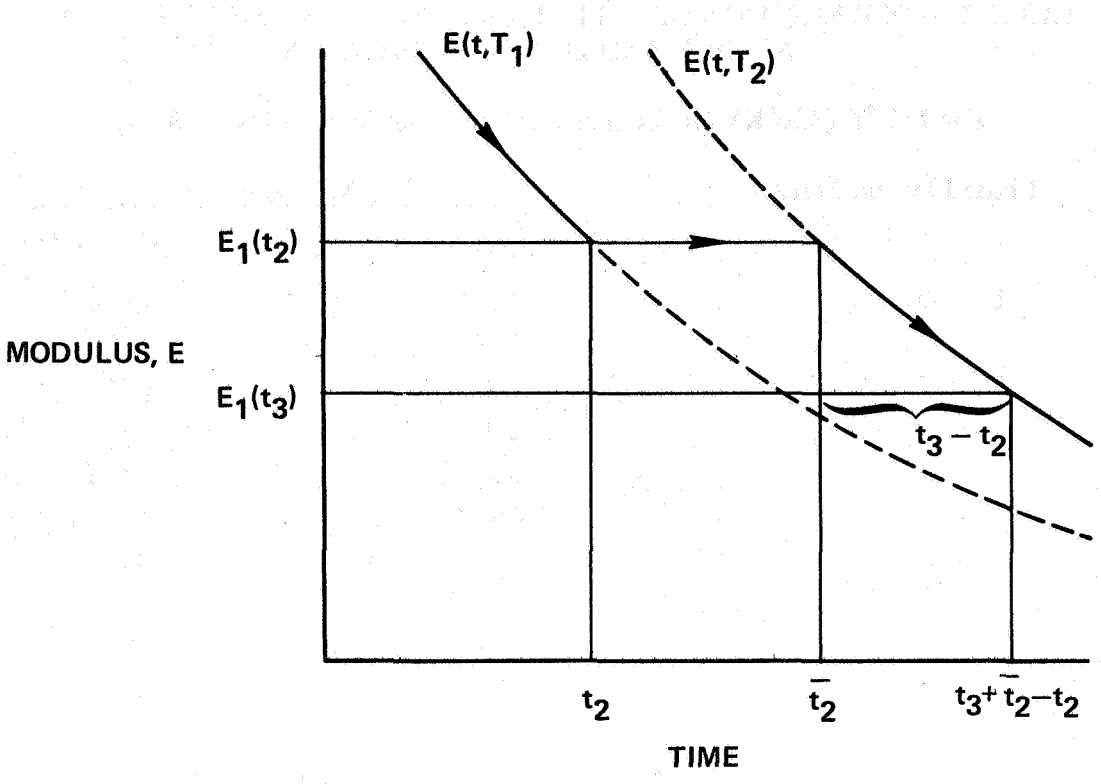

Figure 1. – Change in the response to a step load due to a sudden change in temperature T_1 to T_2 at time t_2.

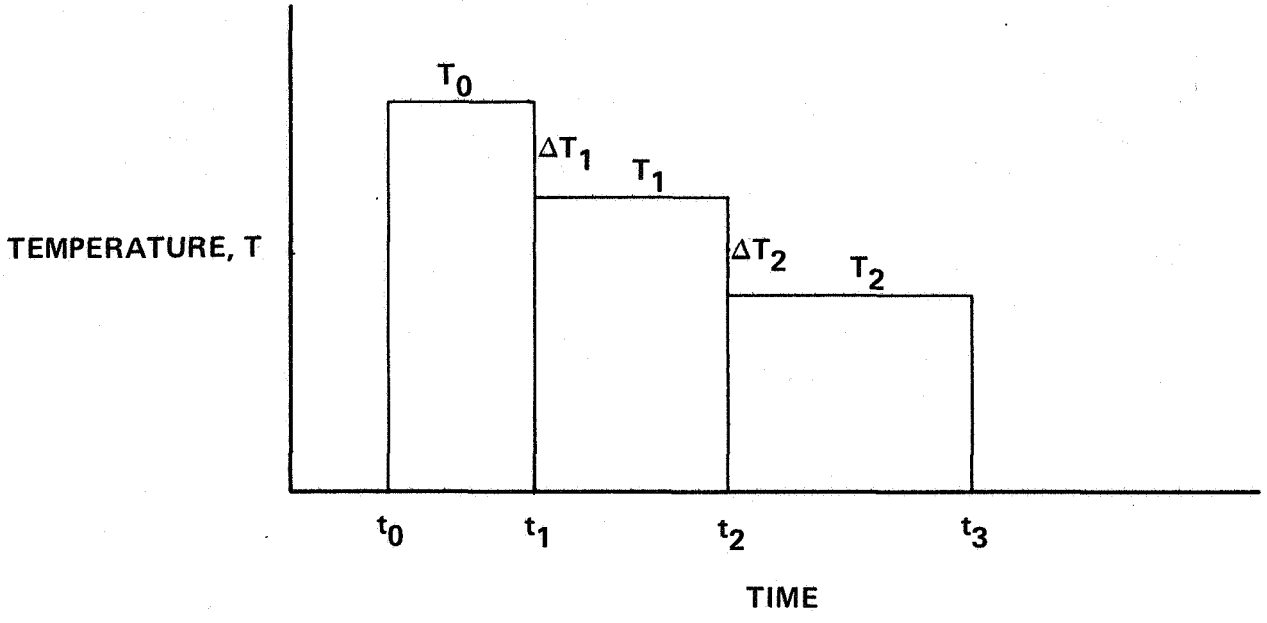

Figure 2. – Nomenclature associated with step function approximation to cooldown time-temperature history.

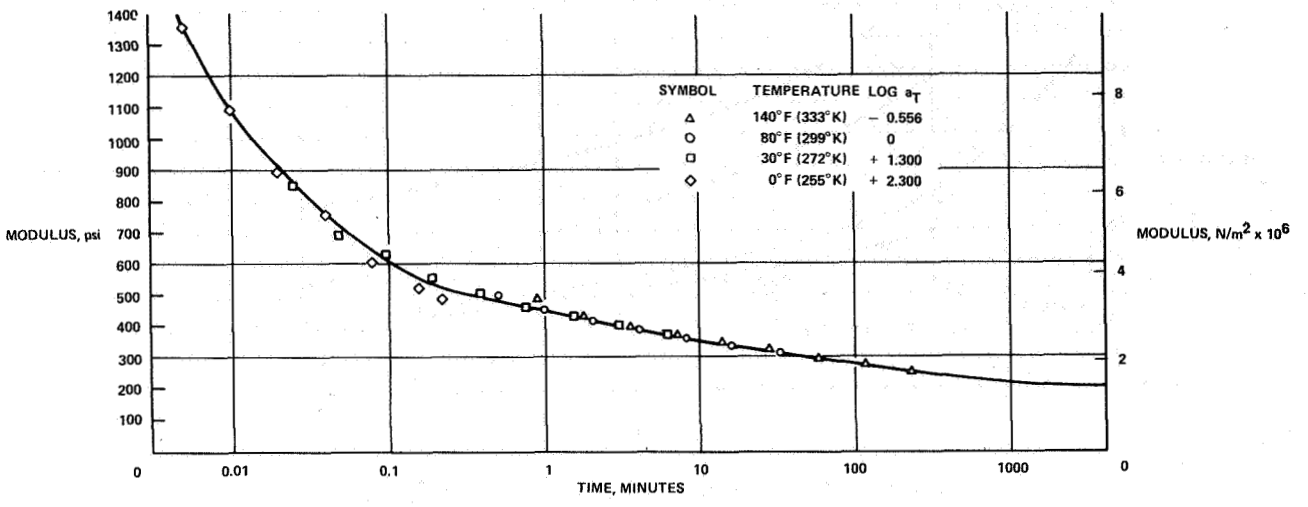

Figure 3. – Master viscoelastic modulus curve at 80°F (299°K) and 2.64% strain for TP-H1011 propellant.

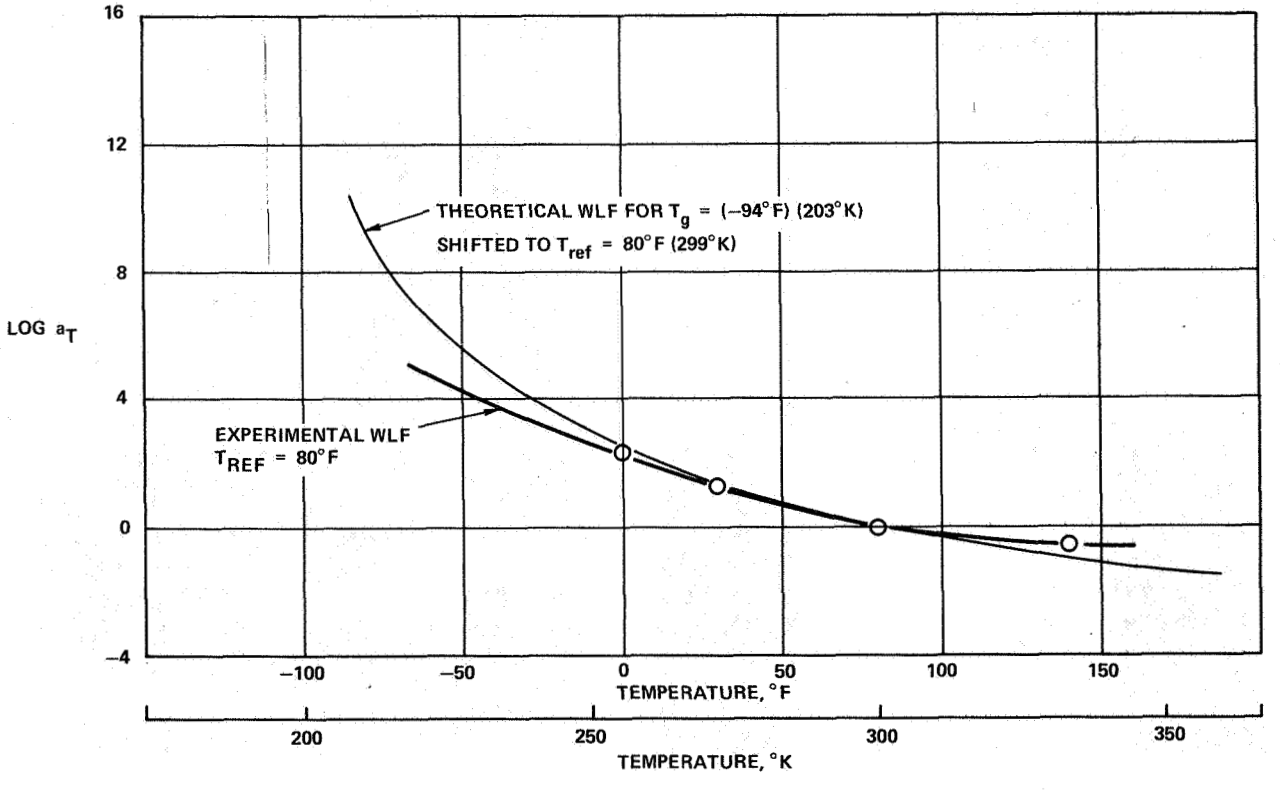

Figure 4. – Time-temperature shift factors as a function of temperature.

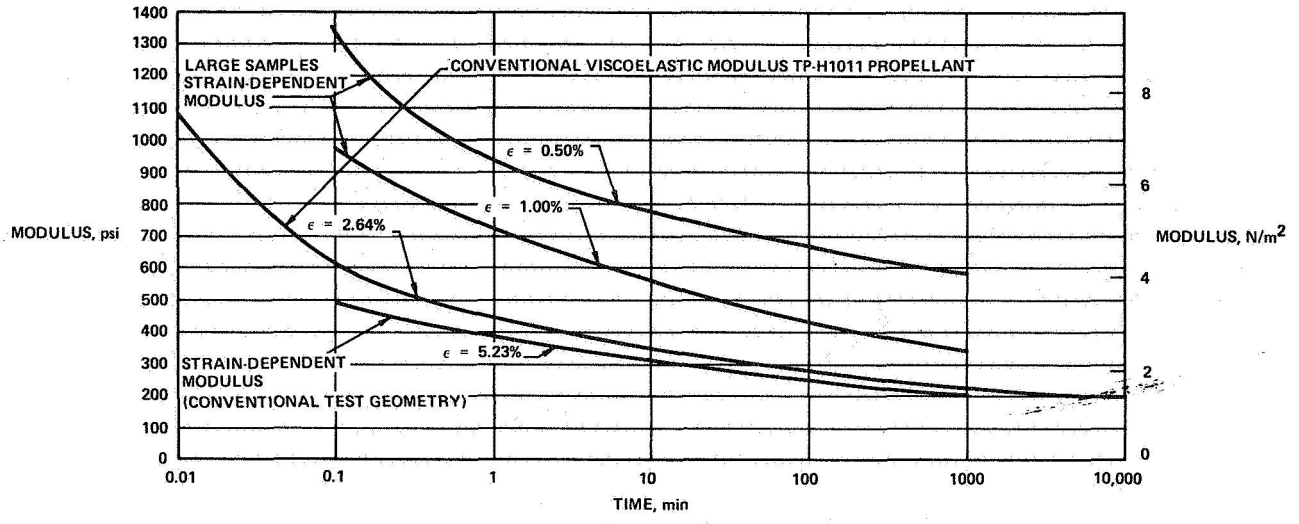

Figure 5. – Conventional viscoelastic modulus data and strain-dependent modulus for TP-H1011 solid propellant.

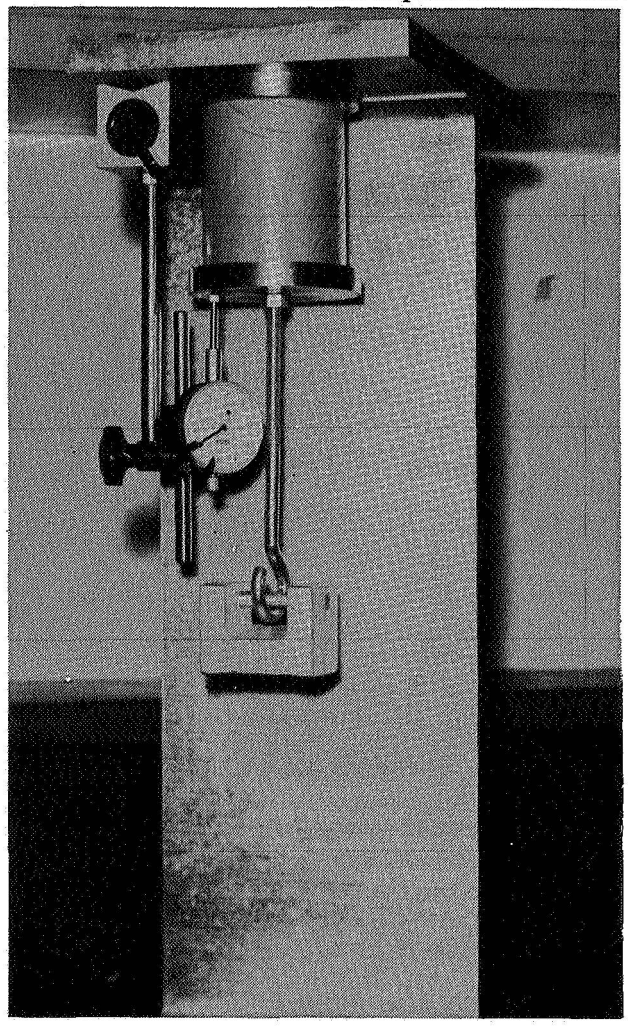

Circular bar specimen constant load

9728-2

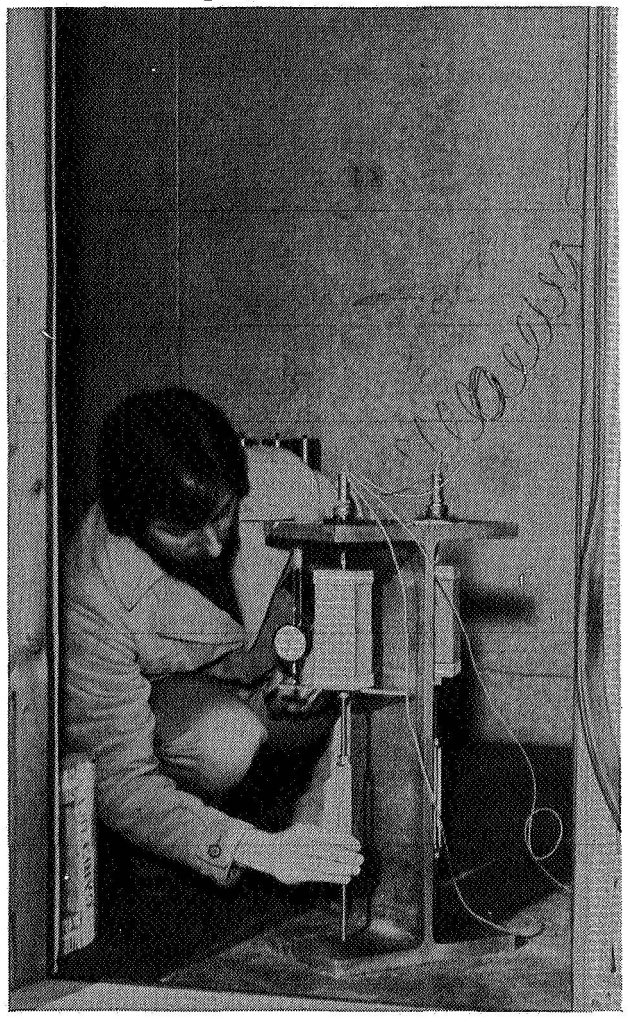

Rectangular bar specimen in constant strain

9731-3

Figure 6. – Large sample in I-beam test fixture.

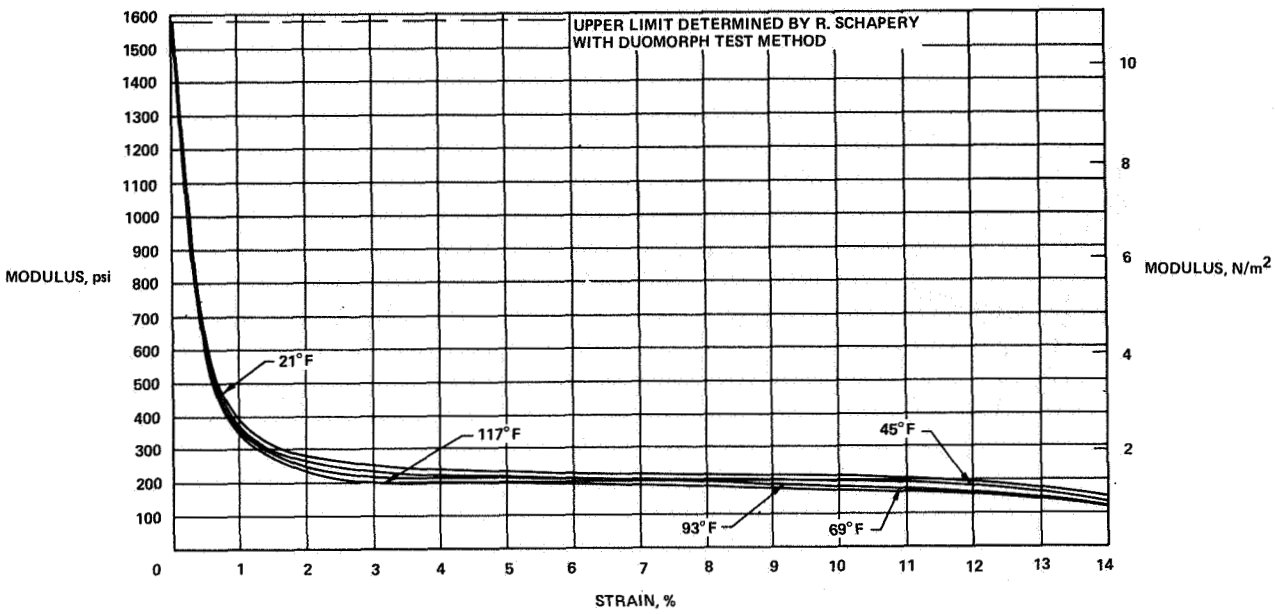

Figure 7. – Propellant modulus-strain behavior at specific motor time-temperature increments.

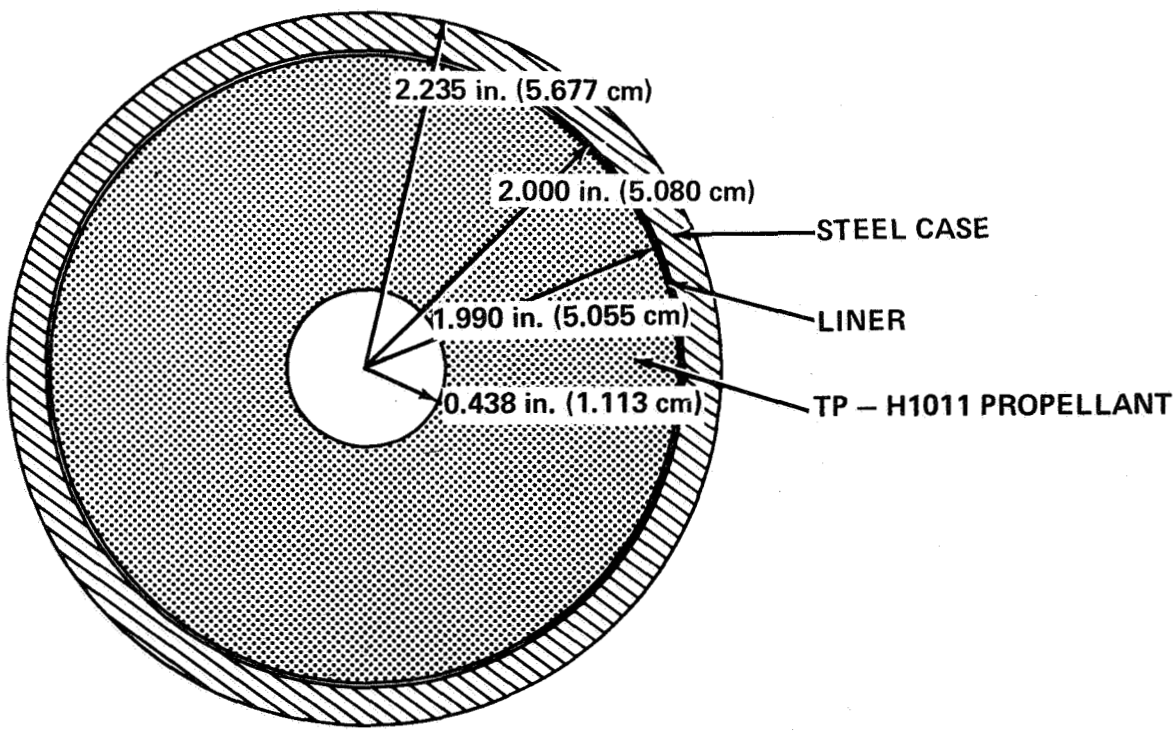

Figure 8. – Cross section of a solid propellant rocket motor.

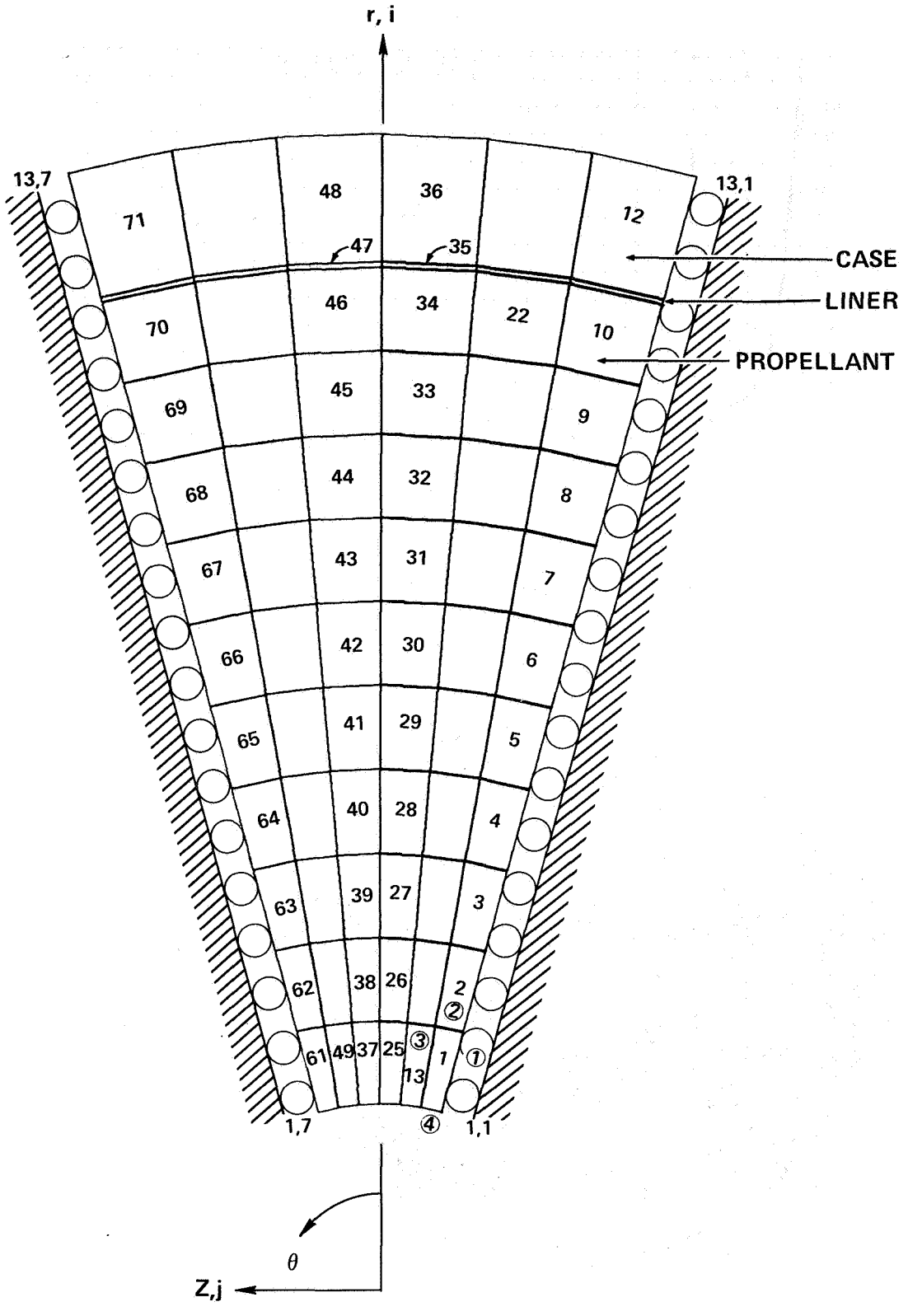

Figure 9. – Finite element grid.

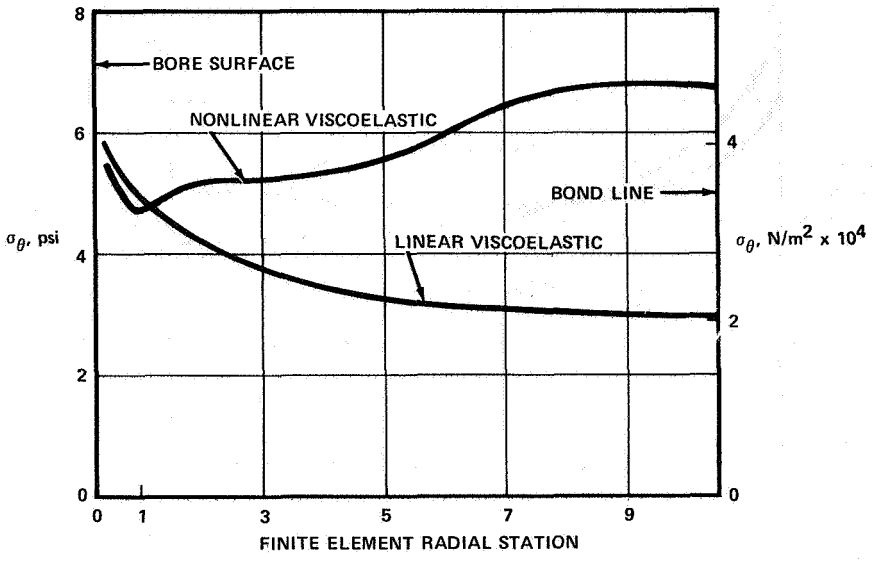

Figure 10. – Distribution of circumferential stress with radius at 117°F (320°K) and 10,000 minutes by linear and nonlinear theory.

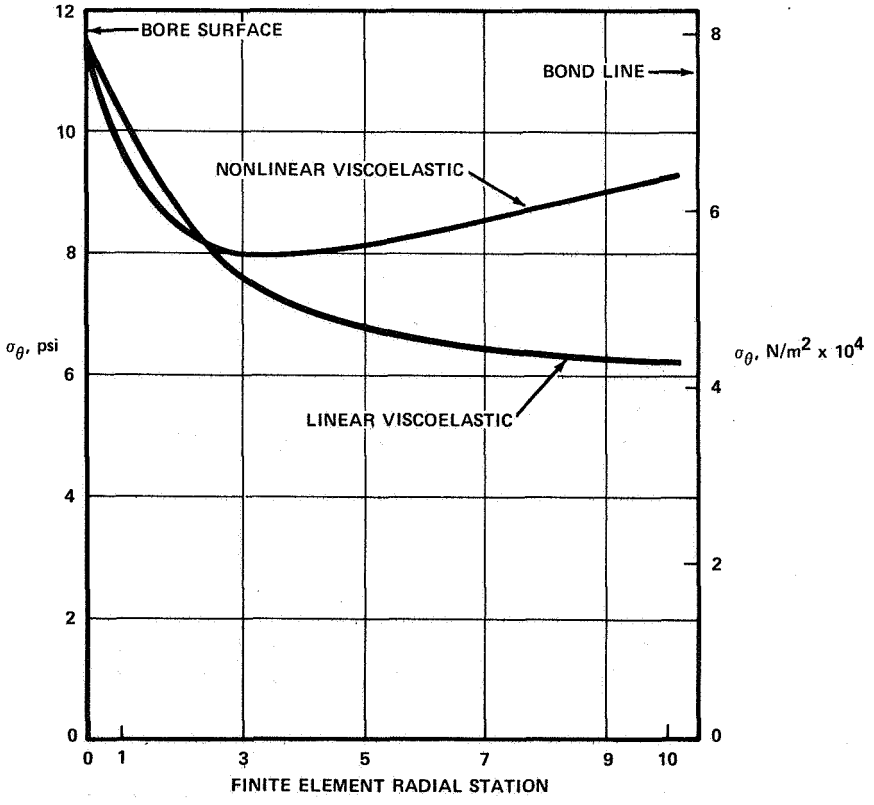

Figure 11. – Distribution of circumferential stress with radius at 93°F (307°K) and 20,000 minutes by linear and nonlinear theory.

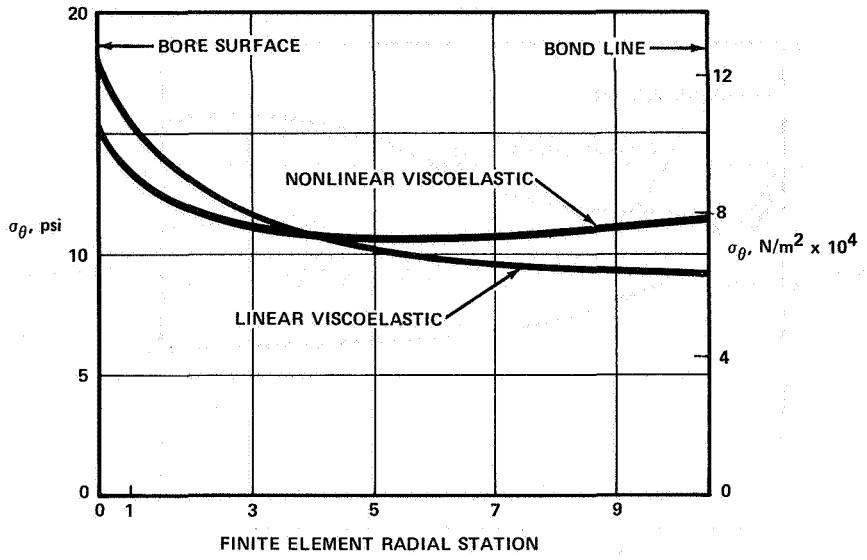

Figure 12. – Distribution of circumferential stress with radius at 69°F (294°K) and 30,000 minutes by linear and nonlinear theory.

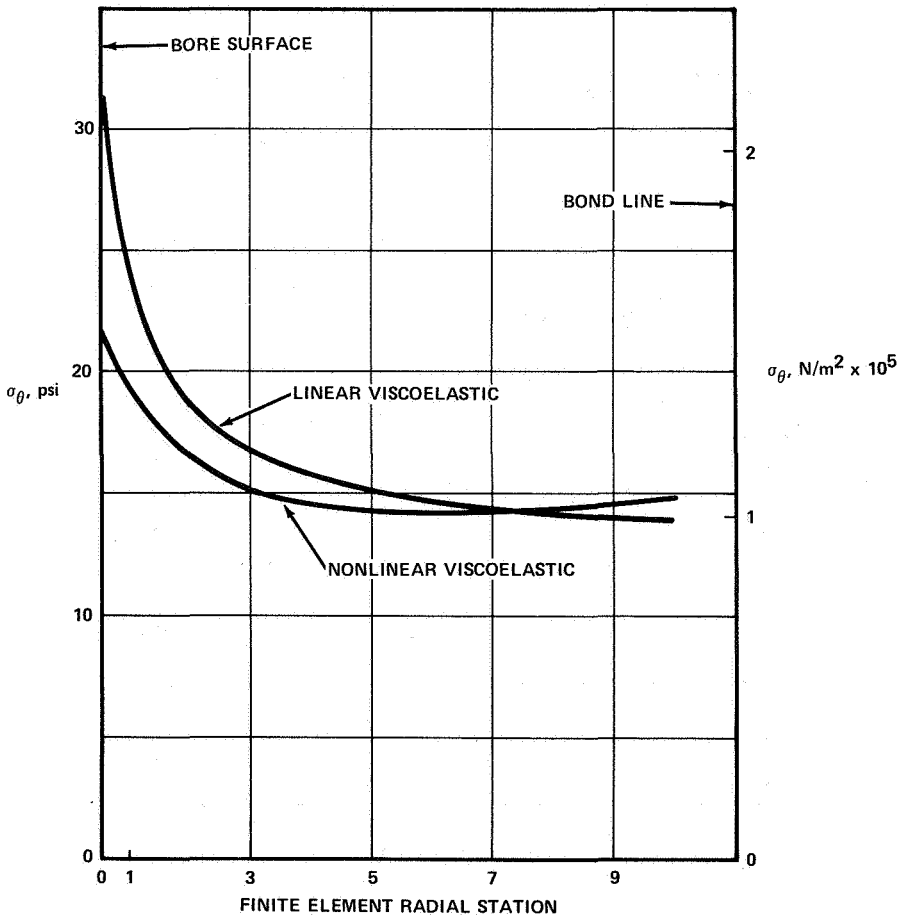

Figure 13. – Distribution of circumferential stress with radius at 45°F (280°K) and 40,000 minutes by linear and nonlinear theory.

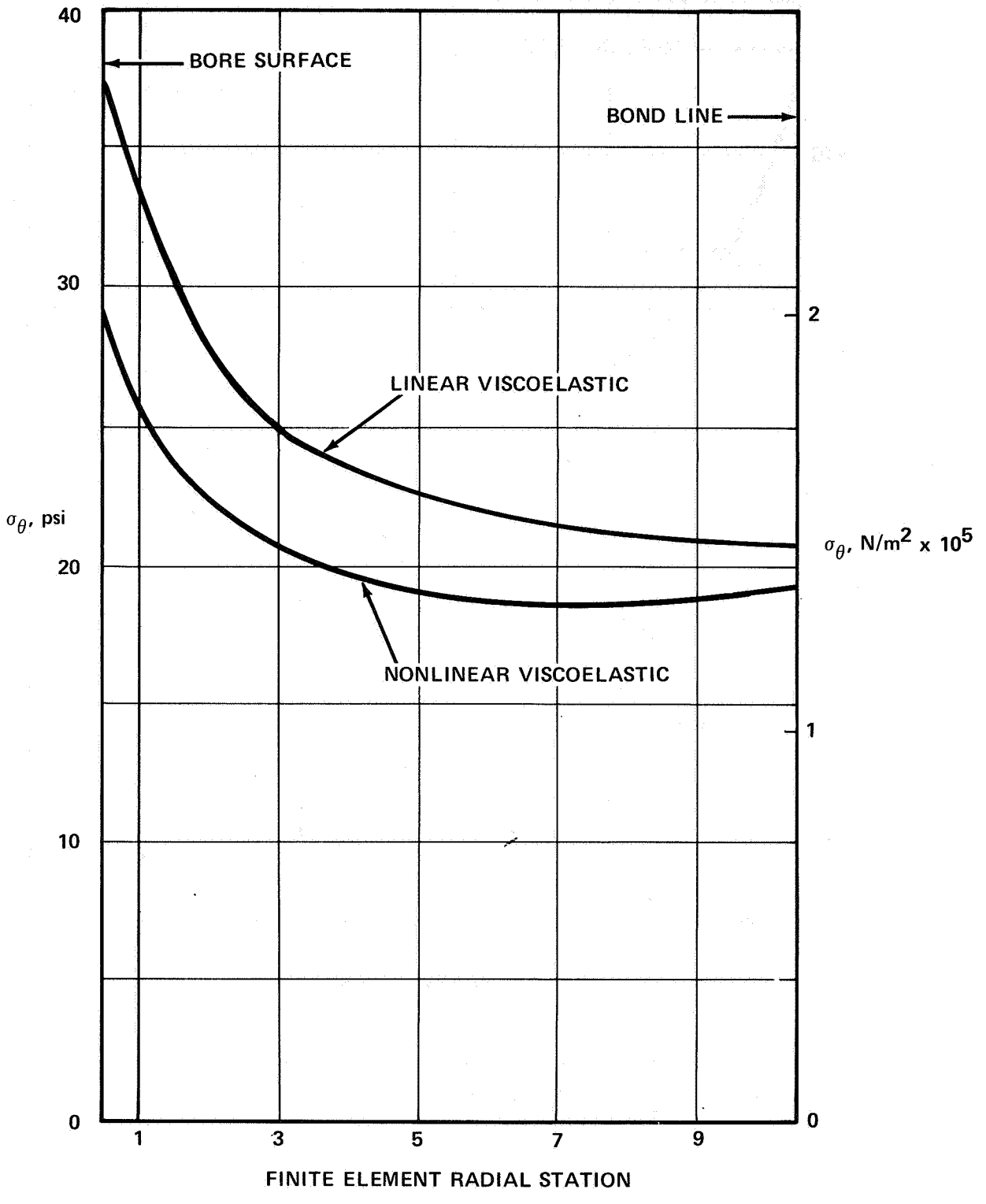

Figure 14. – Distribution of circumferential stress with radius at 21°F (267°K) and 50,000 minutes by linear and nonlinear theory.

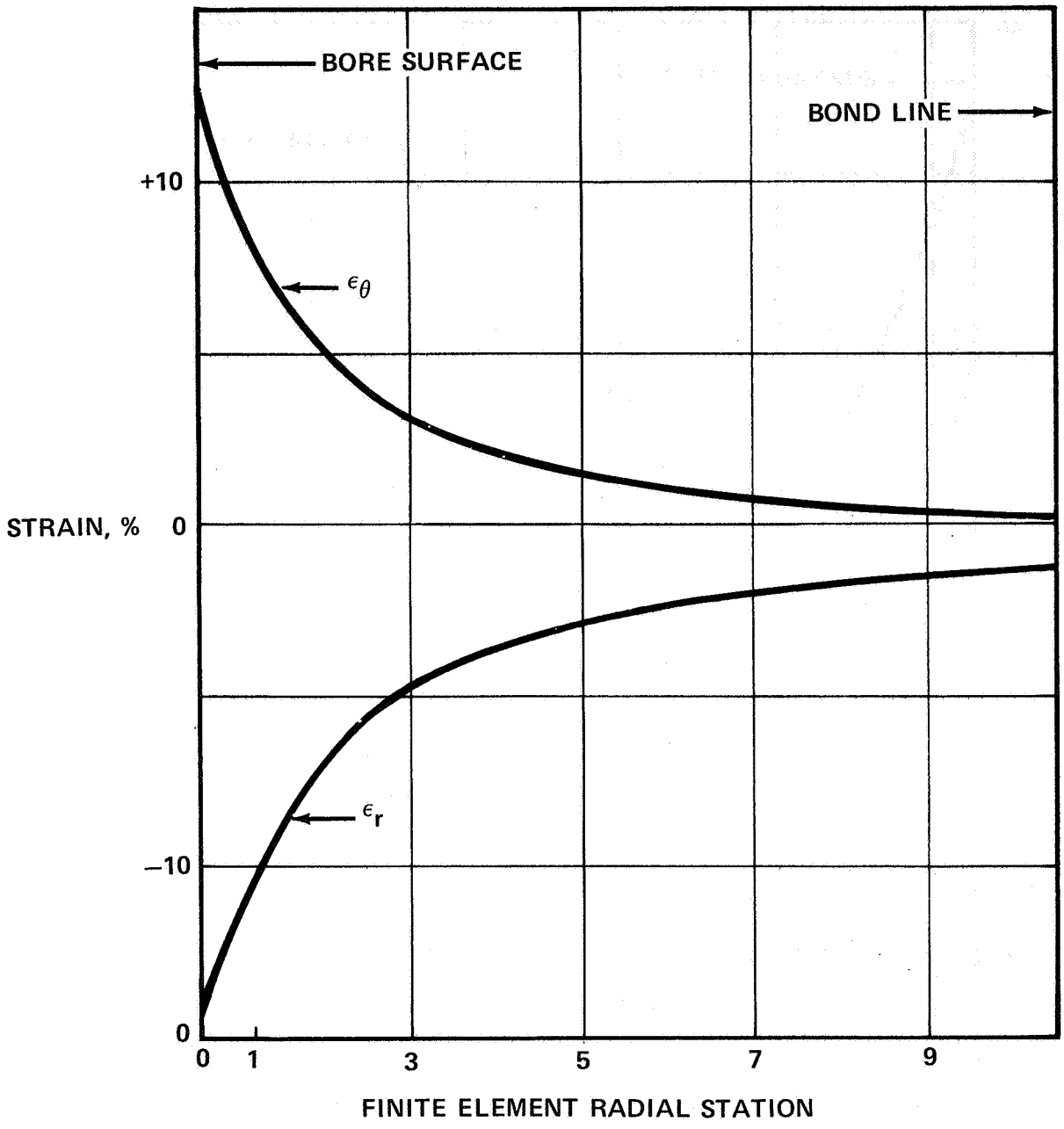

Figure 15. – Distribution of circumferential and radial strain with radius at 45°F.

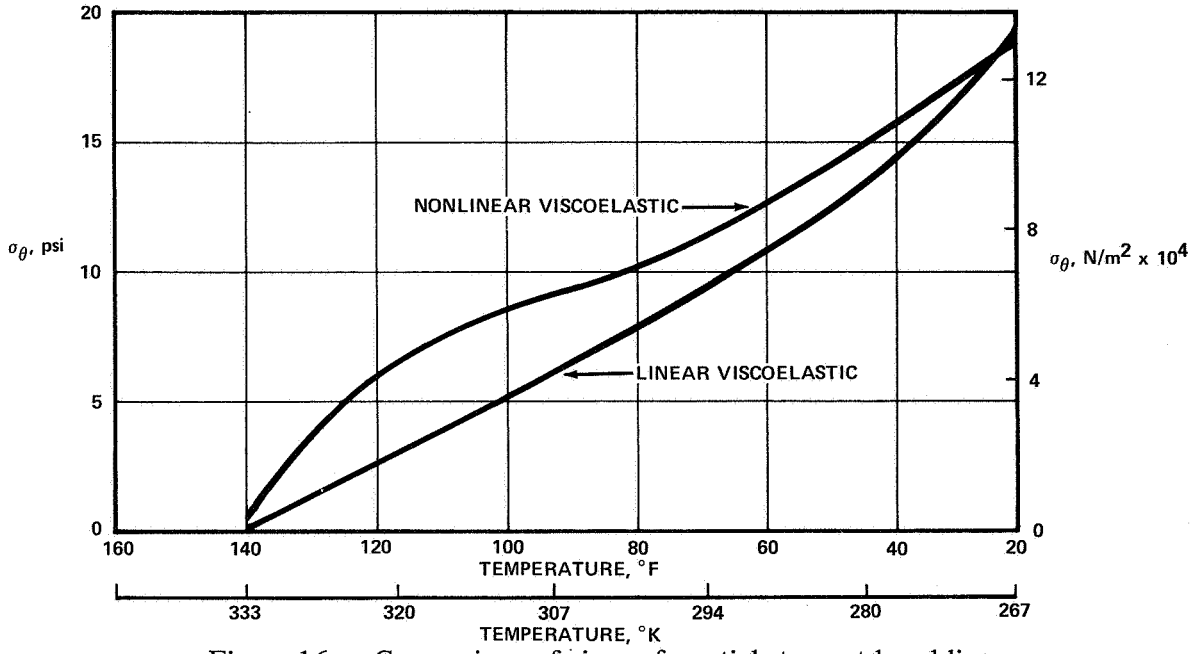

Figure 16. – Comparison of circumferential stress at bond line during cooldown, as calculated by linear and nonlinear methods.

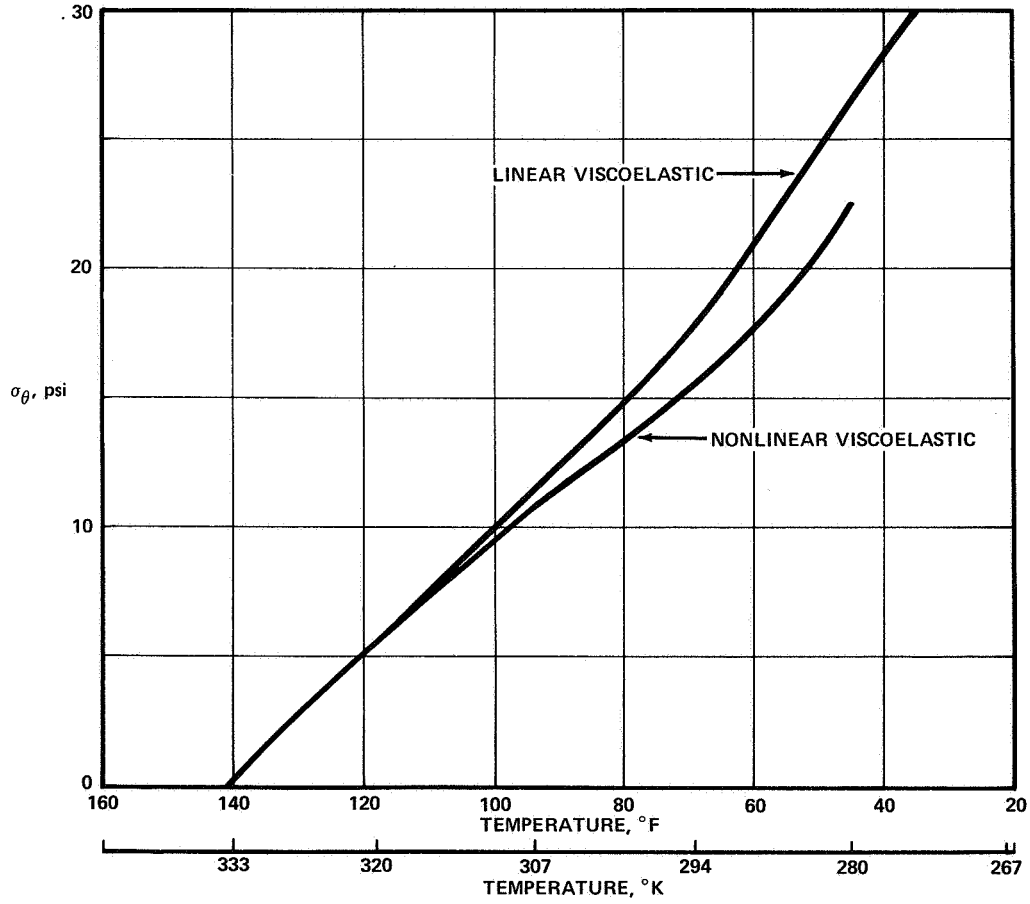

Figure 17. – Comparison of circumferential stress at bore surface during cooldown, as calculated by linear and nonlinear methods.

COMPUTER SIMULATION OF SCREW DISLOCATION IN ALUMINUM

Donald M. Esterling
Joint Institute for Advancement of Flight Sciences
The George Washington University

SUMMARY

The atomic structure in a <110> screw dislocation core for aluminum is obtained by computer simulation. The lattice statics technique is employed since it entails no artificially imposed elastic boundary around the defect. The interatomic potential has no adjustable parameters and was derived from pseudopotential theory. The resulting atomic displacements were allowed to relax in all three dimensions.

INTRODUCTION

Extended defects, such as dislocations and cracks, play a well-known role in determining the mechanical properties of a solid. These defects have been modeled extensively using a continuum approach. In many circumstances, however, final quantification of the model requires an understanding of processes on an atomic scale, e.g. at the crack tip or the dislocation core. Continuum theories typically acquire singularities in these regions, whereas discrete, or lattice models are well behaved. There have been a few attempts to use the latter models for these extended defects (Ref. 1), but usually large scale computer calculations are required in contrast to the analytical solutions available in continuum mechanics. Since little or no experimental data is available concerning these restricted atomic scale regions, reliable calculations will require careful modeling. Some of the necessary precautions will be discussed in the following as well as a brief description of the approach used in this calculation. Calculational details are given in the next section and we conclude with the resulting atomic configuration associated with a <110> screw dislocation in aluminum. This represents the first step in a path which will permit atomic level effects to be incorporated into continuum calculations and subsequent engineering applications. Portions of this work were previously reported (Ref. 2). In that work, the atomic displacements were constrained to lie along the dislocation core axis, whereas in this report full three dimensional relaxations are permitted.

Many computer simulations of dislocations and cracks have employed a molecular dynamics approach with interatomic potentials derived empirically. Some care must be exercised with this approach. The molecular dynamics method embeds a discrete lattice (containing the defect) in a elastic continuum. Computational constraints keep the discrete region small (~1000 atoms) whereas some calculations (Ref. 3) suggest that the discrete region must contain

~10,000 atoms before the elastic predictions are valid for even so simple a defect as a single vacancy in aluminum. In addition, although many simulation results are somewhat insensitive to the choice of interatomic potential within a general class of potentials, the latter area is also one of concern. As an example, a recent atomistic study of hydrogen-enhanced crack propagation in BCC iron (Ref. 4) found very different enhancement effects from the hydrogen depending on the choice of empirical potential. We will now briefly describe an alternative approach which addresses each of these possible problem areas.

We will use a lattice statics technique. This method was first proposed by Matsubara (Ref. 5) for point defects. Maradudin (Ref. 6) applied it to dislocations. More recently, Boyer and Hardy (Ref. 7) have performed calculation quite similar to that described in this paper (but in all of the preceding work, the forces were all restricted to being harmonic or linear in the displacements). For harmonic forces, Fourier transform techniques permit an evaluation of an atomic displacement anywhere in the crystal once the nature of the defect and the force constants are given. The underlying crystal symmetry of the undistorted lattice is exploited as an integral part of the lattice statics method. This leads to computational times on the order of seconds rather than hours as required by a molecular dynamics solution. Eventually, the displacement field approaches the continuum values but no specific boundary is imposed. Even the harmonic approximation breaks down (though no singularities occur) within a few atomic spacings of the defect. We will report the first lattice statics calculation for an extended defect which includes an anharmonic region as well.

In order to complete the solution in the anharmonic region, the entire interatomic potential is required. We will assume pair potentials. This work will not address directly the validity of this approximation. Pseudopotential theory provides a rigorous basis for such an approach, both for simple metals and for certain classes of d-band metals (Ref. 8). More germane to this calculation is the choice between empirical potentials (e.g., Johnson, Born-Mayer, Morse, etc.) and a potential derived from a more fundamental perspective, such as our pseudopotential. A brief summary of the method used to generate an interatomic potential will be given in the next section. At this juncture, we only wish to point out that there are no adjustable parameters (input is based on atomic data), yet the potential accurately describes a wide variety of electronic and lattice properties.

SYMBOLS

H	Hamiltonian
H_{har}	harmonic part of Hamiltonian
H_{anhar}	anharmonic part of Hamiltonian
$u_\alpha(\ell)$	displacement of atom ℓ in direction α

$F_\alpha(\ell)$	force on atom ℓ in direction α
D	force constant
Λ	anharmonic force
F^E	external force
v	effective pair potential between ions
V	electron-ion potential
W	electron-ion pseudopotential
Ψ	wave function
ϕ	pseudowave function
a_o	unit cell dimension
$\vec{a}_1$	primitive fcc lattice vectors
$\vec{b}$	Burger's vector
$\vec{x}_1$	vectors for orthogonal coordinate system
$\hbar$	Planck's constant
m	mass of electron

CALCULATIONAL DETAILS

Lattice Statics

The problem is to find the atomic displacements (u) due to prescribed external and/or internal stress fields. The equilibrium condition is that the sum of all the forces on each atom must vanish or:

$$F_\alpha(\ell) = -\frac{\partial H}{\partial u_\alpha(\ell)} = 0 \qquad (1)$$

where $F_\alpha(\ell)$ is the force on an atom at site ℓ in the α direction, $u_\alpha(\ell)$ is

the corresponding displacement, and H is the Hamiltonian. The Hamiltonian can be written as:

$$H = H_{int} + H_{ext} \tag{2}$$

where H_{ext} is the contribution from external forces and the internal part is a sum of pair potentials:

$$H_{int} = \frac{1}{2} \sum_{\ell,\ell'} v(|r(\ell) - r(\ell')|) \tag{3}$$

We decompose H_{int} further as

$$H_{int} = H_{har} + H_{anhar} \tag{4}$$

where the harmonic contribution is defined as:

$$H_{har} = H_o + \sum_{\ell,\alpha} D_\alpha^\ell u_\alpha(\ell) + \frac{1}{2} \sum_{\substack{\ell,\ell' \\ \alpha,\beta}} D^{\ell\ell'} u_\alpha(\ell) u_\beta(\ell') \tag{5}$$

Note that the sums over lattice sites (ℓ and ℓ') extend over the entire crystal. Such an expression would only be valid if the atoms were everywhere coupled by linear or harmonic restoring forces. Note also that the force constants (D_α^ℓ and $D_{\alpha\beta}^{\ell\ell'}$) are determined by the <u>undistorted</u> crystal. This fact will be the key to the power of the lattice statics method.

The anharmonic contribution, H_{anhar}, involves a sum over lattice sites which are not coupled harmonically. The appropriate harmonic terms are substracted out and the " exact" pair potentials are substituted. Note, however, that this latter set of terms involve only a finite, and typically small, number of sites. The detailed expression for H_{anhar} depends on the defect considered. An explicit expression for a screw dislocation will be given in the next section. Application to a model crack calculation may be found in Reference 9.

The equation of motion can then be obtained from equation (1) and takes the form:

$$F_\alpha(\ell) = -\sum_{\ell',\beta} D_{\alpha\beta}^{\ell\ell'} u_\beta(\ell') + \Lambda_\alpha^\ell(u) + F_\alpha^E(\ell) = 0 \tag{6}$$

(We have assumed inversion symmetry so that D_α^ℓ vanishes.) Here F^E represents the external term force applied to atom ℓ and the term Λ arises from the anharmonic contributions. Note that Λ is functional only of those displacements in the anharmonic region. Equation (6) represents N coupled equations in N unknowns, where $N \sim 10^{23}$. However, we can take advantage of certain properties of $D_{\alpha\beta}^{\ell\ell'}$ to decouple the equations associated with the anharmonic region from those associated with the harmonic region. Some of details can be found in Reference 9, but in essence is described in the following.

As a first step, we wish to obtain $\tilde{D}^{\ell\ell'}_{\alpha\beta}$, where $\tilde{D}$ is the matrix inverse of D. Now $D^{\ell\ell'}_{\alpha\beta}$ retains the full symmetry of the distorted lattice, in particular the lattice translational symmetry. Working, for simplicity, with a Bravais lattice, this is a function of $r(\ell) - r(\ell')$. As such, we may obtain its Fourier transform $D_{\alpha\beta}(q)$ in the usual manner. Fourier transforming back with $\tilde{D}_{\alpha\beta}(q)$ - where we only require the 3 x 3 matrix inversion in the (α,β) coordinates - we finally obtain $\tilde{D}^{\ell\ell'}_{\alpha\beta}$.

Once we have D, the solution immediately follows as:

$$u_\alpha(\ell) = \tilde{D}^{\ell\ell'}_{\alpha\beta} \Lambda^{\ell'}_\beta + \tilde{D}^{\ell\ell'}_{\alpha\beta} F^E_\beta(\ell') \tag{7}$$

The procedure is to first solve Equation (7) self-consistently for the $u_\alpha(\ell)$ in the anharmonic region. This then specifies Λ. We may then obtain displacements anywhere since the right hand side involves all known quantities.

Pseudopotential Theory

The use of pseudopotentials in the theory of simple metals is discussed at length in Reference 10. We give here only a brief outline of the derivation of an interatomic pair potential from pseudopotential theory. The formal result of importance to us is that the total binding energy of a metal such as aluminum can be written, both for the undistorted and the distorted lattice, as:

$$E_{total} = E_o + \frac{1}{2} \sum_{\ell,\ell'} v(|r(\ell)-r(\ell')|) \tag{8}$$

Both E_o and the pair potential v are volume-dependent functionals of an atomic pseudopotential, but their forms are independent of the structure, i.e., the positions of the ions $r(\ell)$ in the metal. All dependence of E_{total} on structure is explicit through the summation over $r(\ell)$ and $r(\ell')$.

Equation (8) is obtained by first exactly transforming the one-electron Schrodinger equation

$$[-\frac{\hbar^2}{2m}\nabla^2 + V(\vec{r})]\Psi_v(\vec{r}) = E_v \Psi_v(\vec{r}) \tag{9}$$

for the true valence eigenstates Ψ_v, to an equivalent pseudo-Schrodinger equation

$$[-\frac{\hbar^2}{2m}\nabla^2 + W]\phi_v(\vec{r}) = E_v \phi_v(\vec{r}) \tag{10}$$

where the full self-consistent potential V is replaced by a weak pseudopotential W and Ψ_v is replaced by a smooth pseudowavefunction ϕ_v. Equation (10) may be solved by perturbation theory for the valence eigenstates E_v. The total energy of the metal can then be calculated by (1) summing E_v over all occupied valence states, (2) adding in the direct Coulomb interaction between ions and (3) substracting off an energy equal to the electron-electron interaction, which is counted twice in the sum over E_v. Equation (8) follows rigorously by terminating the calculation at second-order in W.

The atomic pseudopotential W used in the present work was constructed by John A. Moriarty entirely from first-principles using the zero-order pseudoatom method described in Reference 11 plus one refinement. The exchange correlation contribution to the self-consistent screening of W has been included through the G(q) function of Reference 12 rather than that employed in Reference 11. In the Tables of Ref. 11 are listed various calculated physical properties of aluminum that can be compared with experiment to indicate the reliability of our pseudopotential, and hence our pair potential.

Core Dislocation Structure in Al

Boyer and Hardy have applied the lattice statics method to screw dislocations in cubic metals, including aluminum (Ref. 7). In the following, we will conform to their notation and coordinate system throughout. Further elaboration may be obtained from their paper.

The undistorted lattice sites are at positions:

$$\vec{R}(\ell) = \ell_1\vec{a}_1 + \ell_2\vec{a}_2 + \ell_3\vec{a}_3 \tag{11}$$

where (ℓ_1, ℓ_2, and ℓ_3) are half-odd integers and (a_1, a_2, a_3) are the primitive lattice vectors for the fcc aluminum lattice:

$$\vec{a}_1 = \frac{a_o}{2}\,[011],\quad \vec{a}_2 = \frac{a_o}{2}\,[101],\quad \vec{a}_3 = \frac{a_o}{2}\,[110] \tag{12}$$

where a_o = 7.65278 A.U. is the unit cell dimension. The Burger's vector $\vec{b}$ is taken parallel to the a_3 axis, $\vec{b} = \vec{a}_3$. It will be convenient to introduce an orthogonal coordinate system:

$$\vec{x}_1 = \frac{a_o}{2}\,[\bar{1}10],\quad \vec{x}_2 = \frac{a_o}{\sqrt{2}}\,[001],\quad \vec{x}_3 = \vec{a}_3. \tag{13}$$

Note that the (110) plane has reflection symmetry in both the x_1 and x_2 axes.

Boyer and Hardy did not include anharmonic effects in their calculation. Further, the force constants used in the calculation were obtained by a fit to elastic constant data. As they indicated in an earlier paper (ref. 3), there is a considerable lack of uniqueness associated with this fit. The pseudopotential approach provides the required force constants directly. Further by employing an explicit pair potential we may incorporate anharmonic effects.

The calculation proceeds in two stages. First, the harmonic displacement field is determined as was done in the Boyer/Hardy paper - though using revised force constants. Second, an anharmonic "core" region is chosen. Within this region, all harmonic forces are replaced by the exact forces derived from the pair potential. The assumption is made (for calculational simplicity) that all forces between atoms outside the core or between a pair of atoms located inside and outside the core are harmonically coupled. Clearly for large enough core size this becomes an accurate approximation. These two steps define F^E and Λ respectively and the computation then proceeds as outlined in Section II.

The first stage corresponds to introducing a cut half-plane terminating on the a_3 axis and containing the a_1 axis. In order to form the screw dislocation, bonds which cross this plane are "cut" and then "rejoined" to a partner atom one Burger's vector up (or down, if crossing the cut plane in the opposite direction). Mathematically, this corresponds to introducing a Hamiltonian of the form $(u_\alpha(\ell\ell') \equiv u_\alpha(\ell) - u_\alpha(\ell'))$:

$$H = \frac{1}{4} \sum_{\substack{\ell\ell' \\ \alpha\beta}} D_{\alpha\beta}^{\ell\ell'} [u_\alpha(\ell\ell') - b_\alpha(\ell|\ell')] [u_\beta(\ell\ell') - b_\beta(\ell|\ell')] \qquad (14)$$

Here $(\ell|\ell')$ is defined as +1 if a line from ℓ to ℓ' crosses the cut plane from left to right, -1 if the line crosses the cut plane from right to left, and zero otherwise. If the line crosses the a_3 axis line, then the above prescription is reduced by a factor of 1/2. For b = 0, the above Hamiltonian reduces to the harmonic Hamiltonian, using the symmetry properties of D. By taking $H-H_{har}$, we then define the term H_{ext} in Equation (2) and the "external" force field in Equation (6).

The resulting harmonic displacement field is quite similar to that obtained by Boyer and Hardy and will not be reproduced here. We obtained deviations from the continuum values for the (3/2, -1/2) and (3/2, 1/2) points as -0.01062 and 0.00097 respectively. The rest agreed within about 10% or less. One comment - they obtained a spurious cut over the entire $\ell_2 = 0$ plane, rather than over the chosen half-plane. When performing a certain infinite sum to obtain the function "F(x,y)" in their paper, they did not include an additional contribution to the sum which arises when $x \to 0$ and which becomes proportional to a delta function for an infinite lattice. This term is exactly what is required to restore the cut to the appropriate half plane.

As noted earlier, these harmonic displacements are quite close to the elastic continuum values. The screw dislocation in an fcc lattice retains a very high degree of symmetry which is the basis for this result. The harmonic displacements equal the elastic field values along these axes and, hence, never deviate far from the elastic values. For a defect with lower symmetry (e.g., with the dislocation line at a saddle point configuration) this would no longer be true.

The anharmonic field was obtained by solving Equation (6) where F^E was obtained from the harmonic calculation and Λ is related to appropriate derivatives of the pair potential. The equation of motion, equivalent to Equation (6), becomes for an atom ℓ in the core

$$F_\alpha(\ell) = -\sum_{\ell'\beta} D^{\ell\ell}_{\alpha\beta}[u_\beta(\ell\ell') - b_\beta(\ell|\ell')] + \Lambda^\ell_\alpha = 0 \qquad (15)$$

where the anharmonic force field Λ is

$$\Lambda^\ell_\alpha = -\sum_{\ell'\varepsilon \text{ core}} [\sum_\beta D^{\ell\ell'}_{\alpha\beta} [u_\beta(\ell\ell') - b_\beta(\ell|\ell')]$$

$$+ \frac{1}{R} \left.\frac{\partial v}{\partial R}\right|_{R^o_{\ell\ell'}} R^o(\ell\ell') - \frac{1}{R} \left.\frac{\partial v}{\partial R}\right|_{R_{\ell\ell'}} R_\alpha(\ell\ell')] \qquad (16)$$

In the above equation, v is the effective pair potential, $R(\ell\ell')$ is the magnitude of the separation of lattice sites ℓ and ℓ' ; R_α is the α component of that separation vector, and the superscript o indicates evaluation at the undistorted lattice position.

Note that the above derivations were evaluated at the actual atomic positions in the core region and hence, the solution required an iterative technique. A Newton-Raphson method was used to obtain a consistent solution. The starting configuration was the harmonic field, but the atoms in the core were no longer constrained to maintain a cut across the $\ell_2 = 0$ plane. For computational convenience, the effective ion-ion potential was truncated after fifth nearest neighbors.

The results for an anharmonic core containing an array of atoms 4 x 4 x ∞ in size are displayed in the Table. Translational symmetry leads to the displacement field repeating for each (110) plane. Only the displacements for ℓ_1 positive are listed. The in-plane displacements are odd for $(\ell_1, \ell_2) \rightarrow (-\ell_1, -\ell_2)$, whereas the displacements along the core are even.

The atoms were allowed to relax in the plane as well as along the core (a_3) axis. However, the displayed values should be considered as preliminary. The anharmonic region for this calculation was small and a larger core will be required for the final converged values. These preliminary results are quite interesting. The relaxations in the plane are larger than anticipated and indicate the necessity of in-plane relaxation which were ignored in

earlier calculations. The anharmonic displacements parallel to the core no longer vanish for sites along the x_1 or x_2 axes and are quite different from the values obtained when the in-plane displacements were constrained to vanish. We may anticipate some quantitative changes for large anharmonic cores, but the qualitative results should be retained.

In a later publication, in addition to listing the final converged displacement field, we plan to address configurations relevant to the movement of the dislocation. This includes the displacement field and associated Peierl's barrier when the dislocation is in a saddle point configuration, as well as vacancy-dislocation interactions.

TABLE I

Anharmonic Displacement Field (Units of Bohr Radii)

Parallel to $\vec{x}_1$ axis

ℓ_1/ℓ_2	3/2	1/2	-1/2	-3/2
3/2	0.010	-0.007	-0.240	-0.223
1/2	-0.009	-0.015	-0.336	-0.121

Parallel to $\vec{x}_2$ axis

ℓ_1/ℓ_2	3/2	1/2	-1/2	-3/2
3/2	0.262	0.272	0.050	0.026
1/2	0.325	0.478	-0.011	0.005

Parallel to $\vec{x}_3$ axis

ℓ_1/ℓ_2	3/2	1/2	-1/2	-3/2
3/2	-0.008	0.062	-0.045	-0.003
1/2	-0.107	0.011	-0.004	0.118

REFERENCES

1. Gehlen, P.C.; Beeler, J.R. Jr.; and Jaffee, R.I. (Editors): Interatomic Potentials and Simulation of Lattice Defects. Plenum Press, N.Y., 1972. (A survey of the literature up to 1972).

   Proceedings of the 1976 NBS Conference on Computer Simulation for Materials Applications, Gaithersburg, Md. (A more recent review)

2. Esterling, D.M.; and Moriarty, J.A.: Computer Simulation for Materials Applications. NBS Conference, Gaithersburg, Md., 1976, p. 858.

3. Boyer, L.L.; and Hardy, J.R.: Phys. Rev., B4, 1079, 1971.

4. Gehlen, P.C.; Markworth, A.J.; and Kahn, L.R., NBS Conference, Gaithersburg, Md., 1976, p. 684.

5. Matsubara, T.J.: J. Phys. Soc. Japan, 7, 720, 1952.

6. Maradudin, A.A.: J. Phys. Chem. Solids, 9, 1, 1958.

7. Boyer, L.L.; and Hardy, J.R.: Phil. Mag. 24, 647, 1971.

8. Moriarty, J.A.: Phys. Rev. B5 2066, 1972. and Harrison, W.A.: Phys. Rev. 181, 1036, 1969.

9. Esterling, D.M.: J. Appl. Phys. 47, 486, 1976.

10. Harrison, W.A.: Pseudopotentials in the Theory of Metals, W.A. Benjamin, New York, 1966.

11. Moriarty, J.A.: Phys. Rev. B 10 3075, 1974.

12. Geldart, D.J.W.; and Taylor, R.: Can. J. Phys. 48, 167, 1970.

MOISTURE TRANSPORT IN COMPOSITES*

George S. Springer
The University of Michigan

SUMMARY

The moisture distribution and moisture content of composite materials exposed to humid air or to water are discussed. Expressions are presented for estimating the weight gain of both single and multilayered composites when the moisture content and the temperature of the environment are constant. The parameters needed for solving problems in the time varying environmental conditions are specified, and a numerical approach for the solution of such problems is indicated.

INTRODUCTION

The mechanical and electrical properties of composite materials may change considerably when the material is exposed to a moist environment. Therefore, the response of such materials to moisture must be known in order to utilize their full potential. In this paper the moisture absorption and desorption characteristics of composite materials are described, and the results needed to estimate the moisture content of the material are summarized.

SYMBOLS

a,b,d	constant (dimensionless)
C	moisture concentration (g mm^{-3})
c	specific heat (J g^{-1} K^{-1})
D	mass diffusivity mm^2s^{-1}
G	parameter defined by eq. (14) (dimensionless)
h	thickness (mm)
K	thermal conductivity (W mm^{-1} K^{-1})
m	moisture content in the material (g mm^{-2})
M	percent moisture content in the material (dimensionless)
t	time (s)

* This work was supported by the United States Air Force Materials Laboratory, Air Force Systems Command, Wright-Patterson Air Force Base, Dayton, Ohio.

T	temperature (K)
V_f	volume fraction of fiber (dimensionless)
α, β, γ	fiber orientation with respect to the x, y and z axes (rad)
ϕ	percent relative humidity (dimensionless)
ρ	density (g mm^{-3})

Subscripts

a	ambient condition
d	dry material
f	fiber
i	initial state
j	layer number
m	maximum saturation
r	matrix (resin)
11	in the direction parallel to the fiber
22	in the direction normal to the fiber

THE PROBLEM

The following problem is considered. A plate of thickness h is exposed to a moist environment (Fig. 1). The plate may be made of either homogeneous or composite materials, and may consist of a single layer or of several layers. In the latter case the properties, as well as the thicknesses of the layers, may differ. The characteristics of each subsequent layer are denoted by the subscripts j = 1,2...k. The plate is taken to be infinite in the y and z directions so that the moisture content and the temperature inside each layer vary only in the x direction (one dimensional problem). Initially, (time $t<0$) the temperature T_i and the moisture concentration C_i inside the material is known. T_i and C_i are not necessarily constant, but may vary with position x. The two sides of the plate (x=0 and x=h) are exposed to moist environments where the temperatures are $T_a(0)$ and $T_a(h)$ and the moisture concentrations are $C_a(0)$ and $C_a(h)$. Alternately, one side of the plate may be insulated, so as to be impermeable to both heat and moisture. The objective is to determine the temperature distribution T, the moisture distribution C, and the total moisture content of the material as a function of time. The total mass of the moisture per unit area in the jth layer is given by

$$m_j(t) = \int_0^{h_j} C(t)dx \qquad (1)$$

Generally, the moisture content is expressed in terms of the percent mass (or weight) gain which is defined as

$$M = M(t) = \frac{\text{mass of moist material-mass of dry material}}{\text{mass of dry material}} \times 100 \text{ percent} \quad (2)$$

or

$$M = M(t) = \frac{(m+m_d)-m_d}{m_d} \times 100 = \frac{m}{m_d} \times 100 \text{ percent} \quad (3)$$

When the material is fully saturated $C = C_m$ and eqs. (2) and (3) give the maximum mass or weight gain (maximum saturation level) of the jth layer as

$$(M_m)_j = \frac{(C_m)_j}{\rho_j} \times 100 \quad (4)$$

Note that $m_{d_j} = \rho_j h_j$, where ρ_j is the density of the dry material and h_j is the thickness of the jth layer.

The temperature and the moisture concentration in each layer are described by the Fourier and the Fick equations (e.g. see ref. 1). Solution of these equations is a difficult task and, for most problems, solutions can be obtained only by numerical means. However, even when numerical methods are employed certain assumptions must be made regarding the parameters characterizing the material. Two of the necessary assumptions pertain to the thermal diffusivity $K_x/\rho c$ and the mass diffusivity D_x: (1) In principle, these parameters may depend both on the temperature and on the moisture concentration. In practice, $K_x/\rho c$ and D_x are insensitive to the moisture content and therefore, may be taken to depend on temperature alone (refs. 1, 2). (2) For most materials the ratio $(K_x/\rho c)/D_x$ is of the order of 10^6. Since this ratio represents the "speed" by which the temperature and moisture "fronts" travel inside the material, the high value of the ratio implies that the temperature equilibriates much faster than the moisture content. Thus, the calculations of the temperature and moisture distribution may be decoupled. The temperature distribution can be calculated first by the Fourier equation, followed by the calculation of the corresponding moisture concentration by the Fick equation.

The third assumption which must be made in solving the problem described above pertains to the relationship between the moisture content of the environment and the moisture content at the surface of the material (C_m, Fig. 1). Experimental evidence indicates that for a material exposed to humid air the maximum saturation level M_m is related to the humidity ϕ by the expression

$$M_m = a\,\phi^b \quad \text{(humid air)} \quad (5)$$

For a material immersed in water

$$M_m = d \quad \text{(immersed in water)} \quad (6)$$

a, b and d are constants which depend on the material and on the temperature. The values of these constants must be determined experimentally. The data obtained thus far is for a limited temperature range only (i.e. 300-400K). In this range the constants and M_m appear to be insensitive to temperature. However, there is some evidence that a, b, and d (and consequently M_m) depend on

the temperature when the material is exposed to higher or lower temperatures. Unfortunately, the existing experimental results do not yet provide the needed relationship between the constants and the temperature. Until such information becomes available the solutions must be made on the basis of the assumption that the variation of M_m with temperature is insignificant.

In addition to the maximum moisture content, the mass diffusivity of the material must also be specified. The appropriate expressions for the diffusivity are given below.

DIFFUSIVITY

The diffusivity of the material in the direction normal to the surface is denoted by D_x. For fiber reinforced composites in which the orientations of all the fibers with respect to the x, y, z axes are α, β and γ

$$D_x = D_{11}\cos^2\alpha + D_{22}\sin^2\alpha \tag{7}$$

where D_{11} and D_{22} are the diffusivities in the directions parallel and normal to the fibers. Equation (7) applies to the jth layer and, therefore, all symbols should be subscripted by j. For simplicity, the subscripts were omitted. This practice will be followed throughout this section.

For fiber reinforced composites D_{11} and D_{22} (and consequently D_x) can also be estimated from the expressions (ref. 1)

$$D_{11} = (1-V_f)D_r + V_f D_f \tag{8}$$

$$D_{22} = (1-2\sqrt{V_f/\pi})D_r + \frac{D_r}{B}\left[\pi - \frac{4}{\sqrt{1-(B^2V_f/\pi)}}\tan^{-1}\frac{\sqrt{1-(B^2V_f/\pi)}}{1+\sqrt{(B^2V_f/\pi)}}\right] \tag{9}$$

where D_r and D_f are the diffusivities of the matrix (resin) and the fiber respectively, V_f is the volume fraction of the fiber, and $B=2(D_r/D_f-1)$. Generally, the diffusivity of the fiber is small compared to the diffusivity of the matrix ($D_f << D_r$) and eqs. (8) and (9) reduce to ($V_f < 0.785$)

$$D_{11} = (1-V_f)D_r \tag{10}$$

$$D_{22} = (1-2\sqrt{V_f/\pi})D_r \tag{11}$$

Equations (7), (10) and (11) give D_x.

Comparisons between measured values of D_{22} and values calculated by eq. (11) for composites of Graphite T-300 and Fiberite 1034 are shown in Fig. 2. As can be seen there is good agreement between the measured and calculated diffusivities.

NUMERICAL SOLUTION

As indicated in the problem statement, the temperature distribution, moisture concentration, and weight gain of the material may be calculated by nu-

merical methods when the following parameters are specified in each layer; 1) thickness h_j, 2) density ρ_j, 3) thermal conductivity K_j, 4) diffusivity D_{xj}, 5) maximum moisture content M_{mj}, and 6) the constants a_j, b_j and d_j. In addition, the solution requires that the initial conditions (the initial temperature and moisture distribution inside each layer) and boundary conditions on both sides of the plate (the temperature and humidity of the environment as a function of time) be specified. A computer code providing solutions to such problems has been developed at The University of Michigan and may be obtained from the Fluid Dynamics Laboratory, Department of Mechanical Engineering, The University of Michigan.

STEADY STATE SOLUTION - SINGLE LAYER COMPOSITE

Although the calculation of the moisture content of composite materials requires a numerical procedure, analytical, closed form solutions may be obtained in some special, restricted cases. Analytical solution is feasible when, in addition to the assumptions made earlier (see Problem Statement), the following conditions are met: 1) the plate is made only of a single layer of composite, 2) initially the temperature and moisture concentration inside the plate are uniform, 3) the plate is suddenly exposed to a moist environment in which the temperature and moisture concentration are constant. In this case, at time t the moisture concentration inside the material is (ref. 3)

$$\frac{C-C_i}{C_m-C_i} = 1 - \frac{4}{\pi} \sum_{n=o}^{\infty} \frac{1}{(2n+1)} \sin\frac{(2n+1)\pi x}{h} \exp\left[\frac{(2n+1)^2\pi^2 D_x t}{h^2}\right] \tag{12}$$

and the weight gain of the material is

$$M = G(M_m - M_i) + M_i \tag{13}$$

where

$$G = 1 - \frac{8}{\pi^2} \sum_{n=o}^{\infty} \frac{\exp\left[-(2n+1)^2\pi^2\left(\frac{D_x t}{s^2}\right)\right]}{(2n+1)^2} \tag{14}$$

The foregoing results apply during both desorption and absorption. The results may also be used when the material is exposed on both sides to the same environment (in which case s = h) and when the material is insulated on one side (in which case s = 2h). A comparison between calculated and measured values of moisture contents for composites of Graphite T-300 and Fiberite 1034 is presented in Fig. 3.

It is emphasized that the foregoing simple expressions must be used only when the conditions of the environment are constant. When this is not the case and the environmental conditions vary with time, the use of these expressions may result in considerable error as illustrated in Fig. 4. This figure shows that the results of the "steady state" analysis (eqs. 13 and 14) may underestimate the weight gain by as much as 100 percent.

STEADY STATE SOLUTIONS - LAYERED COMPOSITES

Equations (12), (13) and (14) apply only to single layered composites. These results may be extended to multilayered materials if an appropriate average diffusivity and average maximum weight gain are substituted for D_x and M_m. The average diffusivity may be approximated by

$$D_{x_{avg}} = \frac{h}{h_1/D_{x_1} + h_2/D_{x_2} + \ldots} \tag{15}$$

while the maximum moisture content may be estimated by

$$(M_m)_{avg} = \frac{M_{m_1} h_1 + M_{m_2} h_2 + \ldots}{h} \tag{16}$$

Comparisons between calculated and measured values of D_{avg} and M_{avg} are given in Figs. 5 and 6. The agreement between the calculated and measured results support the validity of the above expressions. However, the values of D_{avg} and $(M_m)_{avg}$ must be used with caution in calculating the moisture contents of layered composites. When the humidity of the environment is changed, for some period of time only the outer layer will sense this change. Depending upon the temperature and the material this time may be as long as 500-1000 hours. Therefore, during this initial time period the moisture content should be calculated by the actual diffusivity and maximum moisture content of the outer layer, and not by the average values. The use of the average values may result in substantial errors in the calculated moisture content.

THERMAL SPIKES

It has been observed that the absroption and desorption characteristics of composite materials change considerably when the material is exposed to very high ($\sim$450K) and very low ($\sim$200K) temperatures. Preliminary data suggest that sudden large temperature changes result in microcracks in the material. Due to these cracks both the diffusivity and the maximum moisture content (maximum saturation level) of the material changes. Thus, to obtain valid results, the calculations described previously must be performed using the proper values of D_x and M_m. If changes in D_x and M_m caused by thermal spikes are neglected the calculated results will, of course, be in error.

REFERENCES

1. Shen, C.H., and Springer, G.S., Moisture Absorption and Desorption of Composite Materials, J. of Composite Materials, Vol. 10, No. 1, Jan. 1976, pp. 2-20.

2. Augl, J.M., and Trabocco, R., Environmental Degradation Studies on Carbon Fiber Reinforced Epoxies, Presented at the "Workshop on Durability of Composite Materials," held on September 30-October 2, 1975 at the Battelle Memorial Institute, Columbus, Ohio.

3. Jost, W., Diffusion in Solids, Liquids, and Gases, Academic Press (1960).

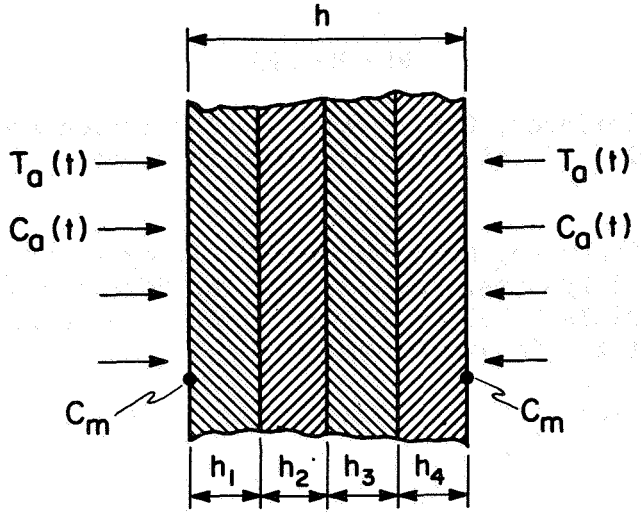

Figure 1.- Illustration of problem.

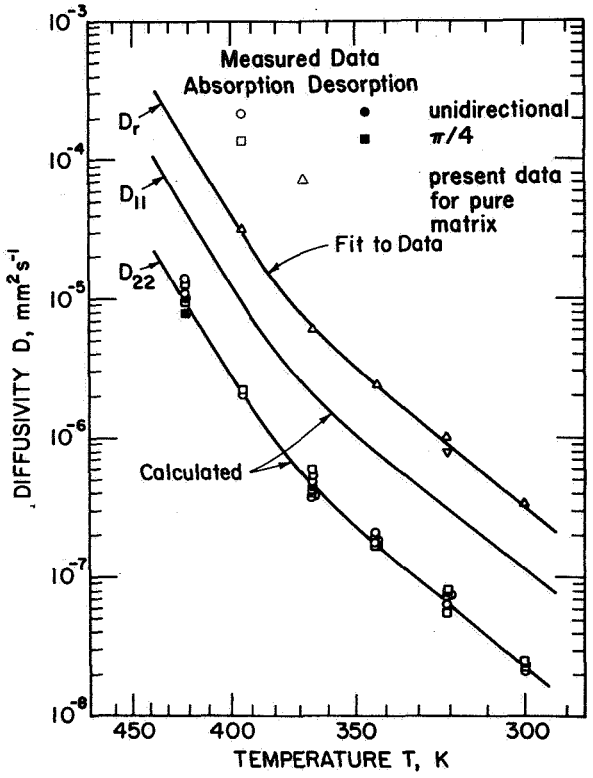

Figure 2.- Matrix diffusivity D_r, transverse diffusivity D_{22}, and longitudinal diffusivity D_{11} of Graphite T-300 and Fiberite 1034 composites. (D_{11} and D_{22} are for $V_f = 0.68$ and $\alpha = 90^o$.)

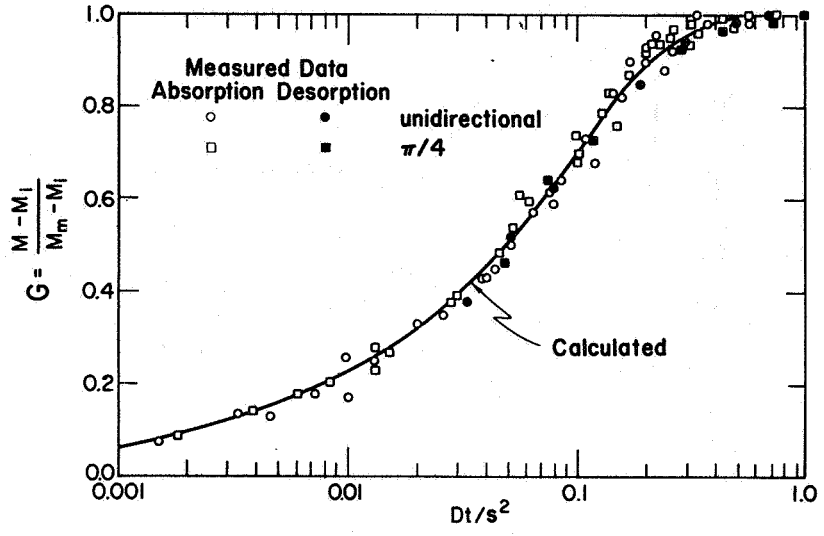

Figure 3.- Comparison of calculated (eq. (14)) and measured G values for unidirectional and π/4 Graphite T-300 and Fiberite 1034 composites (V_f = 0.68 and α = 90°).

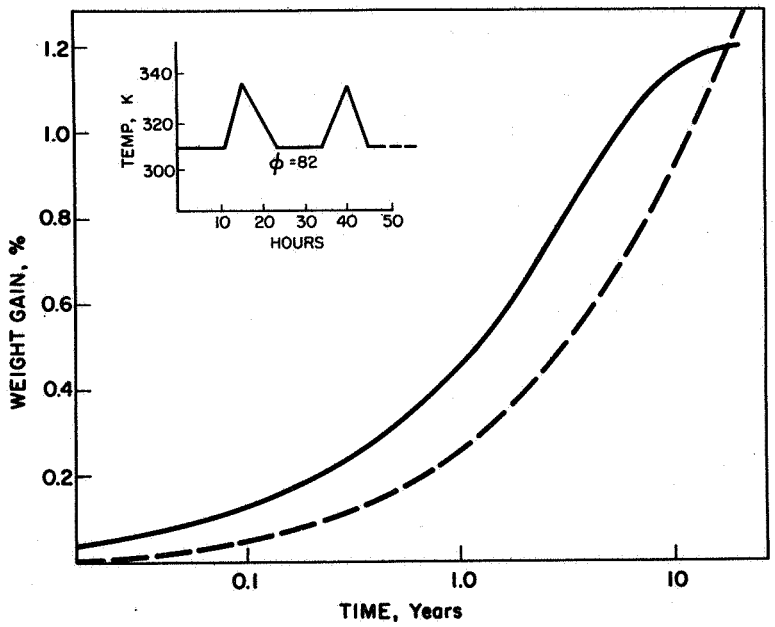

Figure 4.- Weight gain of a 12-mm-thick graphite-epoxy composite. Solid line was calculated for the time varying environment shown. Dotted line was calculated assuming a constant temperature (290 K), constant humidity (82%) environment.

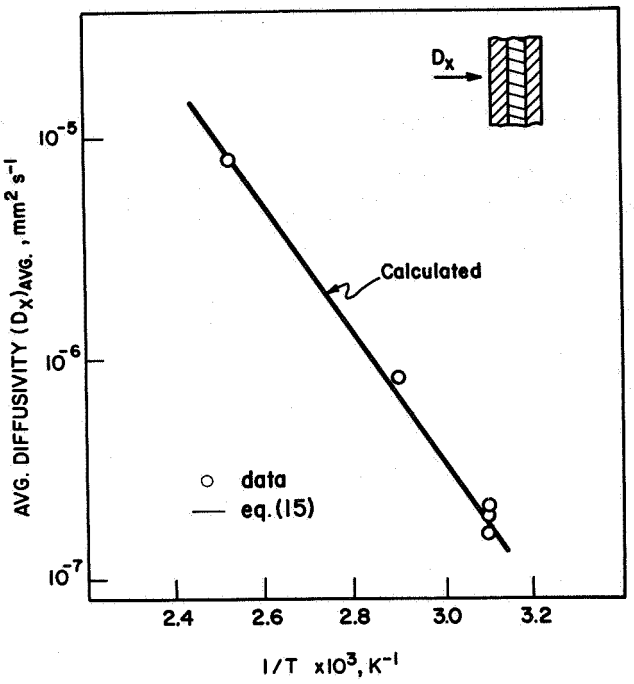

Figure 5.- Average diffusivity as a function of temperature for a 12-mm-thick, layered, graphite-epoxy (48 layers) and boron-epoxy composite (48 layers).

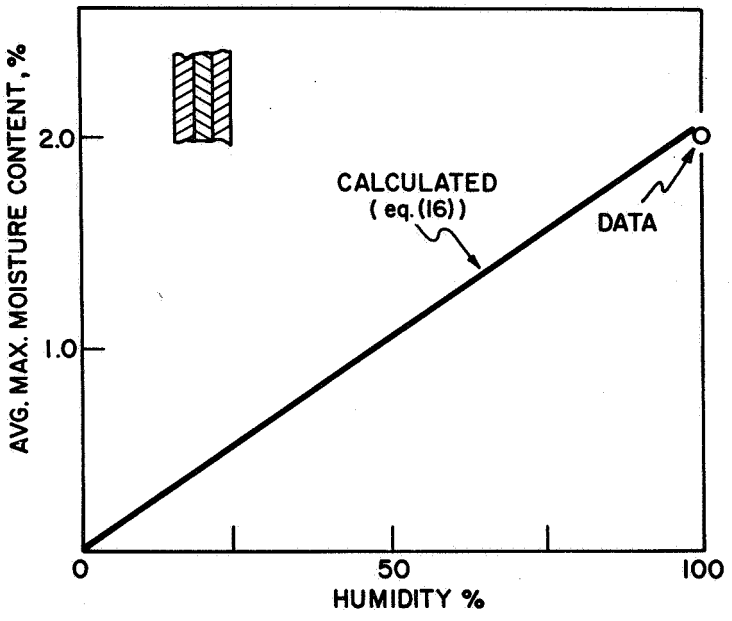

Figure 6.- Average maximum moisture content for a 12-mm-thick, layered, graphite-epoxy (48 layers) and boron-epoxy composite (48 layers).

A HIGH ORDER THEORY FOR UNIFORM AND LAMINATED PLATES

King H. Lo
Washington University

Richard M. Christensen and Edward M. Wu
University of California, Lawrence Livermore Laboratory

SUMMARY

A theory of plate deformation is derived herein which accounts for the effects of transverse shear deformation, transverse normal strain, and a nonlinear distribution of the in-plane displacements with respect to the thickness coordinate. The theory is compared with lower order plate theories through application to a particular problem involving a plate acted upon by a sinusoidal surface pressure. Comparison is also made with exact elasticity solution of this problem. It is found that when the ratio of the characteristic length of the load pattern to the plate thickness is of the order of unity, lower order theories are inadequate and the present high order theory is required to give meaningful results.

Application of the present plate theory to laminated composites is illustrated. Results are given for the bending of symmetric cross-ply and angle-ply laminates. Comparison with exact elasticity solutions indicates that the present plate theory is sufficiently accurate for predicting the behavior of thick laminates.

INTRODUCTION

The development and application of the classical plate theory is one of the achievements of modern engineering. It is continuously being applied to new problems to gain new and needed design information. Despite its successes, however, the inherent limitations of the classical theory necessitate the development of more refined and higher order plate theories for problems where the classical theory is inadequate to describe the behavior of the plates. Such problems concern plates with cutouts, contact problems involving plates, and laminated plates. The present paper concerns the derivation, evaluation, and application of a particular high order theory of plate behavior.

Before describing the present theory, a brief review of some of the developments in the generalization of classical plate theory is in order. Reissner (ref. 1 and ref. 2) obtains a consistent theory which incorporates the effects of transverse shear deformation and transverse normal stress through appropriately assumed stress distributions. The derivation given by Reissner results in a displacement field of the form

$$u = u^{\circ}(x,y) + z\psi_x(x,y),\ v = v^{\circ}(x,y) + z\psi_y(x,y),\ w = w^{\circ}(x,y) \tag{1}$$

where z is the coordinate normal to the middle plane of the plate and ψ_x, ψ_y, and w° are weighted displacement averages. At the same level of approximation Mindlin (ref. 3) employs kinematic assumptions of the form of equation (1), and without introducing corresponding stress distribution assumptions, obtained the governing equations from a direct method. A correction factor is introduced into the shear stress resultants to account for the nonuniform shear stress distributions through the thickness of the plate. The value of the correction factor is evaluated by comparison with an exact elasticity solution.

The next higher order plate theory involves an assumed displacement field of the form

$$u = u^{\circ}(x,y) + z\psi_x(x,y),\ v = v^{\circ}(x,y) + z\psi_y(x,y)$$
$$w = w^{\circ}x,y) + z\psi_z(x,y) + z^2\zeta_z(x,y) \tag{2}$$

which includes the effect of transverse normal strain. Displacement assumptions of the form of equation (2) along with the corresponding stress distribution assumptions has been used by Essenburg (ref. 4) to derive a one-dimensional plate theory. In the context of contact problems, Essenburg (ref. 4) demonstrates the utility and advantages of the theory based upon equation (2) over lower order theories.

Many other high order plate theories that have recently been proposed mainly deal with laminated composite plates. Correction factors are introduced in these theories as in reference 3 to improve the accuracy of the predicted plate behavior. A typical high order laminated plate theory is that given by Nelson and Lorch (ref. 5) with the following assumed displacement field

$$u = u^{\circ}(x,y) + z\psi_x(x,y) + z^2\zeta_x(x,y)$$
$$v = v^{\circ}(x,y) + z\psi_y(x,y) + z^2\zeta_y(x,y)$$
$$w = w^{\circ}(x,y) + z\psi_z(x,y) + z^2\zeta_z(x,y) \tag{3}$$

However, for laminated plates it can be shown that the inclusion of the quadratic terms in the in-plane displacements does not necessarily provide a significant improvement over the lower level theory as that represented by equation (2). Moreover, the use of a large number of correction factors made the application of the plate theory a lot more complicated.

The theory to be presented here is based on the following assumed displacement field:

$$u = u^{\circ}(x,y) + z\psi_x(x,y) + z^2\zeta_x(x,y) + z^3\phi_x(x,y)$$

$$v = v^{\circ}(x,y) + z\psi_y(x,y) + z^2\zeta_y(x,y) + z^3\phi_y(x,y)$$

$$w = w^{\circ}(x,y) + z\psi_z(x,y) + z^2\zeta_z(x,y) \qquad (4)$$

which obviously is of higher order than the theories mentioned previously. The level of truncation in equation (4) is consistent in the sense that the transverse shear stresses due to in-plane displacements u and v are of the same order in z as that determined by the transverse displacement w. The accuracy of this theory in comparison with lower order theories will be assessed by direct comparison with an exact solution from the theory of elasticity. It will be shown that equation (4) gives a far more accurate description of plate deformation behavior under short wave-length conditions than do lower order plate theories. Application of the theory to composite laminates indicates that the present plate theory is sufficiently accurate for predicting the behavior of laminated plates.

SYMBOLS

x,y,z	coordinates of the plate
u,v,w	displacements in the x,y, and z directions, respectively
ψ,ζ,ϕ	displacement coefficients
$^{\circ}$	superscript for quantities in the middle plane of the plate
$M,\overline{M},N,P,$ Q,R,S	Stress resultants
l,m,n,q	equivalent surface tractions
σ,τ	normal and shear stress components
h	thickness of the plate
n,t	normal and tangential directions
q_o	amplitude of surface traction
L	characteristic dimension of the load pattern
C_{ij}	stiffness coefficients
$\overline{w}$	non-dimensional mid-plane deflection

HIGH ORDER PLATE THEORY

Plate theories can be developed by expanding the displacement components in power series of the coordinate normal to the middle plane of the plate. In principle, theories developed by this means can be made as accurate as desired simply by including a sufficient number of terms. In practice, however, a point of diminishing returns is reached whereby the complexity of the resulting theories becomes too great. We here seek the minimum number of terms which include the effects of the transverse shear deformation, transverse normal strain, and warpage of the cross section. Thus the displacement components are taken in the form of equation (4).

The principle of stationary potential energy is used to derive the following governing equilibrium equations and boundary conditions for the present plate theory

$$
\begin{aligned}
&N_{x,x} + N_{xy,y} + q_x = 0;\ N_{y,y} + N_{xy,x} + q_y = 0 \\
&Q_{x,x} + Q_{y,y} + q = 0; \\
&M_{x,x} + M_{xy,y} - Q_x + m_x = 0;\ M_{y,y} + M_{xy,x} - Q_y + m_y = 0 \\
&R_{x,x} + R_{y,y} - N_z + m = 0; \\
&P_{x,x} + P_{xy,y} - 2R_x + n_x = 0;\ P_{y,y} + P_{xy,x} - 2R_y + n_y = 0 \\
&S_{x,x} + S_{y,y} - 2M_z + n = 0; \\
&\bar{M}_{x,x} + \bar{M}_{xy,y} - 3S_x + \ell_x = 0;\ \bar{M}_{y,y} + \bar{M}_{xy,x} - 3S_y + \ell_y = 0
\end{aligned}
\tag{5}
$$

where the stress resultants are defined by

$$
\begin{bmatrix} N_x & N_y & N_z & N_{xy} & Q_x & Q_y \\ \bar{M}_x & \bar{M}_y & \bar{M}_z & \bar{M}_{xy} & R_x & R_y \end{bmatrix} = \int_{-h/2}^{h/2} \begin{Bmatrix} 1 \\ z \end{Bmatrix} [\sigma_x \sigma_y \sigma_z \tau_{xy} \tau_{xz} \tau_{yz}]\, dz \tag{6}
$$

$$
\begin{bmatrix} P_x & P_y & P_{xy} \\ \bar{M}_x & \bar{M}_y & \bar{M}_{xy} \end{bmatrix} = \int_{-h/2}^{h/2} \begin{Bmatrix} z^2 \\ z^3 \end{Bmatrix} [\sigma_x \sigma_y \tau_{xy}]\, dz \tag{7}
$$

and

$$
[S_x \ S_y] = \int_{-h/2}^{h/2} z^2 [\tau_{xz} \tau_{yz}]\, dz \tag{8}
$$

with

$$[q_x\ n_x] = [\tau_{xz}(h/2)-\tau_{xz}(-h/2)][1\ h^2/4]$$

$$[q_y\ n_y] = [\tau_{yz}(h/2)-\tau_{yz}(-h/2)][1\ h^2/4]$$

$$[m_x\ \ell_x] = [\tau_{xz}(h/2)+\tau_{xz}(-h/2)][h/2\ h^3/8]$$

$$[m_y\ \ell_y] = [\tau_{yz}(h/2)+\tau_{yz}(-h/2)][h/2\ h^3/8]$$

$$[q\ \ n] = [\sigma_z(h/2)-\sigma_z(-h/2)][1\ h^2/4]$$

$$m = [\sigma_z(h/2)+\sigma_z(-h/2)]h/2 \tag{9}$$

Finally, the boundary conditions along the edge of the plate require that one member of each of the following eleven products must be prescribed:

$$N_n u_n^\circ,\ N_{nt} u_t^\circ,\ M_n \psi_n, M_{nt}\psi_t, P_n \zeta_n, P_{nt}\zeta_t,$$

$$\overline{M}_n \phi_n, \overline{M}_{nt}\phi_t, Q_n w^\circ, R_n \psi_z \text{ and } S_n \zeta_z \tag{10}$$

where n and t are the directions normal and tangential to the edge of the plate.

When expressed in terms of displacement coefficients, equation (5) comprises a set of eleven coupled second order partial differential equations which govern the behavior of the present plate theory. They can be applied to both homogeneous isotropic as well as anisotropic laminated plates.

EVALUATION OF PLATE THEORY

The present high order theory can be critically assessed by comparing the solutions for a particular problem with the corresponding exact elasticity solutions. The problem of interest here is that of the deformation of an infinite homogeneous isotropic plate of thickness h subjected to a pressure on the top surface z = h/2 of the form

$$\sigma_z = q_o \sin \frac{\pi x}{L} \tag{11}$$

with all other surface tractions vanishing identically. Obviously the solutions for the generalized displacement functions would involve terms proportional to $\sin(\pi x/L)$ and $\cos(\pi x/L)$. Due to limitation on the length of this paper, details of the solutions will not be given here.

The stresses and displacements obtained by the present plate theory are compared with the exact elasticity solutions (ref. 6). Comparisons are also made with the solutions obtained from other lower order approximate plate theories.

Figure 1 shows the maximum deflections of the middle plane of the plate according to various plate theories. It is seen that for values of h/L (i.e. ratio of thickness of plate to characteristic length of the loading pattern) equal to 1.5 the deviations between the approximate theories and the exact results are substantial, and the deviations continue to increase with increasing values of h/L. The present high order theory can be seen to give results closest to the exact solutions.

The flexural stress distributions across the thickness of the plate are shown in figure 2 for h/L = 1.0. All approximate theories give the same linear stress distribution with the exception of the present high order theory. Considering the complex shape of the exact solution stress distribution, the high order theory can be seen to provide a more effective model of plate deformation. In addition, figure 2 reveals the essential presence of the z^3 terms in the displacement field. Comparison of the results given in figure 2 with those given in figure 1 shows that stress distribution is a more sensitive measure of the accuracy of plate theories than is displacement distribution.

APPLICATION TO LAMINATED PLATES

The present theory offers a ready extension to laminated plate problems where the classical plate theory is inadequate for predicting the nonlinear stress and displacement distributions of these laminated structures. The constitutive relations for any layer of the laminate are of the form

$$\begin{bmatrix} \sigma_x \\ \sigma_y \\ \sigma_z \\ \tau_{xy} \end{bmatrix} = \begin{bmatrix} C_{11} & C_{12} & C_{13} & C_{16} \\ C_{12} & C_{22} & C_{23} & C_{26} \\ C_{13} & C_{23} & C_{33} & C_{36} \\ C_{16} & C_{26} & C_{36} & C_{66} \end{bmatrix} \begin{bmatrix} \varepsilon_x \\ \varepsilon_y \\ \varepsilon_z \\ \gamma_{xy} \end{bmatrix} \tag{12}$$

$$\begin{bmatrix} \tau_{yz} \\ \tau_{xz} \end{bmatrix} = \begin{bmatrix} C_{44} & C_{45} \\ C_{45} & C_{55} \end{bmatrix} = \begin{bmatrix} \gamma_{yz} \\ \gamma_{xz} \end{bmatrix} \tag{13}$$

where C_{ij} are the components of the anisotropic stiffness matrix. With the assumed displacement field as given by equation (4), no shear correction factors are needed to relate the transverse components of stress and strain as in other lower order laminated plate theories.

The degree of accuracy of the resulting high order laminated plate model is assessed by comparing the solutions for angle-ply and cross-ply laminates subjected to sinusoidal surface loadings as given by equation (11) with the corresponding exact elasticity solutions.

Angle-ply and Cross-ply Laminates

Numerical results of flexural stress distributions are given in figure 3 for a $[+30°, -30°]_s$ angle-ply laminate and in figure 4 for a $[0°, 90°]_s$ cross-ply laminate. Typical values of stiffness coefficients for high modulus graphite/epoxy composites as given in reference 7 are used.

For the angle-ply laminate, the agreement with exact elasticity solutions (ref. 7) is exceptionally good in the regions of high values of flexural stresses. As the interface between different layers is approached, the stresses in the +30° layer are slightly different from that given by exact elasticity solutions. However, such slight discrepancies are immaterial, especially in the regions of low values of stresses.

The cross-ply laminate serves as a more critical test of the plate theory. As in the case of angle-ply laminate, close agreement of the numerical results with exact elasticity solutions (ref. 8) is again obtained. The relatively large discrepancies in the values of the flexural stresses at the interface between different layers are due to the high discontinuity in the values of the stiffness coefficients across the interface of different layers. As before, such discrepancies occur in the regions of low values of flexural stresses where accurate predictions of the values of the stresses are immaterial.

CONCLUDING REMARKS

By comparing the results obtained with the exact elasticity solutions, the relative accuracy of various approximate theories, including the one presented herein, has been studied. It is obvious that the present high order theory is a much more accurate approximation of the behavior of plates. Due to the high order of terms involved, it is of course not convenient to use. However, for problems with disturbing features, such as holes, cutouts and sub-surface cracks with a characteristic length of the order of the thickness of the plate, a theory at least of the order of the one presented here would be required to properly model the effects of the transverse stress and strain components of the plate.

In addition, the present high order theory has been shown to be sufficiently accurate for predicting the behavior of thick laminates. The use of correction factors to improve the accuracy of the approximated plate behavior is unnecessary.

REFERENCES

1. Reissner, E.: On the Theory of Bending of Elastic Plates. J. Math. Phys., Vol. 23, 1944, pages 184-191.

2. Reissner, E.: The Effects of Transverse Shear Deformation on the Bending of Elastic Plates. J. Appl. Mech., Vol. 12, No. 2, Trans. ASME, Vol. 67, June 1945, pages 69-77.

3. Mindlin, R. D.: Influence of Rotatory Inertia and Shear on Flexural Motions of Isotropic, Elastic Plates. J. Appl. Mech., Vol. 18, No. 1, Trans. ASME, Vol. 73, Mar. 1951, pages 31-38.

4. Essenburg, F.: On the Significance of the Inclusion of the Effect of Transverse Normal Strain in Problems Involving Beams with Surface Constraints. J. Appl. Mech., Vol. 42, Mar. 1975, pages 127-132.

5. Nelson, R. B., and Lorch, D. R.: A Refined Theory of Laminated Orthotropic Plates. J. Appl. Mech., Vol. 41, June 1974, pages 471-476.

6. Little, R. W.: Elasticity. Prentice-Hall, Inc., 1973, pp. 109-112.

7. Pagano, N. J.: Influence of Shear Coupling in Cylindrical Bending of Anisotropic Laminates. J. Comp. Mats., Vol. 4, July 1970, pages 330-343.

8. Pagano, N. J.: Exact Solutions for Composite Laminate in Cylindrical Bending. J. Comp. Mats., Vol. 3, July 1969, pages 398-411.

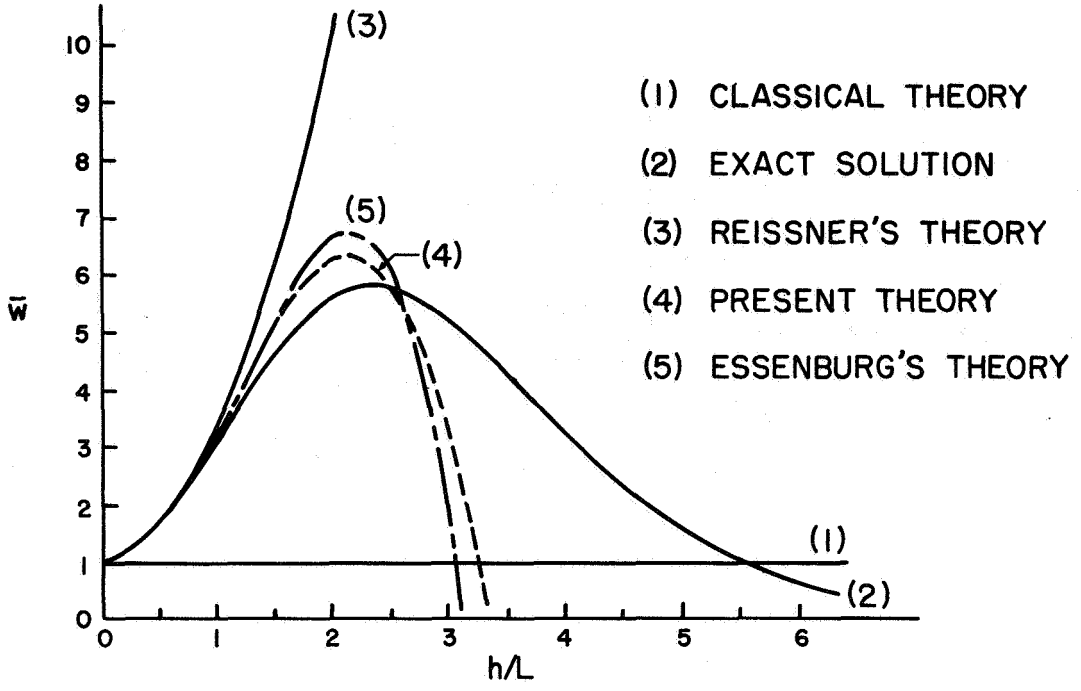

Figure 1.- Mid-plane deflections for a homogeneous isotropic plate.

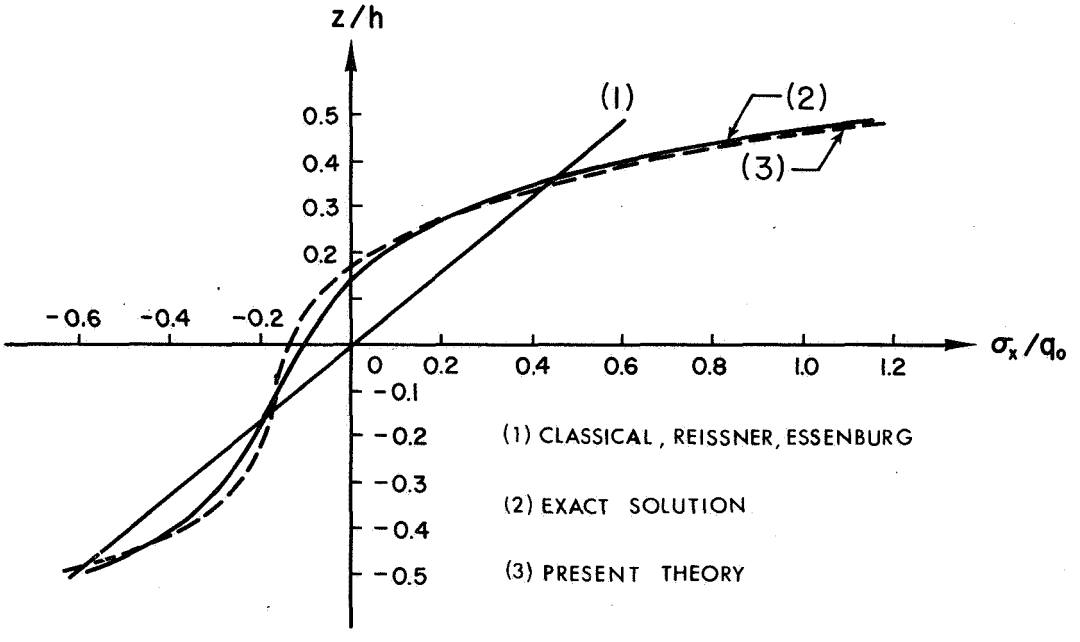

Figure 2.- Flexural stress distributions for a homogeneous isotropic plate at L/h = 1.0.

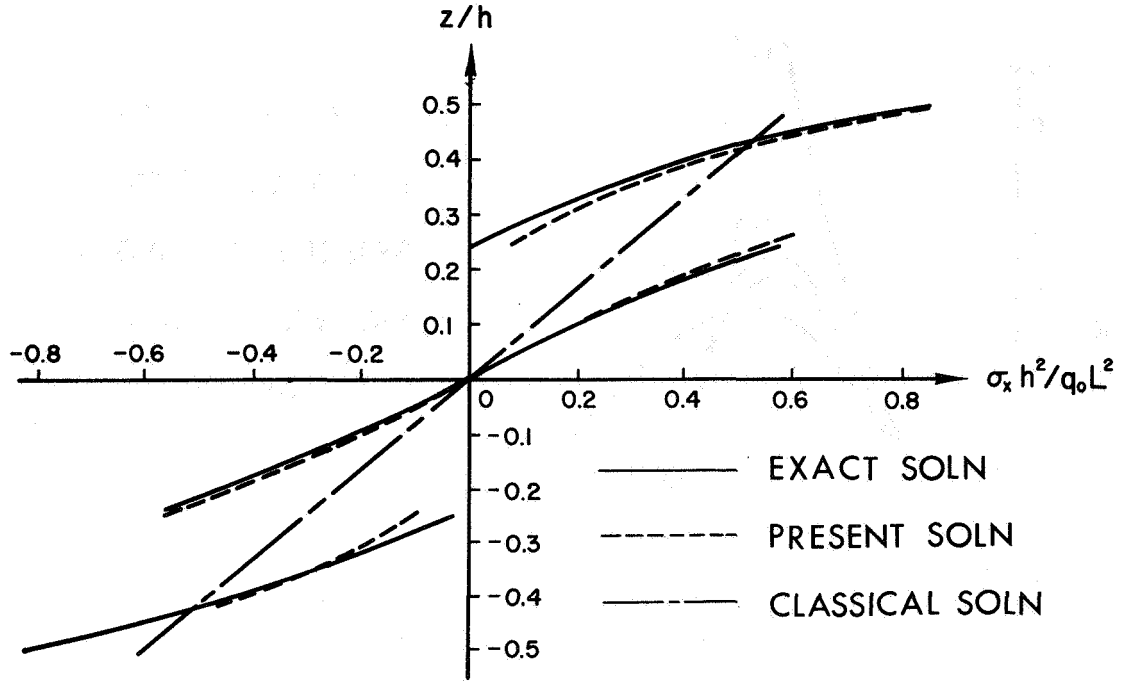

Figure 3.- Flexural stress distributions for a $[+30^o, -30^o]_s$ angle-ply laminate at L/h = 4.0.

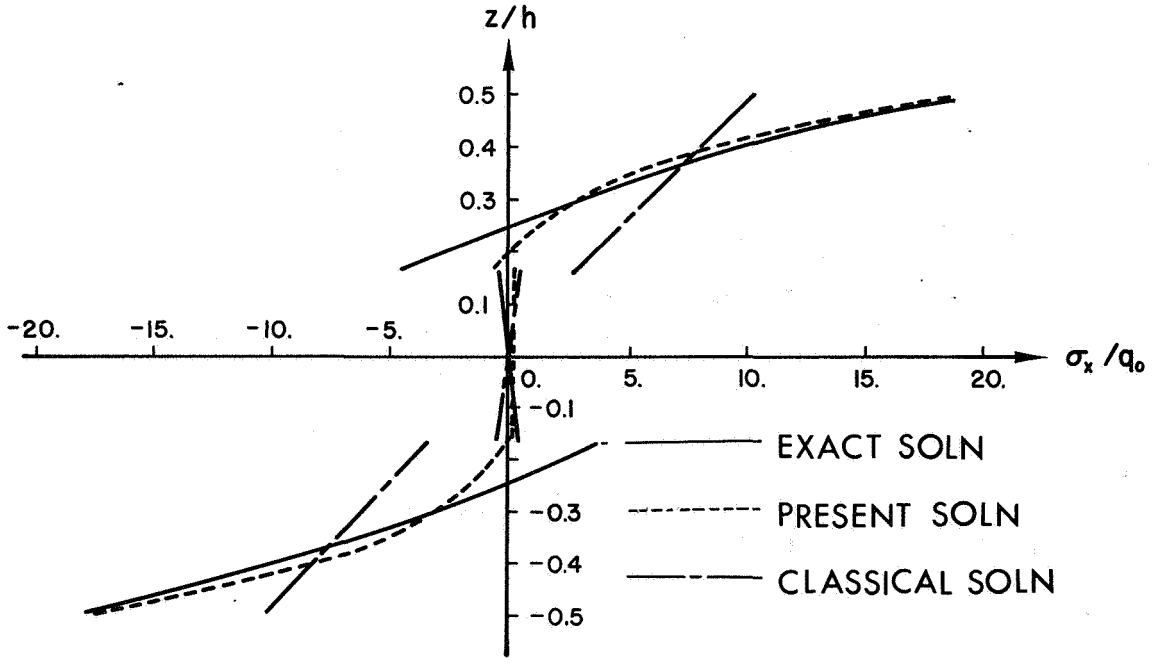

Figure 4.- Flexural stress distributions for a $[0^o, 90^o]_s$ cross-ply laminate at L/h = 4.0.

STOCHASTIC MODELS FOR THE TENSILE STRENGTH, FATIGUE AND STRESS-RUPTURE OF FIBER BUNDLES

S. Leigh Phoenix
Cornell University

SUMMARY

An overview is presented of recent theoretical developments concerning the study of the tensile strength and time-to-failure of fiber bundles under a variety of loadings. The time-to-failure of a single fiber is modeled as a functional of the fiber load history and reasonable forms for this functional are proposed. Earlier models by Daniels and Coleman are shown to be special cases of the proposed model and apparent disparities in their behavior are discussed. Techniques are presented for determining analytically the asymptotic distributions of the tensile strength and time-to-failure for bundles of a large number of fibers. For smaller bundles, exact results are far too cumbersome to be of use so that efficient Monte Carlo simulation procedures are proposed. Using these techniques we consider an example of practical importance and conclusions are drawn regarding the fatigue behavior of cables and other fibrous structures.

INTRODUCTION

Consider a bundle of n parallel fibers to which is applied a nonnegative time-dependent load program $L_s(t)$. As time passes, fibers fail in a random manner that depends on their individual load histories. A fiber supports no load after failing so that the surviving fibers at any time t must share the load according to a specified load sharing rule. We let $T_1,\ldots,T_n$ denote the failure times of the n individual fibers respectively and let $T_{[1]} \leq \ldots \leq T_{[n]}$ be these failure times arranged in increasing order. The time-to-failure of the bundle is then $T_{[n]}$, the failure time of the last surviving fiber. The problem is to determine the probabilistic characteristics of the time-to-bundle failure under reasonable assumptions on single fiber failure, on the load sharing rule, and on the load program $L_s(t)$.

In this paper we will discuss recent theoretical developments regarding the study of this problem. In particular, we will discuss techniques for determining the asymptotic distribution of $T_{[n]}$ when n grows large. For a wide variety of cases $T_{[n]}$ is found to be asymptotically normally distributed. For small n exact results are too cumbersome to be useful. However, efficient Monte Carlo simulation techniques have been developed for use when n is

moderate. We will discuss these techniques briefly and give some results. It will be demonstrated that under reasonable assumptions regarding single fiber behavior, the mean lifetime of a bundle is diminished considerably relative to that of a single fiber under static and dynamic fatigue load programs which are comparable on a load per fiber basis. However, a limit on this reduction is approached as n grows large. But by reducing the bundle load a moderate amount the lost lifetime can be restored. On the other hand, the variability in the time-to-failure of the bundle is reducible simply by increasing the number of fibers. Otherwise the behavior of a large bundle is remarkably similar to that of a single fiber under load programs of engineering significance.

ASSUMPTIONS AND EARLIER ANALYSIS

Assumptions on loading. We naturally ask how the probabilistic characteristics of the bundle time-to-failure compare with those of a single fiber. A fair comparison is made when the load per fiber in the bundle is the same as the total load on the single fiber. Hence we will speak in terms of the nominal fiber load program $L(t) = L_s(t)/n$, though we will often call $L(t)$ simply the load program. Now the actual loads on the fibers of the bundle will generally differ from $L(t)$. For example, the load-strain rules for the fiber may vary from fiber to fiber as a result of say random variations in stiffness, existence of random fiber slack, or mixing of fiber types. Under such conditions results have been obtained for the strength distribution of classic fiber bundles where the strength of each fiber is random but remains fixed in time. (See references 1 to 3 for an extensive treatment). Unfortunately, for the time-dependent problem being considered here, results are available only under the equal load sharing rule for which the surviving fibers at any time t must share the load equally. Here we proceed under the equal load sharing rule so that each fiber of the bundle is thereby subjected to the load

$$L_n(t) = \begin{cases} L(t)/(1-i/n) & \text{for } T_{[i]} \leq t < T_{[i+1]},\ i=0,\ldots,n-1 \\ \\ 0 & \text{for } T_{[n]} \leq t, \end{cases} \tag{1}$$

up to its time of failure, where we set $T_{[0]} \equiv 0$. We call $L_n(t)$ the actual fiber load program. Three particular forms of the load program $L(t)$ are of practical interest. The constant load program

$$L_1(t) = L,\ t \geq 0 \tag{2}$$

where L is a positive constant, is appropriate for studying stress-rupture or static fatigue behavior. The linearly increasing load program

$$L_2(t) = L_0 t, \quad t \geq 0 \tag{3}$$

where the nonnegative constant L_0 is the loading rate, is of interest in considering short-term tensile strength behavior. In dymanic fatigue situations we consider the periodic load program

$$L_3(t) = L_\nu(t-mb), \quad t \geq 0 \tag{4}$$

where the positive constant ν is the frequency of repetition, $b = 1/\nu$ is the period and m is the number of complete cycles that has occurred in the time interval $[0,t]$.

Assumptions on single fiber behavior. We assume that the fibers are sampled independently from a common source which imparts random physical properties to them. Of these properties we are interested in the influence of fiber load history on the fiber time to failure. We assume, then, that a single fiber subjected to the known load history $L(t)$, has a random failure time T with cumulative distribution function (c.d.f.) of the form

$$F(t|L) = 1-\exp\{-\Omega(t;L)\} \tag{5}$$

where $\Omega(t;L)$ is a non-anticipating (history-dependent) functional of $L(t)$ and is non-decreasing in t. We call $\Omega(t;L)$ the fiber hazard functional and assume it to be known for all fiber load histories L that are possible outcomes of L_n. In order to derive meaningful results we restrict our attention to the special fiber hazard functional

$$\Omega(t;L) = \sup\{\Psi[L(\tau), \int_0^\tau \kappa[L(s)]ds]; \ 0 \leq \tau \leq t\} \tag{6}$$

where $\kappa[x]$, $x \geq 0$ is a nonnegative increasing unbounded and continuous function, $\Psi(x,y)$ is a strictly increasing unbounded continuous function of both $x \geq 0$ and $y \geq 0$ for which $\Psi(0,0) = 0$. (Here $\sup\{f(\tau), 0 \leq \tau \leq t\}$ is essentially the maximum value the function $f(\tau)$ achieves in the time interval $[0,t]$. Also a function is increasing (decreasing) if it is nondecreasing (nonincreasing) in its argument). If $L(t)$ is increasing we may drop the sup in equation (6) and put $\tau = t$. In solving specific cases further assumptions on L,ψ and κ will generally be necessary.

Earlier analysis. Previous probabilistic models of the tensile strength and time-to-failure of fiber bundles have been developed under restricted versions of equation (6). In the classic (static) fiber bundle strength problem originally studied by Daniels (ref. 4) and later generalized by Phoenix and Taylor and others (refs. 1,2,3,5), time is not explicitly involved. Specifically the tensile strengths $\zeta_1,\ldots,\zeta_n$ of the n individual fibers are assumed to be fixed in time and to be independent identically distributed (i.i.d.) random variables with common c.d.f. $F_s(x) = 1-\exp\{-\Psi_s(x)\}$, $x \geq 0$ where $\Psi_s(x)$ is a strictly increasing and unbounded function with $\Psi_s(0) = 0$.

It is easily seen that if $\zeta_{[1]} \leq \ldots \leq \zeta_{[n]}$ are $\zeta_1,\ldots,\zeta_n$ arranged in increasing order then the bundle strength Q_n^* is given by

$$Q_n^* = \max\{\zeta_{[1]}, \frac{n-1}{n}\zeta_{[2]},\ldots, \frac{2}{n}\zeta_{[n-1]}, \frac{1}{n}\zeta_{[n]}\} \tag{7}$$

and the time-to-failure under $L(t)$ is $T_{[n]} = \inf\{t \geq 0;\ L(t) \geq Q_n^*\}$, that is $T_{[n]}$ is the smallest time for which the load exceeds the bundle strength. The restriction then for this classic problem is that

$$\Psi(x,y) = \Psi_s(x) \tag{8}$$

so that $\Omega(t;L) = \sup\{\Psi_s(L(\tau));\ 0 \leq \tau \leq t\}$.

Most of the earlier analysis on the time-to-failure of fiber bundles was performed by Coleman (refs. 6 to 12) who essentially assumed the hazard functional to be of the form

$$\Omega(t;L) = \Psi_c\{\int_0^t \kappa[L(s)]ds\} \tag{9}$$

where $\Psi_c(x)$ is an increasing, continuous and unbounded function with $\Psi_c(0) = 0$. We call $\Psi_c(x)$ the hazard form. Although Coleman proposed the model of equation (9), only by taking $\Psi_c(x) = x$ was he able to derive the exact or even the asymptotic probability distribution of the bundle failure time $T_{[n]}$ and most of his analysis dealt with this case. Now the assumption that $\Psi_c(x) = x$ simplifies the analysis greatly but unfortunately it is unduly restrictive in light of available experimental data. More recently, asymptotic normality of the time-to-system failure has been demonstrated by the author in reference 13 for a broad variety of useful hazard forms $\Psi_c(x)$, functions $\kappa(x)$ and loadings $L(t)$. Some of these results will be discussed later. The restriction then for Coleman's time-dependent problem is that $\Psi(x,y) = \Psi_c(y)$. Since the integral in equation (9) is automatically increasing in t, the supremum function in equation (6) is not necessary.

Following Coleman we call the function $\kappa(x)$ the breakdown rule. Of particular interest are the exponential breakdown rule

$$\kappa_1(x) = \alpha \exp(\beta x) \tag{10}$$

and the power law breakdown rule

$$\kappa_2(x) = (x/\ell_0)^\rho \tag{11}$$

where α,β,ℓ_0 and ρ are all nonnegative constants. These two rules lead to

the two common formats for presenting fatigue data, namely the load versus log-time format and the log-load versus log-time format, respectively. Also of interest is the Weibull hazard form

$$\Psi_{cw}(x) = x^r \tag{12}$$

since single fibers under the constant load program $L_1(t) = L$ will have the popular Weibull time-to-failure distribution.

Shortcomings of previous models. One might expect that the classic (static) fiber bundle strength model would be a special case of the time-dependent model introduced by Coleman. For the most part this is not the case. For example, consider the application of the linearly increasing load program $L_2(t)$ to both types of bundles. For the classic bundle the observed strength Q_n^* will be independent of the loading rate L_0 but more important, ties are possible among $T_{[1]},\ldots,T_{[n]}$ and in fact the last few fibers are likely to fail together as the bundle collapses. For the Coleman time-dependent model, the bundle strength will depend on the loading rate and the failure times will generally be distinct with $T_{[1]} < \ldots < T_{[n]}$. Hence the last surviving fiber will support the load for a nonzero time. The difficulty is that in the classic case, jumps in $L(t)$ generally result in jumps in $F(t|L)$, whereas in the Coleman time-dependent model $F(t|L)$ is continuous even under jumps in $L(t)$ as can be seen from the hazard functional given by equation (9). The special fiber hazard functional (eq. (6)) of interest in this paper will alleviate these difficulties, and will give us a more realistic model structure.

CURRENT ANALYTICAL APPROACH

The crux of our approach lies in formulating a bundle model whose statistical properties are equivalent to those of the real bundle but whose time-to-failure may be written in terms of n specific i.i.d. random variables. The benefit is that much is known about the structures of the i.i.d. random variables that arise and we may draw on this knowledge. Of course we must prove the statistical equivalence of the models and unfortunately this is not a simple task. We proceed by formulating the equivalent bundle model.

With the i^{th} fiber we associate the exponential random variable V_i and we assume that $V_1,\ldots,V_n$ are i.i.d. with common exponential c.d.f. $H(x) = 1-\exp\{-x\}$, $x \geq 0$. We let $V_{[1]} \leq \ldots \leq V_{[n]}$ be these random variables arranged in increasing order. Now we define

$$T'_{[i]} = \inf\{t \geq T'_{[i-1]};\ \Omega(t;\ L_{n,i-1}) \geq V_{[i]}\} \tag{13}$$

where $T'_{[0]} \equiv 0$, $L_{n,0}(s) = L(s)$, and

$$L_{n,i}(s) = \begin{cases} L(s) & \text{for } 0 \le s < T'_{[1]} \\ L(s)/(1-1/n) & \text{for } T'_{[1]} \le s < T'_{[2]} \\ \cdots & \\ L(s)/(1-i/n) & \text{for } T'_{[i]} \le s \end{cases} \tag{14}$$

for $i=1,\ldots,n$.

Conjecture: Under reasonable assumptions on $L(t)$ and the behavior of the hazard functional $\Omega(t;L)$, the random vectors $(T_{[1]},\ldots,T_{[n]})$ and $(T'_{[1]},\ldots,T'_{[n]})$ have the same probability distribution.

It is easy to show that the conjecture is true for single fibers, that is, when $n=1$. In fact we may permit $L(t)$ to be a random process when $n=1$. Under reasonable assumptions the author has shown the conjecture to be true for Coleman's time-dependent model where $\Omega(t;L)$ is given by equation (9). (See reference 13). There is very little doubt that the conjecture is true in general, however, the proof is not complete as yet. The benefit of verifying the conjecture is that we need only study the random properties of $T'_{[1]},\ldots,T'_{[n]}$. Henceforth we may drop the primes for convenience.

Equations (13) and (14) yield n expressions relating $T_{[1]},\ldots,T_{[n]}$ and $V_{[1]},\ldots,V_{[n]}$. The objective is to express $T_{[n]}$ in terms of $V_{[1]},\ldots,V_{[n]}$. Then by knowing the random properties of $V_{[1]},\ldots,V_{[n]}$ we may determine the random properties of $T_{[n]}$. In general, the inversions are very difficult to perform analytically. Hence we consider some special cases which illustrate the technique and are tractable.

Constant load program and the special hazard functional. For $L(t) = L_1(t) = L$ and $\Omega(t;L)$ given by equation (6) we may rewrite equations (13) and (14) as

$$T_{[i]} = \inf\{t \ge T_{[i-1]};\ \Psi(nL/(n-i+1),\ \kappa[L]T_{[1]} + \kappa[nL/(n-1)][T_{[2]}-T_{[1]}] + \ldots + \kappa[nL/(n-i+1)][t-T_{[i-1]}]) \ge V_{[i]}\} \tag{15}$$

for $i=1,\ldots,n$. We let $y = \Psi^{-1}(x,u)$ be the solution to $\Psi(x,y) = u$ for $u \ge 0$ with $x > 0$ held fixed. By our earlier assumptions $y \ge 0$ and $\Psi^{-1}(x,u)$ is increasing and continuous in u and decreasing and continuous in x. We let

$$W_{[i]} = \Psi^{-1}(nL/(n-i+1),\ V_{[i]}) \tag{16}$$

and define the random process $W_n(y)$ by

$$W_n(y) = \begin{cases} W_{[1]}, & 0 \le y < 1/n \\ W_{[2]}, & 1/n \le y < 2/n \\ \cdots & \\ W_{[n]}, & (n-1)/n \le y \le 1. \end{cases} \tag{17}$$

Observe that while $V_{[1]} \le \ldots \le V_{[n]}$ are ordered $W_{[1]},\ldots,W_{[n]}$ are not necessarily arranged in increasing order so that $W_n(y)$ is not by nature increasing in y. However we require an associated random process

$$W_n^{\#}(y) = \max[0,\ \sup\{W_n(\tau);\ 0 \le \tau \le y\}] \tag{18}$$

for $0 \le y \le 1$, which is increasing in y. Now in view of equation (16) we may rewrite (15) as

$$T_{[i]} = \inf\{t \ge T_{[i-1]};\ \kappa[L]T_{[1]} + \kappa[nL/(n-1)](T_{[2]} - T_{[1]}) + \ldots + \kappa[nL/(n-i+1)](t - T_{[i-1]}) \ge W_{[i]}\} \tag{19}$$

for $i=1,\ldots,n$. By inspecting equations (19) successively we observe that $T_{[1]} > 0$ if and only if $W_{[1]} > 0$ and for $i=2,\ldots,n$ that $T_{[i]} - T_{[i-1]} > 0$ if and only if $W_{[i]} > \max[0, W_{[j]}]$ for all $j=1,\ldots,i-1$. In fact, we may combine equations (19) in view of equations (17) and (18) to yield

$$\begin{aligned} \kappa[L]T_{[1]} &= W_n^{\#}(0) \\ \kappa[nL/(n-1)](T_{[2]} - T_{[1]}) &= W_n^{\#}(1/n) - W_n^{\#}(0) \\ &\cdots \\ \kappa[nL](T_{[n]} - T_{[n-1]}) &= W_n^{\#}\left(\frac{n-1}{n}\right) - W_n^{\#}\left(\frac{n-2}{n}\right). \end{aligned} \tag{20}$$

By successive substitutions we may combine equations (20) to yield an expression which is equivalent to

$$T_{[n]} = -\int_0^1 \frac{d}{dy}\left\{\kappa\left[\frac{L}{1-y}\right]^{-1}\right\} W_n^{\#}(y)\,dy \tag{21}$$

where we have used the fact that $\kappa(x)$ grows unbounded in x. Equation (21) serves as a starting point for determining the probabilistic characteristics of

the bundle time-to-failure $T_{[n]}$ for we have $T_{[n]}$ written as a linear functional of $W_n^{\#}(y)$ which is a random process involving $V_1,\ldots,V_n$ through their ordered values $V_{[1]} \leq \ldots \leq V_{[n]}$.

Although much is known about the probabilistic characteristics of $V_{[1]},\ldots,V_{[n]}$, the relationship between $T_{[n]}$ and $V_{[1]},\ldots,V_{[n]}$ as given by equation (21) is a very complex one. As a result, an expression for the exact probability distribution of $T_{[n]}$ will be far too cumbersome to be of any use whatsoever, for among other difficulties it will involve an n-fold convolution integral (except perhaps in a few unrealistic special cases). On the other hand Monte Carlo simulation of outcomes for $T_{[n]}$ is straightforward. This is because outcomes for $V_{[1]},\ldots,V_{[n]}$ are easily generated and given $V_{[1]},\ldots,V_{[n]}$, L, κ and Ψ the computation of the integral in equation (21) is a simple task. For large n there is the possibility of determining the asymptotic distribution of $T_{[n]}$. Save for a few technical details in the associated proof, this has been done and will be reported on at a later date. We say more on the approach shortly.

For the more restrictive Coleman hazard functional as given by equation (9), we have $W_{[i]} = \Psi_c^{-1}(V_{[i]})$ so we define $W_i = \Psi_c^{-1}(V_i)$. Now since $\Psi_c^{-1}(y)$ is increasing in $y \geq 0$ we find that $W_{[1]} \leq \ldots \leq W_{[n]}$ are $W_1,\ldots,W_n$ arranged in increasing order. Furthermore since $V_1,\ldots,V_n$ are i.i.d. with common c.d.f. $H(x) = 1-\exp\{-x\}$, $x \geq 0$, then it follows that $W_1,\ldots,W_n$ are i.i.d. with common c.d.f.

$$G(w) = 1-\exp\{-\Psi_c(w)\},\ w \geq 0. \tag{22}$$

Hence $W_{[1]} \leq \ldots \leq W_{[n]}$ are a set of order statistics from $G(w)$. Also $W_n(y)$ is nonincreasing so that $W_n^{\#}(y) = W_n(y)$ where $W_n(y)$, $0 \leq y \leq 1$ is now the quantile process associated with $W_{[1]},\ldots,W_{[n]}$. (Quantile processes are receiving considerable attention in the mathematical statistics literature (refs. 14-16) and may well be the most useful vehicle for determining the asymptotic distribution of $T_{[n]}$). Hence in view of equation (17) we may integrate in equation (21) to obtain

$$T_{[n]} = \sum_{i=1}^{n} C_{ni} W_{[i]} \tag{23}$$

where

$$C_{ni} = \kappa(nL/(n-i+1))^{-1} - \kappa(nL/(n-i))^{-1}. \tag{24}$$

Since the bundle time-to-failure $T_{[n]}$ is a linear combination of the order statistics $W_{[1]},\ldots,W_{[n]}$ we may determine the asymptotic distribution of $T_{[n]}$ as n grows large provided that the weighting constants C_{ni} have the appropriate behavior as $n \to \infty$. Indeed if we require the reasonable conditions that $d\{\kappa[L/(1-y)]^{-1}\}/dy$ be bounded and continuous on $[0,1]$ and that the second moment of $G_c(w)$ exist, then we may use Theorems 1 to 3 together with Remark 2 of Stigler (ref. 14) to assert the following theorem.

Let

$$t_b = \int_0^\infty \phi(1-G(y))dy \tag{25}$$

and

$$\sigma_b^2 = \int_0^\infty\int_0^\infty \phi'(1-G(u))\phi'(1-G(v))\Gamma(u,v)dudv \tag{26}$$

where

$$\phi(x) = \kappa(L/x)^{-1} \tag{27}$$

and

$$\Gamma(u,v) = \begin{cases} G(u)[1-G(v)] & \text{for } u \le v \\ G(v)[1-G(u)] & \text{for } v \le u. \end{cases} \tag{28}$$

and $\phi'(y) = d\phi(y)/dy$. Then we have the main theorem.

Theorem 1: As $n \to \infty$ the standardized system failure time

$$T_n = \sqrt{n}\,\{T_{[n]} - t_b\} \tag{29}$$

is asymptotically normally distributed with mean zero and variance σ_b^2.

Later we examine some practical consequences of Theorem 1, but first we comment on our analytical approach for determining asymptotic results for the special hazard functional. Now in reference 13, we have proven Theorem 1 under slightly more restrictive conditions but by using a different approach. We have operated with the empirical c.d.f. of $W_{[1]},\ldots,W_{[n]}$ which is

$$G_n(w) = \begin{cases} 0 & \text{for } 0 \le w < W_{[1]} \\ i/n & \text{for } W_{[i]} \le w < W_{[i+1]},\ i=1,\ldots,n-1 \\ 1 & \text{for } W_{[n]} \le w. \end{cases} \tag{30}$$

Note that the quantile process $W_n(y)$ is the inverse of the empirical c.d.f. $G_n(w)$. For the Coleman hazard functional we could have written $T_{[n]}$ as

$$T_{[n]} = \int_0^{\infty} \kappa[L/(1-G_n(w))]^{-1} dw. \tag{31}$$

Hence $T_{[n]}$ is a *nonlinear* functional of the empirical c.d.f. $G_n(w)$ and from equation (21) with $W_n^{\#}(y) = W_n(y)$ we see that $T_{[n]}$ is also a linear functional of the quantile process $W_n(y)$. Now it is known that under reasonable conditions both the empirical c.d.f. $G_n(w)$ and the quantile process $W_n(y)$ when properly normalized converge in distribution to specific Gaussian processes respectively. By expanding the functionals for $T_{[n]}$ appropriately about $G(w)$ for the empirical c.d.f. and about $G^{-1}(y)$ for the quantile process we may use results in weak convergence theory to obtain the asymptotic normality of $T_{[n]}$ as given by Theorem 1. Now it is believed that a similar approach may be used for the special hazard functional of equation (6) since it turns out that $T_{[n]}$ as given by equation (21), is still a functional of $W_n(y)$ albeit a much more complicated one. We are pursuing this approach currently, and results will be forthcoming.

Time-dependent load programs and the special hazard functional. When the load program $L(t)$ is an arbitrary function of time, it is not possible to arrive at an expression similar to equation (21) except in some special cases where a convenient factorization arises. For example, under the Coleman hazard functional with $\kappa(x)$ taken as the power law breakdown rule (eq. (11)), a convenient factorization arises which results in the replacement of $T_{[n]}$ with $\int_0^{T_{[n]}} L(s)^{\rho} ds$ and L with unity in equation (21). Hence asymptotic normality of $T_{[n]}$ will result in most cases. (For details the reader is referred to reference 13). If, on the other hand, a convenient factorization does not occur, then it appears possible to generate from equations (19) a stochastic differential equation as $n \to \infty$ involving the limiting Gaussian process of the normalized empirical c.d.f. $G_n(w)$ or quantile process $W_n(y)$ and the limit of an empirical process involving $T_{[1]},\ldots,T_{[n]}$. The solution of this stochastic differential equation would yield the asymptotic distribution of $T_{[n]}$. This approach is being pursued and appears to show promise. Otherwise one may resort to Monte Carlo simulation procedures using equations (15) since outcomes for $V_{[1]},\ldots,V_{[n]}$ are easily generated and the calculation of the associated $T_{[1]},\ldots,T_{[n]}$ is straightforward given $\Psi(x,y)$, $L(t)$ and $\kappa(x)$. Some simulation results will be reported on in a future publication.

PRACTICAL RESULTS

Results of engineering significance have been generated to date only for the Coleman hazard functional given by equation (9) with the hazard form $\psi_c(x)$ taken as the Weibull hazard form (equation (12)) and the breakdown rule $\kappa(x)$ taken as either the exponential breakdown rule (equation (10)) or the power law breakdown rule (equation (11)). Even under these restrictions, the resulting model is surprisingly flexible. In fact the single fiber model generates behavioral features which are remarkably consistent with the current probabilistic view of the stress-rupture, fatigue and tensile strength behavior of structural materials. The single fiber model satisfies a probabilistic interpretation of Miner's fatigue rule because of the integral in equation (9). Also, two popular formats for presenting fatigue and stress-rupture data result. The exponential breakdown rule, $\kappa_1(x)$ is associated with the common load versus log-time format and the associated equiprobability of failure curves under the constant (stress-rupture) load program L_1 and fatigue loading L_3 form a set of straight parallel lines whose spacing is governed by the hazard form $\Psi(x)$. The power law breakdown rule $\kappa_2(x)$ on the other hand generates similar behavior except the format is the log-load versus log-time format. The time-to-failure distribution for single fibers under the constant load program L_1 and the Weibull hazard form Ψ_{cw} is the popular Weibull distribution as is the tensile strength distribution under the power law breakdown rule κ_2 and the linearly increasing load program L_2 but with different parameters. We will not expand in any detail on the above statements but rather we summarize a few practically important asymptotic results for the time-to-failure of a bundle of fibers as compared with that of a single fiber. For a thorough discussion we refer the reader to references 13 and 17. We will restrict our attention to results under the power law breakdown rule, the Weibull hazard form, and the constant load program. These results will illustrate typical behavior.

Single fiber results. For a single fiber under the constant load program L_1, the cumulative distribution function of the time-to-failure T is easily found to be

$$F(t|L_1) = 1-\exp\{-[(L/\ell_0)^{\rho}t]^r\},\ t \geq 0 \tag{32}$$

which is the Weibull distribution with scale parameter $(\ell_0/L)^{\rho}$ and shape parameter r. The mean $E[T]$ and coefficient of variation $CV[T] \equiv \sqrt{Var[T]}/E[T]$ of this distribution are respectively

$$E[T] = (\ell_0/L)^{\rho}\Gamma(1+1/r) \tag{33}$$

and

$$CV[T] = \frac{\{\Gamma(1+2/r)-\Gamma(1+1/r)^2\}^{1/2}}{\Gamma(1+1/r)} \tag{34}$$

the latter being independent of ℓ_0 and ρ. Note that if we fix ℓ_0, $\rho > 0$, we find that a graph of log L versus log E[T] forms a straight line with slope $-1/\rho$. In fact the equiprobability of failure curves for $F(t|L_1)$ also form a set of parallel straight lines with slope $-1/\rho$. We alluded to this behavior earlier.

Fiber bundle results. For a fiber bundle under the constant load program L_1 we consider asymptotic results for large n since exact results are not available as we pointed out earlier. For moderate n, Monte Carlo simulation procedures have been used, and we will include some of those results. Using Theorem 1 and performing the appropriate calculations we find that the time-to-bundle failure $T_{[n]}$ is asymptotically normally distributed with mean

$$t_b = (\ell_0/L)^\rho \rho^{-1/r} \Gamma(1+1/r) \tag{35}$$

and variance

$$\sigma_b^2/n = (\rho \ell_0^\rho / L^\rho)^2 K(\rho,r)/n \tag{36}$$

where

$$K(\rho,r) = \{[\rho(\rho-1)]^{-1/r} - \rho^{-2/r}\}\Gamma(1+1/r)^2 - \frac{2\Gamma(2/r)}{[\rho(\rho-1)]^{1/r} r 2^{2/r}} \{\frac{1}{\rho} + \frac{1}{2\rho^2} + \frac{4r-1}{12r\rho^3} + \ldots\}. \tag{37}$$

We have obtained the above asymptotic expansion because the integral in equation (26) cannot be obtained in closed form. Equations (36) and (37) yield the first few terms of an expansion of Coleman's result in reference 8 for the special case $r=1$. Typically $r<2$ and $\rho>20$ so equations (36) and (37) will yield accurate results. The bundle coefficient of variation defined by $CV_b \equiv \sigma_b/(t_b\sqrt{n})$ is

$$CV_b = \rho^{1+1/r} [K(\rho,r)/n]^{1/2} \Gamma(1+1/r)^{-1}. \tag{38}$$

Comparison of bundle and single fiber results. To illustrate the comparison of bundle and single fiber behavior we have constructed a graph (Figure 1) using estimates of the parameters r, ℓ_0 and ρ based on stress-rupture data for epoxy-impregnated Kevlar-49 strands. (See reference 17 for further details). One impregnated strand plays the role of a single fiber in our model. Resin-impregnated Kevlar-49 strands are being used in the construction of high-strength cables and lines and are becoming an important structural material. First we observe that on a log-log scale the graph of the asymptotic mean time-to-bundle failure t_b is virtually parallel to that for the single strand time-to-failure E[T]. However at all stresses the mean lifetime of the large bundle is almost

two orders of magnitude less than that of a single strand. The appropriate quantity for reflecting this loss is the time-to-failure efficiency $E_t \equiv t_b/E[T]$ which in this case is simply $\rho^{-1/r}$. Second if we stress a large bundle to about 90% of that for a single strand, the mean lifetime of the bundle will approximately equal that for the single strand. The load ratio in this case is simply $\rho^{-1/(r\rho)}$. Interestingly, this ratio is numerically close to the bundle strength efficiency obtained under the linearly increasing load program $L_2(t)$. Third we compare the single fiber coefficient of variation $CV[T]$ with CV_b for the bundle. Numerically we have $CV[T] = 1.15$ whereas $CV_b = 5.08n^{-1/2}$. Evidently a fairly large number of strands is necessary to decrease the bundle coefficient of variation relative to that of a single strand.

The question naturally arises as to the applicability of the asymptotic results for bundles of a moderate number of fibers. In Figure 1 we have plotted Monte Carlo simulation estimates of the mean time-to-bundle failure $E[T_{[n]}]$. We see that the asymptotic results are quite accurate in this respect for $n>50$ say. We are currently studying other aspects of the proximity of the asymptotic time-to-failure distribution to the true distribution of $T_{[n]}$ using Monte Carlo simulation techniques, especially in the very important lower tail regions of the distributions.

The behavior just described is believed to be typical though numerical values will vary substantially over the various fiber types. To what extent the bundle time-to-failure character is altered under the special hazard functional is currently under study.

REFERENCES

1. Phoenix, S.L.; and Taylor, H.M.: The Asymptotic Strength Distribution of a General Fiber Bundle. Advances in Appl. Probability, vol. 5, 1973, pp. 200-216.

2. Phoenix, S.L.: Probabilistic Strength Analysis of Fiber Bundle Structures. Fibre Sci. and Tech., vol. 7, 1974, pp. 15-31.

3. Phoenix, S.L.: Probabilistic Inter-Fiber Dependence and the Asymptotic Strength Distribution of Classic Fiber Bundles. International J. Eng. Sci., vol. 13, 1975, pp. 287-304.

4. Daniels, H.E.: The Statistical Theory of Strength of Bundles of Threads I. Proc. Roy. Soc., vol. A183, 1945, pp. 405-435.

5. Suh, M.W.; Bhattacharyya, B.B.; and Grandage A.: On the Distribution and Moments of the Strength of a Bundle of Filaments. J. Appl. Probability, vol. 7, 1970, pp. 712-720.

6. Coleman, B.D.: Statistics and Time Dependence of Mechanical Breakdown in Fibers. J. Appl. Physics, vol. 29, 1958, pp. 968-983.

7. Coleman, B.D.: Time Dependence of Mechanical Breakdown in Bundles of Fibers IV. Infinite Ideal Bundle Under Oscillating Loads. J. Appl. Physics, vol. 29, 1958, pp. 1091-1099.

8. Coleman, B.D.: Time Dependence of Mechanical Breakdown in Bundles of Fibers III. The Power Law Breakdown Rule. Trans. Soc. Rheology, vol. 2, 1958, pp. 195-218.

9. Coleman, B.D.: Time Dependence of Mechanical Breakdown in Bundles of Fibers II. The Infinite Ideal Bundle Under Linearly Increasing Loads. J. Appl. Physics, vol. 28, 1957, pp. 1065-1067.

10. Coleman, B.D.: Time Dependence of Mechanical Breakdown in Bundles of Fibers I. Constant Total Load. J. Appl. Physics, vol. 28, 1957, pp. 1058-1064.

11. Coleman, B.D.: A Stochastic Process Model for Mechanical Breakdown. Trans. Soc. Rheology, vol. 1, 1957, pp. 153-168.

12. Coleman, B.D.: Time Dependence of Mechanical Breakdown Phenomena. J. Appl. Physics, vol. 27, 1956, pp. 862-866.

13. Phoenix, S.L.: The Asymptotic Time to Failure of Mechanical Parallel Element Systems. (Submitted for publication to SIAM J. Appl. Math.)

14. Stigler, S.M.: Linear Functions of Order Statistics with Smooth Weight Functions. The Annals of Statistics, vol. 2, 1974, pp. 676-693.

15. Shorack, G.R.: Functions of Order Statistics. The Annals of Mathematical Statistics, vol. 43, 1972, pp. 412-427.

16. Shorack, G.R.: Convergence of Reduced Empirical and Quantile Processes with Applications to Functions of Order Statistics in the non i.i.d. case. The Annals of Statistics, vol. 1, 1973, pp. 146-152.

17. Phoenix, S.L.: The Tensile Strength and Time to Failure in Fatigue of Mechanical Parallel Member Systems. (Submitted for publication to AIAA J.)

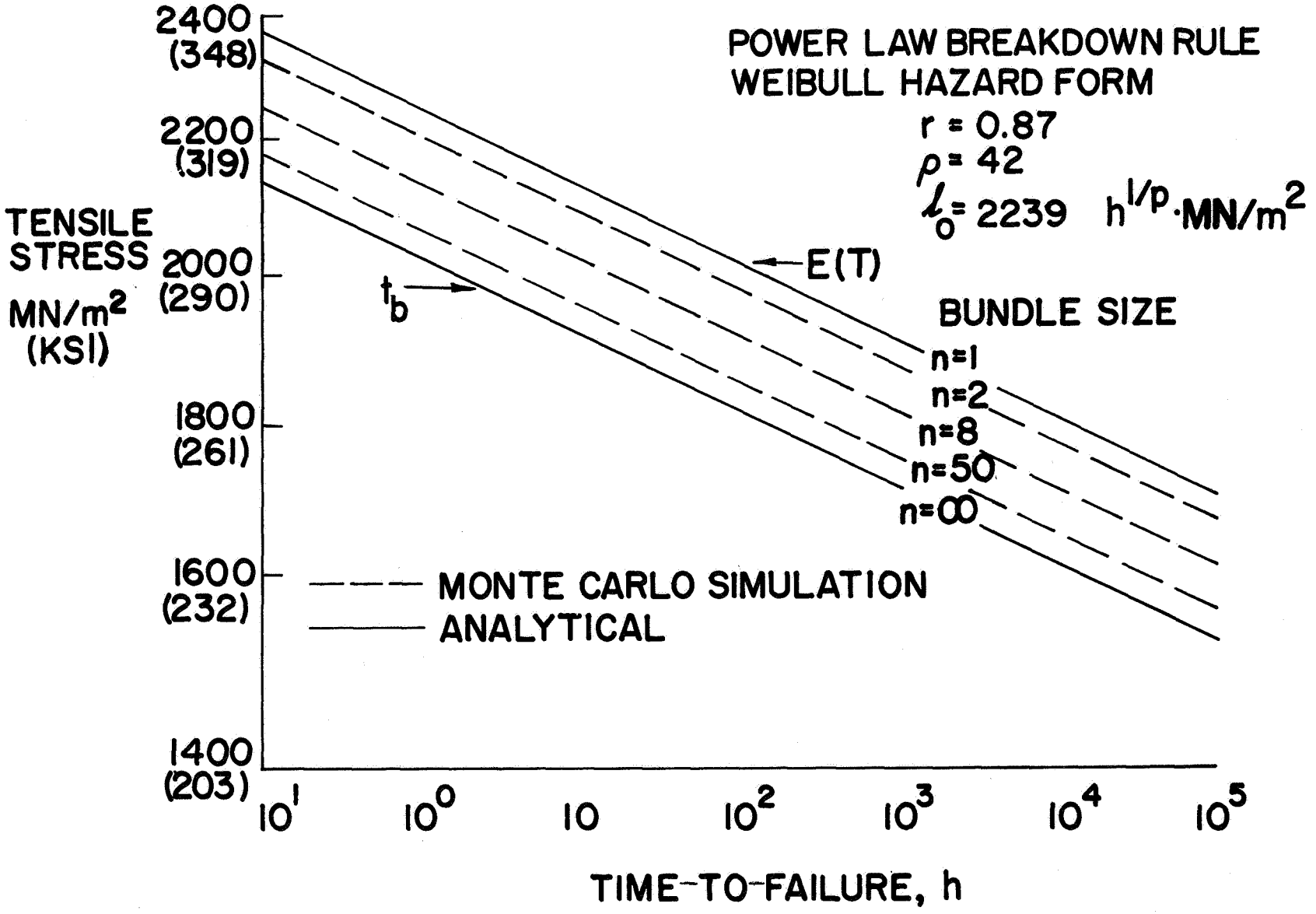

Figure 1.- Bundle time-to-failure in stress rupture.

PROGRESSIVE FAILURE OF NOTCHED COMPOSITE LAMINATES USING FINITE ELEMENTS[1]

Ralph J. Nuismer
University of Utah

Gary E. Brown
United States Air Force Academy
(Formerly University of Utah)

SUMMARY

An incremental, non-linear, finite-element program capable of tracing the damage that occurs in a notched laminated composite, before ultimate failure takes place, is described. The program uses only the properties of the constituent plies to model the progressive failure and to predict the ultimate failure load for the laminate. Computer predictions for the ultimate failure load and failure modes are compared to experimental results for two laminates containing holes and loaded in uniaxial tension. The comparison is quite favorable.

INTRODUCTION

The prediction of the strength of unnotched composite laminates on a macroscopic level has proceeded in a number of directions. For example, one approach has been to use a ply failure criterion, such as the maximum strain or distortional energy criterion, in conjunction with laminated plate theory to predict the failure of the laminate. Although appropriate for predicting first ply failure if one is concerned with the ultimate failure of the laminate, such an approach often results in highly conservative strength estimates because first ply failure usually does not result in the total failure of the laminate. Another approach has been to use a phenomenological failure surface for a laminate (ref. 1). Since this approach does not make use of the known failure characteristics of the constituent plies, however, such a surface must be generated anew for each distinct laminate of a particular material system. An interesting approach that does make use of the individual failure characteristics of the plies, while still accounting for the ultimate failure of the laminate itself through a progressive failure mechanism, is that of Petit and Waddoups (ref. 2). Here, use was made of laminated plate theory and the constitutive relations for the individual plies to predict the stress-strain curve of the laminate in uniaxial tension. This approach was shown to result in reasonable strength predictions for such loadings.

[1]Support from the University of Utah Research Fund for computer time is gratefully acknowledged.

The introduction of through-the-thickness notches in laminates, either by design (e.g., fastener holes) or by accident (e.g., projectile penetration), complicates strength predictions further because of the resulting stress inhomogeneity and biaxiality such notches produce. A relatively simple approach to the prediction of the strength of notched laminates in uniaxial tension has been presented in references 3 and 4. This method has led to satisfactory strength predictions for laminates containing a variety of notch shapes and sizes and has served to provide a simple explanation for the observed hole size effect. However, this approach does not take into account progressive damage of the laminate and the resulting stress redistribution that can occur due to such damage. Furthermore, it does not take into account stress interaction effects on failure and assumes the direction of failure to be known. Where these considerations are of importance, therefore, such as in the case of non-proportional biaxial loadings, the modification of the approach used in references 3 and 4 to account for such effects is not obvious.

To avoid these difficulties as well as to provide additional understanding of the underlying failure process, an approach is presented in this paper that accounts for the progressive failure of a notched or unnotched laminate, that is, for the damage to the matrix and fibers in the individual plies that is known to occur before ultimate failure of the laminate takes place (refs. 5 and 6). The approach taken is similar to that of reference 2, that is, as partial or total failure of a ply takes place, appropriate stiffness changes are made in the laminate via laminated plate theory. However, the more complicated biaxial and inhomogeneous stress field surrounding a through-the-thickness notch makes the problem two-dimensional and of a sufficiently complicated nature to require a computer to follow the progressive failure process. This paper describes an incremental, finite element program developed to trace the damage that leads to ultimate failure of a notched or unnotched laminate under uniaxial or biaxial loading conditions and to predict this ultimate failure load. Comparison of the computer predictions is made with experimental results obtained for several uniaxially loaded graphite-epoxy laminates containing a circular hole.

FAILURE CRITERIA

Since the finite element program which has been developed is inherently dependent on the ply failure criterion and ply post-failure constitutive relations used, these are described in more detail along with how they are combined to trace damage and predict ultimate failure in the laminate. As an individual ply failure criterion, the ultimate strain criterion is used. This criterion assumes failure of the ply to occur in the fiber direction when the strain in that direction reaches a certain value determined from experiment. Similarly, failure of the matrix is assumed to occur when either the transverse or shear strains reach a critical value. This criterion has been chosen, at least initially, partly because of its simplicity but, more importantly, because it enables a physical interpretation of the failure to be made, and this is important in determining the post-failure constitutive relations of the ply. It should be noted that this failure criterion does not account for stress interaction effects on the failure of the ply. How-

ever, these effects are considered to be of secondary importance and, of course, any other ply failure criterion could easily be substituted into the computer program.

Since after failure the ply does not necessarily lose its entire stiffness, post-failure constitutive relations must be developed. To accomplish this, the following assumptions, based on the physical nature of the ultimate strain failure criterion, are made: 1) if a ply fails in the fiber direction, it loses its stiffness in the fiber direction and in shear, but not its stiffness in the transverse direction ($E_{11} = \nu_{12} = G_{12} = 0$, $E_{22} \neq 0$); 2) if a ply sustains matrix failure, whether due to transverse tension or shear, it loses its stiffness in the transverse direction and in shear, but not its stiffness in the fiber direction ($E_{22} = \nu_{12} = G_{12} = 0$, $E_{11} \neq 0$). These assumptions are made primarily for tensile conditions. Modifications would have to be made if loadings were substantially compressive.

The stiffness of the laminate is determined using the ply stiffnesses in conjunction with laminated plate theory. Therefore, before failure of the first ply takes place, the undamaged ply stiffnesses are pieced together in the usual fashion to form the laminate stiffness. If failure of a particular ply occurs, the appropriate reduced stiffness for the type of damage suffered (matrix or fiber failure) is used to replace the original undamaged stiffness of that ply in the laminated plate equations. Thus, for any state of damage of the laminate, an appropriate stiffness can be derived. It should be noted that since only mid-plane symmetric laminates and in-plane loads are considered here, the damage should also be mid-plane symmetric. The use of laminated plate theory is thus justified provided extensive delamination does not precede ultimate failure.

Failure of a particular ply within the laminate is determined by transforming the laminate strains into strains in the ply principal directions and applying the ultimate strain failure criterion, as previously discussed. When damage to a ply occurs, the stiffness of the laminate is changed appropriately, as described in the preceding paragraph. As more load is applied, more and more damage accumulates, until finally the load can no longer be sustained and ultimate failure of the laminate takes place.

NUMERICAL PROCEDURE

In cases where the in-plane stress field is non-homogeneous, such as when the laminate contains a through-the-thickness notch, the failure process is traced by the use of a finite element procedure. Such a procedure becomes necsssary because the different stresses at different points in the laminate cause different states of damage and, therefore, inhomogeneous stiffnesses. The finite-element method is well suited to this problem because the largest stiffness gradients occur where the stress and strain gradients are also largest and because non-linear incremental procedures are well established for this method. An outline of the numerical procedure follows.

The first step in the numerical analysis is the formation of the structural stiffness matrix using standard numerical procedures, the undamaged ply stiffness, and laminated plate theory. A load increment, either applied stress or applied displacement, is applied to the specimen being analyzed, and the stresses and strains in the global coordinate system are determined. Then, for each ply of each element, the strains in the ply principal directions are calculated and compared to the failure values. If either matrix or fiber failure occurs, the change in stiffness of that ply and, therefore, of the laminate for that element is calculated. However, if failure occurs in any element, the lowering of its stiffness implies that the previous values obtained for stress are too large for the given strains, i.e., its load-displacement point lies above the load-displacement curve. To correct for this, an iterative procedure (often called the "incremental-initial strain" method) is used in which iteration back to the actual load curve is accomplished at a constant load value in a saw-tooth fashion. This is accomplished by applying a set of "pseudo" body forces to the nodes to equilibrate the applied loads and then removing them by allowing the structure to deform appropriately. This process is repeated until the stress-strain in each element converges to the actual damaged or undamaged stress-strain curve. Once convergence is achieved, a new increment of load or displacement is applied to the specimen being analyzed and the iteration process is repeated. Total failure of the laminate is considered to take place when equilibrium can no longer be achieved or when the peak load is reached. Further details can be found in reference 7.

An incremental procedure has been used here rather than the direct iteration procedure sometimes used in nonlinear elasticity because the damage process is path dependent. That is, upon loading past failure and then unloading, healing of the damage does not take place; therefore, unloading proceeds along a different curve than does loading. This can be of importance in the analysis of a notched body since failure in a small region of the notch where the initial stress concentration is high can result in an unloading of the surrounding region.

COMPARISON TO TEST DATA

To evaluate the use of the described finite element method as a failure criterion for laminated composites, several test cases were run. These cases were chosen on the basis of availability of the test data and are reasonably representative of problems of interest. In particular, several unnotched uniaxial tensile specimens of various ply orientations were run as an initial check. These were followed by an analysis of specimens of two different ply orientations containing circular holes and subjected to uniaxial tensile loadings. Further analyses are planned to include other notch shapes and biaxial loadings, but these are not yet available.

As an initial check of the program, stress-strain curves were generated using the data of reference 8 for uniaxial tension of various Thornel 300/Narmco 5208 graphite-epoxy laminates. Since this has previously been done by others (e.g. refs. 2 and 9) using similar procedures, it suffices

to say that for the cases run, $(0°/\pm45°/0°)_s$, $(0°/\pm45°/90°)_s$, $(0°/90°/0°/90°)_s$ and $(90°/\pm45°/90°)_s$, the computer results compared very favorably with the data with respect to the point of initial failure, subsequent slopes, and ultimate failure stresses and strains. Of course, the sudden unloading upon failure of a ply that occurs in the present program led to discrete jumps in the computer generated stress-strain curves, but this is not considered to be particularly important in predicting the ultimate failure load, nor, for that matter, the slopes of the stress-strain curve before and after initial ply failure. Furthermore, the smooth experimental stress-strain curves are usually generated by ramp displacement loadings which tend to mask any such discrete jumps that might tend to take place. Finally, in the case of notched laminates, jumps in the load-displacement relationship usually fail to occur because only a few elements fail during each load increment. Thus, the overall stiffness of the specimen suffers no large discontinuities.

A more interesting comparison of the computer generated results was made with the data of reference 4. In this reference, a series of tests was run on specimens of various sizes, ply orientations, material systems, and notch shape and size, all under uniaxial tension. Furthermore, many of these speciments were strain gaged with several vertical gages located across the ligament of the cracked and circularly notched specimens (the readings from these gages were not included in reference 4). Two of the Thornel 300/Narmco 5208 graphite-epoxy specimens of width 7.62 cm (3 inches) containing holes 2.54 cm (1 inch) in diameter were selected for comparison. The ply orientations of these specimens were $(0°/\pm45°/90°)_{2s}$ and $(0°/90°)_{4s}$. These orientations were originally chosen because of the quasi-isotropic nature of the first and large stress concentration factor (5.11) of the second.

The computer simulation of these test specimens was made using a 99 element grid and an applied displacement loading of .002 cm (.0008 inches) per increment. The ply stiffnesses used were those of reference 8 for the same material system. The ply failure strains used were taken from the data of reference 8 as well. Specifically these were taken to be: 1) fiber failure strain, 0.0095; 2) transverse failure strain, 0.0041; and 3) shear failure strain, 0.023.

RESULTS AND DISCUSSION

For the $(0°/\pm45°/90°)_{2s}$ laminate containing a circular hole, eleven increments of the applied displacement were needed to reach the predicted ultimate failure load of 174.4 MN/m^2 (25.3 ksi). The maximum number of iterations needed within a single displacment increment up to this point was 49, which occurred immediately after failure of the fibers in the 0° ply of the element along the horizontal axis closest to the hole. The central processing unit (CPU) time for this computer run was about 2 minutes.

For the $(0°/90°)_{4s}$ laminate containing a circular hole, twelve increments of the applied displacement were needed to reach the predicted ultimate failure load of 286.1 MN/m^2 (41.5 ksi). The maximum number of iterations needed in any one displacement increment up to failure was 105, which

occurred for the last increment due to fiber failures in several elements near the hole boundary. The CPU time for this run was almost 5 minutes.

The computer predicted failure loads were in quite good agreement with the experimentally observed values given in reference 4. In this reference the gross failure stresses were given as 194.4 MN/m^2 (28.2 ksi) and 315.1 MN/m^2 (45.7 ksi) for the 2.54 cm (1 inch) hole diameter specimens of the $(0°/\pm45°/90°)_{2s}$ and $(0°/90°)_{4s}$ graphite-epoxy laminates, respectively. However, there is reason to believe that a more representative failure load for the $(0°/90°)_{4s}$ specimens would be about 275.8 MN/m^2 (40 ksi), as can be seen from the data for failure loads for the same laminate containing smaller holes. This anomaly was referred to in reference 4 as well.

In order to trace the progressive damage that takes place in a laminate before ultimate failure occurs, the computer program prints out the state of damage in each ply of each element after equilibrium is achieved for each increment. Thus, for each displacement increment, whether a particular ply is intact or has failed, in the fibers or matrix or both, is known for the entire laminate. The progressive damage that is predicted to occur for the two examples being considered is shown in figures 1 and 2. To keep these figures reasonably simple, only two distinctions have been made: matrix failure and fiber failure. Matrix failure refers to the failure of the matrix for any ply within that element, with no distinction between plies being shown (although this information is printed out by the computer). Similarly, fiber failure refers to the failure in the fiber direction of any ply within that element. It is interesting to consider the failure progression shown in figures 1 and 2 in more detail.

In figures 1 and 2, the four stages of damage shown correspond to the first failure that occurs, the first fiber failure that occurs, the ultimate load, and the post-failure process where the load rapidly drops off as the applied displacement continues to increase. As expected for both laminates, the first failure is the matrix failure of the 90° plies at the edge of the hole where the highest stress and strain concentrations occur. Up to this point, the load-displacement relation for the specimen is a linear one. After this first failure, the relation becomes only slightly nonlinear until fiber failure of the 0° ply occurs, also in the element along the horizontal axis nearest the hole. This is shown in the second drawing of each figure. In between the first matrix and first fiber failures, damage of the matrix spreads out in both the horizontal and vertical directions. In the $(0°/90°)_{4s}$ laminate, matrix failure of the +45° plies also occurs in the elements nearest the hole. After failure in the fibers of the 0° ply near the hole, the rapid spread of matrix damage is apparent.

Two differences in the failure of the $(0°/\pm45°/90°)_{2s}$ and $(0°/90°)_{4s}$ laminates become noticable in the last two drawings of figures 1 and 2. The first difference is the tendency for matrix failure in the $(0°/90°)_{4s}$ laminate to spread up the outer edges of the specimen. This "columnating" effect is the result of the difference between the stresses near the center of the specimen and near the edge of the specimen (both considered near the top of the specimen away from the hole). Although even initially, before any failures

occur, the $(0°/90°)_{4s}$ specimen has larger stresses toward the edge than in the center than does the $(0°/\pm45°/90°)_{2s}$ specimen, as the ultimate loads for each specimen are reached, this concentration of stress towards the edges becomes even more pronounced for the $(0°/90°)_{4s}$ specimen, whereas for the $(0°/\pm45°/90°)_{2s}$ specimen this does not occur. A more important difference in the predicted failure modes of the two laminates concerns the predicted ultimate path. This is represented in figures 1 and 2 by the blackened elements representing fiber or total failure of that element. Although it is apparent that the last drawing of figures 1 and 2 is calculated for an equilibrium situation when in actuality unstable dynamic conditions would exist at this point for typical experimental conditions, it is expected that the direction of the failure path is at least initially correct. Although not clearly displayed in the photographs of failed specimens in reference 4, examination of the actual failed specimens shows the predicted failure modes to be in close agreement with those observed. Thus, the $(0°/\pm45°/90°)_{2s}$ laminates showed a failure mode that began at the extreme hole edges and propagated essentially straight across the specimen along the horizontal axis of symmetry. Failure of the $(0°/90°)_{4s}$ laminates on the other hand, although beginning at the outer edges of the hole, propagates from the hole in an asymmetric manner, angling up at one edge and down at the other for about a third of the ligament width before becoming horizontal out to the edge.

The comparison of strains across the ligament of the specimen from the hole edge was less successful. Although the predicted strains agreed well with the strain gage data for the gages located away from the hole, the predicted strains very close to the hole (closest element) were much too high once fiber failure of that element occurred. This is thought to happen because of the model of failure used. A failure model which takes into account the unloading process after failure would be expected to at least dimenish this problem. It appears, however, that the present failure model is successful at modeling the decrease in stiffness of the laminate near the hole, thus lowering the stress concentration and redistributing the stress out away from the hole.

CONCLUDING REMARKS

An incremental finite element program capable of modeling damage accumulation in notched composites and predicting ultimate failure loads, from a knowledge of ply behavior alone, has been described. Although reasonably successful in predicting failure strengths and failure modes in two simple examples of notched laminates, definite conclusions regarding the success of this method await comparisons with a great deal more experimental data, including notches under biaxial loadings. Furthermore, a number of significant improvements could be made to the present program, such as including a gradual unloading mechanism after failure of a ply and the known nonlinear behavior of a ply in shear. However, both of these improvements are considered to be of secondary importance in the modeling of damage. It is concluded that the method described, although capable of considerable improvement, can model the damage process on a macroscopic scale and shows considerable promise as an analytical method of predicting the failure of notched composite laminates.

REFERENCES

1. Wu, E. M.: Strength and Fracture of Composites. Fracture and Fatigue, Vol. 5 in Composite Materials, L. J. Broutman and R. H. Krock, Ed., Academic Press, 1974, pp. 191-247.

2. Petit, P. H. and Waddoups, M. E.: A Method of Predicting the Nonlinear Behavior of Laminated Composites. Journal of Composite Materials, Vol. 3, 1969, pp 2-19.

3. Whitney, J. M. and Nuismer, R. J.: Stress Fracture Criteria for Laminated Composites Containing Stress Concentrations. Journal of Composite Materials, Vol. 8, 1974, pp. 253-265.

4. Nuismer, R. J., and Whitney, J. M.: Uniaxial Failure of Composite Laminates Containing Stress Concentrations. Fracture Mechanics of Composites, Spec. Tech. Publ. 593, American Soc. Testing and Mater., 1975 pp. 117-142.

5. McGarry, F. J.: Crack Propagation in Fiber Reinforced Plastic Composites. Fundamental Aspects of Fiber Reinforced Plastic Composites, R. T. Schwartz and H. S. Schwartz, Ed., Interscience Pub., 1968.

6. Rotern, A. and Baruch, J.: Determining the Load-Time History of Fiber Composite Materials by Acoustic Emission. Journal of Materials Science, Vol. 9, 1974, pp. 1789-1798.

7. Brown, G. E.: Progressive Failure of Advanced Composite Laminates Using the Finite Element Method. M. S. Thesis, University of Utah, March 1976.

8. Sendeckyj, G. P., Richardson, M. D., and Pappas, J. E.: Fracture Behavior of Thornel 300/5208 Graphite-Epoxy Laminates Part I: Unnotched Laminates. Air Force Flight Dynamics Lab., AFFDL-TM-74-89-FBC, Wright-Patterson, A.F.B., Ohio, April 1974.

9. Sandhu, R. S.: Ultimate Strength Analysis of Symmetric Laminates. Air Force Flight Dynamics Lab., AFFDL-TR-73-137, Wright Patterson A.F.B., Ohio, 1973.

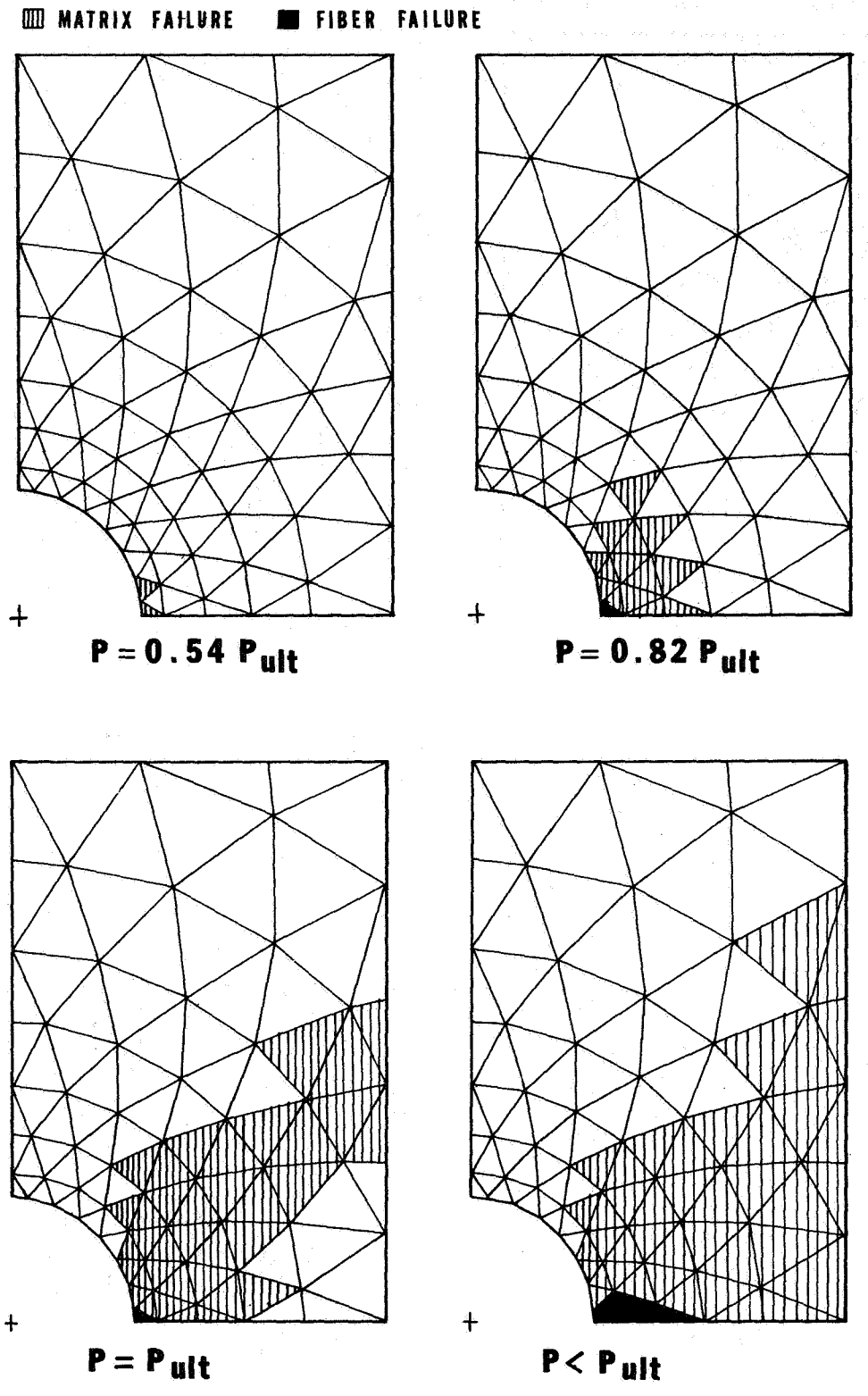

Figure 1.- Progressive failure: $(0/\pm45/90)_{2s}$.

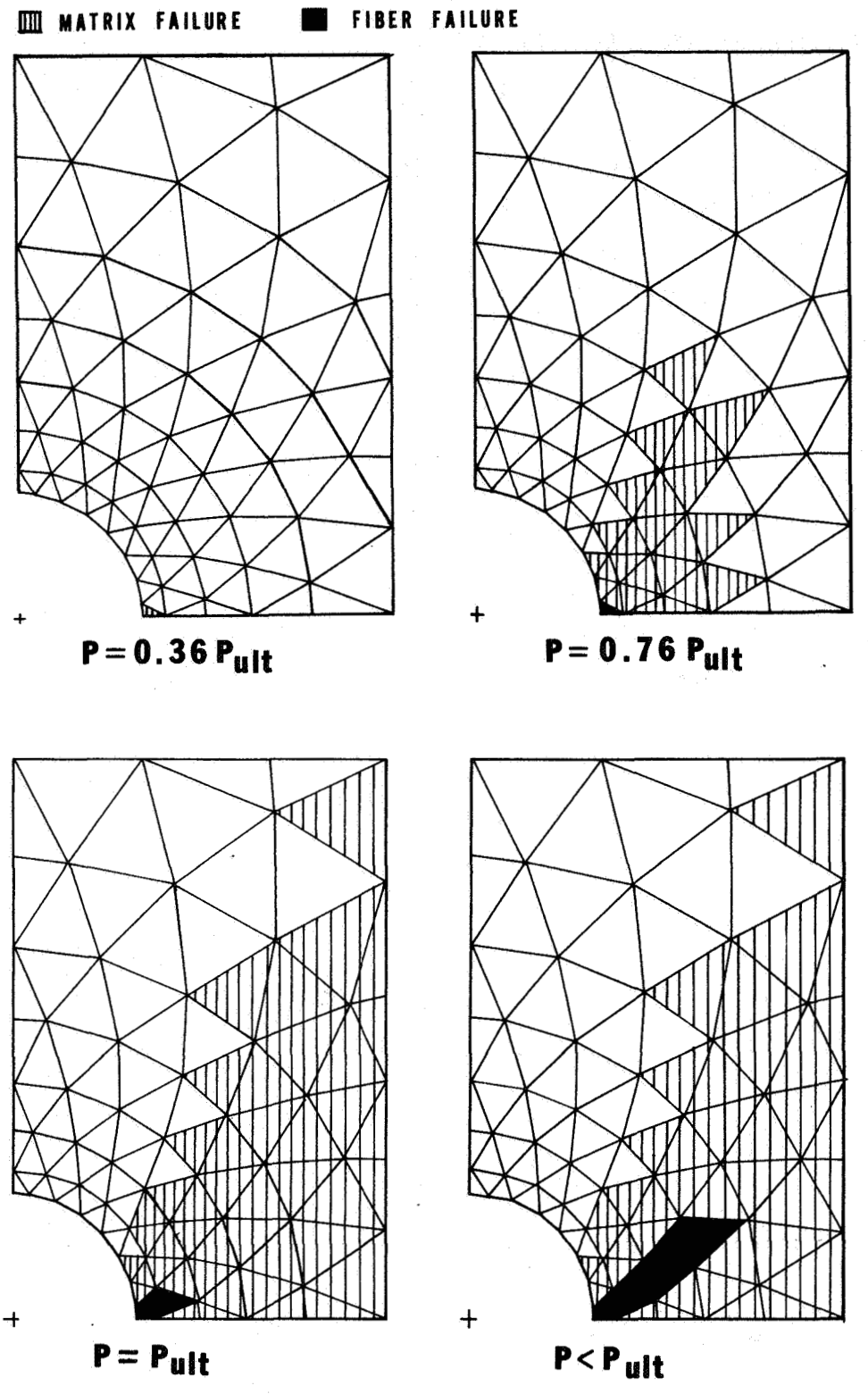

Figure 2.- Progressive failure: $(0/90)_{4s}$.

RESIDUAL STRESSES IN POLYMER MATRIX COMPOSITE LAMINATES

H. Thomas Hahn
University of Dayton Research Institute

SUMMARY

Residual stresses in composites are induced during fabrication and by environmental exposure. The theory formulated can describe the shrinkage commonly observed after a thermal expansion test. Comparison between the analysis and experimental data for $[0_2/\pm 45]_s$ laminates of various material systems indicates that the residual stress-free temperature can be lower than the curing temperature, depending on the curing process. Effects of residual stresses on ply failure including the acoustic emission characteristics are discussed.

INTRODUCTION

By definition a composite is composed of several different material phases and residual stresses are induced due to the heterogeneity. Magnitude of these residual stresses depends on the history of environmental exposure as well as on the constituent properties. Typical residual stresses which are attracting increased attention are the curing stress and the swelling stress. The former is induced by the thermal expansion mismatch during fabrication and the latter by the difference in swelling when moisture is absorbed.

The curing stress in certain graphite/epoxy laminates may be large enough to cause ply failure in the absence of applied stress or premature failure upon tensile loading (refs. 1 and 2). In metal matrix composites such as boron/aluminum, the curing stress may cause plastic deformation in the matrix (ref. 3). The damage observed in boron/aluminum composite after thermal fatigue can be attributed to the curing stress among others (ref. 4).

In the present paper we shall analyze the residual stresses resulting from fabrication and moisture absorption and compare the analytical results with experimental data. Although the analysis method can be extended to

metal matrix composites, the discussion will be limited to thin resin matrix composite laminates. Effects of residual stresses on mechanical behavior will also be discussed.

PREDICTION OF RESIDUAL STRESSES

Whereas the curing stress in advanced composites increases with decreasing temperature, viscosity becomes less influential at room temperature. Furthermore, the swelling stress due to moisture absorption has a negating effect on the resultant residual stress because it is caused by the swelling of matrix in contrast to the curing stress. Thus the total residual stress is likely to be of sufficiently low magnitude as to justify the assumption of elastic behavior (refs. 5 and 6). The assumption of history independence is also necessitated by the difficulty associated with characterizing the actual behavior and implementing it in the subsequent analyses.

Let us consider a homogeneous material subjected to a stress σ_i, at temperature T, and with moisture content H. Measured from a stress-and moisture-free reference configuration at T_o, the total strain can be written as the sum of the mechanical and nonmechanical strains,

$$e_i = e_i^M + e_i^N \quad , \quad (i = 1, 2, 6) \quad .$$

The mechanical strain is assumed to be proportional to the stress,

$$e_i^M = S_{ij}(T,H)\, \sigma_j \quad ,$$

and the nonmechanical strain is divided into the thermal and swelling parts,

$$e_i^N = e_i^T(T) + e_i^H(H) \quad .$$

Note that the compliance depends on T and H in the current state and that any interaction between temperature and moisture is neglected in the nonmechanical strain.

Unidirectional Lamina

Residual stress distribution due to the thermal expansion and swelling can be calculated by following the same procedure as described for the determination of thermal expansion coefficients in references 7 and 8. However, in practical composites uniform distribution can be assumed of the strain in the longitudinal direction and of the stress in the transverse direction. The

equations for the nonmechanical strain, and for the residual stress, of the composite are then formulated in terms of the nonmechanical strains of the constituents.

Similar equations for thermal expansion coefficients were shown to be close to more sophisticated solutions (ref. 7) and also to agree favorably with experimental data for specimens of dimensions large enough to avoid boundary effects (ref. 9). The assumption of longitudinal (average) residual stress being the only nonvanishing component was seen to be valid in the residual fringe patterns in a glass/polyester composite. In fact, the residual stresses calculated from the simple equations described above were in close agreement with those from the residual fringes (ref. 10).

The most important but difficult problem which is not encountered in the usual thermal expansion coefficient analysis is the determination of the residual stress-free temperature T_o. Most matrix materials have larger thermal expansion than fiber materials and the thermal expansion coefficients usually increase with the temperature. Thus a small error in T_o can lead to a large error in the calculated curing stress. Details concerning T_o will be discussed in the following section.

When the thermal and the moisture diffusion occur concurrently, the temperature can be assumed to reach equilibrium instantaneously because the typical ratio of the thermal diffusivity to the moisture diffusivity is of the order of 10^6 (ref. 11). Therefore, changing moisture content may lead to an erroneous measurement of thermal expansion. Shrinkage observed after complete thermal cycles is a direct result of moisture desorption (refs. 12 and 13).

Figure 1 shows the transverse strain observed in a T300/5208 Gr/Ep subjected to two thermal cycles. The heating and cooling curves during the second cycle are almost the same and consequently only one curve is shown. For most resin matrix composites, the moisture content depends on the relative humidity only and the diffusivity on the temperature only. Thus, assuming the relative humidity within the test chamber to be zero, we can apply the method in reference 14 to the present problem.

For the material chosen the diffusivity is

$$D = 0.0849 \quad \exp(-4328/T) \quad cm^2/min$$

Using the approximate equation in reference 11 and the modified time in reference 14, we obtain the weight loss as

$$G = (M-M_i) / (M_f-M_i) = 1- \exp(-7.3\ r^{0.75}) ,$$

$$r = (0.0849/L^2) \int_0^t h(u)du .$$

Here M_i and M_f are the initial and final equilibrium values of the average moisture content M. The thickness L is 1.04 mm and the function h is

$$h(u) = \exp[-4328 / (295+ 2.222\ u)] \quad \text{for heating} ,$$

$$= \exp[-4328 / (450- 2.222\ u)] \quad \text{for cooling} ,$$

The resulting value of G is shown as a function of time in figure 2. The moisture desorption is seen to accelerate during heating but decelerate during cooling. Although one third of the total moisture loss is predicted to occur during the second cycle, no further shrinkage was observed (ref. 13). Therefore, we chose the curve for the second cycle as representative of the true thermal expansion.

From the observed shrinkage of 0.061% and the swelling coefficient of 0.7, we calculate the initial equilibrium content M_i to be 0.29%. The calculated weight loss of 0.087% after one cycle compares favorably with the observed value of 0.08%. The final prediction for the transverse strain in figure 1 is lower than observed. However, limited amount of data available shows that the absorbed moisture produces relatively little swelling until the moisture content reaches a certain level and then increases proportionally to the additional moisture content. Thus, if this threshhold level is incorporated in the analysis, the contraction due to moisture desorption will start at a later stage, resulting in a better correlation.

Multidirectional Laminate

Equations for the curing stress prediction are formulated in reference 5 within the framework of the laminated plate theory. The same equations can be used for general residual stress prediction if we simply replace the thermal strain by the nonmechanical strain.

Analyses have been performed for the curing strain data of reference 15 for $[0_2/\pm45]_s$ laminates of different material systems. Thermophysical and mechanical properties of unidirectional laminae were taken from reference 15 and the curing temperature was taken as the residual stress-free temperature.

The calculated in-plane curing strains of the laminates in three different directions are listed in table I. The normalized transverse and shear stresses included are within 45° plies. Less stresses are predicted within 0° plies. The calculated strains in the 90° direction are higher than the observed in all composites except B/PI. Therefore, it is suspected that the actual stress-free temperature is lower than the curing temperature for the following reasons.

If the true stress-free temperature T_o^{true} is lower than the curing temperature T_o, then the curing strain in table I will be the sum of the true curing strain between T_o^{true} and room temperature and the strain between T_o^{true} and T_o. Since the transverse and shear moduli at T_o are much lower than those at room temperature, the sum of these separate strains will be smaller than the strain based on T_o alone. The difference increases if the thermal expansion increases with temperature, as is the case in most composites.

In the 90° direction 0° plies force 45° plies to contract through the residual stress built up. The magnitude of the residual stress near the curing temperature increases with the degree of curing. As the temperature decreases, 0° plies gain enough stiffness to contract the neighboring 45° plies. However, the overall curing strain at room temperature will be lower in case of incomplete curing. This is exactly the case for Gr/Ep in table I, as shown by the numbers inside the parentheses. Accordingly, the stress-free temperature will be lower for undercured laminates.

As for B/PI which exhibits higher strains than calculated, the readings during curing and postcuring are reported to have been erroneous and the data shown was taken in the subsequent thermal cycling. The analysis shows that the transverse stress is higher than the strength. Thus it is possible that the anomalous behavior might be due to the microcracking caused by the curing stress. However, effect of microcracks on macroscopic response is not well understood at present (cf. ref. 16).

In order to study influence of ply orientation, curing strains and stresses have been calculated for $[0_2/\pm\theta]_s$ Gr/PI, figures 3 and 4. The abscissa in both figures is the angle θ and the stresses are within θ° plies. Again, the analysis yields higher strains than observed (data from ref. 15). The transverse stress increases with θ reaching the maximum at $\theta = 90^{\circ}$. If the assumed T_o is correct, transverse failure of θ° plies is expected for θ greater than about 35°. However, the actual stress will be lower when the correct value is used for T_o.

A direct method of determining T_o suggested in references 6 and 17 makes use of unsymmetric [±θ] laminates. Two measurements are recommended in this method: warpage and the temperature at which the laminates become flat. The warpage is more sensitive to the curing stress than is the curing strain, and therefore depends more critically on T_o. It is interesting to note that the suggested value of T_o for T300/5208 Gr/Ep and Scotchply 1002 Gl/Ep is 394°K while the curing temperature is 450°K (ref.16).

EFFECTS OF RESIDUAL STRESSES

Curing stresses in the transverse direction in table I are higher than the transverse strengths in all cases but B/Ep. Even a conservative estimate based on T_o being about 60% of the curing temperature indicates that the curing stresses can be higher than 50% of the transverse strengths. However, failure of 45° plies has negligible influence on the initial modulus and Poisson's ratio in the 0° direction for $[0_2/\pm45]_s$ laminates (ref. 15). The reason is because even an approximation based on $E_L/2$ yields a fairly accurate modulus. However, in laminates such as $[(\pm45)_2/90_4]_s$ premature failure of 90° plies can clearly be detected by a substantial change in the axial stress-strain relation (ref. 2).

In [0/90] laminates Poisson's ratio is more sensitive to the failure of 90° plies than is the modulus. After 100 thermal cycles between room temperature and 533°K while under 70% of the ultimate load, Poisson's ratio of $[0_2/90_2]_s$ Gr/Ep decreased from an initial value of 0.035 to 0.013, apparently indicating the failure of 90° plies (ref. 15).

Effect of the curing stress can also be seen in the acoustic emission characteristics of composite laminates. In figure 5 two $[0/\pm45/90]_s$ Gr/Ep specimens were preloaded to the levels shown: one at room temperature and the other at 455°K. Both specimens were then tested to failure at room temperature. Preloading produces delayed A.E. activity when the specimen is tested at 455°K. However, the same specimen, when tested later at room temperature, exhibits A.E. activity earlier than it did at 455°K. The reason for this difference is because the curing stress that was absent at 455°K is recovered at room temperature and causes earlier failure of plies. The specimen preloaded at room temperature shows the so-called Kaiser effect, i.e., A.E. activity is negligible until the preload level is exceeded.

In determining the effect of curing stress on ply failure, extra care should be exercised not to expose specimens to moist environment, since absorbed moisture will almost cancel the curing stress. For example, only

about 0.4-0.5% moisture content is required to completely negate the transverse curing strain e_T^T in Gr/Ep. Approximately the same amount of moisture is observed to exist in Gr/Ep exposed to laboratory conditions. In this case the absorbed moisture can eliminate the curing stress and render composite laminates free of residual stress.

CONCLUSIONS

Equations for the analysis of residual stresses have been formulated under the assumption of elastic behavior and within the framework of the laminated plate theory. The formulation includes both the curing stress resulting from fabrication and the swelling stress due to moisture absorption. Comparison between the predictions and experimental data for the laminates studied leads to the following conclusions.

1. The residual stress-free temperature is lower than the curing temperature and depends on the curing process.

2. Curing stress in the transverse direction is higher than 50% of the transverse strength.

3. Moisture absorption under room conditions can render laminates free of residual stress.

4. Shrinkage after thermal cycling is mainly due to moisture desorption and can be predicted.

REFERENCES

1. Doner, D.R. and Novak, R.C.: Structural Behavior of Laminated Graphite Filament Composites. 24th Annual Tech. Conf., SPI, Inc., 1969, paper 2-D.

2. Novak, R.C. and DeCrescente, M.A.: Fabrication Stresses in Graphite Resin Composites. J. Engineering for Power, vol. 92, 1970, pp. 377-380.

3. Chamis, C.C. and Sullivan, T.L.: A Computational Procedure to Analyze Metal Matrix Laminates With Nonlinear Lamination Residual Strains. Composite Reliability, ASTM STP 580, 1975, pp. 327-351.

4. Wright, M.A.: The Effect of Thermal Cycling on the Mechanical Properties of Various Aluminum Alloys Reinforced with Unidirectional Boron Fibers. Met. Trans. A., vol. 6A, 1975, pp. 129-134.

5. Hahn, H.T. and Pagano, N.J.: Curing Stresses in Composite Laminates. J. Composite Materials, vol. 9, 1975, pp. 91-106.

6. Pagano, N.J. and Hahn, H.T.: Evaluation of Composite Curing Stresses. Presented at ASTM 4th Conf. on Composite Materials, May 1976.

7. Schapery, R.A.: Thermal Expansion Coefficients of Composite Materials Based on Energy Principles. J. Composite Materials, vol. 2, 1968, pp. 380-404.

8. Hashin, Z.: Theory of Fiber Reinforced Materials. NASA Contract NAS1-8818, Nov. 1970.

9. Marom, G. and Weinberg, A.: The Effect of the Fiber Critical Length on the Thermal Expansion of Composite Materials. J. Mat. Sci., vol. 10, 1975, pp. 1005-1010.

10. Hahn, H.T. and Morris, D.H.: Anisotropic Photoelasticity with Application to Composites. Presented at 1976 SESA Spring Meeting, May 1976.

11. Shen, C.-H. and Springer, G.S.: Moisture Adsorption and Desorption of Composite Materials, J. Composite Materials, vol. 10, 1976, pp. 36-54.

12. Freeman, W.T. and Campbell, M.D.: Thermal Expansion Characteristics of Graphite-Reinforced Composite Materials. Composite Materials: Testing and Design (Second Conf.), ASTM STP 497, 1972, pp. 121-142.

13. Hofer, K.E., Jr.; Larsen, D.; and Humphreys, V.E.: Development of Engineering Data on the Mechanical and Physical Properties of Advanced Composite Materials. AFML-TR-74-266, Air Force Materials Lab., Feb. 1975.

14. Weitsman, Y.: Diffusion with Time-Varying Diffusivity, with Application to Moisture-Sorption in Composites. To be published in J. Composite Materials, 1976.

15. Daniel, I.M. and Liber, T.: Lamination Residual Stresses in Fiber Composites. NASA CR-134 826, Mar. 1975.

16. Tsai, S.W. and Hahn, H.T.: Failure Analysis of Composite Materials. Inelastic Behavior of Composite Materials, AMD-Vol. 13, ASME, 1975.

17. Tsai, S.W.: Strength Characteristics of Composite Materials. NASA CR-224, Apr. 1965.

TABLE I.- CURING STRAINS AND CURING STRESSES

	$-e_0^T$, %		$-e_{90}^T$, %		$-e_{45}^T$, %		$\frac{\sigma_T}{X_T}$	$\frac{\sigma_{LT}}{X_{LT}}$
	EXP.	CAL.	EXP.	CAL.	EXP.	CAL.		
B/Ep	0.123	0.109	0.234	0.259	0.171	0.184	0.99	0.13
B/PI	0.100	0.075	0.214	0.186	0.163	0.131	4.09	0.33
Gr/Ep	-0.018 (-0.009)	-0.019	0.104 (0.068)	0.122	0.036 (0.026)	0.052	1.09	0.11
Gr/PI	0.002	-0.004	0.031	0.051	0.017	0.028	1.20	0.11
Gl/Ep	0.105	0.117	0.260	0.361	0.182	0.239	1.39	0.65

Remarks: Numbers inside the parentheses for Gr/Ep are measured during the cooling stage of curing and the heating stage of postcuring. X_T and X_{LT} are the transverse and shear strengths, respectively.

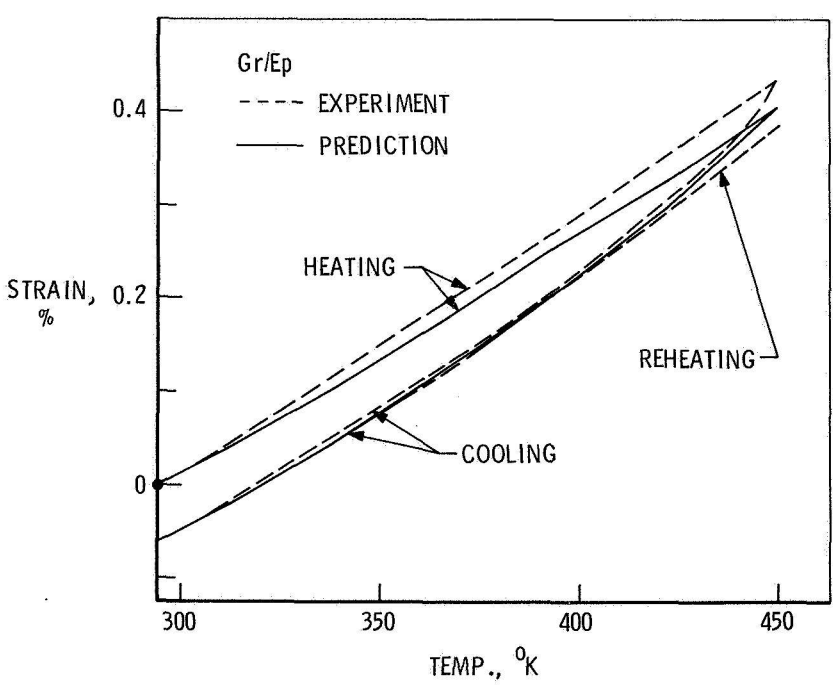

Figure 1.- Transverse strain during thermal cycling.

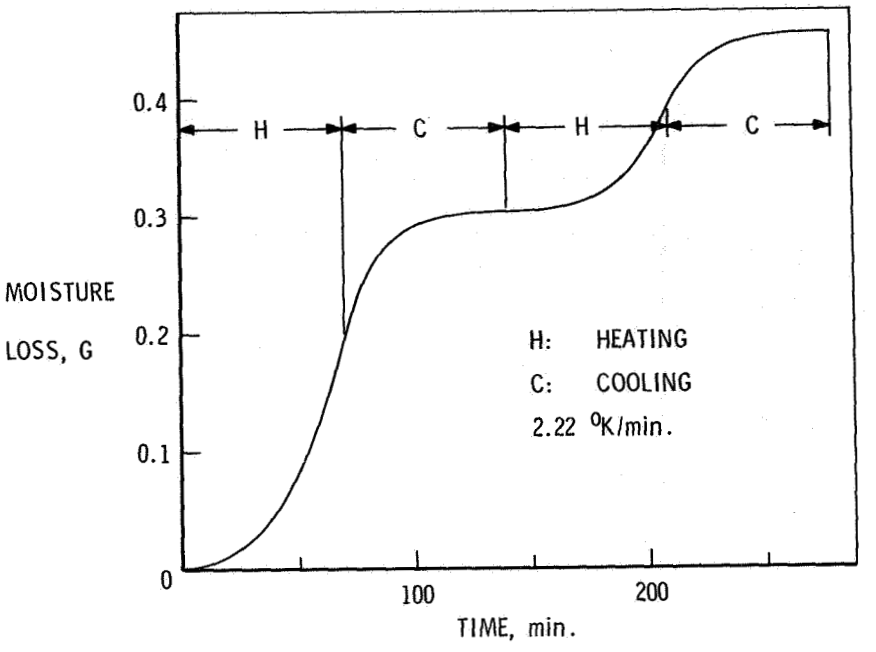

Figure 2.- Moisture desorption during thermal cycling.

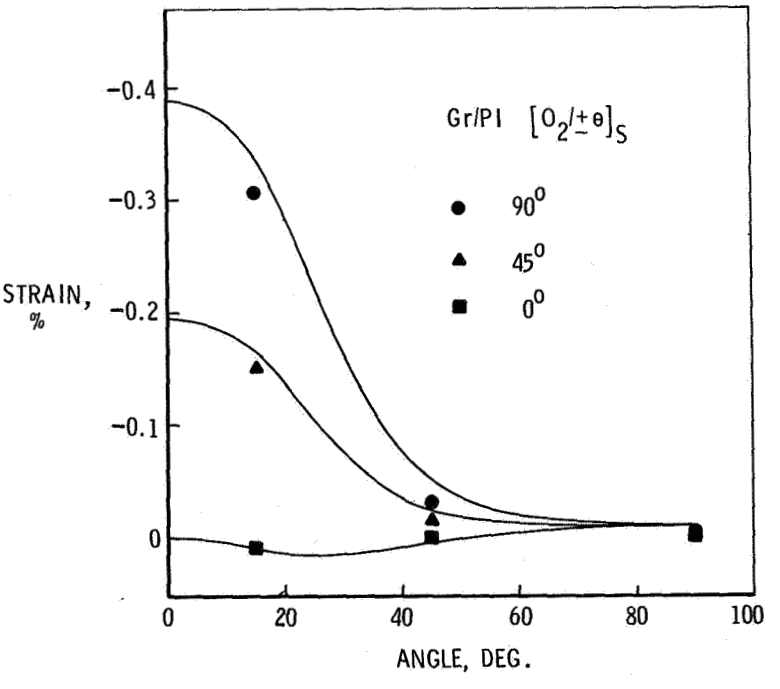

Figure 3.- Curing strains of $[0_2/\pm\theta]_s$ Gr/PI laminates.

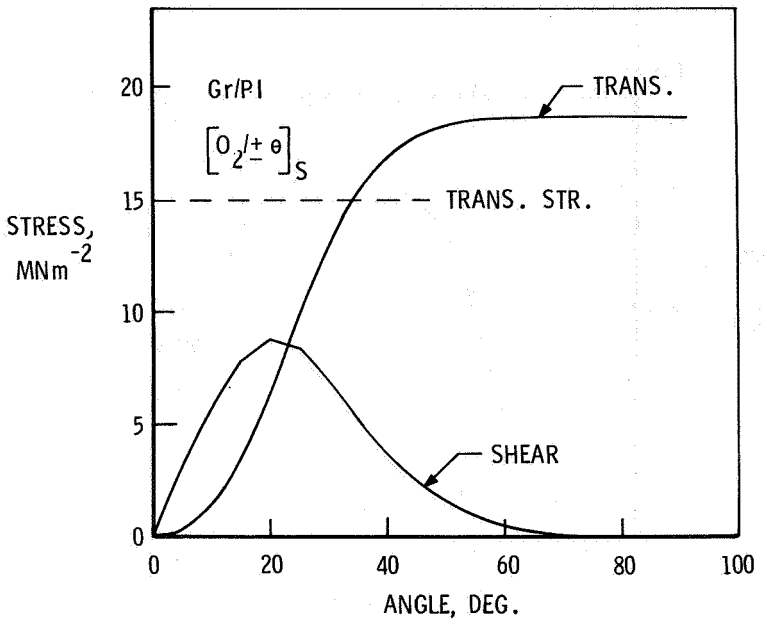

Figure 4.- Curing stresses within θ^{o} plies of $[0_2/\pm\theta]_s$ Gr/PI laminates.

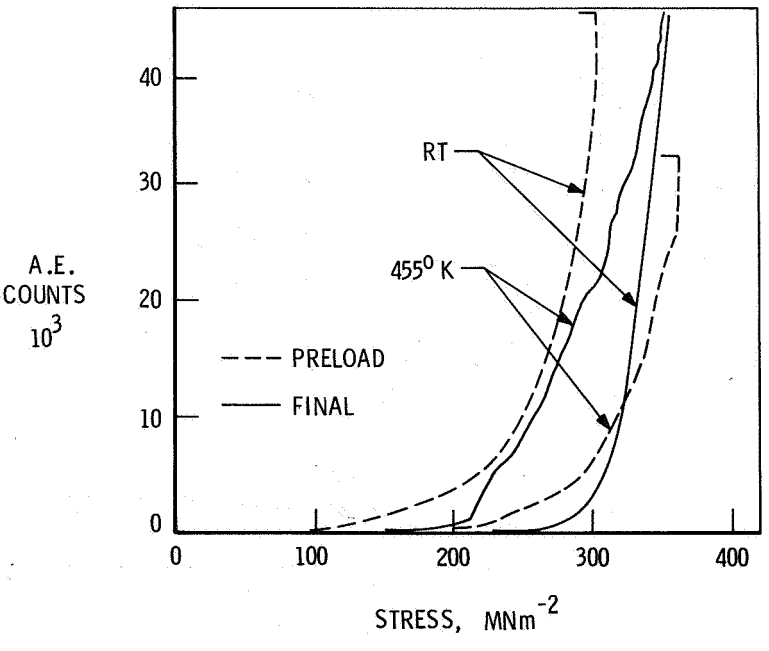

Figure 5.- Effect of preloading on total number of A.E. counts at two different temperatures.

INFLUENCE OF SPECIMEN BOUNDARY ON THE DYNAMIC STRESS INTENSITY FACTOR

E. P. Chen and G. C. Sih
Lehigh University

SUMMARY

The dynamic interaction of a crack with specimen boundaries has received very little attention in the literature mainly because of the difficulties encountered in the analytical treatment. The problem to be considered in this paper is the sudden appearance of a flaw or crack in a strip of material of finite height subjected to tensile loading. Stress waves are generated within the strip and are reflected from boundary to boundary. Of interest is the maximum value of the dynamic stress intensity factor at a given instance of time as the strip height to crack length ratio is varied.

INTRODUCTION

The dynamic interaction of cracks with neighboring free surfaces or boundaries poses difficulties to analytical treatment. Available solutions in this area are meager. The few published results dealt with the steady state diffraction of harmonic waves by a crack near an interface (refs. 1 and 2) and dynamic loading on cracks in specimens with finite dimensions (refs. 3 and 4).

Considered in this paper is the sudden appearance of a finite length crack parallel to the edges of a strip of material. The edges of the strip are pulled apart by equal and opposite tensile stresses. The mixed boundary value problem as formulated by means of Laplace and Fourier transforms can be reduced to the solution of a pair of dual integral equations in the Laplace transform domain. Further reduction leads to a Fredholm integral equation of the second kind. The time dependence of the problem is recovered by utilizing a numerical Laplace inversion scheme developed by Sih, Embley and Ravera (ref. 5).

Numerical values of the dynamic stress intensity factor and the crack opening displacement are obtained as functions of time for various strip height to crack length ratios. The general behavior of the curves is that they all oscillate with decreasing amplitude and reduce to the static values as time becomes infinite. For large cracks confined in a narrow strip, small oscillations in the stress intensity factor $k_1(t)$ curves are observed prior to $k_1(t)$ reaching its maximum value. Similar phenomenon occurs for the crack opening displacement curves. Moreover, the peak values of both the dynamic stress intensity factor and the crack opening displacement are reached simultaneously. As the crack length to strip height ratio is reduced, the reflected boundary waves become

less significant and do not affect the near field result. The larger peaks are predominately caused by the interaction of waves emanating from the crack tip and they are larger than the corresponding static value.

Although only traction boundary condition is considered, other conditions can be prescribed on the strip edges and the problem can be handled in a similar manner without additional difficulties.

FORMULATION OF THE PROBLEM

Consider the case of a strip of material of height 2h containing a crack of length 2a. A set of cartesian coordinates (x,y,z) is attached to the center of the crack. The geometry of the problem is shown in figure 1.

Let the displacement components in the x, y and z directions be denoted by u_x, u_y and u_z, respectively. Under plane strain†, the displacement u_z vanishes everywhere and u_x and u_y are functions of x, y and time t only. In terms of the wave potentials $\phi(x,y,t)$ and $\psi(x,y,t)$, the displacement field may be written as

$$u_x(x,y,t) = \frac{\partial \phi}{\partial x} + \frac{\partial \psi}{\partial y} \tag{1}$$

$$u_y(x,y,t) = \frac{\partial \phi}{\partial y} - \frac{\partial \psi}{\partial x} \tag{2}$$

$$u_z = 0 \tag{3}$$

Through the generalized Hooke's Law and equations (1), (2) and (3), the stress field may also be expressed in terms of the wave potentials. Making use of the equations of motion, the wave equations

$$\nabla^2 \phi = \frac{1}{c_1^2} \frac{\partial^2 \phi}{\partial t^2}, \quad \nabla^2 \psi = \frac{1}{c_2^2} \frac{\partial^2 \psi}{\partial t^2} \tag{4}$$

are obtained. In equations (4), the dilatational and shear wave velocities c_1 and c_2 are given by

$$c_1 = \sqrt{\frac{\lambda+2\mu}{\rho}}, \quad c_2 = \sqrt{\frac{\mu}{\rho}} \tag{5}$$

†Sih (ref. 6) has shown that a state of plane strain always prevails near the edge of a crack.

where λ and μ are the Lamé constants for an isotropic elastic solid and ρ is the mass density of the material. The Laplacian operator ∇^2 stands for $\partial^2/\partial x^2 + \partial^2/\partial y^2$. Note that ϕ and ψ constitute the solution to the problem.

A uniform tensile stress of magnitude σ_0 is applied to the upper and lower boundaries at $y = \pm h$. For the determination of dynamic stress intensity factor, it is only necessary to consider the equivalent problem of specifying $-\sigma_0$ to the upper and lower crack surfaces, i.e.,

$$\sigma_y(x,o,t) = -\sigma_o H(t), \quad |x|<a \tag{6}$$

$$u_y(x,o,t) = 0, \quad |x|\geq a \tag{7}$$

in which H(t) is the Heaviside unit step function. The symbols σ and τ are normal and shear stresses, respectively. Since the problem is symmetric with respect to the xz-plane, an additional condition previals at y=0:

$$\tau_{xy}(x,o,t) = 0, \quad -\infty<x<\infty \tag{8}$$

The equivalent problem requires the surfaces $y = \pm h$ to be free from tractions at all times:

$$\sigma_y(x,\pm h,t) = \tau_{xy}(x,\pm h,t) = 0, \quad -\infty<x<\infty \tag{9}$$

DUAL INTEGRAL EQUATIONS

Applying the Laplace and Fourier transforms to equations (4), the Laplace transform of ϕ and ψ may be written as

$$\phi^*(x,y,p) = \frac{2}{\pi}\int_0^\infty [A_1(s,p)\exp(-\gamma_1 y) + A_2(s,p)\exp(\gamma_1 y)]\cos(sx)ds \tag{10}$$

$$\psi^*(x,y,p) = \frac{2}{\pi}\int_0^\infty [A_3(s,p)\exp(-\gamma_2 y) + A_4(s,p)\exp(\gamma_2 y)]\sin(sx)ds \tag{11}$$

where p is the Laplace variable and γ_j (j = 1,2) are defined by

$$\gamma_j = \sqrt{s^2 + \frac{p^2}{c_j^2}}, \quad j = 1,2 \tag{12}$$

The conditions in equations (8) and (9) require that not all of the functions A_j (s,p) (j = 1,2,3,4) be independent of one another and they can be expressed

in terms of a single unknown as follows:

$$A_j(s,p) = f_j A(s,p),\ j = 1,2,3,4 \tag{13}$$

in which

$$f_1 = 2\gamma_2 m_2 \alpha_1/(m_2 m_3 - m_1 m_4),\ f_2 = m_1 f_1/m_2 \tag{14}$$

$$f_3 = -\exp(\gamma_2 h)[\alpha_3 f_1 \exp(-\gamma_1 h) + \alpha_4 f_2 \exp(\gamma_1 h)]/(2s\gamma_2\alpha_1) \tag{15}$$

$$f_4 = \exp(-\gamma_2 h)[\alpha_4 f_1 \exp(-\gamma_1 h) + \alpha_3 f_2 \exp(\gamma_1 h)]/(2s\gamma_2\alpha_1) \tag{16}$$

The following contractions m_j and α_j $(j = 1,2,3,4)$ have been made:

$$m_1 = 2\alpha_2 + [\alpha_4 \exp(-\gamma_2 h) - \alpha_3 \exp(\gamma_2 h)]\exp(-\gamma_1 h) \tag{17}$$

$$m_2 = 2\alpha_2 - [\alpha_3 \exp(-\gamma_2 h) - \alpha_4 \exp(\gamma_2 h)]\exp(\gamma_1 h) \tag{18}$$

$$m_3 = 2\gamma_1\gamma_2\alpha_1 + [\alpha_4 \exp(-\gamma_2 h) - \alpha_3 \exp(\gamma_2 h)]\exp(-\gamma_1 h) \tag{19}$$

$$m_4 = 2\gamma_1\gamma_2\alpha_1 - [\alpha_3 \exp(-\gamma_2 h) - \alpha_4 \exp(\gamma_2 h)]\exp(\gamma_1 h) \tag{20}$$

$$\alpha_1 = s^2 + \frac{1}{2}\left(\frac{p}{c_2}\right)^2,\ \alpha_2 = s^2\gamma_1\gamma_2 \tag{21}$$

$$\alpha_3 = \alpha_1 + \alpha_2,\ \alpha_4 = \alpha_1 - \alpha_2 \tag{22}$$

Finally, equations (11) and (12) yield a pair of dual integral equations

$$\int_0^\infty A(s,p)\cos(sx)ds = 0,\ x \geq a \tag{23}$$

$$\int_0^\infty sF(s,p)A(s,p)\cos(sx)ds = -\frac{\pi\sigma_0}{4\mu(1-\kappa^2)p},\ x<a \tag{24}$$

from which $A(s,p)$ may be determined. In equation (24), the function $F(s,p)$ is defined by

$$F(s,p) = \frac{1}{s(1-\kappa^2)} \{\alpha_1(f_1+f_2) + s\gamma_2(f_3-f_4)\} \tag{25}$$

with $\kappa^2 = c_2/c_1$. Following the method of Copson (ref. 7), it can be shown from equations (23) and (24) that

$$A(s,p) = -\frac{\pi\sigma_0 a^2}{4\mu(1-\kappa^2)p} \int_0^1 \sqrt{\xi}\Phi^*(\xi,p)J_0(sa\xi)d\xi \tag{26}$$

where J_0 is the zero order Bessel function of the first kind. The function $\Phi^*(\xi,p)$ may be computed numerically from a Fredholm integral equation in the Laplace transform plane:

$$\Phi^*(\xi,p) + \int_0^1 K(\xi,\eta,p)\Phi^*(\eta,p)d\eta = \sqrt{\xi} \tag{27}$$

The symmetric kernel $K(\xi,\eta,p)$ is given as

$$K(\xi,\eta,p) = \sqrt{\xi\eta} \int_0^\infty s[F(s/a,p)-1]J_0(s\xi)J_0(s\eta)ds \tag{28}$$

NUMERICAL RESULTS AND DISCUSSION

Following the same procedure as in reference 5, the in-plane stresses near the crack tip may be expressed in terms of the local polar coordinates r and θ in figure 1 as

$$\sigma_x(r,\theta,t) = \frac{k_1(t)}{\sqrt{2r}} \cos\frac{\theta}{2}\left[1 - \sin\frac{\theta}{2}\sin\frac{3\theta}{2}\right] + O(r^0) \tag{29}$$

$$\sigma_y(r,\theta,t) = \frac{k_1(t)}{\sqrt{2r}} \cos\frac{\theta}{2}\left[1 + \sin\frac{\theta}{2}\sin\frac{3\theta}{2}\right] + O(r^0) \tag{30}$$

$$\tau_{xy}(r,\theta,t) = \frac{k_1(t)}{\sqrt{2r}} \cos\frac{\theta}{2}\sin\frac{\theta}{2}\cos\frac{3\theta}{2} + O(r^0) \tag{31}$$

in which the dynamic stress intensity factor k_1 is defined by

$$k_1(t) = L^{-1}\left\{\frac{\Phi^*(1,p)}{p}\right\} \sigma_0\sqrt{a} \tag{32}$$

In equation (32), the symbol L^{-1} represents the Laplace inversion operator and

$\Phi^*(1,p)$ is value of $\Phi^*(\xi,p)$ at the crack tip (ξ=1). Numerical values of the normalized stress intensity factor $k_1(t)/\sigma_o\sqrt{a}$ in equation (32) are obtained as a function of c_2t/a for a Poisson's ratio of ν = 0.25 and a/h = 0.0, 0.5, 1.0 and 2.0. The general behavior of the curves in figure 2 is that they all oscillate with decreasing amplitude and reduce to the static values in table I as t becomes infinite. Note that the maximum value of $k_1(t)$ increases with a/h and a time delay between each maximum is observed as a/h is increased. For a/h = 2.0, the dynamic stress intensity factor can be one and a half times greater than the corresponding static value. It is interesting to note that for large cracks in a narrow strip or large a/h ratios, small oscillations of the $k_1(t)$ curves for $c_2t/a < 0.5$ are observed. These small peaks are generated by the arrival of the reflected waves from the strip boundaries to the crack tip region. For small values of a/h or as the strip height is increased, the reflected boundary waves become less significant and eventually do not affect the results. The larger peaks as discussed earlier are predominantly caused by the interaction of waves emanating from the crack tips.

Another quantity of interest is the crack opening displacement. It can be calculated from

$$\bar{u}_y = \frac{2\mu u_y(x,o)}{\sigma_o h} = \frac{a}{h(1-\kappa^2)} \int_{x/a}^{1} \sqrt{\xi}\, L^{-1}\left\{\frac{\Phi^*(\xi,p)}{p}\right\} \frac{d\xi}{\sqrt{\xi^2-(x/a)^2}} \qquad (33)$$

Variation of the normalized crack opening displacement $\bar{u}_y$ with the distance x/a is depicted in figure 3 for ν = 0.25, a/h = 0.25 and various c_2t/a values. The elliptic shape of the crack profile is maintained. However, the magnitude of $\bar{u}_y$ oscillates with time. This behavior can better be observed from figure 4 where the crack opening displacement at the center of the crack is plotted against c_2t/a for ν = 0.25 and a/h = 0.25 and 1.0. These curves have essentially the same behavior as the stress intensity factor curves.

REFERENCES

1. Keer, L. M.; Luong, W. C.: Diffraction of Waves and Stress Intensity Factors in a Cracked Layered Composite. J. Acoust. Soc. Am., vol. 56, no. 6, 1974, pp. 1681-1686.

2. Luong, W. C.; Keer, L. M.; Achenbach, J. D.: Elastodynamic Stress Intensity Factors of a Crack Near an Interface. Int. J. Solids Structures, vol. 11, 1975, pp. 919-925.

3. Anderson, J. M.; Aberson, J. A.; King, W. W.: Finite Element Analysis of Cracked Structures Subjected to Shock Loads. Computational Fracture Mechanics, American Society of Mechanical Engineers Publication, 1975, pp. 173-184.

4. Chen, Y. M.: Numerical Computation of Dynamic Stress Intensity Factors By a Lagrangian Finite-Difference Method (The Hemp Code). Eng. Fract. Mech., vol. 7, 1975, pp. 653-660.

5. Sih, G. C.; Embley, G. T.; Ravera, R. S.: Impact Response of a Finite Crack in Plane Extension. Int. J. Solids Structures, vol. 8, 1972, pp. 977-993.

6. Sih, G. C.: Dynamic Aspects of Crack Propagation. Inelastic Behavior of Solids, Edited by M. F. Kanninen, W. F. Adler, A. R. Rosenfeld and R. I. Jaffe, McGraw-Hill Co., 1970, pp. 607-639.

7. Copson, E. T.: On Certain Dual Integral Equations. Proc. Glasgow Math. Assoc., vol. 5, 1961, pp. 21-24.

TABLE I. - STATIC VALUES OF EQUATION (32)

a/h	0.0	0.5	1.0	2.0
$k_1/\sigma_o\sqrt{a}$	1.00	1.26	1.62	3.38

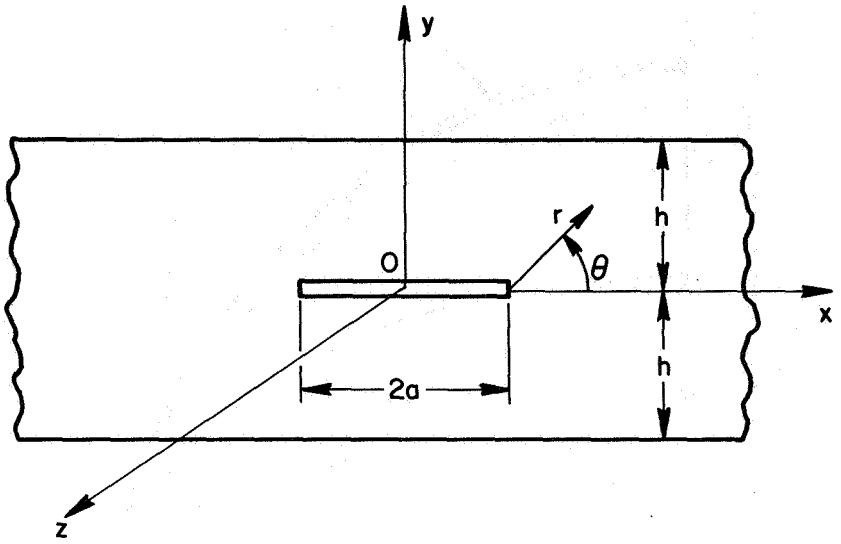

Figure 1.- A strip of material containing a crack.

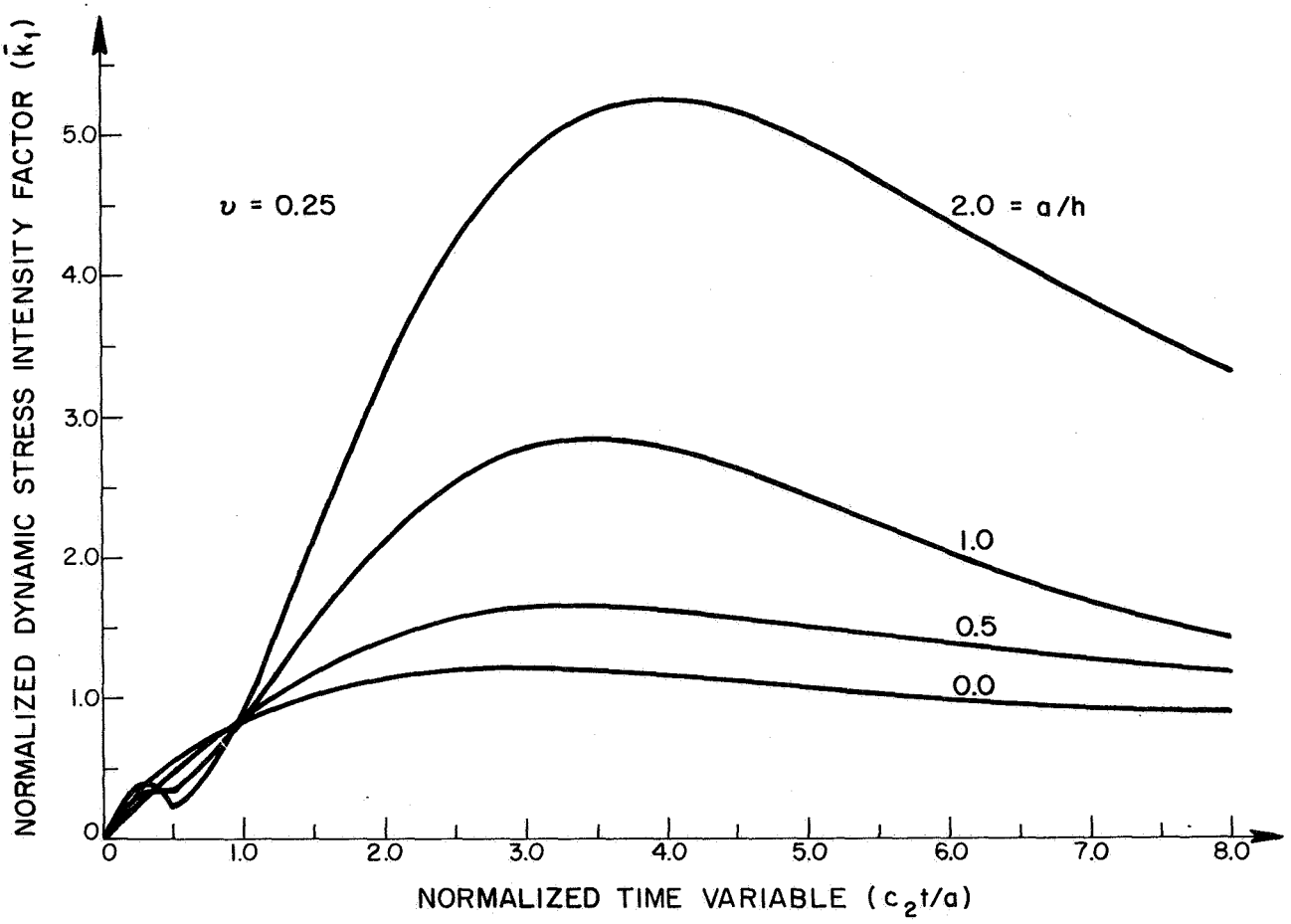

Figure 2.- Normalized dynamic stress intensity factor versus time.

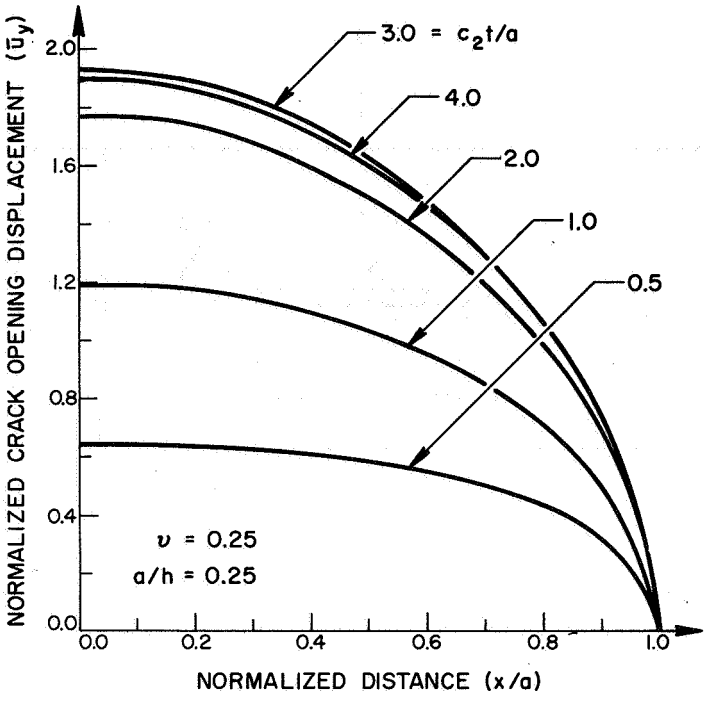

Figure 3.- Normalized crack opening displacement as a function of location.

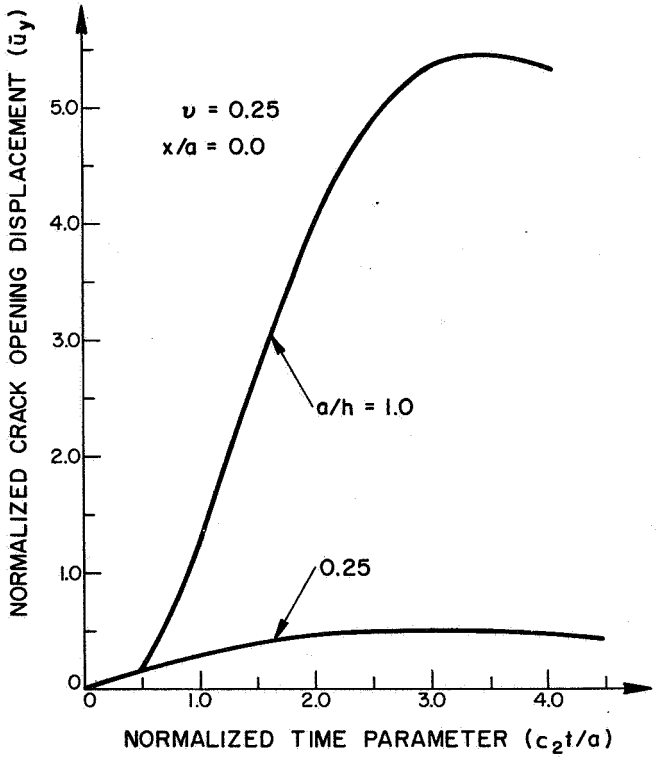

Figure 4.- Normalized crack opening displacement versus time.

FINITE-ELEMENT ANALYSIS OF DYNAMIC FRACTURE*

J. A. Aberson, J. M. Anderson and W. W. King
Georgia Institute of Technology

SUMMARY

Applications of the finite-element method to the two-dimensional elastodynamics of cracked structures are presented. Stress-intensity factors are computed for two problems involving stationary cracks. The first serves as a vehicle for discussing lumped-mass and consistent-mass characterizations of inertia. In the second problem the behavior of a photoelastic dynamic-tear-test specimen is determined for the time prior to crack propagation. Finally, some results of a finite-element simulation of rapid crack propagation in an infinite body are discussed.

INTRODUCTION

During the last few years, the writers and several of their graduate students have been exploring the application of the finite-element method to elastodynamics problems of two-dimensional linear fracture mechanics. This work originated with the development, by Aberson and Anderson (ref. 1), of crack-tip singularity elements for use in equilibrium problems. These elements, one for opening-mode problems and one for mixed-mode problems, are rectangular so as to facilitate their utilization in regular-grid finite-element models. Displacement fields within the elements are represented by a finite series of Williams' eigenfunctions. Subsequently, Morgan (ref. 2) deduced the consistent-mass matrices for these elements and developed a finite-element computer program, employing the Newmark-β method ($\beta = 1/4$) for time integration, for the analysis of transient elastodynamic problems of bodies with stationary cracks. Appraisals of the elastodynamic performances of the singularity elements and the solutions of several problems may be found in references 3 and 4.

Recently the writers have initiated a research program on finite-element simulation of rapidly propagating cracks in order to address questions associated with unstable crack propagation and crack arrest. Initial results of this work have been reported in references 5 and 6.

The purposes of this paper are threefold: (1) to present results of numerical experiments motivated by questions as to the advantages of different mass distribution schemes and time-integration algorithms; (2) to report a finite-element simulation of specimen behavior, prior to crack propagation, in

* The research described in this paper was supported in part by the U.S. Air Force under contract F08635-76-C-0136 with the Armament Development and Test Center, Eglin Air Force Base.

a dynamic tear test; (3) to supplement results of a study (ref. 5) of finite-element simulation of rapid crack propagation in an infinite sheet.

STATIONARY CRACKS

A Test Problem

The scheme for assigning mass distribution in a finite-element model and the choice of time-integration algorithm are worthy of some discussion. The consistent-mass scheme is favored by many vibration analysts primarily for its role in providing upper bounds on fundamental frequencies. However, there is a substantial body of opinion, e.g. references 7 and 8, that lumped-mass characterizations are superior to consistent-mass characterizations of inertia for problems of wave propagation. Neither scheme holds a significant advantage for calculations with the Newmark-β method, since in this implicit method a linear combination of mass and stiffness matrices must be inverted. However, for time integration by the explicit central-difference method, only the mass matrix need be inverted, and this becomes trivial with the lumped-mass scheme, since it results in a diagonal mass matrix. The Newmark-β ($\beta = 1/4$) method which is often called the constant-average-acceleration method has the virtue of unconditional stability, while for stability the central-difference method requires a time step substantially less than the least natural period of the discretized structure under study. Since such a small time step usually is not justified by requirements of accuracy, in many instances the Newmark-β method, with its more complex calculations, may be more economical than the central-difference method. To shed some light on these issues, a series of numerical experiments have been conducted for a problem solved by Chen (ref. 9) using finite differences in space and time.

Chen's problem consists of the plane-strain response of a centrally cracked ($2a = 0.48$ cm) rectangular strip (2 cm $\times$ 4 cm) subjected to suddenly applied and maintained tension σ at each end. Properties of the strip were taken to correspond nominally to steel. The geometry of the problem is shown in figure 1a, where the shaded quadrant indicates the region of 5000 mesh points used by Chen in his finite-difference analysis. A finite-element model composed of constant-strain triangles and singularity-element ABCD and representing this region is shown in figure 1b. Time integration was accomplished by the Newmark-β method with 75 steps, each of 0.2 μs; this choice of time increment was motivated by the transit time (0.22 μs) of a longitudinal wave across the smallest of the triangular elements. Stress-intensity factors obtained from the finite-element model using the consistent-mass and lumped-mass schemes are shown in figure 2. These results are in substantial agreement, the most striking differences occurring around sharp local maxima and minima of the stress intensity factor. In reference 4 the consistent-mass results have been shown to be in excellent agreement with those of Chen. The lumped-mass model predicts a peak stress-intensity factor 5% higher than that reported by Chen while the consistent-mass model predicts a value 2% lower than that of Chen.

Contrary to the contention of Bazant et al (ref. 8), essentially the same results were obtained for each case when the time step was reduced to 0.01 μs

(ref. 10). At this smaller step, central-difference calculations yielded results indistinguishable from those of Newmark-β when plotted to the scale of figure 2. Frick, in reference 10, discovered by numerical experiments that the maximum time step for stable central-difference integration of the lumped-mass model was 0.016 μs. This is surprising in light of the often-used rule that the critical step size will be approximately the longitudinal-wave transit time across the smallest element in the model. This discrepancy apparently is attributable to the stiffness characteristics of the singularity element; when the element was replaced by six constant-strain triangles, the critical time step increased dramatically to about 0.19 μs which is consistent with the transit time of 0.22 μs. Consequently, because of the small time step required, it appears that, when used in conjunction with the singularity element, the central-difference integration scheme offers no computational advantage.

Analysis of a Dynamic Tear Test

Impact of a falling weight with a precracked beam is an experimental method for determination of dynamic fracture toughnesses. Successful interpretation of such tests depends upon an accurate appraisal of the elastodynamics of both the specimen and the hammer; the ideal situation is one in which the hammer may be treated as a rigid body and the specimen behavior is quasi-static. However, often it is not possible to satisfy both of these conditions; in that event a dynamic finite-element analysis may play a useful role in predicting time-dependent stress-intensity factors.

Depicted in figure 3 is a finite-element model of a dynamic-tear-test specimen of Homalite-100, a photoelastic material, with which experiments have been conducted by Kobayashi and Chan (ref. 11). The specimen support and loading configuration is essentially that of a Charpy test except that a translating steel hammer is used in place of a pendulum for the impact source. Since steel has an acoustic impedance of approximately eighteen times that of Homalite-100 and a longitudinal-wave speed of about two and one-half that of Homalite-100, it is reasonable to regard the hammer as a rigid body in an analysis of the specimen. Thus, as is indicated in figure 3, which depicts only half of the specimen because of symmetry, the node corresponding to the impact point is assigned a mass equal to one-half the mass M of the hammer. This node is then given an initial velocity V_o equal to the impact velocity; all other nodes have zero initial velocity.

Since the specimen is relatively thin (0.0095m), plane-stress forms of the elements were used in the computations which were carried out using the consistent-mass Newmark-β scheme (time step = 2 μs) for a crack length of 0.005m. The numerical results are given in figure 4 where the stress-intensity factor and hammer acceleration are plotted for the first 200 μs following contact of the hammer with the specimen. The Kobayashi-Chan experiments were concerned primarily with the crack propagation phase of the motion, and they reported only limited data that bears on the interval prior to propagation. Nonetheless, the experimental evidence suggests that for conditions corresponding to the analytical model, the crack began to extend at some time prior to 200 μs after impact. It should be noted from figure 4 that the static

toughness, k_c = 342 kPa - $\sqrt{m}$, is attained during this interval. Moreover, Professor Kobayashi has communicated to the writers that the peak specimen load, deduced from strain gages on the hammer tup, is in excellent agreement with the peak hammer acceleration deduced from the finite-element model. Of greatest importance, perhaps, is that there is apparently no simple correspondence between the stress-intensity factor and the hammer acceleration (or specimen load). This is not surprising in light of the fact that the time for a longitudinal wave to propagate from the impact point to one of the supports and then to the crack is about 185 μs (the first signal of impact is felt at the crack tip at 44 μs). Thus, for the time interval of interest, the motion of the specimen is definitely not that of a beam.

RUNNING CRACKS

Problems of unstable crack propagation are the subjects of much current research activity, and, in the absence of exact solutions, there is a real need for reliable numerical methods for analyzing the motions of finite bodies containing rapidly propagating cracks. The writers (refs. 5 and 6) and other investigators (refs. 12 and 13) have endeavored to bring the finite-element method to bear on such problems. A problem solved by Broberg (ref. 14) is one of the few genuine initial-value problems of physically meaningful crack extension to which an exact solution has been obtained, and, therefore, it has been selected as a test problem to provide guidance in establishing mesh-size and time-step requirements for finite-element simulation. In this section some results of the first stage of a program of numerical experimentation are presented.

Shown in figure 5 is a finite-element model of one quadrant of a rectangular region of sufficient size to simulate, for the time intervals and crack speeds of interest, the infinite space of Broberg's problem. The problem is that of an infinite body in equilibrium with a uniform uniaxial tension $\sigma_y = \sigma$ prior to t = 0, at which time a crack begins to grow symmetrically, from zero initial length, each tip moving at constant speed c. In the finite-element analysis crack propagation is simulated by the sequential release of restraints on the nodes at the base of the model. Thus, one crack tip starts at the lower left corner of the model (fig. 5) and moves along the x-axis, and a nodal restraint is removed at the time at which the crack tip (from a continuum point of view) reaches the node in question. Each element of the model is a constant-strain triangle, and the characteristic length L is the largest half-length of the crack; the smallest distance between nodes is L/10. For material properties such that the ratio of longitudinal and shear wave speeds $c_1/c_2 = 2$, crack speeds of c/c_2 = 0.2, 0.4, 0.6, and 0.8 have been considered. Introducing dimensionless time, $\tau = c_2 t/L$, the time of propagation is $\tau = 5$, and the interval between releases of adjacent nodes is $\Delta\tau = 0.5$ for the case $c/c_2 = 0.2$. Within this interval the equations of motion were integrated using the consistent-mass Newmark-β method; ten time steps, $\Delta\tau = 0.05$, were used. Ten time steps also were used within an interval of incremental propagation for each of the other crack-speed cases; e.g. at $c/c_2 = 0.8$ the time step was $\Delta\tau = 0.0125$. It should be noted that the largest time step used was the transit time of a longitudinal wave across the smallest element in the model.

Displacements resulting from these calculations have been used to compute stress-intensity factors which were reported in reference 5 . These stress-intensity factors were determined by a least-squares fitting of near-tip nodal displacements to an assumed near-tip displacement field described by a finite series of running-crack eigenfunctions, one of which describes the stress singularity at the crack tip. While stress-intensity factors were determined (for all four crack speeds) to within 15% of the exact solution using one particular pattern of near-tip nodal displacements and a four-term series of eigenfunctions, Malluck (ref. 15) has shown that the results are sensitive to the nodal pattern and number of eigenfunctions employed. Thus, the approach for extracting stress-intensity factors is promising, but additional studies are needed.

One issue of concern is the effect of the necessarily discrete advance of the crack tip in the finite-element simulation. This effect is difficult to identify in the calculated stress-intensity factors because they have been deduced from "averaged" near-tip nodal displacements. It is therefore useful to compare crack-face displacements determined from the finite-element analysis with those deduced by Broberg. With v as vertical displacement and μ as shear modulus, dimensionless displacements $\mu v/\sigma L$ at two points, $x/L = 0$ and 0.5, are plotted in figure 6 against dimensionless time ct/L for the case $c/c_2 = 0.2$. It should be noted that in the finite-element analysis nodal releases occur at $ct/L = 0$, 0.1, 0.2, etc. While the finite-element results generally follow those of Broberg, they oscillate somewhat erratically, which is likely a consequence of the simulation process. Displacements of the same points are plotted in figure 7 for $c/c_2 = 0.8$. For that case the finite-element displacements vary more smoothly with time, although errors are about the same as in the first case. The time span of figure 6 is, of course, four times that of figure 7, and the time steps in the numerical integrations were in the same ratio. However, recent calculations by J. F. Malluck for the case $c/c_2 = 0.2$, using smaller integration steps, indicate that the results shown in figure 6 are not significantly altered by this requirement. It appears, therefore, that a procedure, perhaps similar to that of reference 13, for gradually releasing nodes would be beneficial to the finite-element analysis. An appropriate method for this is being studied currently.

CONCLUDING REMARKS

Successful applications of the finite-element method to a number of stationary-crack elastodynamic problems (of which two have been presented here) support the conclusion that this is a reliable and practical method for computing time-dependent stress-intensity factors even under conditions of stress-wave loading. It is now appropriate to consider engineering applications; foremost among these are impact tests designed to determine fracture toughnesses associated with the onset of crack propagation under high rates of loading. The writers believe that the finite-element approach can play a significant role in the interpretation of current experiments and possibly in the design of improved tests.

Although additional numerical experimentation is required before the finite-element method can be relied upon to provide accurate analyses of rapid crack propagation, initial results are encouraging. For this kind of analysis, there exist many important potential applications, most notably the support of experiments designed to establish criteria for rapid crack propagation and crack arrest.

REFERENCES

1. Aberson, J. A., Anderson, J. M.: Cracked Finite Elements Proposed for NASTRAN. Third NASTRAN User's Colloquium, NASA TMX-2893, NASA Langley Research Center, 1973, pp. 531-550.

2. Morgan, J. D., III: Dynamics of Cracked Structures Using Finite Elements. Ph.D. Thesis, Georgia Institute of Technology, Atlanta, Georgia, 1974.

3. Morgan, J. D., III, Anderson, J. M. and King, W. W.: Elastodynamics of Cracked Structures Using Finite Elements. AIAA Journal, vol. 12, no. 12, 1974, pp. 1767-1769.

4. Anderson, J. M., Aberson, J. A. and King, W. W.: Finite Element Analysis of Cracked Structures Subjected to Shock Loads. Computation Fracture Mechanics, Edited by E. F. Rybicki and S. E. Benzley, American Society of Mechanical Engineers, New York, 1975, pp. 173-184.

5. King, W. W., Malluck, J. F., Aberson, J. A. and Anderson, J. M.: Application of Running-Crack Eigenfunctions to Finite-Element Simulation of Crack Propagation. Mechanics Research Communications, vol. 3, no. 3, 1976, pp. 197-202.

6. Aberson, J. A., Anderson, J. M. and King, W. W.: Singularity-Element Simulation of Crack Propagation. Paper presented at the Symposium on Fast Fracture and Crack Arrest, American Society for Testing and Materials, Chicago, Illinois, June 28-30, 1976.

7. Clough, R. W.: Analysis of Structural Vibrations and Dynamic Response. Recent Advances in Matrix Methods of Structural Analysis and Design, Edited by R. H. Gallagher, Y. Yamada and J. T. Oden, University of Alabama Press, 1971, pp. 441-482.

8. Bazant, Z. P., Glazik, J. L., Jr. and Achenback, J. D.: Finite Element Analysis of Wave Diffraction by a Crack. Journal of the Engineering Mechanics Division, American Society of Civil Engineers, vol. 102, no. EM3, 1976, pp. 479-496.

9. Chen, Y. M.: Numerical Computation of Dynamic Stress Intensity Factors by a Lagrangian Finite-Difference Method (the Hemp Code). Engineering Fracture Mechanics, vol. 7, 1975, pp. 653-660.

10. Frick, T. G.: The Transient Dynamic Analysis of Cracked Structures by the Finite Element Method. M.S. Report, Georgia Institute of Technology, Atlanta, Georgia, 1975.

11. Kobayashi, A. S. and Chan, C. F.: A Dynamic Photoelastic Analysis of Dynamic-tear-test-specimen. Experimental Mechanics, vol. 16, no. 5, 1976, pp. 176-181.

12. Kobayashi, A. S., Emery, A. F. and Mall, S.: Dynamic Finite Element and Dynamic Photoelastic Analyses of Two Fracturing Homalite-100 Plates. University of Washington Technical Report No. 23, Office of Naval Research Contract N00014-76-C-0060, NR 064-478, December, 1975.

13. Yagawa, G., Sakai, Y. and Ando, Y.: Analysis of Rapidly Propagating Crack Using Finite Elements. Paper presented at the Symposium on Fast Fracture and Crack Arrest, American Society for Testing and Materials, Chicago, Illinois, June 28-30, 1976.

14. Broberg, K. B.: The Propagation of a Brittle Crack. Arkiv Fysik, vol. 18, 1960, pp. 159-192.

15. Malluck, J. F.: Crack Propagation in Finite Bodies, Ph.D. Thesis, Georgia Institute of Technology, Atlanta, Georgia, 1976.

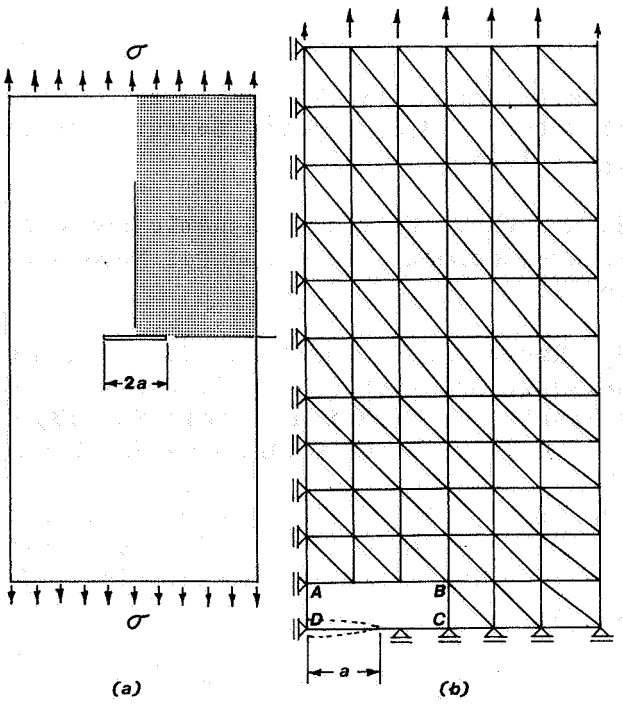

Figure 1.- Chen's problem and the finite-element model.

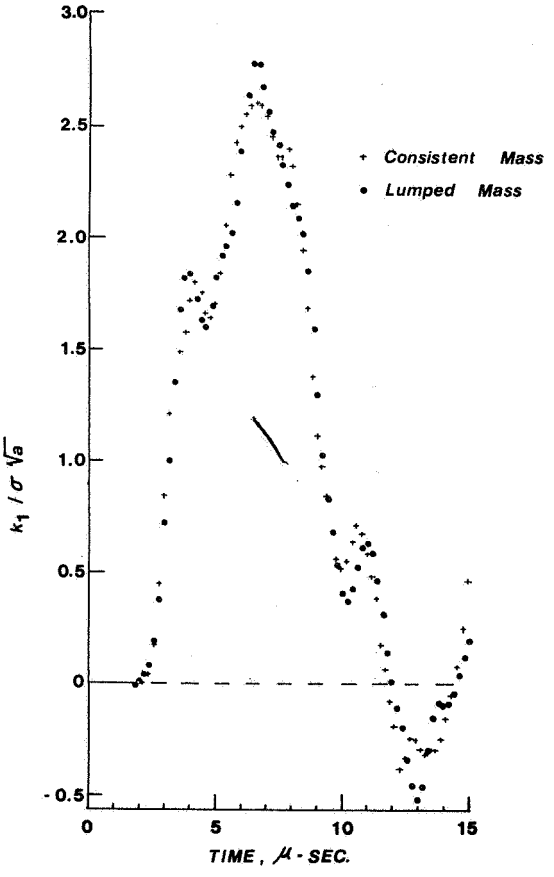

Figure 2.- Stress-intensity factors predicted using different mass distributions.

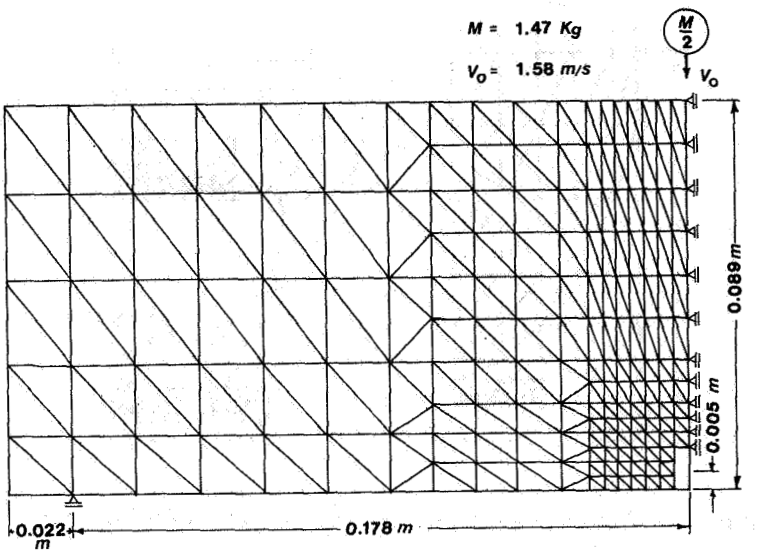

Figure 3.- Finite-element model of a dynamic-tear-test specimen.

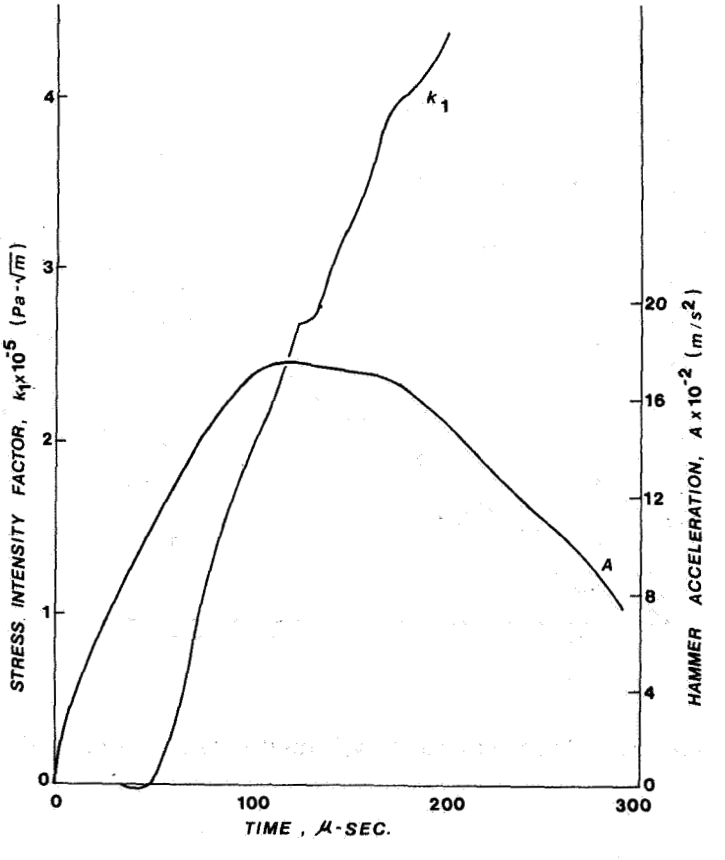

Figure 4.- Stress-intensity factor and hammer acceleration for a dynamic tear test.

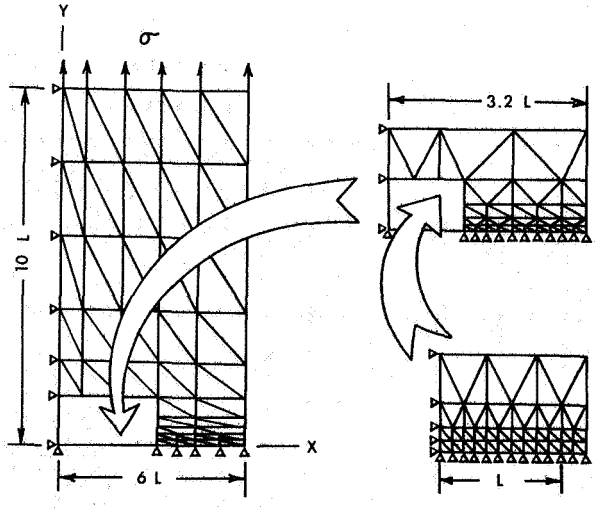

Figure 5.- Finite-element model of Broberg's problem.

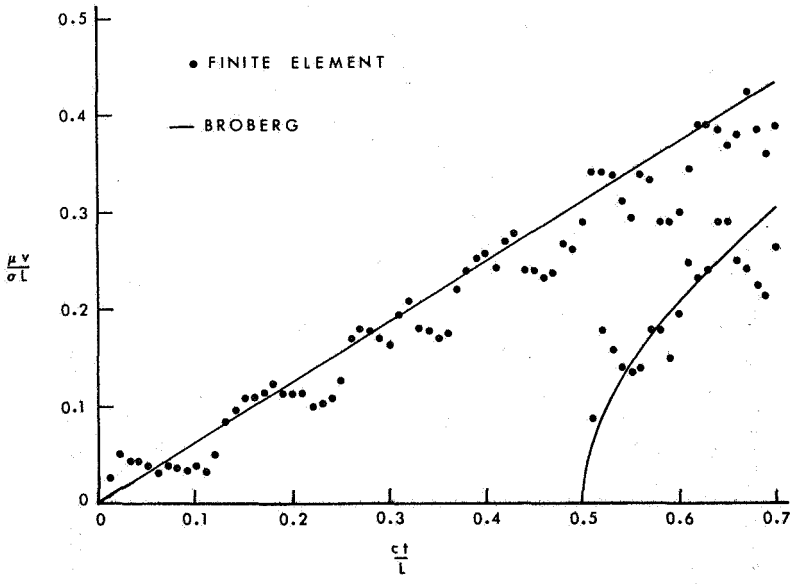

Figure 6.- Crack-face displacements. $c/c_2 = 0.2$.

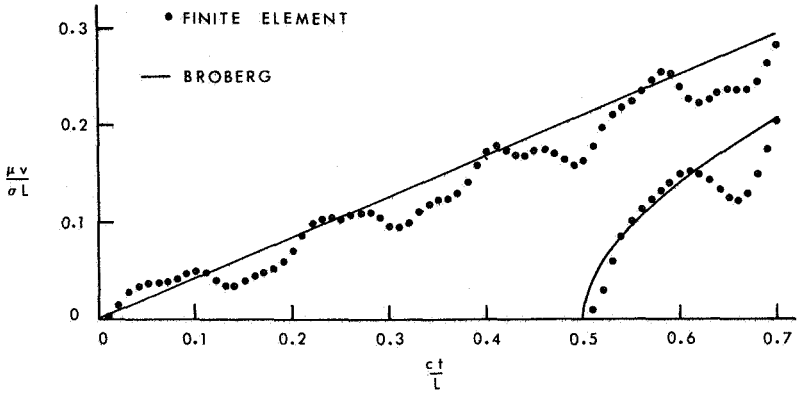

Figure 7.- Crack-face displacements. $c/c_2 = 0.8$.

APPLICATION OF A NOVEL FINITE DIFFERENCE METHOD TO DYNAMIC CRACK PROBLEMS*

Yung M. Chen
State University of New York at Stony Brook

Mark L. Wilkins
Lawrence Livermore Laboratory

INTRODUCTION

A versatile finite difference method (HEMP and HEMP 3D computer programs) has been developed originally for solving dynamic problems in continuum mechanics (refs. 1, 2, 3, 4). Now it has been extended to analyze the stress field around cracks in a solid with finite geometry subjected to dynamic loads and to simulate numerically the dynamic fracture phenomena (refs. 5, 6, 7, 8, 9) with success. This method is an explicit finite difference method applied to the **Lagrangian** formulation of the equations of continuum mechanics in two and three space dimensions and time. The calculational grid moves with the material and in this way it gives a more detailed description of the physics of the problem than the Eulerian formulation.

The important features of these computer programs are:

(a) The first order space partial derivatives of a scalar function are approximated by calculating fluxes through the boundaries. This type of approximation is of second order accuracy. It has the **advantages that the cubical** shaped calculational-grid can be generated to accommodate **free-form boundaries** of a particular object and no change in the computer logic is required if cubes are collapsed to triangles. In actual large-scale computation, using lower order accuracy method with more calculational grids to obtain better accuracy is often preferred to using a higher order method with less calculational grids. This is because less programing effort is needed and less uncertainty is encountered in applying boundary conditions for the lower order methods. The first order time derivative is approximated by the central difference scheme and the time step in calculation is determined automatically by the numerical stability criterion contained in the computer programs. Artificial viscosity is contained in the HEMP programs to damp out the stable numerical oscillations in the neighborhood where the solution has either a discontinuity or a steep gradient (Gibb's phenomenon). With the explicit finite difference method,

* Work done at Lawrence Livermore Laboratory under Energy Research and Development Administration contract No. W-7405-Eng-48 and at Department of Applied Mathematics and Statistics, State University of New York at Stony Brook under U. S. Army Research Office grant No. DAAG 29-76-G-0197.

the integration scheme itself does not impose the large computer-storage requirements that are necessary with the implicit finite difference methods and the well-known finite element methods.

(b) The complex descriptions of material behavior are contained only in the equation of state. Hence for solving problems with different materials (elastic solids, plastic solids, fluids, etc.), there is no change in the main computer program.

(c) A special sub-routine of extrapolation scheme for improving the accuracy of the numerical solution near a singularity is incorporated into the main computer program. A priori knowledge of the type of singularity is needed for the successful application of the extrapolation scheme. It is especially useful for computing the dynamic stress intensity factors. Additional improvement can be obtained by employing Richardson extrapolation.

(d) To simulate the dynamic fracture phenomenon in a solid numerically, the Lagrangian calculational grid must be able to split in order to describe the breakage of the solid. Two sub-routines are available for introducing the desired free-surface boundary conditions: One actually splits the grid (sliding-open-interfaces logic) and the other introduces the effect of the free-surface boundary conditions without actually splitting the calculational grid (method of equivalent free-surface boundary conditions).

(e) Suddenly splitting the calculational grid introduces spurious numerical errors which will then propagate in the calculational grid. In this case, the artificial viscosity in the main computer program is not sufficient for damping out this undesirable phenomenon. Hence a smoothing procedure, the method of artificial velocity, is incorporated in the main computer program to make each incremental volume break up smoothly.

To demonstrate the capability of the numerical technique, dynamic stress intensity factors for crack problems of different three-dimensional finite geometry are calculated.

FINITE DIFFERENCE SCHEME

The partial derivatives of a scalar function $F(x_1,x_2,x_3,t) \equiv F(\underline{r}, t)$ are approximated by

$$\partial F/\partial x_i \Big|_{\underline{r}_o} \simeq \frac{\oint_{\Delta s} F(\underline{n} \cdot \underline{l}_i)\, ds}{\Delta V}, \quad i = 1, 2, 3, \qquad (1)$$

where $\underline{l}_i$ is the unit vector in the direction of x_i, $\underline{n}$ is the outward unit normal vector of the surface Δs enclosing the incremental cubical volume ΔV and $\underline{r}_o$ is the center of ΔV. The surface integral is approximated by the trapezoidal rule. Basically, this type of finite difference scheme is second order. However, if the cubical ΔV is badly deformed from its original shape, this scheme will degenerate into a first order approximation.

For simplicity, only some of the important features are pointed out for the HEMP code. Details are given in references 1, 2, 4, and 7 . The first order space partial derivatives of velocities are computed at the zone center (fig. 1) and the half-integer time step, e. g.

$$\partial\dot{x}/\partial x \Big|_{\substack{t=(n+\frac{1}{2})\Delta t,\\ x=(j+\frac{1}{2})\Delta x,\\ y=(k+\frac{1}{2})\Delta y,}} = \frac{1}{2A_{①}^{n+\frac{1}{2}}}\left[(\dot{x}_2 - \dot{x}_4)(y_3 - y_1) - (\dot{x}_3 - \dot{x}_1)(y_2 - y_4)\right]^{n+\frac{1}{2}} \quad (2)$$

The first order space partial derivatives of stresses are computed at the grid point (fig. 2) and the integer time step, e. g.

$$\partial\sigma_{xx}/\partial x \Big|_{\substack{t=n\Delta t,\\ x=j\Delta x,\\ y=k\Delta y,}} = -4\left[\sigma^n_{xx①}(y^n_{II} - y^n_{III}) + \sigma^n_{xx②}(y^n_{III} - y^n_{IV}) + \sigma^n_{xx③}(y^n_{IV} - y^n_{I}) + \sigma^n_{xx④}(y^n_{I} - y^n_{II})\right]\left[\sum_{i=1}^{4} A_{ⓘ}\right]^{-1} \quad (3)$$

Boundary conditions can be implemented by using only one layer of phantom zones, where the quantities associated with the phantom zones can be adjusted to satisfy the given boundary condition.

THREE-DIMENSIONAL CRACK PROBLEMS

To demonstrate the capability of the HEMP 3D code for solving dynamic problems in linear fracture mechanics, several different crack geometries under Heaviside-function time dependence loads are considered (refs. 6, 7, 9).

First, a centrally embedded elliptical crack in a linear elastic rectangular parallelopiped under normal tension PH(t) with μ = 77 GPa, K (bulk modulus) = 165 GPa and ρ^0 = 7.9 Mg/m^3 is considered. The geometry and zoning of one octant of the actual specimen are shown in figure 3. The calculated k_1/P vs. t curve is shown in figure 4. Its dynamics are similar to the case of central crack in a rectangular bar under plane strain loading. The corresponding semielliptic surface crack is also considered. The geometry and zoning of one quadrant of the actual specimen and the calculated k_1/P vs. t curve are shown in figures 3 and 5, respectively. The maximum value of the dynamic stress intensity factor undergoes a relaxation which can be correlated with the changes in the shape of crack surfaces under the dynamic load.

Next, a section of a pipe with a through-the-thickness crack in either the axial direction or the circumferential direction is shown in figure 6. The material is linear elastic with μ = 76.923 GPa, K = 166.667 GPa, and ρ^0 = 5 Mg/m^3. Symmetry boundary conditions were assumed for each end of the pipe. A sudden pressure PH(t) has been applied to the interior of the pipe. Figures 7 and 8 show $3k_1/4P$ versus radial position R in the cylinder wall at several times for the axial crack with length 64 mm and the circumferential crack with approximate length 68.12 mm, respectively. The calculated time histories of the dynamic stress intensity factors for an axial and a circumferential crack are shown in figure 9. It shows that k_1(t) [axial crack]>> k_1(t) [circumferential crack of approximately equal crack length]. Finally, figure 10 shows

the normalized dynamic stress intensity factor $3k_1/4P$ for axial cracks with different crack lengths. The difference between $k_1(t)$ for the shorter crack length and the longer crack length is completely dynamical.

COMPUTER SIMULATION OF FRACTURE

There are two requirements for computer simulation of the initiation, propagation and arresting of cracks (refs. 1, 2, 7). The first is the physical model represented by a sequence of programing instructions which determine if a crack is going to initiate or to stop and describe the conditions for its propagation. The second requirement is a method to represent a moving crack in the calculational scheme. Due to the complexity of the underlying physics, the first requirement will not be discussed here. Nevertheless, the important point here is that at best the computer can do only what it is instructed to do.

To simulate the dynamic fracture phenomena in a solid numerically, the continuous Lagrangian calculational grid must be able to split in order to describe the breakage of the solid. Two sub-routines are available for introducing the desired free-surface (under tension) and quasi-free-surface (under compression) boundary conditions. One sub-routine does actually split the grid (sliding-open-interfaces logic). It has the advantage of providing accurate fracture geometry and the disadvantage of double storage needed for each grid point. The other introduces the effect of fracturing of a zone without actually splitting the calculational grid (method of equivalent free-surface boundary conditions). However, the fracture geometry here is represented at best by a band of fractured zones with single zone width.

Due to the nature of hyperbolic partial differential equations, sudden splitting (or effectively splitting) of the calculational grid introduces significant disturbances in the stresses and displacements in the neighborhood of the crack tip which will then propagate in the characteristic directions of the calculational grid. In this case, the artificial viscosity imbedded in the main computer program is not sufficient for damping out this undesirable phenomenon. Hence a smoothing procedure, the method of artificial velocity, is incorporated in the main computer program to make each incremental volume break up smoothly. Here in HEMP calculations, when the critical fracture criterion is reached at time t_c, a smoothing parameter

$$F^{n+1} \equiv F \text{ at } (n+1)\Delta t = \frac{t^{n+1} - t_c}{\Delta L}, \quad 0 < F \leq 1, \quad \Delta L = \Delta x / V_c, \tag{4}$$

is calculated.

Here $t^{n+1} = (n+1)\Delta t$ is some time after t_c, Δx is a typical zone dimension and V_c is an estimated artificial crack propagation velocity. The parameter V_c is not critical in the smoothing process here. $F = 1$ denotes complete fracture and $F = 0$ denotes integral material. The parameter F is then used in the acceleration equations to apply free-surface boundary conditions to a zone. This procedure allows a fracture to run smoothly through the grid independent of the zone size. The actual computed fracture velocity will depend on the load, the geometry, and the physical model of the particular problem.

REFERENCES

1. Wilkins, M.L.: Calculation of Elastic-Plastic Flow, Methods in Computational Physics, Vol. 3, ed. by Alder, B., Fernbach, S., and Rotenberg, M., Academic Press, New York, 1964, pp. 211-262.

2. Wilkins, M.L.: Calculation of Elastic-Plastic Flow, Rept. UCRL-7322 Rev. 1, Lawrence Livermore Laboratory, 1969.

3. Wilkins, M.L., French, S.J., and Sorem, M.: Finite Difference Scheme for Calculating Problems in Three Space Dimensions and Time, Lecture Notes in Physics, Vol. 8, ed. by Holt, M. (Proc. 2nd Int. Conf. Numerical Methods in Fluid Dynamics), Springer-Verlag, New York, 1971, pp. 30-33.

4. Wilkins, M.L., Blum, R.E., Cronshagen, E., and Grantham, P.: A Method for Computer Simulation of Problems in Solid Mechanics and Gas Dynamics in Three Space Dimensions and Time, Rept. UCRL-51574, Rev. 1, Lawrence Livermore Laboratory, 1975.

5. Chen, Y.M.: Numerical Computation of Dynamic Stress Intensity Factors by a Lagrangian Finite-Difference Method (the HEMP Code), Eng. Fract. Mech., Vol. 7, 1975, pp. 653-660.

6. Chen, Y.M. and Wilkins, M.L.: Fracture Analysis With a Three-Dimensional Time-Dependent Computer Program, Int. J. Fract., Vol. 12, 1976.

7. Chen, Y.M. and Wilkins, M.L.: Numerical Analysis of Dynamic Crack Problems, Dynamic Crack Propagation, Vol. IV of Mechanics of Fracture, ed. by Sih, G.C., Noordhoff Int. Pub., Leyden, The Netherlands.

8. Chen, Y.M. and Wilkins, M.L.: Numerical Analysis of Notches Under Dynamic Loads, Stress Analysis of Notch Problems, Vol. V of Mechanics of Fracture, ed. by Sih, G.C., Noordhoof Int. Pub., Leyden, The Netherlands.

9. Chen, Y.M. and Wilkins, M.L.: Dynamic Fracture Analysis With a Lagrangian Finite Difference Method, Rept. UCRL-77257 Rev. 1 , Lawrence Livermore Laboratory, 1976.

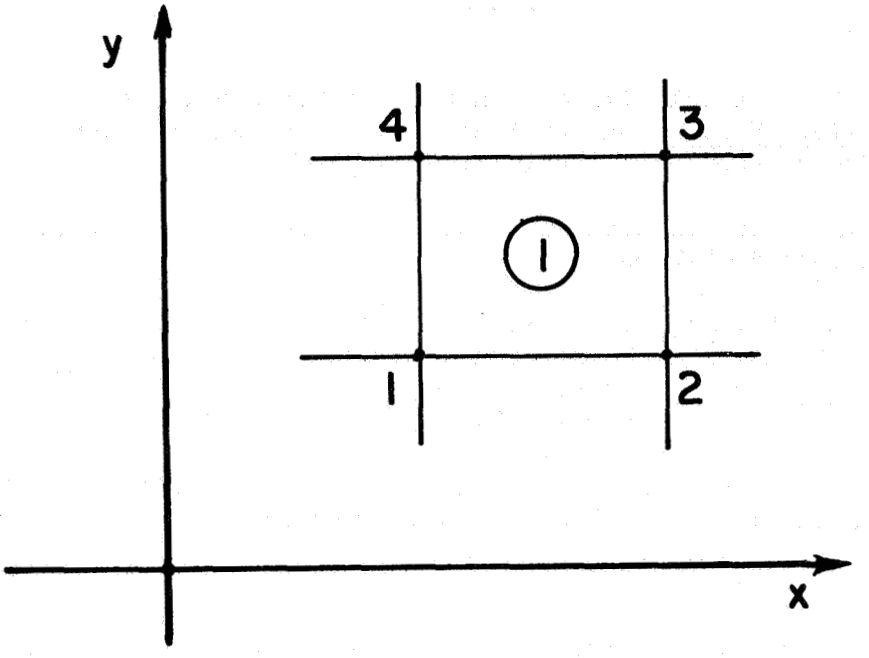

Figure 1.- Finite difference scheme for strains.

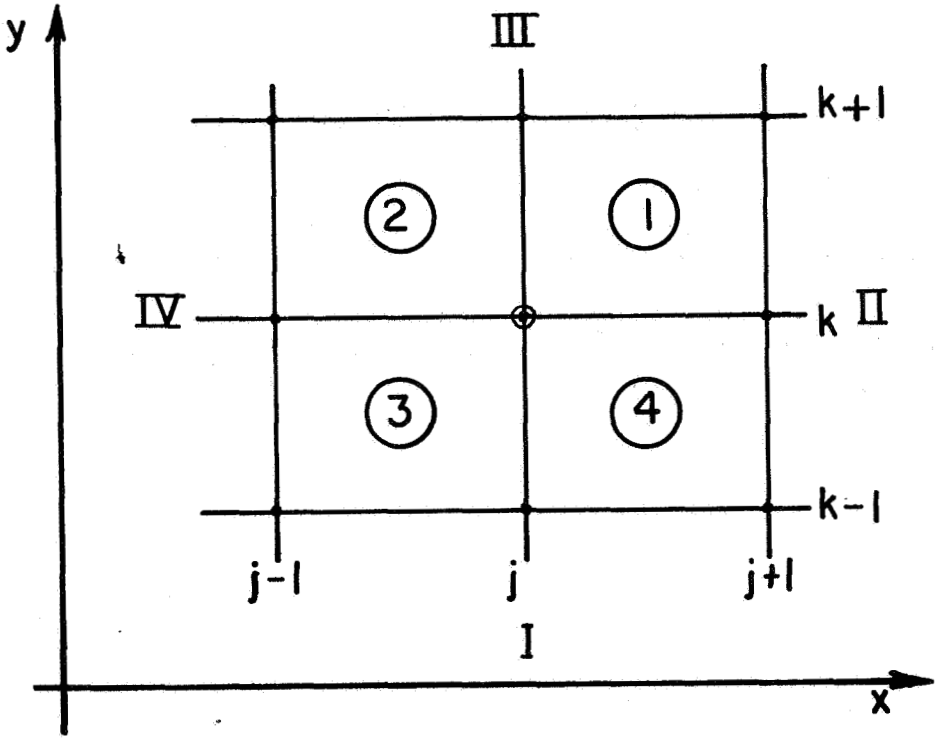

Figure 2.- Finite difference scheme for equations of motion.

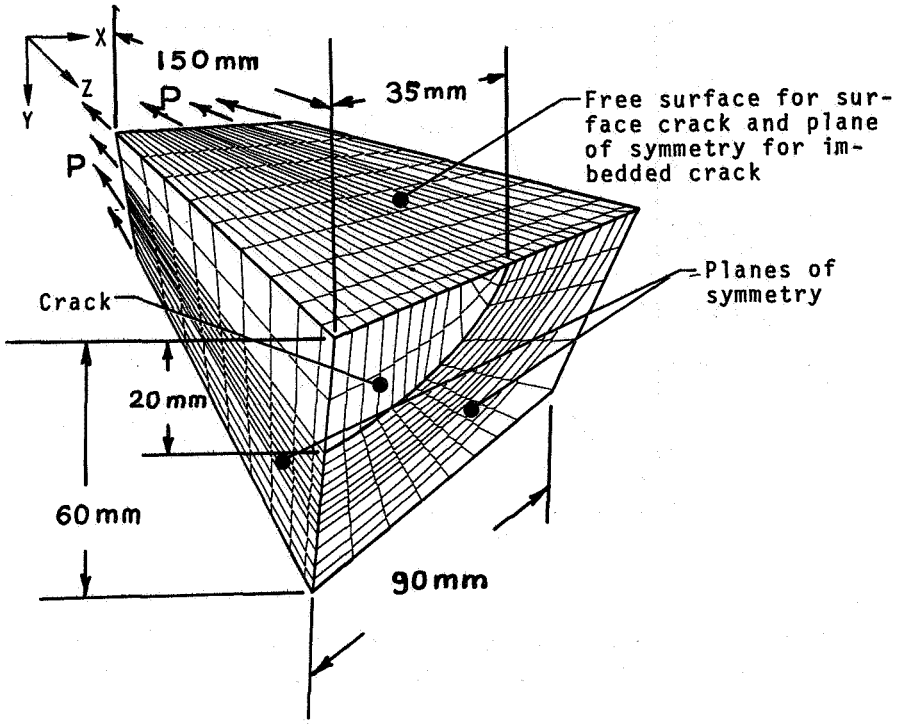

Figure 3.- Lagrange grid used in calculations of a semielliptic surface crack and an imbedded elliptical crack.

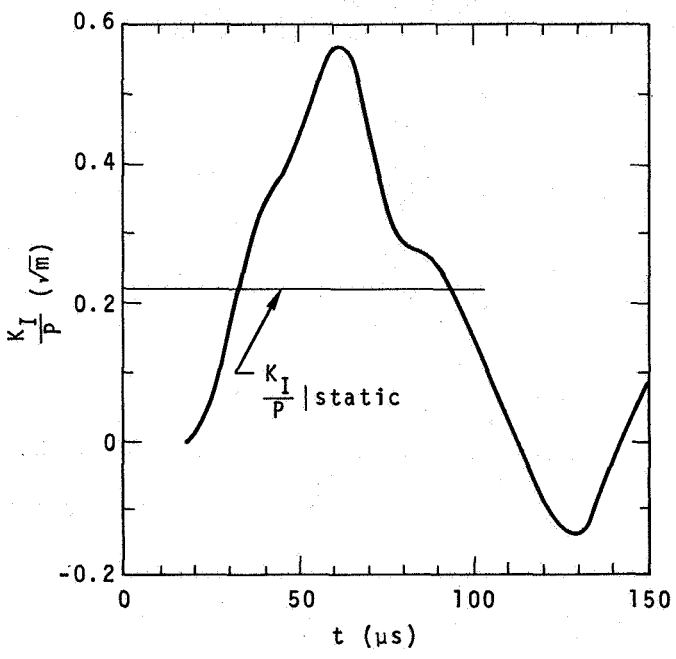

Figure 4.- Normalized stress intensity factor versus time for imbedded elliptical crack.

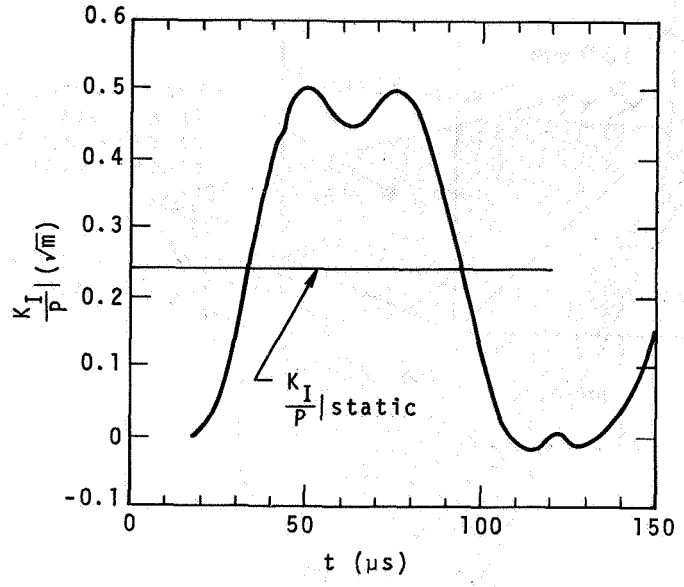

Figure 5.- Normalized stress intensity factor versus time for semielliptic surface crack.

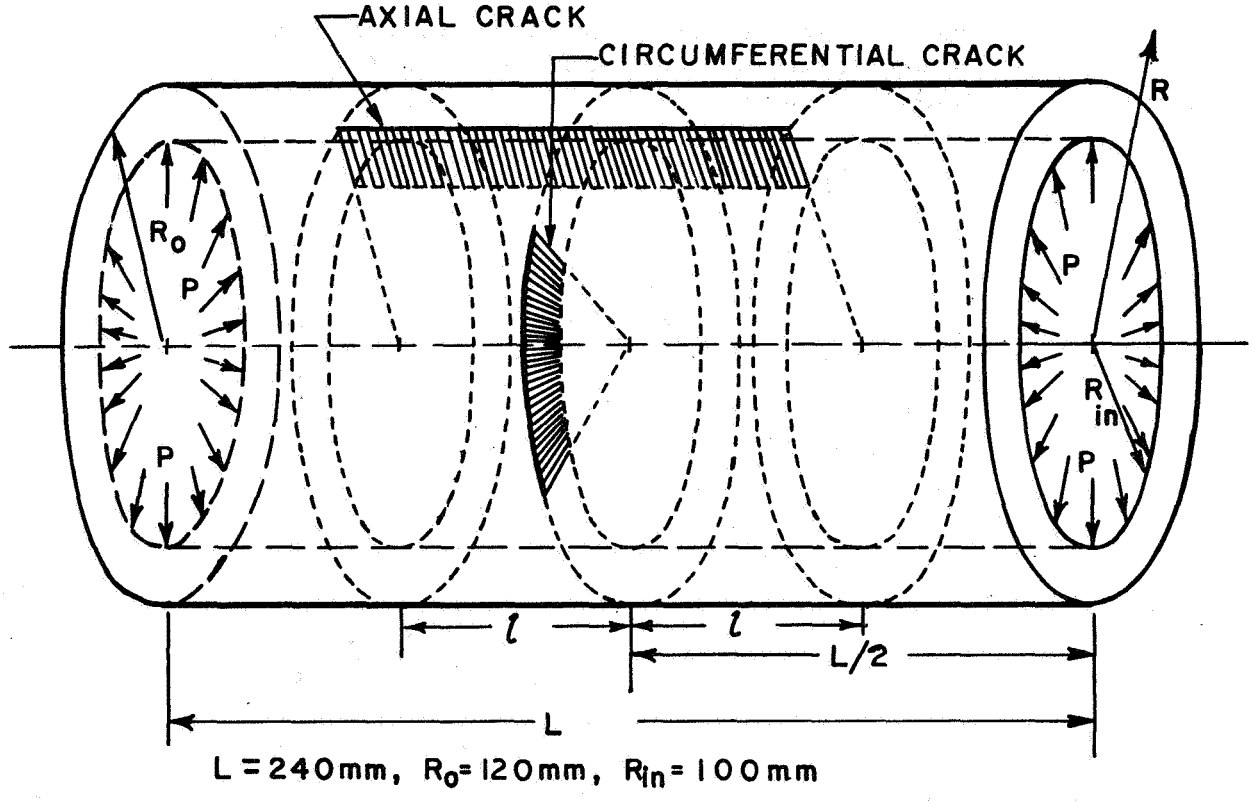

Figure 6.- Geometry of the axial and circumferential cracks in the wall of a section of cylindrical pipe.

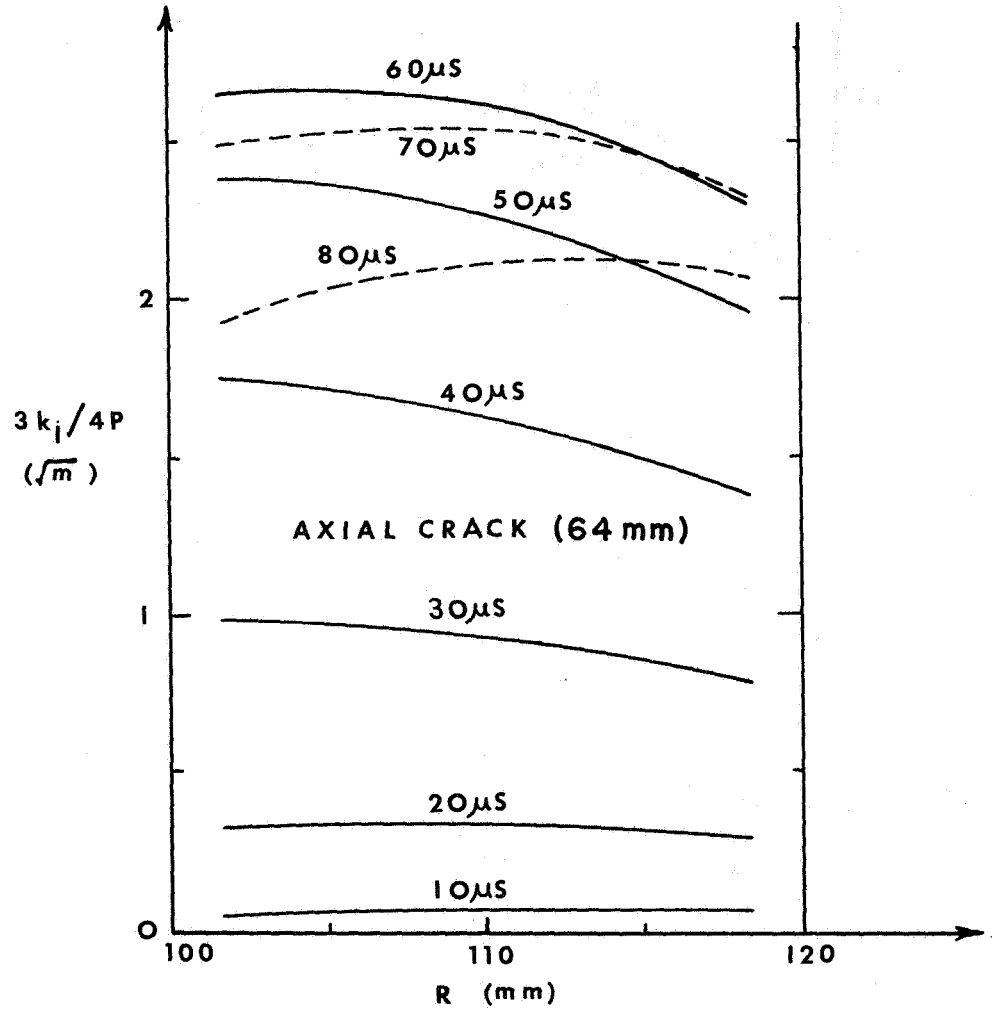

Figure 7.- Normalized stress intensity factor $3k_I/4P$ versus R at several time steps for the axial crack.

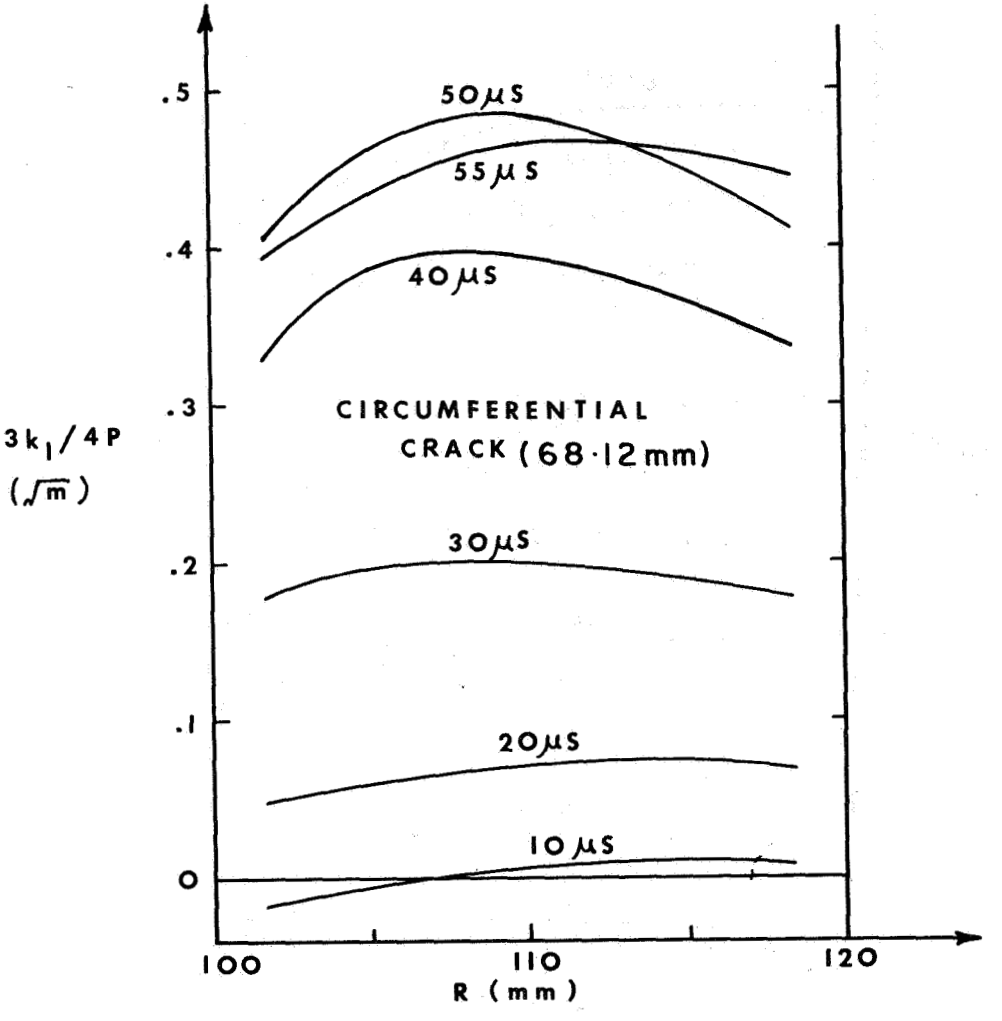

Figure 8.- Normalized stress intensity factor $3k_1/4P$ versus R at several time steps for the circumferential crack.

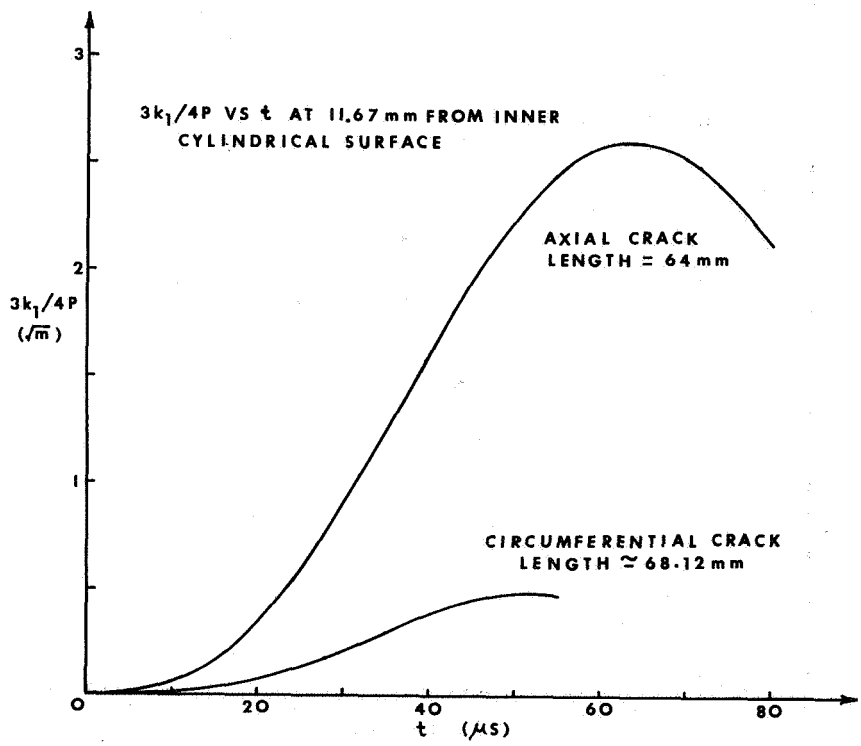

Figure 9.- Normalized stress intensity factor $3k_1/4P$ versus t at a position 11.67 mm from the inner cylindrical surface for the axial and circumferential cracks.

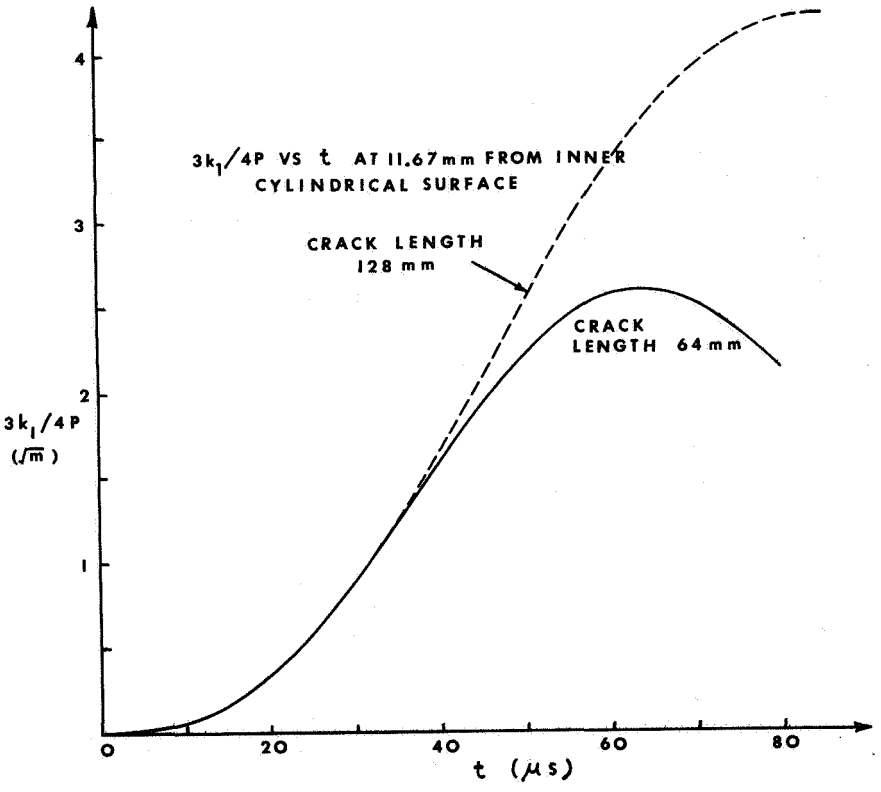

Figure 10.- Comparison of $3k_1/4P$ versus t curves for two axial crack lengths at a position 11.67 mm from the inner cylindrical surface.

RAPID INTERFACE FLAW EXTENSION WITH FRICTION

L. M. Brock
University of Kentucky

INTRODUCTION

Layered dissimilar materials vary from strata in the earth's crust to structural elements such as laminated composites. When appropriate loading is applied the bonding between layers may fail causing rapidly extending interface flaws and stress wave propagation. If complete separation does not occur then this extension process may be characterized by relative slip between the flaw surfaces opposed by friction.

This paper examines an idealized two-dimensional example of such a process. Referring to figure 1 initially undisturbed dissimilar isotropic, homogeneous, linearly elastic half-spaces are perfectly bonded along the interface $y=0$. Quantities associated with the half-space $y \leq 0$ are denoted by the prime superscript or the subscripts 3 or 4 while those in $y \geq 0$ carry the subscripts 1 or 2. At time $t=0$ adjacent material points at $x=0$, $y=\pm 0$ are forced apart horizontally with a constant relative velocity Δv. This results in a zone of bond failure which extends symmetrically along the interface at a constant rate c. The newly created flaw surfaces are in sliding contact resisted by Coulomb friction. The friction coefficient is γ. Stress waves are also generated and we assume that c is subcritical, i.e.,

$$c < c_R, c_R', c_S < c_1, c_2, c_3, c_4, c_m \qquad c_m = \max(c_1, c_3) \qquad (1a,b)$$

Here the odd and even subscripts denote dilatational and rotational wave speeds. Although the case in figure 1 is often treated explicitly the analysis will be valid for all six possible inequality relations between these speeds. The other symbols denote Rayleigh (R) and Stoneley (S) wave speeds. As Cagniard (see ref. 1) has shown the existence of Stoneley waves depends on the half-space properties. To analyze this process we first examine a closely related boundary value problem.

RELATED BOUNDARY VALUE PROBLEM

For $y \geq 0$ the pertinent displacements (u) and stresses (σ) are

$$u = u_r + iu_\theta, \quad s_\theta = \sigma_\theta - i\sigma_{r\theta}, \quad r(\Delta + i2\omega) = (ru)_{,r} - iu_{,\theta} \tag{2a-c}$$

where r,θ are the polar coordinates, Δ and ω are the dilatation and rotation and a subscripted variable after a comma means a derivative with respect to that variable. The constitutive relations are

$$\tau s_\theta = (m_1^2 m_2^{-2} - 1)\Delta - r(r^{-1}u)_{,r} - ir^{-1}u_{,\theta} \quad m_k = c_k/c_m \tag{3a,b}$$

where $1/\tau$ is the shear modulus. The governing equations are

$$c_1^2 \nabla^2 \Delta = \Delta_{,tt} \quad c_2^2 \nabla^2 \omega = \omega_{,tt} \tag{4a,b}$$

where ∇^2 is the Laplacian operator in r,θ. Similar expressions hold for $y \leq 0$. Along the flaw surfaces FG and interface segments AF and GL (see fig. 1), respectively,

$$\sigma_{r\theta} + \gamma\sigma_\theta = 0, \quad s_\theta - s_\theta' = 0, \quad u_\theta - u_\theta' = 0, \quad u_{r,t} - u_{r,t}' = \pm\Delta v \tag{5a-d}$$

$$u - u' = 0, \quad s_\theta - s_\theta' = 0 \tag{6a,b}$$

where equation (5d) holds only at $x = \pm 0$. Arcs AL and ARSL are moving into undisturbed material so that

$$\Delta = s_\theta = u = u_{,t} = 0, \quad \Delta' = s_\theta' = u' = u_{,t}' = 0 \tag{7a,b}$$

respectively. Similarly arcs AMNL and APQL are moving into regions disturbed only by dilatational waves so that, respectively,

$$\omega = 0 \quad \omega' = 0 \tag{8a,b}$$

Clearly the initial conditions are that $u, u' \equiv 0$ for $t \leq 0$. Integrable singularities in the stresses and particle velocities should be expected only at the flaw edges and the Stoneley wavefronts E, H. Finally when $\gamma = 0$ the solution should be antisymmetric about $x = 0$.

METHOD OF ANALYSIS

The differentiability of equations (5c) and (6a) and the absence of a characteristic length in the problem imply that

displacement derivatives are homogeneous of degree 0 in r and t. Thus for $y \geq 0$ we define

$$\phi_1(s,\theta) = c_1^2 \Delta, \quad \phi_2(s,\theta) = -2c_2^2 \omega, \quad s = r/t \tag{9a-c}$$

and equations (4) become hyperbolic for $s \geq c_k$ so that

$$2\phi_k(s,\theta) = f_k^+(\alpha_k+\theta)+f_k^-(\alpha_k-\theta); \quad \alpha_k = \cos^{-1}(c_k/s), \; 0 \leq \alpha_k \leq \pi/2 \tag{10a,b}$$

while for $s \leq c_k$ they are elliptic so that

$$2\phi_k(s,\theta) = \mathrm{Re}\Phi_k(\beta_k+i\theta)+\mathrm{Re}\Psi_k(\beta_k-i\theta); \quad \beta_k = \cosh^{-1}(c_k/s) \geq 0 \tag{11a,b}$$

where Re and Im denote real and imaginary part. Here the real f and complex Φ,Ψ functions are arbitrary. Similar equations hold for $y \leq 0$. The characteristic properties of the f's allow equations (5) to (8) to reduce to coupled conditions on the ϕ's everywhere on the boundaries of the semicircles OLAO, BKSR, CJNM and DIQP (see fig. 1). In view of equation (11) the problem can now be studied by mapping techniques. The transformations

$$z_k = x_k+iy_k = m_k \operatorname{sech}(\beta_k+i\theta) \tag{12}$$

map these semicircles on the upper or lower halves of the complex plane and

$$\Omega_k = \Phi_{k,z_k}\dot{z}_{k,\beta_k}, \quad \omega_k = \Psi_{k,\bar{z}_k}\dot{\bar{z}}_{k,\beta_k}, \quad p_k = (1-z^2/m_k^2)^{-1/2} \tag{13a-c}$$

are defined where the p-functions are analytic in the plane cut along Im $z=0$, $|\mathrm{Re}\,z| < m_k$. It can then be shown that

$$c_m u = J_1[(vt-r/c_m)U(W_1)]-iJ_2[(vt-r/c_m)U(W_2)] \tag{14}$$

$$\tau c_m^2 s_\theta = J_1[V(W_1)]-iJ_2[V(W_2)] \tag{15}$$

$$U(W_k) = [1-\bar{p}_k(v)]\bar{W}_k-[1+p_k(v)]W_k, \quad W_k = \Omega_k(v_k)+\overline{\omega_k(\bar{v}_k)} \tag{16a,b}$$

$$V(W_k) = [2-K(v)\overline{p}_k(v)]\overline{W}_k - [2+K(v)p_k(v)]W_k, \quad K(v) = 2-v^2/m_2^2 \tag{17a,b}$$

formally satisfy equations (1) to (4), (7), (8) and the initial conditions where $-$ denotes complex conjugate. Similar equations hold for $y \leq 0$. Here

$$4J_k(h) = \int_{\xi}^{g_k(\theta)} v^{-3}hdv, \quad \xi = r/c_m t \tag{18a,b}$$

where for $v \leq m_k$ and $m_k \leq v \leq g_k(\theta)$, respectively,

$$v/v_k = \cos\theta + i(1-v^2/m_k^2)^{\frac{1}{2}}\sin\theta, \quad v_k = m_k \sec[\sec^{-1}(v/m_k) \pm |\theta|] \tag{19a,b}$$

for $|\theta| < \pi/2(+)$ and $|\theta| > \pi/2(-)$. In equation (18a)

$$1/g_k(\theta) = |\cos\theta| + (m_k^{-2}-1)^{\frac{1}{2}}\sin|\theta| \tag{20}$$

for $0 \leq |\theta| \leq \cos^{-1}m_k$ and $\pi - \cos^{-1}m_k \leq |\theta| \leq \pi$ but is unity otherwise.

In view of equations (14) to (18) and figure 1 it is readily shown that conditions (5b,c) and (6) will be satisfied if

$$\Omega_1, i\Omega_2 = (hKL'p_2 - Rp_2 - 2hp_4z^2/m_4^2, 2hL' - R' - hKp_1p_4z^2/m_4^2)\frac{F}{S} \tag{21a,b}$$

in the lower half of the complex plane while in the upper half

$$\Omega_3, i\Omega_4 = (hK'Lp_4 - h^2R'p_4 - 2hp_2z^2/m_2^2, 2hL - h^2R - hK'p_2p_3z^2/m_2^2)\frac{F}{S} \tag{22a,b}$$

Identical expressions hold for the ω's in the corresponding opposite half of the complex plane. The arbitrary function F is analytic everywhere except perhaps $\mathrm{Im}z=0, |\mathrm{Re}z| < p$ where $p = c/c_m$ while

$$L = 2-Kp_1p_2, \quad L' = 2-K'p_3p_4, \quad R = 4-K^2p_1p_2, \quad R' = 4-(K')^2p_3p_4 \tag{23a-d}$$

$$S = (h')^2+M^2p_1p_2p_3p_4-N^2p_1p_2-(N')^2p_3p_4-hz^4(p_1p_4+p_2p_3)/m_2^2m_4^2 \tag{24}$$

$$M = K'-hK,\ N = 2-hK,\ N' = 2h-K',\ h = \tau'/\tau,\ h' = 2(1-h) \tag{25a-e}$$

Here R,R' and S are the Rayleigh and Stoneley functions. The origin $s=0$ and the wavefronts at $|\theta|=\pi/2$ are ordinary points while integrable singularities are expected at the flaw edges. Thus

$$F = 0(z^3)\quad F = 0(1)\quad F = 0(|z\pm p|^{-1-\varepsilon})\ (0<\varepsilon<1) \tag{26a-c}$$

for $z\to 0$, $z\to\infty$ and $|z\pm p|\to 0$, respectively. Stoneley waves arise when S has non-zero roots. These roots occur at $z=\pm n$ and exist only if $S(m) > 0$ where

$$n = c_S/c_m\quad n < m\quad m = \min(m_2,m_4) \tag{27a-c}$$

These roots are manifested as logarithmic singularities and jump discontinuities at the Stoneley wavefronts. Finally it can be shown that the limit case $\gamma=0$ will be antisymmetric only if F is imaginary when $\gamma,\mathrm{Re}z=0$. With equations (21) and (22) at hand condition (5a) reduces to a Hilbert form for $\mathrm{Im}z=0, |\mathrm{Re}z| < p$:

$$(A-i\gamma C)F^+ + (A+i\gamma C)F^- = 0,\quad F^{\pm} = F(\mathrm{Re}z\pm i0) \tag{28a,b}$$

$$A = hz^2p_4R/m_4^2+z^2p_2R'/m_2^2,\quad C = hL'R-LR' \tag{29a,b}$$

Here A and C are evaluated on $\mathrm{Im}z=+0$. A solution which accounts for the above observations on F and also condition (5d) is

$$F(z) = Bz^3(p^2-z^2)^{-3/2}\exp\left[\int_{-p}^{p}\frac{b(v)dv}{v-z}\right],\ \pi b(v) = \tan^{-1}\frac{\gamma C}{A} \tag{30a,b}$$

$$I_1B = c_m\Delta v\quad I_1 = \int_0^{\pi/2}\cos A'(v)(p^2+\tan^2 v)^{-3/2}\sin v\sec^3 v\,dv \tag{31a,b}$$

$$A'(v) = 2b(0)\tan^{-1}(p\cot v)+2\tan v\int_0^p\frac{b(w)-b(0)}{w^2+\tan^2 v}\,dw \tag{32}$$

THE COULOMB FRICTION PROBLEM

Although they satisfy all the conditions on the related boundary value problem the previous results will not represent a solution to the original problem unless (I) a compressive stress exists everywhere over the flaw surfaces and (II) the shear stress everywhere opposes the relative slip velocity of the flaw surfaces. It can be shown that these conditions are guaranteed for the following two situations:

$$\Delta v,\gamma,C(v) > 0 \quad \Delta v,\gamma,C(v) < 0 \quad (|v| < p) \tag{33a,b}$$

From a fracture mechanics view point the flaw edges are of interest. It is readily shown that the stresses and relative particle velocities behave as

$$\frac{\tau I_1 c_m}{\Delta v} s_\theta \sim \frac{-(1+i\gamma)C(p)G(p)}{S(p)(2p)^{\beta_\pm}(p-\xi)^{\beta_\mp}} , \frac{I_1}{\Delta v}(u,_t - u',_t) \sim \frac{pG(p)}{(2p)^{\beta_\pm}(p-\xi)^{\beta_\mp}} \tag{34a,b}$$

$$p[1\mp 2b(p)][1+\gamma^2 C^2(p)/A^2(p)]^{\frac{1}{2}}G(p) = \exp[\pm A''(p)], \quad \beta_\pm = \tfrac{1}{2}\pm b(p) \tag{35a,b}$$

$$A''(p) = \int_{-p}^{p} \frac{b(v)-b(p)}{v-p}\,dv \tag{36}$$

on the flaw surface as $x \to \pm ct$. Similar expressions hold on the interface as $x \to \pm ct$. Equations (29) and (30b) demonstrate that $-\frac{1}{2} < b(p) \leq 0$ for both cases (33a,b). In light of (34) it follows that the flaw edge integrable singularities are either stronger or weaker than the square-root singularity associated with a stress-free flaw surface. The functions C and b are plotted vs. the subcritical range of v in figure 2 for various values of the m's and h. The curves indicate a rapid variation with flaw extension rate and that the rate for which the entire flaw surface experiences Coulomb friction may be limited by material properties.

DISCUSSION OF RESULTS

This paper considered interface flaw generation and extension caused by bonding failure and accompanied by Coulomb sliding friction between the flaw surfaces. A closely related boundary value problem was solved and under some restrictions imposed on the material properties and flaw extension rate the solution was found

to represent the process. It was also found that the particle velocities and stresses at the flaw edges exhibit integrable singularities whose order depends on the material properties, friction coefficient and flaw extension rate. Similar behavior occurs in the static analysis of rigid indentation with friction (see ref. 2).

Although such a study is not pursued here, perhaps the boundary value problem can yield further insight. For example the solution restrictions may indicate that the flaw surfaces near the edges completely separate above certain flaw extension rates. Moreover the relative slip-shear resistance relationship along the flaw surface might be of interest. Finally it should be noted that future work will consider the more useful problem of flaw extension with friction due to a specified loading. In regard to the method of analysis used here homogeneous function solution techniques can be applied to a variety of wave propagation problems; see for example the recent work of references 3 and 4.

REFERENCES

1. Cagniard, L.: Reflection and Refraction of Progressive Seismic Waves, McGraw-Hill, 1962, pp. 42-49.

2. Muskhelishvili, N. I.: Some Basic Problems in the Mathematical Theory of Elasticity, Noordhoff, 1963, pp. 493-498.

3. Willis, J. R.: Self-Similar Problems in Elastodynamics, Phil. Trans. Roy. Soc. London, Series A, Vol. 274, 1973, pp. 435-491.

4. Brock, L. M.: Non-Symmetric Extension of a Small Flaw into a Plane Crack at a Constant Rate under Polynomial-Form Loadings, Int. J. Engng. Sci., Vol. 14, 1976, pp. 181-190.

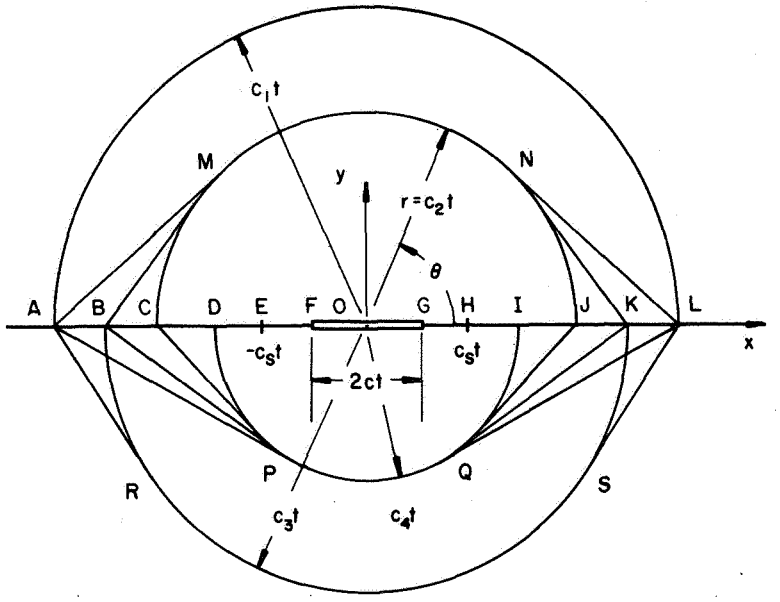

Figure 1.- Pattern of wavefronts for time $t \geq 0$.

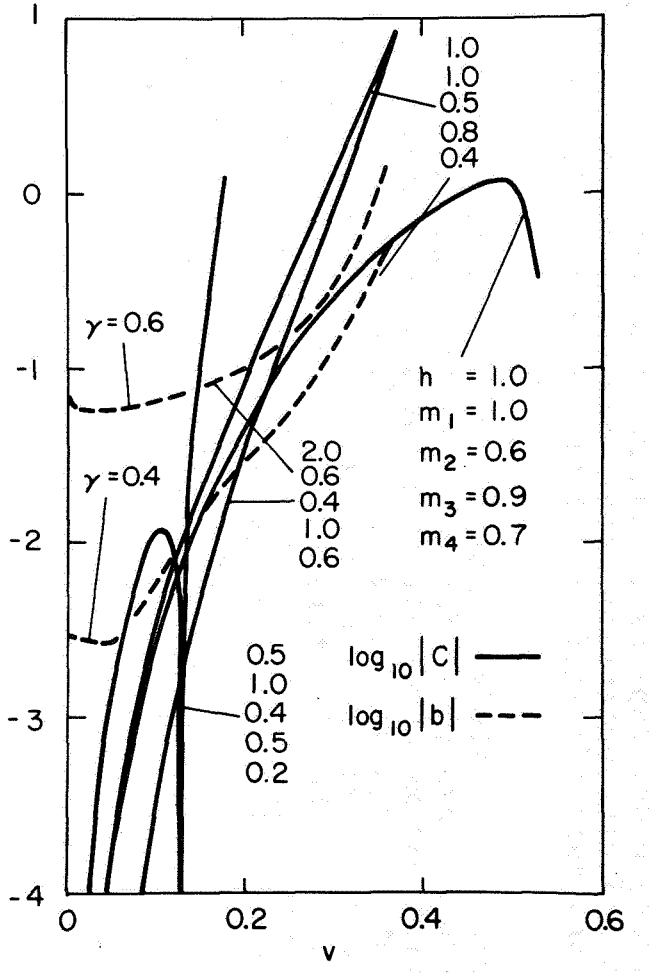

Figure 2.- Parameters C and b versus subcritical flaw extension rate for various solids.

DYNAMIC DUCTILE FRACTURE OF A CENTRAL CRACK*

Y. M. Tsai
Iowa State University

SUMMARY

A central crack, symmetrically growing at a constant speed in a two-dimensional ductile material subject to uniform tension at infinity, is investigated using the integral transform methods. The crack is assumed to be the Dugdale crack, and the finite stress condition at the crack tip is satisfied during the propagation of the crack. Exact expressions of solution are obtained for the finite stress condition at the crack tip, the crack shape, the crack opening displacement, and the energy release rate. All those expressions are written as the product of explicit dimensional quantities and a nondimensional dynamic correction function. The expressions reduce to the associated static results when the crack speed tends to zero, and the nondimensional dynamic correction functions were calculated for various values of the parameter involved.

The finite stress condition is used to determine the plastic zone size. It is shown that the plastic zone width shrinks significantly with increasing crack speed. A general convenient method is described to determine the plastic zone size using the nondimensional dynamic correction curves obtained. Due to the effect of crack propagation, the crack opening displacement and the energy release rate are found to decrease with increasing crack speed.

INTRODUCTION

The Dugdale model was applied to a dynamic problem of a rapidly extending semi-infinite crack under traveling "wedging" pressures (refs. 1 and 2) and to the study of a ductile-crack propagation (ref. 3). The finite stress condition at the crack tip in both the theoretical studies on dynamic ductile fractures (refs. 2 and 3) predicted that the proportion of the plastic zone size to the crack length is independent of crack speed and remains exactly the same as that for the corresponding static problems. However, experimental results indicate that the crack tip plastic zone in steels may shrink as the crack increases in velocity (ref. 4).

The present work, using integral transform methods similar to those used in reference 5, investigates plastic zone size, crack shape, crack opening

*The research is sponsored by the National Science Foundation under Grant No. ENG 74-08147 and by the Engineering Research Institute, Iowa State University, Ames, Iowa.

displacement, and energy release rate of a central crack which is symmetrically growing at a constant speed in a two-dimensional ductile Dugdale material. Exact expressions of solution are obtained which describe the shrinkage of the plastic zone and the variations of crack shape, crack opening displacement, and energy release rate as a function of crack speed, applied stress, and material properties.

CRACK SHAPE AND PLASTIC-ZONE SIZE AT VANISHING CRACK SPEED

Consider a two-dimensional solid material subjected to uniform tensions at infinity. A Dugdale crack starts to propagate in the x-direction at time $t = 0$ in a plane, $y = 0$, perpendicular to the direction of tension. During propagation the crack tip is specified by $\ell(t)$, and the plastic zone tip is $a(t)$. Solution of the problem can be obtained by superposing a uniform tension field p_o and the stress field which is set up by a pressure, p_o, acting on the crack surfaces and the tensile stress, $Y - p_o$, acting in the plastic zone. The latter problem is the main subject of interest in the present work. For convenience, the above normal stresses are described by a function $\sigma(x,t)$, which is equal to $-p_o$ for $x \leq \ell(t)$ and $Y - p_o$ for $\ell(t) < x \leq a(t)$. The dynamic boundary conditions on the crack plane $y = 0$ for $t > 0$ can be prescribed as $\sigma_{xy} = 0$, $V = w(x,t)$ for $x \leq a(t)$ and $\sigma_{xy} = V = 0$ for $x > a(t)$. V is the vertical displacement normal to the crack plane and $w(x,t)$ is an unknown crack shape function to be determined in terms of $\sigma(x,t)$. The methods of integral transforms similar to those used in reference 5 can be used here to solve the equations of motion and the dynamic boundary conditions. After inversions, the normal stress on $y = 0$ can be written as (ref. 5):

$$\sigma_{yy}(x,t) = \sigma^{o}_{yy} - p_o q; \quad p_o q = \rho c_1 I Q_1 + \mu L_2 Q_2 \tag{1}$$

ρ, μ and c_1 are, respectively, the material density, the shear modulus, and the dilatational wave speed. σ^{o}_{yy} as defined in reference 5. IQ_1 and L_2Q_2 are, respectively, equal to Q_1 and L_2Q_2 in reference 5. The operator L_2 over η is the same as L_1 in reference 5 while the operator L defined in the Appendix is a modified form of the integral representation of the zeroth order Bessel function involved in Q_1 of reference 5. Equation (1) may be converted into an integral equation to solve for the unknown w embedded in the integrals on the right hand side of the equation. As shown in detail in reference 5, the equation obtained can be written as

$$w(x,t) = w^{o}(x,t) - 2\, w_q/\pi K;$$

$$w_q = \int_x^a n(n^2 - x^2)^{-1/2} \int_o^n q(n^2 - \lambda^2)^{-1/2}\, d\lambda dn; \quad K = \frac{\mu}{(1 - \nu)} \tag{2}$$

where $$q = q_\ell(x,t),\ x < \ell(t); \quad q = q_r(x,t),\ \ell(t) < x < a(t) \tag{3}$$

w in equation (2) can be determined by the method of successive approximations

(ref. 5). For the first approximation, the wave-effect integrals Q_1 and Q_2 are dropped temporarily and equation (1) reduces to the associated static equation. In terms of σ and $\alpha = p_o/Y$, the reduced equation is integrated to be the first approximation of w as

$$w_1(x,t) = w^o(x,t) = \frac{p_o}{K}\left\{\sqrt{a^2 - x^2} - \frac{1}{\alpha}\frac{2}{\pi}w_q^1\right\} \tag{4}$$

w_q^1 is defined in equation (2) with $q_\ell = -p_o$ and $q_r = Y - p_o$. In terms of equation (4), the first approximation of σ_{yy} in equation (1) for $x > a$ is obtained as

$$\sigma_{yy}^1 = \sigma_{yy}^o = p_o\left\{x\left[1 - (1 - 2\sin^{-1}(\ell/a)/\pi)/\alpha\right](x^2 - a^2)^{-1/2} - 1 - \frac{2}{\pi}\int_\ell^a (x^2 - n^2)^{-1/2}(n^2 - \ell^2)^{-1/2} n^{-1}\ell x\,dn/\alpha\right\} \tag{5}$$

If there is no plastic zone where ℓ is equal to a, equation (5) reduces to the corresponding elastic solution (ref. 5). If the finite stress condition at the crack tip is imposed, equation (5) exactly gives the well known equation, i.e., B = 0 in equation (6) for determining the plastic zone size obtained by Dugdale (ref. 1) from a different approach. The equation is to be shown as a part in the dynamic equation for determining the plastic zone size as a function of crack speed.

DYNAMIC CRACK SHAPE

The successive approximations of w can be obtained from equation (2) in terms of $p_o q$ in equation (1). To obtain closed-form solutions, it is assumed that the crack tip and the plastic zone tip are running at constant speeds of e and v, respectively; i.e., $\ell = et$ and $a = vt$. Under this assumption, the cosine transform of equation (4) and its derivative can be obtained and used to obtain the first approximation of L_2Q_2 as

$$L_2Q_2^1 = BQ_{21} + L_2Q_{22}^1,\quad B = 1 - \left(1 - \frac{2}{\pi}\sin^{-1}\frac{\ell}{a}\right)/\alpha \tag{6}$$

$$\text{where}\quad L_2Q_{22}^1 = \frac{2e^2p_o}{\pi\alpha K}\frac{\partial}{\partial x}L_2\int_o^\infty \sin(sx)\int_o^t \cos[sc_2\eta(t-\tau)]\,\tau\int_1^{v/e}\frac{\lambda J_o(s\ell\lambda)\,d\lambda}{\sqrt{\lambda^2 - 1}}\,d\tau ds \tag{7}$$

where J_o is the Bessel function and Q_{21} is identical with L_1Q_2 in reference 5 if K_D there is replaced by K here. The integrated results can be obtained from reference 5 as

$$Q_{21} = p_o v_2^2 L_2 D_2(\eta, v_2)/K, x < a \tag{8}$$

$$\text{and}\quad Q_{21} = p_o v_2^2 L_2 D_6(\eta, v_2, x/c_2t, x/a, 1)/K \quad , a < x < c_2t\ (c_2 = \sqrt{\mu/\rho}) \tag{9}$$

where D_2 and D_6 are nondimensional dynamic functions which are defined in terms of $v_2 = v/c_2$ in the Appendix. Equation (7) involves an additional integration over λ compared to Q_{21}. However, the procedures for integration are very similar. For $x < \ell$, $L_2Q_{22}^1$ is similar to Q_{21} for $x < a$ in equation (8) and can be written in terms of D_7 in the Appendix as:

$$\mu L_2 Q_{22}^1 = p_o D L_2 D_7(\eta, e_2, 1)/\alpha, x < \ell;\ D = 2(1 - \nu)e_2^2/\pi, e_2 = e/c_2 \tag{10}$$

For $\ell < x < a$, $L_2Q_{22}^1$ is similar to the combination of equations (8) and (9), and the results can be written as:

$$\mu L_2 Q_{22}^1 = p_o D L_2[D_8(\eta, e_2, x/\ell) + D_7(\eta, e_2, x/\ell)]/\alpha, \ell < x < a \tag{11}$$

D_8 is defined in the Appendix. Similarly, the first approximation of LQ_1 can be written as

$$LQ_1^1 = BQ_{11} + LQ_{12}^1 \tag{12}$$

$$\text{where}\quad LQ_{12}^1 = \frac{2ep_o}{\pi\alpha K}\frac{\partial}{\partial t} L \int_o^\infty \cos(sx) \int_o^t \sin[sc_1\eta(t - \tau)] \int_\ell^a \frac{nJ_o(sn)dn}{\sqrt{n^2 - \ell^2}}\, d\tau ds \tag{13}$$

Q_{11} is identical with Q_1^1 if cosh ξ is replaced by η in reference 5. Integration of Q_1^1 in reference 5 was explained in detail, and the integrated forms of Q_{11} are found to be the same as the expressions on the right-hand sides of Q_{21} in equations (8) and (9) if c_2, v_2, and L_2 are, respectively, replaced by c_1, $v_1 = v/c_1$, and $_1L_1$, which is defined in the Appendix. The procedures for integrating LQ_{12} are similar to those for $L_2Q_{22}^1$. The integrated forms of LQ_{12}^1 in equation (13) are identical with the expressions on the right-hand side of $L_2Q_{22}^1$ in equations (10) and (11) if c_2 and L_2 are replaced by c_1 and L_1, respectively.

In terms of equations (6) and (12), the first approximation of p_oq can now be written as follows:

$$p_oq_1 = p_oBq_o + p_og_1/\alpha, x \le \ell\ ;\ p_oBq_o + p_oh_1/\alpha, \ell < x \le a \tag{14}$$

$$\text{where}\quad q_o = e_2^2(1 - \nu)(L_1 + L_2)D_2(\eta, v_i),\ g_1 = D(L_1 + L_2)D_7(\eta, e_i, 1) \tag{15}$$

$$h_1 = D(L_1 + L_2)[D_8(\eta, e_i, x/\ell) + D_7(\eta, e_i, x/\ell)] \tag{16}$$

where the subscript i is 1 for the operator L_1 and becomes 2 for the operator L_2. The quantity e_1 is equal to e/c_1 and D_8 is defined in the Appendix. The above procedures can be continued to obtain higher order approximations. As a continuation of equation (14), p_oq is found to be an alterating series of the general expressions as follows:

$$g_j = D^j(L_1 + L_2)D_{7j}(\eta, e_i, 1) \tag{17}$$

and $$h_j = D^j(L_1 + L_2)[D_{8j}(\eta, e_i, x/\ell) + D_{7j}(\eta, e_i, x/\ell)] \tag{18}$$

The time derivative of h_j leads to $\bar{E}_{j+1}$ in the Appendix. A clear pattern can be seen in the process of higher order approximations. After infinitely many approximations, the final form of w is found as follows:

$$w = w^o - \frac{P_o}{K}\left[\bar{B}\, q_o\, (a^2 - x^2)^{1/2} + \frac{2}{\pi\alpha}\, w_{\bar{q}}\right] \tag{19}$$

where $\bar{B}$ is found to be the product of two series, one of which can be written into a simple form as follows:

$$\bar{B} = \Delta\left[1 + \sum_{j=1}^{\infty} (-1)^j q_o^j\right] = \frac{\Delta}{1 + q_o}\,, \quad \Delta = B + \frac{1}{\alpha}\sum_{j=1}^{\infty} (-1)^j \epsilon_j \tag{20}$$

where $$\epsilon_j = \left[g_j \sin^{-1}\frac{\ell}{a} + \int_{\ell}^{a} h_j (a^2 - \lambda^2)^{-1/2} d\lambda\right] 2/\pi \tag{21}$$

Equation (2) defines $w_{\bar{q}}$ if q is replaced by $\bar{q}$ which is equal to $\bar{g} = \sum_{j=1}^{\infty} (-1)^{j+1} g_j$ for $x < \ell$ and $\bar{h} = \sum_{j=1}^{\infty} (-1)^{j+1} h_j$ for $\ell < x < a$. It will be shown later that Δ, and hence $\bar{B}$, must be vanishing in order to satisfy the finite-stress condition at the extended crack tip of the Dugdale crack.

DYNAMIC PLASTIC-ZONE SIZE

The plastic zone size can be determined by satisfying the condition that the stress singularities at the crack tips vanish. In order to satisfy this finite stress condition, the normal stress σ_{yy} in equation (1) must be calculated. In terms of equation (19), it is obtained that for $x < a$, σ_{yy} in equation (1) exactly reduces to the surface stress prescribed. Following the techniques similar to those for equation (5), the integration over s gives for $x > a$:

$$\sigma^o_{yy}/p_o = x(x^2 - a^2)^{-1/2}\left[(1 - \bar{B}q_o) - (1 - \frac{2}{\pi}\sin^{-1}\frac{\ell}{a})/\alpha - \frac{2}{\pi}\left(\bar{g}\sin^{-1}\frac{\ell}{a} + \int_{\ell}^{a} \bar{h}(a^2 - \lambda^2)^{-1/2}\, d\lambda\right)/\alpha\right] - (1 - \bar{B}q_o) + \bar{g}/\alpha$$

$$+ \frac{2}{\pi}\frac{1}{\alpha}\int_{\ell}^{a} \frac{x\ell}{\sqrt{x^2 - n^2}}\left(\frac{1 - \bar{g}}{n\sqrt{n^2 - \ell^2}} + \frac{\partial}{\partial n}\int_{\ell}^{n} \frac{\bar{h}\, d\lambda}{\ell\sqrt{n^2 - \lambda^2}}\right) dn \tag{22}$$

$p_o q$ in equation (1) can be integrated in terms of equation (19) by using the methods similar to those for equations (10) and (11) and the techniques used in reference 5. The integrations are obtained for $x > a$ as follows:

$$p_o q = p_o(L_1 + L_2)\left\{(1 - \nu)\bar{B}v_2^2\left[D_4(\eta,v_i)(x\,(x^2 - a^2)^{-1/2} - 1) + D_5(\eta,v_i,x/c_i t)\right] + \frac{D}{\alpha}\int_1^{v/e}\lambda\left[(\lambda^2 - 1)^{-1/2} + \sum_{j=1}^{\infty}(-1)^j D^j E_{j+1}(e_2,\lambda)\right] D_6(\eta,\lambda e_i, e_i x/\ell, x/\ell, \lambda)\,d\lambda\right\} \tag{23}$$

If equations (22) and (23) are substituted into equation (1), the normal stress on $y = 0$ is obtained and the finite stress condition at the crack tips can be written in terms of equations (6), (15), and (20) into the following exact expression:

$$\Delta\, K_I/(1 + q_o) = 0,\quad K_I = 1 - (1 - \nu)v_2^2(L_1 + L_2)D_4(\eta,v_i) \tag{24}$$

Equation (24) is satisfied if Δ or K_I vanishes. In fact, Δ vanishes at lower crack speed than K_I does. Therefore, the vanishing of Δ in equation (20) determines the size of the plastic zone. If crack speed vanishes, all ϵ_j become zero and equation (20) reduces to the corresponding static condition of $B = 0$. In equation (20) Δ can be seen as an alternating power series of e_2^2. The first power term of Δ, ϵ_1, is found numerically to be of the order of 10^{-1}, and the second power term ϵ_2 is 10^{-3}. It appears that Δ in equation (20) converges very rapidly. The calculations were carried out by means of the regular four point integration formula using an IBM 360/65 electronic computer. It appears practically accurate enough to include only ϵ_1 in calculating Δ in equation (20). The value of ϵ_1 was calculated for various values of e_2 and ℓ/a at $\nu = 0.3$ and shown in figure 1. The value of B in equation (6) was also calculated and shown in figure 1. The intersection of the curves for B and ϵ_1/α gives the nondimensional quantity ℓ/a for determining the plastic-zone size. The width of the plastic zone is $a - \ell$, and the ratio of the width to the half crack length is determined as shown in figure 2 for various values of α and e_2 at $\nu = 0.3$. For values of α and e_2, different from those in figure 2, the plastic zone size can also be determined by interpolating the value of ϵ_1 and B in figure 1 at a proper ℓ/a which makes Δ in equation (20) vanishing. It can be seen from figure 2 that the plastic zone width expressed in $(a - \ell)/\ell$ shrinks significantly with increasing crack speed in terms of $e_2 = e/c_2$. For $\alpha = p_o/Y = 0.8$, the reduction of the plastic zone width at $e_2 = 0.6$ is 85% of the corresponding static plastic zone width at $e_2 = 0$. This is clearly consistent with the experimental findings of the transition of ductile fracture to brittle fracture at sufficiently high crack speeds (ref. 4).

CRACK OPENING DISPLACEMENT AND ENERGY RELEASE RATE

The crack opening displacement (C.O.D.) can be obtained from equation (19) with $\bar{B} = 0$ for satisfying the finite-stress condition as $w_\ell = p_o \ell f_w(e_2,\alpha,\nu)/K$. The nondimensional dynamic C.O.D. correction function is obtained as:

$$f_w = \sqrt{(v/e)^2 - 1} - \frac{1}{\alpha}\int_1^{v/e} m\left[1 - \frac{2}{\pi}\sin^{-1}\frac{1}{m} + \sum_{j=1}^{\infty}(-1)^j \epsilon_j\right](m^2 - 1)^{-1/2}dm \tag{25}$$

The value of f_w above was calculated by the computer as shown in figure 2. Similarly, the dynamic crack shape in equation (19) with $\bar{B} = 0$ can also be calculated. In energy consideration, it is assumed that the method of calculation for the work done to an elastic medium in equilibrium (ref. 6) can also be used in the elastodynamic problem. Therefore, the release rate of the work W_k done to the medium by the crack surface pressure can be calculated in terms of equation (19) as

$$\partial W_k/\partial \ell = 2(1 - \nu^2)p_o^2 \pi \ell \, f_R(\alpha,e_2,\nu)/E \tag{26}$$

where E is Young's modulus and the nondimensional dynamic correction function for the energy release rate is

$$f_R = (1 - \frac{1}{\alpha})\, v^2/e^2 - \frac{\bar{g}}{\alpha} + \frac{2v}{\pi e \alpha}\left[(1 - e^2/v^2)^{1/2} + \frac{v}{e}\sin^{-1}\frac{e}{v}\right] - \frac{4}{\pi\alpha}\int_1^{v/e} m\left[(1 - \frac{1}{\alpha})\frac{\pi}{2} + \frac{1}{\alpha}\sin^{-1}\frac{1}{m}\right]\left[1 - \frac{2}{\pi}\sin^{-1}\frac{1}{m} + \sum_{j=1}^{\infty}(-1)^j \epsilon_j\right]dm \tag{27}$$

The value of f_R was calculated by the computer and also plotted in figure 2. Both the C.O.D. and the energy release rate can be seen as functions with an explicit factor of the crack length ℓ and reduce to the associated static expressions as the crack speed, e, tends to zero. The crack opening displacement and the energy release rate can be seen to be decreasing with increasing crack speed in figure 2.

APPENDIX

$$Lf = \frac{2}{\pi}\int_1^{\infty}(\eta^2 - 1)^{-1/2} f(\eta)d\eta, \quad L_1 f = \frac{2}{\pi}\int_1^{\infty}\eta(\eta^2 - 1)^{-1/2} f(\eta)d\eta$$

$$D_2(\eta,v_2) = \frac{1}{(\eta^2 - v_2^2)^{3/2}}\left\{2\eta \ell n\left[\sqrt{\frac{\eta - v_2}{2v_2}} + \sqrt{\frac{\eta + v_2}{2v_2}}\right] - (\eta^2 - v_2^2)^{1/2}\right\}$$

$$D_5(\eta,v_2,x/c_2t) = \frac{\eta}{(\eta^2 - v_2^2)^{3/2}} \ln \frac{\sqrt{\eta^2 - x^2/c_2^2/t^2}[1 + \eta(\eta^2 - v_2^2)^{-1/2}]}{x/c_2t + \eta(\eta^2 - v_2^2)^{-1/2}\sqrt{x^2/c_2^2t^2 - v_2^2}}$$

$$D_6(\eta,v_2,x/c_2t,x/a,\lambda) = D_4(\eta,v_2)\left[\frac{x/a}{\sqrt{x^2/a^2 - \lambda^2}} - 1\right] + D_5(\eta,v_2,x/c_2t)$$

$$D_4(\eta,v_2) = (\eta^2 - v_2^2)^{-1}, \quad D_7(\eta,e_i,x/\ell) = \int_{x/\ell}^{v/e} \lambda\,(\lambda^2 - 1)^{-1/2} D_2(\eta,\lambda e_i)d\lambda$$

$$D_8(\eta,e_i,x/\ell) = \int_1^{x/\ell} \lambda(\lambda^2 - 1)^{-1/2}\, D_6(\eta,\lambda e_i,e_i x/\ell,x/\ell,\lambda)d\lambda$$

$$\bar{E}_2(\eta,e_i,\xi) = \frac{\xi^2}{\sqrt{\xi^2 - 1}} \frac{1}{\eta^2 - e_i^2\xi^2} - \xi \frac{\eta}{(\eta^2 - e_i^2\xi^2)^{3/2}} \ln \frac{\sqrt{\eta^2 - e_i^2\xi^2} + \eta}{e_i\xi}$$

$$+ \xi \int_1^{\xi} \frac{\eta}{(\eta^2 - \lambda^2 e_i^2)^{3/2}} \left\{ \frac{e_i^2\xi}{\eta^2 - e_i^2\xi^2} + \frac{1 + \eta(\eta^2 - \lambda^2 e_i^2)^{-1/2}\xi(\xi^2 - \lambda^2)^{-1/2}}{\xi + \eta(\eta^2 - \lambda^2 e_i^2)^{-1/2}(\xi^2 - \lambda^2)^{1/2}} \right\} d\lambda$$

$$- \xi \int_0^{\pi/2} \left[\frac{1}{\eta^2 - Z(\xi,1,\theta)e_i^2} - 2e_i^2\xi \frac{\cos^2\theta}{[\eta^2 - Z(\xi,1,\theta)e_i^2]^2} \right] d\theta$$

$$Z(\xi,\lambda,\theta) = \xi^2 - (\xi^2 - \lambda^2)\sin^2\theta, \quad k^2 = 2(1 - \nu)/(1 - 2\nu)$$

$$E_j(e_2,m) = \int_1^m \left[L_1\bar{E}_j(\eta,ke_2,\xi) + L_2\bar{E}_j(\eta,e_2,\xi) \right] \left(m^2 - \xi^2\right)^{-1/2} d\xi$$

$$D_{7j}(\eta,e_i,x/\ell) = \int_{x/\ell}^{v/e} E_j(e_i,m)mD_2(\eta,me_i)dm$$

$$D_{8j}(\eta,e_i,x/\ell) = \int_1^{x/\ell} E_j(e_i,m)mD_6(\eta,me_i,e_i x/_{\ell},x/\ell,m)dm$$

REFERENCES

1. Dugdale, D. S.: Yielding of Steel Sheets Containing Slits. J. Mech. Phys. Solids, vol. 8, 1960, pp. 100-104.

2. Goodier, J. N.; and Field, F. A.: Plastic Energy Dissipation in Crack Propagation. Fracture of Solids. Edited by D. C. Drucker and J. J. Gilman, Interscience, New York, 1963, pp. 103-118.

3. Kanninen, M. F.; Mukherjee, A. K.; Rosenfield, A. R.; and Hahn, G. T.: The Speed of Ductile-Crack Propagation and the Dynamics of Flow in Metals. Mechanical Behavior of Materials under Dynamic Loads. Edited by U. S. Lindholm, Springer-Verlag, New York, 1968, pp. 96-133.

4. Felbeck, D. K.; and Orowan, E.: Experiments on Brittle Fracture of Steel Plates. Welding Res. Suppl., vol. 34, 1955, pp. 570S-575S.

5. Tsai, Y. M.: Propagation of a Brittle Crack at Constant and Accelerating Speeds. Int. J. Solids Structures, vol. 9, 1973, pp. 625-642.

6. Sneddon, I. N.: Fourier Transforms. McGraw Hill, New York, 1951, p. 430.

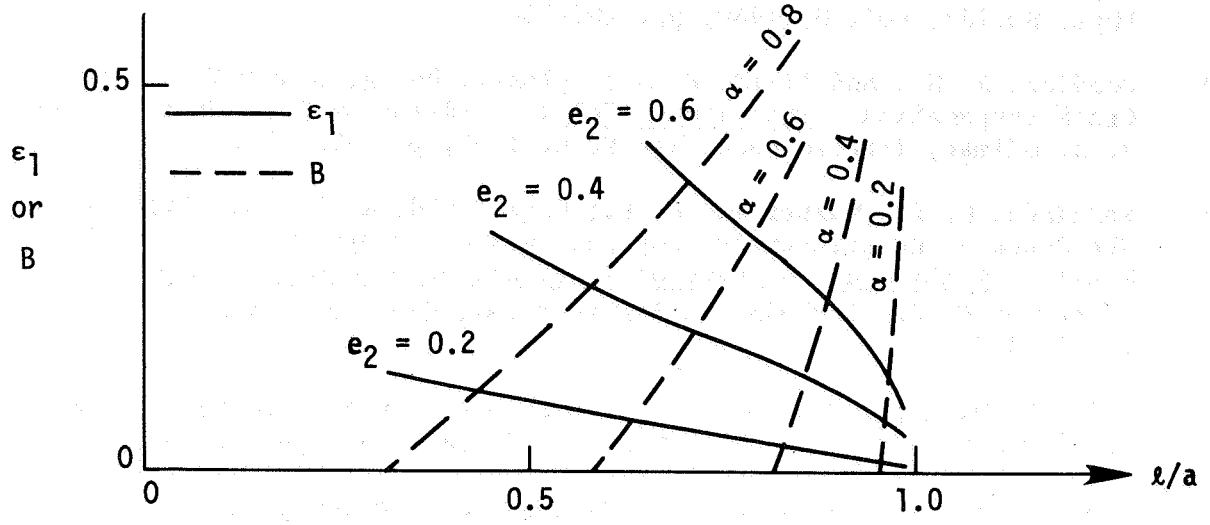

Figure 1.- Nondimensional curves of ε_1 and B for determining the plastic-zone size.

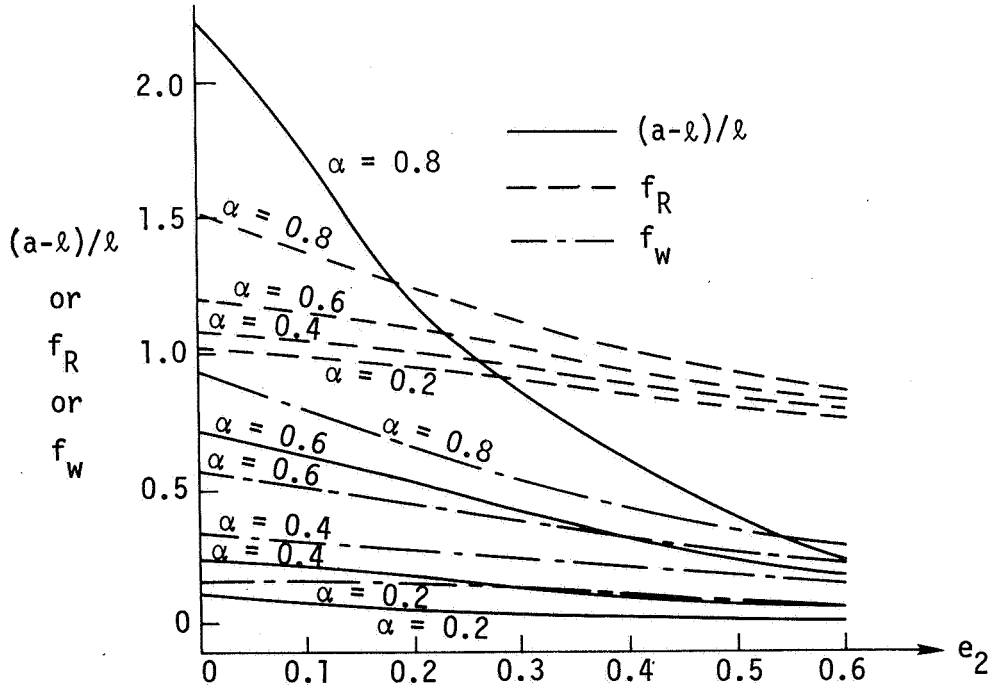

Figure 2.- Normalized plastic-zone width (a - ℓ)/ℓ and the nondimensional dynamic correction curves of f_w for the C.O.D. and f_R for the energy release rate.

A STUDY OF THE EFFECT OF SUBCRITICAL CRACK GROWTH ON THE GEOMETRY DEPENDENCE OF NONLINEAR FRACTURE TOUGHNESS PARAMETERS

D. L. Jones, P. K. Poulose, and H. Liebowitz

The George Washington University

ABSTRACT

The effect of subcritical crack growth on the geometry dependence of nonlinear fracture toughness parameters was studied by comparing the toughness values for different specimen geometries at the onset of subcritical crack growth and at the initiation of unstable crack propagation. Center-cracked thin sheet specimens of 2024-T3 and 7075-T6 aluminum alloys were tested by varying the specimen length L , width w , and crack length-to-width ratio c/w . When the onset of unstable crack propagation was selected as the critical point, the nonlinear energy toughness $\tilde{G}_c$ and the R curve toughness G_R increased with increasing w and decreasing L and c/w. However, when the onset of subcritical crack growth was taken as the critical point, G_c and the linear toughness values were independent of these geometrical variables.

The effect of thickness on the nonlinear energy toughness $\tilde{G}_{Ic}$, the J integral J_{Ic} , and the linear toughness $\overline{G}_{Ic}$ values was investigated by testing compact tension specimens of 2124-T851 aluminum alloy. At the onset of unstable crack propagation the toughness values increased with decreasing specimen thickness, but at the point of crack growth initiation they were independent of thickness and were almost the same as the G_{Ic} value for specimens that met the thickness requirement according to ASTM E399.

INTRODUCTION

In brittle materials for which the linear elastic fracture mechanics(LEFM) analysis is valid, the critical values of load and crack length in fracture toughness testing are easily identified since the common fracture mechanics specimen geometries do not exhibit subcritical crack growth. On the other hand, in semibrittle materials crack-tip plastic deformation and subcritical crack growth introduce ambiguities in the determination of the critical point and, consequently, in the fracture toughness values. Two points have received considerable attention as critical points: (i) the onset of subcritical crack growth and (ii) the initiation of unstable crack propagation, which usually corresponds to the peak load.

The occurrence of subcritical crack growth introduces analytical and experimental complexities in addition to those caused by crack-tip plastic deformation. Since an exact elastic-plastic solution for crack-tip stresses and displacements is not available today, most of the nonlinear methods suggested as fracture criteria are modifications of the linear toughness criterion and represent approximations to the actual situation. Further, all of these methods, except the R curve, are considered to be valid only when there is no subcritical crack growth. Critical examinations of the analytical bases of several of these methods have been given in references 1 and 2, and experi-

mental comparisons have been given in references 3,4, and 5. The R curve method (ref.6) was introduced specifically for situations involving subcritical crack growth, as is commonly observed in the fracture of thin sheet materials. This method evaluates the fracture toughness from the peak load and the critical crack length at the initiation of unstable crack propagation. It has the disadvantage that elastic formulas are employed to determine fracture toughness values even though subcritical crack growth and crack-tip plasticity clearly represent inelastic processes. A further disadvantage of this method is that determination of the critical crack size is by far the most difficult measurement in a fracture toughness test.

The nonlinear energy fracture toughness $\tilde{G}_c$ has also been proposed(ref.1) as a fracture toughness parameter based on the application of a general energy balance criterion to a cracked body. For an arbitrarily shaped, plane body having a through-the-thickness crack of length c, $\tilde{G}_c$ is defined as

$$\tilde{G}_c = \frac{\partial W}{\partial c} - \frac{\partial U_e}{\partial c} - \frac{\partial U_p}{\partial c} = \frac{\partial \Gamma}{\partial c} \tag{1}$$

where W is the work done, U_e is the elastic strain energy, U_p is the plastic strain energy, and Γ is the surface energy. It is emphasized that equation(1) is based on a general energy balance which permits the incorporation of large-scale plasticity and subcritical crack growth into the fracture toughness determination. However, no procedure has yet been established that is capable of evaluating equation(1) exactly for a practical fracture mechanics geometry. Therefore, an approximate method for evaluating $\tilde{G}_c$ has been developed(ref.1) that is based on the Ramberg-Osgood representation of the load-displacement record

$$v = \frac{F}{M} + k\left(\frac{F}{M}\right)^n . \tag{2}$$

In equation 2, M is the initial tangent modulus and n and k are constants for a given test. From equation(2) an expression for $\tilde{G}_c$ has been obtained as

$$\tilde{G}_c = \left[1 + \frac{2nk}{n+1}\left(\frac{F}{M}\right)^{n-1}\right]\bar{G}_c = \tilde{C}\bar{G}_c \tag{3}$$

where $\bar{G}_c$ is the linear toughness value employing the initial crack length and the load corresponding to the critical point, and $\tilde{C}$ is primarily a measure of the curvature of the load-displacement record.

Another fracture toughness parameter J_{Ic} based on the J integral(ref.7), has been proposed for situations of elastic-plastic material response in the absence of crack growth. The J integral was originally defined only for nonlinear elastic material response and was also shown to be given by

$$J = -\frac{\partial P}{\partial c} \tag{4}$$

where P is the global elastic potential energy. This definition was used by Begley and Landes(ref.8) as a basis for determining J_{Ic} at the onset of subcritical crack growth. Hence, J_{Ic} can be considered a nonlinear elastic extension of the linear elastic toughness criterion G_{I_c}, valid only in the

absence of subcritical crack growth.

The purpose of this paper is to discuss the dependence of several fracture toughness parameters on the specimen geometry and on the choice of critical points. The results are based on comparisons that were made at the onset of subcritical crack growth and at unstable fracture. The linear, R curve, and nonlinear energy toughness parameters were evaluated for the thin sheet specimens. For the compact tension specimens the linear, J integral, and nonlinear energy toughness parameters were evaluated and compared. Then, the relative merits of the various nonlinear fracture toughness methods were compared and discussed.

EXPERIMENTAL PROCEDURE

The influence of subcritical crack growth on geometry dependence was studied using center-cracked, 1.6mm(0.063in.) thick sheet specimens of 7075-T6 and 2024-T3 aluminum alloys and compact tension specimens of 2124-T851 alloy. In center-cracked specimens the displacements were measured at the loading points. The gauge length was nominally 76.2mm(3in.) less than the specimen length. The notch tip was filed to a radius of 0.076-0.127mm(0.003-0.005in.). The tests were conducted in load control, and slow crack growth was monitored visually using a 10X magnifier and lines scribed at intervals of 1.27mm(0.05in.). Three series of tests were performed on each alloy in the L-T orientation by varying: (i) the length L from 254 to 890mm(10 to 35in.), (ii) the width w from 102 to 356mm(4 to 14in.), and (iii) the crack length-to-width ratio c/w from 0.3 to 0.6, while keeping the other parameters constant in each series. Duplicate tests were conducted for each geometry, and anti-buckling guides were not used.

The effect of specimen thickness on the nonlinear fracture toughness values was examined using compact tension specimens of 2124-T851 with thicknesses above and below the ASTM minimum requirement for plane strain fracture (E399). The specimens conformed to the ASTM standard except for the thickness. Since it was not possible to directly measure the subcritical crack growth in these specimens, indications of crack growth were obtained from sudden changes in the slope of the load-displacement curves.

Nonlinear Energy Method.— The experimental procedure for evaluating equation(4) is straightforward due to the separation of the linear and nonlinear portions of G_c. $\overline{G}_c$ can be obtained directly from standard expressions for the stress intensity factors and the appropriate G-K relations. It has been shown(eq.3) that $\tilde{C}$ can be evaluated by the equation

$$\tilde{C} = 1 + \frac{2n(1-\alpha_2)}{\alpha_2(n+1)} \tag{5}$$

where

$$n = 1 + \ell n \frac{\alpha_1(1-\alpha_2)}{\alpha_2(1-\alpha_1)} \Big/ \ell n \frac{F_2}{F_1} . \tag{6}$$

In these equations the values of F_1 and F_2 are obtained from reduced modulus secant lines drawn to the nonlinear load-displacement curve. The second secant line with slope $\alpha_2 M$ should intersect the load-displacement record at the critical point($F_2=F_c$), and the first should approximately bisect the angle between

the tangent modulus M and $\alpha_2 M$.

R Curve.— For the center-cracked panels tested, significant measurable subcritical crack growth was observed prior to unstable fracture. Therefore, the fracture toughness G_R according to the R curve method was evaluated for comparison with the nonlinear energy fracture toughness. According to recent discussions on the R curve method(ref.2,6), G_R is evaluated by substituting the crack size and load at the instability point into the appropriate linear stress intensity factor. For the center-cracked sheets, the ASTM polynomial was employed in the form

$$G_R = \frac{K_c^2}{E} = \frac{\sigma_c^2 \pi c_c}{E}\left[1 - 0.1\left(\frac{c_c}{w}\right) + \left(\frac{c_c}{w}\right)^2\right]^2 . \tag{7}$$

It is acknowledged, however, that measurement of the critical crack size is difficult, especially for materials such as 2024-T3 aluminum in which the transformation from subcritical cracking to unstable fracture occurs gradually rather than instantaneously.

J Integral.— For determining J_{Ic} toughness values from the compact tension specimens, an approximate procedure suggested for bend type specimens(ref.8,9) was followed from which J_{Ic} was obtained as

$$J_{Ic} = \frac{2A}{B(w-c)} . \tag{8}$$

In equation(8) the area A under the load-load point displacement curve was obtained from the Ramberg-Osgood representation as

$$A = \frac{\tilde{C} F_c^2}{2M} . \tag{9}$$

RESULTS AND DISCUSSION

The tests conducted on the center-cracked and compact tension specimen geometries covered a wide range of geometrical variables. The selection of the critical point on the load-displacement curve corresponding to the onset of unstable fracture was easy since it corresponded to the peak load. However, load-displacement diagrams for the center-cracked specimens did not exhibit a marked change in slope at the onset of subcritical crack growth; therefore, the exact point of crack extension was not readily determined. Hence for these specimens, load versus crack length plots were made, and the loads corresponding to one percent crack growth were chosen to represent the initiation of slow crack growth. For the compact tension specimens, the onset of subcritical crack growth was detected by sudden changes in the slope of the load-displacement curve.

The results of the tests of the effects of specimen length on fracture toughness values for 7075-T6 center-cracked sheets are shown in figure 1. Since the R curve toughness G_R is applicable only at the maximum load, the nonlinear energy toughness $\tilde{G}_c$ was compared with G_R only at this point. At the onset of subcritical crack growth, the nonlinear energy toughness $\tilde{G}_{sc}$ was compared with the linear toughness $\bar{G}_{sc}$. At the peak load, both $\tilde{G}_c$ and G_R increased

with decreasing specimen length, with $\tilde{G}_c$ consistently larger than G_R. It is noted that, as the gauge length decreased, the difference between $\tilde{G}_c$ and G_R increased significantly. The authors feel that this difference is due to the nonlinearity in the load-displacement record resulting from crack-tip plasticity, since the R curve method does not incorporate crack-tip plasticity into the G_R toughness values. At the onset of stable crack growth, both $\tilde{G}_{sc}$ and $\overline{G}_{sc}$ remained practically independent of specimen length. The difference between $\tilde{G}_{sc}$ and $\overline{G}_{sc}$ also increased slightly as the gauge length decreased. This difference is clearly caused only by nonlinearity in the load-displacement record resulting from crack-tip plasticity, since the only difference between the two toughness values is $\tilde{C}$. The most direct comparisons of the effect of subcritical crack growth are obtained between $\tilde{G}_c$ and $\tilde{G}_{sc}$, when the nonlinearity of the load-displacement response is included, and between G_R and $\overline{G}_{sc}$, when the nonlinearity is not considered. In both cases it is seen that a severe penalty in terms of decreased toughness values is paid whenever subcritical crack growth is excluded from consideration.

In the more ductile 2024-T3 alloy, the variation of $\tilde{G}_c$ and G_R with length at peak load was greater than for the 7075-T6(fig.2), but both alloys displayed the same trend. As in the case of 7075, the toughness parameters for 2024 also exhibited a length independency when evaluated at the onset of stable crack growth. However, it is also noted that the differences between $\tilde{G}_c$ and G_R are much greater for 2024-T3 than for 7075-T6. This result shows more dramatically the decreased toughness values which result when the crack-tip plasticity is not considered. When both crack-tip plasticity and subcritical crack growth are taken into account, figure 2 shows that the highest toughness value $\tilde{G}_c$ (for the shortest gauge length), is approximately four times the lowest $\overline{G}_{sc}$. The width series and c/w series tests, which are not included in this paper, showed that both $\tilde{G}_c$ and G_R determined at peak load increased with increasing width and decreasing c/w in 2024, while this effect was less pronounced in 7075. The toughness values determined at the onset of stable crack growth in these alloys exhibited little dependency on width and c/w.

The R curve method has not been suggested for thick specimens. Hence in compact tension specimens, the nonlinear energy toughness $\tilde{G}_{Ic}$, the J integral, J_{Ic}, and the linear toughness $\overline{G}_{Ic}$ were compared. The variation of $\tilde{G}_{Ic}$, J_{Ic}, and $\overline{G}_{Ic}$ on compact tension specimens of 2124-T851 with thickness is illustrated in figure 3. Also included in figure 3 are the values of these toughness parameters evaluated at the onset of subcritical crack growth and designated $\tilde{G}_{Isc}$, J_{Isc}, and $\overline{G}_{Isc}$ respectively. As in the center-cracked specimens, the toughness parameters determined at peak load showed a geometry dependence; they increased with decreasing thickness, and all three parameters varied in a similar manner. The $\tilde{G}_{Ic}$ and J_{Ic} values behaved in a similar manner, with $\tilde{G}_{Ic}$ consistently larger than J_{Ic}, and their difference from $\overline{G}_{Ic}$ increased with decreasing thickness. The J_{Ic} and $\tilde{G}_{Ic}$ values agreed with the ASTM value G_{Ic} when the thickness was sufficient to cause plane strain fracture. Therefore, these toughness

values for the two thickest specimens were not included in figure 3 since they overlapped $\tilde{G}_{Isc}$, J_{Isc}, and $\bar{G}_{Isc}$. When determined at the onset of subcritical crack growth, $\bar{G}_{Isc}$, $\tilde{G}_{Isc}$, and J_{Isc} were within ten percent of each other, and the values remained unchanged with changes in specimen thickness.

The linear toughness values determined at the onset of subcritical crack growth $\bar{G}_{Isc}$ remain essentially constant in the entire thickness range with no appreciable differences between $\tilde{G}_{Isc}$ and the linear toughness. Thus, it was concluded that valid linear toughness values can be obtained from specimens much thinner than that required by ASTM E399 by evaluating $\bar{G}_{Isc}$. As compared to the agreement between $\bar{G}_{Isc}$, $\tilde{G}_{Isc}$, and J_{Isc} values at all thicknesses, the differences of $\tilde{G}_{Ic}$ and J_{Ic} values from $\bar{G}_{Ic}$ increase with decreasing thickness. The extent of subcritical crack growth also is larger when the thickness is smaller. This indicates that the nonlinearity due to crack-tip plastic deformation before crack growth initiation is very limited and that the major contribution to nonlinearity is due to subcritical crack growth and plastic deformation after the onset of stable crack growth.

CONCLUSIONS

The effect of subcritical crack growth on the geometry dependence of the linear and several nonlinear toughness parameters was investigated by varying the specimen length, width, and crack length-to-width ratio in center-cracked specimens and by varying the thickness in compact tension specimens. It was observed that the geometry dependence of various toughness parameters was dependent on the choice of the critical point. The following conclusions were made.

1. In thin sheet specimens, when the peak load was chosen as the critical point $\tilde{G}_c$ and G_R increased with increasing width and decreasing length and c/w. When the critical point was the onset of crack growth initiation, the geometry dependence was negligibly small. The geometry dependence was more pronounced in the more ductile 2024-T3 than in the more brittle 7075-T6.
2. In the compact tension specimens $\bar{G}_{Ic}$, $\tilde{G}_{Ic}$, and J_{Ic} increased with decreasing thickness in a similar fashion when the peak load was chosen as the critical point. When the onset of subcritical crack growth was used as the critical point, all of the toughness parameters were independent of specimen thickness.
3. The results of these experiments indicate that valid G_{Ic} values can be obtained from specimens of thickness much lower than that required by ASTM E399, if the onset of subcritical crack growth is chosen as the critical point.

4. The contribution of nonlinear effects to toughness values is very small prior to crack growth initiation; the major contribution arises from subcritical crack growth and plasticity after the onset of stable crack growth.

REFERENCES

1. Eftis, J.; Jones, D. L.; and Liebowitz, H.: On Fracture Toughness in the Nonlinear Range. Eng. Fract. Mech., vol. 7, 1975, pp. 491-504.

2. Eftis, J.; and Liebowitz, H.: On Fracture Toughness Evaluation for Semibrittle Fracture. Eng. Fract. Mech., vol. 7, 1975, pp. 101-136.

3. Jones, D. L.; Poulose, P. K.; and Liebowitz, H.: A Comparison of the Effect of Specimen Thickness and Subcritical Crack Growth on Several Nonlinear Fracture Toughness Parameters. Presented at the Int. Conf. Mech. Behavior of Mater. II, Boston, 1976.

4. Liebowitz, H.; Jones, D. L.; and Poulose, P. K.: Development of the Nonlinear Energy Method for Determination of Fracture Toughness Values. Prospects of Fracture Mechanics, ed. by Sih, Van Elst and Broek, Noordhoff, 1974, pp. 103-123.

5. Liebowitz, H.; Jones, D. L.; and Poulose, P. K.: Theoretical and Experimental Comparisons of the Nonlinear Energy Method to the J Integral, R Curve and COD Methods in Fracture Toughness Testing. Proc. 1974 Sym. Mech. Behavior of Mater., vol. 1, Society of Materials Science, Japan, 1974, pp. 1-20.

6. Fracture Toughness Evaluation by R Curve Methods. Spec. Tech. Pub. 527, American Soc. Testing & Mater., 1973.

7. Rice, J. R.: A Path Independent Integral and the Approximate Analysis of Strain Concentration by Notches and Cracks. J. Appl. Mech., 1968, p. 379.

8. Landes, J. D.; and Begley, J. A.: Test Results from J Integral Studies - An Attempt to Establish a J_{Ic} Testing Procedure. Sci. Paper 73-1E7-FMPWR-P3, Westinghouse Research Laboratories, 1973.

9. Rice, J. R.; Paris, P. C.; and Merkle, J. G.: Some Further Results of J Integral Estimation Procedures. Progress in Flaw Growth and Fracture Toughness Testing, Spec. Tech. Pub. 536, American Soc. Testing & Mater., 1973, p. 231.

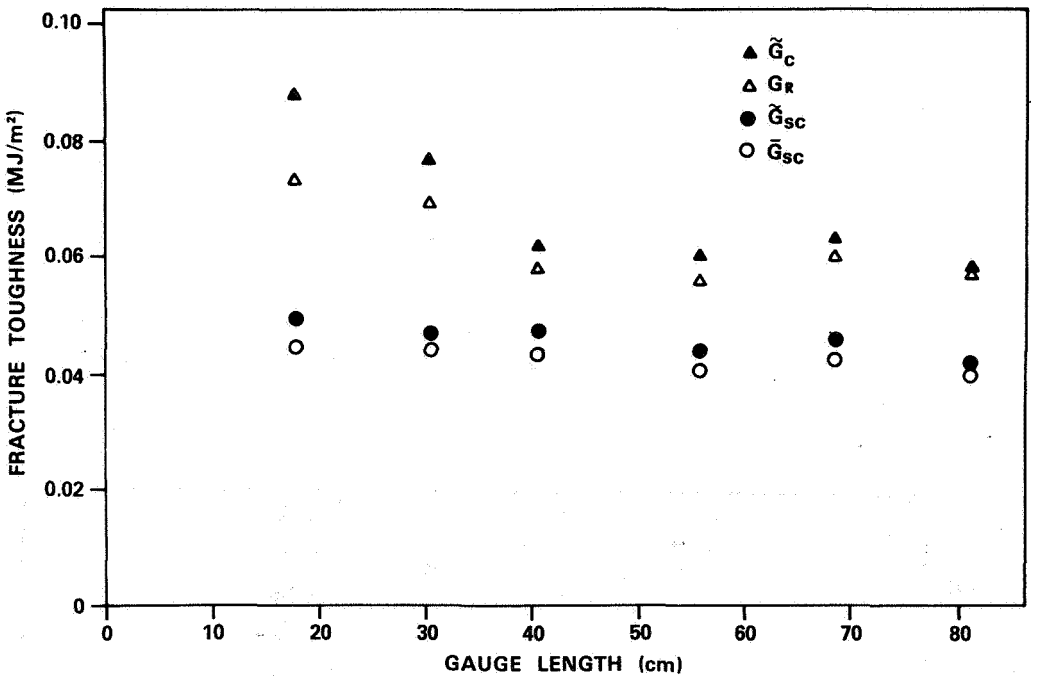

Figure 1.- Fracture toughness of 7075-T6 sheets as a function of gauge length, evaluated at the onset of subcritical crack growth and at peak load.

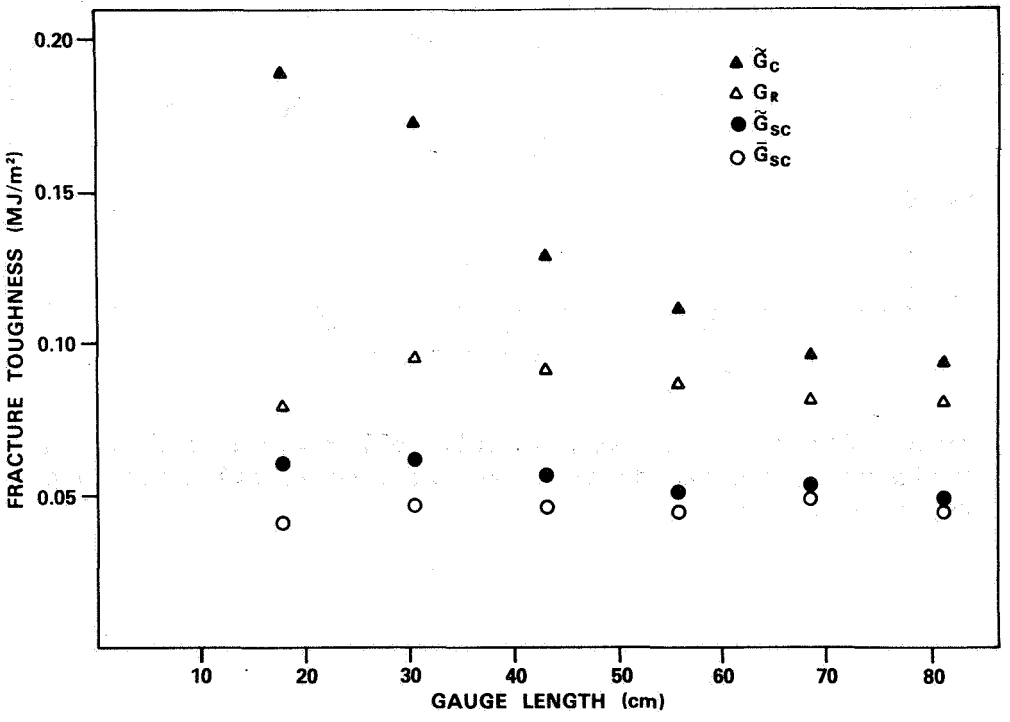

Figure 2.- Fracture toughness of 2024-T3 sheets as a function of gauge length, evaluated at the onset of subcritical crack growth and at peak load.

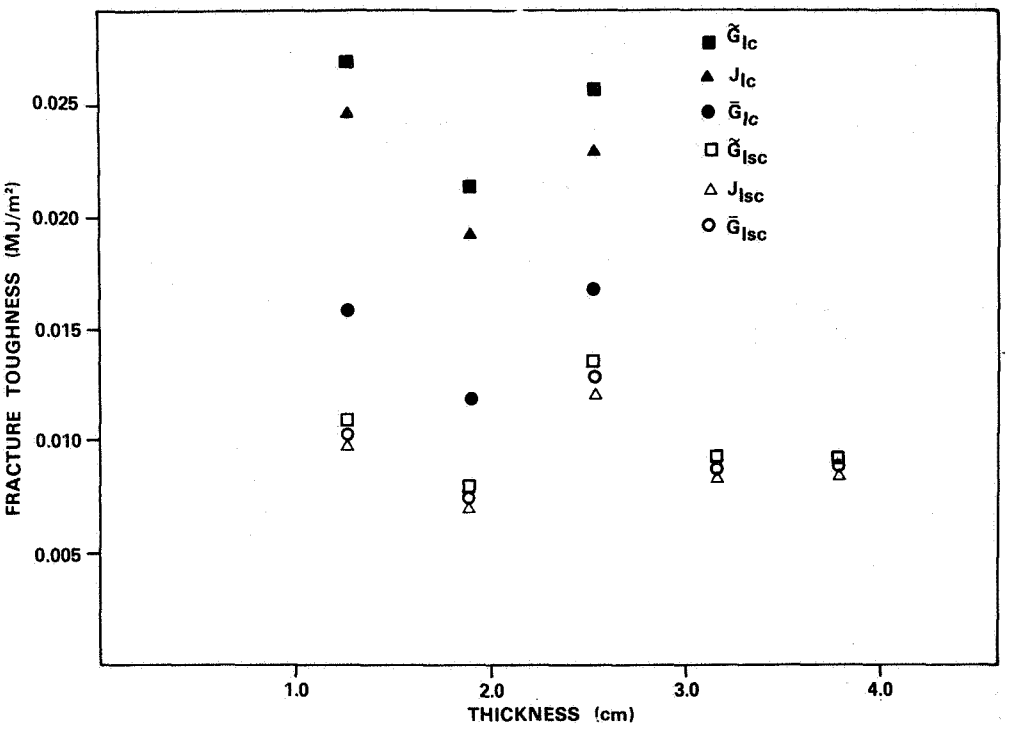

Figure 3.- Fracture toughness of 2124-T851 alloy as a function of thickness, evaluated at the onset of subcritical crack growth and at peak load.

ON A 3-D "SINGULARITY ELEMENT" FOR COMPUTATION OF COMBINED MODE STRESS INTENSITIES*

Satya N. Atluri and K. Kathiresan
Georgia Institute of Technology

ABSTRACT

A special three-dimensional "singularity" element is developed for the computation of combined modes I, II and III stress intensity factors, which vary along an arbitrarily curved crack front in three-dimensional linear-elastic fracture problems. The finite element method is based on a "displacement-hybrid" finite element model, based on a modified variational principle of potential energy, with arbitrary element-interior displacements, inter-element boundary displacements, and element boundary tractions as variables. The special crack-front element used in this analysis contains the square root singularity in strains and stresses, where the stress-intensity factors K_I, K_{II}, and K_{III} are quadratically variable along the crack front and are solved directly along with the unknown nodal displacements. Stress intensity factors for buried elliptical flaws of various aspect ratios, semi-elliptical flaws of various aspect ratios and crack-depth/specimen thickness ratios, and quarter-elliptical corner flaws of various aspect ratios, in a finite-sized uni-axial tension specimen are presented. The qualitative nature of these results is discussed.

INTRODUCTION

The problem of computing stress-intensity factors (SIF) for three-dimensional crack geometries is receiving considerable attention currently. This task, however, is a formidable one, with analytical solutions being limited to simple embedded crack geometries in an infinite space. The problems of embedded circular or elliptical flaws near a free surface have been studied using the Schwarz-Newmann alternating technique for instance (ref. 1,2). Part circular and semi-elliptical cracks intersecting with a free surface ("surface-cracks") have also been studied (ref. 3,4) by the alternating technique. However, as is now widely recognized, the alternating technique suffers from an intrinsic difficulty when the crack intersects a free surface, viz., at each alternating step where residuals are removed from the crack faces, a singular spike of residual normal stress is introduced on the free surface which intersects the crack. Treatment of embedded and surface flaws through the boundary-integral equation method have also been presented (ref. 5) for mode I type

* This work was supported by AFOSR Grant 74-2667, and in some parts by NSF grant ENG-74-21346. We gratefully acknowledge these, and the encouragement of Dr. W.J. Walker.

problems. The procedure used in reference 5 is to use the usual boundary-integral-equation type modelling of the three-dimensional cracked body; however, with a finer surface element breakdown near the crack-front. The SIF in mode I were then computed in reference 5 from the computed crack-opening displacements. The object of the present paper is to describe an "embedded-singularity," special crack front element based on the hybrid-displacement model, which is used to compute directly the combined modes I, II, and III SIF variations along a crack front.

BRIEF DESCRIPTION OF "EMBEDDED-SINGULARITY", SPECIAL CRACK FRONT ELEMENT

Consider a triad of orthonormal coordinates: "t" tangential to crack border; 'n', local outward normal to the crack border and lying in the crack plane; and 'z' normal to both the 't' and 'n' axes. From the well-known, general solution of an embedded elliptical crack the asymptotic solution for displacements near the crack front is known to be,

$$U_i^a \sim \left[U_i^a \ (\sqrt{r},\theta) \right] \begin{Bmatrix} K_I(t) \\ K_{II}(t) \\ K_{III}(t) \end{Bmatrix} \tag{1}$$

where r,θ are polar coordinates centered at a point on the crack border and in the n-z plane, and the index $i = 1,2,3$ is used such that $U_1 \equiv U_t$, $U_2 \equiv U_n$ and $U_3 \equiv U_z$. Our aim is to embed the above asymptotically correct singular displacements, and the corresponding singular stresses, in finite elements immediately near to the crack front. To keep the size of the finite element optimally finite, we include also regular, arbitrary order, polynomial displacement assumptions in these near field elements. In doing so, interelement displacement compatibility and traction equilibrium cannot be achieved in a trivial manner. To this end, we use the displacement-hybrid finite element model (refs. 6,7) which enforces these interelement conditions through a Lagrange Multiplier technique. It has been shown in reference 6 that the variational principle governing this hybrid finite element model for linear elastic problems, is $\delta\pi = 0$, where

$$\pi \left[U_i, V_i, T_{Li} \right] = \sum_{m=1}^{M} \left\{ \int_{\Omega_m} \left[\frac{1}{2} E_{ijk\ell} \epsilon_{ij} \epsilon_{k\ell} - \bar{F}_i U_i \right] d\Omega - \int_{s_{\sigma_m}} \bar{T}_i U_i \ ds \right.$$

$$\left. + \int_{s_{u_m}} T_i (U_i - \bar{U}_i) \ ds - \int_{\rho_m} T_{Li} (U_i - V_i) \ d\rho \right\} \tag{2}$$

where Ω_m is the domain of m^{th} element, $\varepsilon_{ij} = 1/2(U_{i,j} + U_{j,i})$ is strain, $E_{ijk\ell}$

are elastic constants, U_i are displacements in the interior of the element, ρ_m is the interelement boundary, V_i is independently assumed interelement boundary displacement (at ρ_m) and T_{Li} are Lagrange Multipliers (which are physically the independently assumed boundary tractions) at ρ_m, needed to enforce the constraint of interelement compatibility, $U_i = V_i$ at ρ_m for adjoining elements. In developing the 'singularity element', we then make the following assumptions for each of such elements:

$$U_i = \left[U_i^R\ (r,\theta,t)\right]\{\beta\} + \left[U_i^a\ (\sqrt{r},\theta)\right]\begin{Bmatrix} K_I(t) \\ K_{II}(t) \\ K_{III}(t) \end{Bmatrix} \tag{3}$$

where superscript R is used to denote regular, arbitrary order, polynomials,

$$V_i = [L_s]\ \{q\} \quad \text{and} \quad T_{Li} = [R_s]\ \{\alpha\} \tag{4}$$

We note that boundary displacements L_s contain $\sqrt{r}$ variation on appropriate boundaries and likewise boundary tractions R_s contain $1/\sqrt{r}$ variation on appropriate boundaries, of a singular element. Referring to reference 7 for all the intermediate details of assumed functions and the variational procedure to obtain the final matrix equations, we note that the above hybrid-displacement method, as applied to fracture calculations, leads to the final equations:

$$\begin{bmatrix} \mathbb{K}_o & \mathbb{K}_1^T \\ \hline \mathbb{K}_1 & \mathbb{K}_2 \end{bmatrix} \begin{Bmatrix} \underset{\sim}{q}^* \\ \hline \underset{\sim}{K} \end{Bmatrix} = \begin{Bmatrix} Q_1^* \\ \hline Q_2^* \end{Bmatrix}$$

where

$$\left[\underset{\sim}{k}\right] = \left[K_I^J,\ K_{II}^J,\ K_{III}^J\right]$$

are the combined mode stress intensities at all nodes at the crack front, J = 1,2...m, and thus these are calculated directly. Some applications of the present method are given below.

BURIED ELLIPTICAL CRACK IN A FINITE SPECIMEN

The specimen dimension is 2H × 2H × 2H, H = 5. The area of quarter ellipse, viz., $(\pi/4)$ ab is kept constant, and the aspect ratio (a/b) is varied from 4 to 1 (fig. 1). In this and all the following cases, the Poisson's ratio $\nu = .3$. The exact solution for a buried elliptical crack in an infinite solid is displayed in figure 2 for convenience, and the finite element modelling of the present finite-sized specimen is shown in figure 3. The computed K_I variations and their comparison with the infinite-domain exact solution are shown in figure 4 for various (a/b) ratios. We note that the normalizing factor used in figure 4 is the exact K_I solution for a buried circle

of radius b, in an infinite solid. It is seen that when (a/b) = 4 (and corresponding a/H = .4 and b/H = .1) the finite-width correction is about +20% at the ellipse major axis location, and this correction drops to about +5% near the minor axis location where the stress-intensity is the maximum. These finite-width corrections reduce progressively as a/b decreases, and when a/b = 1 (buried circular crack) the finite-width correction is +3%. We note that the boundary-integral method (BIE) (ref. 5) for the identical problem yields little or no finite-width corrections to the infinite-domain solutions for all aspect ratios. Part of this discrepancy in reference 5 could be due to the fact the solutions reported in reference 5 were normalized w.r.t. the numerical solution, obtained through BIE method, for the buried-circle crack. However, it appears that in reference 5 the numerical solution of the buried circular crack was 8-10% lower than the corresponding infinite-domain solution.

SEMI-ELLIPTICAL SURFACE FLAWS IN A FINITE SPECIMEN

The K_I variations for the surface crack, for various a/b ratios, normalized with respect to the solution of a buried crack of the same aspect ratio and in an infinite solid, are shown in figure 5. Unfortunately, in varying a/b ratio, because H was kept constant, the depth ratio b/H (and hence a/H) also varied continuously. It is seen that for a/b = 4 (a/H = .4 and b/H = .1) the maximum stress intensity magnification occurs near the free surface. This free-surface stress-intensity magnification factor decreases continuously as a/b is decreased. At a/b = 1 (semi-circular surface flaw) the obtained solution is found to agree well with reference 4. It is interesting to note that as a/b becomes less than 1, the maximum stress-intensity magnification occurs at the point of deepest penetration, rather than at the free surface. It is seen from figure 5, that for a/b = 0.25 (a/H = .1, b/H = .4) i.e., when the crack depth is 40% of the specimen thickness, the stress-intensity magnification at point of deepest penetration is about 17% higher than that of the free surface. For this case of a narrow and deep surface flaw, it may be expected that the K_I value in the neighborhood of the free surface approaches that of a through-the-thickness crack, and the presently computed results appear to confirm this. The present results, however, are found to differ significantly from those in reference 5 for identical problems. Further comparison of the present results with those in reference 5 is omitted here for want of space.

QUARTER-ELLIPTICAL CORNER CRACKS IN A FINITE SPECIMEN

The K_I variations, normalized using the same procedure as in figure 5, are shown in figure 6 for various a/b ratios. Once again, it is seen that the maximum stress-intensity magnification occurs near the point of intersection of the major axis of the ellipse, the crack front, and the free surface, as may be expected. This maximum stress-intensity magnification drops as a/b decreases, until when a/b = 1, this quantity is the same at both points of intersection of the crack front with the free surfaces. Once again, the present

results differ significantly from those in reference 5, and further discussion of this is omitted for want of space. However, one reason for this discrepancy may be the particular normalization procedure, mentioned earlier, that is used in reference 5.

CLOSURE

An efficient embedded singularity element is developed and applied in several problems of buried, surface, and corner cracks that usually occur in practical situation. However, since the developed procedure hinges on embedding a $1/\sqrt{r}$ type stress singularity near the crack front, it cannot be expected to yield any new insights into the nature or strength of singularity right at the intersection of the crack front with a free surface.

REFERENCES

1. Smith, F. W.; and Alavi, M. J.: Engineering Fracture Mechanics, vol. 3, 1974, pp. 241-254.

2. Shah, R. C.; and Kobayashi, A. S.: International Journal of Fracture, vol. 9, 1973, pp. 133-146.

3. Hartrauft, R. J.; and Sih, G. C.: Chapter 4, Methods of Analysis and Solutions of Crack Problems, (G. C. Sih, Editor) Noordhoff Publ. Leyden, 1973.

4. Kobayashi, A. S.; Polvanich, N.; Emery, A. F.; and Love, W. J.: Proceedings of 12th Annual Meeting of Society of Engineering Science, Austin, Texas, 1975, pp. 343-353.

5. Cruse, T. A.: Boundary-Integral Equation Method for Three-Dimensional Elastic Fracture Mechanics Analysis, AFOSR-TR-75-0813, May 1975, Accession No. ADA011660.

6. Atluri, S. N.; Kobayashi, A. S.; and Nakagaki, M.: International Journal of Fracture, vol. 11, no. 2, 1975, pp. 257-271.

7. Atluri, S. N.; Kathiresan, K.; and Kobayashi, A. S.: Paper L-7/3, Trans. of 3rd Internation Conference on Structural Mechanics in Reactor Technology, CECA, CEE, CEEA, Luxembourg, 1975.

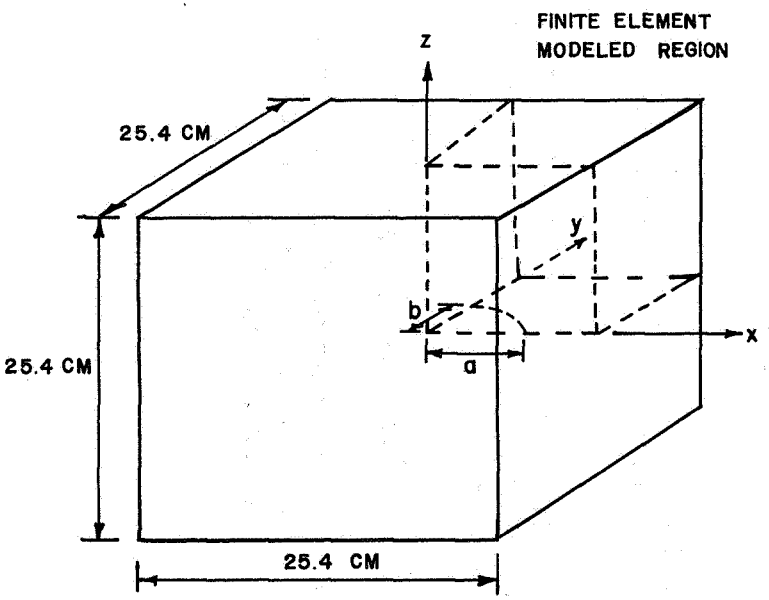

AREA OF QUARTER ELLIPSE = $\frac{\pi}{4} \times 2.54^2$ CM^2

ASPECT RATIOS: a/b = 0.25, 0.5, 0.667, 1.0, 1.5, 2.0, 4.0

Figure 1.- Problem definition (cube containing buried elliptical crack).

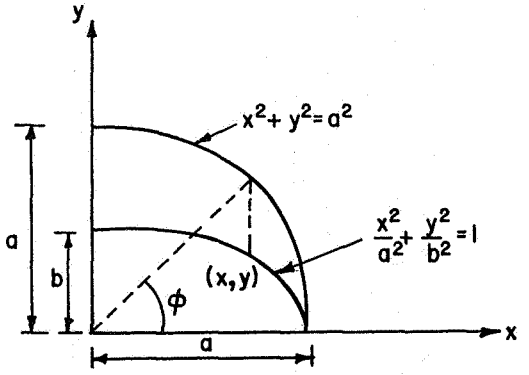

$$K_I = \frac{\sigma\sqrt{\pi b}}{E(k)}\left\{\sin^2\phi + \left(\frac{b}{a}\right)^2\cos^2\phi\right\}^{1/4} \quad a > b$$

ϕ = ELLIPTICAL ANGLE

σ = STRESS NORMAL TO PLANE OF ELLIPSE

$$E(k) = \int_0^{\pi/2}\sqrt{1-k^2\sin^2\psi}\;d\psi$$

$$= \frac{\pi}{2}\left[1-(1/2)^2k^2-\left(\frac{1}{2}\cdot\frac{3}{4}\right)^2\frac{k^4}{3}-\left(\frac{1}{2}\cdot\frac{3}{4}\cdot\frac{5}{6}\right)^2\frac{k^6}{5}-\ldots\right]$$

$$k^2 = 1-b^2/a^2$$

Figure 2.- Exact solution for buried elliptical crack in an infinite solid.

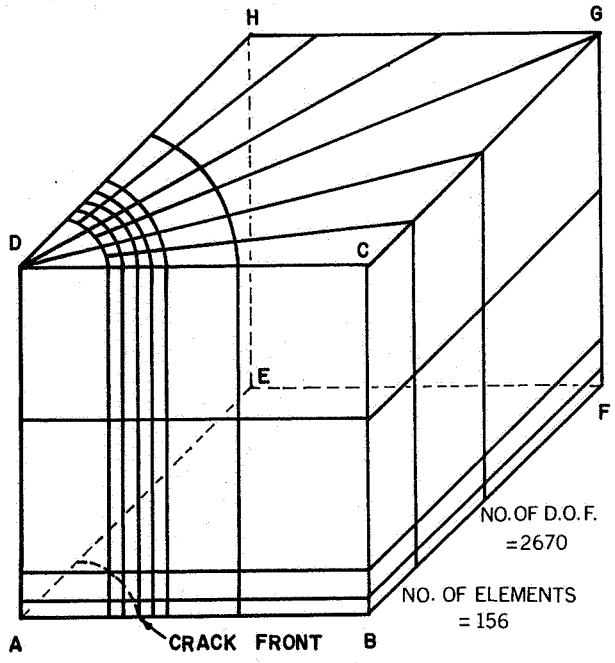

ON FACES ABCD, ADHE AND ABFE BOUNDARY CONDITIONS CAN BE APPLIED APPROPRIATELY TO GENERATE BURIED, SURFACE AND CORNER CRACK PROBLEMS

Figure 3.- Finite element breakdown for circular and elliptical crack problems.

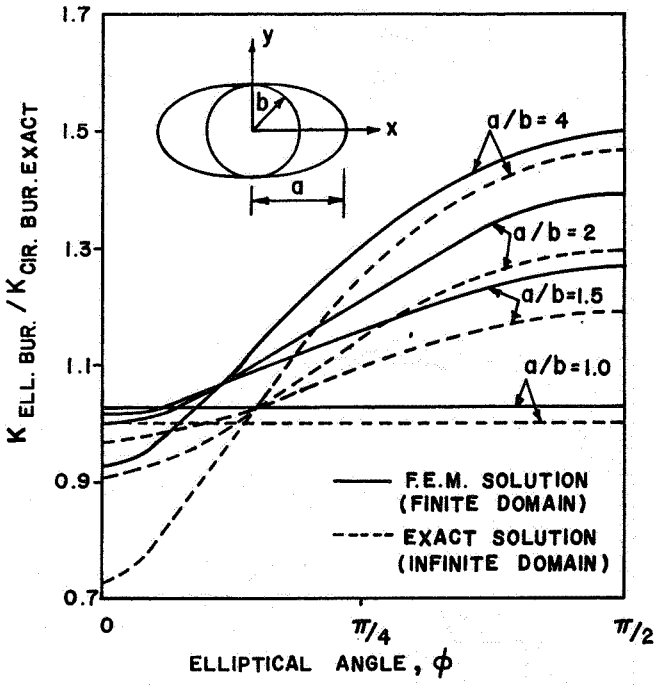

Figure 4.- Variation of stress-intensity factors for buried elliptical cracks.

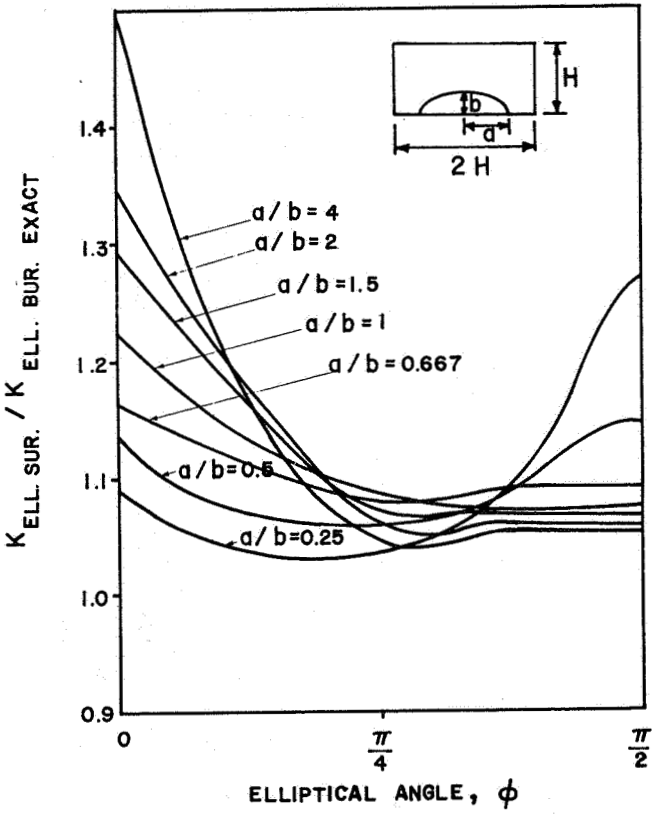

Figure 5.- Variation of stress-intensity factors for semi-elliptical surface cracks.

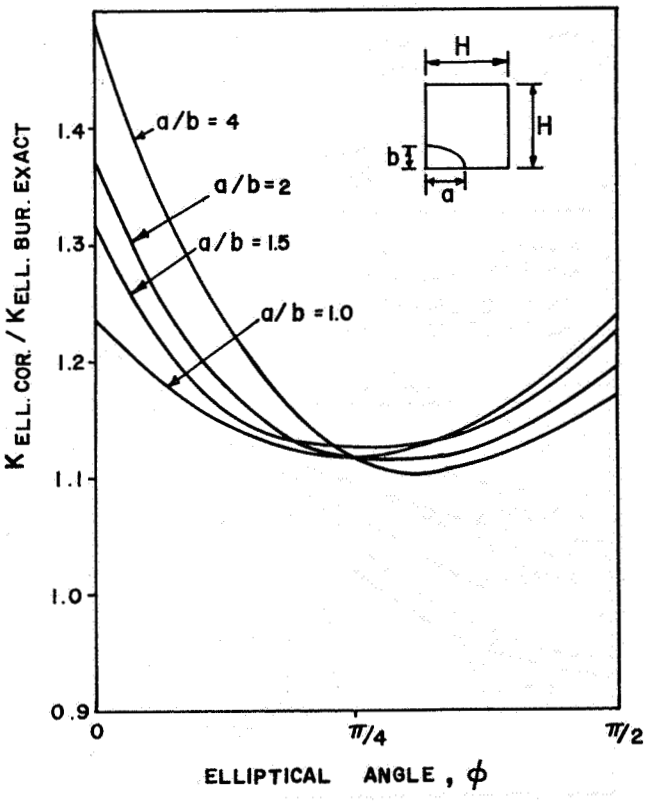

Figure 6.- Variation of stress-intensity factors for quarter-elliptical corner cracks.

INFLUENCE OF A CIRCULAR HOLE UNDER UNIFORM NORMAL PRESSURE ON THE STRESSES AROUND A LINE CRACK IN AN INFINITE PLATE

Ram Narayan and R. S. Mishra
Banaras Hindu University, India

SUMMARY

Based on the two-dimensional theory of elasticity and by the use of Muskhelishvili's technique, the influence of a circular hole, under uniform normal pressure, on the stresses around a line crack in an infinite plate subjected to tension is discussed. Numerical calculations were carried out and the variation of the crack-tip stress intensity factor due to the geometry was clarified.

INTRODUCTION

The regions near crack tips are usually in an elastoplastic stress state for which analytical solutions are difficult to obtain except for quite simple cases. In the design of aircrafts, ships, and other machines, it is often important to know the state of stress and strain around cracks in sheet structures.

The study in crack problems was first initiated by Inglis (ref. 1); however, the interest in such problems stemmed from Griffith's paper (ref. 2). The cases of straight crack, circular crack, star crack, and penny-shaped crack have been studied by many investigators. The problem of an infinite plate containing a circular hole was discussed by Green (ref. 3) and others. The problem of a circular hole under uniform normal pressure in an infinite plate was considered in reference 4. An effort to combine the above two problems forms the subject matter of the present paper.

This paper deals with the problem of an infinite isotropic elastic material called matrix containing a straight crack from (a,0) to (b,0) and a circular hole of radius R with center at any point M (M may be complex). The crack and the hole do not overlap. The rims of the crack are free from external tractions and the boundary of the circular hole is subjected to a uniform normal pressure P. The matrix is subjected to a load at infinity (see fig. 1). It is assumed that rotation at infinity is zero, as it does not affect the stresses. A dual homogeneous Hilbert problem is formulated for two functions $\phi(z)$ and $\Omega(z)$ by using the condition given at the rims of the crack. Solution of the Hilbert problem is obtained by the use of the complex

variable technique developed by Muskhelishvili. Once the functions $\phi(z)$ and $\Omega(z)$ are known, the elastic field in the region under consideration can be determined very easily.

SYMBOLS

σ_x, σ_y, τ_{xy}	Cartesian stress components
σ_r, σ_θ, $\tau_{r\theta}$	polar stress components
u_x, u_y	Cartesian displacement components
$\phi(z)$, $\Psi(z)$	complex potential for sheet
μ, ν	shear modulus and Poisson's ratio of sheet, respectively
κ	for plane deformation, $3-4\nu$, for generalized plane stress, $(3-\nu)/(1+\nu)$
N_1, N_2	values of principal stresses at infinity
β	angle between the principal axis, corresponding to N_1 and x-axis
A_n, B_b, D_n, E_n	parametric coefficients included in $\phi(z)$ and $\Psi(z)$

BASIC EQUATIONS

The fact that the solution of a two-dimensional elasticity problem depends upon finding two holomorphic functions $\phi(z)$ and $\Psi(z)$ is well-known. The stress and displacement components are related to the functions $\phi(z)$ and $\Psi(z)$ by the following relations:

$$\sigma_x + \sigma_y = 2[\phi(z) + \overline{\phi(z)}]$$

$$\sigma_y - i\,\tau_{xy} = \phi(z) + \overline{\phi(z)} + \overline{z\phi'(z)} + \overline{\Psi(z)} \tag{1}$$

$$2\mu(u_{x,x} + i\,u_{y,x}) = \kappa\phi(z) - \overline{\phi(z)} - \overline{z\phi'(z)} - \overline{\Psi(z)}$$

where the bar denotes the complex conjugate and the comma after the function stands for partial differentiation with respect to subscripts following it.

We define a new function $\Omega(z)$ as follows:

$$\Omega(z) = \overline{\phi(z)} + z\overline{\phi}'(z) + \overline{\Psi}(z) \tag{2}$$

Hence,

$$\Psi(z) = -\phi + \overline{\Omega}(z) - z\overline{\phi}'(z) \tag{3}$$

Substitution of $\Omega(z)$ instead of $\Psi(z)$ in equation (1) leads to

$$\begin{aligned} \sigma_y - i\,\tau_{xy} &= \phi(z) + \Omega(\bar{z}) + (z-\bar{z})\bar{\phi}'(\bar{z}) \\ 2\mu(u_{x,x} + i\,u_{y,x}) &= \kappa\phi(z) - \Omega(\bar{z}) - (z-\bar{z})\,\bar{\phi}'(\bar{z}) \end{aligned} \tag{4}$$

Thus, for the function $\Psi(z)$, the stresses and displacements are expressed in terms of two functions $\phi(z)$ and $\Omega(z)$.

BOUNDARY CONDITIONS

The boundary conditions of the problem can be stated as follows:

(i) At infinity,

$$\phi(z) = \Gamma_o + O(z^{-2}),\ \Omega(z) = \Gamma_o + \bar{\Gamma}_1 + O(z^{-2}) \tag{5}$$

where

$$\Gamma_o = \frac{1}{4}(N_1 + N_2)\quad \Gamma_1 = -\frac{1}{2}(N_1 - N_2)\,e^{-2i\beta}$$

(ii) On the rims of the crack L, $\sigma_y^{\pm} - i\,\tau_{xy}^{\pm} = 0$

$$\phi^+(t) + \Omega^-(t) = 0,\ \phi^-(t) + \Omega^+(t) = 0 \tag{6}$$

where t is the coordinate of the point on the cut L and superscripts + and - refer to the boundary values of the functions as z approaches t from the upper and lower half-plane respectively.

(iii) On the circular hole $r = R$, when origin is considered at M,

$$\begin{aligned} \sigma_r + i\,\tau_{r\theta} &= -P \\ \phi(Re^{i\theta}) + \bar{\phi}(Re^{-i\theta}) - Re^{-i\theta}\,\bar{\phi}'(Re^{-i\theta}) - e^{-2i\theta}\,\bar{\Psi}(Re^{-i\theta}) &= -P \end{aligned} \tag{7}$$

COMPLEX POTENTIALS FOR THE PLATE

Since equations (6) are dual homogeneous Hilbert problems for two functions $\phi(z)$ and $\Omega(z)$, which are analytic in the entire plane cut along L, the complex potentials $\phi(z)$ and $\Omega(z)$ can readily be constructed for the infinite plate which satisfy the conditions in equations (5) and (6) by the use of Muskhelishvili's technique. Taking account of the fact that $\phi(z)$ and $\Omega(z)$ could have poles of various orders at $z = M$, we can write them as follows:

$$\left.\begin{matrix}\phi(z)\\ \Omega(z)\end{matrix}\right\} = \mp \frac{1}{2}\bar{\Gamma}_1 \pm \frac{1}{2}\sum_{n=2}^{\infty} A_n\{\frac{1}{z-M}\}^n + \frac{1}{2}X(z)[(2\Gamma_o + \bar{\Gamma}_1)\{z - \frac{a+b}{2}\} + \sum_{n=1}^{\infty} B_n\{\frac{1}{z-M}\}^n] \tag{8}$$

where

$$X(z) = (z-a)^{-\frac{1}{2}}(z-b)^{-\frac{1}{2}} \tag{9}$$

Equation (9) means that the branch is analytic in the entire plane cut along L such that $X(z) \to (1/z)$ for $|z| \to \infty$. The coefficients A_n and B_n are to be determined by equation (7).

The origin of the coordinate system is now shifted to M. The functions $\{\phi(z), \Psi(z)\}$ transform to new functions $\{\phi_1(z_1), \Psi_1(z_1)\}$. We drop the subscript 1 for convenience but remember these are the potentials obtained after shifting the origin to M.

The function $\phi(z)$ in equation (8) and the corresponding potential $\Psi(z)$ obtained from equation (3), can be expanded in the following Laurent series,

$$\phi(z) = \sum_{n=-\infty}^{\infty} D_n z^n, \quad \Psi(z) = \sum_{n=-\infty}^{\infty} E_n z^n \tag{10}$$

where

$$D_n = \frac{1}{2}[-\bar{\Gamma}_1\delta_{o,n} + (2\Gamma_o + \bar{\Gamma}_1)\, p_{n-1}\,(1 - \delta_{o,n}) + \frac{1}{2}(2\Gamma_o + \bar{\Gamma}_1)\{M - \frac{a+b}{2}\}\, p_n + \sum_{k=1}^{\infty} p_{n+k}\, B_k] \quad (n \geq 0) \tag{11a}$$

$$D_{-n} = \frac{1}{2}[A_n(1 - \delta_{1,n}) + \sum_{k=0}^{\infty} p_k\, B_{n+k}] \quad (n \geq 1) \tag{11b}$$

$$E_n = \frac{1}{2}[(\Gamma + \bar{\Gamma}_1)\delta_{o,n} + \{(\Gamma_1 - \bar{\Gamma}_1) - n(2\Gamma_o + \bar{\Gamma}_1)\}p_{n-1}\,(1 - \delta_{o,n}) +$$

$$+ \{(M - \frac{a+b}{2})\{(\Gamma_1 - \bar{\Gamma}_1) - n(2\Gamma_o + \bar{\Gamma}_1)\} - (n+1)(2\Gamma_o + \bar{\Gamma}_1)(M - \bar{M})\}p_n +$$

$$+ (2\Gamma_o + \bar{\Gamma}_1)(M - \bar{M})(M - \frac{a+b}{2})(n+1)p_{n+1} + \sum_{k=1}^{\infty}\{\{\bar{B}_k - (n+1)B_k\}p_{n+k} -$$

$$- (M - \bar{M})(n+1)B_k\, p_{n+k+1}\}] \quad , \quad (n \geq 0) \tag{12a}$$

$$E_{-n} = \frac{1}{2}[\{n-1)A_n - \bar{A}_n + (M - \bar{M})(n-1)A_{n-1}(1 - \delta_{2,n})\}\ (1 - \delta_{1,n}) +$$

$$+ \sum_{k=0}^{\infty}\{\{(n-1)B_{n+k} + \bar{B}_{n+k}\}p_k + (M - \bar{M})(n-1)B_{n+k}p_{k+1}\}] \ , \ (n \geq 1) \tag{12b}$$

Here $\delta_{m,n}$ is Kronecker delta. The constants p_n's are known quantities determined from the relation

$$\sum_{n=0}^{\infty} p_n z^n = (z + M - a)^{-\frac{1}{2}} (z + M - b)^{-\frac{1}{2}} \tag{13}$$

Using equation (7) along with equation (10), one may obtain

$$R^n D_n + (n + 1)R^{-n} \bar{D}_{-n} - R^{-n-2} \bar{E}_{-n-2} = - P \delta_{o,n} \quad (n \geq 0) \tag{14}$$

$$R^{-n} D_{-n} - (n - 1)R^n \bar{D}_n - R^{n-2} \bar{E}_{n-2} = 0 \quad (n \geq 1) \tag{15}$$

When (14) and (15) are solved, the following expressions are obtained:

$$D_{-1} = 0 \tag{16}$$

$$D_{-n} = (n - 1)R^{2n} \bar{D}_n + R^{2n-2} \bar{E}_{n-2} \quad (n \geq 2)$$

$$E_{-1} = 0 \tag{17}$$

$$E_{-n-2} = (R^n P + D_o + \bar{D}_o)R^2\delta_{o,n} + R^2\{R^{2n} \bar{D}_n + (n + 1)D_{-n}\}(1 - \delta_{o,n}) \quad (n \geq 0)$$

By equations (11) and (12) and (16) and (17)

$$A_n = - \sum_{k=0}^{\infty} p_k B_{n+k} + 2\{(n - 1)\bar{D}_n + R^{-2} \bar{E}_{n-2}\} R^{2n} \quad (n \geq 2) \tag{18}$$

$$\sum_{k=0}^{\infty} p_k B_{k+1} = 0 \qquad \sum_{k=0}^{\infty} p_k \bar{B}_{k+1} = 0 \tag{19}$$

$$\sum_{k=0}^{\infty} [2p_k \bar{B}_{n+k+2} - (M - \bar{M})(n + 1)\{p_k B_{n+k+1}(1 - \delta_{o,n}) - p_{k+1}B_{n+k+2}\}]$$

$$= 2R^2 (R^nP + D_o + \bar{D}_o) \delta_{o,n} + 2R^{2n+2} \bar{D}_n (1 - \delta_{o,n}) + 2\{(n^2 - 1)R^{2n+2} \bar{D}_n +$$

$$+ (n + 1) R^{2n} \bar{E}_{n-2}\}(1 - \delta_{o,n} - \delta_{1,n}) + 2\{(n + 1)R^{2n+4} D_{n+2} + R^{2n+2} E_n\} -$$

$$-2\{(n + 1)^2 R^{2n+4} \bar{D}_{n+2} + (n + 1) R^{2n+2} \bar{E}_n\}$$

$$-2(M - \bar{M})\{n(n + 1)R^{2n+2} \bar{D}_{n+1} + R^{2n} \bar{E}_{n-1}\}(1 - \delta_{o,n}) \quad (n \geq 0) \tag{20}$$

Since D_n and E_n are linear functions of B_n's, equations (19) and (20) solve completely the problem of determining the coefficients B_n, when the values of Γ_o, Γ_1, m, a, b, and R are known. The values of A_n's are determined from equation (18) using the values of B_n's determined earlier. Thus the potentials $\{\phi(z), \Psi(z)\}$ are completely known.

NUMERICAL EXAMPLES

In order to clarify the effect of a hole under uniform normal pressure on the crack-tip stress intensity factor, some numerical calculations were carried out for the following values:

$a = -0.5 \quad b = 0.5 \quad M = (0,-2) \quad R = 0.5(.25)1.75 \quad \Gamma_o = \Gamma_1 = 0$

Here, it is noted that the stress intensity factor decreases as the radius of the hole decreases (see fig. 2).

It may be verified from the theoretical results given in this paper that when $P \to 0$ and $R \to 0$, we revert to the case of a matrix with a single crack under tension at infinity. Also, when the length of the crack and tractions at infinity vanish, we get the results of circular cavity under uniform normal pressure in an infinite elastic plate.

REFERENCES

1. Inglis, C. E.: Stresses in a Plate Due To the Presence of Cracks and Sharp Corners. Transactions of the Institute of Naval Architects. London, England, Vol. 60, 1913, p. 219.

2. Griffith, A. A.: The Phenomena of Rupture and Flow in Solids. Phil. Trans., A 221, 1921, p. 163.

3. Green, A. E.: General Biharmonic Analysis For A Plate Containing Circular Holes. Proc. Roy. Soc. London, 1940, p. 176.

4. Muskhelishvili, N. I.: Some Basic Problems of the Mathematical Theory of Elasticity. P. Noordhoff, Ltd. (Groningen), 1953.

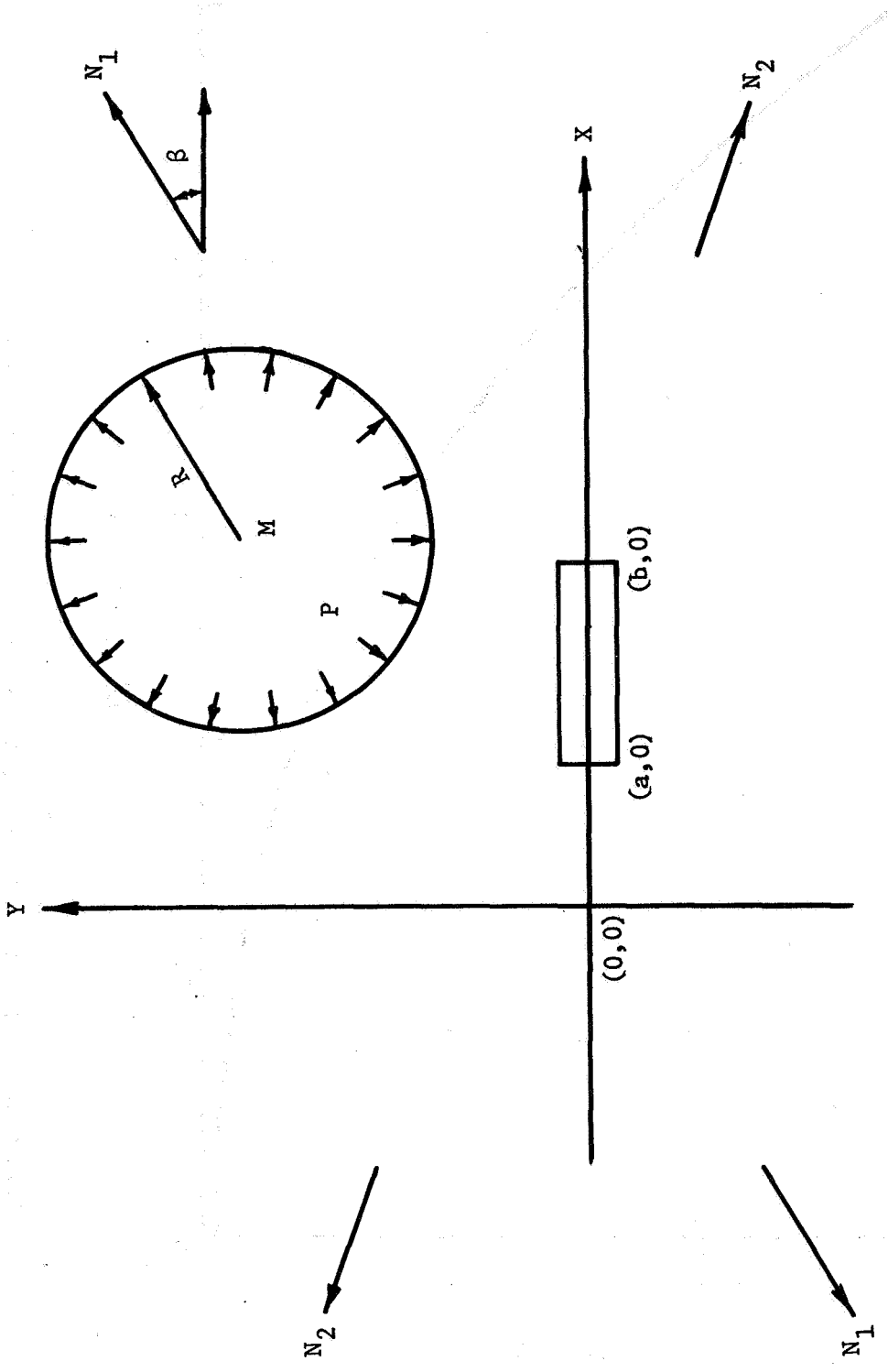

Figure 1.- Configuration and coordinate system.

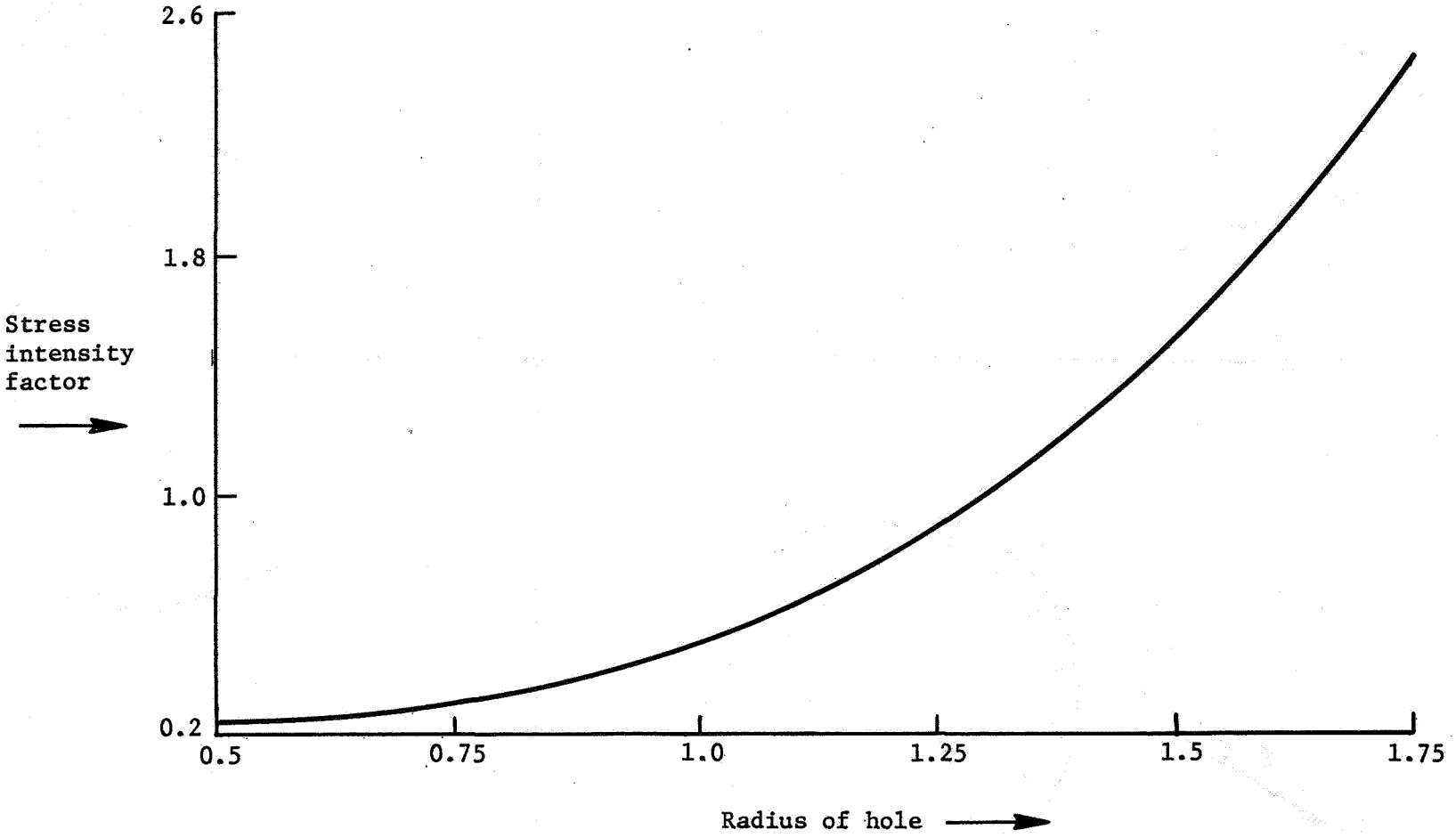

Figure 2.- Crack-tip stress intensity factor versus radius of hole.

THE EFFECT OF SEVERAL INTACT OR BROKEN STRINGERS ON THE STRESS INTENSITY FACTOR IN A CRACKED SHEET*

K. Arin
Lehigh University

ABSTRACT

The effect of several stringers on the stress intensity factors at the tips of a crack is considered. The stringers which are continuously attached to the plate and placed perpendicular to the crack may be partially debonded due to high stress concentrations. Since the stringers may even break under excessive loading conditions, both intact and broken stringers are considered to investigate the effect of rupture. The continuity of displacements along the bond lines leads to an integral equation which is solved to give the shear stress distribution in the adhesive and the stress intensity factors at the crack tips.

INTRODUCTION

Stiffened panels, i.e. metal sheets with stringers continuously bonded through an adhesive have long been of major interest (refs. 1-6). Greif and Sanders have given the solution of a stringer perfectly bonded to a cracked sheet (ref. 1). On the other hand, the case with riveted stringers - both intact and broken - has been treated by Poe (refs. 2 and 3). Furthermore, the problem of a cracked isotropic plate stiffened by a stringer which may be partially debonded has been considered by Arin (ref. 4). It has been concluded that the debonding process as well as the stringer placing are quite important as far as the stiffening effect of the stringer is concerned. In a separate work (ref. 5) the effect of lateral bending stiffness of the stringer has been investigated.

However, due to high load levels stringer breakage can occur in addition to debonding. Also, in actual structures several stringers are present instead of one. Hence the problem of several intact or broken stringers will be considered in this paper. The method employed here is the same as the one used in reference 4 and therefore most of the results will be used without derivation.

---

* This work has been supported by the National Aeronautics and Space Administration under the Grant NSG 1178.

For intact stringers the case where the loads are applied on the crack surfaces will be considered (see figure 1). This will also give the singular part of the solution around the crack tips. The actual problem where the loads are applied at infinity can be obtained by a simple superposition. However, for broken stringers the actual problem will be treated as it is (see figure 2) due to difficulties involved in superposition. In all these cases, loads will be considered uniform.

The technique used here makes it possible to consider any number of stringers located at arbitrary locations. For the sake of simplicity the numerical results will be given for uniformly spaced stringers all located along the positive x axis. However, the results for the stringers located along the negative x axis can be obtained by simply substituting for d_o - the distance of the first stringer to the y axis - its value with a negative sign.

FORMULATION OF THE PROBLEM

The problem will be formulated using the same notation* as in reference 4. Also, due to symmetry only the upper half of the plate will be considered. The adhesive will be treated as a shear spring and the shear stresses will be considered as body forces in the plate solution (generalized plane stress). Let q represent the uniform pressure applied on the crack surfaces in the case of intact stringers (see figure 1) and the uniform tension applied at infinity in the case of broken stringers (see figure 2). Then the continuity of displacements can be written as (ref. 4)

$$v_p(z) - v_s(z) = \frac{h_a}{d_s \mu_a} P(z) \quad , \quad z \text{ on } L \tag{1}$$

Here, L denotes the union of straight lines L_j defined by $x=c_j$, $b_j \leq y < \infty$; $j=1,\ldots n_s$ where n_s is the number of stringers, b_j is the half debond length of the j th stringer. For uniformly spaced stringers we have

$$c_j = d_o + (j-1)d_1 \tag{2}$$

where d_1 is the stringer spacing and d_o is the distance of the first stringer to the mid-point of the crack.

---

*(E,ν): Elastic constants of the plate. $\mu_p=E/2(1+\nu)$, $\kappa=(3-\nu)/(1+\nu)$ for generalized plane stress.
(E_s,A_s): Elastic modulus and cross-sectional area of the stringer.
μ_a: Shear modulus of the adhesive.
(h_p,h_a): Thicknesses of the plate and the adhesive.
a: Half crack length.
d_s: Stringer width.
$v_p(z)v_s(z)$: Displacements of the plate and the corresponding stringer at z location.
P(z): Shear stress in the adhesive at z location.
σ_y: Stress in the y direction.

Moreover, for broken stringers, the equilibrium equations can be stated as follows:

$$\int_{L_j} P(z_o)\,dy_o = \begin{cases} -\dfrac{1+\kappa}{8\mu_p} E_s A_s q & \text{if the load at infinity is also transferred to the stringer} \\ 0 & \text{if the end of the stringer at infinity is stress free} \end{cases}$$

$$j=1,\ldots n_s \qquad (3)$$

where $y_o = \mathrm{Im}(z_o)$.

Hence, using the appropriate displacement expressions equation (1) will give the integral equation of the problem as

$$P(z) + \int_L k(z,z_o)P(z_o)\,dy_o + \frac{d_s\mu_a}{h_a} C = \frac{d_s\mu_a}{h_a} q\, k_o(z), \quad z \text{ on } L \qquad (4)$$

which will be considered together with equation (3) and solved for the shear stress distributions and the rigid body displacements. Note that C in equation (4) which represents the rigid body displacements assumes a different constant value on each broken stringer, i.e., $C=C_j$, $j=1,\ldots n_s$.

Here, the kernels $k(z,z_o)$ and $k_o(z)$ can be obtained similarly as in reference 4.

The stress intensity factor is defined as

$$K = \lim_{x\to a} \left[\sqrt{2(x-a)}\right] \sigma_y(x,0) \qquad (5)$$

and given in figures 3,4,5,6, and 7.

NUMERICAL RESULTS AND CONCLUSION

The numerical results are obtained for the following data:

Plate: $\nu = 0.30$, $E = 703000$ kg/cm^2 (10^7 psi), $h_p = 0.229$ cm (0.09 in)

Stringer: $A_s = 1.065$ cm^2 (0.165 in^2), $E_s = 871720$ kg/cm^2 (1.24×10^7 psi)

Adhesive: $\mu_a = 11600$ kg/cm^2 (1.65×10^5 psi), $h_a = 0.01$ cm (0.004 in)

q = constant

Intact Stringers: The effect of debond length b_1 of the first stringer is illustrated in figure 3. It is seen that for $b_1/a > 2$ the stiffening effect will decrease appreciably even if the other stringers still remain perfectly bonded to the plate. One can show that (ref. 6) the effect of a stringer is most significant if it is located between the crack tips. The number of stringers is less significant if these stringers are placed away from the crack tips. The effect of the location of the first stringer (d_o), is shown in figure 4. It is observed that for $d_o/a > 2$ all $K/q\sqrt{a}$ values rapidly approach unity.

Broken Stringers: In this case, the results are obtained for both crack surface loading (perturbation problem) and the loading at infinity (the actual problem). The solution to the first case is given to make a comparison with the intact stringer problem.

Figure 5 indicates a similar trend as in figure 3 and can be interpreted the same way. The stress intensity factors have considerably higher values if the loads are applied at infinity. This important result is shown in figure 6. $K/q\sqrt{a}$ values decrease with increasing debond length b_1. The effect of d_o is illustrated in figure 7 for crack surface loading where $K/q\sqrt{a}$ values approach unity as d_o increases.

More details and numerical results can be found in reference 6.

REFERENCES

1. Greif, R. and Sanders, J. L., Jr.: The Effect of a Stringer on the Stress in a Cracked Sheet. Trans ASME, Ser. E, J. of Applied Mechanics, vol. 32, 1965, pp. 59-66.

2. Poe, C. C., Jr.: Stress Intensity Factor for a Cracked Sheet with Riveted and Uniformly Spaced Stringers. NASA Technical Report, NASA TR R-358, 1971.

3. Poe, C. C., Jr.: The Effect of Broken Stringers on the Stress Intensity Factor for a Uniformly Stiffened Sheet Containing a Crack. NASA Technical Memorandum, NASA TMX-71947, 1973.

4. Arin, K.: A Plate with a Crack Stiffened by a Partially Debonded Stringer, Eng. Fract. Mech., vol. 6, 1974, pp. 133-140.

5. Arin, K.: A Note on the Effect of Lateral Bending Stiffness of Stringers Attached to a Plate with a Crack. Eng. Fract. Mech., vol. 7, 1975, pp. 173-179.

6. Arin, K.: A Cracked Sheet Stiffened by Several Partially Debonded Intact or Broken Stringers — Reinforcement (Structures) and Structural Stability of Metal Sheets. NASA CR-144952, 1975.

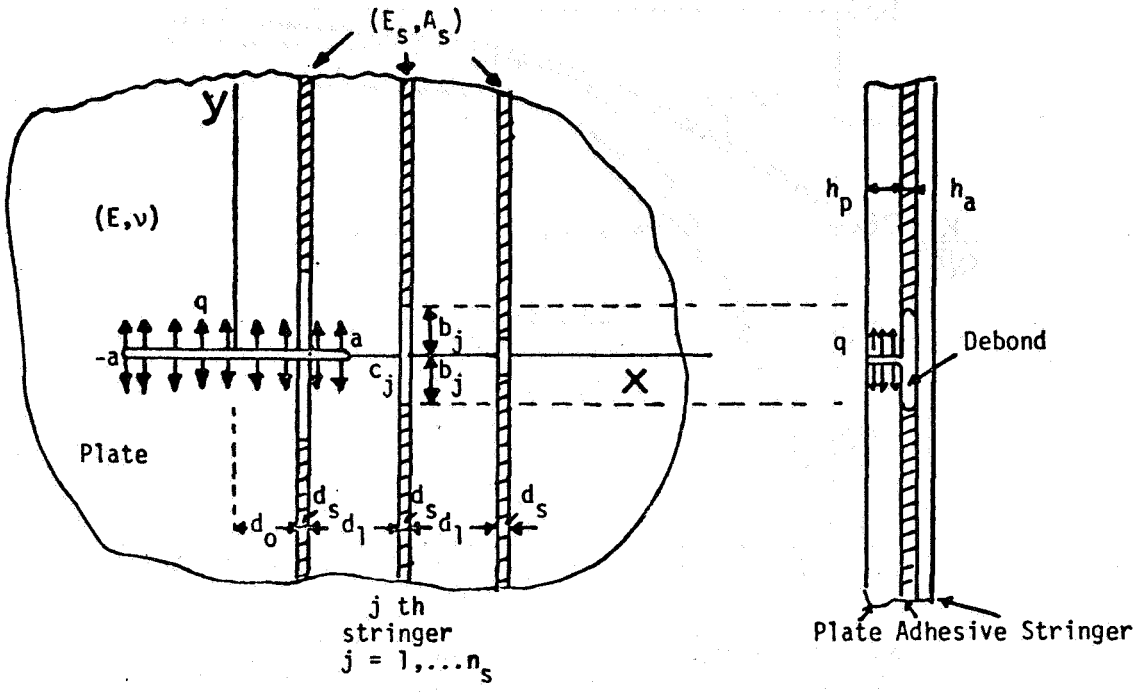

Figure 1.- Geometry of the problem (intact stringers).

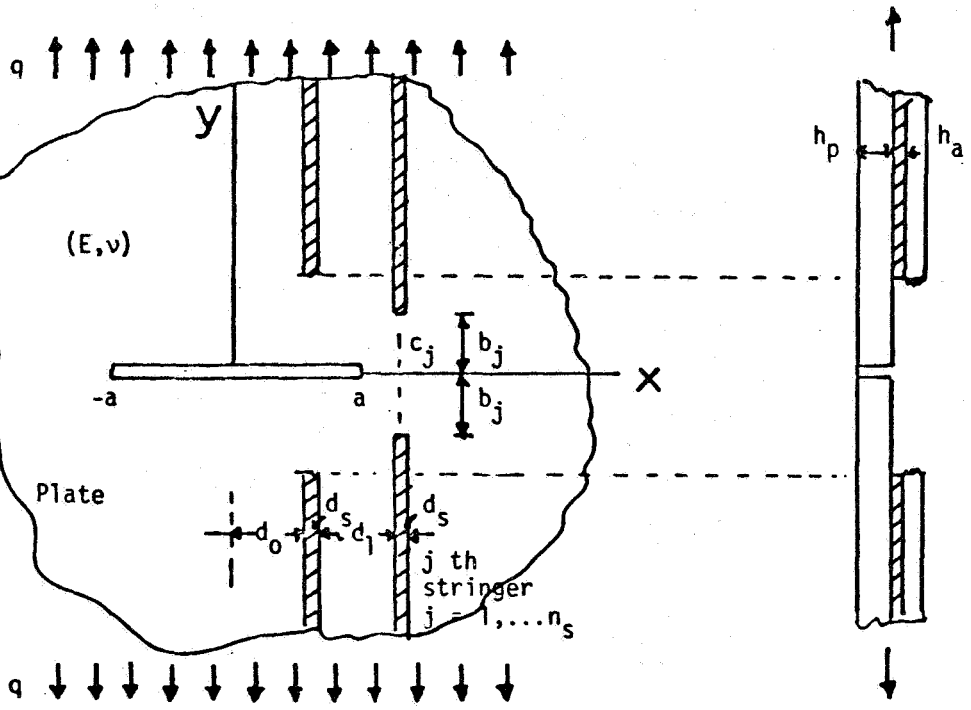

Figure 2.- Geometry of the problem (broken stringers).

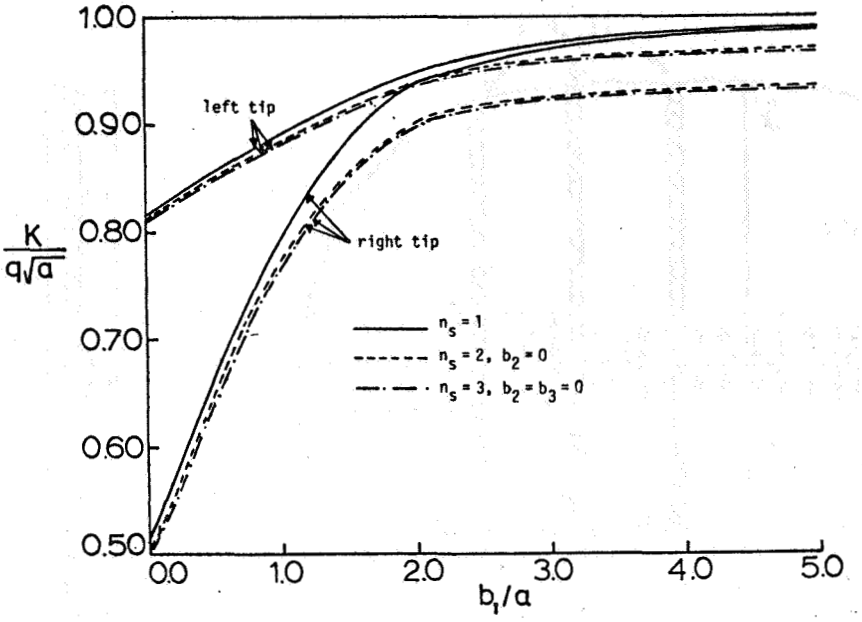

Figure 3.- $K/q\sqrt{a}$ vs. b_1/a (intact stringer, $d_o/a = 0.5$, $d_1/a = 1.0$, $d_s/a = 0.2$).

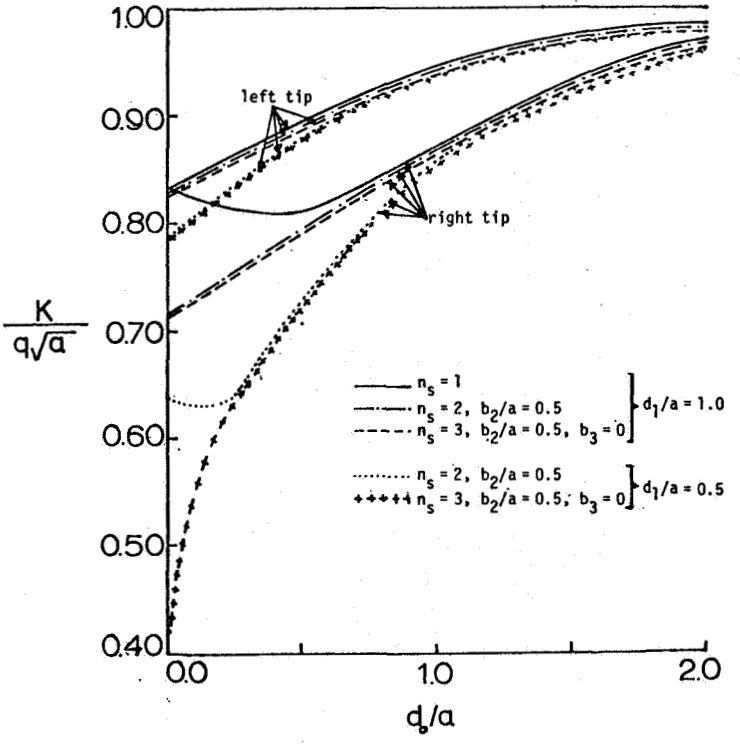

Figure 4.- $K/q\sqrt{a}$ vs. d_o/a (intact stringer, $b_1/a = 1.0$, $d_s/a = 0.2$).

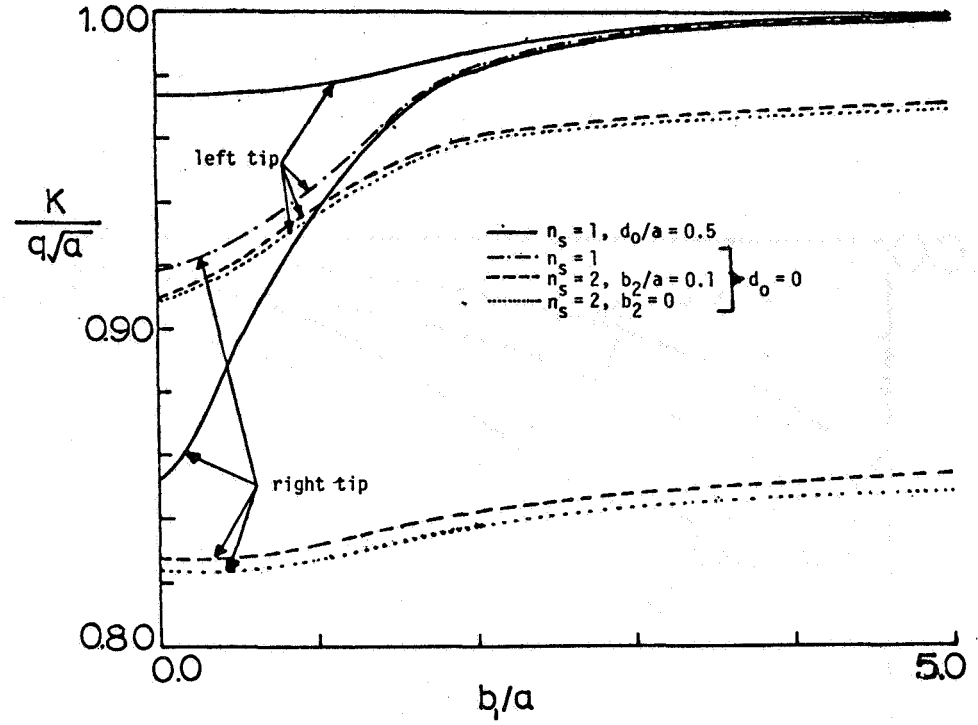

Figure 5.- $K/q\sqrt{a}$ vs. b_1/a (broken stringer, loading on the crack surfaces, $d_1/a = 0.5$, $d_s/a = 0.2$).

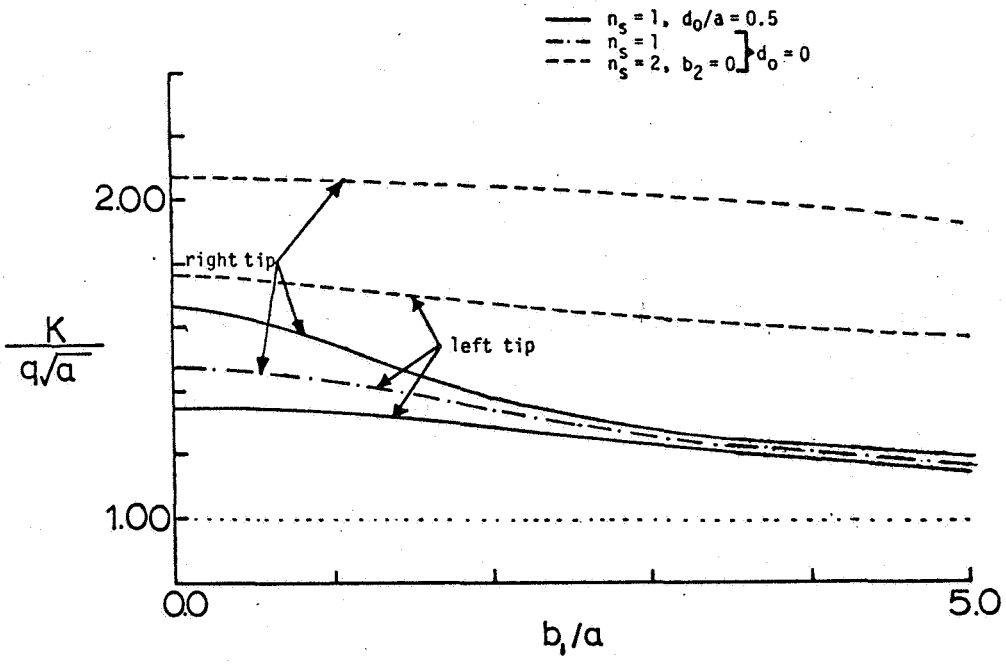

Figure 6.- $K/q\sqrt{a}$ vs. b_1/a (broken stringer, loading at infinity, $d_1/a = 0.5$, $d_s/a = 0.2$).

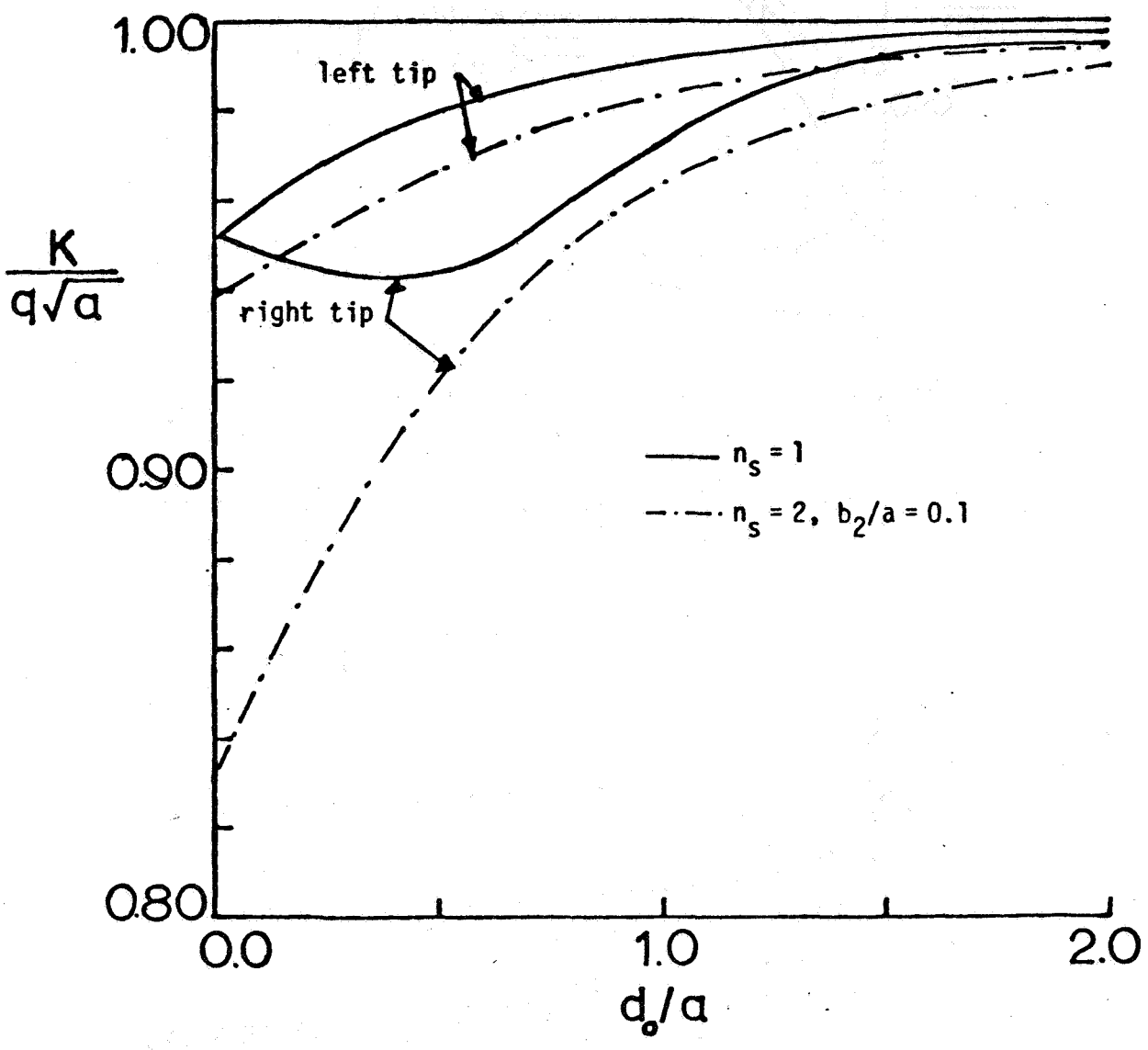

Figure 7.- $K/q\sqrt{a}$ vs. d_o/a (broken stringer, loading on the crack surfaces, $b_1/a = 1.0$, $d_1/a = 0.5$, $d_s/a = 0.2$).

ON THE PROBLEM OF STRESS SINGULARITIES IN BONDED ORTHOTROPIC MATERIALS*

F. Erdogan and F. Delale
Lehigh University

SUMMARY

The problem of stress singularities at the leading edge of a crack lying in the neighborhood of a bimaterial interface in bonded orthotropic materials is considered. The main objective of the paper is to study the effect of material orthotropy on the singular behavior of the stress state when the crack touches or intersects the interface. The results indicate that, due to the large number of material constants involved, in orthotropic materials the power of stress singularity as well as the stress intensity factor can be considerably different than that found in the isotropic materials with the same stiffness ratio perpendicular to the crack.

INTRODUCTION

In the design of a structural component in which fracture failure is a prime consideration, at one point it is necessary to apply a failure criterion which is usually the comparison of a "characteristic strength parameter" of the material with a "critical load factor". The strength parameter represents the resistance of the material for the particular mode of fracture failure and is an experimentally measured quantity. The load factor, on the other hand, is a measure of the intensity of applied loads and the severity of component geometry, and generally is a calculated quantity. It is therefore clear that in any given situation the specific choice of fracture criterion and the corresponding strength parameter and load factor will have to depend on the particular mode of fracture which may be the most likely mechanism of failure.

If the material is homogeneous and isotropic in its strength as well as its mechanical properties, particularly in the absence of large scale plastic deformations, the fracture process is relatively well-understood and the techniques dealing with the related problems are sufficiently well-developed. On the other hand in composites, particularly in fiber-reinforced laminates, the situation is much more complicated not only because of the nonhomogeneity and anisotropy of the medium which make it difficult to analyze the problem, but also because of the highly nonhomogeneous and nonisotropic distribution of the strength parameter which makes the development and application of a proper fracture criterion also very difficult. In such materials it is quite possible

*This work was supported by NASA-Langley under the Grant NGR 39-007-011.

that the concept of the progressive growth of a dominant flaw with a well-defined leading edge may not be appropriate to model the gross fracture behavior. Very often somewhat irregular and diffused damage zones may develop around the flaw and the fracture process may be governed by a principle of "weakest link", the local fracture propagation being progressive or in discrete steps. Nevertheless, whatever the gross mechanism governing the fracture failure of the medium, one may nearly always assume that locally fracture initiation and propagation will take place along the leading edges of existing imperfections where the conditions of the relevant fracture criterion are satisfied. Thus, in order to treat the local fracture phenomenon in composites quantitatively, one needs the solution of the mechanics problem for flaws or cracks located at or near the phase boundaries or bimaterial interfaces.

For composites which consist of bonded isotropic materials a wide variety of problems have been solved in which either the asymptotic behavior of the stress state around the points of geometric singularity or the results for a specific idealized crack geometry have been discussed (see, for example, refs. 1 to 5). Compared to the isotropic case, the crack problems for the anisotropic materials remain relatively unexplored. The existing solutions refer to either an infinite homogeneous plane with a crack (refs. 6,7), or two bonded semi-infinite planes with an interface crack (ref. 8). These solutions indicate that for the crack geometries under consideration the singular behavior of the stress state around the crack tips is essentially identical to the corresponding isotropic problems, namely square root power singularity for the crack in a homogeneous medium and oscillating stress singularity with a one-half power for the interface crack. The problems regarding the cracks in the neighborhood of or intersecting the bimaterial interfaces in anisotropic nonhomogeneous materials do not seem to have been investigated. In this paper this question is discussed for a group of plane problems in which the specific geometry used is that of periodically arranged two different sets of bonded orthotropic strips. The primary emphasis in the paper is on the examination of the effect of material orthotropy on the behavior of the stresses around the singular points.

FORMULATION OF THE PROBLEM

If u and v respectively correspond to the x and y components of the displacement vector, for an orthotropic plane the equations of equilibrium may be expressed as follows (see, for example, ref. 9):

$$\left.\begin{aligned} \beta_1 \frac{\partial^2 u}{\partial x^2} + \frac{\partial^2 u}{\partial y^2} + \beta_3 \frac{\partial^2 v}{\partial x \partial y} = 0 \\ \frac{\partial^2 v}{\partial x^2} + \beta_2 \frac{\partial^2 v}{\partial y^2} + \beta_3 \frac{\partial^2 u}{\partial x \partial y} = 0 \end{aligned}\right\} \tag{1}$$

where the elastic constants β_1, β_2, and β_3 are given by

$$\beta_1 = \frac{E_x}{(1-\nu_{xy}\nu_{yx})G_{xy}} \quad , \quad \beta_2 = \frac{E_y}{E_x}\beta_1 \quad , \quad \beta_3 = 1 + \nu_{yx}\beta_1 \tag{2}$$

for generalized plane stress, and

$$\beta_1 = b_{11}/b_{66} \quad , \quad \beta_2 = b_{22}/b_{66} \quad , \quad \beta_3 = 1 + b_{12}/b_{66} \tag{3}$$

for plane strain. Here the engineering material constants and the matrix $B=(b_{ij})$ are defined by the following standard relations (ref. 9):

$$\begin{aligned}
&\varepsilon = A\sigma \quad , \quad A = (a_{ij}) \quad , \quad (i,j=1,..,6) \quad , \quad B = A^{-1} \\
&a_{11} = 1/E_x \quad , \quad a_{12} = -\nu_{xy}/E_x \quad , \quad a_{13} = -\nu_{xz}/E_x \quad , \quad a_{14} = a_{41} = 0,... \\
&..... \\
&a_{44} = 1/G_{yz} \quad , \quad a_{55} = 1/G_{xz} \quad , \quad a_{66} = 1/G_{xy} \quad , \\
&E_y\nu_{xy} = E_x\nu_{yx} \quad , \quad E_z\nu_{yz} = E_y\nu_{zy} \quad , \quad E_x\nu_{zx} = E_z\nu_{xz} \quad , \\
&\sigma_1 = \sigma_{xx} \quad , \quad \varepsilon_1 = \varepsilon_{xx} \quad , \ ... \ , \quad \sigma_4 = \sigma_{yz} \quad , \quad \varepsilon_4 = 2\varepsilon_{yz} \quad , \ ...
\end{aligned} \tag{4}$$

Consider now the periodically arranged bonded orthotropic strips shown in figure 1a. Let the plane be loaded uniformly parallel to the interfaces and away from the region of cracks. Then the solution of the problem may be written as the sum of a uniform solution obtained from the plane without cracks and under given applied loads, and a perturbation solution obtained from the cracked plane in which self-equilibrating crack surface tractions are the only external loads. From the fracture viewpoint the relevant solution is the latter. Noting that x and y are local axes of symmetry, the solution of equations (1) may be expressed as

$$\begin{aligned}
u_j(x_j,y) &= \frac{2}{\pi}\int_o^\infty f_j(\alpha,x_j)\cos\alpha y \, d\alpha + \frac{2}{\pi}\int_o^\infty h_j(\alpha,y)\sin\alpha x_j d\alpha \\
v_j(x_j,y) &= \frac{2}{\pi}\int_o^\infty m_j(\alpha,x_j)\sin\alpha y \, d\alpha + \frac{2}{\pi}\int_o^\infty n_j(\alpha,y)\cos\alpha x_j d\alpha \quad ,
\end{aligned} \tag{5}$$

where j=1,2 refer to strips 1 and 2, respectively. Substituting equations (5) into equations (1), one obtains a system of ordinary differential equations which are coupled in pairs. Solving these equations and using the symmetry conditions the unknown functions are obtained in the following form:

$$f_j(\alpha,x_j) = A_j(\alpha)(e^{s_{j1}\alpha x_j} - e^{-s_{j1}\alpha x_y})$$

$$+ B_j(\alpha)(e^{s_{j2}\alpha x_j} - e^{-s_{j2}\alpha x_j})$$

. . . . . (6)

where A_j, B_j, (j=1,2) are unknown functions and s_{j1} and s_{j2} are the roots of the following characteristic equation

$$s^4 + \beta_{j4}s^2 + \beta_{j5} = 0 \quad , \quad (j=1,2;\ s_{j3}=-s_{j1},\ s_{j4}=-s_{j2})$$

$$\beta_{j4} = (\beta_{j3}^2-\beta_{j1}\beta_{j2}-1)/\beta_{j1} \quad , \quad \beta_{j5} = \beta_{j2}/\beta_{j1} \quad , \quad (j=1,2) \quad . \tag{7}$$

In addition to A_j and B_j, (j=1,2) which appear in the expressions of f_j and m_j, the solution contains four more unknown functions C_j and D_j appearing in the expressions of h_j and n_j, (j=1,2). In most orthotropic materials such as boron-epoxy, graphite-epoxy, or fiberglass laminates β_4 is negative. Therefore, the four roots of the characteristic equation (7) are either all real in which case the material is said to be of type I, or all complex in which case the material is said to be of type II.

In the crack problem described by figure 1a, there are six homogeneous conditions which may be used to eliminate six of the eight unknowns, A_j, B_j, C_j, and D_j, (j=1,2). These are the four conditions of continuity of displacement and stress vectors along the interface ($x_1=h_1$, $x_2=-h_2$, $0\le y<\infty$), and two conditions of vanishing shear stress on y=0 plane in the strips 1 and 2. The remaining two functions are determined from the following two mixed boundary conditions:

$$\left.\begin{aligned} &\sigma_{1yy}(x_1,0) = -p_1(x_1) \quad , \quad -a<x_1<a \quad , \\ &\phi_1(x_1) = \frac{\partial}{\partial x_1} v_1(x_1,0) = 0 \quad , \quad a<|x_1|<h_1 \quad , \end{aligned}\right\} \tag{8}$$

$$\left.\begin{aligned} &\sigma_{2yy}(x_2,0) = -p_2(x_2) \quad , \quad c<|x_2|<d \quad , \\ &\phi_2(x_2) = \frac{\partial}{\partial x_2} v_2(x_2,0) = 0 \quad , \quad |x_2|<c \quad , \quad d<|x_2|<h_2 \end{aligned}\right\} \tag{9}$$

where the single-valuedness condition requires that

$$\int_{-a}^{a} \phi_1(t)dt = 0 \quad , \quad \int_{c}^{d} \phi_2(t)dt = 0 \quad . \tag{10}$$

After some very lengthy manipulations it can be shown that all eight unknown functions A_j, B_j, C_j, and D_j, (j=1,2) can be expressed in terms of ϕ_1

and ϕ_2, and the mixed boundary conditions (8) and (9) can be reduced to a system of integral equations of the following form:

$$\frac{1}{\pi}\int_{-a}^{a}\left[\frac{1}{t-x_1}+k_{11}(x_1,t)\right]\phi_1(t)\,dt$$

$$+\int_{c}^{d}k_{12}(x_1,t)\,\phi_2(t)\,dt=-\frac{1}{M_1}\,p_1(x_1)\quad,\quad -a<x_1<a\quad,$$

$$\int_{-a}^{a}k_{21}(x_2,t)\,\phi_1(t)\,dt \tag{11}$$

$$+\frac{1}{\pi}\int_{c}^{d}\left[\frac{1}{t-x_2}+\frac{1}{t+x_2}+k_{22}(x_2,t)\right]\phi_2(t)\,dt=-\frac{1}{M_2}\,p_2(x_2)\quad,\quad c<x_2<d$$

where the kernels k_{ij} and the crack surface tractions p_i, $(i,j=1,2)$ are known functions, and M_1 and M_2 are known material constants. In orthotropic materials the expressions for k_{ij} (which also depend on the elastic constants of the two materials) and M_i $(i,j=1,2)$ are very complicated and for bonded strips of material type I may be found in reference 10(*).

SOLUTION AND SOME RESULTS

If the cracks are fully imbedded into the homogeneous media 1 and 2 as shown in figure 1a, then the kernels k_{ij} (x_i,t), $(i,j=1,2)$ given in equations (11) are bounded functions and the integral equations may be solved in a straightforward manner. In this case the stress state around the crack tips has the standard square root singularity. If, on the other hand, one of the strips is fully ruptured or the crack tip touches the interface, using the complex function technique it can be shown that, for exampke, for $a=h_1$, $d<h_2$ (see ref. 10)

$$\phi_1(x_1)=F_1(x_1)(h_1^2-x_1^2)^{-\gamma}\quad,\quad \sigma_{kij}(r,\theta)\simeq\frac{1}{r^{\gamma}}\,f_{kij}(\theta)\quad, \tag{12}$$

$$\Delta_1(\gamma)=0,k=1,2\quad,\quad (i,j)=(r,\theta)\quad,\quad f_{2\theta\theta}(0)/2^{\gamma}=k_a$$

where (r,θ) are the polar coordinates at the crack tip with $r<<h_1$, (see fig. 1b) k_a is defined as the stress intensity factor, and $\Delta_1(\gamma)$ is the characteristic function for the material pair 1 and 2. The power of stress singularity γ is

*The results for material type II may be found in a Technical Report by F. Delale, submitted to the Materials Division, NASA, Langley, March 1976, Grant No. NGR 39-007-011.

a real number between 0 and 1 for all material combinations and generally $\gamma \neq 1/2$ if the materials 1 and 2 are not identical.

Similarly, if the crack crosses the interface, i.e., if $a=h_1$, $d=h_2$, $c>0$, then the intersection of the crack line and the interface is a point of singularity, and again it can be shown that

$$\phi_1(x_1) = G_1(x_1)(h_1^2-x_1^2)^{-\beta} \quad , \quad \phi_2(x_2) = G_2(x_2)(x_2+h_2)^{-\beta}(-x_2-c)^{-0.5} \quad ,$$

$$(-a<x_1<a \quad , \quad -h_2<x_2<-c) \quad , \quad \sigma_{kij}(r,\theta) \simeq \frac{1}{r^\beta} g_{kij}(\theta) \quad , \tag{13}$$

$$\Delta_2(\beta) = 0 \quad , \quad k=1,2 \quad , \quad (i,j) = (r,\theta) \quad , \quad f_{2\theta\theta}(\tfrac{\pi}{2})/2^\beta = k_{xx}$$

$$f_{2r\theta}(\tfrac{\pi}{2})/2^\beta = k_{xy}$$

where (r,θ) are the polar coordinates around the singular point $x_1=a$, $y=0$ (see fig. 1c), $\Delta_2(\beta)$ is the related characteristic function, k_{xx} and k_{xy} are the stress intensity factors (which are linearly dependent), the power of singularity β is real, and $0 \leq \beta < 1/2$. Unlike the corresponding isotropic case, in orthotropic materials the characteristic functions $\Delta_1(\beta)$ and $\Delta_2(\beta)$ are quite complicated. It appears that these functions contain six independent material parameters and hence do not lend themselves to a simple systematic study. However, once the material pair is specified the roots γ and β can be calculated very accurately.

To give an idea about the influence of the material orthotropy on the power of singularity γ for a crack terminating at the interface and β for a crack crossing the interface some of the calculated results are shown in table 1. The elastic properties of ten different materials used in these calculations are given in table 2. Here the materials 3, 4, and 6 are essentially isotropic and the remaining materials are orthotropic. Also, for the first eight materials the roots of the characteristic equation (7) $s_1,..,s_4$ are real, meaning that these materials are of type I. Materials 9 and 10 are of type II. The materials are boron-epoxy or graphite-epoxy laminates with various ply orientations.

As indicated before, the solution of the integral equations (11) for cracks fully imbedded into the homogeneous strips is quite straightforward. Figure 2 shows some sample results for a crack in strip 1. In order to show the effect of material orthotropy on the stress intensity factor, in the examples given in this figure the longitudinal stiffness ratio and the crack length were fixed ($E_{1y}/E_{2y} = 5.5$, $a/h_1 = 0.8$) and the stress intensity factor k_a was calculated for various material combinations.

DISCUSSION AND SOME CONCLUSIONS

Aside from the examples shown in figure 2 and table 1, large number of calculations were done by fixing longitudinal stiffnesses E_{1y} and E_{2y}, systematically varying one at a time the remaining six constants and evaluating the stress intensity factor k_a for the configuration shown in figure 2 and powers of stress singularity γ and β (see figure 1b and c). The general trend was the following: As the elastic constants E_{1x}, G_{1xy}, and ν_{1xy} of the medium 1 containing the crack were increased, k_a and γ increased, and as E_{2x}, G_{2xy}, and ν_{2xy} were increased k_a and γ decreased. Among these variables the most significant factor influencing k_a and γ appeared to be the ratio G_{1xy}/G_{2xy} which may clearly be observed from table 1 and figure 2. In figure 2 for the material combinations I, III, IV, and V this ratio is 0.2, 2.58, 5.75, and 70.8, respectively. From figure 2 it may also be observed that for $h_2 \to 0$ as expected all results converge to the solution for collinear periodic cracks in a homogeneous isotropic plane.

A close examination of the results given in table 1 would indicate that, generally there is a relaxation in the stress singularity at the point of intersection of a through crack and the interface (see figure 1c) if the adjoining materials are orthotropic. This may be seen by comparing the β values for various material combinations given in table 1. In fact for certain combinations it is even possible to obtain $\beta = 0$ (i.e., to have bounded stresses at the apex of two rectangular wedges shown in figure 1c), whereas for isotropic materials β is known to be always positive (e.g., refs. 1 and 4). The value of β has, of course, an important bearing on the initiation of a possible delamination fracture from the stress-free boundaries in bonded materials. At first the result regarding the possibility of $\beta = 0$ may appear to be somewhat paradoxical or unexpected. However, considering the fact that in two bonded isotropic wedges forming a half plane β may be zero for certain ranges of the wedge angles, the result is not unreasonable. The possibility of reduction or complete elimination of singularity power β by varying secondary material constants seems to introduce an added flexibility in designing against edge delamination.

REFERENCES

1. Hein, V. L. and Erdogan, F.: Stress Singularities in a Two-Material Wedge. Int. J. Fract. Mech., vol. 7, 1971, pp. 317-330.

2. Bogy, D. B.: On the Plane Elastostatic Problem of a Loaded Crack Terminating at a Material Interface. J. Appl. Mech., vol. 38, Trans. ASME, 1971, pp. 911-919.

3. Erdogan, F. and Gupta, G. D.: The Inclusion Problem with a Crack Crossing the Boundary. Int. J. of Fract., vol. 11, 1975, pp. 13-27.

4. Erdogan, F. and Biricikoglu, V.: Two Bonded Half Planes with a Crack Going Through the Interface. Int. J. Engng. Sci., vol. 11, 1973, pp. 745-766.

5. Erdogan, F. and Bakioglu, M.: Fracture of Plates which Consist of Periodic Dissimilar Strips. Int. J. of Fract., vol. 12, 1976, pp. 71-84.

6. Sih, G. C., Paris, P. C. and Irwin, G. R.: On Cracks in Rectilinearly Anisotropic Bodies. Int. J. Fract. Mech., vol. 1, 1965, pp. 189-203.

7. Krenk, S.: The Stress Distribution in an Infinite Anisotropic Plate with Collinear Cracks. Int. J. Solids Structures, vol. 11, 1975, pp. 449-460.

8. Clements, D. L.: A Crack Between Dissimilar Anisotropic Media. Int. J. Engng. Sci., vol. 9, 1971, pp. 257-265.

9. Lekhnitskii, S. G.: Anisotropic Plates. Gordon & Breach, New York, 1968.

10. Delale, F.: Fracture of Composite Orthotropic Plates Containing Periodic Buffer Strips. Ph.D. Dissertation, Lehigh University, 1976.

TABLE 1.-THE POWER OF STRESS SINGULARITY γ FOR A CRACK IN MEDIUM 1 TERMINATING AT THE INTERFACE AND β FOR A CRACK CROSSING THE INTERFACE. THE PROPERTIES OF MATERIALS USED IN VARIOUS COMBINATIONS ARE GIVEN IN TABLE 2.

Comb.	Materials		Power of Sing.		$\frac{E_{1y}}{E_{2y}}$	$\frac{G_{1xy}}{G_{2xy}}$
	Med.1	Med.2	α	β		
I	1	2	0.55048	0	5.50	0.20
II	3	2	0.65699	0.04248	5.02	2.48
III	4	2	0.66549	0.04887	5.50	2.58
IV	4	6	0.68914	0.14547	5.50	5.75
V	4	5	0.80352	0.05354	5.50	70.8
VI	7	8	0.74523	0.05197	22.5	1.40
VII	2	1	0.42258	0	0.182	5.00
VIII	2	3	0.36911	0.04248	0.199	0.403
IX	9	10	0.61554	0.08520	3.88	2.6
X	10	9	0.43410	0.08520	0.268	0.384

TABLE 2.-ELASTIC CONSTANTS OF THE MATERIALS USED IN NUMERICAL CALCULATIONS.

Mat No.	E_x / $10^9 N/m^2$ (10^6psi)	E_y / $10^9 N/m^2$ (10^6psi)	G_{xy} / $10^9 N/m^2$ (10^6psi)	ν_{xy}
1(0)	55.16 (8.0)	170.8 (24.75)	4.82 (0.7)	0.036
2(0)	134.42 (19.5)	31.01 (4.5)	24.12 (3.5)	0.650
3(0)	154.7 (22.447)	155.8 (22.6)	59.65 (8.655)	0.300
4(I)	167.5 (24.3)	170.8 (24.75)	62.4 (9.05)	0.300
5(0)	10.06 (1.46)	31.01 (4.5)	8.825 (0.128)	0.036
6(I)	30.04 (4.4)	31.01 (4.5)	10.82 (1.57)	0.400
7(0)	44.82 (6.5)	155.1 (22.5)	4.83 (0.7)	0.020
8(0)	34.48 (5.0)	6.895 (1.0)	3.45 (0.5)	0.350
9(0)	21.37 (3.1)	66.88 (9.7)	17.93 (2.6)	0.200
10(0)	17.24 (2.5)	17.24 (2.5)	6.895 (1.0)	0.760

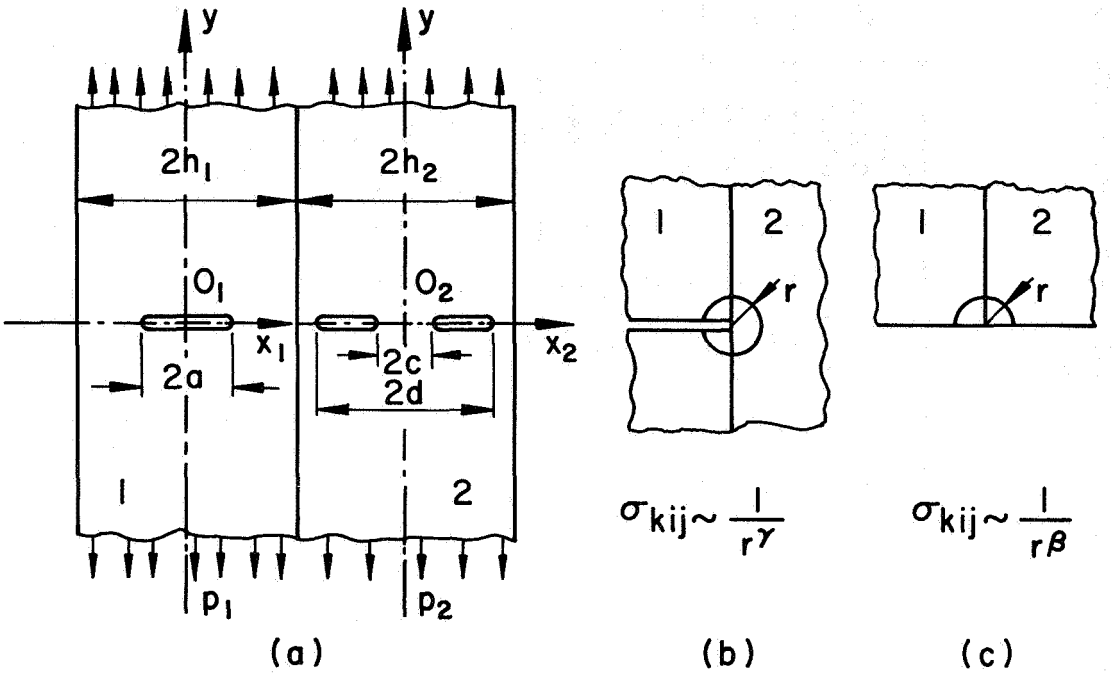

Figure 1.- Crack geometry for the composite medium.

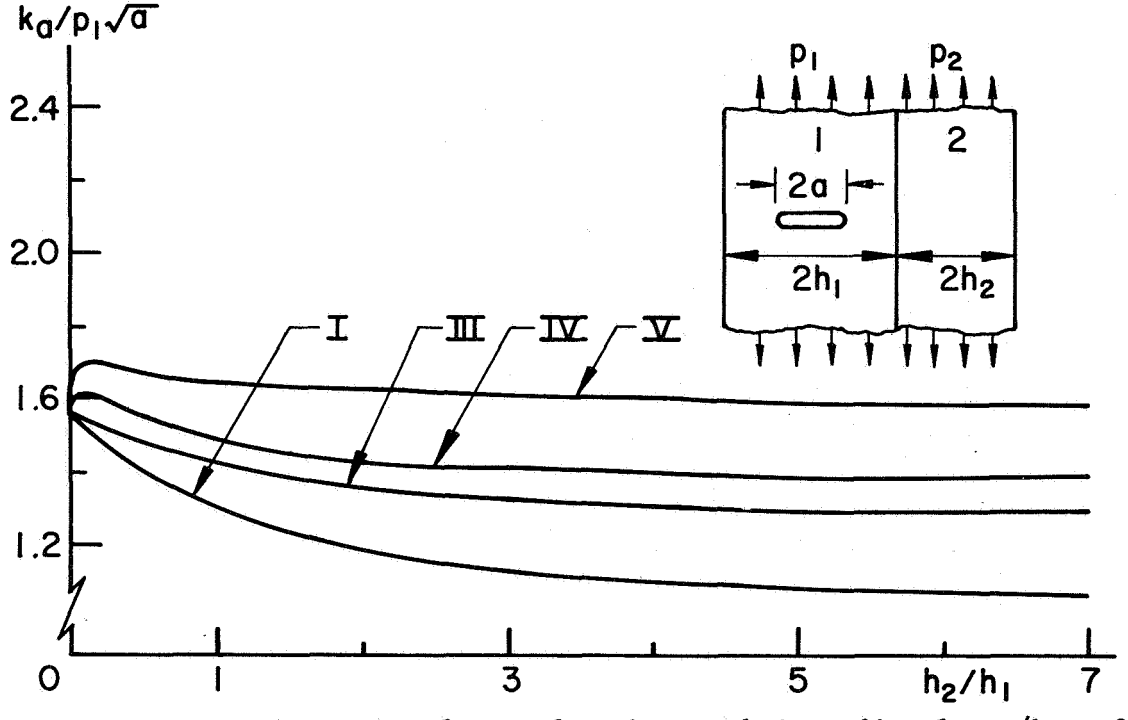

Figure 2.- Stress intensity factor for the crack in medium 1. $a/h_1 = 0.8$, $E_{1y}/E_{2y} \cong 5.5$ (see tables 1 and 2 for material properties).

HIGHER-ORDER EFFECTS OF INITIAL DEFORMATION ON THE VIBRATIONS OF CRYSTAL PLATES*

Xanthippi Markenscoff
Virginia Polytechnic Institute and State University

SUMMARY

A system of plate equations for the thickness-shear and flexural vibrations superposed on large initial deflection due to bending is derived; in the stress-strain relations the terms associated with the fourth-order elastic stiffness coefficients are retained. An explicit formula for the change in the fundamental cut-off thickness shear frequency is obtained and the effects of the terms associated with the fourth-order constants appear to be significant for large gradients of the rotation angles.

INTRODUCTION

The changes in the resonance frequencies of crystal plates subjected to initial stresses have been studied both experimentally and theoretically in the last twenty years (ref. 1). The ratio of the frequency change to the resonance frequency without initial stress, $f-f_o/f_o$, has an order of magnitude of 10^{-5} to 10^{-8} but accurate predictions of it have been obtained (refs. 1,2) by including in the stress-strain relation the nonlinear terms associated with the third-order elastic constants and taking into account the initial deformations. However, in the case of a plate subjected to large initial bending some discrepancies have been observed between experimental and both analytical and numerical results as described in reference 2. It was conjectured that including the fourth-order elastic constants in the stress-strain relations would accommodate these differences.

In reference 1 the basic plate equations of the theory of small deformations superposed on finite deformations are derived in Lagrangian formulation while in the stress-strain relations terms up to quadratic in the strain are kept. In the present paper the cubic terms in the strain, associated with the fourth-order elastic coefficients have been included and plate equations are derived to accommodate the thickness-shear and flexural vibrating of rotated Y-cuts of quartz superposed on a state of large initial bending. The initial strain components are assumed small but large deflection gradients and rotation angles are allowed. An explicit formula is obtained for the change of the fundamental thickness-shear frequencies in terms of the initial deformation and second-, third- and fourth-order constants.

---

*This work was supported by NSF Grant No. ENG 75-11875. To appear in the Journal of the Acoustical Society of America.

The higher-order elastic constants can be measured by observations in phenomena in which the elastic nonlinearity is manifested. For a detailed discussion on this the reader is referred to Thurston (ref. 3). Measurements of some of the fourth-order elastic constants have already been made. Based on the phenomena of intermodulation in thickness-shear and trapped energy resonators Tiersten obtained an estimate of C_{6666} for AT-cut quartz (ref. 4). Using shock-compression experiments Fowles (ref. 5) and Graham (ref. 6) have measured the longitudinal constants C_{1111}, C_{3333} for different cuts of quartz and sapphire. Their technique, however, is restricted to solids that can sustain large elastic compressions in uniaxial strain and to longitudinal elastic coefficients only. Some fourth-order constants for several cesium halides have been measured by ultrasonic techniques (ref. 7) and combinations of fourth-order constants of fused quartz have been determined in uniaxial tension experiments (ref. 8). Also Thurston and Shapiro demonstrated that the growth of the third harmonic in an initially sinusoidal finite-amplitude wave depends on both third- and fourth-order elastic constants (ref. 9).

In this work a different method for the determination of the fourth-order constants is presented. The constants C_{6611}, C_{6633}, C_{6655} can be determined to accommodate the differences between experiments and analytical predictions. As it appears from figure 6 and in particular figure 7 - where the differences are more pronounced - of reference 2, a symmetric function in ψ with respect to $\psi = 180°$ is needed and the additional quadratic terms included in the formula for $\Delta f/f$ provide qualitatively this type of distribution. The order of magnitude of the fourth-order constants involved may be seen to be the same as that of the constants measured by the previously mentioned investigators.

STRESS-STRAIN RELATION

The notation followed here is the same as in reference 1 - also shown in table 1 - and the formulation of the problem is Lagrangian. At the present final state and the initial static one the stress-strain relations are expressed, respectively, by

$$\overline{T}_{ij} = C_{ijk\ell}\overline{E}_{k\ell} + \frac{1}{2} C_{ijk\ell mn}\overline{E}_{k\ell}\overline{E}_{mn} + \frac{1}{6} C_{ijk\ell mnpq}\overline{E}_{k\ell}\overline{E}_{mn}\overline{E}_{pq} + \text{higher order terms in } \overline{E}_{k\ell} \tag{1}$$

$$T_{ij} = C_{ijk\ell}E_{k\ell} + \frac{1}{2} C_{ijk\ell mn}E_{k\ell}E_{mn} + \frac{1}{6} C_{ijk\ell mnpq}E_{k\ell}E_{mn}E_{pq} + \text{higher order terms in } E_{k\ell} \tag{2}$$

and their difference is defined as the incremental stress-strain relation

$$t_{ij} = C_{ijk\ell}\eta_{k\ell} + C_{ijk\ell mn}E_{k\ell}\eta_{mn} + \frac{1}{2} C_{ijk\ell mnpq}E_{k\ell}E_{mn}\eta_{pq} + \text{higher order terms} \tag{3}$$

where the products of the incremental strain have been omitted, the superposed motion being infinitesimal. Following Mindlin's (ref. 10) general procedure of series expansion in the thickness coordinate x_2, equations (2) and (3) yield

$$T_{ij}^{(e)} = \sum_{f} a_{(ef)} C_{ijk\ell} E_{k\ell}^{(f)} + \frac{1}{2} \sum_{f,g} a_{(efg)} C_{ijk\ell mn} E_{k\ell}^{(f)} E_{mn}^{(q)}$$

$$+ \frac{1}{6} \sum_{f,g,h} a_{(efgh)} C_{ijk\ell mnpq} E_{k\ell}^{(f)} E_{mn}^{(g)} E_{pq}^{(h)} \tag{4}$$

$$t_{ij}^{(e)} = \sum_{f} a_{(ef)} C_{ijk\ell} \eta_{k\ell}^{(f)} + \sum_{f,g} a_{(efg)} C_{ijk\ell mn} E_{k\ell}^{(f)} \eta_{mn}^{(g)}$$

$$+ \frac{1}{2} \sum_{f,g,h} a_{(efgh)} C_{ijk\ell mnpq} E_{k\ell}^{(f)} E_{mn}^{(g)} \eta_{pq}^{(h)} \tag{5}$$

where $a_{(efgh\ldots)} = \begin{cases} 2b^{s+1}/s+1 & (s \text{ even}) \\ 0 & (s \text{ odd}) \end{cases}$

$s = e + f + g + h + \ldots$, and $2b$ is the plate thickness.

Truncating the infinite series and retaining terms of orders zero and one only, the stress-strain relations in equations (4) and (5) reduce to

$$T_p^{(0)} = 2b(C_{pq} + \frac{1}{2} C_{pq}^{(0)} + \frac{1}{6} C_{pq}^{(00)}) E_q^{(0)} + \frac{b^3}{3} (C_{pq}^{(1)} + C_{pq}^{(10)}) E_q^{(1)} \tag{6}$$

$$T_p^{(1)} = \frac{2b^3}{3} (C_{pq} + C_{pq}^{(0)} + \frac{1}{2} C_{pq}^{(00)} + \frac{b^2}{10} C_{pq}^{(11)}) E_q^{(1)} \tag{7}$$

$$t_p^{(0)} = 2b(C_{pq} + C_{pq}^{(0)} + \frac{1}{2} C_{pq}^{(00)} + \frac{b^2}{6} C_{pq}^{(11)}) \eta_q^{(0)} + \frac{2b^3}{3} (C_{pq}^{(1)} + C_{pq}^{(10)}) \eta_q^{(1)} \tag{8}$$

$$t_p^{(1)} = \frac{2b^3}{3} (C_{pq}^{(1)} + C_{pq}^{(01)}) \eta_q^{(0)} + \frac{2b^3}{3} (C_{pq} + C_{pq}^{(0)} + \frac{1}{2} C_{pq}^{(00)} + \frac{3b^2}{10} C_{pq}^{(11)}) \eta_q^{(1)} \tag{9}$$

where the abbreviated Voigt notation is used (ref. 1) and

$$C_{pq}^{(\alpha)} = C_{pq} E_q^{(\alpha)}$$
$$C_{pq}^{(\alpha\beta)} = C_{pqrs} E_r^{(\alpha)} E_s^{(\beta)} \qquad (\alpha,\beta = 0,1) \tag{10}$$

INCREMENTAL MOTION SUPERPOSED ON INITIAL BENDING

In this paper the initial stress-strain-displacement fields for a plate subjected to initial bending are taken the same as in reference 2, where a detailed analysis is presented. The initial strains $E_i^{(0)}$ (i = 1,6) are assumed small but the initial rotation angles of the plate elements $U_1^{(1)}$, $U_3^{(1)}$, as well as the deflection gradients $U_{2,1}^{(0)}$, $U_{2,3}^{(0)}$ are considered large and terms up to quadratic in these quantities and their derivatives are retained. Therefore, under these assumptions terms in $C_{pq}^{(01)}$, $C_{pq}^{(00)}$ are discarded.

The stress-equations of motion for vibrations superposed on initial bending are presented in reference 2 (eq. (23)). Substituting the stress in terms of the strain according to equations (6)-(9) and using the strain-displacement relations (eqs. (27) and (28)) of reference 2, the displacement equations of motion in the thickness-shear and flexural modes are obtained:

$$\begin{aligned} P_1 u_{1,11}^{(1)} + P_2 u_{2,1}^{(0)} + P_3 u_1^{(1)} &= \rho \ddot{u}_1^{(1)} \\ P_4 u_{2,11}^{(0)} + P_5 u_{1,1}^{(1)} &= \rho \ddot{u}_2^{(0)} \end{aligned} \tag{11}$$

where

$$P_1 = C_{11} + C_{11}^{(0)} + 2C_{11}E_1^{(0)} + \frac{3b^2}{10} C_{11}^{(11)}$$

$$\begin{aligned} P_2 = &- \frac{3k^2}{b^2} C_{66} + kC_{16,1}^{(1)} + kC_{56,3}^{(1)} + k(C_{66,1}^{(1)} + C_{46,3}^{(1)})U_1^{(1)} \\ &- (C_{11,1}^{(1)} + C_{15,3}^{(1)})U_1^{(1)} - (C_{15,1}^{(1)} + C_{55,3}^{(1)})U_3^{(1)} - C_{11}^{(1)}U_{1,1}^{(1)} \\ &- C_{55}^{(1)}U_{3,3}^{(1)} - C_{15}^{(1)}(U_{3,1}^{(1)} + U_{1,3}^{(1)}) + C_{11}U_{2,11}^{(1)} + C_{55}U_{2,33}^{(1)} \\ &- \frac{3k^2}{b^2}[C_{66}^{(0)} + C_{66}U_{1,1}^{(0)} + C_{66}U_2^{(1)} + C_{56}U_3^{(1)} + C_{12}(U_1^{(0)})^2] - \frac{k^2}{2} C_{66}^{(11)} \end{aligned}$$

$$P_3 = -\frac{3k^2}{b^2} C_{66} + k(C^{(1)}_{16,1} + C^{(1)}_{56,3}) + k(C^{(1)}_{66,1} + C^{(1)}_{46,3})U^{(1)}_1$$

$$+ C_{11}\,(U^{(1)}_1 U^{(1)}_{1,1})_{,1} + C_{13}(U^{(1)}_3 U^{(1)}_{1,3})_{,1} + \frac{3}{2b^3}\,(T^{(1)}_{6,1} + T^{(1)}_{4,3})$$

$$- \frac{3k^2}{b^2}\,[C^{(0)}_{66} + 2C_{66}E^{(0)}_1] - \frac{k^2}{2}\,C^{(11)}_{66}$$

$$P_4 = k^2 C_{66} + k^2 C^{(0)}_{66} + 2k^2 C_{66} U^{(1)}_2 + C_{56}(U^{(0)}_{2,3} - U^{(1)}_3) + \frac{b^3 k^2}{3}\,C^{(11)}_{66}$$

$$P_5 = k^2 C_{66} + k^2 C_{66}(U^{(0)}_{1,1} + (U^{(1)}_1)^2 + U^{(1)}_2) + kC_{56}U^{(0)}_{2,3}$$

$$- \frac{1}{2b}\,U^{(1)}_1 (T^{(1)}_{1,1} + T^{(1)}_{5,3} + T^{(0)}_6) + \frac{b^3 k^2}{3}\,C^{(11)}_{66}$$

The displacement equations of motion accounting for the coupling with the $u^{(1)}_3$ mode as well and variations of the incremental motion in the $-X_3$ direction have been derived, but being very lengthy are not reported here. They will be published in a subsequent Technical Report.

In the previous studies (references 1,2) of plate vibrations it was shown that differences between the changes in the fundamental thickness-shear cut-off frequency at zero wave number and the changes in the thickness-shear frequencies are very small. A simplified formula is obtained in a similar fashion as in reference 2 for the variation of the fundamental cut-off frequency of rotated Y-cuts of quartz:

$$\frac{\Delta f}{f_o} = E^{(0)}_1 + \frac{C^{(0)}_{66}}{2C_{66}} - \frac{b^2}{\sqrt{3}\,\pi\,C_{66}}\,[C^{(1)}_{16,1} + C^{(1)}_{56,3} + (C^{(1)}_{66,1} + C^{(1)}_{46,3})U^{(1)}_3$$

$$+ \frac{1}{k}\,C_{11}(U^{(1)}_1 U^{(1)}_{1,1})_{,1} + \frac{1}{k}\,C_{13}(U^{(1)}_3 U^{(1)}_{1,3})_{,1} + \frac{3}{2b^3 k}\,(T^{(1)}_{6,1} + T^{(1)}_{4,3})$$

$$- \frac{k}{2}\,C^{(11)}_{66}] + \text{higher order terms} \qquad (12)$$

where

$$C^{(0)}_{66} = C_{661}E^{(0)}_1 + C_{662}E^{(0)}_2 + C_{663}E^{(0)}_3 + C_{664}E^{(0)}_4 \qquad (13)$$

$$C^{(1)}_{16,1} = C_{165}E^{(1)}_{5,1} \qquad C^{(1)}_{56,3} = C_{561}E^{(1)}_{1,3} + C_{563}E^{(1)}_{3,3} \tag{14}$$

$$C^{(11)}_{66} = C_{6611}(E^{(1)}_1)^2 + C_{6633}(E^{(1)}_3)^2 + C_{6655}(E^{(1)}_5)^2 \tag{15}$$

$k^2 = \frac{\pi^2}{12}$, k being a correction factor (reference 1).

As it may be seen from equation (12), the frequency change depends on the longitudinal strain $E^{(0)}_i$ (i.e. stretching of the middle plane) directly as well as through the third-order elastic constants (eq. (13)), and on shear strain (eq. (14)) and longitudinal strain due to bending (eq. (15)). For $E^{(1)}_{i,j} \approx E^{(1)}_i \approx 0.1$ (in the case of the plate of reference 2 this would result in strain at the outer fibers of $\approx 0.05\%$), the contribution of the terms appearing in equation (15) is of the same order as those in equation (14), provided that the associated fourth-order constants are bigger than the third-order ones by a factor of 10 - which is to be expected given the order of magnitude found for the fourth-order constants by the previously mentioned investigators. An estimate is not made here, however, because more data are needed and further experiments required. It may be seen, however, that the order of magnitude of the fourth-order constants must be the same as that found by the other investigators, if the discrepancies between theoretical predictions and experimental data are to be explained this way.

The phenomenon of small amplitude vibrations or wave motion superposed as a state of initial bending could be used to determine the fourth-order elastic coefficients. A shortcoming of this method is that the higher-order terms related to the fifth-order and higher constants do not vanish in formula (eq. (12)). A thorough study of wave-motion superposed on large bending is required in order to obtain all of the fourth-order elastic coefficients and this constitutes a topic for further research.

REFERENCES

1. P.C.Y. Lee, Y.S. Wang, and X. Markenscoff, "High Frequency Vibrating of Crystal Plates under Initial Stresses", J. Acoust. Soc. Am., 57, 95-105, 1975.

2. P.C.Y. Lee, Y.S. Wang, and X. Markenscoff, "Nonlinear Effects of Initial Bending on the Vibrations of Crystal Plates", J. Acoust. Soc. Am., 59, 90-96, 1976.

3. R.N. Thurston, Handbuch der Physik, Vol. VI a/4 (ed. C. Truesdell) Berlin-Heidelberg-New York: Springer, 1974.

4. H.F. Tiersten, "Analysis of Intermodulation in Thickness-Shear and Trapped Energy Resonators", J. Acoust. Soc. Am., 57, 667-681, 1975.

5. R. Fowles, "Dynamic Compression of Quartz," J. Geophys. Res., 72, 5729-5742, 1967.

6. R.A. Graham, "Determination of Third- and Fourth-Order Longitudinal Elastic Constants by Shock Compression Techniques - Application to Sapphire and Fused Quartz", J. Acoust. Soc. Am., 51, 1576-1581, 1972.

7. Z.P. Chang and G.R. Barsch, "Nonlinear Pressure Dependence of Elastic Constants and Fourth-Order Elastic Constants of Cesium Halides", Phys. Rev. Lett., 19, 1381-1382, 1967.

8. B.E. Powell and M.J. Skove, "Combinations of Fourth-Order Elastic Constants of Fused Quartz", J. Appl. Phys., 41, 4913-4917, 1970.

9. R.N. Thurston and M.J. Shapiro, "Interpretation of Ultrasonic Experiments on Finite Amplitude Waves", J. Acoust. Soc. Amer., 41, 1112-1125, 1967.

10. R.D. Mindlin, "An Introduction to the Mathematical Theory of Vibrations of Elastic Plates", Monogr. U.S. Army Signal Corps Eng. Labs, Fort Monmouth, N.J., 1955.

Table 1

	Total (at present state)	Initial (at initial state)	Incremental
Displacement	$\overline{U}_i$	U_i	$u_i = \overline{U}_i - U_i$
Kirchhoff-Piola Stress	$\overline{T}_{ij}$	T_{ij}	$t_{ij} = \overline{T}_{ij} - T_{ij}$
Lagrangian Strain	$\overline{E}_{ij}$	E_{ij}	$\eta_{ij} = \overline{E}_{ij} - E_{ij}$

BIODYNAMICS OF DEFORMABLE HUMAN BODY MOTION*

Alvin M. Strauss and Ronald L. Huston
Engineering Analysis Dept., University of Cincinnati

SUMMARY

The objective of this paper is to construct a framework wherein the various models of human biomaterials fit in order to describe the biodynamic response of the human body. The behavior of the human body in various situations, from low frequency, low amplitude vibrations to impact loadings in automobile and aircraft crashes, is very complicated with respect to all aspects of the problem: Materials, Geometry and Dynamics. The materials problem is the primary concern here, but the materials problem is intimately connected with geometry and dynamics.

INTRODUCTION

There are unique difficulties associated with describing in vivo biomaterials. First, the material properties of human tissues vary significantly with the individual. And at this time there do not exist standards applicable to the material properties of human tissues. Even for design purposes there is no agreement on the moduli of bone, muscle or tendon. Moreover, if standards existed they would be restricted to a given age, weight, and sex. The mechanical properties of bone, for example, reach their optimum values when the individual is in his or her early twenties and they deteriorate slowly thereafter. The mechanical properties of the various human tissues also vary with the weight and physical dimensions of the individual. Diet has an influence as does training and disease. If these problems concerned with the variability of physical properties were the only difficulties involved it would not be beyond our creativity to construct a rational process for obtaining numbers, as inputs and constants, in the various biodynamic problems of interest. However, there are significant problems involved in performing measurements of even the most basic material properties, such as the modulus

*This work was partially supported by grants ENG 75 21037 and ENG 75 06619 from the National Science Foundation.

of elasticity, of any human tissue. It is almost impossible to implant instruments in the human body to obtain data. Moreover, even if it were technically feasible to make some of the desired measurements, we cannot violate medical ethics and the civil rights of individuals by surgically implanting instruments and then having the subjects perform the required controlled tasks. It is also extremely difficult to implant devices in animals to obtain biomaterials data. However, this data is essential, because it has been shown many times that the mechanical properties of living subjects are significantly different from those of cadavers. And the mechanical properties of even the most stable of human tissues such as bone are different in vivo from those of a cadaver or of an embalmed specimen (refs. 1 and 2).

SYMBOLS

$a_{\ell p}$	see equation (1)
A_o	function of invariants
B_o	function of invariants
e_{ijk}	permutation symbol
f_ℓ	see equation (3)
$\underset{\sim}{F}$	force vector
F_{jk}	resultant applied force
F_ℓ	generalized active forces
I_j	invariants
I_{ijk}	centroidal inertia dyadics
m_i	masses
$\underset{\sim}{M}$	moment vector
M_{jk}	moment
N	number of rigid bodies
$\underset{\sim}{Q}$	functional operator

t	present time
V_{ijk}	partial rate of change of position
X_j	generalized coordinate, position vector
α	constant
τ	time variable
ω_{ijk}	partial rate of change of orientation

BIOMATERIALS

The human skeletal system is composed of 206 distinct bones, 26 in the vertebral column, 22 in the skull, 25 ribs and sternum, the hyoid bone, 6 auditory ossicles, 64 comprising the upper extremities and 62 comprising the lower extremities. The stress-strain curves for these bones show a definite viscoelastic behavior (refs. 3 to 5). Thus in many situations it will be necessary to model bone as a viscoelastic material.

It is more clear that muscle, tendon, skin, vascular walls, ligaments, and the various internal organs are viscoelastic (refs. 6 to 14). The state-of-the-art in biodynamic modeling can be gleaned from the papers in (ref. 15).

There are no widely accepted models of human biomaterial response for any portion of the human body. For example, the human head has been modeled as a rigid tube, a spherical shell with an elastic core, a spherical elastic shell with a viscoelastic core, a viscoelastic shell and core, a static empty shell, a layered shell, a spherical shell with a fluid core, a rigid spherical shell with an elastic/viscoelastic core among others (ref. 16). This serves to point out that even though there may be agreement on the qualitative properties of human biomaterials there is no agreement towards a rational approach to modeling any portion of the human body in a given biodynamic situation.

Thus a basic problem confronting the mechanicist is how to develop a biomaterials model that will interface in an efficient manner with models for other portions of the human body. For example, to develop a model of the human head for predicting its response to impact loads, one might need to develop a model for the scalp, outer table of the skull, diploe layer, inner table of the skull, meninges and cerebrospinal fluid and the brain. In this case a gross continuum model with one

constitutive equation for the entire head would not yield any useful results, but perhaps the scalp-skull system could be modeled by a single constitutive relation instead of the four suggested above. Often the results desired may determine the sensitivity built into the mathematical model.

This contribution is directed towards developing biomaterials models for use in gross human body modeling. As such only a general finite deformation model will be developed to be used for large portions of the human body as a first step with the second step being a model where bone and muscle-tendon systems are modeled separately and interdigitated with the dynamics of human body.

DYNAMICS

Recently a number of finite-segment human body models have been developed to study the dynamics of the head-neck system, spine deformation, and crash victim motion (refs. 17 to 25). Basically, these models are gross-motion simulators. They are composed of rigid bodies shaped to simulate the human skeletal system and flesh structure. The bodies are generally connected by ball-and-socket, hinge, or sliding joints. The muscles, ligaments, and joint tissue are usually modeled by springs and dashpots. It is at this point that the constitutive equations developed in this paper can make their contribution to deriving more sophisticated and sensitive models.

Consider the model developed by Huston, et.al. (refs. 24 to 28). This model makes use of a set of governing dynamical equations of motion, for the description of the dynamics of the human body, in the form,

$$a_{\ell p}\,\ddot{X}_p = f_\ell \qquad (\ell=1,\ldots,3N+3) \tag{1}$$

where p is summed from 1 to 3N+3 and where $a_{\ell p}$ and f_ℓ are given by,

$$a_{\ell p} = m_j\, V_{jpk}\, V_{j\ell k} + I_{jkn}\, \omega_{jpm}\, \omega_{j\ell k} \tag{2}$$

and

$$f_\ell = -(F_\ell + m_j V_{j\ell k} \dot{V}_{jqk} \ddot{X}_q + I_{jkn} \omega_{j\ell n} \dot{\omega}_{jqk} \ddot{X}_q$$

$$+ e_{nmk} \omega_{jqn} \omega_{jqr} \omega_{j\ell k} I_{jmr} \dot{X}_q \dot{X}_s) \qquad (3)$$

where j, q, and s are summed from 1 to N and the other repeated indices are summed from 1 to 3.

N is the number of rigid bodies in the model and the X_j, where j=1,...,3N+3, are the generalized coordinates of the model system [3 for the translation of the first rigid body and 3 for the rotations of each of the N bodies].

The ω_{ijk} and V_{ijk} (i=1,...,N; j=1,...,3N+3; k=1,2,3) are the partial rates of change of orientation and position (ref. 29) of the bodies and their mass centers.

m_i and I_{ijk} (i=1,...,N; j,k=1,2,3) are the masses and centroidal inertia dyadics of the N bodies. e_{ijk} (i,j,k=1,2,3) is the standard permutation symbol. The F_ℓ (ℓ=1,...,3N+3) are the generalized active forces on the system, and they are given by,

$$F_\ell = V_{j\ell k} F_{jk} + \omega_{j\ell k} M_{jk} \qquad (4)$$

where the F_{jk} and M_{jk} are the components of the resultant applied force and moment on body B_j.

These applied forces and moments can arise externally due to the action of gravity, seat belts, or impact and also arise internally on account of the response of the joint tissue. The modeling of the tissue response by means of spring and dashpot models has been one of the weakest links in existing gross biodynamic motion simulators (ref. 30). Therefore we derive immediately below, a constitutive theory of human tissue response in a force moment formalism.

BASIC FINITE MODEL

Let us assume that, for example, the mechanical properties of the human leg can be described by a single constitutive relation. In other words we assume we can write a mathematical relation and say "this is the constitutive equation that describes

the response of the human leg". This implies that we have assumed the leg to be made of a single material, call it leg material. We, of course, know that the leg is made up of bone, muscle, tendon, various fluids, blood vessels, skin, etc., but the kind of answers we are looking for do not demand the refinement of a composite-solid-fluid analysis. We can, however, describe the leg as an anisotropic material - a refinement well within the capability of the analysis and needed to provide the accurate numbers needed for a sufficiently valid description of the biodynamic response of the human body.

The human leg can also be modeled with the framework of the UCIN model (ref. 24) if the human leg is assumed to be made up of alternating concentric cylinders of rigid material and deformable material. This type of model is subsumed by the finite segment model discussed above. In either case the constitutive relations developed below will hold.

Consider a generic particle that is initially unloaded. We wish to develop a history dependent relationship between the force vector $\underset{\sim}{F}$ and the moment vector $\underset{\sim}{M}$. Assume the moment at the present time t depends on the past history of the force, or

$$\underset{\sim}{M}(t) = \underset{\sim}{Q}[\underset{\sim}{F}(t-\tau)] \tag{5}$$

over the interval $\tau\varepsilon[0,\infty)$ and $\underset{\sim}{Q}$ is the functional operator.

It can be shown (refs. 31 and 32) that if the material is isotropic then we may write Q in the form,

$$\underset{\sim}{Q}=\underset{\sim}{Q}^{(1)}[\underset{\sim}{F}(t-\tau);\ I_1,\ I_2] + \underset{\sim}{Q}^{(2)}[\underset{\sim}{F}(t-\tau_1)x\underset{\sim}{F}(t-\tau_2);\ I_1,\ I_2] \tag{6}$$

where

$$I_1 = \underset{\sim}{F}(t-\tau_1) \cdot F(t-\tau_2) \tag{7}$$

$$I_2 = \underset{\sim}{F}(t-\tau_1) \cdot \underset{\sim}{F}(t-\tau_2) \times \underset{\sim}{F}(t-\tau_3) \tag{8}$$

The functionals $\underset{\sim}{Q}^{(1)}$ and $\underset{\sim}{Q}^{(2)}$ are linear in the forces. The linear approximation to the constitutive relation can be written as

$$\underset{\sim}{M}(t) = \int_o^\infty A_o(t)\ \underset{\sim}{F}(t-\tau)d\tau \tag{9}$$

where A_o is a function of I_1 and I_2. For more significant nonlinear behavior one may write

$$\underset{\sim}{M}(t) = \int_o^\infty A_o(\tau)\ \underset{\sim}{F}\ (t-\tau)d\tau \ + \int_o^\infty \int_o^\infty B_o(\tau_1,\tau_2)\underset{\sim}{F}(t-\tau_1)\ x$$

$$\underset{\sim}{F}(t-\tau_2)d\tau_1\ d\tau_2 \tag{10}$$

where B_o is also a function of I_1 and I_2.

A differential approximation to equation (10) may be obtained by writing the Taylor series,

$$\underset{\sim}{F}(t-\tau) = \sum \frac{1}{n!}\ (-\tau)^n\ \underset{\sim}{F}^{(n)}\ (t) \tag{11}$$

yielding

$$\underset{\sim}{M}(t) = \sum \alpha_n\ \underset{\sim}{F}^{(n)}(t) + \sum \sum \alpha_{mn}\ \underset{\sim}{F}^{(m)}\ (t)\ x\ \underset{\sim}{F}^{(n)}\ (t) \tag{12}$$

where

$$(-1)^n\ n!\ \alpha_n = \int_o^\infty A[I_1,I_2;\tau]\tau^n\ d\tau \tag{13}$$

$$(-1)^{m+n}\ m!\ n!\ \alpha_{mn} = \int_o^\infty \int_o^\infty B[I_1,I_2;\tau_1,\tau_2]\tau_1{}^m\tau_2{}^n d\tau_1 d\tau_2 \tag{14}$$

If the material is assumed to be transversely isotropic one may write (ref. 31)

$$\underset{\sim}{Q} = \underset{\sim}{Q}^{(1)}\ [\underset{\sim}{F}(t-\tau);\ I_1,I_2,I_3] +$$

$$\underset{\sim}{Q}^{(2)}\ [\underset{\sim}{F}(t-\tau_1)\ x\ \underset{\sim}{F}(t-\tau_2);\ I_1,\ I_2,I_3] +$$

$$\underset{\sim}{Q}^{(3)}\ [1,\ I_1,\ I_2,\ I_3] \tag{15}$$

where

$$I_3 = F_3(t-\tau). \tag{16}$$

DISCUSSION AND CONCLUSIONS

Until this time biomaterial modeling in gross-motion simulators has been performed with springs and dampers. And whereas this has been marginally successful, it has often required many hours of "tuning" and adjusting constants to match some experimental data. Equations (9) and (10) provide a means of avoiding this problem. Indeed, since the gross-motion simulators such as UCIN are generally developed to numerically accept arbitrary moment functions, the relation described above can be used directly upon writing of suitable computer algorithms for their inclusion in the computer codes.

REFERENCES

1. Gang, D. P.; and Ross, M. A.: Vertical Mode Human Body Vibration Transmissibility. IEEE Trans. Systems, Man and Cybernetics, vol. SMC-6, no. 2, Feb. 1976, pp. 102-112.

2. Hirsch, A. E.; and White, L. A.: Mechanical Stiffness of Man's Lower Limbs. ASME Paper No. 65-WA/HUF-4, 1965.

3. McElhaney, J. H.: Dynamic Response of Bone and Muscle Tissue. J. Applied Physiology, vol. 21, 1966, pp. 1231-1236.

4. Sedlin, E.: A Rheological Model for Cortical Bone. Acta Orthoped. Scand., vol. 36, suppl. 83, 1965.

5. Davis, C. F.: On the Mechanical Properties of Bones and a Poroelastic Theory of Stresses in Bone Elements. Ph.D. Dissertation, University of Delaware, 1970.

6. Blix, M.: Die Lange und die Spannung des Muskels. Skand. Arch. Physiol., vol. 4, 1893, pp. 399-409.

7. Levin, A.; and Wyman, J.: The Viscous Elastic Properties of Muscles. Proc. Roy. Soc. Ser. B, vol. 101, 1927, pp. 218-243.

8. Paslay, P. R.; et.al.; A Quantitative Model for Partially Activated Skeletal Muscle. J. Appl. Mech., Dec. 1974, pp. 849-854.

9. Little, R. C.: Dynamics of Stress Relaxation in Skeletal Muscle. Am. J. Physiol., vol. 217, 1969, pp. 1665-1671.

10. Aubert, X.; Le Couplage energetique de la Contraction Musculaire. Editions Arscia, Brussels, 1956.

11. Chaplain, R. A.; and Frommelt, B.: A Mechanochemical Model for Muscular Contraction, J. Mechanochem. Cell Motility, vol. 1, no. 1, 1971, pp. 41-56.

12. Apter, J. T.; and Cummings, D. H.: Correlation of Viscoelastic Properties of Large Arteries with Microscopic Structure. Circulation Res., vol. 19, 1966, pp. 104-121.

13. Pell, K. M.; and Stanfield, J. W.: Mechanical Model of Skeletal Muscle. Am. J. Physical Medicine, vol. 51, no. 1, 1972, pp. 23-38.

14. Alexander, R. M.: Animal Mechanics. Univ. of Washington Press, Seattle, 1968.

15. Saczalski, K.; et.al.(eds): Aircraft Crashworthiness. Univ. Press of Virginia, Charlottesville, 1975.

16. King, A. I.: Survey of the State of the Art of Human Biodynamic Response. Aircraft Crashworthiness, 1975, pp. 83-120.

17. Robbins, D. H.; et.al.: The MVMA Two-Dimensional Crash Victim Simulations. Proceedings of the 18th Stapp Car Crash Conference, 1974, pp. 657-678.

18. Glancy, J. J.; and Larsen, S. E.: Users Guide for Program SIMULA. Dynamic Science Report TDR No. 72-23, 1972.

19. Karnes, R. N.; et.al.: Prometheus--A Crash Victim Simulation. Aircraft Crashworthiness, University Press of Virginia, Charlottesville, 1975, pp. 327-346.

20. Robbins, D. H.; et.al.: User Oriented Mathematical Crash Victim Simulator. Proceedings of the 16th Stapp Car Crash Conference, 1972, pp. 128-148.

21. Young, R. D.; et.al.: Simulation of the Pedestrial During Vehicle Impact. Proceedings of the 3rd International Congress on Automotive Safety, paper no. 27, vol. ii, 1974.

22. Furusho, H.; and Yokoya, K.: Analysis of Occupant's Movement in Head-On Collision. Transactions of the Society of Automotive Engineers of Japan, no. 1, 1970, pp. 145-155.

23. Fleck, J. T.: CALSPAN 3-D Crash Victim Simulation Program. Aircraft Crashworthiness, University Press of Virginia, 1975, pp. 299-310.

24. Huston, R. L.; et.al.: Dynamics of a Crash Victim--A Finite Segment Model. AIAA Journal, Feb. 1976, pp. 173-178.

25. Huston, R. L.; et.al.: The UCIN 3-D Aircraft-Occupant. Aircraft Crashworthiness, University Press of Virginia, 1975, pp. 311-324.

26. Advani, S.; et.al.: Human Head Impact Response-Experimental Data and Analytical Simulations. Proceedings 2nd International Conference Biomechanics of Serious Trauma, Birmingham, England, 1975, pp. 153-163.

27. Advani, S.; et.al.: Human Head-Neck Dynamic Response: Analytical Models and Experimental Data. Aircraft Crashworthiness, University Press of Virginia, 1975, pp. 197-212.

28. Huston, J. C.; et.al.: Numerical Prediction of Head/Neck Response to Shock-Impact. Measurement and Prediction of Structural and Biomechanical Crash-Impact Response, ASME Winter Annual Meeting, 1976.

29. Kane, T. R.: Dynamics. Holt, Rinehart, and Winston, New York, 1968.

30. King, A. I.; and Chou, C. C.: Mathematical Modelling, Simulation and Experimental Testing of Biomechanical System Crash Response. AIAA Annual Meeting and Technical Display, Washington, D.C., Feb. 1975.

31. Rivlin, R. S.: Constitutive Equations Involving Functional Dependence of One Vector on Another. J. Appl. Math. Phys. (ZAMP), vol. 12, no. 5, 1961, pp. 447-452.

32. Pipkin, A. C.; and Rivlin, R. S.: Phenomenological Theory of Magnetic Hysteresis. J. Math. Phys., vol. 8, no. 4, 1967, pp. 878-883.

IMPACT TENSILE TESTING OF WIRES

T. H. Dawson
U. S. Naval Academy

SUMMARY

A simple impact test is examined for determining the dynamic tensile response of metal wires. The test consists of fixing one end of a wire specimen and allowing a threaded falling weight to strike the other. Assuming the dynamic stress in the wire to be a function only of its strain, energy considerations show for negligible wire-inertia effects that the governing dynamic stress-strain law can be determined directly from impact-energy vs. wire-elongation data. Theoretical calculations are presented which show negligible wire-inertia effects for ratios of wire mass to striking mass of the order of 10^{-2} or less. The test method is applied to soft copper wires and the dynamic stress-strain curve so determined is found to be about 30 percent higher than the corresponding static curve.

INTRODUCTION

The impact testing of wires and rods provides a subject of continuing interest in the field of mechanics (ref. 1). The experimental problem is complicated by the fact that under impact loading the inertia on the material can become important and thus invalidate assumptions of uniform stress and strain such as customarily employed in simple quasi-static testing. For this reason, modern impact studies generally take into account the wave character of the problem and involve dynamic measurements at various positions along the specimen. Technological interest remains, however, in a simple yet reliable impact test to determine dynamic material response. The present paper discusses such a test and gives experimental results for the case of soft copper wires.

SIMPLE THEORETICAL MODEL

The situation considered is that of a wire fixed at one end and struck at the other by a threaded falling weight (fig. 1). The inertia of the wire is assumed small in comparison with that of the striking mass so that the stress and strain along the wire may be regarded as uniform, or approximately so. In addition, the response of the wire is assumed such that the dynamic stress in the wire is a function only of its strain. Under these circumstances, the initial kinetic energy of the striking mass and the work done by it as it falls through the maximum end displacement of the wire must equal the uniform internal work done by the wire as it stretches. This fact is expressed mathematically by

the equation:

$$\frac{1}{2}\frac{MV_o^2}{AL} + \frac{Mg}{A}\varepsilon_m = \int_o^{\varepsilon_m} \sigma\,(\varepsilon)\,d\varepsilon \tag{1}$$

where M and V_o denote the mass and striking velocity of the falling weight, A and L denote the initial sectional area and length of the wire, g denotes the acceleration of gravity, σ and ε denote nominal (or engineering) stress and strain and ε_m denotes the maximum strain induced in the wire by the impact.

On writing the total impact energy appearing on the left-hand side of equation (1) as

$$T = \frac{1}{2}\frac{MV_o^2}{AL} + \frac{Mg}{A}\varepsilon_m \tag{2}$$

and differentiating with respect to the maximum strain ε_m, it thus follows that

$$\frac{dT}{d\varepsilon_m} = \sigma\,(\varepsilon_m) \tag{3}$$

so that the stress σ associated with the strain ε_m is given directly by the corresponding rate of change of the impact energy with respect to the maximum strain. Once the condition for negligible wire-inertia effects used in writing equation (1) has been established, this last equation can then be used to determine the governing impact stress-strain law from experimentally determined impact-energy vs. wire elongation date.

Equations similar to those given above have previously been employed by W. Soper (ref. 2) in interpreting compression data from impact tests on thin aluminum discs. In Soper's work, the neglect of specimen inertia was based on a rough estimate of the number of wave passes through the specimen during its compression. It will be seen in the next section that the question may be analyzed in an altogether different way.

WIRE INERTIA EFFECTS

The condition for ensuring negligible wire-inertia effects in the above described impact test is subject to exact theoretical determination, although the problem is extremely complex. When, for instance, the falling weight strikes the end of the wire, tension waves are propagated upward, followed by less intense unloading waves caused by the slowing of the weight. These waves reflect an increase in strength at the fixed end and then race back down the wire, increasing the stress as they go. Upon reaching the struck end, they again reflect an increase in strength and the entire wave process is repeated. In this way the wire force acting on the impacting weight is progressively increased and its downward speed continually reduced.

To untangle the above waves and analyze the stress distribution in the wire as the striking weight is brought to rest is a difficult problem which has not yet been undertaken. Fortunately, however, the details of these waves can be side-stepped altogether and the impact mechanics analyzed approximately using a lumped-mass numerical model. Such a model is illustrated in figure 2 where the mass of the wire has been assumed concentrated at eleven equally spaced positions along the wire, with ten massless wire elements connecting them. The stress-strain law governing the wire elements has been assumed, somewhat arbitrarily, to be the same as that governing quasi-static deformations of soft copper wires. This law is shown in figure 2.

If u_1, u_2, ... denote the displacements of the concentrated masses shown in figure 2 and if σ_1, σ_2, ... denote the stresses in the corresponding wire elements, the equations governing the motion of the masses may be written as

$$\begin{aligned}
\frac{d^2u_1}{dt^2} &= \frac{V_o^2\,(\sigma_2 - \sigma_1)}{2\,\alpha\,\ell\,T_K} \\
\frac{d^2u_2}{dt^2} &= \frac{V_o^2\,(\sigma_3 - \sigma_2)}{2\,\alpha\,\ell\,T_K} \\
&\vdots \\
\frac{d^2u_{10}}{dt^2} &= \frac{V_o^2\,(\sigma_s - \sigma_{10})}{(20 + \alpha)\,\ell\,T_K}
\end{aligned} \tag{4}$$

where t denotes the time, ℓ denotes the length of the individual wire elements, V_o denotes the striking velocity of the falling weight, and α, T_K and σ_s are defined by

$$\alpha = \frac{m}{M}, \quad T_K = \frac{1}{2}\frac{MV_o^2}{AL}, \quad \sigma_s = \frac{Mg}{A} \tag{5}$$

with m denoting the total wire mass and, as earlier, M, A, L and g denoting, respectively, the mass of the striking weight, the sectional area and length of the wire and the acceleration of gravity.

These equations may be integrated numerically starting from time t = 0 using initial conditions corresponding to all displacements zero and all velocities zero except that of the struck end where the velocity there initially equals the impact velocity V_o.

This numerical program has been carried out using a standard fourth-order Runge-Kutta integration scheme and an integration time-step interval of 0.001 ℓ/V_o. To fix numbers, the following typical constants were assumed

$$T_K = 4.28 \text{ N/mm}^2, \qquad \sigma_s = 8.56 \text{ N/mm}^2$$

corresponding in the case of negligible wire inertia to a maximum induced strain ε_m of 0.05 and an impact-energy division such that

$$\frac{Mg}{A}\,\varepsilon_m = 0.10\,\left(\frac{1}{2}\,\frac{MV_o^2}{AL}\right)$$

in equation (1). From the above set of governing equations it can be seen that these two constants, together with the mass ratio α, are sufficient to allow determination of the dimensionless displacements u_1/ℓ, u_2/ℓ, ... in terms of the dimensionless time tV_o/ℓ. Using the dimensionless displacements, the strains in the individual wire elements can, of course, also be determined.

Figure 3 shows typical strain-time histories at the wire ends for the case where the ratio of wire mass to striking mass is equal to 0.01. Also shown is the average strain-time history calculated by dividing the struck-end displacement by the total wire length. It will be seen that the strain variations are negligibly small for this mass ratio. Moreover, as expected, when significantly larger mass ratios are examined, the strain variations become more pronounced. On the basis of these results, it may therefore be concluded that the strain - and hence the stress - variations along the wire may safely be ignored for ratios of wire mass to striking mass of the order of 10^{-2} or less.

IMPACT TESTS ON COPPER WIRES

Impact tests satisfying the above condition for negligible wire-inertia effects have been carried out using soft copper wires having initial diameters of 0.079 cm and various initial lengths. The static deformation of these wires is characterized by the stress-strain law given earlier in figure 2.

Table 1 lists impact data for these wires, with U_m denoting the maximum displacement of the struck end. The first set of data refers to tests where the impact energy was held fixed (within 5 percent) at 7.3 N/mm^2. The maximum strains ε_m determined from these data are plotted against their maximum strain rates V_o/L in figure 4. It will be seen that the strains are sensibly independent of these ratios so that the material may thus be regarded as rate insensitive over this range of rates. This result is in agreement with earlier work on hardened copper wires (ref. 3).

Figure 5 shows impact-energy vs. strain data as determined from the above data as well as the remaining data of Table 1. Also shown is a theoretical curve calculated from equation (1) using the static stress-strain law of figure 2. The large differences between the two clearly indicate that the governing impact stress-strain law is considerably different from the static one. This is shown more clearly in figure 6 where impact stress-strain data, as determined from the smoothed curve in figure 5 and equation (3), are contrasted with the static curve. It will be seen, in agreement with other more sophisticated

studies (ref. 4-5), that the impact curve is about 30 percent higher than the static curve.

REFERENCES

1. Bell, J. F.: The Experimental Foundations of Solid Mechanics, Encyclopedia of Physics, Vol VIa/1, Springer-Verlag, Berlin, 1973.

2. Soper, W. G.: Wedge Penetration in a Thick Target, Proceedings ASME Colloquium on the Behavior of Materials Under Dynamic Loading, Chicago, 1965.

3. Dawson, T. H.: On the Applicability of One-Dimensional Non-Viscous Dynamic Plasticity Theory, Int. J. Mech. Sci., Vol. 14, 1972, p. 43.

4. Kolsky, H. and L. S. Douch: Experimental Studies in Plastic Wave Propagation, J. Mech. and Phys. of Solids, Vol. 10, 1962, p. 195.

5. Santosham, T. V. and H. Ramsey: Small Plastic Strain Wave Propagation in Prestressed Soft Copper Rods, Int. J. Mech. Sci., Vol. 12, 1970, p. 447.

TABLE I. IMPACT DATA FROM COPPER WIRES

V_o	L	M	m/M	T	U_m*
cm/sec	cm	kg	-	N/mm^2	cm
CONSTANT IMPACT ENERGY					
89	88.9	3.76	0.001	7.66	4.92
127	63.5	2.00	0.001	7.17	3.10
183	24.9	0.50	0.002	7.42	1.27
254	41.4	0.43	0.004	7.33	2.03
279	50.8	0.43	0.005	7.24	2.54
305	78.7	0.57	0.006	7.50	4.14
406	141.0	0.57	0.011	7.48	7.14
406	36.3	0.15	0.010	7.05	1.75
495	54.1	0.15	0.016	7.07	3.02
VARIABLE IMPACT ENERGY					
173	50.8	0.29	0.008	1.80	0.64
122	31.8	0.57	0.002	2.99	0.64
305	88.9	0.29	0.013	3.22	2.34
356	97.8	0.29	0.015	3.97	2.82
318	66.0	0.29	0.010	4.71	2.51
229	37.1	0.36	0.005	5.45	1.42
254	63.5	0.57	0.005	6.55	3.10
318	68.6	0.43	0.007	6.90	3.02
292	136.9	1.07	0.006	8.24	8.08
305	55.9	0.50	0.005	9.10	3.10
254	56.4	0.78	0.003	10.42	4.01
229	45.7	0.86	0.002	11.17	3.25
254	55.9	0.86	0.003	11.66	4.22
381	105.9	0.78	0.006	12.28	9.36

*Average of two tests

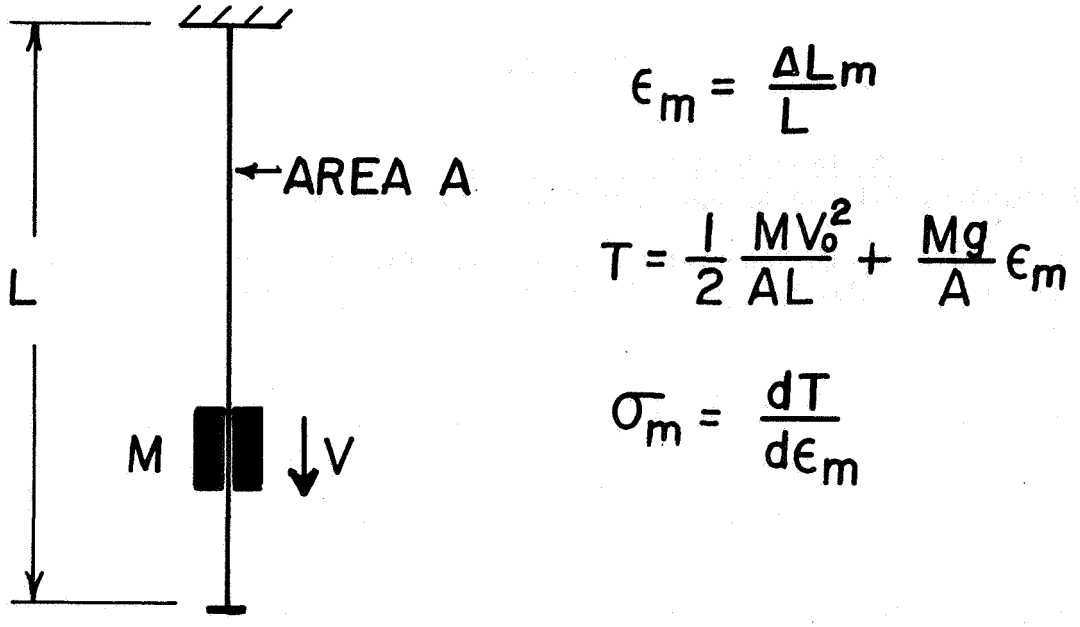

Figure 1.- Simple impact tensile test.

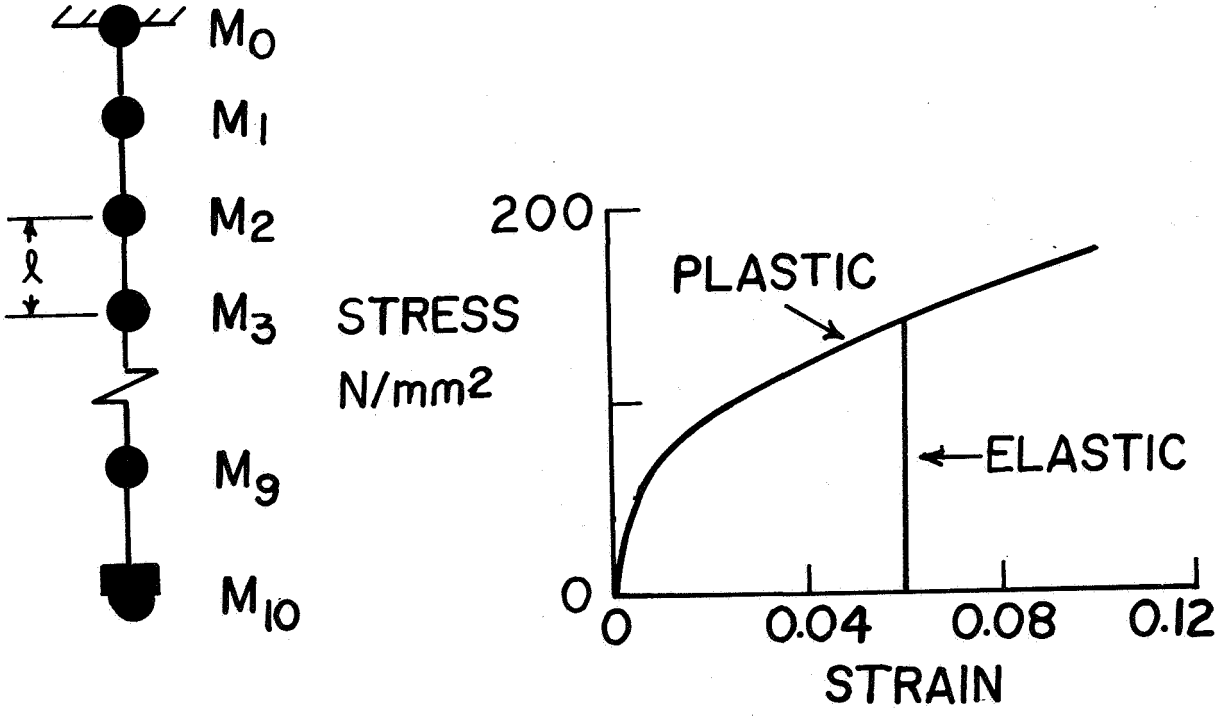

Figure 2.- Numerical model for analyzing impact.

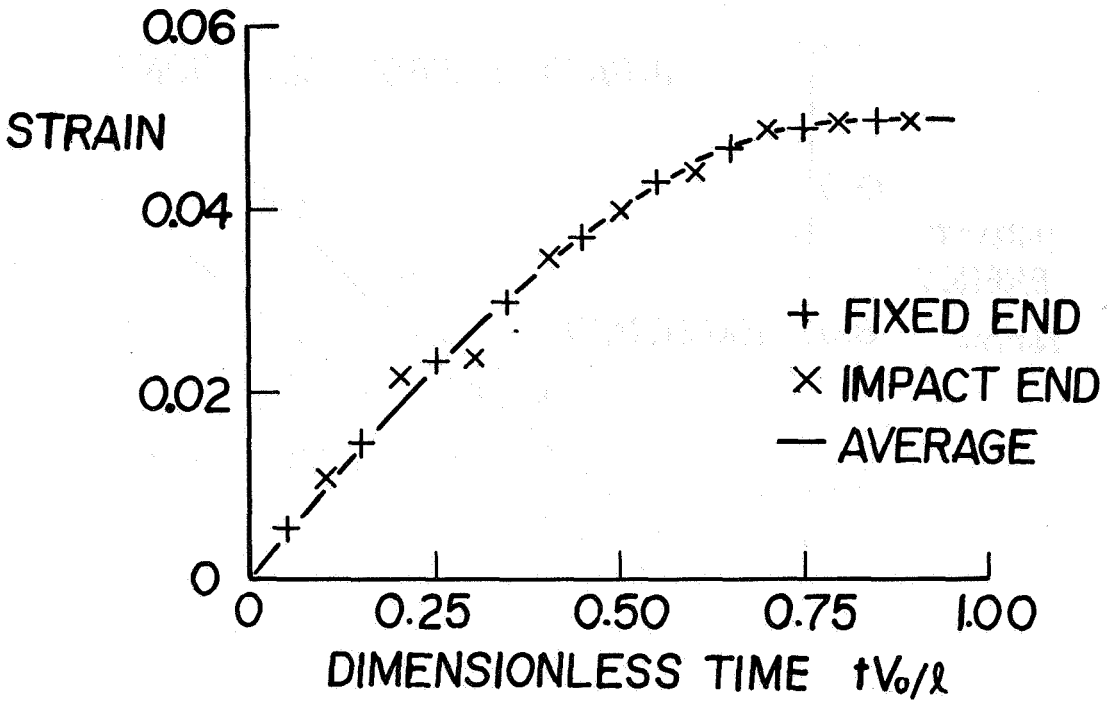

Figure 3.- Theoretical strain histories for case where the ratio of wire mass to striking mass equals 0.01.

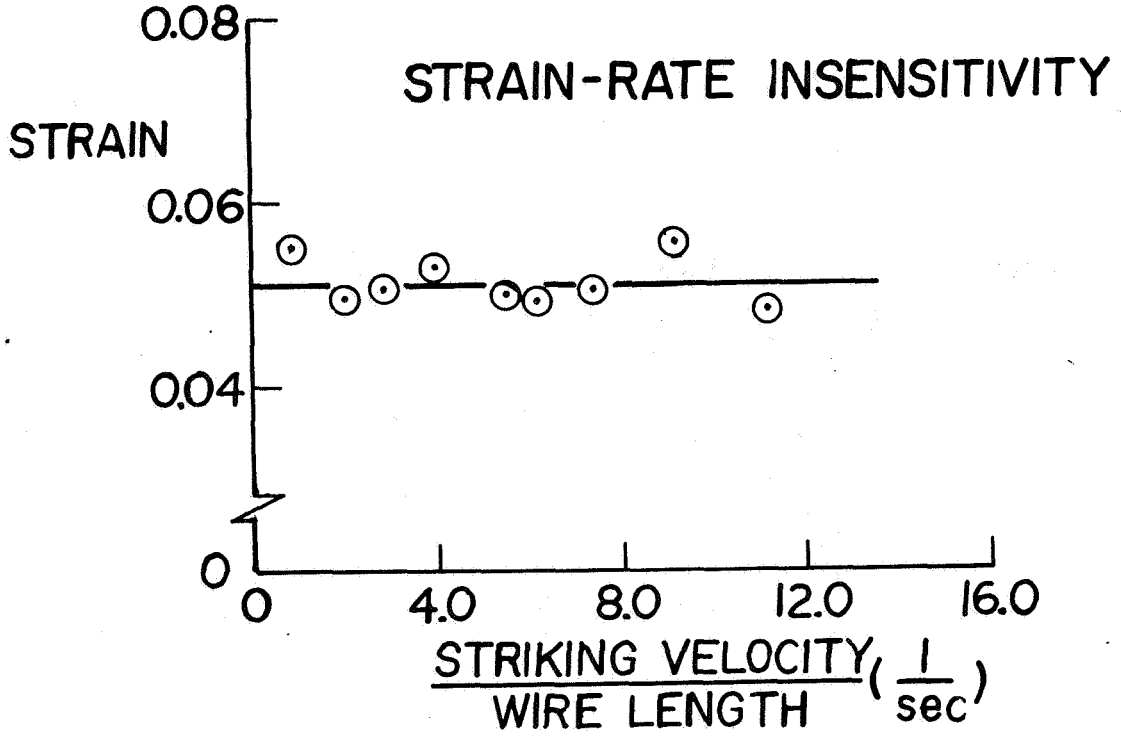

Figure 4.- Experimental data from copper wires showing strain-rate insensitivity.

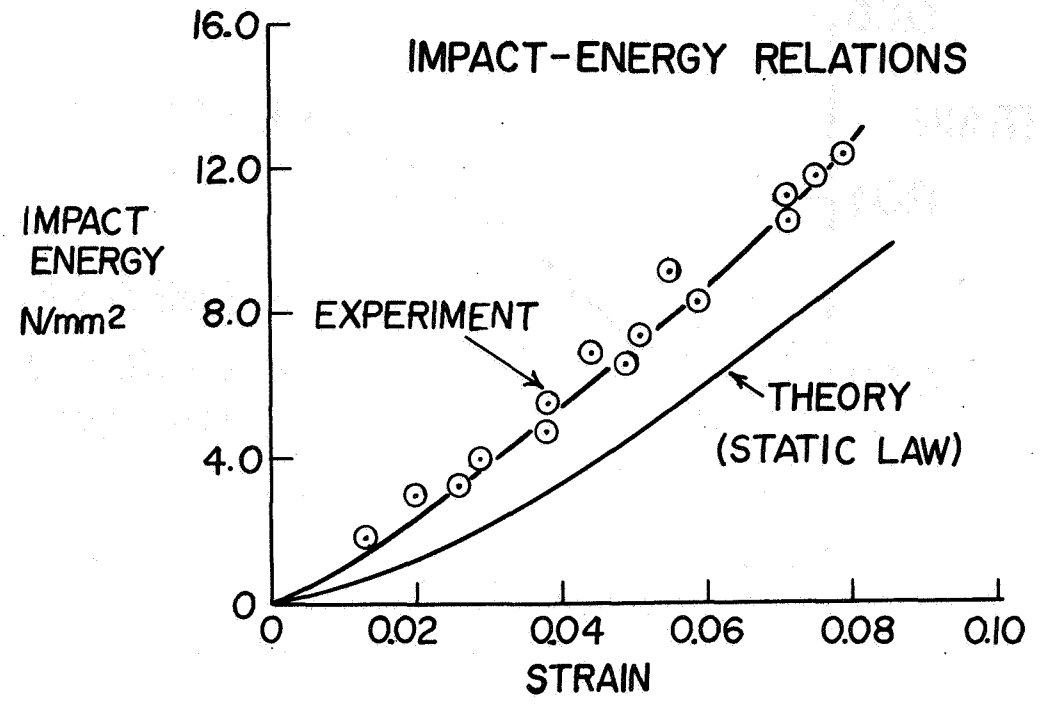

Figure 5.- Impact-energy relations for copper wires.

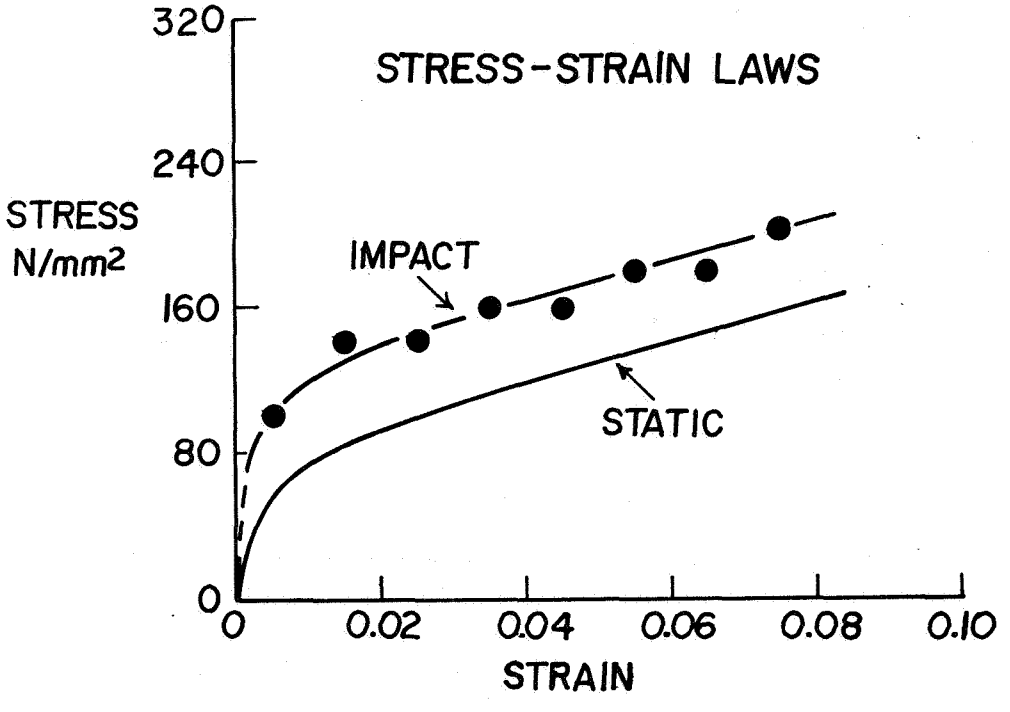

Figure 6.- Comparison of impact and static stress-strain laws for copper wires.

NUMERICAL DETERMINATION OF THE TRANSMISSIBILITY CHARACTERISTICS OF A SQUEEZE FILM DAMPED FORCED VIBRATION SYSTEM

Michael A. Sutton
Babcock and Wilcox Company

Philip K. Davis
Southern Illinois University at Carbondale

SUMMARY

Numerical solutions of the governing equations of motion of a liquid squeeze film damped forced vibration system were carried out to examine the feasibility of using a liquid squeeze film to cushion and protect large structures, such as buildings, located in areas of high seismic activity. The mathematical model used was that for a single-degree-of-freedom squeeze film damped spring-mass system. The input disturbance was simulated by curve fitting actual seismic data with an eleventh order Lagrangian polynomial technique. Only the normal component of the seismic input was considered. The exact solution to the fluid flow equations, as developed by Ishizawa (ref. 1) for the liquid squeeze film undergoing oscillatory motion, was used to include the damping force in the equation of motion of the vibratory system. The non-linear, non-homogeneous governing differential equation of motion was solved numerically to determine the transmissibility over a wide range of physical parameters using a fourth-order Runge-Kutta technique. It is determined that a liquid squeeze film used as a damping agent in a spring-mass system can, for certain combinations of the physical parameters of the system, significantly reduce the response amplitude for a seismic input disturbance.

INTRODUCTION

The term "liquid squeeze film" as used herein is defined as the liquid located between two nearly parallel plane surfaces which are closely spaced compared to the dimensions defining the boundary surfaces. The fluid motion which results from the approach or separation of the surfaces is called "squeezing flow". If the surfaces are in relative oscillatory motion, the fluid will dissipate energy and damp the motion. If the squeezing motion is slow enough that the fluid inertia can be neglected, the resulting fluid flow conforms to Reynold's theory (ref. 2). However, most vibration problems are inherently dynamic in nature and therefore fluid inertia is not expected to be negligible. An interest in the possible application of liquid squeeze films to cushion and protect large structures, such as buildings, located in areas of high seismic activity led to this study which examines the transmissibility characteristics of a liquid squeeze film damped forced vibration system.

A literature search has shown that little research has been carried out concerning the application of liquid squeeze films as a damping agent in forced vibration systems. It was suggested by Sommer (ref. 3) that a liquid squeeze film might serve well as a damping agent in practical applications in which high damping is required but space is limited. The importance of the non-linear

inertia terms in the liquid squeeze flow equations was first discussed by Jackson (ref. 4). Jackson and Kuzma (ref. 5) obtained approximate solutions to these equations with some of the fluid inertia terms included. However, Ishizawa (ref. 1) obtained an exact solution to the complete liquid squeeze film equations in a "multifold" infinite series form, using only the assumptions that the fluid was incompressible and the oscillatory flow was axisymmetric. Theoretical and experimental studies of liquid squeeze film damping were completed by Yabe and Davis (ref. 6) for a single-degree-of-freedom system undergoing free vibrations.

In the absence of previous research, it was decided to carry out a theoretical investigation of the transmissibility characteristics of a liquid squeeze film damped spring-mass system subjected to the normal component of a seismic disturbance. The transmissibility characteristics were studied as the physical properties of the system were varied. The results indicate that under certain conditions a liquid squeeze film might be used to effectively cushion a structure subjected to forced oscillatory input motions.

SYMBOLS

Values are given in both SI and U.S. Customary Units.

Amo	maximum output amplitude, cm (in)
Ami	maximum input amplitude, cm (in)
a	acceleration, cm/s^2 (in/sec^2)
$\frac{d(\ )}{dt}$	total derivative with respect to time
F_b	force of liquid squeeze film, N (lb)
F_s	force of spring, N (lb)
h(t), H(t)	gap width between mass and support at any time, cm (in)
h_o, H_o	Initial gap width between mass and support, cm (in)
J	Variable to account for entrance flow effects. J = 1 if h greater than h_o. J = 0 if h is less than h_o.
k	Spring constant, N/cm (lb/in)
KK	numerically approximated derivative
m	mass, kg (slug)
Q_1	$m\nu/\rho r_o^4 \ h_o \ \omega_n$
Q_2	$\nu/h_o^2 \ \omega_n$

r_o	radius of circular cylindrical mass, cm (in)
t	time, s (sec)
Δt	numerical time step, s (sec)
v	velocity, cm/s (in/sec)
X(t), X	Input displacement as function of time, cm (in)
$\dot{X}(t), \dot{X}$	Input velocity as a function of time, cm/s (in/sec)
$\ddot{X}(t), \ddot{X}$	Input acceleration as a function of time, cm/s^2 (in/sec^2)
X*(t), X*	Non-dimensional input displacement
$\dot{X}^*(t), \dot{X}^*$	Non-dimensional input velocity
$\ddot{X}^*(t), \ddot{X}^*$	Non-dimensional input acceleration
x(t), x	Response displacement as a function of time, cm (in)
$\dot{x}(t), \dot{x}$	Response velocity as a function of time, cm/s (in/sec)
$\ddot{x}(t), \ddot{x}$	Response acceleration as a function of time, cm/s^2 (in/sec^2)
x*(t), x*	Non-dimensional response displacement
$\dot{x}^*(t), \dot{x}^*$	Non-dimensional response velocity
$\ddot{x}^*(t), \ddot{x}^*$	Non-dimensional response acceleration
π	3.14159
ρ	Density of squeeze film fluid, kg/cm^3 ($slugs/in^3$)
ν	Kinematic viscosity of squeeze film fluid, cm^2/s (in^2/sec)
ω_n	natural frequency of the spring-mass system, 1/s (sec^{-1})
Σ	Summation symbol

THEORETICAL DEVELOPMENT

A simplified schematic diagram of the squeeze film spring-mass system, which is used as a basis for developing the governing differential equation of motion, is presented in figure 1.

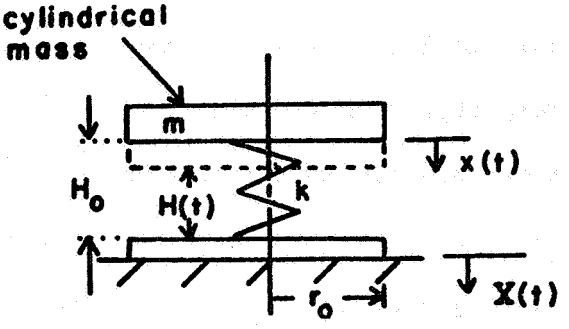

Figure 1: Schematic of Spring-Mass Squeeze Film System

The equation governing the displacement of the mass m is obtained by use of Newton's Second Law,

$$\Sigma\vec{F} = \frac{d(m\vec{v})}{dt} \tag{1}$$

The forces on the mass include the force of the spring

$$Fs = k\,[x(t) - X\,(t)] \tag{2}$$

and the pressure force due to the liquid squeeze film. The latter force is incorporated by retaining the five primary components of the infinite series solution to the fluid flow equations for a liquid squeeze film undergoing oscillatory motion as determined by Ishizawa (ref. 1)

$$F_b = \rho\nu^2 \left(\frac{-3\pi}{2}\right)\left(\frac{r_o}{h}\right)^4 \left[\frac{h\,\dot{h}}{\nu} + \frac{(h)^3\,\ddot{h}}{10(\nu)^2} - \left(\frac{5}{28} - \frac{J}{12}\right)\right.$$

$$\left.\left(\frac{h\,\dot{h}}{\nu}\right)^2 + \frac{(h)^4\,\dot{h}\,\ddot{h}}{260\,(\nu)^3} - \frac{277\,(h)^3\,(\dot{h})^3}{323\,(400)\,(\nu)^3}\right] \tag{3}$$

The squeeze film gap width as a function of time is

$$h = h_o + X - x \tag{4}$$

The time derivatives of equation (4) are as follows:

$$\dot{h} = \dot{X} - \dot{x}$$

$$\ddot{h} = \ddot{X} - \ddot{x}$$

$$(\dot{h})^2 = (\dot{X})^2 - 2\,(\dot{X})\,(\dot{x}) + (\dot{x})^2$$

$$(\dot{h})^3 = (\dot{X})^3 - 3\,(\dot{X})^2\,(\dot{x}) + 3\,(\dot{X})\,(\dot{x})^2 - (\dot{x})^3$$

$$(\dot{h})\ (\ddot{h}) = \ddot{X}\quad \dot{X} - \ddot{X}\ (\dot{x}) - \dot{X}\ (\ddot{x}) + \ddot{x}\ (\dot{x}) \tag{5}$$

Utilizing equations (2), (3), (4) and (5), equation (1) is transformed to

$$\left(m + \frac{3\pi\rho r_o^4}{20\ (h_o + X-x)} + \frac{3\pi\rho r_o^4\ (\dot{X}-\dot{x})}{520\nu}\right)\ddot{x}$$

$$- \frac{3(277)\pi\rho r_o^4\ (\dot{x})^3}{800(323)\nu\ (h_o + X-x)} + \left(\frac{3\pi\rho r_o^4\ (5/28 - J/12)}{2\ (h_o + X - x)^2}\right.$$

$$\left. + \frac{9(277)\ \pi\rho r_o^4\ \dot{X}}{323(800)\nu(h_o+X-x)}\right)(\dot{x})^2 + \left(\frac{3\pi\rho r_o^4\ \nu}{2\ (h_o+X-x)^3}\right.$$

$$\left. - \frac{3\pi\rho r_o^4\ (5/28-J/12)\ \dot{X}}{(h_o + X - x)^2} + \frac{3\pi\rho r_o^4\ \ddot{X}}{520\nu}\right.$$

$$\left. - \frac{9(277)\pi\rho r_o^4\ (\dot{X})^2}{323(800)\ (h_o + X - x)\ \nu}\right)\ \dot{x} + k(x) = k\ (X) +$$

$$\frac{3\pi\rho r_o^4\ \nu\dot{X}}{2(h_o + X - x)^3} + \frac{3\pi\rho r_o^4\ \ddot{X}}{20(h_o+X-x)} - \frac{3\pi\rho r_o^4\ (5/28-J/12)\ (\dot{X})^2}{2\ (h_o + X - x)^2} +$$

$$\frac{3\pi\rho r_o^4\ \dot{X}\ \ddot{X}}{520\ \nu} - \frac{3(277)\pi\rho r_o^4\ (\dot{X})^3}{800(323)\ \nu\ (h_o + X - x)} \tag{6}$$

Equation (6) is the dimensional governing equation for the problem. For large values of m, k, h_o, and r_o, large differences of the order of 10^5 in some cases between the values of the ratios of these constants do occur. In computer techniques, disparities of this order can cause serious problems. One method of minimizing the effects of these disparities is to non-dimensionalize the equation. Equation (6) is non-dimensionalized by using a pertinent length (h_o) and time (ω_n). The non-dimensional relationships are:

$$X = X^*\ h_o \qquad x = x^*\ h_o$$

$$\dot{X} = \dot{X}^*\ h_o\ \omega_n \qquad \dot{x} = \dot{x}^*\ h_o\ \omega_n$$

$$\ddot{X} = \ddot{X}^*\ h_o\ \omega_n^2 \qquad \ddot{x} = \ddot{x}^*\ h_o\ \omega_n^2 \tag{7}$$

Substitution of these relationships into equation (6) and division by the arbitrarily chosen non-dimensional parameter grouping

$$\frac{\rho r_o^4\ h_o^2\ \omega_n^3}{\nu}$$

gives the following non-dimensional equation of motion for the single degree of freedom spring-mass squeeze film system shown in figure 1:

$$\left[Q(1) + \frac{3\pi Q(2)}{20(1 + X^* - x^*)} + \frac{3\pi(\dot{X}^* - \dot{x}^*)}{520}\right] \ddot{x}^*$$

$$- \left(\frac{3(277)\pi}{323(800)\ (1 + X^* - x^*)}\right) (\dot{x}^*)^3 + \left(\frac{3\pi(5/28 - j/12) \cdot Q(2)}{2(1 + X^* - x^*)^2}\right.$$

$$\left. + \frac{9(277)\pi\dot{X}^*}{323(800)\ (1 + X^* - x^*)}\right) (\dot{x}^*)^2 + \left(\frac{3\pi(Q(2))^2}{2(1 + X^* - x^*)^3}\right.$$

$$\left. - \frac{3\pi(5/28 - j/12)\dot{X}^*\ Q(2)}{(1 + X^* - x^*)^2} + \frac{3\pi\ddot{X}^*}{520} - \frac{9(277)\pi(\dot{X}^*)^2}{323(800)\ (1 + X^* - x^*)}\right)$$

$$(\dot{x}^*) + Q(1)\ x^* = Q(1)\ X^* + \frac{3\pi\dot{X}^*\ (Q(2))^2}{2(1 + X^* - x^*)^3} + \frac{3\pi\ddot{X}^*\ Q(2)}{20(1 + X^* - x^*)}$$

$$+ \frac{3\pi\ddot{X}^*\dot{X}^*}{520} - \frac{3\pi(\dot{X}^*)^2(5/28 - j/12)\ Q(2)}{2(1 + X^* - x^*)^2} - \frac{3(277)\pi(\dot{X}^*)^3}{323(800)\ (1 + X^* - x^*)} \qquad (8)$$

where $Q(1) = \dfrac{m\nu}{\rho r_o^4 h_o\ \omega_n}$

and $Q(2) = \dfrac{\nu}{h_o^2 \omega_n}$

Inspection of equation (8) shows that the solution to the equation is a function of the input forcing function X, the time derivatives of X, Q(1), Q(2) and the time t. This is true for constant values of h_o and ω_n, which are the parameters used to non-dimensionalize the dimensional seismic input data prior to insertion into equation (8). Therefore, it is reasonable to expect that equation (8) can be solved for fixed values of h_o and ω_n. The parameter h_o is limited in magnitude by the radius of the cylindrical mass, r_o, since the ratio h_o/r_o is generally taken to be equal to or less than 0.10 to assure that "squeezing flow" will result. Also, ω_n is determined by the mass, m, and the spring constant, k, such that $\omega_n = \sqrt{k/m}$. Since h_o and ω_n may vary from one structure to another, the solutions to equation (8) were charted for varying values for ω_n and h_o.

Equation (8) is a second order, non-linear, non-homogeneous ordinary differential equation with variable coefficients. Since the existence of a closed form solution to this type of equation is unknown, a numerical solution was carried out.

COMPUTER TECHNIQUES

Equation (8) was solved on an IBM-370 digital computer using a fourth-order Runge Kutta technique attributed to Kutta;

$$KK_1 = f\ (ti,\ xi)$$

$$KK_2 = f\ [ti + \Delta t/2,\ xi + (\Delta t/2)\ (KK_1)]$$

$$KK_3 = f\ [ti + \Delta t/2,\ xi + (\Delta t/2)\ (KK_2)]$$

$$KK_4 = f\,[ti + \Delta t,\ xi + (\Delta t)\ (KK_3)]$$

$$\text{and}\quad X_{i+1} = \frac{\Delta t}{6}\ (KK_1 + 2KK_2 + 2KK_3 + KK_4)$$

Where KK values are approximate derivatives of the object function, X, at various points in the time interval, Δt. The value of the time step, Δt, was required to be less than 1/20th of the period of oscillation of the object function. By trial and error, the value of Δt used herein was set at 0.01 seconds.

The input disturbance, X, and its derivatives are based on actual seismic data from a San Fernando earthquake occurring in 1971. Figure 2 shows the seismic displacement function used. A Lagrangian eleventh order finite difference interpolation routine was developed and used to obtain values of X, $\dot{X}$ and $\ddot{X}$ at intervals of 0.01 second.

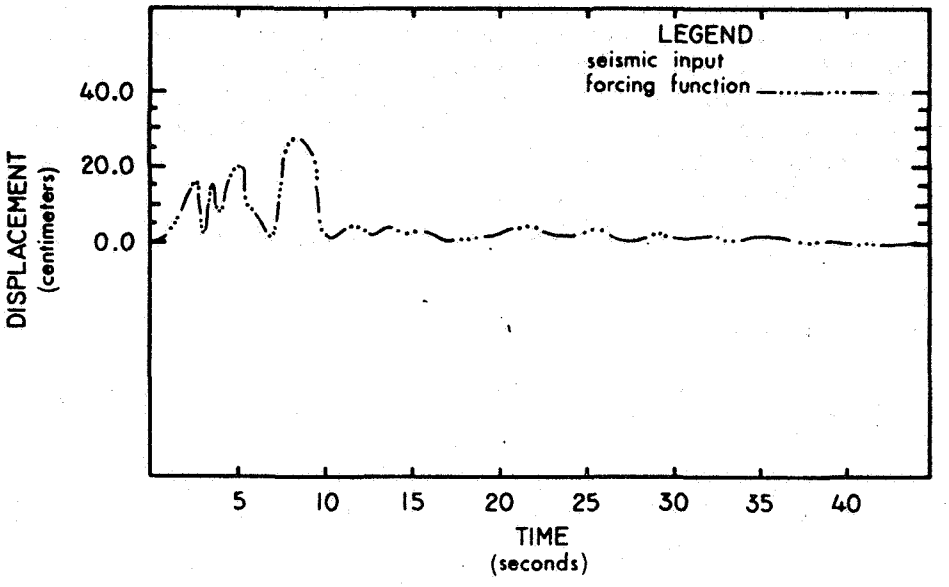

Figure 2: Seismic Input Displacement Function Versus Time

Equation (8) was then solved using a computer technique which is based on the synthesis of these numerical procedures. The results of this study are presented in plots of the transmissibility versus Q(1) for five values of Q(2) with h_o and ω_n held constant. Transmissibility as used herein, is defined as the ratio of the maximum response amplitude (Amo) of the mass to the maximum input disturbance amplitude (Ami). Table 1 shows the parameter values used to obtain the data presented in each figure.

Figure Number	Range of Q(1) Values	Range of Q(2) Values	h_o (cm)	ω_n (Sec^{-1})
3	10^6 to 10^{-6}	10^{-7} to 10^1	57.42	125.66
4	10^6 to 10^{-6}	10^{-7} to 10^1	57.42	6.2832
5	10^6 to 10^{-6}	10^{-7} to 10^1	57.42	0.062832

6	10^{6} to 10^{-6}	10^{-7} to 10^{1}	177.8	125.66
7	10^{6} to 10^{-6}	10^{-7} to 10^{1}	177.8	6.2832
8	10^{6} to 10^{-6}	10^{-7} to 10^{1}	177.8	0.062832

TABLE 1: Parameter Values Used in Figures 3 Through 8

DISCUSSION OF RESULTS

The transmissibility of the system, Amo/Ami, would be unity if a rigid connection existed between the mass and the support. However, as the data indicate, it is possible to have combinations of the physical parameters such that Amo/Ami is greater than unity. Such conditions are undesirable when the purpose is to protect the model from input seismic disturbances.

Several conclusions can be drawn from the data shown in figures 3, 4 and 5. The effect of ω_n on the transmissibility can best be observed by considering all three figures together. For values of $\omega_n \lesssim 1$, the transmissibility is reduced to levels significantly below unity. Figure 5 shows the most intriguing results. These results indicate that for certain values of Q(1) and Q(2), zero transmissibility exists.

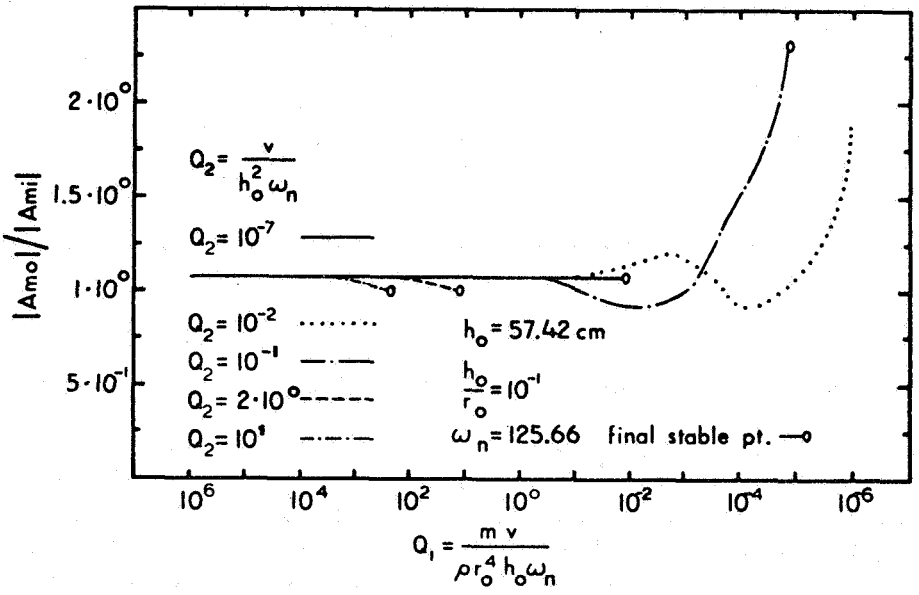

Figure 3: A_{mo}/A_{mi} Versus Q_1 for Five Values of Q_2 with h_o = 57.42 cm and ω_n = 125.60 rad/s.

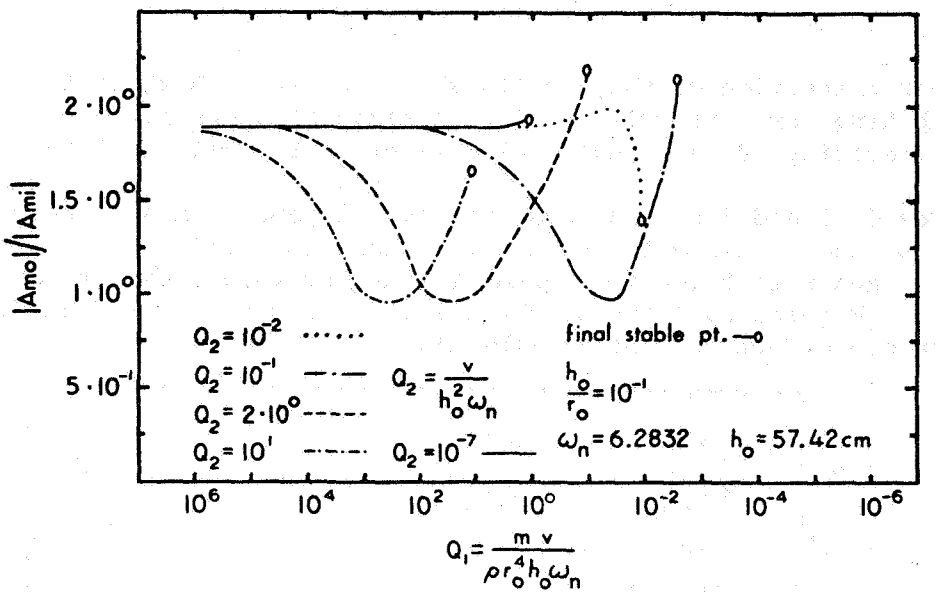

Figure 4: A_{mo}/A_{mi} Versus Q_1 for Five Values of Q_2

with h_o = 57.42 cm and ω_n = 6.2832 rad/s

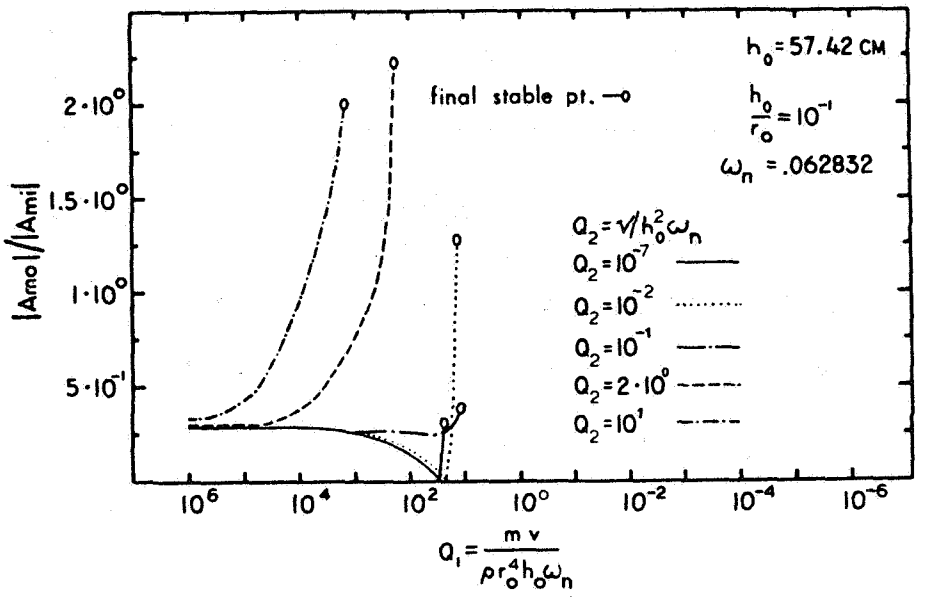

Figure 5: A_{mo}/A_{mi} Versus Q_1 for Five Values of Q_2

with h_o = 57.42 cm and ω_n = 0.062832 rad/s

The values of h_o and ω_n were again held constant for the data shown in figures 3, 4 and 5. If the values of ρr_o^4 also were assumed to be fixed, then Q(1) is only a function of ν and Q(2) is a function of the product, $m\nu$. Therefore, as shown in figures 3, 4 and 5, for each value of kinematic viscosity, ν, there appears to exist a value of mass, m, for which minimum trans-

missibility occurs.

Further inspection of the results shown in Figure 5 shows that for those cases exhibiting zero transmissibility, a range of approximately 10^5 in kinematic viscosity (ν) has negligible effect on transmissibility.

Figures 6, 7 and 8 portray essentially the same trends as shown in Figures 3, 4 and 5. Since the value of h_o used to obtain the data shown in Figures 6, 7 and 8 is three fold greater than the values used to obtain the data shown in Figures 3, 4 and 5, the results indicate that h_o has a small but discernible effect on transmissibility.

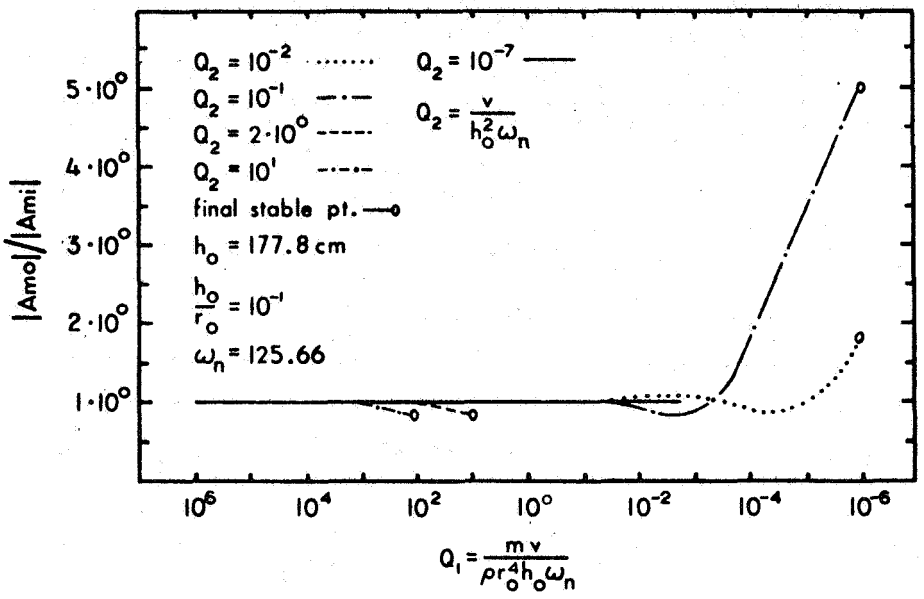

Figure 6: A_{mo}/A_{mi} Versus Q_1 for Five Values of Q_2 with h_o - 177.8 cm and ω_n - 125.66 rad/s

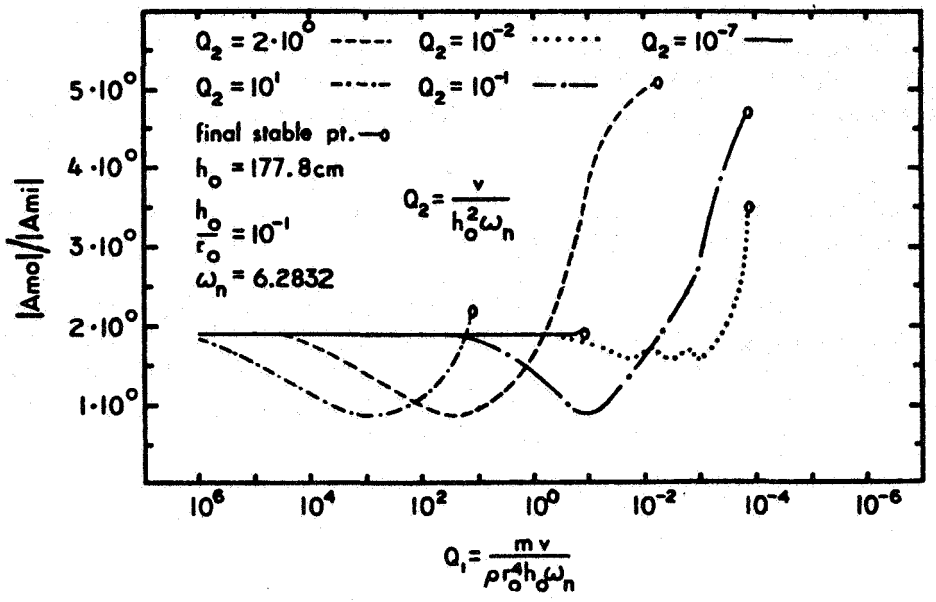

Figure 7: A_{mo}/A_{mi} Versus Q_1 for Five Values of Q_2 with h_o = 177.8 cm and ω_n = 6.2832 rad/s

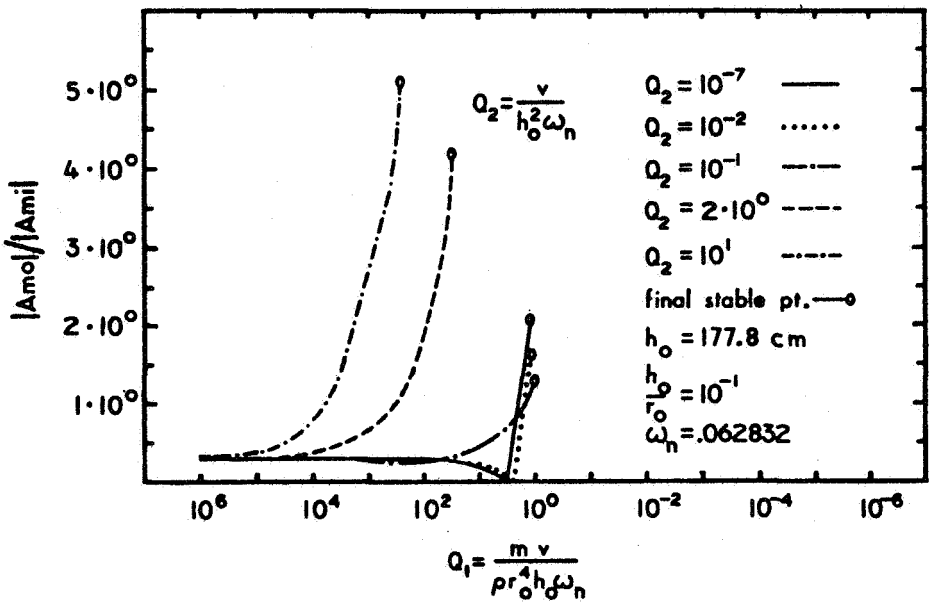

Figure 8: A_{mo}/A_{mi} Versus Q_1 for Five Values of Q_2 with h_o = 177.8 cm and ω_n = 0.062832 rad/s

CONCLUSIONS

1. The results demonstrate that a liquid squeeze film used as a damping agent in a spring-mass system can, for certain combinations of the physical parameters, significantly reduce the response amplitude of the mass with respect to

the input amplitude for seismic input disturbances applied normal to the base of the model. The data therefore indicate that under certain conditions a liquid squeeze film might be used in the system to effectively cushion or partially isolate a structure, e.g. a building, from the normal component of a seismic disturbance.

2. The effect of the initial squeeze thickness (h_o) on transmissibility was found to be small for the range of data taken.

3. For values of ω_n greater than unity, the transmissibility was greater than unity for most values of Q(1) and Q(2). For values of ω_n less than unity, the transmissibility is reduced to levels significantly below unity for most values of Q(1) and Q(2). Furthermore, for $\omega_n = 0.062832$ and for certain values of Q(1) and Q(2), a point of zero transmissibility was predicted.

4. In general, for constant values of ρr_o^4, h_o, ω_n and ν, there exists a value of mass (m) for which minimum transmissibility occurs.

REFERENCES

1. Ishizawa, S. (1966), "The Unsteady Laminar Flow Between Two Parallel Discs with Arbitrarily Varying Gap Width," Bulletin of the Japanese Society of Mechanical Engineers, Volume 9, Number 35, pp. 533-550.

2. Reynolds, O., (1886) "On the Theory of Lubrication and its Application to Mr. Beauchamp Tower's Experiments, Including an Experimental Determination of the Viscosity of Olive Oil", Royal Society of London, Part I, Volume 177, 157-234.

3. Sommer, E.A., (1966) "Squeeze Film Damping," Machine Design, Volume 38 pp. 163-167.

4. Jackson, J.D., (1962), "A Study of Squeezing Flow," Applied Science Research, A Volume 11, pp. 148-152.

5. Kuzma, D.C., (1967), "Fluid Inertia Effects in Squeeze Films," Applied Science Research, Volume 18, pp. 15-20.

6. Yabe, T. and Davis, P.K., (1971) "Damping Characteristics of a Liquid Squeeze Film," Developments in Theoretical and Applied Mechanics, Volume 5, pp. 23-54.

A MODEL STUDY OF LANDING MAT SUBJECTED TO C-5A LOADINGS*

P. T. Blotter, F. W. Kiefer, V. T. Christiansen
Utah State University

INTRODUCTION

A variety of light weight panels have been developed to provide expedient landing surfaces for different generations of aircraft and military conditions. Chambers (ref. 1) reviewed different types of landing mat and the design requirements as related to such factors as mat weight, minimum subgrade strengths, wheel loads, tire pressure, number of landings and placement rates. Chambers' state of the art review noted that little quantitative information was available relative to the dynamic mat response to moving loads applied by the aircraft wheels.

In 1970, attention focused on the dynamic response of landing mat when a section of AM2 mat failed during the fourth landing of the C-5A aircraft at Dyess AFB (refs. 2 to 4). A bow wave formed in the runway in front of the decelerating aircraft which was eventually overrun. Panels were disconnected, hurled into the air and considerable damage was done. As a consequence, a model study was initiated to analyze the dynamic response of AM2 mat subjected to C-5A landings. In reference 5, Kiefer reported the results of the initial 1/7 scale physical model. The model simulated the buckling failure which occurred at Dyess AFB and verified the modeling concept. Model tests on possible mat modification showed there was no significant improvement in the stability of AM2 mat with increased friction at the mat-subgrade interface. Cleats attached to the bottom of mat panels were not effective. Longitudinal pretensioned bands along the top of the runway were effective and no buckling occurred despite increased deceleration rates. However, longitudinal stiffeners connecting three or four panels together did not eliminate buckling. The laying pattern and geometry of the mat seemed to influence the mat behavior and suggested additional testing.

Blotter (ref. 6) developed an analytical model to parallel the 1/7 scale physical model in the simulation of prototype mat behavior. The analytical model consisted of discrete rigid elements interconnected and suspended by springs and dashpots and provided a rapid and inexpensive prediction of dynamic mat performance as related to horizontal thrust, soil stiffness, mat geometry, panel connections, damping, aircraft velocities and other parameters.

The initial physical model study considered only the 0.61 x 3.66 m (2 x 12 ft) AM2 mat. The content of this paper is related to subsequent model studies where both 1.22 x 1.37 m (4 x 4.5 ft) and 0.60 x 2.74 m (2 x 9 ft) Dow truss web mat were studied.

---

*Work supported under contract number F29601-73-C-0131 for USAF/AFWL, Kirtland AFB, N.M.

MODEL DEVELOPMENT

Similitude conditions relating the model C-5A landing gear and the expedient landing strip to the prototype system were developed by Kiefer (ref. 5). The fundamental independent variables considered in the physical model are given in table 1. Mat performance ψ was the dependent variable and was a function of seven dimensionless parameters given in equation (1).

$$\psi = \text{function}\left(\frac{W}{\rho g \lambda^3}\right), \left(\frac{a}{g}\right), \left(\frac{E}{\rho g \lambda}\right), \left(\frac{v^2}{g\lambda}\right), \left(\frac{p}{\rho g \lambda}\right), f, N \qquad (1)$$

The prototype to model density ratio ρ_r and the gravitational acceleration ratio g_r were set equal to unity. The linear scale ratio of prototype to model was arbitrarily set equal to n. Other prototype to model relations follow as given in table 2. For this model study the value of n was chosen as 7.

The model aircraft tare weight was 5.9 kN (1330 lb) to simulate the 2.02 MN (455,000 lb) prototype. Each of the four bogies consisted of six wheels with 0.1 m (4 in) and 0.2 m (8 in) outside diameter rubber tires with the tread ground down and inflated to approximately 83 kPa (12 psi). A hydraulically operated caliper type disk brake was attached to each wheel pair as shown in figure 1. The braking and steering of the model aircraft were done by a pilot on board. The model aircraft is shown in figure 2. The model aircraft was suspended by steel rollers and accelerated along a track. Touchdown was made as the rubber wheels first contacted the landing mat while the model descended along the final portion of the track cantilevered over the runway at a 3 degree slope and the steel rollers were lifted off the acceleration track. Touchdown was made at the same longitudinal location each landing; however, the transverse position varied according to a random distribution pattern over a 0.56 m distance either side of the centerline. Model touchdown velocities were at least 12.2 m/sec and deceleration rates ranged from 2.4 m/sec^2 to 9.9 m/sec^2.

The model runway was 37 m long and 4.3 m wide. Additional effective lengths were modeled by adding end weights to the runway. The subgrade was prepared by excavating and backfilling with 0.3 m (1 ft) of blow sand. The sand had a modulus of subgrade reaction of 108.6 MPa/m to 135.7 MPa/m (400 to 500 psi/in) after drying and was covered with a sheet of polyvinylchloride upon which the landing mat was placed. The runway had a 2 1/2% slope down from the centerline to the edges and the complete runway was covered with a building.

Models of the 1.22 x 1.37 m and 0.60 x 2.74 m Dow truss web mat were constructed of a styrofoam core sandwiched between two sheets of fiberglass with aluminum edge pieces bonded to the fiberglass. The mat edges were made of

extruded aluminum shaped to resemble the prototype male, female and edge connectors reduced to 1/7 scale. The kinetics of the mat were given design priority and the model mats closely simulated the size, shape and joint movement of the prototype. However, the flexural stiffness of the model was about 1.8 times the correct value and the tensile strength exceeded the proper value. The model mats weighed approximately 1.6 N and varied plus or minus 5% from the scaled-down prototype weight.

Static measurements of longitudinal and lateral mat displacements were made. Dynamic measurements of longitudinal, vertical and rotational mat displacements and velocities were also completed. The model aircraft velocities were measured with a radar speedgun. A high speed camera mounted on the model aircraft monitored the mat kinematics in front of the wheels. Measurement details are given in reference 5.

TEST RESULTS

The runway patterns tested are identified in figure 3. In the standard brick pattern, the unrestrained (no runway end weights) 0.6 x 2.74 m mat runway buckled after 12 landings and the buckling force was estimated at 1100 N (85,000 lb prototype). In the same pattern, the 1.22 x 1.37 m model mat showed no signs of buckling after 60 landings. A buckling failure was eventually produced by adding weights to the end of the runway. A typical buckling failure is shown in figure 4. Approximately 2300 N (180,000 lb prototype) force was required for buckling. The 1.22 x 1.37 m mat was more stable than the 0.60 x 2.74 m mat in the standard brick pattern.

Only the 1.22 x 1.37 m mat was tested in the alternate brick pattern and 90^{o} rotated brick pattern. Total landings on these two patterns with continuous longitudinal joints were respectively 100 and 300 without buckling failure. Elimination of the transverse hinged joint made a much more stable runway and reduced longitudinal movement.

Simulated edge tie downs were tested on the 0.60 x 2.74 m mat in the standard brick patterns. A staple attaching the edge mats to a buried wood anchor provided a tie down of approximately 31 N (2400 lb prototype). This tie down was ineffective in the prevention of buckling. A spike driven through the edge mats into the wooden anchor reduced the edge movement; however accumulated displacement at the centerline resulted in a five panel wave after 28 landings. A positive edge fix results in severe in-plane distortion and high connector stresses.

In other tests the touchdown end of the runway was anchored to restrict the horizontal displacement of the forward edge. In the standard brick pattern with the far end of the mat anchored to simulate an additional 39 m of model

mat, the runway survived 100 test landings on both the 0.60 x 2.74 m and 1.22 x 1.37 m mat without buckling. Even with increased decelerations, the mat was stable. The leading anchor tended to restore the mat and the joints remained sufficiently open to eliminate any compression build-up and eventual buckling of the mat.

The 26^{o} diagonal pattern with the model 1.22 x 1.37 m mat was only slightly more stable than the standard brick pattern. The results of the tests are summarized in table 3. Landing tests with lighter model weights and/or lower decelerations which did not produce buckling are not included in table 3; however such tests were completed and are documented in reference 5.

CONCLUSIONS

1. The 1.22 x 1.37 m mat runway in the standard brick pattern with transverse hinged joints is more stable and less susceptible to a buckling failure than the 0.60 x 2.74 m mat runway.

2. Use of tension anchors appears to be a feasible means of controlling longitudinal displacement of the runway and potential runway buckling. Anchors appear to be a practical means to reduce maintenance on mat runways.

3. The 1.22 x 1.37 m mat in the alternate brick pattern or the 90^{o} rotated standard brick pattern forms a dynamically more stable runway with a high resistance to buckling failure. The runway in these patterns is much stiffer and longitudinal movement was less than for the standard brick pattern. In these two patterns there is a continuous longitudinal joint which may lead to rutting problems on soft subgrades. Sliding along the continuous longitudinal joints was not a problem.

4. The model 1.22 x 1.37 m alternate brick pattern runway was difficult to assemble and extremely difficult to take apart. A prototype runway in this pattern would require development of special adapters or techniques to replace damaged interior panels.

5. The diagonal angle for the transverse joint of the standard brick pattern must be greater than 26^{o} to have any significant influence on the mat stability and buckling potential.

6. Edge tie down anchors are not effective in preventing mat buckling.

7. Anchoring the runway edge by pins prevented longitudinal movement along the runway edge but displacment at the runway center line was large enough to develop a buckling failure. With the braking force applied near the runway center line and the fixed points at the edge, a large in-plane mat bow develops putting severe stresses on the mat end joints.

REFERENCES

1. Chambers, Richard E., Development of Concepts for a Structural Module for Air Force Construction., AFWL-TR-71-11, Air Force Weapons Laboratory, Kirtland AFB, N.M., July 1971.

2. Barker, Walter R., Memorandum for Record; AM2 Landing Mat Performance under C-5A Traffic at Dyess AFB, Texas, Waterways Experiment Station, Vicksburg, Mississippi, 3 November 1970.

3. Currin, David D., C-5A Ground-Flotation Test on a Landing Mat Runway, Technical Report No. AFWL-TR-71-45, Air Force Weapons Laboratory, Kirtland, AFB, Kirtland, N.M., July 1971.

4. Green, H. L., Observation of C-5A Operation on Landing Mat Test Facility, Dyess Air Force Base, Texas, Miscellaneous Paper S-72-10, U.S. Army Engineer Waterways Experiment Station, Vicksburg, Mississippi, March 1972.

5. Kiefer, F. W., P. T. Blotter, and V. T. Christiansen, Model Study of C-5A Landings on AM-2 Landing Mat, AFWL-TR-72-210, Air Force Weapons Laboratory, Kirtland AFB, N.M., August 1973.

6. Blotter, P. T., Kiefer, F. W., and Daltarian, K., "A Kinetic Model of Landing Mat Performance," Journal of Aircraft, AIAA, November 1975.

TABLE 1

FUNDAMENTAL VARIABLES CONSIDERED IN THE PHYSICAL MODEL

Symbol	Definition	Basic Dimensions - FLT
ψ	Performance (bow wave, failure, etc.)	-
W	Weight of aircraft	F
λ	All other distances or lengths	L
ρ	Density of materials	FT^2L^{-4}
E	Stiffness modulus of all materials	FL^{-2}
g	Acceleration of gravity	LT^{-2}
a	Other acceleration	LT^{-2}
v	All velocities	LT^{-1}
f	All coefficients of friction	FL^{-2}
N	Number of landings or coverages	-
P	Pressure-tire and soil	FL^{-2}

TABLE 2

SIMILITUDE CONDITIONS FOR THE PHYSICAL MODEL

Variable and Scale Factor		Comments
$W_r = n^3$	$\left(\frac{W}{\rho g \lambda^3}\right) = \left(\frac{W}{\rho g \lambda^3}\right)_m$	Model weight $1/n^3$ that of the prototype
$a_r = 1$	$\left(\frac{a}{g}\right) = \left(\frac{a}{g}\right)_m$	accelerations the same in model and prototype
$f_r = 1$	$(f) = (f)_m$	same coefficient of friction in model and prototype
$N_r = 1$	$(N) = (N)_m$	same number of coverages in model and prototype
$V_r = \sqrt{n}$	$\left(\frac{V^2}{g\lambda}\right) = \left(\frac{V^2}{g\lambda}\right)_m$	model velocities $1/\sqrt{n}$ that of prototype
$E_r = n$	$\left(\frac{\rho g \lambda}{E}\right) = \left(\frac{\rho g \lambda}{E}\right)_m$	stiffness modulus of materials in model 1/n that of prototype
$P_r = n$	$\left(\frac{p}{\rho g \lambda}\right) = \left(\frac{p}{\rho g \lambda}\right)_m$	pressure and stress in model 1/n that of prototype
$t_r = \sqrt{n}$		time in model $1/\sqrt{n}$ that of prototype
$k_r = 1$	FL^{-3}	modulus of soil reaction the same in model and prototype (plate bearing test)
$I_r = n^5$	FLT^2	mass moment of inertia of model landing mat about longitudinal axis $1/n^5$ that of prototype mat

TABLE 3

SUMMARY OF LANDING MAT TESTS

Prototype Mat (m)	Laying Pattern	End Weights Touch-down End (N)	End Weights Far End (N)	Model Vehicle Mass (kg)	Nominal Deceleration Rate (m/s^2)	Number of Landings	Comments
1.22 x 1.37	Standard Brick	445	512	757	2.7	21	No buckling
1.22 x 1.37	Standard Brick	445	512	757	3.6	20	No buckling
1.22 x 1.37	Standard Brick	445	2865-4300	757	3.6	9	Buckled on 7th landing
1.22 x 1.37	Alternate Brick Pattern	445	512	757	2.7	20	No buckling
1.22 x 1.37	Alternate Brick Pattern	445	512	757	3.6	20	No buckling
1.22 x 1.37	Alternate Brick Pattern	445	7500	757	2.7-3.6	240	No buckling
0.6 x 2.74	Standard Brick	445	512	603	2.7	15	Buckled 12th landing
0.6 x 2.74	Standard Brick with Stapled Down Edges	445	512	603	2.7	10	Buckled on 7th landing
0.6 x 2.74	Standard Brick Pattern Nailed Down Edges	445	512	603	2.7	22	Buckled 21st landing
0.6 x 2.74	Standard Brick Pattern Nailed Down Edges	445	512	757	3.6	6	Buckled on 2nd landing
0.6 x 2.74	Standard Brick Pattern	Tension Anchors	7428	757	3.6	81	No buckling
1.22 x 1.37	90^{o} Rotated Standard Brick	445	7428	757	3.0-4.9	80	No buckling
1.22 x 1.37	Standard Brick Pattern	Tension Anchors	7428	757	3.6	100	No buckling
1.22 x 1.37	26.5^{o} Rotated Standard Brick Pattern	445	512	757	3.6	31	Buckled on landings 25-31

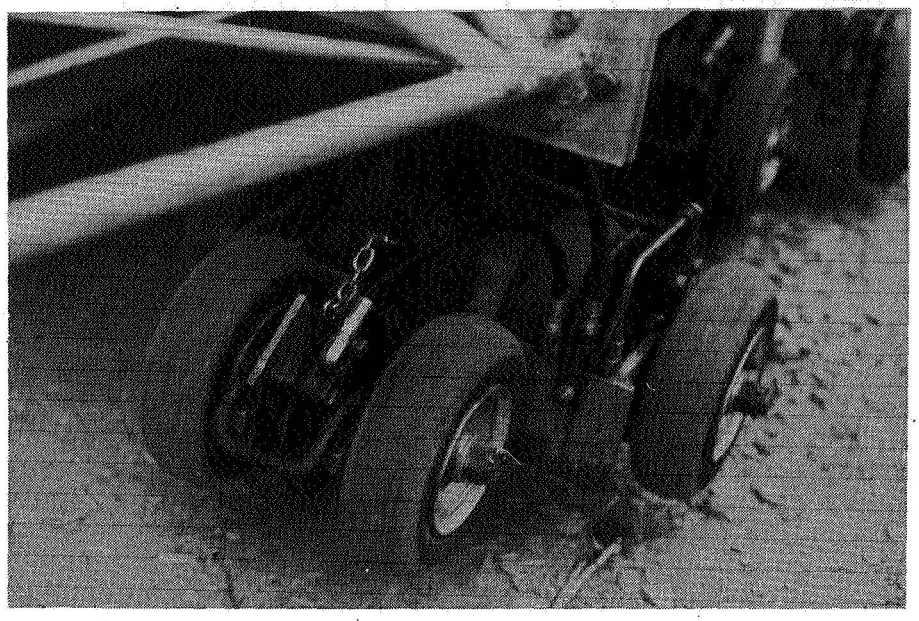

Figure 1.- Model landing gear wheel assembly.

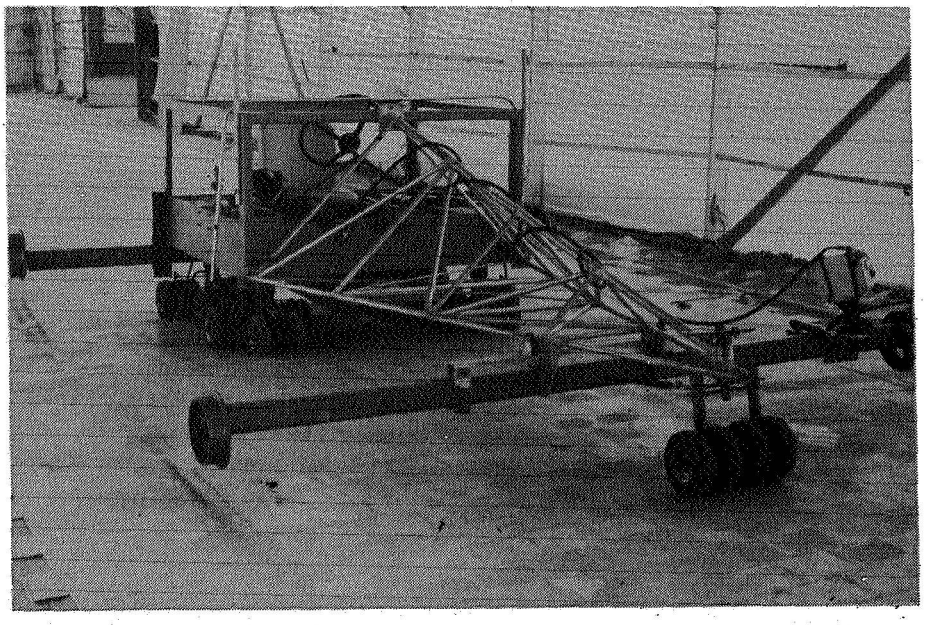

Figure 2.- Model aircraft.

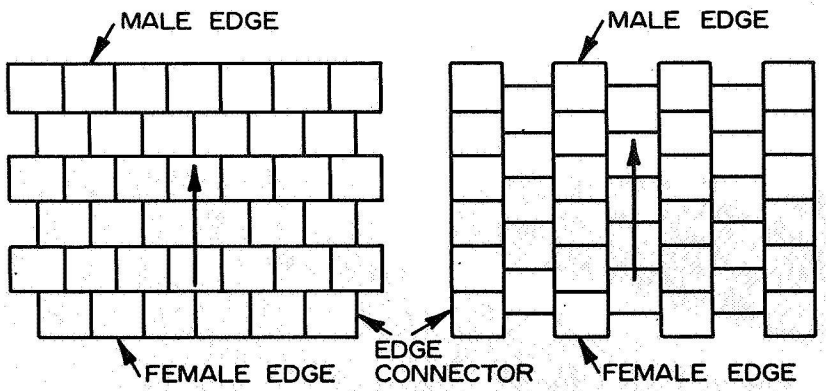

(a) Standard brick pattern. (b) Alternate brick pattern.

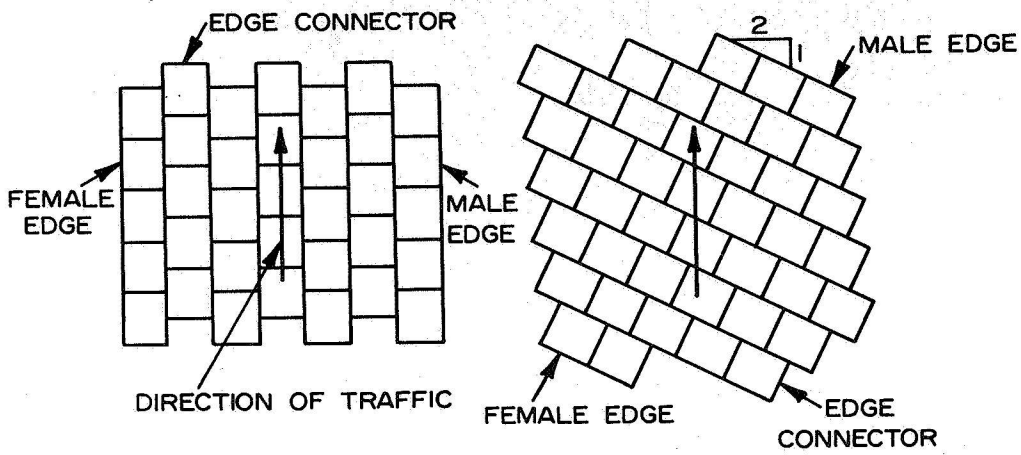

(c) 90° rotated standard brick pattern. (d) Diagonal pattern.

Figure 3.- Mat laying patterns.

Figure 4.- A typical buckling failure.

ROCK FAILURE ANALYSIS BY COMBINED THERMAL WEAKENING AND WATER JET IMPACT†

Adnan H. Nayfeh
Aerospace Engineering Department
University of Cincinnati

SUMMARY

The influence of preheating on the initiation of fracture in rocks subjected to the impingement of a continuous water jet is studied. Preheating the rock is assumed to degrade its mechanical properties and strength in accordance with existing experimental data. The water jet is assumed to place a quasi-static loading on the surface of the rock. The loading is approximated by elementary functions which permit analytic computation of the induced stresses in a rock half-space. The resulting stresses are subsequently coupled with the Griffith criteria for tensile failure to estimate the change, due to heating, in the critical stagnation pressure and velocity of the water jet required to cause failure in the rock. When the results are specialized to the representative Charcoal Granite rock it is shown that the critical jet pressure and velocity are reduced substantially even for moderate amounts of preheating.

INTRODUCTION

As nations become increasingly urbanized, use of underground space for transportation and utility systems becomes more attractive for both economic and environmental reasons. The more recent quickening of needs for drilling and fracturing of geologic formations for recovery of energy and mineral resources has clearly increased the interest and potential payoff of improved excavation technology. Thus, it became necessary for researchers to investigate a variety of novel techniques that appear to be promising alternatives to the drill-and-blast methods that are often employed for rock disintegration. One of these techniques, rock cutting and fragmentation by high velocity water jets, has received considerable attention both experimentally (refs. 1 to 10) and analytically (refs. 1, 10, and 11). Although it is recognized

† This research was supported in parts by the National Science Foundations Grants GI-39224 and ENG 7520850.

that the processes by which a water jet fractures the rock are highly complicated and so far poorly understood, the general conclusion is that water jets hold near-future strong potential for fragmenting hard rocks.

It now appears that such techniques may be made more efficient by coupling water jet impacts and thermal weakening. In fact, the recent experiments of Thirmulai and McNary (ref. 12) and Thirmulai (ref. 13) have shown that preheating the rock reduces its specific fragmentation energy by about one order of magnitude. This enhanced fragmentation is believed to be caused by the creation, upon heating, of intergranular microcracks which both weaken the rock and provide additional channels for the water jet to penetrate below the rock surface, increasing the pore pressure and promoting erosion.

The exact process of the thermal microcracking of rocks is unfortunately not known. However, existing experimental evidence suggests that many rocks lose strength when heated. Ide (ref. 14) has reported decreases in elastic wave speeds when rocks were heated to successively higher temperatures. Ide's results have been confirmed by the recent measurements of Wingquist (ref. 15) Barbish and Gardner (ref. 16), and more recently by those of Sprunt and Brace (unpublished) on a variety of rocks.

The importance of the interactions between thermal microcracking and hydraulic jet erosion has been recognized by Fletcher (ref. 17) who also obtained a patent based on this novel method of rock fragmentation. In this context we also indicate that the establishment of thermally induced stresses in rock as an adjunct to mechanical fragmentation techniques has been evaluated by Clark et al (ref. 18) and Lauriello and Chen (ref. 19).

It thus seems possible that hard rocks, such as granite and basalt, might become susceptible to cutting by relatively low speed continuous jets if preheating is employed. A quantitative understanding of these combined processes is desirable in order to select advantageous combinations of thermohydraulic loading conditions for a given rock type.

In this paper the thermally degraded properties of rocks as measured by Wingquist (ref. 15) will be used to calculate the state of stress in the rock due to the impinging water jet. The water jet will be assumed to place a quasi-static pressure loading on the free surface of a rock half space. This loading will be approximated by elementary functions which permit analytic computation of the stresses in the half space. Existing theories of fracture mechanics, namely, the Griffith Criteria (see for example refs. 10, 11, 19, and 20) will then be employed to estimate the decrease in the critical stagnation pressure and velocity of the jet required to cause failure in the rock. Here it is appropriate to

indicate that any adopted fracture criterion should somehow reflect the influence of the fluid pore pressure. However, the complicated dependence of this pore pressure on the permeability of the thermally cracked rock will lead to complications in the present treatment which cannot be resolved now and are being referred to a further investigation.

CHARACTERIZATION OF THE JET'S PRESSURE LOADING

The experimental evidence indicates that a steady state continuous water jet applies a quasi-static pressure loading to the flat rock surface. Leach and Walker (ref. 1), for example, measured the steady-state pressure distribution imposed upon a rigid flat surface by a continuous jet impinging normally at relatively low speed. They also presented an empirical fit to the measurements which Powell and Simpson (ref. 11) later used as the loading function to calculate the axisymmetric stress field induced in a homogeneous linear elastic solid by such a nonpenetrating jet.

The surface pressure fit utilized by Powell and Simpson is

$$P(r) = \frac{1}{2}\rho v^2\left[1 - 3\left(\frac{r}{b}\right)^2 + 2\left(\frac{r}{b}\right)\right]^3 \quad \text{for} \quad r < b$$

$$= 0 \quad \text{for} \quad r \geq b \qquad (1)$$

where P is the pressure, ρ is the density of water, v is the jet velocity and b is an "effective radius" related to the radius of the jet, r_o, by $b = r_o\sqrt{20/3}$

As is generally the case in problems in elasticity of this kind, the mathematical problem is formulated in terms of the well-known Airy stress function ϕ which satisfies the compatibility condition

$$\nabla^4\phi = 0 \qquad (2)$$

where ∇ is the Laplace operator in cylindrical coordinates. By applying the boundary condition that the normal stress on the rock surface equals $-P(r)$ as given in Eq. (1), one may formally obtain the induced stresses in the half space. As pointed out by Powell and Simpson, however, the exact analytic solution of the biharmonic equation subjected to the particular form of the surface pressure given in Eq. (1) is impossible by conventional methods such as integral transforms. Accordingly, they extended the results obtained by Timoshenko and Goodier (ref. 21) for the stress response to a normally applied point load and were able to obtain numerical stress distributions in the rock in terms of infinite series expansions. Then the computer stress distribution was used,

together with a fracture criterion derived from the Griffith theory of crack propagation in solids, to predict the rock cutting properties of water jets in relation to the mechanical strength of the target rock. More recently, Forman and Secor (ref. 10) allowed the water jet to penetrate the rock, utilized the surface distribution (Eq. (1)) and investigated the combined effects of the pore pressure and surface loadings using finite element methods.

In the present analysis we propose the following alternative approximation to the surface pressure (Eq. (1)):

$$P(r) = a\, r_o^2\, f(r,r_o) + b\, r_o^3 \frac{d}{dr_o} f(r,r_o) + c\, r_o^4 \frac{d^2}{dr_o^2} f(r,r_o) \qquad (3)$$

where

$$f(r,r_o) = P_s \frac{r_o}{(r_o^2 + r^2)^{3/2}} \quad , \qquad (4)$$

P_s is the stagnation pressure $\rho\, v^2/2$ and a, b, c constants are given as

$$a = 1.02134 \ , \quad b = 0.2169 \ , \quad c = -0.01459 \ .$$

The pressure distribution (Eq. (3)) has the advantage of being made up of an elementary combination of the elementary function $f(r,r_o)$ and its derivatives. It also has the advantage of leading to simple classical analytic solutions for the distribution of stresses in the half space. In Figure 1, this proposed pressure distribution is compared with Leach and Walker's data and empirical fit.

STRESS DISTRIBUTION IN THE HALF SPACE

In this section we calculate the stresses induced in a preheated rock half space subjected to the mechanical surface loading (Eq. (3)). It is assumed that heating will not change the basic mechanical behavior of the rock from being linear elastic. In the analysis, the properties of the rock will be assumed to depend upon the temperature in an arbitrary manner. However, the final results will be specialized to Charcoal Granite whose properties are known to depend upon the temperature in the manner depicted in Table 1. In this table, the variations of the mechanical properties E and ν are obtained from the experimental data of Wingquist (ref. 15) whereas the variation in the strength S is deduced from the experimental data of Barbish and Gardner (ref. 16) which relate the variation of the tensile strength of Charcoal Granite to its Young's Modulus. The room temperature value of the strength $S_o = 0.15$ kbar is the experimental value obtained by Savanick and Johnson (ref. 22). [1 kbar = 100 MPa].

TABLE 1

VARIATION OF CHARCOAL GRANITE PROPERTIES WITH TEMPERATURE

T(°C)	Young's Modulus, E,kbar	Poisson's Ratio, ν	Tensile Strength, S,kbar
27	865	0.246	0.15
100	760	0.184	0.127
200	572	0.075	0.105
300	420	-0.014	0.0927
400	314	-0.076	0.08
500	158	-0.167	0.052
600	84	-0.211	0.031
700	95	-0.204	0.035
800	126	-0.186	0.044
900	106	-0.198	0.038

From these data a polynomial fit to the variation of $S(T)$ with $E(T)$ is constructed as

$$S(T) = 55.49\ E(T) - 11.437\ E^2(T) + 0.09697\ E^3(T) \qquad (5)$$

where $E(T)$ is given in Table 1. For a detailed discussion of this fit we refer the reader to (ref. 23).

Now, since we are dealing with a linear problem, if the response $F_i(r,z)$, $i = r, \theta, z, r_z$, produced by the loading $f(r,r_o)$ is found, the complete stress distribution $\sigma_i(r,z)$ can be constructed in accordance with Eq. (3) as

$$\sigma_i(r,z) = r_o^2\, P_s\left[a\, F_i(r,z) + b\, r_o \frac{dF_i}{dr_o}(r,z) + c\, r_o^2 \frac{d^2F_i}{dr_o^2}(r,z)\right] \qquad (6)$$

The response $F_i(r,z)$ to the load $f(r,r_o)$ is however known and is given in (ref. 24) as

$$F_z = -[r_o r^2 + (r_o+z)^2(3z+r_o)]R^{-5}; \quad F_{rz} = -3rz(r_o+z)R^{-5} \qquad (7,8)$$

$$F_r = -\{3r^2z + r_o[r^2 + (r_o+z)^2]\}R^{-5} - (1-2\nu)(R-r_o-z)R^{-1}\, r^{-2} \qquad (9)$$

$$F_\theta = -\, r_o R^{-3} + (1-2\nu)\,\{(r_o+z)[2r^2 + (z+r_o)^2] - 1\}R^{-3}\, r^{-2} \qquad (10)$$

where $R = [r^2 + (z + r_o)^2]^{1/2}$

Substitution from Eqs. (7 to 10) into Eq. (6) gives the complete stress distribution in the rock half space. Notice that σ_z and σ_{rz} will not depend upon the properties of the medium and that σ_r and σ_θ will depend upon the Poisson's ratio ν. In the present context these stresses depend upon the temperature in an implicit manner through their dependence on ν.

GRIFFITH FRACTURE CRITERIA

Having determined the stress distributions and their implicit dependence upon the temperature in the rock half space, we now proceed to use the Griffith criteria for tensile failure of rocks to estimate the critical pressure needed to initiate fractures. For this criteria to be applicable, the material under consideration must contain incipient microcracks having uniform and random distribution and orientation. In the present application, the presence of such cracks are assured, at least, due to heating.

The features of the stress distribution required for the application of the Griffith theory are most concisely defined in terms of the maximum and minimum principal stresses σ_{max} and σ_{min}, respectively. The principal stresses σ_1, σ_2 and σ_3 are defined in terms of the triaxial stress σ_r, σ_θ, σ_z, and σ_{rz} as:

$$\sigma_{1,2} = \frac{\sigma_r + \sigma_z}{2} \pm \left[\left(\frac{\sigma_r - \sigma_z}{2}\right)^2 + \sigma_{rz}^2\right]^{1/2} \quad ; \quad \sigma_3 = \sigma_\theta \tag{11}$$

For the present application, the Griffith condition required to propagate the cracks may be stated as

$$\frac{[\sigma_{max}(T) - \sigma_{min}(T)]^2}{[\sigma_{max}(T) + \sigma_{min}(T)]} = -8\,S(T) \tag{12}$$

for $\sigma_{max}(T) - \sigma_{min}(T) > 0$ and $3\sigma_{max}(T) + \sigma_{min}(T) < 0$

In the (r-z) plane, Eq. (12) determines the contours along which fracture will just occur for jet pressures which are multiples of S(T). These contours will have the form of surfaces of revolution about the z-axis and will in particular intersect it.

Since we are mainly interested in calculating the values of the critical pressures needed to start failure, and, since the fracture contours intersect the line $r = 0$, great simplifications in the analysis leading to the calculation of such critical values can be affected by specializing our subsequent analysis to the limit $r \to 0$. This will undoubtably restrict our information regarding the fracture regions off the $r = 0$ axis but in no way

will influence the values of the critical pressures. Moreover, since r and r_o are treated to be independent of each other, one can easily show that the final results are the same whether the limit $r \to 0$ is reached before or after differentiation with respect to r_o as required in Eq. (6).

Thus, in the limit as $r \to 0$, equations (7 to 10) reduce to

$$F_z = -\frac{3z + r_o}{(r_o+z)^3} \quad , \quad F_r = F_\theta = \frac{1 - 2\nu}{2(r_o+z)^2} - \frac{r_o}{(r_o+z)^3} \quad , \quad F_{rz} = 0 \tag{13}$$

Equations (13) when substituted in Eq. (6) and Eq. (11) yield

$$\frac{\sigma_{max}}{P_s} = \frac{\sigma_1}{P_s} = a\,\frac{(1-2\nu)\gamma-(1+2\nu)}{2(1+\gamma)^3} + b\,\frac{(1+2\nu)-2(1-\nu)\gamma}{(1+\gamma)^6} - 3c\,\frac{(3-2\nu)\gamma+(1+2\nu)}{(1+\gamma)^5} \tag{14}$$

$$\frac{\sigma_{min}}{P_s} = \frac{\sigma_2}{P_s} = -a\,\frac{3\gamma+1}{(\gamma+1)^3} + 2b\,\frac{4\gamma+1}{(\gamma+1)^4} - 6c\,\frac{5\gamma+1}{(\gamma+1)^5} \tag{15}$$

Which, if further used in Eq. (12) finally yield

$$S(T) = \frac{P_s}{16\eta^5}\left[\frac{(-a\eta^2\{(2\eta-7)\eta+6\}+2b\eta\{(2\nu-10)\eta+9\}-6c\{(2\nu-13)\eta+12\})^2}{-a\eta^2\{(2\nu+5)\eta-2\}+2b\eta\{(2\nu+6)\eta-3\}-6c\{(2\nu+7)\eta-4\}}\right] \tag{16}$$

where $\gamma = z/r_o$ and $\eta = \gamma + 1$ (17)

Before proceeding to calculate the critical pressures as functions of the temperature increase, we shall compare our room temperature results with those predicted by Forman and Secor (ref. 10) and Powell and Simpson (ref. 11). Using the room temperature values $\nu = 0.25$ and $S_o = 0.15$ kbar for Charcoal Granite (see Table 1), Eq. (16) dictates that failure will first occur when P_s reaches $P_s^* = 19.63\ S_o \equiv 2.94$ kbar at a distance of about $\eta = 2.25$ (equivalent to 0.625 nozzle diameter beneath the surface). Compared with these results, Forman and Secor predicted the value $P_s^* = 18.8\ S_o$ that occurs at a distance of about 0.75 nozzle diameter below the rock surface. Powell and Simpson (ref. 11) on the other hand did their calculations for $\nu = 0.3$ and predicted the value $P_s^* = 20\ S_o$, which may be compared to the present prediction $P_s^* = 21\ S_o$ also calculated for $\nu = 0.3$.

The threshold pressure (P_s^*) associated with the remaining temperature-dependent Poisson's ratios and strengths listed in Table 1 are normalized with respect to the room temperature value of 19.63 S_o and are plotted as functions of temperature in Figure 2. As can be seen from Figure 2, P_s^* decreases with increasing temperature up to about 600°C. For higher temperatures, the threshold pressure increases then decreases again. This behavior is due to a phase change in the quartz at about 573°C. Using $P_s^* = \rho_o (u_o^*)^2/2$, with ρ = 1 g/cm^3 and using S_o = 0.15 kbar, Figure 2 is replotted in Figure 3 for the variation of the threshold jet speed u_o^* with temperature.

CONCLUSIONS

In conclusion, we have demonstrated that preheating the rock weakens it and makes it more susceptible to breakage by continuous water jets or other mechanical methods. Specifically, the applied water jet pressure required to initiate fracture at a specified location is reduced by an order of magnitude (relative to room temperature) if the rock surface is first heated to about 300°C.

REFERENCES

1. Leach, S.J. and Walker, G.L., "Some Aspects of Rock Cutting by High Speed Water Jets," Phil. Trans. Royal Soc., A260, 1966, pp. 295-308.
2. Farmer, I.W. and Attewell , P.B., "Rock Penetration by High Velocity Water Jet," Intern. J. Rock Mech. and Mining Sci., Vol. 2, No. 2, 1965, pp. 135-153.
3. Brunton, J.H., "High Speed Liquid Impact," Phil. Trans. Royal Soc., A260, 1966, pp. 79-85.
4. Field, J.E., "Stress Waves, Deformation and Fracture Caused by Liquid Impact," Phil. Trans. Royal Soc., A260, 1966, pp. 86-93.
5. Brook, N. and Summers, D.A., "Penetration of Rock by High-Speed Water Jets," Intern. J. Rock Mech. and Mining Sci., Vol. 6, No. 3, 1969, pp. 249-258.
6. Huck, P.J. and Singh, M.M., "Rock Fracture by High-Speed Water Jet," IIT Research Institute, Report FRA-RT-71-58, 1970.
7. Cooley, W.C. and Brockert, P.E., "Rock Disintegration by Pulsed Liquid Jets," Terraspore Research Report No. TR-4032, 1972.
8. Summers, D.A. and Henry, R.L., "Water Jet Cutting of Sedimentary Rock," Jour. Pet. Tech., July 1972.
9. Crow, S.C., "The Mechanics of Hydraulic Rock Cutting," Proc. 2nd International Symposium on Jet Cutting Technology, Cambridge, 1974.
10. Forman, S.E. and Secor, G.A., "The Mechanics of Rock Failure Due to Water Jet Impingement," Sixth Conference on Drilling and Rock Mechanics, Austin, Texas, January 22-23, 1973.
11. Powell, J.H. and Simpson, S.P., "Theoretical Study of the Mechanical Effects of Water Jets Impinging on a Semi-Infinite Elastic Solid," Inter. J. Rock Mech. and Mining Sci., Vol. 6, No. 4, 1969, pp. 353-364.
12. Thirmulai, D. and McNary, O., "Development and Testing of a Thermohydraulic Process for Hard Rock Cutting," Proc. for AIME Annual Meeting, Chicago, Preprint No. 73-AM-45, 1973.
13. Thirmulai, K., "Water Jet Cutting and Excavation of Hard Rocks by Thermohydraulic Method," Proc. 2nd Int. Symposium on Jet Cutting Technology, Cambridge, 1974.
14. Ide, J.M., "Velocity of Sound in Rocks and Glasses as a Function of Temperature," J. of Geol. 45, 1937, p. 689.
15. Wingquist, C.F., "Elastic Modulii of Rock at Elevated Temperatures," U.S. Bureau of Mines, Twin Cities Mining Research Center Report No. 7269, 1969.

16. Barbish, A.B. and Gardner, G.H.F., "The Effects of Heat on Some Mechanical Properties of Igneous Rocks," Proc. 4th Conf. on Drilling and rock Mech., Austin, Texas, 1969, p. 138.

17. Fletcher, R.A., "Method of Fluid Jet Cutting for Materials Including Rock and Compositions Containing Rock Aggregates," U.S. Patent No. 3,704,914, 1972.

18. Clark, G.B., et al., "An Investigation of Thermal-Mechanical Fragmentation of Rock," University of Missouri, Rola No. USD, 402100 28, 1972.

19. Lauriello, P.J. and Chen, Y., "Thermal Fracturing of Hard Rock," Journal of Applied Mechanics, Vol. 40, Series E, No. 4, 1973.

20. Griffith, A.A., "Theory of Rupture," Proceedings First Int. Cong. Appl. Mech., Delft, 1924, pp. 55-63.

21. Timoshenko, S. and J.N. Goodier, Theory of Elasticity, McGraw-Hill, 1951.

22. Savanick, G.A. and Johnson, D.I., "Adhesion at Crystal Line Interfaces in Rocks," U.S. Bureau of Mines, Twin Cities Mining Research Center Report 7709, 1972.

23. Pritchett, J.W., et al., "Thermohydraulic Rock Disintegration - Theoretical Analysis of Rock Cutting by Combined Thermal Weakening and High-Speed Water Jet Impact," Systems, Science and Software, LaJolla, California, Report SSS-R-75-2507, December, 1974.

24. Sneddon, I.N., Fourier Transforms, McGraw-Hill, New York, 1951.

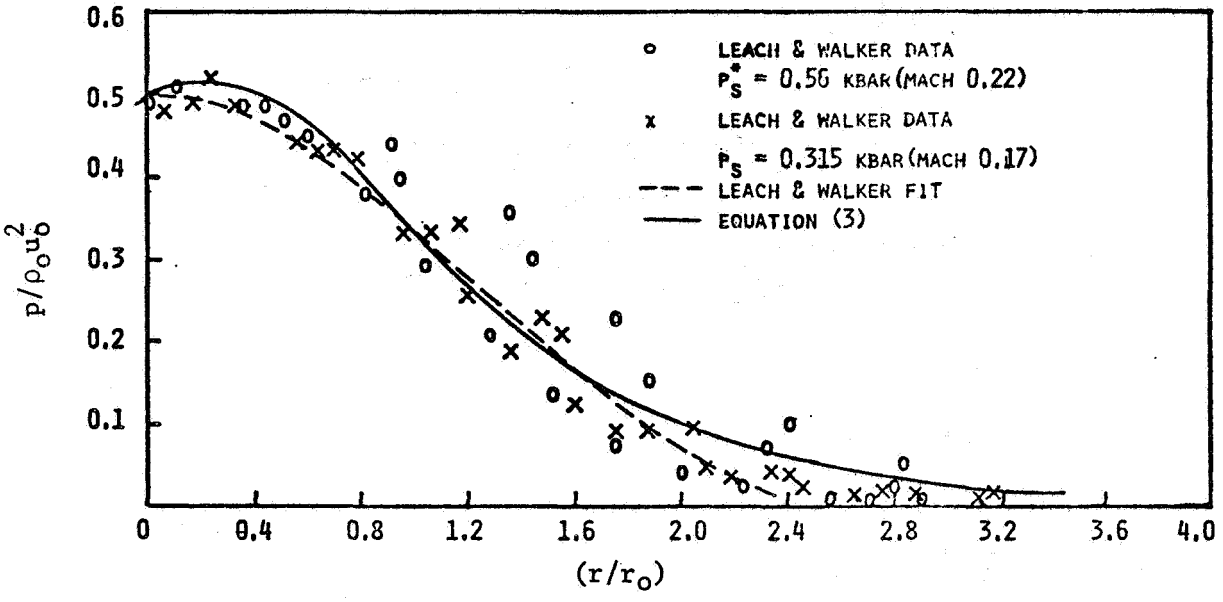

Figure 1.- Steady-state pressure distribution due to incompressible axisymmetric jet impacting rigid flat plate.

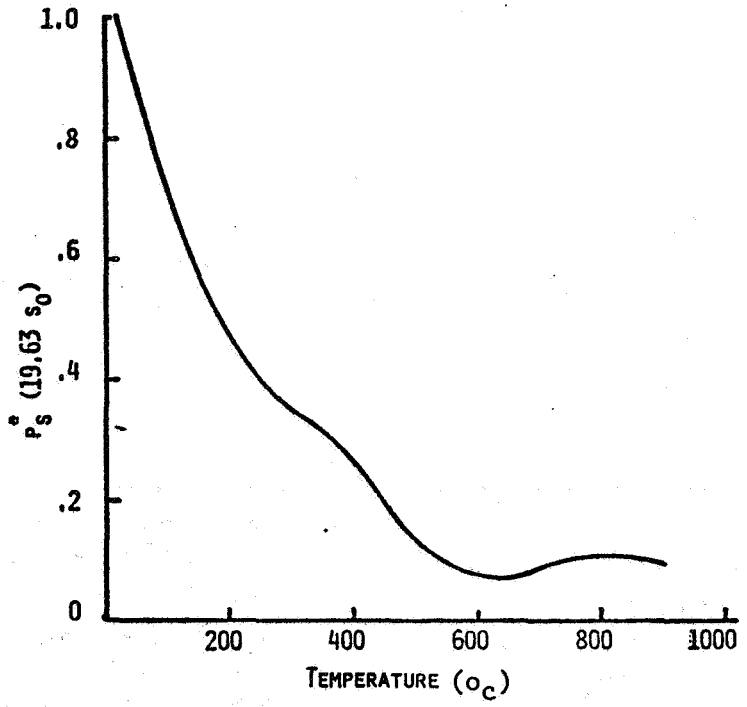

Figure 2.- Variation of threshold pressure (p_s^*) with temperature.

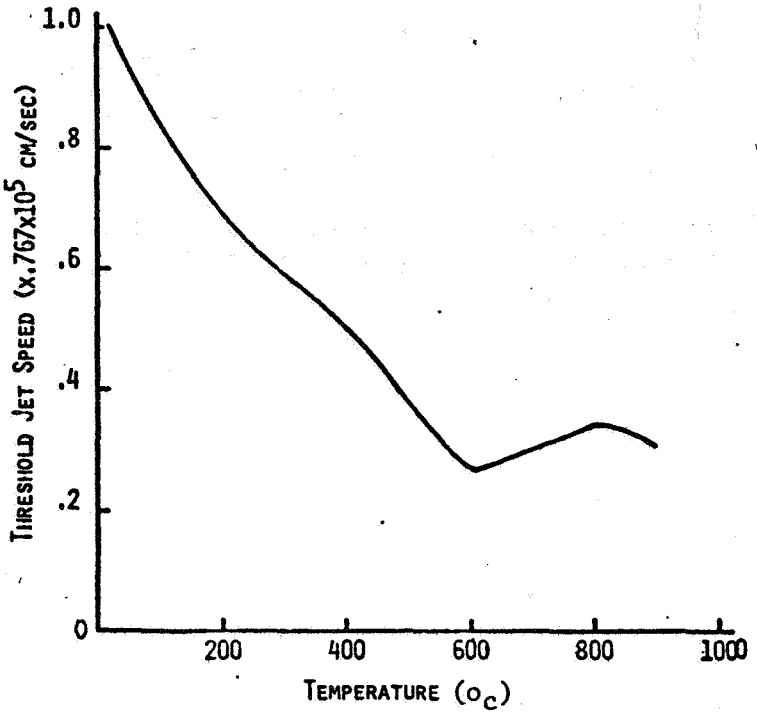

Figure 3.- Variation of threshold jet speed (u_o^*) with temperature.

NASA-Langley, 1976

NATIONAL AERONAUTICS AND SPACE ADMINISTRATION
WASHINGTON, D.C. 20546

OFFICIAL BUSINESS
PENALTY FOR PRIVATE USE $300

SPECIAL FOURTH-CLASS RATE BOOK

POSTAGE AND FEES PAID
NATIONAL AERONAUTICS AND SPACE ADMINISTRATION
451

U.S.MAIL

POSTMASTER: If Undeliverable (Section 158 Postal Manual) Do Not Return

"The aeronautical and space activities of the United States shall be conducted so as to contribute . . . to the expansion of human knowledge of phenomena in the atmosphere and space. The Administration shall provide for the widest practicable and appropriate dissemination of information concerning its activities and the results thereof."

—NATIONAL AERONAUTICS AND SPACE ACT OF 1958

NASA SCIENTIFIC AND TECHNICAL PUBLICATIONS

TECHNICAL REPORTS: Scientific and technical information considered important, complete, and a lasting contribution to existing knowledge.

TECHNICAL NOTES: Information less broad in scope but nevertheless of importance as a contribution to existing knowledge.

TECHNICAL MEMORANDUMS: Information receiving limited distribution because of preliminary data, security classification, or other reasons. Also includes conference proceedings with either limited or unlimited distribution.

CONTRACTOR REPORTS: Scientific and technical information generated under a NASA contract or grant and considered an important contribution to existing knowledge.

TECHNICAL TRANSLATIONS: Information published in a foreign language considered to merit NASA distribution in English.

SPECIAL PUBLICATIONS: Information derived from or of value to NASA activities. Publications include final reports of major projects, monographs, data compilations, handbooks, sourcebooks, and special bibliographies.

TECHNOLOGY UTILIZATION PUBLICATIONS: Information on technology used by NASA that may be of particular interest in commercial and other non-aerospace applications. Publications include Tech Briefs, Technology Utilization Reports and Technology Surveys.

Details on the availability of these publications may be obtained from:

SCIENTIFIC AND TECHNICAL INFORMATION OFFICE

NATIONAL AERONAUTICS AND SPACE ADMINISTRATION

Washington, D.C. 20546